Université de Montréal

La recherche de naines brunes et étoiles de faible masse dans les associations cinématiques jeunes du voisinage solaire

par

Jonathan Gagné

Département de physique

Faculté des arts et des sciences

Thèse présentée à la Faculté des études supérieures

en vue de l'obtention du grade de

Philosophiae Doctor (Ph.D.)

en physique

Avril, 2015

Université de Montréal

Faculté des études supérieures

Cette thèse intitulée :

La recherche de naines brunes et étoiles de faible masse dans les associations cinématiques jeunes du voisinage solaire

présentée par :

Jonathan Gagné

a été évaluée par un jury composé des personnes suivantes :

Pierre Bergeron,	Président-rapporteur
David Lafrenière & René Doyon,	Directeurs de recherche
Pierre Bastien,	Membre du jury
Emily L. Rice,	Examinatrice externe
Richard Martel,	Représentant du Doyen de la FES

Thèse acceptée le : 15 Juillet 2015

Sommaire

L'objectif principal de cette thèse est d'identifier les étoiles de faible masse et naines brunes membres d'associations cinématiques jeunes du voisinage solaire. Ces associations sont typiquement âgées de moins de 200 millions d'années et regroupent chacune un ensemble d'étoiles s'étant formées au même moment et dans un même environnement. La majorité de leurs membres de $\gtrsim 0.3\ M_{\odot}$ sont déjà connus, cependant les membres moins massifs (et moins brillants) nous échappent encore. Leur identification permettra de lever le voile sur plusieurs questions fondamentales en astrophysique. En particulier, le fait de cibler des objets jeunes, encore chauds et lumineux par leur formation récente, permettra d'atteindre un régime de masses encore peu exploré, jusqu'à seulement quelques fois la masse de Jupiter. Elles nous permettront entre autres de contraindre la fonction de masse initiale et d'explorer la connection entre naines brunes et exoplanètes, étant donné que les moins massives des naines brunes jeunes auront des propriétés physiques très semblables aux exoplanètes géantes gazeuses.

Pour mener à bien ce projet, nous avons adapté l'outil statistique BANYAN I pour qu'il soit applicable aux objets de très faibles masses en plus de lui apporter plusieurs améliorations. Nous avons entre autres inclus l'utilisation de deux diagrammes couleur–magnitude permettant de différencier les étoiles de faible masse et naines brunes jeunes à celles plus vieilles, ajouté l'utilisation de probabilités *a priori* pour rendre les résultats plus réalistes, adapté les modèles spatiaux et cinématiques des associations jeunes en utilisant des ellipsoïdes gaussiennes tridimensionnelles dont l'alignement des axes est libre, effectué une analyse Monte Carlo pour caractériser le taux de faux-positifs et faux-négatifs, puis revu la structure du code informatique pour le rendre plus efficace.

Dans un premier temps, nous avons utilisé ce nouvel algorithme, BANYAN II, pour identi-

fier 25 nouvelles candidates membres d'associations jeunes parmi un échantillon de 158 étoiles de faible masse (de types spectraux $\geq$M5) et naines brunes jeunes déjà connues. Nous avons ensuite effectué la corrélation croisée de deux catalogues couvrant tout le ciel en lumière proche-infrarouge et contenant $\sim$500 millions d'objets célestes pour identifier environ 100 000 candidates naines brunes et étoiles de faible masse du voisinage solaire. À l'aide de l'outil BANYAN II, nous avons alors identifié quelques centaines d'objets appartenant fort probablement à une association jeune parmi cet échantillon et effectué un suivi spectroscopique en lumière proche-infrarouge pour les caractériser.

Les travaux présentés ici ont mené à l'identification de 79 candidates naines brunes jeunes ainsi que 150 candidates étoiles de faible masse jeunes, puis un suivi spectroscopique nous a permis de confirmer le jeune âge de 49 de ces naines brunes et 62 de ces étoiles de faible masse. Nous avons ainsi approximativement doublé le nombre de naines brunes jeunes connues, ce qui a ouvert la porte à une caractérisation statistique de leur population. Ces nouvelles naines brunes jeunes représentent un laboratoire idéal pour mieux comprendre l'atmosphère des exoplanètes géantes gazeuses. Nous avons identifié les premiers signes d'une remontée dans la fonction de masse initiale des naines brunes aux très faibles masses dans l'association jeune Tucana-Horologium, ce qui pourrait indiquer que l'éjection d'exoplanètes joue un rôle important dans la composition de leur population. Les résultats du suivi spectroscopique nous ont permis de construire une séquence empirique complète pour les types spectraux M5–L5 à l'âge du champ, à faible (β) et très faible (γ) gravité de surface. Nous avons effectué une comparaison de ces données aux modèles d'évolution et d'atmosphère, puis nous avons construit un ensemble de séquences empiriques de couleur–magnitude et types spectraux-magnitude pour les naines brunes jeunes. Finalement, nous avons découvert deux nouvelles exoplanètes par un suivi en imagerie directe des étoiles jeunes de faible masse identifiées dans ce projet. La future mission GAIA et le suivi spectroscopique complet des candidates présentées dans cette thèse permettront de confirmer leur appartenance aux associations jeunes et de contraindre la fonction de masse initiale dans le régime sous-stellaire.

Mots-clés : Naines brunes — Cinématique — Spectroscopie — Associations jeunes

Abstract

The main objective of this thesis is the identification of low-mass star and brown dwarf members of young moving groups in the solar neighborhood. These associations are typically younger than 200 million years and include stars formed at the same time and in the same environment. The majority of their members with masses $\gtrsim 0.3\ M_{\odot}$ have already been discovered, however the less massive, fainter members are still elusive. Their identification will allow us to address several fundamental questions in astrophysics. In particular, uncovering young objects that are still warm because of their recent formation will allow us to probe masses down to only a few times the mass of Jupiter, a mass regime which is still poorly understood. They will allow us to constrain the initial mass function and explore the connection between brown dwarfs and exoplanets, given that the least massive brown dwarfs have physical properties similar to those of gaseous giant exoplanets.

In order to carry through this project, we have adapted the BANYAN I statistical tool to make it applicable to very low-mass objects in addition to bringing several improvements to the tool. We have included the use of two near-infrared color–magnitude diagrams that allow differentiating young low-mass stars and brown dwarfs from older objects, we added the use of *prior* probabilities to make its results more realistic, we adapted spatial and kinematic models of moving groups using tridimensional gaussian ellipsoids with axes free to rotate, we performed a Monte Carlo analysis to characterize the rate of false-positive and false-negatives, and we revised the structure of its source code to make it more efficient.

As a first step, we have used this new algorithm, BANYAN II, to identify 25 new candidate members among a sample of 158 known young low-mass stars (with spectral types $\geq$ M5) and brown dwarfs. We have then performed a cross-correlation of two all-sky near-infrared catalogs

consisting of $\sim$500 million celestial objects to identify approximately 100 000 brown dwarf and low-mass star candidates in the solar neighborhood. We have identified a few hundred promising young association members in this sample with the BANYAN II tool, and have performed a near-infrared spectroscopic survey to characterize them.

The work presented here has led to the identification of 79 candidate young brown dwarfs and 150 candidate young low-mass stars, and a spectroscopic follow-up allowed us to confirm the young age of 49 brown dwarfs and 62 low-mass stars. We have thus boosted the number of known young brown dwarfs by a factor $\sim$2, opening the door to a statistical characterization of their population. These new young brown dwarfs represent an ideal laboratory to better understand the atmospheres of gaseous giant exoplanets. We have identified the first signs of a turn-up in the initial mass function of very low-mass brown dwarfs in the Tucana-Horologium association, which could indicate that exoplanet scattering plays a significant role in composing their population. Results from this spectroscopic follow-up has allowed us to construct an complete empirical sequence of spectral types M5–L5 for field dwarfs, low-gravity (β) and very low-gravity (γ) dwarfs. We have performed a comparison of these new data with evolution and atmosphere models, and constructed a set of empirical spectral type–magnitude and color–magnitude sequences for young brown dwarfs. Finally, we have discovered two new exoplanets from a direct-imaging follow-up of low-mass stars discovered as part of this project. The future GAIA mission and the complete spectroscopic follow-up of the candidates presented in this thesis will allow to confirm their membership and to constrain the initial mass function in the substellar regime.

Subject headings: Brown dwarfs — Kinematics — Spectroscopy — Young associations

Table des matières

Liste des figures

Liste des tableaux

Abréviations

βPMG :β Pictoris moving group

ρOPH : ρ Ophiucus star-forming region

JWST : James Webb Space Telescope

2MASS : Two Micron All-Sky Survey

AAS : American Astronomical Society

ABDMG :AB Doradus moving group

AIC : Absorption Induite par Collisions

AJ : Association Jeune (ou Astronomical Journal dans la liste de références)

AMNH : American Museum of Natural History

ARG : Argus / IC 2391 association

AURA : Association of Universities for Research in Astronomy

A&A : Astronomy and Astrophysics

AllWISE : Combination of WISE and NEOWISE catalogs

BANYAN : Bayesian Analysis for Nearby Young AssociatioNs

BASS : BANYAN All-Sky Survey

BD : Brown Dwarf

CADC : Canadian Astronomy Data Centre

CARN : Carina-Near moving group

CAR : Carina association

CAS : Castor stream

CDF : Cumulative Density Function

CDS : Centre de Données astronomiques de Strasbourg

CFBDSIR : Canada-France Brown Dwarf Survey InfraRed

CFBDS : Canada-France Brown Dwarf Survey

CHA : Chamaeleon I star-forming region

CIA : Collision-Induced Absorption

CIFIST : Cosmological Impact of the First Stars

CMD : Color-Magnitude Diagram

CNS : Catalogue of Nearby Stars

CNTAC : ChileaN Telescope Allocation Commitee

COL : Columba association

CONICYT : Comisión Nacional de Investigación Científica y Tecnológica

CPAPIR : Caméra PAnoramique Proche-InfraRouge.

CPA : Convergent Point proper motion Analysis

CRSNG : Conseil de recehrche en Sciences Naturelles et en génie du Canada

CSS : Catalina Sky Survey

DEC : DEClination

DENIS : Deep Near Infrared Survey of the Southern sky

DES : Distribution d'Énergie Spectrale

DSS : Digitized Sky Survey

EELT : European Extremely Large Telescope

EW : Equivalent Width

FIRE : Folded port InfraRed Echellette

FLAMINGOS 2 : Near-infrared wide field imager and multi-object spectrometer for use on Gemini-South

FLA : Fonction de Luminosité Actuelle

FLD-G : Field-gravity

FLI : Fonction de Luminosité Initiale

FMA : Fonction de Masse Actuelle

FMI : Fonction de Masse Initiale

FRQ-NT : Fond de Recherche du Québec – Nature et Technologies

GAIA : Global Astrometric Interferometer for Astrophysics

GALEX : GALaxy evolution EXplorer

GJ : Gliese–Jahreiβ catalog

GMOS : Gemini Multi-Object Spectrographs

GMT : Giant Magellan Telescope

GNIRS : Gemini Near-InfraRed Spectrograph

GN : Gemini-North

GCRV : General Catalogue of stellar Radial Velocities

GSC : Guide Star Catalog

GS : Gemini-South

HD : Henry Draper catalog

HIP : Hipparcos catalog

Her-Lyr : Hercules-Lyrae moving group

HR : Yale catalog of bright stars, based on the Harvard Revised photometry catalog

HYA : Hyades association

Hipparcos : HIgh Precision PARallax COllecting Satellite

IAU : International Astronomical Union

IDL : Interactive Data Language

IMF : Initial Mass Function

INT-G : Intermediate-gravity

IPAC : Infrared Processing and Analysis Center

IPAG : Institut de Planétologie et d'Astrophysique de Grenoble.

IRAF : Image Reduction and Analysis Facility

iREX : Institut de Recherche sur les EXoplanètes.

IRSA : InfraRed Science Archive

IRTF : InfraRed Telescope Facility

JPL : Jet Propulsion Laboratory

LCC : Lower Centurus Crux association

LEL : Limite d'Épuisement du Lithium

LMS : Low-Mass Star

LP-BASS : Low-Priority BASS

LSPM : Lépine–Shara Proper Motion catalog

LSST : Large Synoptic Survey Telescope

MagE : Magellan Echellette

MASE : MagE Spectral Extractor

MK : (Classification de) Morgan et Keenan

MSR : Mass Segregation Ratio

MST : Minimum Spanning Tree

NACO : Nasmyth adaptive optics system near-infrared imager and spectrograph

NASA : National Aeronautics and Space Administration

NEOWISE : Near-Earth Object WISE

NGC : New General Catalogue

NIR : Near-InfraRed

NLTT : New Luyten Two-Tenths Catalogue

NOMAD : Naval Observatory Merged Astrometric Dataset

NSERC : Natural Sciences and Engineering Research Council of Canada

NSF : National Science Foundation

OMC : Orion Molecular Complex

OMM : Observatoire du Mont-Mégantic

PDF : Probability Density Function

PLE : Pleiades association

PPMXL : Positions and Proper Motions star catalogue eXtended-Large

PRE-BASS : Preliminary BASS

PSO : Pan-STARRS Object

RA : Right Ascension

ROSAT : RÖntgen SATellite

RV : Radial Velocity

S/N : Signal-to-Noise ratio

SCC : Scorpius-Centaurus Complex

SDSS : Sloan Digital Sky Survey

SED : Spectral Energy Distribution

SFR : Star-Forming Region

SIMON : Spectromètre Infrarouge du MONt-Mégantic.

SIMP : Sondage Infrarouge de Mouvement Propre.

SKM : Spatial and Kinematic Model

SPIRou : Spectro-Polarimètre InfraRouge

SQL : Structured Query Language

SSS : SuperCOSMOS Sky Survey

SIMBAD : Set of Identifications, Measurements and Bibliography for Astronomical Data

SpT : Spectral Type

SpeX : Cross-dispersed near-infrared spectrograph

TAU : Taurus star-forming region

THA : Tucana-Horologium Association

TMT : Thirty Meter Telescope

TWA : TW Hydrae Association

UCAC : US Naval Observatory CCD Astrograph Catalog

UCL : Upper Centaurus Lupus association

UMA : Ursa Major moving group

URL : Ultra-Red L dwarf

USCO : Upper Scorpius association

USNO : United States Naval Observatory

UT Universal Time

UV : Ultra-violet

UdeM : Université de Montréal

VL-G : Very low-gravity

WISEP : WISE Preliminary catalog

WISE : Wide-Field Survey Explorer

YMG : Young Moving Group

Remerciements

Je remercie mes directeurs de recherche David Lafrenière et René Doyon, qui ont su concevoir un projet qui a suscité un grand intérêt dans la communauté scientifique et qui m'a permis d'en apprendre énormément sur plusieurs sphères de la recherche en astrophysique. Étienne Artigau, Lison Malo et Loïc Albert ont aussi joué un rôle important dans mon apprentissage et ont été d'une disponibilité irréprochable pour répondre à mes questions. Merci René pour ton enthousiasme enflammé, David pour tes idées scientifiques remarquables, Étienne pour ton imagination inépuisable, Loïc pour ta patience infinie et Lison pour ton entraide incroyable.

Je remercie aussi tous ceux qui m'ont supporté tout au long de mes études ayant mené à la complétion de ce doctorat, notamment ma famille : Joanne, Louis, Kathy et Mickaël. Merci à Amélie pour son support constant et pour avoir partagé avec moi ces dernières années tellement excitantes et mouvementées ! Merci à Corinne, François-René, Nicolas, Sandie, Marie-Eve, Patrice, Jean-François et Simon pour tous les beaux moments passés dans les dernières années. Je dois remercier en particulier Christof pour m'avoir servi de mentor en programmation dans l'autobus scolaire avec une calculatrice TI-83, ainsi qu'à Édouard pour m'avoir permis d'appronfondir ces connaissances à travers les difficultés rencontrées dans la construction de ses jeux plus imaginatifs les uns que les autres. Je remercie Maxime, Antoine, Sylvain et Pierre-Luc pour avoir montré un intérêt incroyable dans mes recherches et pour avoir cru en moi depuis toujours. Merci à Peter et Hao, ainsi qu'Isadora et Mike pour les moments incroyables que nous avons passés durant l'été 2014 en Californie. Merci à Noé pour ses découvertes artistiques étranges et sa compagnie dans les multiples cafés de Montréal, dans lesquels plusieurs parties de cette thèse ont été écrites. Merci aussi pour tes discussions

sur les mathématiques abstraites qui me forcent toujours à faire travailler mon imagination.

Je remercie également les nombreux collaborateurs qui m'ont énormément apporté, autant dans ma compréhension scientifique que dans mes capacités à communiquer mes recherches oralement ou par écrit, particulièrement en anglais. Ceux-ci incluent Jackie Faherty, Kelle Cruz, Peter Plavchan, Philippe Delorme, Robert Simcoe, Michael Cushing, Adric Riedel, Rebecca Oppenheimer, Eric Mamajek, Brendan Bowler, David Rodriguez, Mike Liu, Katelyn Allers, Joshua Schlieder, Serge Dieterich, Ben Zuckerman, John Gizis, Adam Burgasser, André-Nicolas Chené, Emily Rice, Céline Reyé, France Allard, Will Best, David Blank, Amélie Simon, Gilles Fontaine et Daniella Bardalez Gagliuffi. Toutes ces personnes m'ont poussé à donner le meilleur de moi-même en recherche.

Finalement, je remercie aussi tous les techniciens de télescope et observateurs en mode queue qui m'ont aidé à accumuler les données présentées dans cette thèse, notamment Alberto Pastén, Rachel Mason, Stuart Ryder, Rubén Díaz, Stéphanie Côté, John Blakeslee, Mischa Schirmer, Andrew McNichols, Dave Griep, Brian Cabreira, Tony Matulonis, German Gimeno, Steve Margheim, Percy Gomez, René Rutten, Bernadette Rodgers, Tim Davidge, Pierre-Luc Lévesque, Ghislain Turcotte, Bernard Malenfant, Jaehyon Rhee Jay, Inger Jørgensen, Thomas Hayward, Andrew Cardwell, Blair Conn, Eleazar Rodrigo Carrasco Damele, David Krogsrud, Eduardo Marin, Erich Wenderoth, Fredrik Rantakyro, Joanna Thomas-Osip, Pablo Patricio Candia, Pascale Hibon, Cláudia Winge, Benoit Neichel, Peter Pessev, Matthew Bayliss et Anne Sweet.

À Joanne et Louis

Chapitre 1

Introduction

1.1 Les naines brunes

1.1.1 Caractéristiques

Les naines brunes sont des objets similaires aux étoiles, cependant plusieurs caractéristiques les en distinguent, notamment–et principalement–le fait qu'elles effectuent le brûlage du deutérium et du lithium (pour la plupart) mais pas le brûlage de l'hydrogène comme dans le cas des étoiles. Nous verrons que la capacité d'un objet astronomique à brûler ces éléments dépend principalement de sa masse. Selon les connaissances actuelles, les naines brunes pourraient se former d'une façon similaire aux étoiles à partir d'un nuage moléculaire. À mesure que des instabilités hydrodynamiques se développent à l'intérieur de celui-ci, plusieurs régions commencent à se fragmenter ; c'est alors que s'amorce leur contraction gravitationnelle (Figure 1.1). En effet, lorsqu'un fragment du nuage moléculaire de composition solaire et de masse supérieure à environ 78.5 fois celle de Jupiter (M_{Jup}), ou 0.075 fois celle du Soleil ($M_{\odot}$; Burrows et al. 2001) se contracte, il atteint un point où sa température et sa pression centrales sont suffisamment élevées pour que s'initient au coeur de la protoétoile des réactions thermonucléaires transformant l'hydrogène en hélium ($\approx 3 \times 10^6$ K ; Burrows et al. 2001). Ce procédé est très fortement exothermique, c'est-à-dire qu'à mesure que la fusion s'opère, une grande quantité d'énergie est libérée. Conséquemment, le gaz ambiant se réchauffe et se dilate, ce qui vient contrebalancer la contraction gravitationnelle.

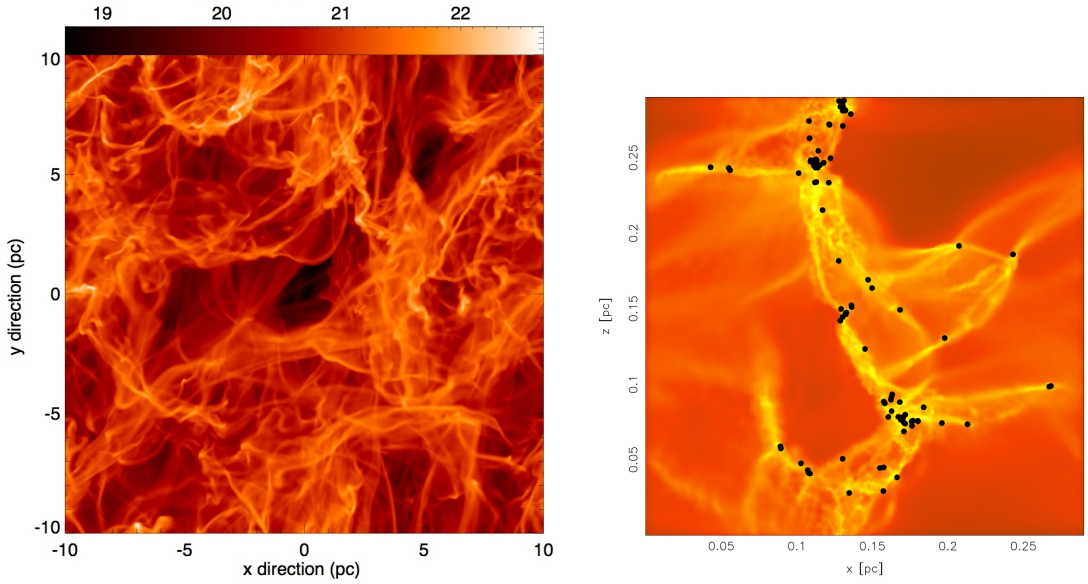

FIGURE 1.1 À gauche : fenêtre de 20 pc sur une simulation de fragmentation d'un nuage moléculaire. Figure tirée de Glover & Mac Low (2007). À droite : gros plan sur une région de 0.3 pc d'une simulation similaire. Les régions plus claires sont plus denses, excepté pour les points noirs qui correspondent à des étoiles et naines brunes en formation. Figure tirée de Jappsen et al. (2005).

On dit que ces réactions nucléaires sont stables car si le taux de réaction s'emballait, le gaz se dilaterait davantage. Ceci contribuerait alors à rabaisser le taux de réactions nucléaires. Si au contraire le taux de réactions devenait trop bas, le gaz se contracterait, se réchaufferait et rétablirait encore une fois le taux de réactions nucléaires. Ainsi, cet effet qu'on qualifie parfois de *thermostat* permet à l'étoile d'atteindre une température stable, en compensant l'énergie perdue par son rayonnement par celle que dégage la fusion nucléaire. Ce phénomène permet aux étoiles de stabiliser leur rayon, luminosité et température durant typiquement plusieurs milliards d'années (selon la masse de l'étoile). On dit alors qu'elles se trouvent sur la séquence principale. Cependant, dans le cas d'un fragment de nuage moléculaire dont la masse est inférieure à environ 78.5 M_{Jup}, le scénario est différent. Pour une telle masse, l'énergie libérée par la contraction gravitationnelle sera moins importante, ainsi sa température interne sera moins grande que celle d'une étoile. C'est alors un autre phénomène physique qui viendra freiner la contraction gravitationnelle, avant que la fusion de l'hydrogène ne puisse s'opérer. On appelle cet effet la pression des électrons dégénérés : si l'on augmente graduellement la

densité d'un gaz tout en veillant à ce que sa température reste suffisamment basse, l'étendue spatiale de la fonction d'onde quantique décrivant les particules qui composent le gaz tendra à augmenter. Pour chaque particule, cette étendue spatiale est de l'échelle d'une quantité physique que l'on nomme la longueur d'onde thermique de de Broglie :

$$\lambda_{\text{th}} = \frac{h}{\sqrt{2\pi m k_B T}}, \tag{1.1}$$

où h est la constante de Planck, m la masse des particules considérées, k_B la constante de Boltzmann et T la température du gaz. Lorsque cette quantité devient comparable à l'espace interatomique, des phénomènes d'interférence statistique se produisent et le gaz cesse de suivre les lois de la thermodynamique classique. Il faut alors faire intervenir la mécanique quantique pour bien décrire le comportement du gaz en question ; si les particules considérées sont des fermions (ce qui est le cas pour les électrons), une répulsion statistique aura lieu, produisant une pression appelée de dégénérescence. Cette répulsion statistique est une conséquence du principe d'exclusion de Pauli, selon lequel deux fermions ne peuvent occuper simultanément le même état quantique. En observant l'Équation (1.1), on remarque deux choses : premièrement, il est nécessaire de garder la température suffisamment basse pour que le phénomène se produise et deuxièmement, les particules de plus petite masse, c'est-à-dire les électrons, subiront les effets de répulsion statistique en premier. On dit souvent que les naines brunes peuvent être vues comme des étoiles manquées, en ce sens qu'elles ne sont jamais devenues étoiles par l'apport d'énergie provenant des réactions thermonucléaires. Puisque c'est la pression des électrons dégénérés qui retient leur effondrement gravitationnel, il n'y a pas d'effet thermostat ou d'apport d'énergie par les réactions thermonucléaires comme dans le cas des étoiles. Ceci engendre un refroidissement graduel des naines brunes à mesure qu'elles vieillissent. En conséquence, la masse d'une naine brune ne peut être déduite uniquement à partir de sa température, comme on peut le faire pour une étoile sur la séquence principale. Il faudra effectivement tenir compte à la fois de son âge et de sa température pour estimer sa masse.

L'une des caractéristiques intéressantes des naines brunes est que sur une large gamme

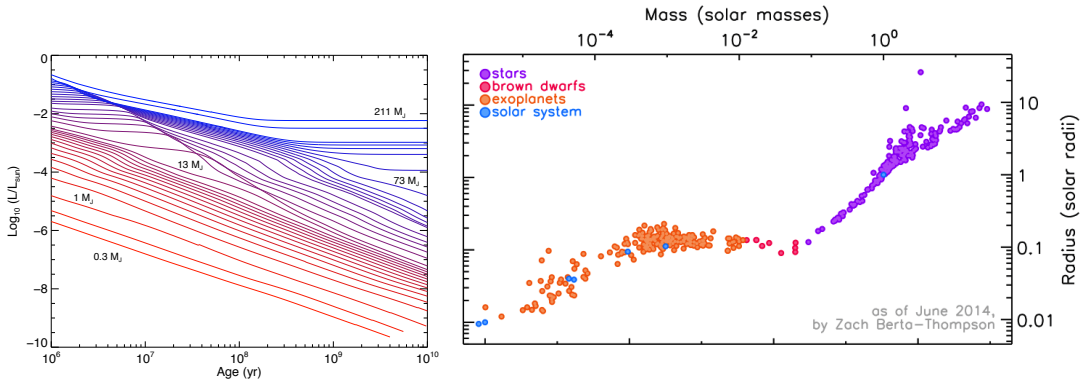

FIGURE 1.2 À gauche : modèles de luminosité en fonction de l'âge pour les étoiles (traits bleus), naines brunes (traits mauves) et planètes gazeuses (traits rouges). On voit que seules les étoiles finissent par voir leur luminosité se stabiliser lorsqu'elles atteignent la séquence principale. Figure adaptée de Burrows et al. (2001) par Michael C. Cushing et construite à partir des modèles d'évolution AMES-Cond (Baraffe et al. 2003). À droite : rayon en fonction de la masse pour ces mêmes types d'objets, cette fois provenant d'observations empiriques. On voit que dans le domaine des naines brunes, le rayon reste dans l'ordre de grandeur de $1\,R_{\mathrm{Jup}}$, alors qu'il augmente de façon abrupte en fonction de la masse dans le régime stellaire. Figure créée par Zachory K. Berta-Thompson à partir de données provenant de Torres et al. (2010); Irwin et al. (2011); Triaud et al. (2013) et la base de données *exoplanets.org*.

de masses, leur rayon à l'âge du champ est toujours voisin (à 10–15% près) du rayon de Jupiter (voir Figure 1.2). Ceci découle de la concurrence entre deux phénomènes physiques contribuant à leur pression interne. Le premier phénomène, la pression des électrons dégénérés, domine l'équation d'état des naines brunes aux plus grandes masses. Dans l'approximation complètement dégénérée, ceci entraîne une dépendance $R \propto M^{-1/3}$. À mesure que l'on tend vers les masses plus petites, la contribution de la pression de Coulomb devient plus importante. Une fois bien en-deçà de $13\,M_{\mathrm{Jup}}$, cette dernière finit alors par dominer l'équation d'état. À ce moment, la relation entre le rayon et la masse devient plutôt $R \propto M^{1/3}$. Entre ces deux cas limites, les deux contributions compétitionnent pour donner lieu à un plateau dans la relation masse–rayon des naines brunes (Chabrier et al. 2009 ; voir Figure 1.2). On catégorise habituellement les étoiles et les naines brunes en construisant une séquence empirique à partir d'un ensemble de *distributions d'énergie spectrale*[1] (DES) observées selon une méthodologie inspirée de la classification MK, du nom des astronomes Morgan & Keenan l'ayant proposée (Morgan et al. 1943). En se fiant à certaines caractéristiques, comme par exemple la présence

[1]Dans le langage courant, on dit simplement un *spectre*.

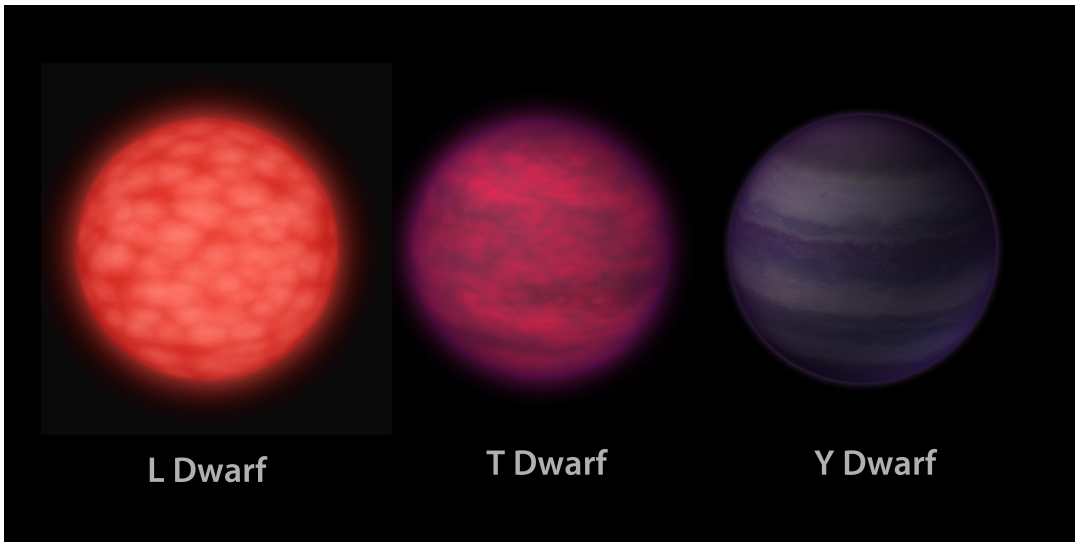

FIGURE 1.3 Vue d'artiste d'objets de types spectraux L, T et Y (de gauche à droite), tels que perçus dans le domaine visible. À mesure qu'on parcourt les types spectraux de la classe L à la classe T, la couleur des objets tend vers le magenta. Ceci est dû à l'absorption par le sodium et le potassium présents dans leur atmosphère, absorbant les longueurs d'onde vertes (Burrows et al. 2001). On voit aussi l'apparition de régions plus sombres, dues à la présence de nuages de poussière. À partir du type spectral Y, on commence à voir apparaître des bandes longitudinales colorées, rappelant l'apparence de Jupiter. Celles-ci seraient causées par la présence de composés chimiques complexes (tels que des glaces d'ammoniaque) et délimitées par de puissants vents méridionaux formés par des instabilités hydrodynamiques. Cette figure est une courtoisie de la NASA.

d'une raie d'absorption particulière ou la forme du continu, on assigne une lettre à chaque grande classe de DES, puis un chiffre de 0 à 9 permettant d'ordonner de façon continue les objets à l'intérieur d'une classe spectrale. Dans l'ordre, les classes spectrales introduites par Morgan et al. (1943) sont OBAFGKM. Le type spectral O, à l'extrémité que l'on qualifie de *précoce*, correspond aux étoiles les plus chaudes et massives sur la séquence principale. À l'autre extrémité, les astres dits *tardifs* correspondent à des objets de plus en plus froids.

La classe spectrale M, correspondant généralement aux étoiles de faible masse, a été développée plus en détail par Boeshaar, P. C. (1976), Henry (1991) et Kirkpatrick et al. (1991). Depuis, cette classification a été étendue aux objets les plus froids ($\lesssim 2300\,\mathrm{K}$; Stephens et al. 2009) avec les classes spectrales L (Kirkpatrick et al. 1999; Martín et al. 1999), T (Kirkpatrick et al. 1999; Burgasser et al. 1999; Geballe et al. 2002; Burgasser et al. 2006) et Y (Kirkpatrick et al. 1999; Cushing et al. 2011; Kirkpatrick et al. 2012). Celles-ci correspondent aux naines

brunes et, dans certains cas, aux objets de masse planétaire ($\gtrsim$L2 à <40 Mans ou $\gtrsim$Y0 à <1 Gan). À la Figure 1.3 sont présentées certaines caractéristiques visuelles des classes L, T et Y dans les longueurs d'onde visibles. Une caractéristique notable qui démarque ces classes spectrales de celles plus précoces est la complexité de la chimie atmosphérique des objets à ces basses températures. Entre autres, des condensats de VO, d'eau, de méthane et d'ammoniac peuvent se former à différentes couches atmosphériques dépendant de la température et de la pression atmosphérique. Ceux-ci peuvent donner lieu à des motifs météorologiques à la surface des naines brunes (Figure 1.4).

Les plus froids d'entre eux n'atteignant pas la séquence principale et sont donc des objets dits sous-stellaires (ce qui inclut les naines brunes). Les plus tardifs sont moins massifs pour une population d'âge fixe, ou plus vieux pour une population de masse fixe. Il y a une raison historique à l'appellation précoce/tardif ; on croyait à l'origine que les objets précoces étaient simplement plus jeunes que les objets tardifs même dans le cas des étoiles, ce qui s'est révélé faux, du moins pour les étoiles sur la séquence principale. La limite correspondant à la transition entre étoiles et naines brunes en est une sur la masse, comme on l'a décrit plus haut. Le type spectral précis où elle est atteinte dépend donc de l'âge de l'objet. Pour les objets relativement âgés ($\gtrsim 1$ Gan), la transition se produit aux environs du type spectral L2. Pour ce qui est de la limite de $13\,M_{\mathrm{Jup}}$ correspondant au régime des masses planétaires, elle se situe environ au type spectral Y0 à ce même âge. Pour un objet relativement plus jeune, à 100 Mans par exemple, cette limite se situe plutôt autour du type spectral T2. On voit donc qu'en général, pour les objets sous-stellaires, il n'est pas simple de convertir directement un type spectral en propriétés physiques (masse, rayon, température ou gravité de surface). On peut toutefois relier de façon relativement précise l'échelle des types spectraux à une échelle de température[2], puisque que c'est le paramètre influant la DES de la façon la plus directe. Par contre, il faut ensuite connaître l'âge de l'objet de façon relativement précise pour en déduire sa masse, mais cette mesure est généralement difficile à obtenir. Il est à noter que la métallicité d'un objet, en d'autres mots sa composition chimique, influence aussi la DES dans une moindre mesure (voir Section 1.1.5).

[2]L'incertitude typique sur une telle conversion est d'environ 150 K (Jeffries 2012).

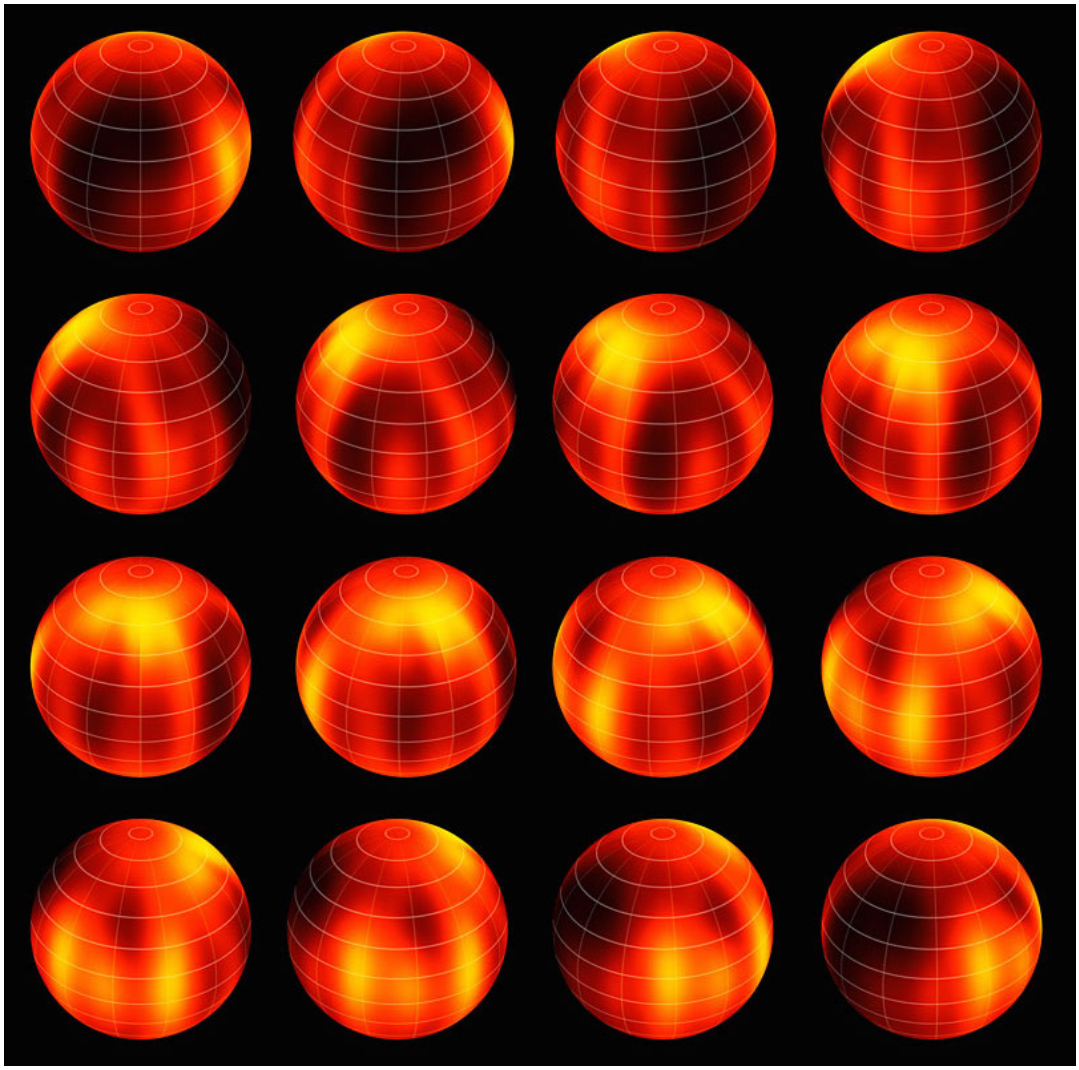

FIGURE 1.4 Carte de la température de surface de la naine brune Luhman 16, obtenue par imagerie Doppler. On peut dinstinguer les régions plus froides (plus sombres sur l'image) qui correspondent à une couverture nuageuse plus épaisse masquant les régions profondes et plus chaudes de l'atmosphère. Figure tirée de Crossfield et al. (2014)

1.1.2 Le régime de masse planétaire

L'Union Astronomique Internationale (UAI) définit une naine brune comme un objet d'au moins $13\,M_{\rm Jup}$, la masse nécessaire au brûlage du deutérium. Le deutérium (^{2}H ou D) est un isotope stable de l'hydrogène formé lors de la nucléosynthèse primordiale et présent à l'état de traces dans l'Univers. En ce moment, on compterait environ 10 milliards d'atomes d'hydrogène pour un seul atome de deutérium (Spite & Spite 1982). La température de fusion du deutérium ($\approx 10^6\,$K) est beaucoup plus basse que celle de l'hydrogène, ce qui explique pourquoi les objets aussi peu massif que $13\,M_{\rm Jup}$ puissent le brûler (Burrows et al. 2001). Toutefois, puisque cet isotope se trouve à l'état de traces seulement, il s'épuise rapidement et ceci ne permet pas aux naines brunes d'atteindre la séquence principale.

Il n'existe pas encore de définition officielle pour les objets isolés dont la masse est inférieure à $13\,M_{\rm Jup}$: ceux-ci possèdent des propriétés physiques semblables à celles des exoplanètes géantes gazeuses, cependant la définition d'une planète selon l'UAI requiert que celle-ci soit en orbite autour d'une étoile. De plus, il est plausible que les objets isolés de $\leq 13\,M_{\rm Jup}$ proviennent de deux populations bien distinctes, soit des planètes géantes éjectées de leur système stellaire peu après leur formation, ou des objets formés de façon similaire aux étoiles et aux naines brunes, directement par la fragmentation d'un nuage moléculaire. La nomenclature pour ces objets est au centre de nombreux débats dans la communauté scientifique : devrait-on adapter la définition de planète à tout objet isolé de masse inférieure à $13\,M_{\rm Jup}$, ou devrait-on plutôt exiger qu'une planète ait nécessairement été formée dans un disque circumstellaire ? Cette deuxième définition a l'avantage de préserver la vision traditionnelle selon laquelle une planète est liée à une étoile, cependant elle est pratiquement inapplicable dans le cas d'une exoplanète géante éjectée de son système. En effet, si un tel objet s'éloigne suffisamment de son système stellaire, il deviendra impossible de retracer son origine. La définition basée sur la masse plutôt que le mécanisme de formation demande un changement de paradigme, mais présente l'avantage d'être reliée à la structure de l'objet et donc mesurable, même dans le cas de planètes éjectées (Basri & Brown 2006).

1.1.3 Comment et pourquoi étudier les naines brunes

Comme mentionné plus tôt, les naines brunes sont en général plus froides que les étoiles plus précoces. Si l'on fait la grossière approximation que les étoiles et naines brunes émettent à la façon d'un corps noir, on peut s'attendre à ce que la loi du déplacement de Wien soit valide :

$$\lambda_{\max} = \frac{hc}{xk_BT}, \tag{1.2}$$

$$x \approx 4.96511, \tag{1.3}$$

où c est la vitesse de la lumière dans le vide et $\lambda_{\max}$ la longueur d'onde à laquelle le rayonnement est maximal pour un corps noir de température T. Typiquement, une naine brune de 78.5 M_{Jup} à un âge typique du voisinage solaire (~ 8 Gan) aura une température effective d'environ 1500 K (type spectral $\approx$ L6 ; Stephens et al. 2009), correspondant à $\lambda_{\max} \approx 1.9\,\mu$m. Ceci démontre que les naines brunes émettent surtout aux longueurs d'onde proche-infrarouges plutôt que dans les longueurs d'onde visibles ($\approx$ 400–700 nm). Si l'on utilise une bande passante uniforme et d'une largeur correspondant à 20% de la longueur d'onde centrale, la densité d'énergie lumineuse émise par un corps noir de 1500 K à 700 nm est environ 75 fois plus faible qu'à 1.9 μm. La loi de Stefan-Boltzmann indique également qu'un corps noir plus froid émet moins d'énergie lumineuse au total. Il est donc difficile d'identifier ou d'étudier les naines brunes dans les longueurs d'onde visibles. C'est principalement pour cette raison qu'il a fallu attendre les sondages infrarouges à grande couverture tels que le *Two Micron All-Sky Survey* (2MASS ; Skrutskie et al. 2006 ; observations menées entre 1997 et 2001) et le *DEep Near-Infrared Survey of the southern sky* (DENIS ; Epchtein 1998 ; observations menées entre 1996 et 2001), pour identifier la majorité des naines brunes connues à ce jour.

Une méthode efficace pour identifier de nouvelles naines brunes consiste à concentrer les recherches dans le voisinage solaire (à moins de ≈ 100 pc) en ciblant les objets astronomiques à grand mouvement propre. D'abord, en comparant les positions des étoiles dans deux images infrarouges prises à quelques années d'écart, on identifie celles qui se sont significativement déplacées par rapport aux autres. D'une façon statistique, ces objets à grand mouvement

propre ont beaucoup plus de chances de se trouver à proximité. Étant donné que les naines brunes sont très peu brillantes, il serait de toute façon difficile d'identifier les naines brunes plus lointaines. Ensuite, en utilisant l'un des multiples sondages visibles accessibles tels que le *Sloan Digital Sky Survey* (SDSS ; York et al. 2000 ; observations menées depuis 2000), on peut s'assurer que les objets en question soient significativement moins brillants dans les longueurs d'onde visibles par rapport à l'infrarouge. Il faut ensuite confirmer hors de tout doute la nature des objets en question en mesurant leur DES infrarouge et en les comparant soit à celles de naines brunes connues, soit aux DES provenant de modèles d'atmosphère de naines brunes.

Il existe plusieurs motivations pour étudier les naines brunes, l'une d'entre elles étant de comprendre leur mécanisme de formation : se forment-elles toutes dans un nuage moléculaire à la façon des étoiles, ou plus souvent dans les disques circumstellaires d'étoiles jeunes telles les planètes géantes ? Quels sont les intervalles de masse que permettent de former chacun de ces deux procédés, et à quelle fréquence ? Toutes ces questions sont reliées au concept de la fonction de masse initiale (FMI), dont nous discuterons plus loin. Historiquement, la première motivation de trouver des naines brunes fut de déterminer si elles pouvaient combler la masse manquante dans la Galaxie, appelée matière sombre. Nous savons maintenant que la densité spatiale des naines brunes dans le voisinage solaire est d'environ $14 \pm 2 \cdot 10^{-3}\,\mathrm{pc}^{-3}$ (types spectraux L2–Y1; Kirkpatrick et al. 2012; Burningham et al. 2013; Marocco et al. 2015; Reylé et al. 2010), ce qui est plus de 6 fois inférieur à la densité spatiale des étoiles sur la séquence principale ($9.3 \times 10^{-2}\,\mathrm{pc}^{-3}$; Chabrier 2005). On obtient donc une de masse totale d'approximativement $\rho \approx 0.8^{+0.5}_{-0.3}\,M_{\mathrm{Jup}}\,\mathrm{pc}^{-3}$ pour les naines brunes, ce qui est nettement insuffisant pour expliquer la nature de la matière sombre, sa densité locale étant estimée à $\rho \approx 8.8\,M_{\mathrm{Jup}}\,\mathrm{pc}^{-3}$ (Bovy & Tremaine 2012).

Un autre objectif de l'étude des naines brunes est de décrire la structure interne et l'atmosphère de ces objets avec les modèles théoriques. Ceci permettrait entre autres de sonder certaines conditions physiques inaccessibles aux laboratoires actuels. En outre, un nouvel aspect de cet objectif s'est dessiné avec la récente découverte des premières exoplanètes : la compréhension de la connection entre les naines brunes de faible masse et les exoplanètes géantes gazeuses. Ces connaissances permettront notamment de tester les modèles théoriques

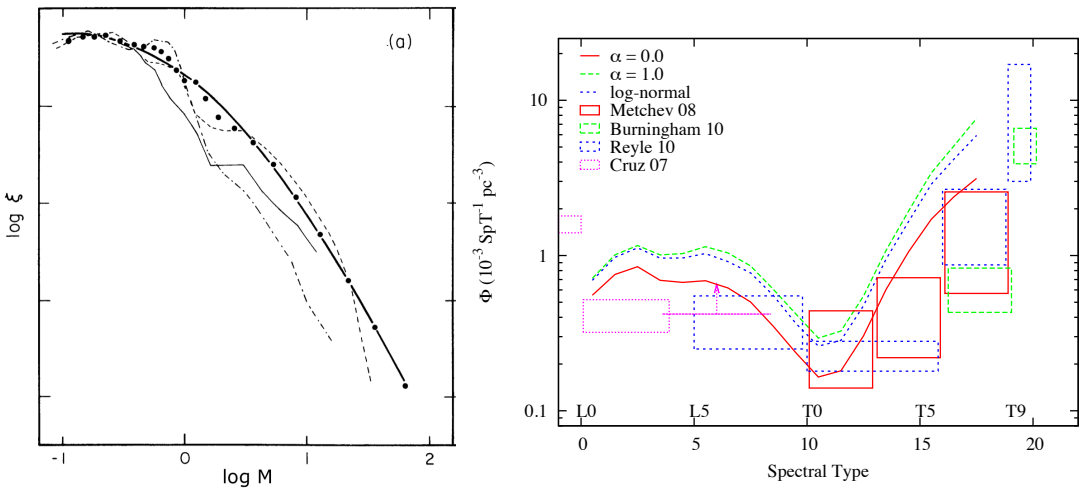

(a) FMI du champ Dwarf

(b) FMA sous-stellaire du champ Dwarf

FIGURE 1.5 À gauche : Comparaison de la FMI du champ mesurée dans plusieurs études. Les points représentent les données de Miller & Scalo (1979). Trait large : Ajustement en loi log-normale ; trait mince : Salpeter (1955) ; trait pointillé : Sandage (1957) ; trait alternant points et tirets : Schmidt (1959). Figure tirée de Miller & Scalo (1979). À droite : FLA pour les objets sous-stellaires du champ. Les résultats de simulations basées sur des modèles théoriques utilisant différentes formes de FMI sont superposés aux échantillons identifiés dans la légende (Burgasser 2007). La pente aux faibles masses est encore mal contrainte, mais les observations récentes semblent favoriser une pente $\alpha \leq 0$. Le comportement de la FMI aux types spectraux plus tardifs que T9 reste grandement incertaine. On s'attend à trouver une éventuelle coupure en masse, en deçà de laquelle la formation par contraction gravitationnelle est impossible, mais il est encore trop tôt pour confirmer exactement à quelle masse cet effet se produit. Figure tirée de Jeffries (2012).

et éventuellement de savoir déterminer de façon précise la masse et les propriétés physiques des exoplanètes à partir de leur DES.

1.1.4 La fonction de masse initiale

Lorsqu'un nuage moléculaire se fragmente, il amorce la formation d'étoiles et de naines brunes d'une grande variété de masses. Si on porte leur distribution de masses en histogramme, on obtient la fonction de masse initiale (FMI). Il est d'un intérêt majeur de connaître celle-ci avec précision. En effet, l'évolution d'une étoile à travers le temps est déterminée principalement par sa masse et sa composition initiale. Ainsi, la connaissance précise de la FMI nous permettrait de mieux connaître l'évolution de la population d'étoiles de la Galaxie dans son ensemble. On a d'ailleurs introduit en astronomie galactique le théorème de Davé, selon le-

quel chacun des problèmes majeurs dans ce domaine peut être réglé par un choix approprié de la FMI (Bastian et al. 2010). Une meilleure connaissance de la FMI fournirait aussi des contraintes observationnelles sur les modèles théoriques de formation stellaire, décrivant l'effondrement de nuages moléculaires en faisant intervenir des procédés physiques relativement complexes. La FMI est un ingrédient fondamental pour comprendre l'évolution des galaxies.

La FMI est toutefois extrêmement difficile à mesurer pour plusieurs raisons : 1. Il est très difficile de mesurer directement la masse des étoiles. Il est beaucoup plus facile de mesurer leur luminosité intrinsèque pour mesurer la fonction de luminosité initiale (FLI), qu'on devra ensuite relier à la FMI par des considérations physiques ; 2. Les naines brunes n'atteignent jamais une séquence principale où leur luminosité et température resteraient stables durant plusieurs milliards d'années. Ainsi, il sera nécessaire de tenir compte de l'évolution temporelle de celles-ci si l'on veut relier la FLI à la FMI dans le régime sous-stellaire ; 3. Pour une population d'âge fixe, les étoiles les plus massives ont déjà quitté la séquence principale pour devenir des géantes rouges, naines blanches, étoiles à neutrons ou trous noirs. Ainsi, la fonction de masse actuelle (FMA) et la fonction de luminosité actuelle (FLA) sont respectivement différentes de la FMI et la FLI ; 4. En ce qui concerne les étoiles de faible masse et les naines brunes, il est encore très difficile d'en étudier un échantillon suffisamment complet à cause de leur luminosité intrinsèque très faible. De plus, à défaut de connaître précisément la distance de chaque étoile pour construire un échantillon complet dans un volume fixe de l'espace, il faut corriger le biais de Malmquist (Malmquist 1936), qui a un impact sur la FLA observée. Ce biais est dû au fait que les étoiles plus massives et plus brillantes peuvent être détectées à une distance plus grande. Ainsi, si l'on étudie un échantillon limité par la sensitivité instrumentale et conséquemment par la magnitude apparente des étoiles, nous verrons les étoiles massives plus loin dans l'espace. Ceci augmentera donc artificiellement leur population dans notre échantillon.

Au début du vingtième siècle, on a commencé à obtenir des mesures empiriques de la FLA (van Rhijn 1936 ; Luyten 1941) à partir de catalogues d'étoiles suffisamment complets. Ceci permit à Salpeter (1955) de la relier à la FMA en utilisant les relations approximatives disponibles à l'époque permettant de relier la masse et la luminosité des étoiles. En supposant

un taux de formation stellaire constant pour estimer la fraction d'étoiles massives ayant déjà terminé leur vie, il parvint à relier la FMA à la FMI. Il obtint alors une distribution qu'il paramétra par une loi de puissance logarithmique :

$$\phi\left(\log m\right) = \frac{\mathrm{d}N}{\mathrm{d}\log m} \propto m^{1-\alpha}, \tag{1.4}$$

où N est le nombre d'étoiles et m leur masse. Cette fonction est appelée la loi de Salpeter. Avec son échantillon d'étoiles dont les masses étaient comprises entre 0.4 et 10 $M_{\odot}$, il trouva que la pente logarithmique décrivant le mieux ses observations correspondait à $\alpha = 2.35$. Ensuite, ce sont Miller & Scalo (1979) qui entreprirent l'étape suivante en améliorant la FLA à l'aide de données plus actuelles et en utilisant un taux de formation stellaire dépendant du temps. Pour ce faire, ils firent la supposition qu'aucune discontinuité n'était admise dans la FMI aux masses correspondant aux étoiles présentement en fin de vie. Cette supposition est fondée sur le fait qu'il n'y a pas de raison pour que l'époque actuelle, où la FMA est mesurée, possède un caractère unique ou qu'un changement physique significatif s'opère dans la structure des étoiles à cette masse particulière. Par cette méthode, ils mesurèrent un taux de formation d'étoiles environ 2 fois plus élevé qu'à la naissance de la galaxie. Ils obtinrent finalement une FMI bien paramétrée par une loi log-normale :

$$\phi\left(\log m\right) = \exp\left(-\frac{\left(\log m - \log m_c\right)^2}{2\sigma^2}\right), \tag{1.5}$$

où m_c correspond à la *masse caractéristique* où la FMI atteint son maximum, puis σ à la largeur caractéristique de la courbe. Les paramètres obtenus par Miller & Scalo (1979) sont $m_c = 0.1\,M_{\odot}$ et $\sigma = 0.7$ pour un échantillon d'étoiles entre 0.1 et 50 $M_{\odot}$, ce qui est cohérent avec les résultats de Salpeter (voir Figure 1.5). Ce type de paramétrisation porte le nom de loi log-normale.

En utilisant un modèle semi-empirique de formation d'étoiles, Adams & Fatuzzo (1996) ont démontré que la masse d'une étoile donnée est le résultat du produit d'un grand nombre de variables indépendantes et aléatoires (i.e., ces variables étant des fonctions de différents paramètres physiques). Dans une telle situation, il est mathématiquement justifiable de s'attendre

à ce que la FMI suive une loi log-normale. En effet, le théorème de la limite centrale stipule que lorsqu'un suffisamment grand nombre de variables aléatoires indépendantes sont additionnées, des déterminations successives de la quantité résultante suivront une distribution normale. Ainsi, en considérant $M_\star$ la masse d'une étoile et l'ensemble des variables aléatoires α_i qui la déterminent, on a :

$$M_\star = \prod_i \alpha_i \Rightarrow \ln M_\star = \sum_i \ln \alpha_i, \tag{1.6}$$

d'où on tire la conclusion que $\ln M_\star$ devrait suivre une loi normale et conséquemment que $M_\star$ devrait suivre une loi log-normale, si les conditions mentionnées plus haut sont respectées. La FMI porte donc une information sur le fait que les paramètres α_i soient corrélés ou en nombre restreint, auquel cas elle s'éloignera d'une forme log-normale (Adams & Fatuzzo 1996).

Il existe d'autres problèmes que nous n'avons pas encore mentionnés concernant la construction d'un échantillon complet pour la détermination d'une FMI. Si l'échantillon est limité par la magnitude, il sera sujet à un biais additionel. En effet, une fraction significative des étoiles sont binaires ($\sim 60\%$ pour les G–K, $\sim 40\%$ pour les M0–M4 et $\sim 20\%$ pour les plus tardives ; Chabrier 2005). Une grande partie des étoiles d'un échantillon typique étant trop éloignées pour qu'on puisse résoudre les composantes du système, la distance à laquelle l'échantillon est limité sera erronée d'un facteur $\sqrt{2}$. De plus, on oublie une étoile dans le décompte à chaque fois où l'on traite une binaire non-résolue comme une étoile simple. Dans le cas où l'on tente de limiter l'échantillon au voisinage solaire en considérant seulement les étoiles à grand mouvement propre, on est alors sujet à un autre biais. Étant donné que certaines étoiles du voisinage solaire ont une vitesse spatiale semblable à celle du Soleil, leur mouvement propre nous apparaîtra très faible et elles seront exclues de l'échantillon étudié, peu importe leur distance. Finalement, même si l'on avait à notre disposition une mesure de distance trigonométrique pour une grande quantité d'étoiles, un autre biais viendrait déformer les résultats. Ceci provient du fait qu'on utilise typiquement une fonction de densité de probabilité gaussienne pour décrire une mesure associée à une incertitude. Cependant, il est mathématiquement inexact de traiter ainsi les mesures de distance à cause du terme r^2 dans le jacobien en géométrie sphé-

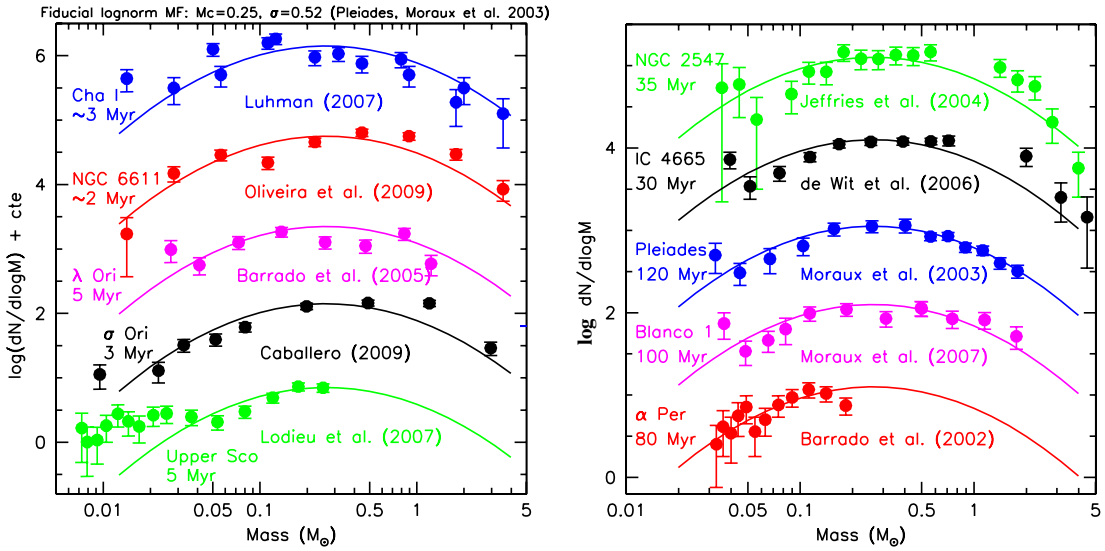

FIGURE 1.6 FMA pour les membres de diverses associations jeunes, auxquelles sont ajustées des distributions en loi log-normale. On remarque plusieurs choses : 1. La FMI ne varie pas de façon drastique d'une association à l'autre ; 2. Les distributions sont raisonnablement bien représentées par des lois log-normales, mais on remarque des déviations ; 3. L'association Upper Scorpius semble avoir un surplus inexpliqué d'objets aux faibles masses. Il reste encore à déterminer si ceci est dû à un biais de sélection ou s'il y a une explication physique sous-jacente. Figures tirées de Jeffries (2012).

rique, celui-là même qui est responsable du fait qu'on trouvera en moyenne plus d'étoiles dans une coquille couvrant r à $r + \mathrm{d}r$, que dans une autre coquille couvrant $r - \mathrm{d}r$ à r. Ceci aura pour effet que les distances d'un ensemble d'étoiles seront systématiquement sous-estimées et que la FMA mesurée dans un échantillon limité par la distance sera conséquemment sur-estimée. Pour compenser cet effet nommé le biais de Lutz-Kelker, un facteur de correction dépendant de la précision des mesures de distance doit être appliqué (Lutz & Kelker 1973). On comprend donc que la FMI est une quantité qui doit être mesurée avec prudence et en tenant compte de ces multiples effets systématiques.

Contraindre la FMI dans le régime des faibles masses pourrait distinguer quelle forme paramétrique est la plus indiquée, ainsi que de tester les premières mesures semblant démontrer qu'il y aurait dans le voisinage solaire une très grande quantité d'objets isolés de masses planétaires (environ 2 objets de masse similaire à Jupiter par étoile ; Sumi et al. 2011). Il sera aussi intéressant de vérifier si la FMI chute de façon drastique à une masse donnée[3].

[3]Les modèles théoriques décrivant la fragmentation de nuages moléculaires suggèrent actuellement des

Toutes ces informations pourraient aider à faire la lumière sur les procédés physiques en jeu lors de la formation des étoiles et des naines brunes. Malheureusement, les choses se compliquent lorsqu'on tente de mesurer la FMI des naines brunes. Puisque les naines brunes sont intrinsèquement moins brillantes, elles sont plus difficiles à étudier et nécessitent de travailler dans l'infrarouge, un domaine relativement récent de l'astrophysique. Conséquemment, nous ne disposons de mesures de distances trigonométriques que pour très peu de naines brunes, la plupart de ces mesures étant très récentes (Dupuy & Liu 2012; Faherty et al. 2012; Dieterich et al. 2014). Nous devrons donc nécessairement nous fier à de plus petits échantillons. Par ailleurs, en se servant uniquement de séquences photométriques, il est pratiquement impossible de distinguer efficacement les étoiles de faible masse contaminant un échantillon de naines brunes à cause de leurs couleurs[4] relativement dispersées et de leur nombre nettement plus grand. Il est donc nécessaire de mesurer la DES pour chacun des objets dans un échantillon afin de bien distinguer les naines brunes des étoiles. L'obtention d'une telle mesure pour chaque objet dans un échantillon relativement grand est très coûteuse en terme de temps de télescope.

Même une fois qu'un échantillon acceptable est construit, il reste d'autres problèmes à surmonter. On se souvient que la luminosité et la température d'une naine brune évoluent constamment dans le temps. Ainsi, nous devons nécessairement connaître la distribution en âge d'une population de naines brunes pour transformer ces quantités en masse. On doit donc connaître le taux de formation de naines brunes en fonction du temps pour relier la FLA à la FMA. Ensuite, la conversion de types spectraux en température permet seulement d'obtenir cette dernière à une précision de $\pm\,150\,\mathrm{K}$. Ceci se répercute à son tour en une incertitude sur la masse allant jusqu'à un facteur 2 à un âge donné (Burrows et al. 1997). En plus, les objets du champ montrent une certaine dispersion en métallicité, qu'on doit mesurer pour contraindre précisément les propriétés d'une naine brune.

Finalement, il existe plusieurs incertitudes systématiques dans l'utilisation de modèles pour transformer la température et l'âge d'une naine brune en masse. Il y a plusieurs facteurs

masses minimales dans l'intervalle de $1\,M_{\mathrm{Jup}}$ (Whitworth & Stamatellos 2006) à $10\,M_{\mathrm{Jup}}$ (Low & Lynden-Bell 1976).

[4]Par couleur, on entend le flux relatif à deux longueurs d'onde différentes.

qui ne sont pas tenus en compte par les modèles théoriques d'évolution et d'atmosphère les plus actuels. Ceux-ci incluent les effets de la rotation, la présence de champs magnétiques et l'entropie initiale. En pratique, ces deux premiers effets peuvent être mesurés et pourront éventuellement être inclus dans des modèles plus réels. Cependant, l'entropie initiale, laquelle est reliée à la température initiale lors de la formation d'une naine brune, restera probablement une quantité impossible à mesurer directement. Les conséquences de l'entropie initiale sur la structure d'une naine brune s'estompent au fil du temps, ainsi la méconnaissance de cette quantité ne fera pas obstacle à l'estimation précise de la masse des naines brunes de plus de quelques centaines de Mans. Les modèles d'évolution les plus couramment utilisés dits à *départ chaud* et correspondant à une entropie initiale maximale ($\approx 12\,k_B$/baryon) fournissent seulement une limite inférieure sur la masse estimée d'une naine brune, et il est attendu que ces derniers sous-estiment la masse des objets à *départ froid* (entropie initiale de $\approx 7\,k_B$/baryon), typiquement d'un facteur de l'ordre de deux (Marleau & Cumming 2014).

Nous pourrions donc être tentés de nous tourner vers une méthode purement empirique pour déterminer la masse d'une naine brune. Or, l'une des seules méthodes nous permettant de le faire est la mesure complète de l'orbite de binaires visuelles. Pour illustrer ceci, portons nous vers la 3$^{\text{e}}$ loi de Kepler :

$$(m_1 + m_2) = \frac{4\pi^2}{G}\frac{a^3}{P^2}, \tag{1.7}$$

où m_i est la masse de la composante i, a est le demi grand-axe, G est la constante gravitationnelle et P est la période orbitale du système. On voit que pour un système de faible masse, soit l'orbite sera relativement compacte, soit la période orbitale sera relativement élevée. En particulier, si l'on requiert que la période orbitale d'un système de masse totale $\leq 0.3\,M_\odot$ ne dépasse pas la dizaine d'années pour des fins pratiques et que l'on considère le cas optimiste où le système se situe à seulement 10 pc du Soleil, le demi grand-axe correspondra à seulement ≤ 0.3 seconde d'arc sur le ciel. Il est difficile de résoudre un tel système et par conséquent, il n'y a que très peu de naines brunes pour lesquelles nous avons une mesure directe de la masse (Lane et al. 2001; Bouy et al. 2004; Dupuy et al. 2009a,b,c, 2010; Konopacky et al. 2010;

Dupuy et al. 2014, 2015). Malgré ces difficultés, plusieurs équipes ont tout de même entrepris de mesurer la FMI sous-stellaire du champ (Allen et al. 2005; Cruz et al. 2007; Metchev et al. 2008; Reylé et al. 2010; Burningham et al. 2010; Burgasser 2007; Kirkpatrick et al. 2011; Sumi et al. 2011). Le portrait global favorise actuellement une loi de Salpeter avec $\alpha \leq 0$ (voir Figure 1.5).

Les populations d'associations jeunes (AJs) sont des échantillons tout indiqués pour mesurer plus facilement la FMI des naines brunes. Effectivement, leurs membres font partie d'un environnement de composition chimique uniforme et ont vécu sous les mêmes conditions d'irradiation, s'étant formés à partir du même nuage moléculaire. Leur âge est relativement bien connu et étant donné leur jeunesse, les naines brunes sont plus chaudes, donc plus brillantes et ainsi plus faciles à étudier. Ces populations ne présentent pas que des avantages cependant. Par exemple, les étoiles jeunes possèdent généralement des champs magnétiques plus intenses. Or les modèles d'atmosphère actuels n'en tiennent pas du tout compte. Même sans compter cet effet, nous avons vu plus tôt que les modèles théoriques actuels présentent des erreurs systématiques importantes pour la détermination précise de la masse d'objets jeunes. De plus, les AJs contiennent une moins grande quantité d'objets que le champ, cela s'ajoutant au fait que le recensement de leurs membres est probablement encore bien incomplet dans le domaine sous-stellaire.

On peut considérer qu'il y a deux classes d'AJs : les très jeunes ($\lesssim 10$ Mans) et les plus vieilles (≈ 10–200 Mans ; Jeffries 2012). Les membres des premières ont le défaut d'être relativement distantes et ainsi sujettes à l'extinction par la présence de matière interstellaire, en plus d'avoir une DES fortement affectée par de possibles disques d'accrétion n'ayant pas encore été dissipés. Ceci est très problématique, surtout si on considère le débat actuel voulant que la DES de ces systèmes puisse même dépendre de l'historique d'accrétion de la naine brune, une information hors de notre portée (Baraffe & Chabrier 2010). Finalement, pour des objets aussi jeunes, une petite déviation sur l'âge entraîne une grande déviation sur les estimés de la masse. Ainsi, puisque l'âge n'est pas connu très précisément pour les AJs et qu'il serait possible que leur population montre une dispersion d'âge intrinsèque (Huff & Stahler 2006), une détermination de la masse de leurs membres est difficile. En ce qui concerne les AJs

de plus de 10 Mans, il est possible que plusieurs objets, en particulier ceux de faible masse, aient été éjectés ou pire, évaporés par la radiation intense des étoiles géantes (De Marchi et al. 2010). Dans une mesure moins importante, il est aussi possible que les objets de faible masse couvrent un volume plus grand que les objets massifs, un effet appelé la ségrégation de masse. Ceci serait dû à l'équipartition de l'énergie cinétique au sein des membres de ces groupes qui, suite à plusieurs interactions, fournirait de plus grandes vitesses aux membres moins massifs. Ceci n'a cependant pas encore été confirmé par les observations dans le cas des AJs (De Marchi et al. 2010).

Malgré ces difficultés, plusieurs équipes se sont déjà attaqué à l'étude de la FMI sous-stellaire dans les AJs (voir Figure 1.6). Entre autres, Moraux et al. (2003) ont choisi les Pléïades pour effectuer une telle étude, étant donné que la distance et l'âge de cette association sont relativement bien connus et que la position de ses membres est bien contrainte sur la Sphère céleste (découlant du fait que les Pléïades sont situées relativement loin à $\approx 133\,\mathrm{pc}$). Leurs résultats indiquent qu'une loi de Salpeter avec $\alpha = 0.60 \pm 0.11$ est satisfaisante entre 0.03 et $0.45\,M_{\odot}$, mais qu'une loi log-normale reproduit bien les données sur une plus grande plage de masses (jusqu'à $2\,M_{\odot}$), avec $m_c = 0.25\,M_{\odot}$ et $\sigma = 0.52$. Plusieurs autres équipes se sont plutôt concentrées sur les groupes α Persei, NGC 2547, IC 4665 et Blanco I (des AJs beaucoup plus distantes à ≈ 250–$650\,\mathrm{pc}$). Les résultats obtenus sont généralement cohérents (Figure 1.6). Cependant, puisque que ces AJs sont trop distantes, il est actuellement impossible de mesurer la DES de la plupart de leurs membres. Il faut donc nécessairement faire confiance aux modèles d'évolution et d'atmosphère pour convertir la FLA en FMA, ce qui reste imprécis. De plus, ces études se concentrent sur le centre spatial des associations en question pour éviter une contamination trop grande. Comme nous l'avons mentionné, il est donc possible que les objets aux faibles masses soient sous-représentés dans leur échantillon de membres. D'autres groupes ont aussi mené ce travail sur des associations très jeunes (≈ 5–$10\,\mathrm{Myr}$) telles que Chamaeleon, NGC 6611, σ Orionis, λ Orionis et Upper Scorpius. Encore une fois, les résultats sont cohérents avec le portrait global, à l'exception d'Upper Scorpius qui semble posséder un excès de naines brunes. Il reste encore à déterminer si ceci est le résultat d'un biais observationnel ou d'une FMI fondamentalement différente.

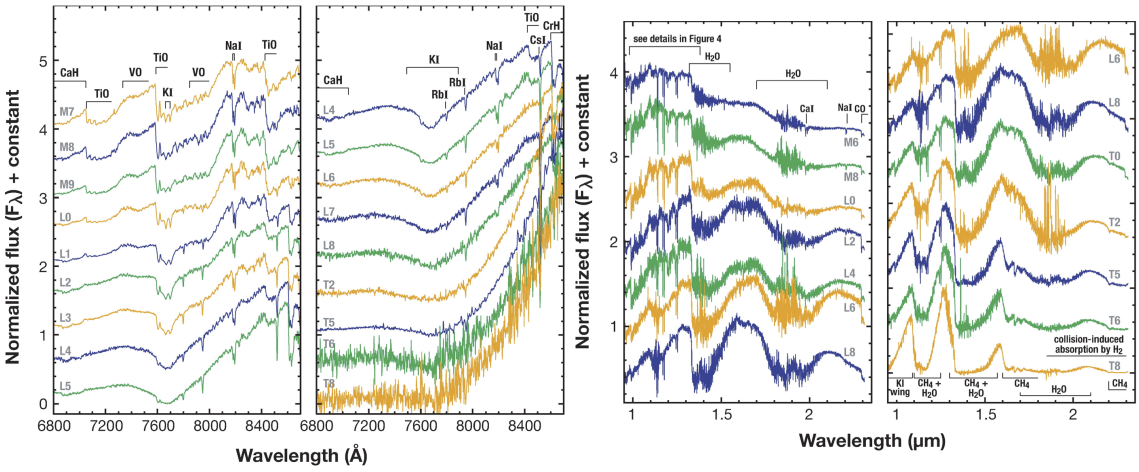

(a) Naines Brunes en Spectroscopie Optique (b) Naines Brunes en Spectroscopie Proche-Infrarouge

FIGURE 1.7 DES pour les étoiles de faible masse et naines brunes de types spectraux M6 à T8, dans les longueurs d'onde visibles (à gauche) et infrarouges (à droite). Les DES sont composées d'un *continu* provenant de l'émission thermique redistribuée par collision induite par absorption de la molécule H_2 (Chabrier et al. 2000), lequel est sculpté par diverses sources d'opacité identifiées sur les figures. On peut voir la présence de plusieurs raies d'absorption telles que le sodium et le potassium et des bandes d'absorption plus larges dues à des molécules, telles l'eau et le méthane. Figures tirées de Kirkpatrick (2005).

Dans le futur, l'avènement de nouveaux instruments permettra de faire avancer les connaissances sur la FMI aux faibles masses. Entre autres, la mission GAIA (Perryman et al. 2001) permettra de mesurer la distance trigonométrique des objets avec $V < 19$ (correspondant au type spectral M6 à 50 pc). L'instrument SPIRou (Spectro-Polarimètre InfraRouge; Delfosse et al. 2013) permettra également d'étudier les propriétés de naines brunes binaires. La complétion des populations des AJs restera un élément clé pour approfondir nos connaissances sur la FMI, particulièrement dans le régime sous-stellaire. Entre autres, la découverte de naines brunes binaires dans les AJs du voisinage solaire sera particulièrement intéressante pour contraindre leur FMI et les modèles théoriques d'évolution et d'atmosphère.

1.1.5 La distribution d'énergie spectrale des naines brunes

On étudie généralement la luminosité des étoiles de faible masse et des naines brunes à travers l'ensemble de filtres passe-bande détaillés à la Table 1.1. Ceux-ci ont été conçus entre autres pour correspondre à des régions intéressantes de la DES des naines brunes, ainsi que

Table 1.1. Principaux filtres photométriques standards en astronomie

Bande	Moyenne (μm)	Largeur Eff. (μm)	Bande	Moyenne (μm)	Largeur Eff. (μm)
U	0.3531	0.0657	J	1.2350	0.1624
B	0.4430	0.0973	H	1.6620	0.2509
G	0.4877	0.1304	K_S	2.1590	0.2619
V	0.5537	0.0890	L'	3.7757	0.6831
R	0.6582	0.1184	$W1$	3.3526	0.6626
I	0.8229	0.2025	$W2$	4.6028	1.0423
Z	0.8828	0.0988	$W3$	11.5608	5.5056
Y	1.0319	0.0876	$W4$	22.0883	4.1017

Les paramètres des filtres G, R, I et Z sont donnés dans le système CFHT, ceux des filtres U, B et V dans le système Johnson, ceux des filtres J, H et K_S dans le système *2MASS*, ceux des filtres $W1$, $W2$, $W3$ et $W4$ dans le système *WISE*, ceux du filtre L' dans le système Keck (NIRC2), puis ceux du filtre Y dans le système UKIRT (Voir `http://svo2.cab.inta-csic.es/svo/theory/fps3/`).

pour éviter les régions où l'absorption tellurique est forte[5], en particulier dans le cas des filtres infrarouges. Si on définit $F_\lambda(\lambda)$ comme la DES d'une étoile à une longueur d'onde λ, la densité moyenne de flux mesurée dans la bande J par exemple sera donnée par :

$$F_J = \frac{\int_0^\infty F_\lambda(\lambda)\phi_J(\lambda)\,\mathrm{d}\lambda}{\int_0^\infty \phi_J(\lambda)\,\mathrm{d}\lambda}, \tag{1.8}$$

où $\phi_J(\lambda)$ correspond à la transmission du filtre passe-bande J en fonction de la longueur d'onde. En astronomie, on travaille habituellement avec la quantité logarithmique appelée magnitude, définie comme :

$$m_A = -2.5\log_{10}\left(\frac{F_A}{F_{V,A}}\right), \tag{1.9}$$

où A correspond à une bande quelconque et $F_{V,A}$ au flux de l'étoile Véga dans cette bande.

Il est intéressant de remarquer que les DES des étoiles de faible masse et naines brunes correspondent à des spectres en absorption. On entend par là qu'elles sont formées par un continu[6] provenant de l'émission thermalisée[7] des couches atmosphériques internes et chaudes,

[5] L'absorption tellurique est principalement due à l'eau dans l'atmosphère terrestre.

[6] Ceci correspond à une émission variant très peu sur un grand domaine de longueurs d'onde.

[7] L'émission est dite thermalisée lorsque la lumière subit un grand nombre d'interactions permettant au gaz

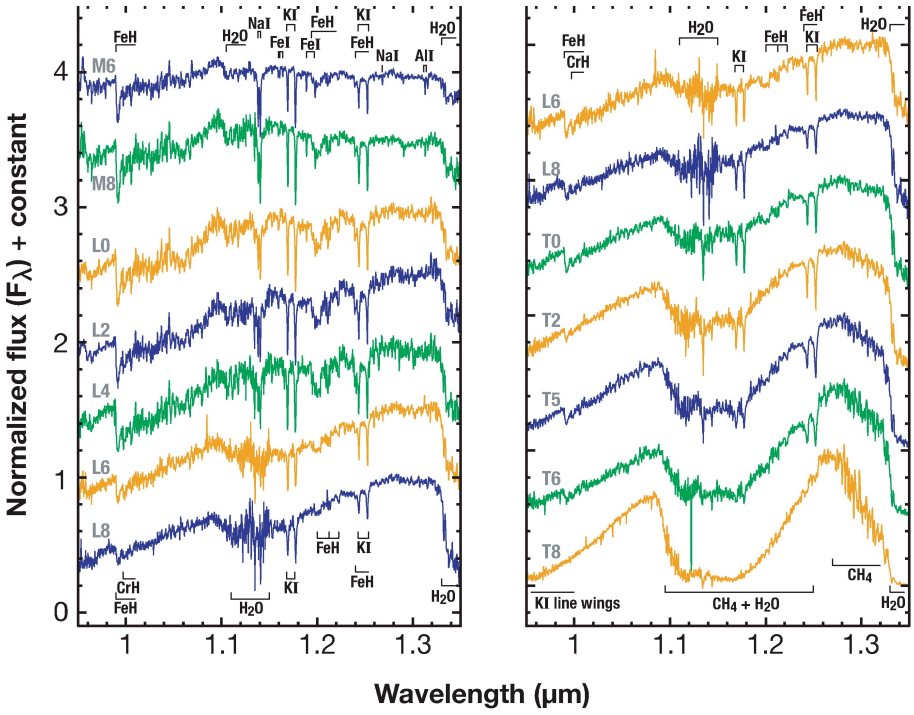

FIGURE 1.8 DES de la bande J en haute résolution pour les étoiles de faible masse et naines brunes de types spectraux M6 à T8. On voit la présence d'une grande quantité de raies d'absorption causées par le potassium, le sodium, le fer et l'aluminium. On remarque aussi qu'aux types spectraux $\geq$ T0, le méthane et l'eau scindent en deux la bande J. Figure tirée de Kirkpatrick (2005).

duquel plusieurs sources d'absorption localisée dans les couches atmosphériques externes et froides viennent retirer une partie du flux pour le redistribuer à différentes longueurs d'onde. Par exemple, les atomes absorbent la lumière à une série de longueurs d'ondes précises via leurs transitions électroniques, ce qui se solde par plusieurs raies d'absorption généralement très étroites (voir Figures 1.7 et 1.8).

Plusieurs phénomènes physiques peuvent contribuer à élargir les raies atomiques. Le plus fondamental correspond à l'élargissement naturel, décrit en mécanique quantique par la relation d'incertitude temps–énergie d'Heisenberg :

$$\sigma_t \sigma_E \geq \hbar \tag{1.10}$$

d'être à l'équilibre thermodynamique local, et donc d'émettre une DES de corps noir.

Ici, σ_t est la déviation standard de la durée des procédés d'émission, σ_E est la déviation standard associée à l'énergie de la transition associée à cette émission, puis $\hbar$ est la constante de Planck réduite. On voit que si les temps de vie typiques associés aux procédés d'émission sont petits, l'incertitude statistique sur l'énergie du photon émis ou absorbé par la transition électronique s'en trouve augmentée. Étant donné que les transitions électroniques ont une durée de vie finie, on comprend que la largeur des raies ainsi formées est non nulle. Un autre phénomène généralement plus important en astrophysique est l'élargissement par effet Doppler. Comme son nom l'indique, celui-ci est dû au fait que les particules du gaz observé possèdent une grande variété de vitesses le long de la ligne de visée de l'observateur. L'effet Doppler décrivant la relation entre la longueur d'onde émise par une source lumineuse et la vitesse de cette dernière s'écrit comme :

$$\lambda_m = \left(1 + \frac{\delta v}{c}\right)^{-1} \lambda_s \tag{1.11}$$

où λ_m est la longueur d'onde mesurée dans le référentiel d'un observateur, λ_s est la longueur d'onde émise dans le référentiel de la source et δv la différence de vitesses entre l'observateur et la source, le long de la droite qui les sépare. Les particules de masse m d'un gaz classique à une température T ont une distribution de vitesses d'une largeur de l'ordre de $\sqrt{k_B T/m}$: on peut donc voir que la largeur de la raie d'émission dépendra aussi de la température du gaz. Il est aussi à noter que la présence d'un champ magnétique affectera la largeur des raies d'absorption par l'effet Zeeman et la rotation stellaire élargira aussi les raies d'absorption par l'effet Doppler. À la Section 1.2.3, nous verrons qu'il existe d'autres phénomènes physiques contribuant à élargir les raies spectrales.

La présence de molécules dans l'atmosphère des naines brunes joue aussi un rôle important dans la formation de leur DES. Étant donné que les molécules possèdent une grande quantité de degrés de liberté incluant la rotation et la vibration, leur interaction avec la lumière s'en trouve plus riche et leur absorption est alors efficace sur un domaine de longueurs d'onde plus large. Par exemple, la molécule d'eau est responsable en grande partie des creux entre

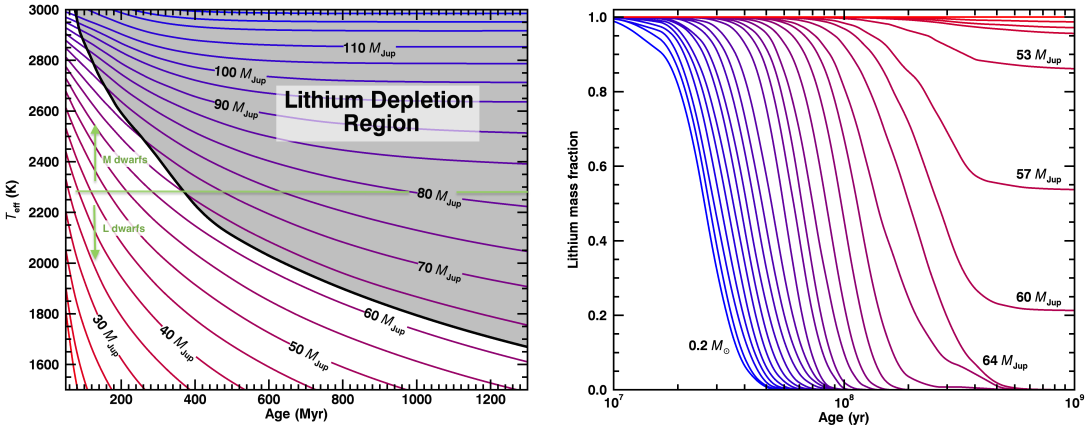

FIGURE 1.9 À gauche : Limite d'épuisement du lithium (LEL ; trait noir épais) en fonction de l'âge et de la température effective des objets, à laquelle sont superposées des courbes de masse constante. Si on détermine qu'une population stellaire d'un âge fixe présente du lithium seulement aux températures inférieures à 2400 K p.ex., alors on peut en tirer un âge de $\sim$350 Mans. On remarque aussi qu'un objet de moins de $\sim 60\,M_{\rm Jup}$ n'atteindra jamais la LEL. La présence ou l'absence de lithium dans l'atmosphère d'un objet de température connue permet aussi de poser une contrainte sur sa masse. Figure inspirée de Basri (1998). À droite : Évolution de la fraction de masse du lithium pour les étoiles de faible masse et naines brunes. On peut y voir que les naines brunes de $\sim$50–60 $M_{\rm Jup}$ détruiront une partie de leurs réserves de lithium, mais le brûlage cessera après $\sim$300 Mans.

les bandes J, H et K autour du type spectral L0 (voir Figure 1.7). Aux types spectraux plus tardifs, le méthane commence aussi à jouer un rôle important, par exemple en scindant en deux parties la bande J (voir Figure 1.8). Nous verrons aussi plus tard que l'absorption induite par collisions de la molécule H_2 joue un rôle important dans le modelage de la DES des naines brunes.

1.2 Les indicateurs d'âge des naines brunes et étoiles de faible masse

Dans cette section, nous décrirons les principaux observables permettant de poser des contraintes sur l'âge des étoiles. Nous déterminerons alors quelles méthodes seront applicables de façon efficace dans le régime des étoiles de faible masse et des naines brunes.

1.2.1 L'abondance du lithium

Le lithium est un élément présent dans l'univers à l'état de traces et ayant été créé en majeure partie sous forme d'isotopes ^{6}Li et ^{7}Li durant la nucléosynthèse primordiale immédiatement après le Big Bang. Une certaine quantité est aussi produite dans une moindre mesure par deux autres phénomènes : la décomposition radioactive d'éléments plus lourds tels que ^{7}Be et ^{10}Be, ainsi que la spallation, c'est-à-dire le bris d'atomes plus lourds, par interaction avec les rayons cosmiques à haute énergie. Le lithium fait partie des éléments qui sont créés par la fusion nucléaire au coeur des étoiles, mais il est aussitôt détruit à cause de la température très élevée de ce milieu. C'est effectivement un atome dont la température de fusion est très basse ($\approx 2.5 \times 10^{6}\,\mathrm{K}$), d'une façon semblable au deutérium. Ainsi, il ne survivra pas longtemps dans les objets de plus d'environ $60\,M_{\mathrm{Jup}}$, car ceux-ci atteindront les conditions nécessaires pour le brûler. On peut donc utiliser la présence des raies Li (6103 et 6707.8 Å ; Soderblom 2010) dans l'atmosphère d'une étoile ou d'une naine brune relativement massive comme un indicateur de jeunesse (voir Figure 1.9). De plus, à l'intérieur d'un certain intervalle de types spectraux, on peut aussi l'utiliser pour avoir une idée de la masse d'un objet. Par exemple, un objet de type spectral M9 d'environ 200 Mans aura une masse avoisinant les $60\,M_{\mathrm{Jup}}$, la limite permettant d'éliminer le lithium (Figure 1.9). La présence de lithium dans son atmosphère nous indiquera donc directement s'il est âgé de plus d'environ 200 Mans ou non. Habituellement, on utilise aussi le test de la *limite d'épuisement du lithium* (LEL) pour mesurer l'âge d'un groupe d'étoiles. Pour ce faire, on dresse une séquence en températures ou types spectraux pour le groupe en question et on détermine à partir de quelle température les objets montrent du lithium dans leur DES. En utilisant ensuite les modèles d'atmosphère pour déterminer cette LEL de façon théorique, on peut alors déterminer l'âge de la population en question (voir la Figure 1.9). Cette méthode a permis de déterminer l'âge de plusieurs amas ouverts et AJs (Soderblom et al. 1990, 1993c,b,a; Jeffries et al. 2013; Malo et al. 2014b; Kraus et al. 2014b; Mamajek & Bell 2014)

Cependant, il est important de noter qu'une détermination précise de la LEL est une tâche complexe présentant des subtilités que nous n'aborderons pas en détails. En effet, la présence de convection peut grandement accélérer la destruction du lithium en le transportant

de l'atmosphère vers les couches internes d'un objet suffisamment lourd pour le brûler. La rotation peut aussi créer des courants méridionaux, transportant le lithium plus efficacement vers le coeur (Pinsonneault 2010). En revanche, la présence d'un champ magnétique ou de rotation peut influencer la structure interne d'une étoile et diminuer sa température centrale. Ceci aura pour effet de déplacer la LEL vers les masses plus grandes (Opitz & Gallardo 2011). Il est donc crucial de construire des modèles théoriques complets incluant entre autres les effets des champs magnétiques, pour interpréter de façon précise la présence de lithium dans l'atmosphère des objets d'intérêt.

On remarque à la Figure 1.9 que plus un objet est froid, moins la mesure du lithium est un diagnostic efficace pour contraindre son âge. Par exemple, la présence de lithium dans un objet de 2300 K pose une contrainte à $\lesssim 400$ Mans sur son âge, tandis que la même mesure pour un objet de 1800 K pose une contrainte à $\lesssim 1$ Gan seulement. De surcroît, mesurer l'abondance de lithium d'une naine brune est une tâche généralement difficile. Celle-ci nécessite l'obtention d'un spectre à très haute résolution dans les longueurs d'onde visibles, un domaine où les naines brunes sont beaucoup moins brillantes. Le fait que l'on doive sacrifier l'intensité du signal lumineux pour obtenir une meilleure résolution en spectroscopie ajoute à l'ampleur de ce problème : il faudra investir une quantité de temps significative sur de grands télescopes pour effectuer cet type de mesure. C'est pour ces deux raisons que la mesure de lithium n'est pas un diagnostic d'âge très efficace pour les naines brunes, contrairement aux étoiles.

1.2.2 La rotation

Lorsqu'une étoile se forme par l'effondrement d'un fragment de nuage moléculaire, sa vitesse de rotation initiale se trouve amplifiée de façon à ce que le moment cinétique total soit conservé. Il existe cependant certains mécanismes pouvant ralentir ou même renverser cette accélération de la rotation. Par exemple, une étoile très jeune possédant un disque d'accrétion peut redistribuer une partie de son moment cinétique au disque à travers l'interaction entre son champ magnétique et le gaz chaud. Ce mécanisme, nommé verrouillage du disque ou *disk locking*, ralentit l'accélération de la vitesse de rotation durant les premiers ~ 10 Mans (Bodenheimer 1995). La vitesse de rotation est ensuite libre d'augmenter à mesure que s'opère la

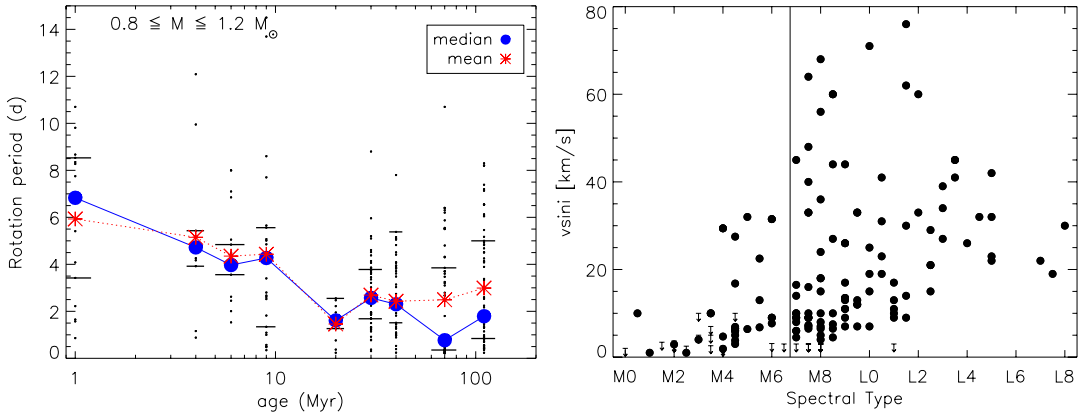

FIGURE 1.10 À gauche : Période de rotation en fonction de l'âge pour les étoiles membres d'AJs. On peut voir qu'à mesure que les objets se contractent, la rotation s'accélère par conservation du moment d'inertie. Après plusieurs dizaines de Mans, le mécanisme de freinage magnétique domine et la vitesse de rotation commence alors à se stabiliser et à décroître. Figure tirée de Messina et al. (2011). À droite : Vitesse de rotation des étoiles de faible masse et naines brunes du champ en fonction du type spectral. On remarque que la dispersion augmente considérablement à partir du type spectral M7. Ceci est dû en partie à l'atmosphère devenue trop froide pour que le freinage magnétique s'effectue de façon efficace. Figure tirée de McLean et al. (2012).

contraction gravitationnelle, jusqu'à ce qu'un autre mécanisme prenne le dessus après environ ~ 100 Mans. C'est alors le vent stellaire, constitué de particules ionisées, qui peut dérober une partie du moment cinétique de son étoile par son interaction avec le champ magnétique. Ce mécanisme se nomme le freinage par le vent stellaire, ou *wind braking* (voir Figure 1.10 et Messina et al. 2011).

Dans le cas des naines brunes, l'évolution temporelle de la vitesse de rotation obéit aux mêmes principes, avec l'exception que le freinage par le vent stellaire est beaucoup moins efficace. La raison pour cela est que le couplage entre le champ magnétique et l'atmosphère des naines brunes est beaucoup plus faible. Pour la même raison, on ne s'attend pas à observer des éjections de masse significatives par les naines brunes ; celles-ci n'interagiraient de toute façon que très peu avec son champ magnétique dû à leur température trop basse. Les naines brunes à l'âge du champ posséderont donc une vitesse de rotation significativement plus élevée que les étoiles du même âge. Cet effet a effectivement été mesuré par (Zapatero Osorio et al. 2006 ; voir Figure 1.10). Dans le cas des naines brunes jeunes, l'observation d'une large gamme de vitesses

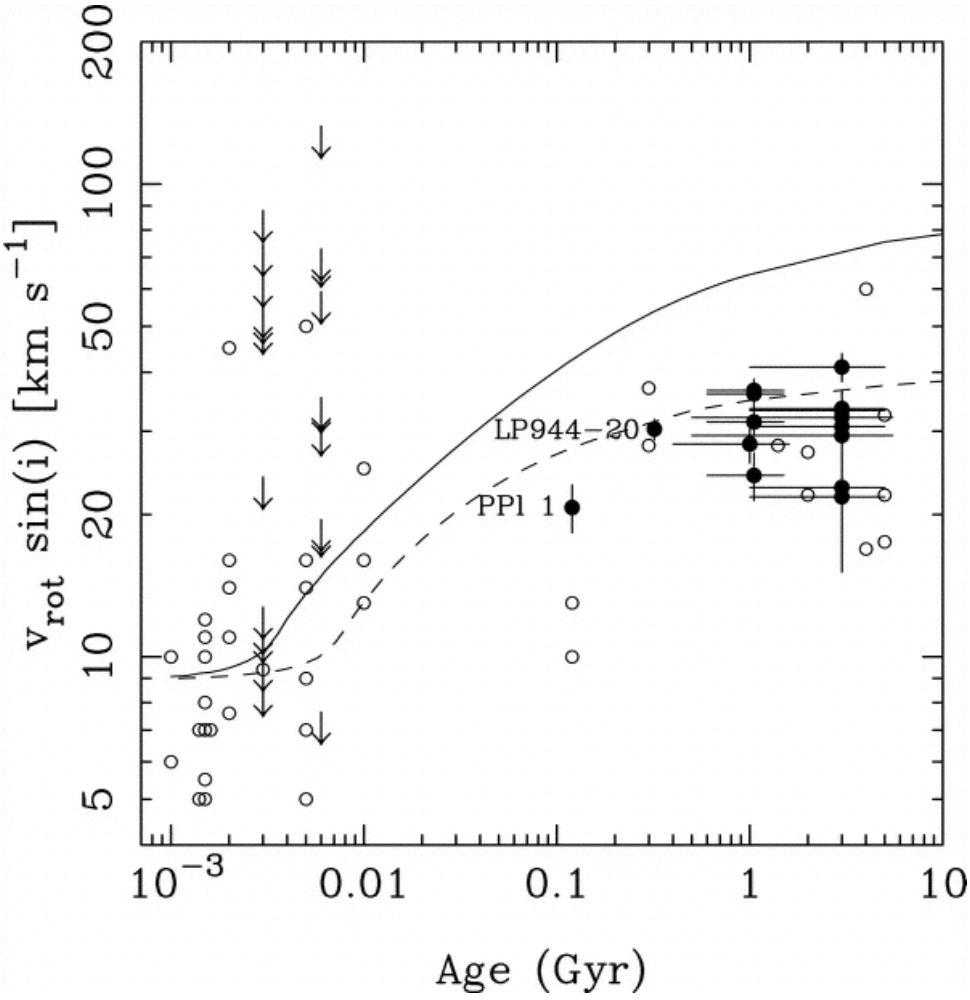

FIGURE 1.11 Évolution temporelle de la vitesse de rotation des naines brunes du champ. Les flèches pointant vers le bas représentent des limites supérieures. Les cercles noirs proviennent de Zapatero Osorio et al. (2006) et les cercles blancs proviennent de sources additionelles dans la littérature. Les traits solide et pointillé représentent les courbes théoriques d'évolution pour une naine brune de 30 et 70 $M_{\rm Jup}$, respectivement. On remarque une tendance similaire aux étoiles où la rotation accélère à mesure que la contraction gravitationnelle s'effectue, cependant certaines naines brunes jeunes ont une vitesse de rotation aussi élevée que les naines brunes de plusieurs Gans, pour une raison encore mal comprise. On remarque aussi que, contrairement aux étoiles, le freinage magnétique ne ralentit pas la rotation des naines brunes entre $\sim$100–600 Mans. Figure tirée de Zapatero Osorio et al. (2006).

de rotation (voir Figure 1.11) nous indique qu'il existe à la fois des mécanismes de freinage, en plus de cas particuliers où la vitesse de rotation est beaucoup plus élevée qu'attendu. Ces mécanismes sont encore mal compris, en particulier dans le cas des naines brunes jeunes à très haute vitesse de rotation. Pour les autres, il est probable que le freinage magnétique soit plus efficace à ce moment étant donné qu'elles sont plus chaudes de par leur formation récente. Une autre possibilité serait qu'elles possèdent à ce moment une chromosphère beaucoup plus chaude que leur atmosphère, de façon similaire au Soleil.

Comme on peut le voir à la Figure 1.11, une naine brune à grande vitesse de rotation pourrait donc aussi bien avoir quelques Mans ou plusieurs Gans. Nous pouvons en conclure que la vitesse de rotation n'est pas un diagnostic d'âge efficace pour les naines brunes, contrairement aux étoiles. L'intensité de l'activité magnétique est souvent utilisée comme indicateur de jeunesse dans le cas des étoiles. Cette méthode est efficace étant donné que la rotation est le moteur de l'effet dynamo qui maintient le champ magnétique des étoiles et des naines brunes. Cependant, la mesure de l'activité magnétique ne sera pas un bon indicateur de jeunesse pour les naines brunes, étant donné que la rotation n'est pas bien corrélée avec l'âge pour celles-ci.

1.2.3 La gravité de surface

Comme nous l'avons mentionné plus tôt, une naine brune relativement jeune n'a pas achevé sa contraction gravitationnelle. Conséquemment, son rayon est jusqu'à environ 3 fois plus grand qu'une naine brune vieille de la même masse (Burrows et al. 2001). En d'autres mots, la gravité de surface d'une naine brune jeune augmentera graduellement jusqu'à ce que celle-ci atteigne son rayon final après ~ 150 Mans. Ainsi, la mesure de la gravité de surface peut fournir une information précieuse quant à l'âge d'une naine brune. La gravité de surface affecte directement la pression atmosphérique d'une naine brune, laquelle a des répercussions directes sur sa DES. D'ailleurs, Kirkpatrick (2005), Kirkpatrick et al. (2006) et Cruz et al. (2009) ont introduit les suffixes α, β, γ et δ qu'ils ajoutent aux types spectraux des naines brunes jeunes pour différencier celles, plus âgées, du champ (sans suffixe, ou avec le suffixe α) à celles montrant les signes de faible gravité les plus marqués (δ).

Une des conséquences de la pression atmosphérique plus basse chez les naines brunes jeunes

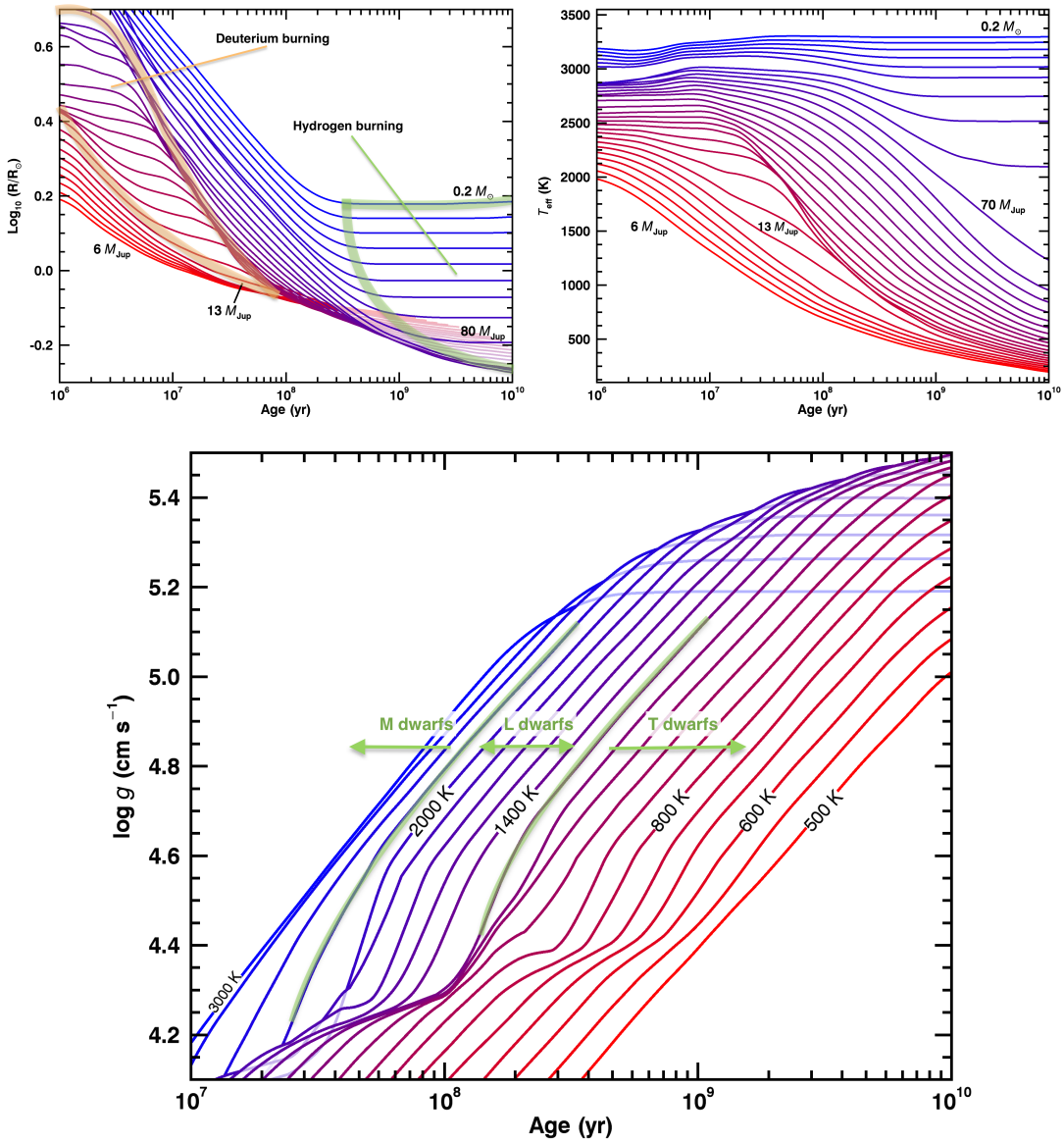

FIGURE 1.12 En haut à gauche : Évolution temporelle du rayon des étoiles de faible masse et naines brunes. On peut voir que la phase de contraction gravitationnelle se poursuit de façon significative jusqu'à quelques centaines de Mans, selon la masse de l'objet. On remarque que les phases de brûlage du deutérium (orange) et de l'hydrogène (vert) ont pour effet de stabiliser de le rayon de ces objets. En haut à droite : Évolution temporelle de la température effective des étoiles de faible masse et naines brunes. Les étoiles entretiennent une température stable une fois qu'elles atteignent la séquence principale, cependant les naines brunes se refroidissent continuellement avec le temps. En bas : Évolution temporelle de la gravité de surface des étoiles de faible masse et naines brunes de températures fixes. Les deux effets expliqués ci-haut contribuent à diminuer la gravité de surface des objets jeunes à une température donnée. Par exemple, une naine brune jeune de type spectral L sera moins massive et aura un rayon plus grand qu'une naine brune plus vieille du même type spectral. Ces figures ont été construites à partir des modèles d'évolution AMES-Cond (Baraffe et al. 2003).

est reliée à l'importance de l'absorption induite par collisions (AIC) de la molécule H_2. L'AIC se produit lorsque des molécules possédant un moment dipolaire suffisamment grand entrent fréquemment en collision inélastique. Cet effet prend donc place dans les gaz relativement denses. En effet, un ensemble de molécules peut agir de façon instantanée comme une super-molécule, laquelle possède des niveaux d'énergie différents des molécules individuelles. Ainsi, ce comportement collectif permet aux molécules d'un gaz d'absorber ou d'émettre la lumière à des longueurs d'onde différentes que les composantes individuelles du gaz ne le permettraient normalement. En l'absence d'AIC, la bande H d'une naine brune est majoritairement sculptée par l'absorption de la molécule H_2O, ce qui lui donne une forme triangulaire distinctive. Dans le cas des naines brunes plus vieilles, où la pression atmosphérique est plus grande, l'AIC de la molécule H_2 devient importante et vient aplatir la bande H, qui n'est alors plus triangulaire. Ainsi, une bande H de forme triangulaire est un signe typique de faible gravité (et donc de jeunesse) chez les naines brunes (Figure 1.13). La bande K est aussi affectée par l'AIC de la molécule H_2, cependant cet effet est plus subtil (Canty et al. 2013; Allers & Liu 2013).

Une deuxième conséquence importante de la pression atmosphérique plus basse chez les objets jeunes correspond à une diminution de la largeur équivalente des raies d'absorption de plusieurs espèces chimiques (voir Figures 1.14 et 1.15). La largeur équivalente est une méthode permettant de mesurer l'importance d'une raie d'absorption ou d'émission par rapport au niveau du continu ; plus une raie est large ou profonde, plus sa largeur équivalente est grande. Cette quantité correspond en fait à la largeur qu'une portion du continu devrait prendre pour couvrir la même *aire*[8] que la raie d'absorption. Le phénomène physique derrière cette variation de la largeur équivalente en fonction de la pression locale est appelé l'élargissement par la pression[9]. On peut dénombrer deux causes à ce phénomène. La première, l'élargissement dû aux impacts, est reliée au fait qu'à chaque impact entre deux particules, les niveaux d'excitation de leurs électrons sont affectés de façon abrupte. Ceci a pour effet d'interrompre les procédés d'émission en cours ce qui, en moyenne, diminuera le temps de vie des états excités. Souvenons-nous maintenant de la relation d'incertitude temps-énergie d'Heisenberg (Équation 1.10) ; si le temps de vie typique des transitions électroniques est diminué, l'incertitude

[8] On parle ici d'une aire dans le plan longueurs d'onde–flux.
[9] En anglais, on l'appelle *pressure broadening*.

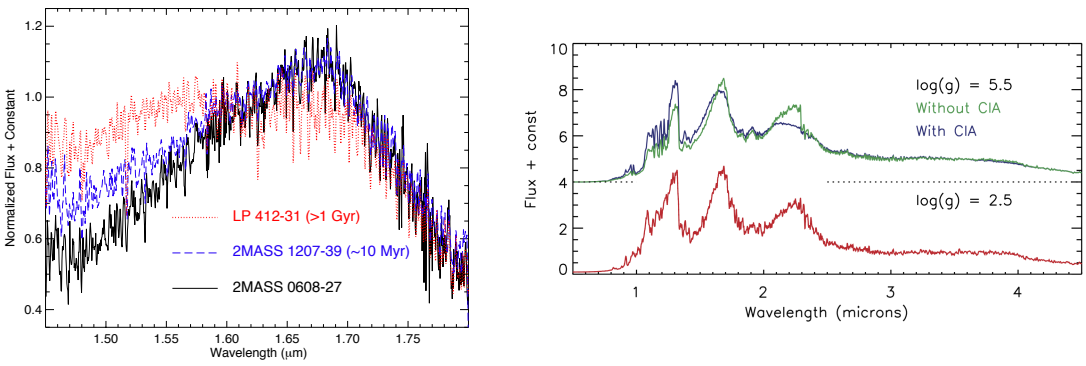

(a) Forme du *continu* en bande H

(b) Effets de l'AIC sur le *continu*

FIGURE 1.13 À gauche : Démonstration empirique de la forme triangulaire de la bande H des naines brunes jeunes. On y montre 2MASS J0608–27 (20–40 Mans) et 2MASS J1207–39 (5–15 Mans), des membres confirmés des associations β Pictoris et TW Hydrae respectivement, puis un objet à l'âge du champ (LP 412–31). Figure tirée de Rice et al. (2010). À droite : DES synthétiques pour un objet de type spectral M8 à deux gravités de surface (traits rouge et bleu), puis à haute gravité de surface, mais en ignorant artificiellement les effets de l'AIC (trait vert). On peut voir que la bande H est triangulaire en l'absence de l'AIC, peu importe la gravité de surface. La forme triangulaire de la bande H est causée par l'absorption de la molécule d'eau. C'est l'AIC de la molécule H_2 qui vient aplatir la bande H lorsque la gravité de surface est suffisamment élevée pour que l'AIC devienne plus efficace. Figure tirée de Rice et al. (2011).

statistique sur l'énergie associée à cette interaction s'en trouvera augmentée. On peut donc imaginer que la raie d'absorption observée est le résultat de la combinaison d'un grand nombre de raies très minces, mais dont la position de chacune diffère d'une quantité de l'ordre de :

$$\sigma_\lambda = \frac{hc}{\sigma_E}. \tag{1.12}$$

Il en résulte donc un élargissement de la raie. Le deuxième phénomène, qu'on appelle l'élargissement quasi statique, est dû au fait que la présence de particules environnantes perturbe les niveaux d'énergie d'une particule, et donc encore une fois la longueur d'onde précise associée au procédé d'absorption ou d'émission donnant lieu à une raie spectrale. Ceci entraînera un élargissement et un léger déplacement de la raie en question. Les espèces chimiques dont les raies d'absorption sont les plus fortement affectées par la gravité de surface sont : Na I (0.8183, 0.8195, 1.13 et 1.14 μm), K I (0.7665, 0.7699, 1.17 et 1.24 μm), FeH (0.8692, 0.98 et

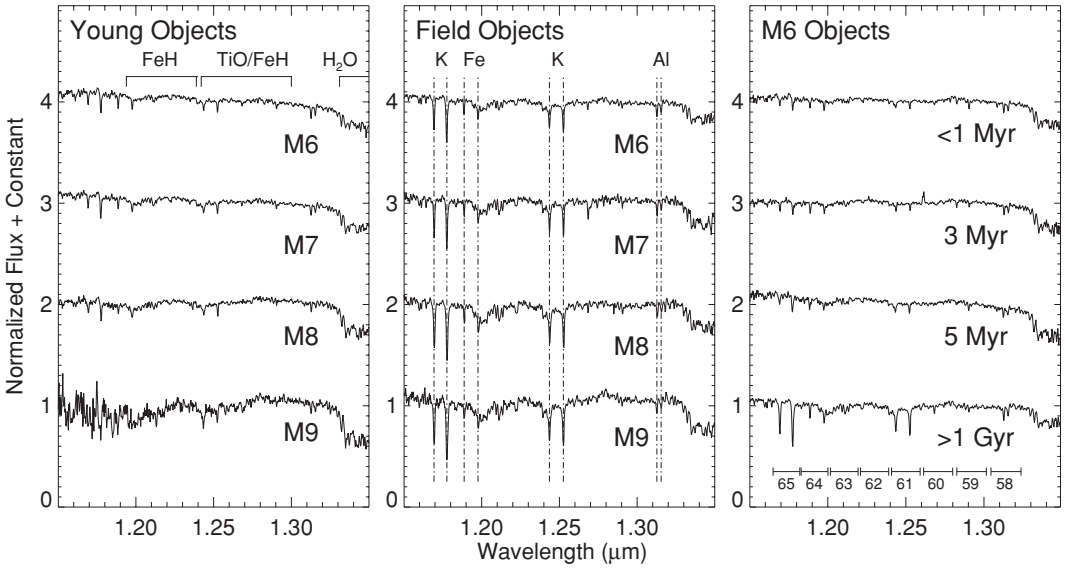

FIGURE 1.14 Raies d'absorption de divers éléments en spectroscopie infrarouge en fonction de l'âge des objets. On voit que pour des objets jeunes, les raies du potassium et du fer sont significativement moins profondes. Figure tirée de Rice et al. (2010).

1.19 μm), TiO (0.8432 μm) et CrH (0.8611 μm ; Cruz et al. 2009). Étant donné que la largeur équivalente de ces raies dépend aussi fortement de la température d'un objet, il est nécessaire de construire une séquence pour chacune de ces espèces chimiques en fonction de la température (ou du type spectral) des objets à plusieurs âges caractéristiques (voir Figure 1.15). Ainsi, lorsqu'un objet montre des raies d'absorption très faibles à un type spectral donné, on peut en déduire que sa gravité de surface est plus faible que la normale.

Il est aussi à noter que les bandes d'absorption de la molécule VO (0.730–0.755, 0.785–0.800 et 1.05 μm) sont plus fortes dans les objets jeunes. On peut voir cet effet à la Figure 1.16 dans le cas de la raie à 1.05 μm. On associe ce phénomène à la présence de condensats épais plus haut dans leur haute atmosphère, une autre conséquence de la pression atmosphérique plus faible (Allers et al. 2007). Les grains de poussière formés dans les atmosphères à basse pression sont aussi de plus grande taille–ces deux effets ont pour conséquence de déplacer le flux lumineux provenant des longueurs d'onde proche-infrarouges ($\approx$ 1–3 μm) à des longueurs d'onde plus grandes ($\gtrsim$ 5 μm ; Faherty et al. 2012, 2013b; Liu et al. 2013b, J. K. Faherty et al., en préparation). Nous verrons à la prochaine section les conséquences de cette caractérisique sur les couleurs photométriques et la magnitude absolue des naines brunes jeunes.

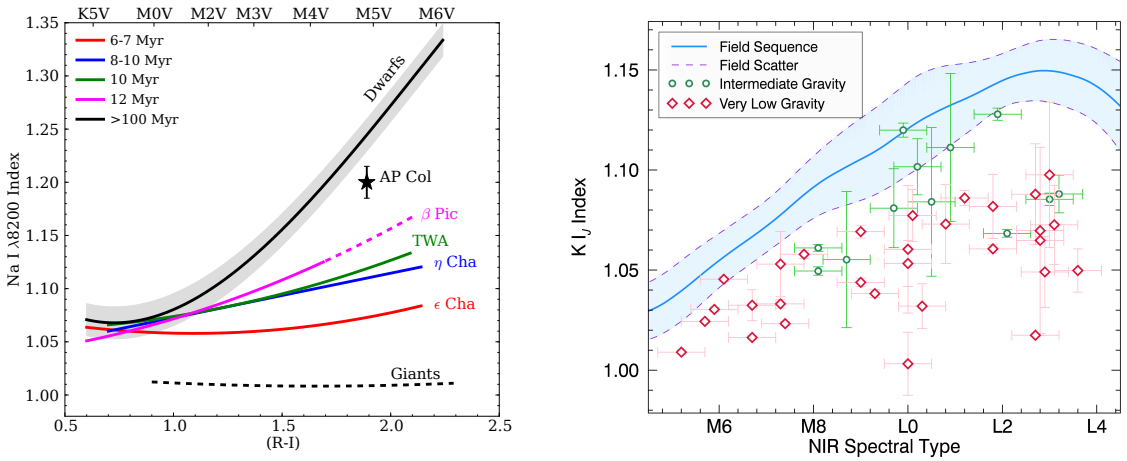

(a) Absorption due au Sodium

(b) Absorption due au Potassium

FIGURE 1.15 À gauche : Largeur équivalente de la raie d'absorption du Na I dans la lumière visible, pour les objets du champ et ceux de plusieurs AJs. On y montre également la séquence d'étoiles géantes rouges, dont la gravité de surface est encore plus faible que celles des étoiles jeunes. L'étoile AP Col montrée sur la figure a été proposée comme membre de l'association Argus. Figure tirée de Riedel et al. (2014). À droite : Indice spectral sensible à la largeur équivalente de l'atome neutre K I dans l'infrarouge, pour les objets du champ (trait bleu et région bleue pâle), à gravité de surface intermédiaire (cercles verts) et à gravité de surface très faible (losanges rouges). Figure tirée de Allers & Liu (2013).

1.2.4 Les séquences couleur–magnitude

Nous avons mentionné précédemment que les naines brunes jeunes possèdent un rayon jusqu'à 3 fois plus grand que celui des naines brunes à l'âge du champ, n'ayant pas encore complété leur contraction gravitationnelle. Il en résulte que le flux observé à une distance fixe devrait être jusqu'à 9 fois plus élevé que pour une naine brune vieille à la même température. Il est donc tentant de construire un diagramme couleur–magnitude absolue[10] pour identifier les objets jeunes qui devraient se trouver au-dessus de la séquence des objets vieux. Étant donné que la couleur dépend directement de la température d'un objet[11] et non de son rayon, cela mettra directement en évidence les objets les plus brillants à une température donnée. Il s'est avéré que cette méthode fonctionne relativement bien, mais pas pour cette raison ! Il a fallu attendre jusqu'à très récemment pour avoir à notre disposition les mesures

[10] La magnitude absolue est définie comme la magnitude pour un observateur à une distance de 10 pc.

[11] Les objets les plus froids montrent des couleurs généralement plus rouges dans les longueurs d'onde proche-infrarouges.

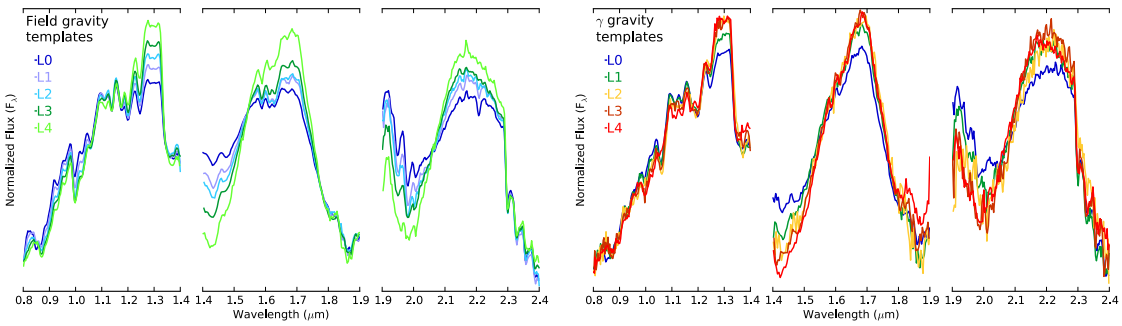

FIGURE 1.16 Séquence de naines brunes du champ (gauche) et jeunes (droite) aux types spectraux L0–L4. On remarque que la pente en bande J (0.8–1.4 μm) des naines brunes jeunes est plus accentuée et sculptée par des raies d'absorption moins profondes. La bande H (1.4–1.8 μm) est quand à elle plus triangulaire chez les naines brunes jeunes. La seule bande d'absorption moléculaire étant plus forte dans le cas des naines brunes jeunes est celle due à la molécule VO à 1.06 μm (ne pas confondre avec la raie due à la molécule FeH à 1.0 μm). Ces caractéristiques sont expliquées par une pression atmosphérique plus basse, des nuages plus épais et une plus grande quantité de condensats de la molécule VO en haute atmosphère, tous ces effets découlant à leur tour d'une masse plus petite et d'un rayon plus grand à un type spectral fixe. Figures tirées de Kelle L. Cruz et al. (en préparation).

de distances trigonométriques pour un ensemble complet de naines brunes de différents âges. À la Figure 1.17, on peut voir une séquence type spectral–magnitude absolue, construite en utilisant uniquement des mesures de distance trigonométriques et donc fiables. On peut y voir que, contrairement à ce qui était attendu, les objets plus jeunes de types spectraux L ne sont pas plus brillants dans la bande spectrale considérée ! La tendance va même jusqu'à se renverser aux types spectraux $\geq$ L4.

Par contre, on voit aux Figures 1.17 et 1.18 que les naines brunes jeunes sont beaucoup plus rouges que la séquence du champ à un type spectral fixe. On interprète ces données comme la conséquence d'une quantité de poussière beaucoup plus grande dans l'atmosphère des objets jeunes (Faherty et al. 2012), comme il a été démontré pour les exoplanètes géantes gazeuses HR 8799 b et c (Currie et al. 2011). Ceci aurait pour effet de masquer les couches internes plus chaudes, ce qui viendrait diminuer la luminosité pour compenser le rayon plus grand. Pour la même raison cependant, la DES s'en trouve plus rouge. On comprend donc que l'utilisation d'un diagramme couleur–magnitude absolue est finalement justifiée pour repérer les objets jeunes, étant donné que le déplacement d'une séquence vieille vers le haut ou vers la

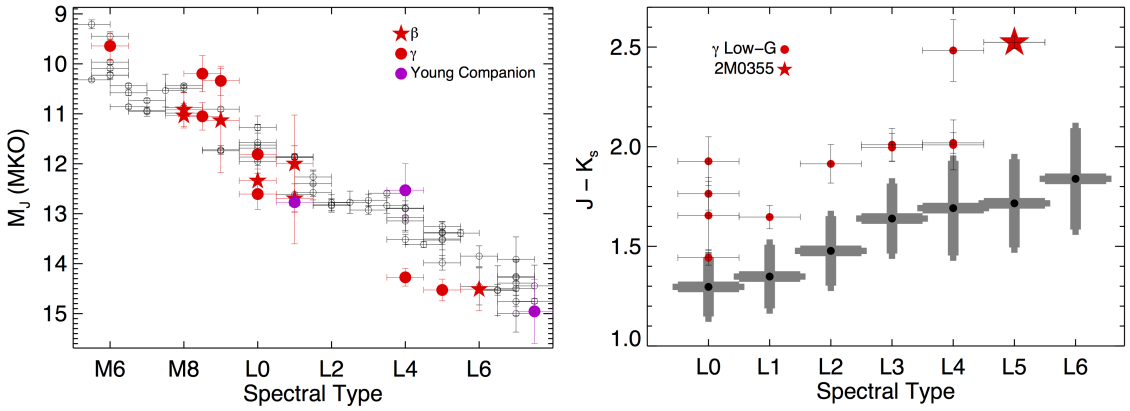

FIGURE 1.17 À gauche : Séquence magnitude absolue–type spectral pour des objets à l'âge du champ (noir) et des objets jeunes avec mesures de distance trigonométrique (rouge et mauve). On voit que les objets jeunes de types spectraux L ne sont pas systématiquement plus brillants que la séquence du champ. À droite : Séquences couleur–type spectral pour des objets du champ (noir) et des objets à faible gravité de surface et donc jeunes (rouges). On voit bien la tendance des objets plus jeunes à démontrer des couleurs plus rouges dans les longueurs d'onde proche-infrarouges. Figures tirées de Faherty et al. (2012).

droite aura la même conséquence. Il faudra cependant en tenir compte si on souhaite estimer le type spectral d'un objet à partir de ses couleurs. Il est à noter que par définition de la température effective, une naine brune vieille aura une luminosité totale plus faible qu'une naine brune jeune à la même température puisque le rayon de cette dernière est plus grand. Cependant, il faudra considérer une gamme de longueurs d'onde plus large (p.ex. couvrant ≈ 0.8–$10\,\mu$m) pour observer cet effet puisque les condensats atmosphériques de la naine brune jeune redirigent une partie du flux aux longueurs d'onde $\gtrsim 5\,\mu$m.

1.3 Les associations cinématiques jeunes

1.3.1 Caractéristiques

L'une des principales caractéristiques des AJs est le fait que leurs membres possèdent des positions galactiques et des vitesses spatiales semblables. La raison pour cela est qu'ils se seraient formés récemment au sein d'un même nuage moléculaire, lequel commence tout juste à se disperser dans l'espace dû aux interactions avec son environnement (Zuckerman & Song 2004). La vitesse spatiale UVW d'une étoile est celle mesurée dans un système de

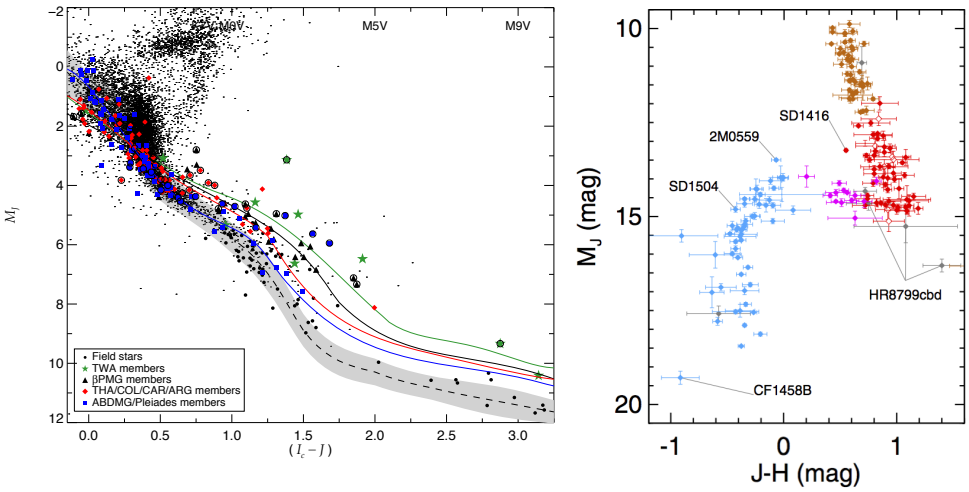

FIGURE 1.18 À gauche : Séquence couleur–magnitude absolue pour les étoiles du champ et les membres d'AJs faisant intervenir les bandes I_C (0.8 μm) et J (1.2 μm). On remarque que les objets jeunes sont plus lumineux que la séquence du champ, ceci étant dû à leur rayon plus grand. Figure tirée de Malo et al. (2013). À droite : Séquence couleur-magnitude pour des objets du champ de types spectraux M (orange), L (rouge) et T (bleu). Les points roses représentent les objets à la transition L/T. Les planètes géantes du système jeune HR 8799 bcd sont indiquées en gris. Elles sont rouges et sous-lumineuses par rapport aux naines brunes à l'âge du champ : ceci est dû à leur gravité de surface plus faible permettant à des nuages de poussière plus épais de se former dans leur haute atmosphère. Figure tirée de Dupuy & Liu (2012).

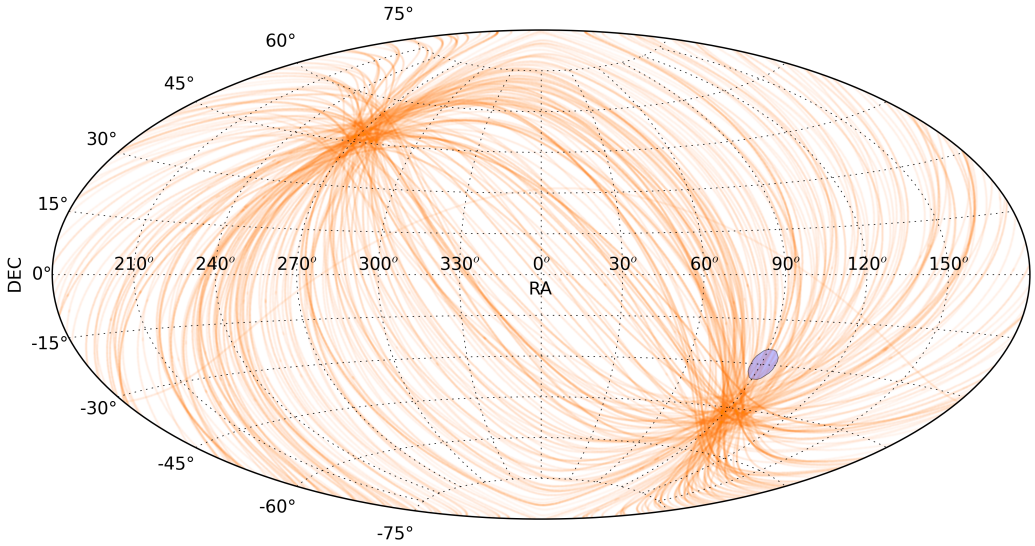

(a) AB Doradus

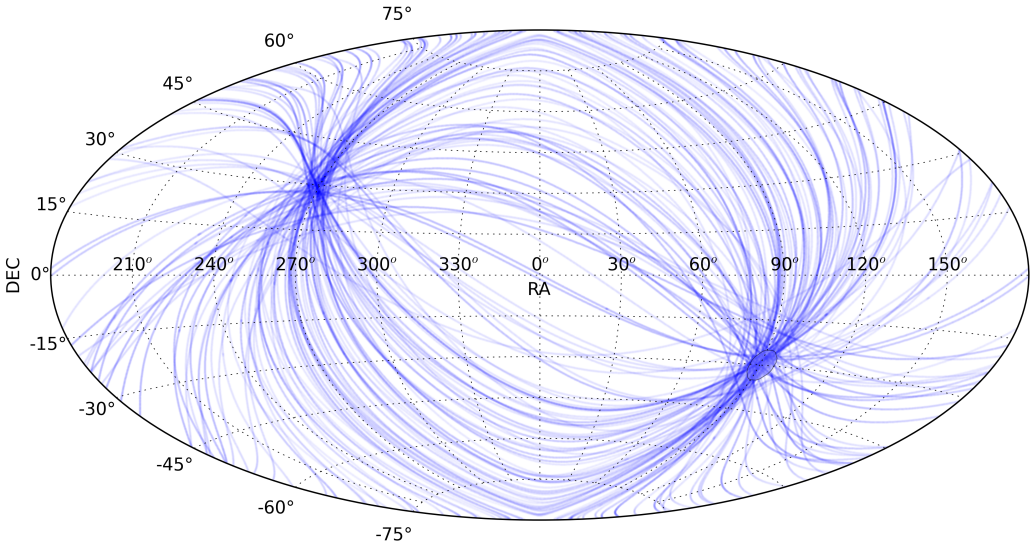

(b) β Pictoris

FIGURE 1.19 Distribution des grands cercles tracés par la direction du mouvement propre des membres des AJs AB Doradus (orange) et β Pictoris (bleu) sur la Sphère céleste. On peut voir la tendance qu'ont les membres d'une association cinématique à pointer vers un point commun appellé l'apex. Ainsi, un membre qui serait situé vis-à-vis l'apex de l'association aurait une vélocité pointant exactement dans la direction opposée à nous. Les cercles bleus marquent la position de l'apex solaire, c'est-à-dire la direction vers laquelle pointe la vélocité du Soleil. Figures construites par Adric R. Riedel (voir Riedel 2012b).

coordonnées cartésien, dont les directions U, V et W pointent respectivement vers le centre de la Voie Lactée, dans le sens de sa rotation[12], et vers le pôle Nord galactique[13] (Johnson & Soderblom 1987). La position galactique XYZ d'une étoile correspond quant à elle à sa coordonnée dans un système cartésien dont l'origine est le Soleil et les axes sont alignés avec ceux du référentiel UVW (Torres et al. 2008). Il est donc possible de convertir l'ensemble des coordonnées $XYZUVW$ d'une étoile en coordonnées célestes (ascension droite et déclinaison), mouvement propre, vitesse radiale[14] et distance, et vice-versa (Johnson & Soderblom 1987).

En raison de leur proximité au Soleil, les AJs étudiées ici ne sont pas regroupées dans de petites régions sur la Sphère céleste. Effectivement, les membres des AJs du voisinage solaire sont éparpillés un peu partout à travers le ciel. L'effet de projection de leurs vitesses spatiales similaires sur la Sphère donne lieu à un phénomène de convergence des mouvements propres vers un point appelé l'apex (Figure 1.19). Cette proximité rend beaucoup plus difficile l'identification de membres d'AJs dans le voisinage solaire. La recherche de nouveaux membres est d'autant plus difficile étant donné qu'elle nécessite la mesure de la vitesse radiale et la distance de chacun, deux quantités dont la mesure est coûteuse en temps de télescope. De plus, il est généralement accepté qu'avant de déterminer qu'un objet est membre d'une AJ, il est nécessaire de montrer qu'il possède des signes de jeunesse en plus d'une cinématique cohérente avec l'AJ. Ceci est nécessaire à cause du fait que les objets du champ ont une distribution de coordonnées UVW beaucoup plus étendue que les membres d'AJs et recouvrant entièrement leur intervalle de paramètres. Ainsi, d'une façon statistique il y aura une certaine quantité d'objets du champ qui auront une cinématique similaire à chacune des AJs par pure coïncidence, sans que ceux-ci ne soient de réels membres (Zuckerman & Song 2004).

L'identification d'une majeure partie des AJs a suivi de près la sortie du catalogue *HIgh Precision PARallax COllecting Satellite* (Hipparcos) en 1993 (Perryman et al. 1997), fournissant la distance trigonométrique de plus de 100 000 étoiles jusqu'aux magnitudes $V \sim 12.5$[15]. Ainsi, en utilisant des catalogues de vitesse radiale tels que GCRV (Wilson 1953), il devenait

[12] Si on regarde la Voie Lactée du haut du pôle Nord galactique, elle tourne dans le sens anti-horaire. On choisit U, V et W de façon à ce qu'ils soient en moyenne nuls pour les objets du voisinage solaire, ce qui correspond au référentiel cinématique au repos local, ou le *kinematic local standard of rest*.

[13] Le Nord terrestre pointe vers l'hémisphère Nord galactique.

[14] La vitesse radiale correspond à la vitesse d'un objet le long de notre ligne de visée.

[15] Correspond approximativement à la magnitude limite pour un télescope amateur de 10 cm.

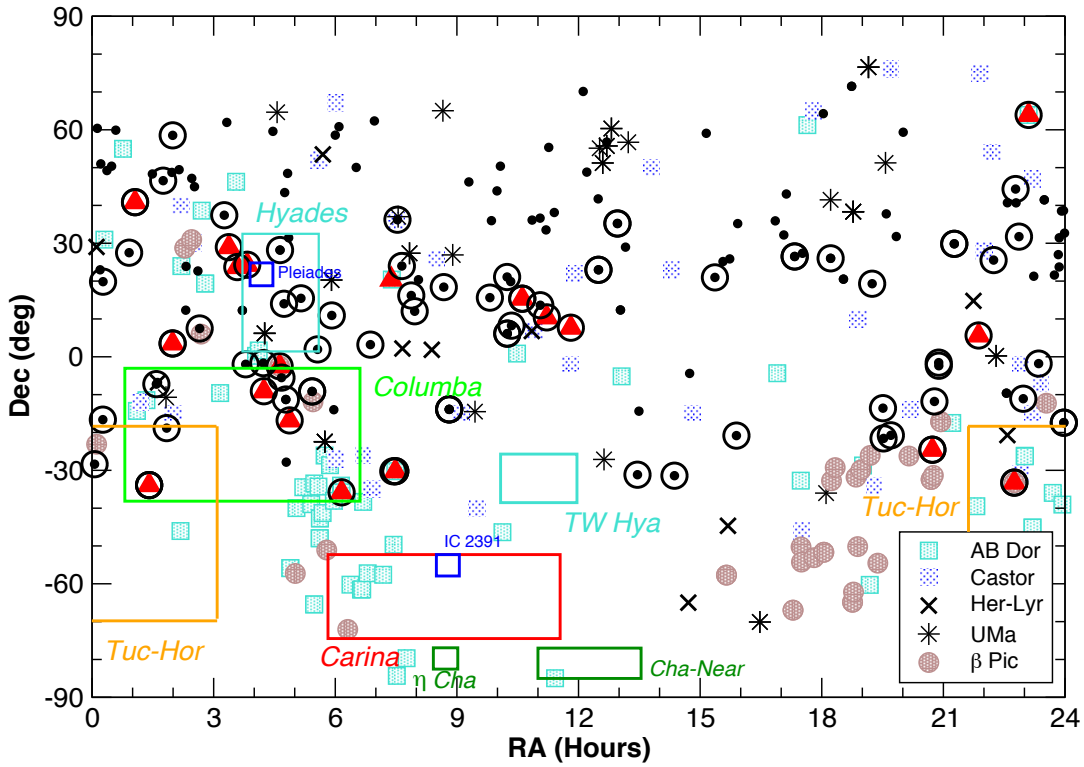

FIGURE 1.20 Distribution des membres d'AJs sur la Sphère céleste. Celles plus éloignés et dont l'étendue angulaire est moindre sont identifiées par des régions rectangulaires. Les points noirs et les triangles rouges correspondent à des candidates membres des associations AB Doradus, β Pictoris, Ursa Major et Hercules-Lyrae et du courant cinématique Castor identifiées par Shkolnik et al. (2012). Figure tirée de Shkolnik et al. (2012).

possible de calculer les coordonnées UVW pour un grand ensemble d'étoiles. C'est en faisant cela que l'on s'est rendu compte que plusieurs étoiles jeunes possèdent des positions galactiques et vitesses spatiales très rapprochées, bien qu'elles soient éloignées sur la Sphère céleste. Étant donné qu'Hipparcos se limite aux étoiles les plus brillantes, les premiers membres d'AJs identifiés correspondent à des étoiles de types spectraux $\leq$ K0 ($\gtrsim 0.8\,M_{\odot}$). Ce domaine d'étude est extrêmement actif et nous continuons aujourd'hui à découvrir de nouvelles AJs (Table 1.2).

1.3.2 Les associations jeunes connues

Dans la Table 1.2, nous présentons un recueil des AJs connues à l'intérieur de 100 pc. À la Figure 1.20, nous présentons la distribution céleste de la plupart de celles-ci. Ensuite, nous présentons à la Figure 1.21 la distribution de ces associations en termes de coordonnées

galactiques. Il a été démontré que les associations cinématiques Castor (Barrado y Navascués et al. 1998), Pléïades (ou l'Association Locale), Hyades et Sirius (parfois qualifiées de super amas) sont composées de membres de compositions et d'âges hétérogènes. Ces trois dernières sont à ne pas confondre avec les amas des Pléïades, des Hyades et Sirius. Il est probable que les associations cinématiques mentionnées plus tôt soient des courants cinématiques ne permettant pas de poser une contrainte sur l'âge de leurs membres (Famaey et al. 2008; Mamajek et al. 2013). Pour cette raison, celles-ci ne sont pas pas inclus dans la Table 1.2.

1.4 Description du projet et de la stratégie adoptée

Le projet entrepris ici consiste en la recherche de nouvelles naines brunes et étoiles de faible masse jeunes membres d'AJs. Comme nous l'avons mentionné plus tôt, la plupart des membres d'AJs connus à ce jour sont des étoiles relativement massives ($\gtrsim 0.5\,M_{\odot}$). Ainsi, leurs types spectraux sont généralement $\lesssim$M0, bien que plusieurs équipes aient entrepris d'identifier les membres de types spectraux M0–M6 au cours des dernières années (Malo et al. 2013; Shkolnik et al. 2012; Schlieder et al. 2010, 2012a,b; Rodriguez et al. 2011, 2013; Moór et al. 2013; Murphy & Lawson 2015; Kraus et al. 2014b; Riedel et al. 2014, 2011; Malo et al. 2014a). Nous nous concentrerons dans ce projet sur l'identification d'objets de types spectraux $\geq$M5.

1.4.1 Buts

La recherche de naines brunes jeunes est un domaine en pleine effervescence ; plusieurs équipes à travers le monde y participent activement et notre perception des problèmes rencontrés évolue rapidement. Il y a deux principales raisons expliquant l'évolution rapide de ce domaine. Premièrement, la technologie en place ne nous permet d'étudier les naines brunes jeunes que depuis très récemment. Ensuite, les objectifs scientifiques encourus sont multiples et de grande importance en astrophysique. Parmi ceux-ci, on compte :

- La complétion de la population de faible masse des AJs qui servira à étudier la FMI dans différents environnements.
- La compréhension des mécanismes de formation de naines brunes et exoplanètes. En

Table 1.2. Liste des associations jeunes à l'intérieur de 100 pc

Nom	Âge (Myr)	Distance (pc)	Références
HD 141569	2–8	93–112	1
η Chamaeleontis[a]	2–18	93–100	2, 3, 4, 5
ϵ Chamaeleontis[b]	2–18	93–123	3, 4, 5, 6, 7, 8, 9
TW Hydrae	5–15	40–62	3, 5, 6, 7, 9, 11, 12, 13, 14, 15, 16, 17, 18, 19, 20, 21, 22, 23, 24, 25, 26, 27
β Pictoris[c]	20–26	18–40	3, 6, 7, 8, 9, 20, 21, 22, 24, 25, 26, 27, 28, 29, 30, 31, 32, 33, 34, 35, 36, 37, 38, 39, 40
Octans	$\sim$ 20	82–175	6, 7, 24, 25, 41
32 Orionis[d]	$\sim$ 25	$\sim$ 90	5, 42, 43
Tucana-Horologium	20–40	38–51	3, 5, 6, 7, 8, 9, 20, 21, 22, 24, 25, 26, 27, 37, 44, 45, 46
Columba	20–40	26–63	6, 7, 9, 21, 22, 24, 25, 27, 37, 45, 47
Carina	20–40	11–42	6, 7, 9, 21, 24, 25, 37
Argus[e]	30–50	15–48	6, 7, 9, 21, 24, 25, 27, 37, 45, 48, 49, 50, 51, 52, 53, 54
AB Doradus	110–130	19–50	3, 5, 6, 7, 9, 20, 21, 22, 24, 25, 26, 27, 32, 33, 34, 35, 40, 45, 55, 56, 57, 58
Carina-Near	150–250	10–53	5, 22, 59
Hercules-Lyrae	$\sim$ 200	10–24	9, 60, 61, 62, 63
Ursa Major	300–600	9–123	3, 5, 9, 20, 27, 50, 51, 53, 54, 64, 65
Coma Berenices	$\sim$ 600	86–88	65, 66
Hyades	625–650	32–62	3, 9, 50, 51, 53, 54, 64, 65, 66

[a] Aussi appelée Mamajek 1.

[b] Aussi appelée Cha-Near.

[c] Plus rarement appelée Beta-Cap, car elle contient l'association Capricornius.

[d] Aussi appelée Mamajek 3.

[e] Inclut l'amas ouvert IC 2391.

Références : 1 : Aarnio et al. 2008, 2 : Lawson et al. 2001, 3 : Zuckerman & Song 2004, 4 : Jilinski et al. 2005, 5 : Mamajek 2010, 6 : Torres et al. 2008, 7 : da Silva et al. 2009, 8 : Kiss et al. 2011, 9 : Shkolnik et al. 2012, 11 : de la Reza et al. 1989, 12 : Kastner et al. 1997, 13 : Zuckerman & Webb 2000, 14 : Gizis 2002, 15 : Mamajek 2005, 16 : de La Reza et al. 2006, 17 : Looper et al. 2007a, 18 : Rodriguez et al. 2011, 19 : Schneider et al. 2012a, 20 : Allers & Liu 2013, 21 : Malo et al. 2013, 22 : Rodriguez et al. 2013, 23 : Weinberger et al. 2013a, 24 : Malo et al. 2014a, 25 : Malo et al. 2014b, 26 : Manjavacas et al. 2014, 27 : Riedel et al. 2014, 28 : Zuckerman et al. 2001a, 29 : Ortega et al. 2002, 30 : Lépine & Simon 2009, 31 : Rice et al. 2010, 32 : Schlieder et al. 2010, 33 : Schlieder et al. 2012b, 34 : Schlieder et al. 2012a, 35 : Faherty et al. 2013b, 36 : Liu et al. 2013b, 37 : Moór et al. 2013, 38 : Binks & Jeffries 2014, 39 : Mamajek & Bell 2014, 40 : Schneider et al. 2014, 41 : Murphy & Lawson 2015, 42 : Mamajek 2006, 43 : Jilinski et al. 2009, 44 : Zuckerman et al. 2001b, 45 : Zuckerman et al. 2011, 46 : Kraus et al. 2014b, 47 : Hinkley et al. 2013, 48 : Eggen 1991, 49 : Makarov & Urban 2000, 50 : Montes et al. 2001, 51 : Mamajek 2010, 52 : Riedel et al. 2011, 53 : Gálvez-Ortiz et al. 2014, 54 : Klutsch et al. 2014, 55 : Luhman et al. 2005, 56 : Ortega et al. 2007, 57 : Liu et al. 2013a, 58 : Gizis et al. 2015, 59 : Zuckerman et al. 2006, 60 : Gaidos 1998, 61 : Fuhrmann 2004, 62 : López-Santiago et al. 2006, 63 : Eisenbeiss et al. 2013, 64 : Eggen 1958, 65 : van Leeuwen 2009, 66 : Johnson & Knuckles 1955.

particulier, l'intervalle d'âges des AJs permet de sonder l'échelle de temps correspondant à la formation de planètes terrestres ($\lesssim$30 Mans) et de géantes gazeuses ($\lesssim$10 Mans ; Song et al. 2003) à partir d'un disque d'accrétion.

- La recherche d'exoplanètes par imagerie directe : les exoplantètes géantes gazeuses jeunes sont encore chaudes et émettent de la lumière dans les longueurs d'onde proche-infrarouge. On peut complémenter cet effet par la recherche d'exoplanètes autour d'étoiles de faible masse (et donc moins brillantes) afin de minimiser le contraste de luminosité étoile–planète et de faciliter leur détection.
- La connaissance précise de l'âge d'un système planétaire est une caractéristique clé permettant de caractériser la masse de ses constituants.
- La construction d'une collection de DES visibles et infrarouges pour une variété d'objets tardifs et jeunes servira à contraindre les modèles d'atmosphère et construire une séquence empirique des propriétés des étoiles et naines brunes jeunes à différents âges.
- Les propriétés atmosphériques (basse température et basse pression) des naines brunes jeunes sont similaires à celles des exoplanètes géantes gazeuses. Cependant, les naines brunes sont beaucoup plus faciles à étudier car elles ne sont pas liées à une étoile-hôte beaucoup plus brillante.

1.4.2 Méthode

Comme mentionné plus tôt, il y a deux difficultés majeures qui doivent être surmontées pour identifier les membres de faible masse aux AJs du voisinage solaire : ceux-ci sont éparpillés sur la Sphère céleste, et nous ne disposons que de très peu de mesures pour la grande majorité des étoiles de faible masse et naines brunes du voisinage solaire. Pour la plupart de ces objets, nous ne disposons que de photométrie dans le visible ou l'infrarouge à un nombre limité d'époques, typiquement espacées de quelques dizaines d'années. Nous devrons donc identifier dans un premier temps les membres potentiels d'AJs sans connaître leurs coordonnées $XYZUVW$ complètes.

L'inférence bayésienne est une méthode tout indiquée pour restreindre notre recherche à un nombre plus limité d'objets lorsque certaines mesures ne sont pas accessibles. En effet,

Malo et al. (2013) ont démontré l'efficacité de cette méthode en construisant l'outil *Bayesian Analysis for Nearby Young AssociatioNs* (BANYAN) pour identifier de nouveaux membres d'AJs aux types spectraux M0–M6, pour lesquelles les vitesses radiales et distances n'avaient pas été mesurées. L'outil BANYAN compare les magnitudes d'une étoile en bandes I_C (rouge) et J (proche-infrarouge), ainsi que son mouvement propre et ses coordonnées célestes (ascension droite et déclinaison) à celles prédites selon des modèles d'AJs et des étoiles du champ, pour assigner une probabilité d'association à chacune de ces AJs (ou au champ) selon le théorème de Bayes. Un diagramme couleur–magnitude tel que présenté à la Figure 1.18 est utilisé pour s'assurer que la distance correspondant à la meilleure hypothèse est cohérente avec la séquence couleur–magnitude à l'âge en question. Cette méthode, complémentée par la mesure subséquente de vitesses radiales (Malo et al. 2014a) et distances (Riedel et al. 2014) des candidates les plus prometteuses, a permis d'identifier plus de 200 nouvelles candidates membres d'AJs de types spectraux M0–M6 à partir de catalogues d'étoiles possiblement jeunes avec une couverture partielle de la sphère céleste (Riaz et al. 2006).

Nous allons utiliser une méthode similaire pour mener à bien ce projet. Cependant, nous allons utiliser seulement la photométrie en longueurs d'onde infrarouge étant donné que nous ciblerons des objets plus froids. Une difficulté supplémentaire à laquelle nous ferons face est le fait que la plupart des objets jeunes aux types spectraux $\geq$ M5 du voisinage solaire sont encore inconnus, en plus qu'aucune mesure de leur mouvement propre ne soit disponible. Nous utiliserons les catalogues 2MASS et WISE (le *Wide-field Infrared Survey Explorer* ; Wright et al. 2010 ; observations menées entre 2009 et 2011) qui contiennent chacun la photométrie et les coordonnées célestes de plus de 300 millions d'objets dans l'infrarouge. Étant donné que ces deux missions ont été menées à $\approx$ 11 ans d'écart, nous pourrons mesurer le mouvement propre de chaque objet en effectuant une corrélation croisée des deux catalogues. Nous allons ainsi développer une version modifiée de l'outil BANYAN que nous utiliserons conjointement avec cet ensemble volumineux de données pour identifier des membres potentiels aux AJs du voisinage solaire de types spectraux $\geq$ M5, et ce pour toute la Sphère céleste. Les connaissances actuelles sur les séquences couleur–magnitude que nous avons présentées à la Section 1.2.4 seront utilisées pour construire les séquences couleur–magnitude à l'âge du champ et des AJs,

lequelles feront partie du nouvel outil BANYAN II. Nous choisirons alors les candidates avec les plus grandes probabilités d'appartenance aux AJs pour entreprendre un programme de spectroscopie infrarouge et visible à résolution moyenne ($R \sim 1000$) afin de corroborer leur type spectral et leur jeune âge. Nous utiliserons en particulier les effets de la faible gravité de surface sur leur DES pour identifier les candidates jeunes.

Au Chapitre 2, nous présenterons une description détaillée de l'outil BANYAN II et nous caractériserons son efficacité à discerner les vrais membres d'AJs des étoiles du champ possédant une cinématique similaire. Nous utiliserons aussi cet outil pour identifier de nouvelles candidates membres d'AJs parmi les naines brunes jeunes déjà connues. Au Chapitre 3, nous présenterons une nouvelle liste de nouvelles candidates naines brunes membres d'AJs, construite à partir d'une corrélation croisée entre les catalogues proche-infrarouges 2MASS et WISE et de l'outil BANYAN II. Nous poursuivrons en présentant au Chapitre 4 le suivi spectroscopique de 2MASS 12074836–3900043, une nouvelle naine brune jeune de type spectral L1, candidate membre de l'association TW Hydrae. Cette naine brune est la membre candidate la plus froide de TW Hydrae et sa masse estimée se trouve dans le régime planétaire (11–13 $M_{\rm Jup}$). Nous présentons ensuite au Chapitre 5 le suivi spectroscopique de SIMP J21543454–1055308, une autre naine brune jeune de masse planétaire (10–11 $M_{\rm Jup}$) membre candidate à l'association jeune Argus. La culmination de ce projet sera présentée au Chapitre 6, où nous décrirons les résultats du suivi spectroscopique de 240 candidates membres identifiées au Chapitre 3. Nous utiliserons les résultats de ce suivi spectroscopique pour mieux caractériser les propriétés des naines brunes jeunes, entre autres en construisant de nouvelles séquences type couleur–type spectral et couleur–magnitude, en ajustant des modèles théoriques d'atmosphère et de structure interne aux observations, puis en posant des contraintes sur la fonction de masse initiale de l'association jeune Tucana-Horologium. Nous présentons la conclusion de cet ouvrage au Chapitre 7.

Certains résultats corollaires à ce projet seront présentées en Appendice: l'Appendice A décrit les résultats préliminaires d'un suivi spectroscopique des étoiles de faible masse identifiées lors de ce projet et l'Appendice B décrit brièvement la découverte de la potentielle planète

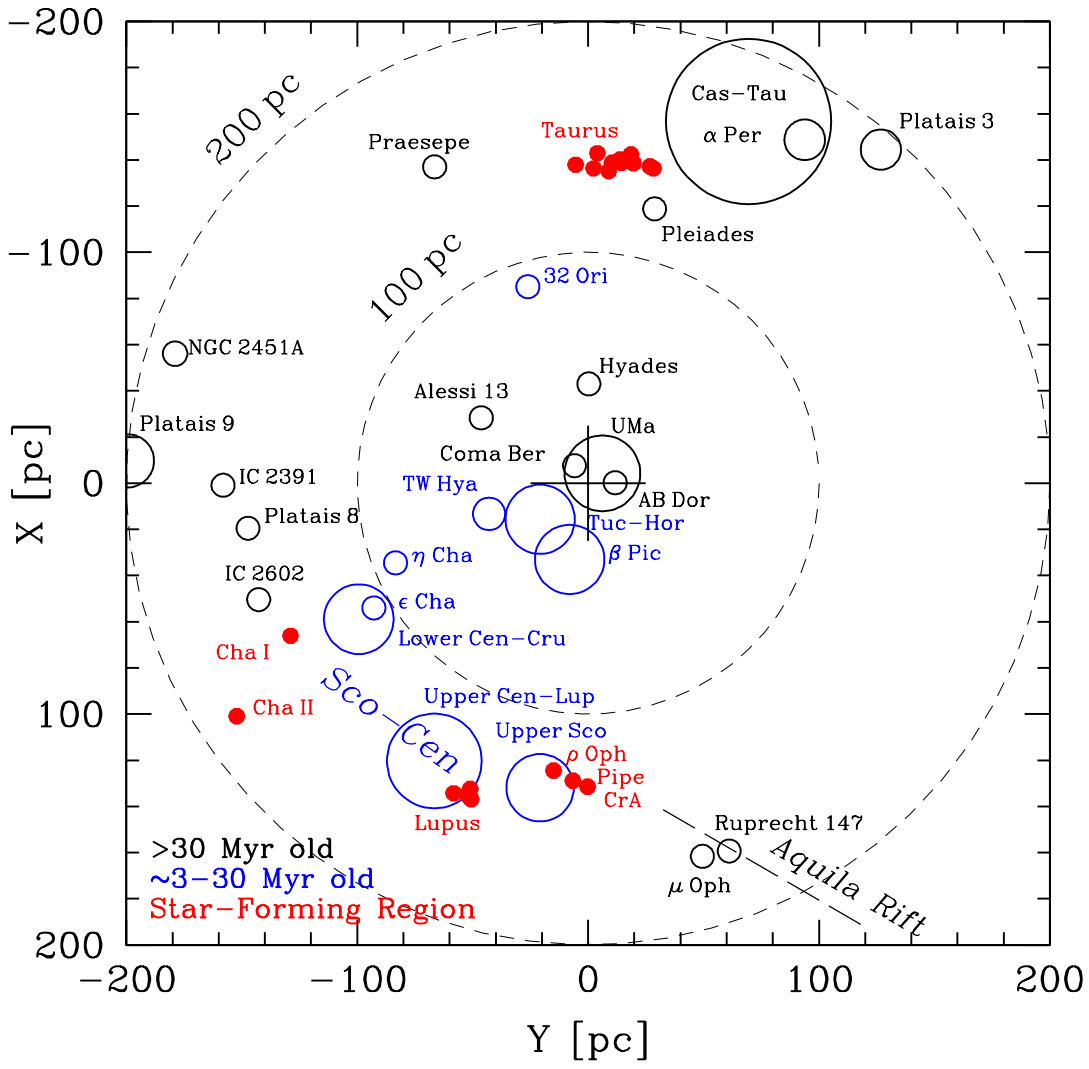

FIGURE 1.21 Position galactique des AJs à l'intérieur de 200 pc. On voit que les régions de formation d'étoiles, qui sont plus jeunes, sont aussi plus compactes. En contraste, les associations cinématiques, un peu plus vieilles, montrent une plus grande couverture spatiale, au point où les plus rapprochées englobent même le système solaire. Ceci explique le fait que leurs membres soient répandus sur l'ensemble de la Sphère céleste. L'association Ruprecht 147 n'est pas incluse dans la Table 1.2 dû à son âge plus élevé (2.5 Gan). Figure tirée de Rice et al. (2011).

flottante CFBDSIR 2149 à l'aide entre autres de l'outil BANYAN II. Dans les Appendices C et D sont brièvement présentées les découvertes de deux compagnons planétaires à des étoiles de faible masse identifiées lors de ce projet, respectivement 2MASS J01033563–5515561 (AB)b et 2MASS J02192210–3925225 b. Nous présentons également à l'Appendice E une compilation des articles, compte-rendus de conférence et affiches présentés dans le cadre de ce projet.

1.5 Déclaration de l'étudiant

J'ai rédigé la totalité des articles présentés aux Chapitres 2, 3, 4, 5 et 6 ainsi qu'à l'Appendice A et j'ai mené les travaux qui y sont présentés. J'ai également créé toutes les figures à l'exception de la plupart de celles présentées au Chapitre 1. Dans ces cas, la référence est mentionnée dans la légende. J'ai écrit l'entièreté du code informatique BANYAN II sur lequel est basée cette thèse, en m'inspirant de la méthode et du théorème mathématique sous-jacent à BANYAN I, lequel a été présenté dans la thèse de Lison Malo. J'ai effectué moi-même les compilations des données de la littérature présentées au sein des Chapitres 2, 3 et 6, avec l'exception de la liste de membres bona fide des associations jeunes présentée au Chapitre 2, pour laquelle j'ai complémenté la liste compilée par Lison Malo (Malo et al. 2013). J'ai construit tous les codes informatiques IDL sur lesquels les travaux de cette thèse sont basés, avec l'exception de librairies de base telles que l'*astrolib* et la librairie publique de Craig B. Markwardt (voir aussi la discussion sur *krEllipsoidFit.pro*, qui a été écrit par Ronn Kling, au Chapitre 2). J'ai effectué la corrélation croisée des catalogues 2MASS et WISE (en utilisant en partie les outils fournis par *irsa.ipac.caltech.edu*), construit et appliqué les filtres de sélection et effectué la recherche littéraire pour mettre sur pied les catalogues BASS et LP-BASS présentés au Chapitre 3 et aux Annexes 3.A et 3.B. Sauf mention contraire dans cette section, j'ai effectué toute l'analyse scientifique ayant donné lieu aux articles présentés dans cette thèse.

J'ai écrit les codes de réduction en language IDL pour les instruments Flamingos-2 et GMOS. J'ai utilisé et modifié le code Firehose qui m'a été fourni par Robert Simcoe pour réduire les données de l'instrument FIRE. J'ai aussi utilisé et modifié le code spextool qui m'a été fourni par Michael C. Cushing pour réduire les données de l'instrument SpeX. Les trois spectres GNIRS présentés au Chapitre 6 ont été réduits par Rachel Mason et Andrew

McNichols dans le cadre du développement du pipeline de réduction XDGNIRS qui sera offert aux utilisateurs GNIRS. Le spectre TripleSpec présenté au Chapitre 6 m'a été fourni par Kelle L. Cruz et 14 des 134 spectres SpeX présentés au même chapitre m'ont été fournis par Adam J. Burgasser (13) et John E. Gizis (1). La classification spectrale des 3 spectres en longueurs d'onde visible présentés au Chapitre 6 a été effectuée par Kelle L. Cruz. Les spectres présentés au Chapitre 4 ont été observés par Jacqueline K. Faherty, puis celui présenté au Chapitre 5 a été observé par David Lafrenière, Lison Malo et Jasmin Robert dans le cadre du projet *SIMP* (J. Robert et al., en préparation).

Deux des 27 nuits d'observation avec l'instrument SpeX ont été effectuées par Lison Malo, puis celle-ci m'a assisté durant deux nuits supplémentaires avec ce même instrument. Jacqueline K. Faherty a effectué les neuf nuits d'observation avec l'instrument FIRE. J'ai planifié toutes les observations en mode classique et préparé toutes les observations en mode queue effectuées avec les instruments GNIRS, Flamingos-2 et GMOS, puis les observations ont été effectuées par les équipes d'observations à Gemini-Nord et Gemini-Sud. Étienne Artigau, David Lafrenière et René Doyon m'ont grandement aidé pour apprendre à utiliser les outils mis à notre disposition pour préparer les observations en mode queue.

J'ai écrit l'entièreté des 25 demandes de temps de télescope associées à cette thèse, ce qui n'inclut pas les trois demandes de temps reliées à l'instrument FIRE, lesquelles ont été écrites par Jacqueline K. Faherty. Ces dernières ont été utilisées pour accumuler des données non seulement dans le cadre de cette thèse, mais aussi pour d'autres projets. J'ai écrit et préparé toutes les conférences et les affiches qui sont également présentées à l'Appendice E. Ceci inclut les compte-rendus de conférence sur lesquels je suis identifié comme premier auteur. Mes contributions détaillées concernant les articles sur lesquels je suis listé comme co-auteur sont détaillées individuellement à l'Appendice E.

David Lafrenière, René Doyon et tous les coauteurs identifiés sur les articles ont contribué soit au développement des études, à la prise des données, à certaines parties de l'analyse et/ou à la révision du texte. Ils ont permis d'améliorer grandement la qualité de la structure et du contenu des articles présentés dans le cadre de cette thèse. Finalement, je dois les idées de base et la vision incroyable ayant permis d'entreprendre un projet aussi fructueux à David

Lafrenière et René Doyon. Étienne Artigau, Lison Malo, Jacqueline K. Faherty, Kelle L. Cruz, Philippe Delorme, Robert Simcoe, Michael C. Cushing, Loïc Albert, Adric Riedel, Rebecca Oppenheimer, Eric E. Mamajek, Brendan Bowler, David Rodriguez, Michael C. Liu, Amélie Simon, Gilles Fontaine, Katelyn Allers, Joshua Schlieder, Sergio B. Dieterich, Benjamin M. Zuckerman, John Gizis, André-Nicolas Chené, Sarah Jane Schmidt, Simon Coudé, Emily Rice, Céline Reyé, France Allard, Will Best, David Blank et Daniella C. Bardalez Gagliuffi ont également entretenu avec moi des discussions scientifiques enrichissantes ayant permis d'améliorer le contenu de cette thèse.

Chapitre 2

BANYAN. II. VERY LOW MASS AND SUBSTELLAR CANDIDATE MEMBERS OF NEARBY, YOUNG KINEMATIC GROUPS WITH PREVIOUSLY KNOWN SIGNS OF YOUTH

Jonathan Gagné, David Lafrenière, René Doyon, Lison Malo, and Étienne Artigau

Département de Physique and Observatoire du Mont-Mégantic, Université de Montréal, C.P. 6128 Succ. Centre-ville, Montréal, Qc H3C 3J7, Canada

Received 2013 August 21; accepted 2013 December 19

Published in *The Astrophysical Journal*,

March 2014, *Vol.* 783, *page* 121

2.1 Abstract

We present Bayesian Analysis for Nearby Young AssociatioNs II (BANYAN II), a modified bayesian analysis for assessing the membership of later-than-M5 objects to any of several young moving groups (YMGs). In addition to using kinematic information (from sky position and proper motion), this analysis exploits 2MASS-WISE color-magnitude diagrams in which old and young objects follow distinct sequences. As an improvement over our earlier work, the spatial and kinematic distributions for each association are now modeled as ellipsoids whose axes need not be aligned with the Galactic coordinate axes, and we use prior probabilities matching the expected populations of the YMGs considered versus field stars. We present an extensive contamination analysis to characterize the performance of our new method. We find that bayesian probabilities are generally representative of contamination rates, except when a parallax measurement is considered. In this case contamination rates become significantly smaller and hence bayesian probabilities for YMG memberships are pessimistic. We apply this new algorithm to a sample of 158 objects from the literature that are either known to display spectroscopic signs of youth or have unusually red near-infrared colors for their spectral type. Based on our analysis, we identify 25 objects as new highly probable candidates to YMGs, including a new M7.5 bona fide member to Tucana-Horologium, making it the latest-type member. In addition, we reveal that a known L2 γ dwarf is co-moving with a bright M5 dwarf, and we show for the first time that two of the currently known ultra red L dwarfs are strong candidates to the AB Doradus moving group. Several objects identified here as highly probable members to YMGs could be free-floating planetary-mass objects if their membership is confirmed.

2.2 Introduction

Young moving groups (YMGs) provide a unique means of studying the formation processes and physical properties of stars and brown dwarfs (BDs) at ages ranging from 8 Myr to 120 Myr. Since these associations are close-by and believed to have formed coevally, each of them consists of an easily accessible sample of objects at the same age. Furthermore, their

relative youth means that they have not dispersed significantly yet, and hence that their members still share similar space velocities, within a few $\mathrm{km\,s^{-1}}$. The advent of the Hipparcos catalog has revealed several YMGs within 100 pc. The main ones that are well-defined and younger than 120 Myr include TW Hydrae (TWA; 8 - 12 Myr; Zuckerman & Song 2004), β Pictoris (βPMG; 12–22 Myr; Zuckerman et al. 2001a), Tucana-Horologium (THA; 20–40 Myr; Torres et al. 2000, Zuckerman 2001), Carina (CAR; 20–40 Myr; Torres et al. 2008), Columba (COL; 20–40 Myr; Zuckerman et al. 2011), Argus (ARG; 30–50 Myr; Zuckerman et al. 2011) and AB Doradus (ABDMG; 70–120 Myr ; Zuckerman et al. 2004). However, since Hipparcos is limited to bright stars, it uncovered only the most massive (F, G and K) members of YMGs. Since the initial mass function (IMF) peaks around $0.3\,M_{\odot}(\gtrsim$M3), most of the members to YMGs remain to be identified, a challenge that has only recently been tackled (Zuckerman & Song 2004, Torres et al. 2008, Cruz et al. 2009, Malo et al. 2013, Rodriguez et al. 2013, Faherty et al. 2013a, Liu et al. 2013b and references therein). Finding these low-mass members would be of great interest for several reasons. It would allow us to study the low-mass end of the IMF in different environments while providing a unique test bench for evolutionary models at young ages, in addition to providing a sample of age-calibrated young systems in the solar neighborhood. The latter is particularly interesting for the dynamic field of exoplanet imaging: low-mass stars (LMSs) or BDs are intrinsically fainter than their more massive equivalents, and young planets are hotter (thus brighter) than older ones because of the thermal energy stored during their initial contraction. Those two effects both reduce the contrast ratio between a planet and its host star, thus facilitating their detection. Yet the identification of such low-mass objects is a difficult task because (1) members of YMGs are spread over very large portions of the sky, and (2) their colors can be confused with those of the overwhelmingly more numerous field stars and BDs. In the case of the youngest YMGs, objects later than $\sim$ L1 could have masses down into the planetary regime, which would provide an easy way of studying the atmosphere of such objects. YMGs represent interesting test benches for planetary formation theories, since 10 and 30 Myr respectively correspond to the formation timescales of giant and terrestrial planets (Song et al. 2003).

Recently, Malo et al. (2013) proposed a new quantitative method, Bayesian Analysis for

Nearby Young AssociatioNs (BANYAN), to assess the probability that a given object belongs to such YMGs through bayesian inference. With the use of this method, they identified an M5 + M6 binary bona fide member to the βPMG, 16 very strong K5–M5 candidates to YMGs with radial velocity and parallax measurements, as well as 167 strong candidates without available radial velocity or parallax measurements. We define bona fide members in a way similar as Malo et al. (2013, Section 4.3; see also Section 2.5.3 of this paper) : we thus consider that bona fide members are objects with a good measurement of proper motion, radial velocity and parallax which show Galactic position, space motion and youth indicators consistent with the properties of a YMG.

Later-type candidates could not be efficiently uncovered with the method of Malo et al. (2013), because they made use of the $I_C - J$ colors to calibrate the probabilities over the distances considered, where I_C magnitude is generally not available for very low-mass stars and BDs. Adapting the tool of Malo et al. (2013) to enable the identification of very low-mass stars and BDs in YMGs is the main focus of this work. Since the spectral energy distribution (SED) shifts to the near-infrared (NIR) at later spectral types, it is thus necessary to use yet redder colors to identify the latest members of YMGs. For this purpose, we use here two colors based on filters from the 2MASS and WISE surveys. We also implement several other modifications to the approach of Malo et al. (2013) to bring the bayesian probabilities closer to physically meaningful values. The new method presented here has already identified a candidate free-floating planetary-mass object (*planemo*) member to ABDMG (Delorme et al. 2012) and a binary M5 candidate to THA around which a 12–14 $M_{\rm Jup}$ object was directly imaged (Delorme et al. 2013; J. Gagné et al., in preparation).

This paper starts by describing the current known population of late type ($>$ M5) dwarfs showing signs of youth or NIR colors redder than normal. Then, we describe the bayesian statistical method used for finding new candidate members to YMGs. Since this statistical tool needs an input model for every hypothesis under test, namely the membership to a given YMG or to the field, we describe how to build photometric, spatial and kinematic models that can be compared against observables. This is followed by a Monte Carlo analysis to assess the reliability of the probabilities yielded by this bayesian method. Finally, we apply this analysis

to our sample to identify several new very low-mass, highly probable candidate members to YMGs, one new bona fide member, as well as a bright co-moving M5 dwarf to a known, young L2 γ dwarf.

2.3 Young late-type objects in the literature

Several LMSs and BDs have been previously identified as young objects either because (1) their optical or NIR spectra display lower-than normal Na I (8183 and 8195 Å; 1.13 and 1.14 μm), K I (7665 and 7699 Å; 1.17 and 1.24 μm), FeH (8692 Å; 0.98 and 1.19 μm), TiO (8432 Å) or CrH (8611 Å) equivalent widths due to a lower pressure in their photosphere (due to low surface gravity ; Cruz et al. 2009), (2) their spectra show stronger-than-normal VO bands, indicative of lower surface gravity (Allers et al. 2007), (3) their NIR spectra display a triangular-shaped H-band continuum due to decreased H_2 collision-induced absorption which is also a consequence of low gravity, (4) they display signs of accretion, (5) they display lithium at a temperature where old objects would have completely destroyed it, (6) they are over-luminous because of their inflated radius, (7) they display unusually red NIR colors for their spectral type because of a greater amount of dust in their photosphere, (8) they are fast rotators, and/or (9) they display a high level of chromospheric activity, either through high levels of X-ray, radio, UV or Hα emission. Based on our review of the literature, we have compiled a list of 158 currently known later-than-M5 young objects ; the observational properties of these candidates are given in Table 2.4, along with the YMG association to which they were previously identified, when applicable. Since the 2MASS and WISE catalogs provide a sufficiently good baseline (typically $\approx$ 11 yr) to achieve proper motion measurements with errors typically lower than 10 mas yr^{-1}, we have used them to measure the proper motion for all objects in our sample and combined them with already existing NIR proper motion measurements when available. For some cases where a parallax solution had been measured for a given object, a very precise proper motion measurement was available and was preferred over the less accurate proper motion provided by 2MASS and WISE. There are two exceptions where a proper motion could not be measured this way: G 196–3B because the WISE source is masked by its bright primary, and 2MASS J00250365+4759191 because it is absent from

the WISE catalog. For both of them, other measurements were available in the literature so we have used those. We have included in Table 2.4 a subsample of *Possibly Young Objects* with marginal indicators of youth, yet with NIR colors unusually red for their spectral type. This subsample includes the 11 URLs that have been identified by Looper et al. (2008b), Kirkpatrick et al. (2008), Kirkpatrick et al. (2010), Mace et al. (2013a) and Thompson et al. (2013). These URL objects display very red colors but no other signs of low-gravity, which brings the question whether they are unusual young objects, or just old objects with very dusty atmospheres. It has also been hypothesized that these objects could have an anomalously high metallicity. In Section 2.8, we will assess whether those objects could plausibly be members of YMGs using a modified bayesian analysis.

2.4 A modified bayesian inference

The new method presented here is a modified version of the bayesian analysis described in Malo et al. (2013), based on a naive bayesian classifier. This statistical tool has already shown its high potential in other branches of astrophysics (see Bazell & Aha 2001, Norman et al. 2004, Zhang 2004, Picaud et al. 2005, Ptak 2007, Mahabal et al. 2008, Burnett & Binney 2010 and Broos et al. 2011). We use the position and proper motion of a given object, along with its spectral type and 2MASS J, H, K_s and WISE $W1$ and $W2$ magnitudes, altogether defining a set of observables $\{O_i\}$, to assess the probability that it is a member of any of several YMGs, or to the field (old or young; see Section 2.4.3); these possibilities define the set of hypotheses H_k. When such a measurement is available, radial velocity and/or parallax can be added to the observables to get an updated membership probability that is subject to less false positives. However, since these measurements are generally not available, the general case is developed whereby both radial velocity and distance are treated as marginal parameters.

By following the principles of a naive bayesian classifier i.e. by treating every observable as an independent variable, one can write a generalization of Bayes' theorem including a set of N hypotheses $\{H_k\}$ and M observables $\{O_i\}$ associated with a single astrophysical object $\mathcal{O}$, where its unknown radial velocity ν and trigonometric distance ϖ are treated as two

additional marginal parameters. Following Bayes' theorem, the probability that $\mathcal{O}$ satisfies H_k given its observables $\{O_i\}$ (the set $\{O_i\}$ does not include ν and ϖ) is :

$$P(H_k|\{O_i\}) = \frac{P(H_k)}{P(\{O_i\})} \int_0^\infty \int_{-\infty}^\infty P(\{O_i\}, \nu, \varpi|H_k)\ d\nu\ d\varpi. \tag{2.1}$$

The i and j indices always refer to an observable whereas k and l always refer to an hypothesis. The list of hypotheses H_k considered here are given in Table 2.1. The *prior probability* $P(H_k)$ is the *a priori* probability that $\mathcal{O}$ respects hypothesis H_k before having performed the bayesian analysis, and is discussed in Section 2.4.1. $P(\{O_i\})$ is called the *evidence*, and acts as a normalization factor. It represents the probability that an object displays the set of observables $\{O_i\}$ irrespective of the hypothesis H_k it verifies. It is simply given by the sum of those probabilities over each hypothesis considered :

$$P(\{O_i\}) = \sum_{l=1}^{N} P(H_l) \int_0^\infty \int_{-\infty}^\infty P(\{O_i\}, \nu, \varpi|H_l)\ d\nu\ d\varpi. \tag{2.2}$$

In practice, a numerical integration of Equation (2.1) is done on a regular 500×500 grid of distances and radial velocities varying from 0.1 to 200 pc and –35 to 35 $\mathrm{km\,s^{-1}}$, respectively. These intervals ensure that no object in our sample has a prior or likelihood probability density function (PDF) that peaks near or outside the limits of the grid. At each position of this grid, we evaluate the PDF of the *likelihood* that an hypothesis H_k generates the set of observables $\{O_i\}$ by making the assumption that $\{O_i\}$, ν and ϖ are independent :

$$P(\{O_i\}, \nu, \varpi|H_k) = P(\nu|H_k)\ P(\varpi|H_k) \prod_{j=1}^{M'} P(Q_j|H_k, \nu, \varpi), \tag{2.3}$$

where $\{Q_j\} = \{Q_j(\{O_i\}, \nu, \varpi)\}$ is a set of M' quantities obtained through a transformation of the M observables $\{O_i\}$ and/or ν and ϖ. The purpose of transforming observables is to obtain quantities Q_j which can be represented by a normal distribution for each hypothesis H_k :

$$P(Q_j|H_k, \nu, \varpi) = \frac{1}{\sqrt{2\pi}\sigma_j} e^{-(Q_j - \bar{Q_j})^2/2\sigma_j^2}, \tag{2.4}$$

where $\bar{Q}_j$ and σ_j are the mean value and standard deviation describing the normal PDF of Q_j if $\mathcal{O}$ respects the hypothesis H_k. The transformed quantities Q_j considered in this work are described in sections 2.5.1 and 2.5.2. The quantities $P(\nu|H_k)\ d\nu$ and $P(\varpi|H_k)\ d\varpi$ are generally not well represented by normal distributions, but rather by complex PDFs arising from the transformation of several normal PDFs. These distributions are determined through a numerical Monte Carlo analysis. Each time, we draw a million synthetic objects from the spatial and kinematic models (SKMs) of each H_k (see Section 2.5.1) and compute the radial velocity and distance of each one of them. We then build a normalized PDF for ν and ϖ on the same grid as previously described (see Figure 2.1). The $P(\{O_i\}, \nu, \varpi|H_k)$ represent 2D PDFs for the radial velocity and distance of an object verifying hypothesis H_k (see Figure 2.10 for an example). The position of the peak and its characteristic width give the most probable radial velocity and parallax of the object if the hypothesis is true, along with their respective 1σ errors. When the radial velocity and/or the distance are known, we remove them from the set of marginal parameters and insert them back into the set of observables $\{O_i\}$. We take measurement errors $\{\Delta O_i\}$ into account by propagating them to the modified observables $\{Q_j\}$, and then by widening their PDFs (see Equation 2.4) by replacing σ_j with $\sigma'_j = \sqrt{\sigma_j^2 + \Delta Q_j^2}$. For simplicity, we will refer to the bayesian probabilities with the P_{H_k} notation instead of $P(H_k|\{O_i\})$ in the remainder of this work.

2.4.1 The definition of prior probabilities

The prior probability $P(H_k)$ represents the probability that an object $\mathcal{O}$ verifies the hypothesis H_k before having performed bayesian inference. Hence, this quantity should depend on the population of objects from hypothesis H_k that could mimic the properties of $\mathcal{O}$. For simplicity reasons, we only consider observables that significantly affect this population estimate, namely the magnitude of proper motion, the Galactic latitude, radial velocity and distance. We define the population fraction $\xi_{O_i;\ k}$ of objects from hypothesis H_k that have the observable O_i comparable to $\mathcal{O}$'s measurement $O_{i;\ m}$ that has a measurement error $\sigma_{i;\ m}$ as :

$$\xi_{O_i;\ k} = \frac{1}{\sqrt{2\pi}\sigma_{i;\ m}} \int e^{-\ (x\ -\ O_{i;\ m})^2/2\sigma^2_{i;\ m}}\ P(O_i = x|H_k)\ dx, \tag{2.5}$$

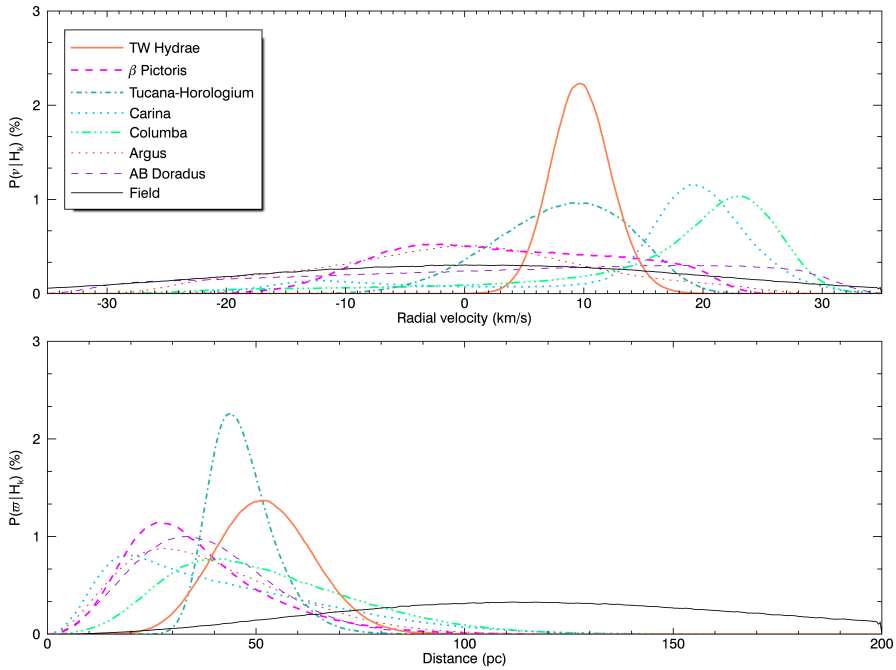

FIGURE 2.1 Prior distributions $P(\nu|H_k)\ d\nu$ and $P(\varpi|H_k)\ d\varpi$ for the two marginalized parameters in our analysis : distance and radial velocity. It can be clearly seen that most of these distributions would be poorly represented by a normal PDF. Each distribution is normalized such that the total area under its curve is equal to unity. We did not show separately young and old field populations, since their prior distributions are similar.

where the integral is performed over the range where O_i is defined, and $P(O_i = x|H_k)$ represents the value for the likelihood PDF $P(O_i|H_k)$ at $O_i = x$. For example, the population fraction $\xi_{\varpi;\ k}$ corresponding to an object $\mathcal{O}$ with a distance measurement $\varpi \pm \sigma_\varpi$ would be :

$$\xi_{\varpi;\ k} = \frac{1}{\sqrt{2\pi}\sigma_\varpi} \int_0^\infty e^{-\ (x\ -\ \varpi)^2/2\sigma_\varpi^2}\ P(\varpi = x|H_k)\ dx. \tag{2.6}$$

In an ideal case where the measurement error would be strictly zero, one would find :

$$\xi_{O_i;\ k} = P(O_i = O_{i;\ m}|H_k). \tag{2.7}$$

We thus define the prior probability that an object $\mathcal{O}$ verifies H_k by :

$$P(H_k) = \frac{N_k \prod_i \xi_{O_i;\ k}}{\sum_l N_l \prod_i \xi_{O_i;\ l}}, \tag{2.8}$$

where N_k is the expected total population of objects that verify H_k and indice i runs over all available observables from the magnitude of proper motion, Galactic latitude, radial velocity and distance. The denominator serves as a normalization factor so that all prior probabilities sum up to unity. In order to estimate N_k, we define our sample as dwarfs later than M5, younger than 1 Gyr and lying within 200 pc of the Sun. We choose 1 Gyr as a conservative limit to ensure that any field object that could imitate the properties of YMG members is included in the *young field* hypothesis. The reason for choosing such an old limit compared to the oldest YMG considered (ABDMG at 70–130 Myr) is that BDs (especially objects with masses around $\sim 80\,M_{\rm Jup}$) significantly younger than 1 Gyr might not have reached their equilibrium radius yet (Burrows et al. 2001), which means that they could display signs of low-gravity. A conservative limit is preferred since spectral properties of low-mass objects do not allow to make a precise statement on their age. The 200 pc limit was chosen to match with the grid over which we marginalize distance (see Equation 2.2 as well as explanations following it).

We cannot estimate the number of YMG members in this sample in a precise manner since their population is still largely incomplete for such late type objects. For this reason, we estimate N_k by supposing that YMGs are complete in the A0–M0 spectral type range, then using a log-normal IMF with $m_c = 0.25\ M_\odot$and $\sigma = 0.5$ dex (Jeffries 2012; Chabrier 2005) to estimate the expected number of objects later than M5 in each YMG. To avoid small number statistics, we have combined together bona fide members of all YMGs considered here, and estimated that the total expected late-type population should be approximately 616 objects. Since we do not want to make any predictive statement on the relative population of each YMG, we have thus used an averaged population $N_k = 88$ for every of the seven YMGs considered here. We do not state that this necessarily represents the real low-mass end of the IMF, since it is not well known yet. We rather use this as the best *a priori* estimate that one can make at this time.

We define $N_{\rm field}$ as the total number of objects in our field model (see Section 2.5.1). It is probable that some A0–M0 stars are still missing in the census of YMGs, the effect here would be that we may underestimate bayesian probabilities $P(H_k)$ for the YMG hypotheses,

and hence that our membership probabilities, as well as our contamination rates (see Section 2.6) would be too conservative. It should be stressed that including such priors in our analysis does not significantly affect the relative classification ranking of different objects, but changes the absolute values of the bayesian probabilities that each objects are members of a specific YMG. In particular, bayesian probabilities calculated this way will be significantly lower than those reported in Malo et al. (2013), who set all priors to unity. In the present work, we use Bayes' theorem to try and assess the probability that objects belong to several YMGs, consisting of our different hypotheses H_k. However, since we use a naive bayesian classifier in the sense that we treat input parameters as independent variables, we expect that the bayesian probabilities $P(H_k|\{O_i\})$ we derive this way will be biased (Hand & Yu 2001). Because of this, we will perform a Monte Carlo analysis (see Section 2.6) to estimate un-biased membership probabilities, as well as the recovery rate of our method. We strongly advise that the bayesian probabilities should always be interpreted together with the prior assumptions that were made, and the reader should keep in mind that even if the relative ranking of each hypothesis is preserved for a given object, the absolute bayesian probabilities remain inevitably biased.

2.4.2 The equal-luminosity binary hypothesis

In the case of objects for which youth is uncertain, we expect that part of the false-positive candidate members identified with our method will be unresolved field binaries, since such objects would fall higher than the old sequence in a color-magnitude diagram (CMD), and could thus be misinterpreted as earlier, brighter and/or redder (young) objects. For this reason, for each group in our analysis, including the field, we add an *equal luminosity binary* hypothesis, which has the exact same SKM, but with a CMD shifted up by 0.7 magnitudes. This ensures that objects falling above the old CMD sequence but with position or kinematics not coherent with any YMG would not be interpreted as candidate members. Hence, our membership probabilities will be more conservative by including those binary hypotheses. Higher probabilities for the binary hypotheses (compared to the single-object hypotheses) will also flag the potentially unresolved binaries in our sample. However, since the photometric properties of young systems are not very well defined yet, we do expect a fraction of false-positives amongst the

systems we flag as possible binaries. Objects for which the binary hypothesis of the most probable YMG has a higher probability than the single-object hypothesis are indicated as *possible binaries* in the following. For simplicity, we did not use different priors for single and binary hypotheses. This is equivalent to the prior supposition that the binary fraction of young or old, late-type objects is 50%, regardless of their membership.

2.4.3 Modeling field stars

We have used a Besançon Galactic model (A. C. Robin et al., in preparation; Robin et al. 2012) to compute the values in Tables 2.1 and 2.2, for both the *field* and *young field* hypotheses, consisting of objects with ages more or less than 1 Gyr, respectively. The main differences between those two populations are (1) that the old one is larger in number and has a larger kinematic scatter, and (2) that younger objects have different photometric properties (early-type objects are intrinsically brighter, whereas late-type objects are redder; see Section 2.5.2). When one computes the bayesian probability that an object is a member of YMGs, both field hypotheses should be included in the bayesian algorithm, unless the object displays evidence for low-gravity, hence youth. In the latter case, the *old field* hypothesis should not be included. As explained earlier, we have included only objects within 200 pc having spectral types M5 or later and luminosity class V (see Section 2.4.1). Since these models do not include objects at spectral types later than M9, we have used the same IMF as described in Section 2.4.1 to estimate the population of objects later than M9, which are included in the numbers reported in Table 2.1. We thus find that the expected number of objects for the young and old field populations are 390 007 and 1 601 130, respectively. Since the estimated field population is much higher than that of YMGs, the bayesian probability that any object belong to YMGs will be significantly decreased in comparison with Malo et al. (2013) where they set prior probabilities to unity. This reflects the fact that an object randomly chosen in an all-sky sample with the aforementioned properties has a much larger probability to be a field object than being a member of a YMG.

Table 2.1. Properties of Young Local Associations

Name of Group	Age[a] Range (Myr)	Distance (ϖ) (pc)	RV (ν) ($\mathrm{km\,s^{-1}}$)	Bona Fide Members[b]
TW Hydrae	$8-12$	$40-62$	$7-12$	18
β Pictoris	$12-22$	$18-40$	$-9-16$	33
Tucana-Horologium	$20-40$	$38-51$	$3-14$	52
Columba	$20-40$	$26-63$	$19-26$	21
Carina	$20-40$	$11-42$	$16-23$	8
Argus	$30-50$	$15-48$	$-10-9$	11
AB Doradus	$70-120$	$19-50$	$-11-29$	54
Young Field	$0-1000$	$66-169$	$-19-19$	–
Old Field	$1000-8000$	$70-177$	$-34-32$	–

[a]We do not suggest those as robust age estimates for NYAs, which is out of the scope of this work. These age ranges result instead from a collection of the different ages proposed in the literature for each NYA. The relative age of the different associations should be correct, however.

[b]See Section 2.5.3

Table 2.2. Mean Galactic Motion and Position in Rotated Reference Frames

Name of group	UVW ($\mathrm{km\,s^{-1}}$)	$\phi_D\theta_D\psi_D$ (°)	$\sigma_{U'V'W'}$ ($\mathrm{km\,s^{-1}}$)	XYZ (pc)	$\phi_S\theta_S\psi_S$ (°)	$\sigma_{X'Y'Z'}$ (pc)
TWA	$-11.12, -18.88, -5.63$	$-158.7, -55.3, -5.4$	$0.90, 1.56, 2.78$	$19.10, -54.16, 21.54$	$25.3, 60.8, 80.4$	$4.98, 7.16, 22.57$
βPMG	$-11.03, -15.61, -9.24$	$-113.0, -70.3, 76.6$	$1.38, 1.72, 2.50$	$7.58, -3.52, -14.53$	$-90.2, 65.1, -77.9$	$8.22, 13.52, 30.67$
THA	$-9.70, -20.47, -0.78$	$-52.0, -30.2, 1.6$	$1.05, 1.68, 2.38$	$6.74, -21.79, -36.05$	$-28.2, 263.1, 21.1$	$3.90, 10.62, 20.10$
COL	$-12.14, -21.29, -5.61$	$143.4, 22.7, -68.8$	$0.51, 1.27, 1.69$	$-28.11, -25.78, -28.56$	$-25.7, -35.5, -62.2$	$10.55, 17.63, 28.33$
CAR	$-10.72, -22.23, -5.67$	$-68.0, -61.6, -86.4$	$0.31, 0.65, 1.08$	$10.09, -51.63, -14.85$	$18.4, -16.5, -64.9$	$5.78, 11.34, 29.79$
ARG	$-21.54, -12.24, -4.63$	$76.1, 55.9, 29.4$	$0.87, 1.67, 2.74$	$15.04, -21.69, -8.09$	$-12.4, -73.0, -51.9$	$12.07, 15.51, 27.43$
ABDMG	$-6.96, -27.23, -13.90$	$-54.4, 185.8, 10.7$	$1.18, 1.68, 1.94$	$-2.53, 1.28, -16.34$	$57.3, 51.9, 88.7$	$16.33, 19.95, 23.47$
Young Field	$-11.21, -18.57, -6.94$	$69.0, -89.3, -69.8$	$7.74, 12.46, 19.58$	$2.82, 0.07, -13.14$	$52.6, -30.0, 27.5$	$79.63, 80.37, 80.81$
Old Field	$-11.00, -37.25, -6.93$	$68.8, -89.8, -69.0$	$18.59, 28.73, 40.15$	$2.55, 0.01, -2.71$	$-113.1, 0.3, 0.0$	$79.43, 79.56, 96.06$

2.5 Modeling nearby, young associations

In the current model, we have included only YMGs younger than 130 Myr that lie within 100 pc of the Sun and have at least 6 bona fide members. Those associations, along with some of their properties, are listed in Tables 2.1 and 2.2. In the following sections, we will refer only to associations in this list when we use the term YMG.

2.5.1 A new spatial and kinematic model for young moving groups

In the previous bayesian inference method described in Malo et al. (2013), the SKM was defined by fitting an error function to the cumulative density function (CDF) of the Galactic

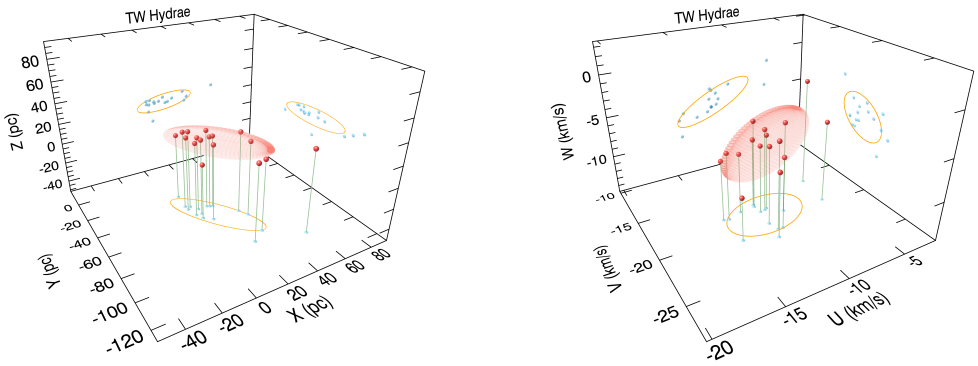

FIGURE 2.2 Spatial and kinematic models for TWA (red ellipsoids) derived from its bona fide members (red dots). We show their respective projections as orange lines and blue dots, such that the misalignment of TWA with the local galactic coordinate axes is obvious. Similar figures for all NYAs considered here are available at our group's website *www.astro.umontreal.ca/~gagne*.

position XYZ and spatial velocities UVW distributions of the bona fide members in each association. Then, it was assumed that the SKM could be described as a normal distribution having the corresponding mean and standard deviation, for each of the aforementioned parameters. In other words, it was assumed that both the 3D XYZ and UVW ellipsoids fitting the bona fide members' positions and velocities *necessarily had their principal axes aligned with the local Galactic coordinate axes*. As can be seen in Figure 2.2, this is generally not the case. To address this issue, we have modified the SKM used here in the following way. (1) For each association, we use the *krEllipsoidFit* IDL procedure[1] to find the *centers of mass*, respectively C_D (dynamic) and C_S (spatial), and principal axes of the UVW and XYZ distributions of the bona fide members, as well as the standard deviation of the distribution in the direction of the principal axes. (2) We calculate the sets of three $\phi_{\rm D}\theta_{\rm D}\psi_{\rm D}$ (dynamic) and $\phi_{\rm S}\theta_{\rm S}\psi_{\rm S}$ (spatial) Euler angles needed to make the rotations that bring each ellipsoid's principal axes along the local Galactic reference frame's axes[2]. The correct procedure to transform UVW coordinates to the $U'V'W'$s is to (1) subtract the C_D center of mass to the UVWs, (2) build a rotation

[1] *krEllipsoidFit* uses a special algorithm for 3D ellipsoids fitting from Ronn Kling and Jerry Lefever, described at *http://www.rlkling.com*

[2] Two different rotated reference frames are defined: one for the XYZ and another one for the UVW coordinates.

matrix from the $\phi_D\theta_D\psi_D$ Euler angles[3], (3) apply it to the UVWs and (4) add back C_D to the result of this rotation. The XYZ coordinates are transformed in the same way. For each association, the principal axes of the $X'Y'Z'$ (or $U'V'W'$) distribution of bona fide members should then fall along the axes of those new frames of reference. In the bayesian inference method described in the previous section, the $X'Y'Z'$ and $U'V'W'$ coordinates belong to the set $\{Q_j\}$ of transformed observables, whose PDFs can be represented by normal distributions. The parameters of these reference frames and the associated coordinates of YMGs are listed in Table 2.2. The parameters determined for the Carina SKM deserve close examination as they are based on only 7 bona fide members, compared to more than 15 for all other associations. By fitting ellipsoids using only subsets of the other associations, we determined that having only 7 objects yields an uncertainty of up to a factor of 2 in the velocity dispersions, while the effect on the spatial distribution is much smaller. In Figure 2.2, we show the adopted ellipsoids for TWA as an example.

2.5.2 Photometric properties as a function of age

Using a set of known old field LMS later than M5 and BDs with parallax measurements from the Dwarfarchives[4] (Dupuy & Liu 2012; Faherty et al. 2012), along with similar young Upper Scorpius objects from Lodieu et al. (2011) and Dawson et al. (2011), we have defined two CMDs based on 2MASS and WISE photometry that best separate the old and young subsets. These two CMDs are (1) M_{W1} versus $J-K_s$ and (2) M_{W1} versus $H-W2$ (see Figure 2.3). In both cases, the average color of the old sequence was defined by minimizing the reduced χ^2 of data points in bins of 0.7 mag in the vertical ($W1$) direction. The scatter associated with this value has been computed by finding the values at which the reduced χ^2 has a p-value of 68%. Since there are only a few young objects, especially at the red end of both CMDs, we have proceeded in a different way to build the young sequence PDF. The shape of the young sequence is taken to be the shape of the $+1\sigma$ old sequence, but shifted to the right. The reason why we used the shape of the rightmost 1σ limit of the field sequence to build the young PDF is that it becomes redder at later spectral types, which is more representative

[3] A sample IDL routine to achieve this is provided in the electronic version of this paper.
[4] *http://ldwarf.ipac.caltech.edu*

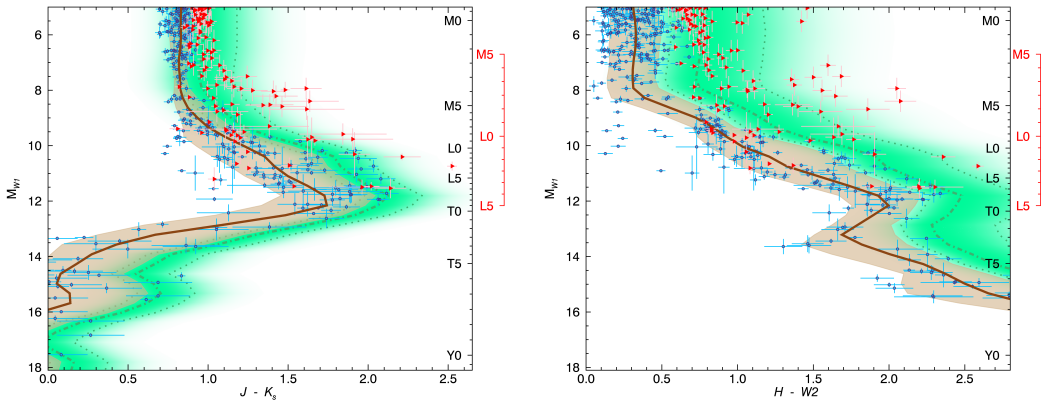

FIGURE 2.3 Color-magnitude diagrams for young (red dots) and old (blue dots) objects with parallax measurements. The thick, brown line and its shaded region respectively represent the old, field sequence and its 1σ scatter. See the text for a description of the way the young sequence PDF (green region) was constructed. The thick dash-dotted green line is the field sequence and both dotted green lines delimit its $\pm 1\sigma$ scatter regions. The rightmost black (red) axis indicates the spectral type of an old (young) dwarf at this absolute $W1$ magnitude.

of the general distribution of young objects in the CMDs, especially in the case of J - K_s. The shift was determined in the following manner : first, we built a 2D PDF distribution composed of a sum of 2D normal distributions, located at the positions of each young data point (the red dots in Figure 2.3). The vertical and horizontal characteristic widths of each normal distribution were set respectively to the vertical and horizontal measurement errors of the corresponding data points. Then, we determined what horizontal shift to the $+1\sigma$ field sequence was needed so that half of the total area of the previously described 2D PDF was to its left. The width of the young PDF was then taken as the width for which 68% of the total area of the 2D distribution was encompassed. The resulting young PDF is shown in Figure 2.3 for each of the two CMDs. We do not pretend that young objects should necessarily fall along these defined sequences, but rather use them only to represent the fact that younger objects are redder (and/or brighter) than the old sequence.

We have built an absolute magnitude–spectral type sequence in a similar way (see Figure 2.4). For young objects later than L6, no data with a parallax measurement is currently available. Hence, in this domain we have set the young sequence equal to the old one with a larger scatter to account for the fact we do not know well how those objects behave. Thus,

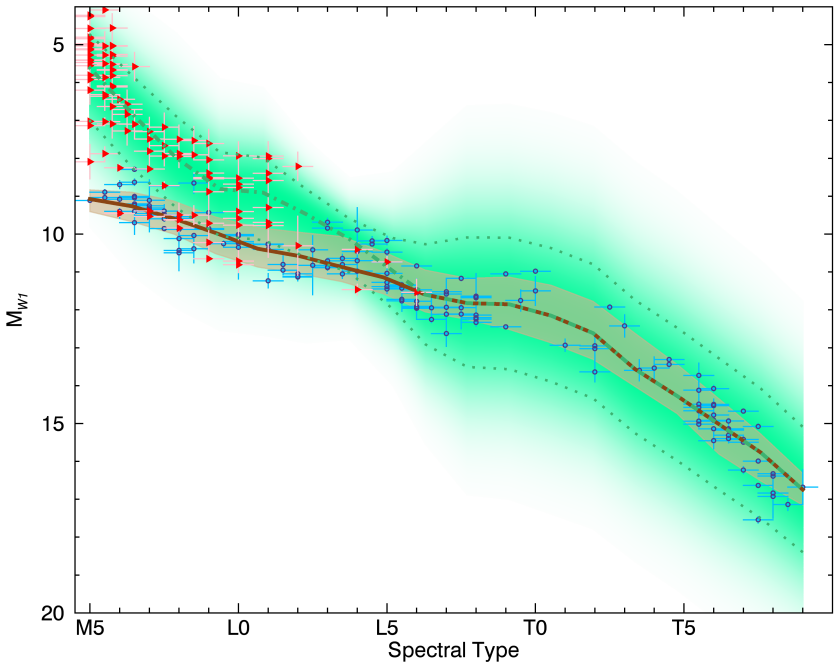

FIGURE 2.4 Absolute WISE $W1$ magnitude as a function of spectral type for young (red dots) and old (blue dots) objects with parallax measurements. The old sequence is defined by the thick brown line and its 1σ scatter represented by the shaded region. The young sequence (green dash-dotted line) was built from young objects only for spectral types $<$ L6. We have set it equal to the old sequence for later objects, but with a larger scatter (1.5 mag was added in quadrature to the field scatter), since the over- or under-luminosity of very late, young objects is not well known yet. The dotted green lines delimit the young sequence $\pm1\sigma$ scatter limits. The green region represents the young sequence PDF. Both sequences serve as spectroscopic distance calibrators in our bayesian analysis.

any young candidate with spectral type later than $\sim$L6 unveiled from our analysis should be taken with caution. These three sequences serve as photometric models in the bayesian inference method described in the last section. More precisely, the absolute $W1$ magnitude is computed at each distance on the grid (which is described in Section 2.4) and then, for this value of $W1$, we draw expected J - K_s and H - $W2$ colors from the magnitude–spectral type sequence, and compare them to the actual measurements. Thus, J - K_s, H - $W2$ and the spectral type are included in the set of observables $\{Q_j\}$. Including such photometric models has the effect of providing a spectrophotometric distance calibration, as well as increasing the probability that very red objects belong to moving groups or the young field hypothesis (in cases where youth is not well established prior to the bayesian inference).

2.5.3 Definition of YMG bona fide members

In order to define a robust subset of bona fide members to YMGs from which we will build their SKMs, we have started with a sample containing only objects with (1) signs of youth that are consistent with the age of the YMG they belong to, (2) a radial velocity measurement with an error < 5 km s^{-1}, (3) a parallax measurement with an error < 7 pc and (4) a proper motion measurement with a significance higher than 5σ. This first set of filters has removed 7 members that are considered as bona fide members to YMGs in Malo et al. (2013), namely : HIP 22738 and WX Col A from the ABDMG; 2MASS J06085283–2753583 from the βPMG ; HIP 46063 from CAR ; TWA 19 A from TWA ; HIP 1910 AB, HIP 3556 and HIP 104308 from THA. Here we consider multiple objects as only one system, so that we do not artificially double the weight for their position or kinematics. We then build a SKM model from the resulting list and compute the $XYZUVW$ standard deviation of each object with respect to its SKM model, and reject those with a standard deviation greater than 4. We repeat these steps independently for each YMG until no further objects are removed. This has removed 9 additional objects from our subset : HD 178085 from ABDMG; HIP 50156 and HIP 95261 A from βPMG; and HIP 17782, HIP 24947, GJ 490, HIP 83494, HIP 84642 and HIP 105404 from THA. We do not want to state that those rejected objects are not members. Instead, we consider that either we need more precise measurements or that they are possibly kinematic outliers, even if they were members. By rejecting such objects, we will get SKM models that have smaller dispersions and we will reduce the number of false-positives, with the price of possibly missing some new outlier members. We have also removed κ And from the COL bona fide members, since new estimates for this system's age are inconsistent with that of COL (Hinkley et al. 2013). We have added 16 new bona fide members not present in the list of Malo et al. (2013) either from the objects that they propose as new bona fide members, or from new members identified in Weinberger et al. (2013a) and Shkolnik et al. (2012) : G 269–153 A, HIP 107948, CD-35 2722 and BD+20 1920 in ABDMG : 2MASS J03350208+2342356, 2MASSJ01112542+1526214, HIP 23418 ABCD and GJ 3331 in βPMG : TWA 28, TWA 2 A, TWA 12, TWA 13 A, TWA 5 A, TWA 23, TWA 25 and TWA 20 in TWA. We have verified that all of these objects fall within 4σ of the SKM of their corresponding YMG. The membership

of TWA 9 system has recently been subject to discussion : Weinberger et al. (2013a) indicated that its space motion does not agree with other TWA members in a traceback analysis. Another problem concerning this system is its discrepant age (63 Myr for TWA 9 A, 150 Myr for TWA 9 B) from BCAH98 models fitting, reported by Webb et al. (1999). More recently, Pecaut & Mamajek (2013) proposed that the Hipparcos distance of this object might be off by at least 3σ, which would explain both its kinematic and photometric (and thus age estimate) discrepancies. They also suggested that TWA 9 should still be considered as a bona fide member to TWA. Because of these uncertainties, we chose not to include this object in our construction of the SKM model of TWA to be more conservative. The final SKM obtained through this procedure are the ones used for all further analyses in this paper; their properties are given in Table 2.2.

2.5.4 A summary of differences in this modified analysis

We briefly summarize here the differences between the analysis presented here and that of Malo et al. (2013).

- We use $W1$ versus $H-W2$ and $W1$ versus $J-K_s$ CMDs instead of I_C versus I_C-J, which allows to apply the method to objects later than M5.
- When available, we use the spectral types in the input observables.
- We consider the fact that the positions and kinematics of YMGs might be spread as ellipsoids whose major axes are not aligned with axes of the Galactic position reference frame (see Section 2.5.1).
- We include the error on measurements that feed the bayesian analysis.
- We have slightly modified the list of bona fide members to define a more robust and conservative list of core members (see Section 2.5.3).
- We estimate prior probabilities with the ratio of expected number of objects in each hypotheses, instead of setting them all to unity. Because of this, bayesian probabilities associated to YMG hypotheses in this work are dramatically lower compared with those reported in Malo et al. (2013).
- We use a Besançon Galactic model (Robin et al. 2012) to build the young and old field

hypotheses.

– We consider a *young field* hypothesis consisting of < 1 Gyr field objects from the Besançon Galactic model.
– The bayesian analysis directly compares $X'Y'Z'U'V'W'$ instead of the proper motions, the former being better represented by normal distributions. A consequence is the need to marginalize radial velocity and distance, which in turn necessitates the use of prior distributions displayed in Figure 2.1.

2.6 Contamination rates

As mentioned earlier, the fact that we use dependent observables in a naive bayesian algorithm means that the bayesian probabilities derived in this work are subject to be biased. To verify this, we have performed a Monte Carlo simulation, in which we draw 50 000 random synthetic objects from every SKM model described in Table 2.2 and use their synthetic characteristics to compute bayesian probabilities in the same way than described earlier. Since we know from which SKM these synthetic objects were drawn in the first place, we can use this to assess the performance of our bayesian analysis. We have assumed an IMF described in Section 2.4.1 to assign masses to these synthetic objects, and in turn converted them to M_{W1} magnitudes using the AMES-Cond isochrones (Baraffe et al. 2003) in combination with CIFIST2011 BT-Settl atmosphere models (Allard et al. 2013, Rajpurohit et al. 2013). In doing so, we have assumed a uniform age distribution spanning the age range of the hypothesis from which the synthetic object was drawn. Using M_{W1}, we have then assigned synthetic spectral types and NIR colors by using the photometric models described in Section 2.5.2. We have only included the young field hypothesis (not the old one) in this Monte Carlo analysis. Hence, the contamination rates that we derive in this section (and that are shown in Figures 2.5–2.7) are to be compared only to objects that display signs of youth. We discuss the contamination rates of objects with no evidence of youth at the end of this section. We have completed this Monte Carlo analysis four times: (1) without using neither radial velocity nor distance in the bayesian analysis, (2) by using radial velocity only, (3) by using distance only and (4) by using both radial velocity and distance. The contamination rates are obtained by choosing a lower

limit $P_{\rm low}$ to the bayesian probability, then counting the number of times $N_{H_k \to H_l}$ where a synthetic object originating from the SKM of hypothesis H_k has $P_{H_l} > P_{\rm low}$. We then define the correspondent fraction of contaminants as :

$$f_{H_l \to H_k}\left(P_{\rm low}\right) = \frac{N_{H_l \to H_k}\left(P_{\rm low}\right)}{N_{\rm synth}}. \tag{2.9}$$

where $N_{\rm synth} = 50\,000$ is the number of synthetic objects considered. We then rescale these synthetic populations according to the prior probabilities $P(H_l)$ described in Section 2.4.1. In the cases where we do not have a distance or radial velocity measurement for a given object $\mathcal{O}$, we use statistical predictions yielded by our bayesian analysis to adjust the population numbers $P(H_l)$ considered in this section. By doing this, we are counting how many synthetic objects drawn from every SKM could have properties alike those of a given object $\mathcal{O}$, for which we want to estimate the contamination probability. We thus expect that a total number $f_{H_l \to H_k}\left(P_{\rm low}\right) \cdot P(H_l)$ of objects drawn from the SKM of hypothesis H_l will end up as contaminant candidates to hypothesis H_k with $P_{H_k} > P_{\rm low}$. Consequently, there will be a fraction of contaminants $\mathcal{C}_{H_k}$ with similar properties to $\mathcal{O}$, which is a function of the low-cut bayesian probability $P_{\rm low}$:

$$\mathcal{C}_{H_k}\left(P_{\rm low}\right) = \frac{\sum_l f_{H_l \to H_k} \cdot P(H_l) \;-\; f_{H_k \to H_k} \cdot P(H_k)}{\sum_l f_{H_l \to H_k} \cdot P(H_l)}, \tag{2.10}$$

The denominator corresponds to the total number of objects that end up as candidates to H_k with $P_{H_k} > P_{\rm low}$, coming from all possible SKMs. The numerator is the same quantity, from which we subtract the number of objects that really originated from the SKM of H_k in the first place. Hence, the numerator is equal to the number of objects from all associations *other than* H_k that ended up as contaminant candidates to H_k, i.e. the number of contaminants.

In Figure 2.5, we present the fraction of young field contaminants without taking account of cross contamination between YMGs :

$$C_{H_k}\left(P_{\rm low}\right) = \frac{f_{yf \to H_k} \cdot P(H_{yf})}{f_{yf \to H_k} \cdot P(H_{yf}) + f_{H_k \to H_k} \cdot P(H_k)}, \tag{2.11}$$

where index $l = yf$ refers to the *young field*. Since the value for $P(H_k)$ is dependent on the object $\mathcal{O}$ for which we want to estimate the contamination rate (see Section 2.4.1), we cannot

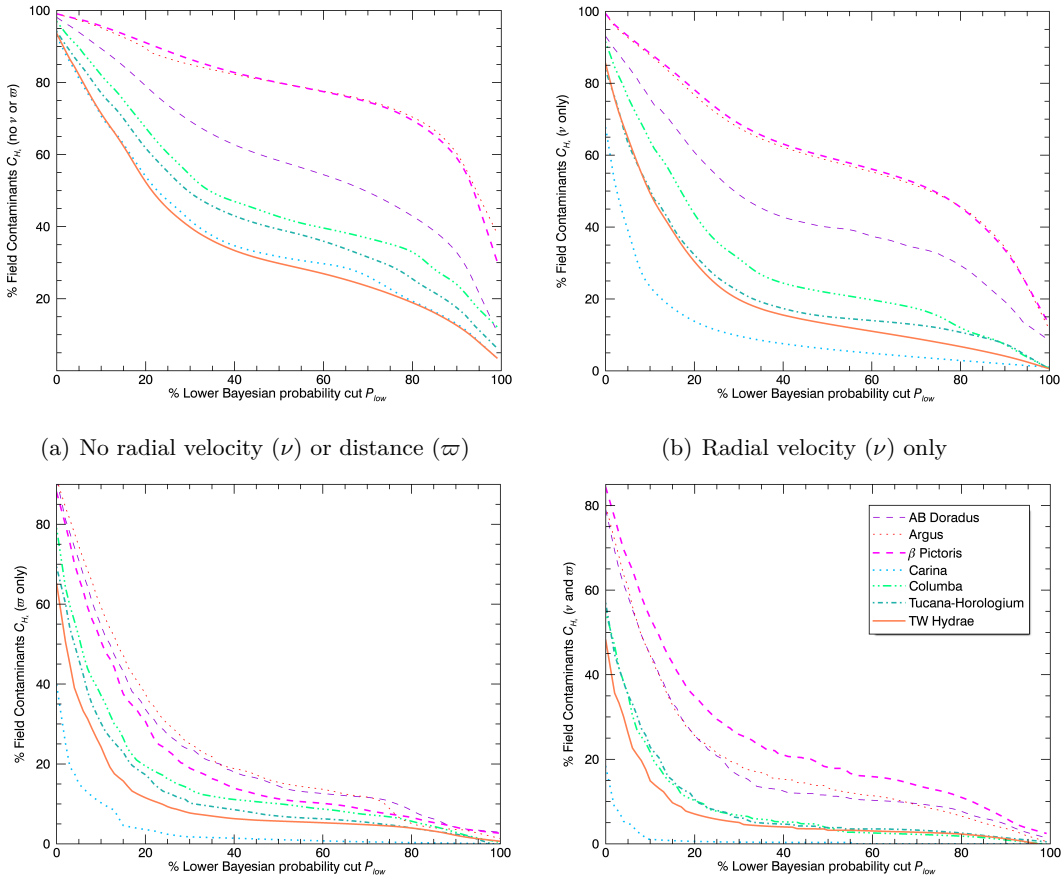

FIGURE 2.5 Field contamination rates in different YMGs, as a function of the chosen lower limit on bayesian probability P_{H_k}. A fraction of $C_{H_k}(P_{\rm low})$ of objects ending up in H with $P_{H_k} > P_{\rm low}$ will be field contaminants. From upper-left to lower right, we show results by taking into account (1) no radial velocity and no parallax, (2) radial velocity only, (3) parallax only and (4) both radial velocity and parallax. In most cases, the field makes up for all contaminants. Exceptions where some YMGs contaminate other YMGs are shown in Figure 2.7.

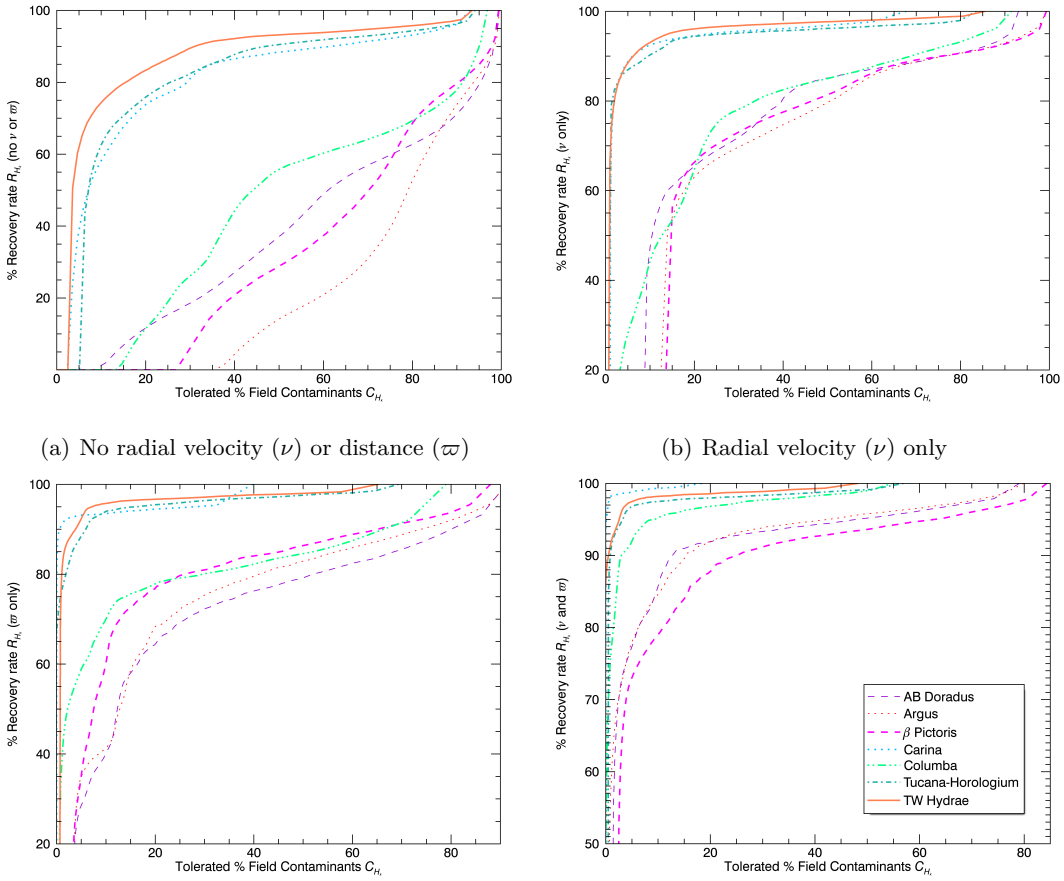

(a) No radial velocity (ν) or distance (ϖ)

(b) Radial velocity (ν) only

(c) Distance (ϖ) only

(d) Radial velocity (ν) and distance (ϖ)

FIGURE 2.6 Recovery rates in different YMGs, as a function of the tolerated field contamination C_{H_k}. A fraction of objects $R_H(P_{\rm low})$ originating from hypothesis H will be recovered by our method with a bayesian probability $P_{H_k} > P_{\rm low}$ allowing in a fraction C_{H_k} of field contaminants. The members of the closest YMGs such as βPMG, ARG and ABDMG are harder to recover without prior knowledge of radial velocity or distance, because their prior PDFs for radial velocity resemble that of the field (see Figure 2.1).

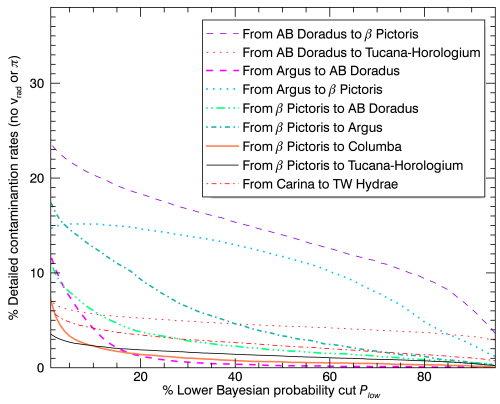

(a) No radial velocity (ν) or distance (ϖ), part 1

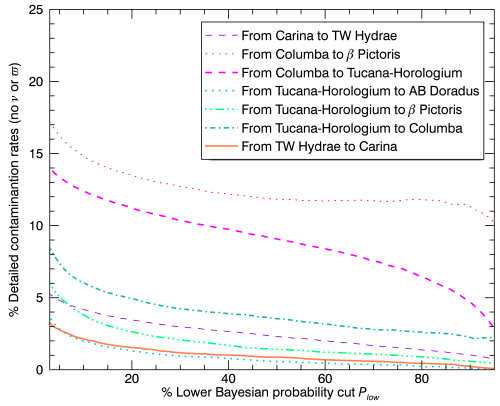

(b) No radial velocity (ν) or distance (ϖ), part 2

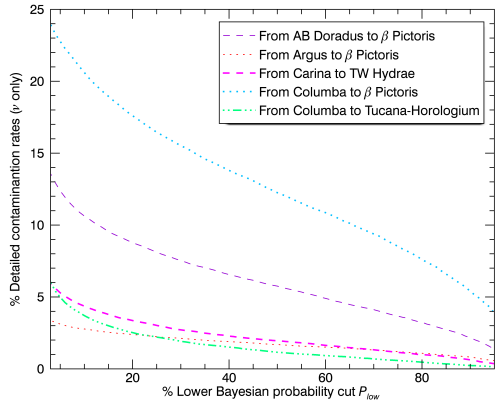

(c) Radial velocity (ν) only

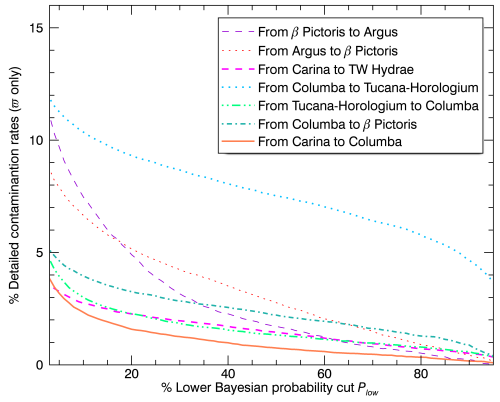

(d) Distance (ϖ) only

FIGURE 2.7 Cross contamination rates for YMGs considered in this work. Each curve represents a combination of contaminant to contaminated YMG. We only show the detailed contamination rates which have at least 3% for a bayesian probability $P_{H_k} = 5\%$.

capture all the information in only one such figure ; we would rather need such a figure for each object. We have thus chosen to display here a typical case by using values for $P(H_k)$ that vary smoothly and monotonically as a function of bayesian probability in the same way that was observed in our sample, since object with a higher bayesian probability of verifying a given H_k generally have a higher prior $P(H_k)$. We can see that (1) the bayesian probabilities derived in this work are generally biased, but comparable to the probability $(1 - C_{H_k})$ that an object is not a field contaminant, (2) close-by YMGs such as ABDMG, βPMG and ARG, for which members are the most spread out in the whole sky, have a greater young field contamination rate, (3) adding a measurement of distance and radial velocity produces bayesian probabilities that are even more biased towards the field and thus more conservative. This is particularly true whenever a distance measurement is used : then, even objects with very low (e.g. 30%) bayesian probabilities are unlikely ($< 30\%$) to be young field contaminants. It is interesting to note that the general shape of contamination rates indicate that bayesian probabilities in the cases where $P_{H_k} > 50\%$ tend to be overestimated whereas those with $P_{H_k} < 50\%$ tend to be underestimated, with an apparent lack of objects having bayesian probabilities around 50%. This is precisely the expected behavior of a naive bayesian classifier receiving dependent input variables (Hand & Yu 2001, Russek et al. 1983). For a given hypothesis, there is always a maximum value for the bayesian probability, which is close to but not exactly $P_{H_k} = 100\%$. The reason for this is that even if we consider an object whose $XYZUVW$ would lie exactly at the center of the SKM of a given YMG, there would be associated small, but non-zero bayesian probabilities for every other hypothesis. Since the sum of all probabilities must be normalized to unity, no object will ever have exactly $P_{H_k} = 100\%$ for a particular hypothesis H_k, with the effect that the curves show large random excursions at $P_{H_k} > 95\%$. We have found that this generally happens around $P_{H_k} = 95\%$ for most YMGs. For this reason, even if we have used a very large number of synthetic objects in our Monte Carlo simulation, small number statistics inevitably occur at these very high bayesian probabilities. We have thus corrected the contamination curves in this regime with polynomial fitting to avoid effects of the small number statistics. We remind that the results in Figure 2.6 rely on the assumption that objects under study display signs of youth. We expect to overestimate the contamination rates for

objects with ages significantly lower than this, because there will be less field contaminants at lower ages. We chose not to include this consideration in the prior probabilities because one cannot efficiently constrain the age of a low-mass object based only on signs of low-gravity.

In Figure 2.6, we present the recovery rate $R_{H_k} = f_{H_k \to H_k}(C_{\rm low})$, the fraction of synthetic objects drawn from H_k ending up as candidates to H_k. Hence, R_{H_k} represents the expected fraction of true YMG members that will be recovered with the bayesian method described here, depending on how many contaminants we allow in our output candidates sample. It can be seen that adding radial velocity or parallax measurements significantly increase the recovery rate. Furthermore, we can see that in absence of radial velocity and parallax measurements, our method will yield relatively small recovery rates for COL, ABDMG, βPMG and ARG unless we consider candidates with relatively high field contamination rates (by considering objects with low bayesian probabilities). It should also be considered that lower-mass members to YMGs could be spread further than the bona fide members considered in building our SKM models. If this is the case, then the recovery rates presented here will be underestimated, since our SKMs will not be a fair representation of reality.

In Figure 2.7, we show the cross-contamination rates $\mathcal{C}_{H_l \to H_k}(P_{\rm low})$ between YMGs :

$$\mathcal{C}_{H_l \to H_k}(P_{\rm low}) = \frac{f_{H_l \to H_k} \cdot P(H_l)}{\sum_l f_{H_l \to H_k} \cdot P(H_l)}, \tag{2.12}$$

where l does not include the field, for every combination yielding a contamination fraction higher than 3% when considering bayesian probabilities $P_{H_k} > 5\%$. These contamination rates apply to objects which are not field contaminants, and hence are applicable regardless of their age. In the case where neither radial velocity nor parallax is known, there are 3 combinations where we expect the cross-contamination rates to be relatively high (larger than 15% for small bayesian probabilities) : from ABDMG to βPMG, from ARG to βPMG and from COL to βPMG. When only radial velocity is known, this only happens from COL to βPMG, whereas when only parallax is known, the cross-contamination rates drop below 20% for every YMG combination at any bayesian probability. If both radial velocity and parallax are known, the cross-contamination rates drop even more, to rates always lower than 3%.

There is a subclass of red objects considered in this work for which we do not have any

other signs of youth. For those objects, we have used a similar contamination analysis than described here, but consider both (young and old) field hypotheses. We have found that the contamination rates do not significantly differ from those given in Figure 2.5 for a given bayesian probability, which means that our bayesian probabilities are biased in the same way whether or not we include the old field hypothesis.

2.6.1 Statistical predictions for distance and radial velocity

We have used the Monte Carlo analysis described in the previous section to assess the performance of our bayesian method in predicting the distance and radial velocity of a given object. To do this, we compare statistical distances and radial velocities to the actual values of input synthetic objects, in the case where we do not use radial or distance as input parameters in our bayesian analysis. We have only included objects ending up as YMG candidates in this figure, since the predictions for field hypotheses are less precise, due to the intrinsic larger scatter in the likelihood PDFs of field objects. We show the results in Figure 2.8, as well as a similar analysis applied to known bona fide members of YMGs. In the latter case. We find that the agreement is generally very good between predictions and true values, with reduced χ^2 values of 1.1 and 1.6 for the radial velocity and distance predictions, respectively. Our analysis can thus predict distances to precisions of 8.0% and radial velocities to 1.6 $\mathrm{km\,s^{-1}}$. The higher χ^2 value corresponding to distance predictions can be assigned to the fact that distance estimates tend to be slightly underestimated at large distances. A small fraction of bona fide members have outlier $XYZUVW$ parameters compared to the locus of their YMG, which is reflected in a larger scatter in their radial velocity and distance predictions, compared to synthetic objects. We also show that statistical predictions agree well with actual measurements for young objects in our sample.

2.7 Analysis of present faint, bona fide members

We have applied our modified bayesian analysis to all currently known bona fide members (see Section 2.5.3) that have absolute $W1$ magnitudes higher than 3, so that we can use the photometric models described in Section 2.5.2. The young field contamination rates as a

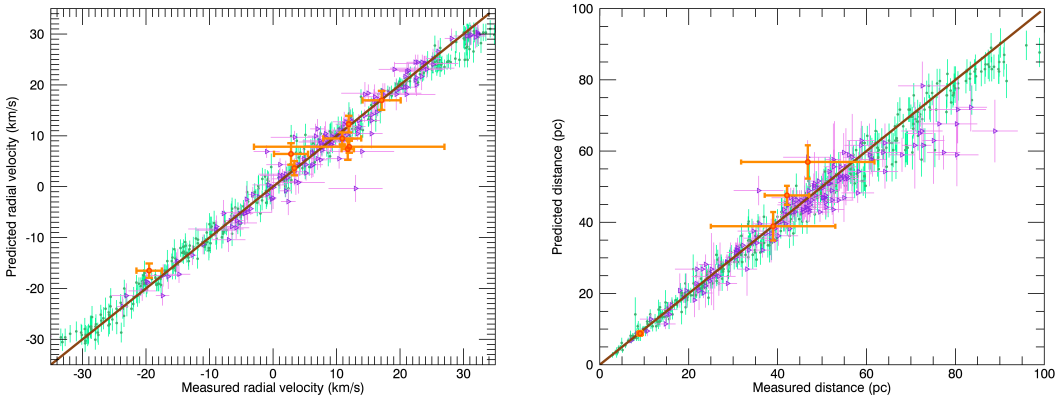

FIGURE 2.8 Performance of the statistical radial velocities and distances predictions for YMG candidates. Results from the Monte Carlo contamination analysis (small green dots), for existing bona fide members (purple open triangles) and candidates in our sample (orange, thick open circles) are displayed. For a better clarity, we only show 30 synthetic (green) data points per bins of 5 $\mathrm{km\,s^{-1}}$ or 5 pc. The reduced χ^2 values of the blue dots (including those not displayed) are 1.1 and 1.6, respectively.

function of bayesian probability is displayed in Figure 2.9(a) for each object in this sample. We can see that some outlier members presently considered as bona fide have bayesian probabilities down to $P_{H_k} \sim 25\%$, but that they generally have low contamination rates $C_{H_k} \lesssim 12\%$, with the exception of 3 objects that we did not display : 2MASS J17383964+6114160, 2MASS J05365509–4757481 and 2MASS J05365685–4757528 have contamination rates of 78%, 41% and 37%, respectively. All of them are 1.2 to 2.2 σ away from the locus of their YMG. In Figure 2.9(b), we display this N_σ distance as a function of the bayesian probability. We obtain N_σ by propagating the error of the 6-dimensional distance of each object in the $XYZUVW$ parameter space, where we treat the width of each axis in the SKM as a measurement error over the central position of the SKM. We can see that objects with lower bayesian probabilities are generally further from the center of the SKM. In particular, objects within 1σ of the SKM center always have $P_{H_k} > 99\%$. Both P_{H_k} and C_{H_k} provide a quantitative framework for qualifying the membership of bona fide objects. Core members generally have high bayesian probabilities $P_{H_k} \gtrsim 50\%$ and C_{H_k} less than a few %, while peripheral ones are those characterized by lower P_{H_k} (25–50%), yet with a modest contamination rate i.e., $C_{H_k} \lesssim 12\%$.

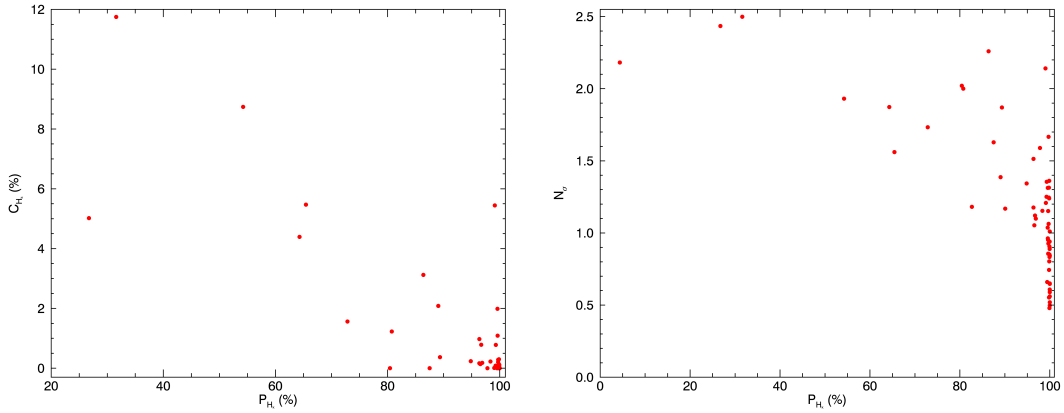

FIGURE 2.9 Resulting bayesian probability P_{H_k} and young field contamination rates C_{H_k} for bona fide members with $M_{W1} > 3.0$ in the literature, analyzed with our modified bayesian method (left). N_σ distance from the center of the respective SKM of each object in this bona fide sample, as a function of the resulting P_{H_k} (right). One can see that objects further from the center ($N_\sigma > 1.0$) generally have lower P_{H_k}, and that C_{H_k} is anti-correlated with P_{H_k}, as expected. Bona fide members can have bayesian probabilities as low as $P_{H_k} = 25\%$, but they generally have $C_{H_k} \lesssim 12\%$.

2.8 Results and discussion

In Table 2.3, we list all candidate members to YMGs from the input sample of young or red dwarfs described in Section 2.3 that were recovered by our modified bayesian analysis with a bayesian probability P_{H_k} corresponding to a field contamination rate C_{H_k} lower than 90%. We remind that bayesian probabilities reported here cannot be directly compared to the values in Malo et al. (2013), because of the different prior probabilities we have used. If we had set them to unity so that a comparison was possible, every object in the three sections of Table 2.3 would have $P_{H_k} \gtrsim 90\%$. We report even candidates with contamination rates as high as $C_{H_k} \sim 90\%$ to ensure high recovery rates (see Figure 2.6). Only in the cases where objects display signs of youth, we have not included the *old field* hypothesis in our bayesian analysis. For all objects, we have used sky position, proper motion, NIR photometry, spectral types, radial velocity and trigonometric distance whenever they were available. There are a few objects for which a very low precision radial velocity is available (Kirkpatrick et al. 2010), which we did not use because we have to assume that measurement errors are small in order to propagate them to errors on spatial velocities. We find a few core and peripheral

bona fide members, 35 very strong candidate members for which C_{H_k} is less than 15%, 15 modest candidate members with C_{H_k} between 15 and 70%, and 6 low-probability candidate YMG members with C_{H_k} between 70 and 90%. For each of them, we give their NIR or optical spectral type, as well as the bayesian probability, predicted radial velocity and distance associated with the YMG they most probably belong to. We use the J, H, K_s, $W1$ and $W2$ apparent magnitudes and statistical distances (or parallax measurements) for each object, along with the age of their most probable association, to determine their most probable mass using AMES-Cond isochrones (Baraffe et al. 2003) in combination with CIFIST2011 BT-Settl atmosphere models (Allard et al. 2013, Rajpurohit et al. 2013) in a likelihood analysis. We thus report several *planemo* candidates whose mass estimates lie entirely inside the planetary-mass regime, 9 of them being new, very strong candidates. In Figure 2.10, we show an example of the $P(\{O_i\}, \nu, \varpi|H_k)$ PDF for the ABDMG bona fide member 2MASS J03552337+1133437. The very good agreement between measurements and predicted values for distance and radial velocity associated with the most probable hypothesis (ABDMG) illustrates the robustness of our analysis. Radial velocity and distance measurements were *not* used as input parameters to generate this PDF. Similar figures for all objects in our sample are available at our group's website *www.astro.umontreal.ca/~gagne*. We give all the details on the output of our bayesian analysis for each object in our sample in Tables 2.5 and 2.6.

2.8.1 Comments on individual objects

In this section, we comment on the properties and previous knowledge of individual objects displayed in the first two sections of Table 2.3. Those are objects that we identify as candidate members to YMGs, with a probability lower than 70% of being field or young field contaminants. We also comment on objects for which our conclusions are different from those of other authors.

2.8.1.1 Bona fide members

2MASS J01231125–6921379 (2MUCD 13056) is a young M7.5 BD with Li absorption (Reiners & Basri 2009). We find that it is a strong candidate to the THA with a predicted

radial velocity of 9.9 ± 2.5 $\mathrm{km\,s^{-1}}$ and distance of 47.4 ± 3.2 pc. Reiners & Basri (2009) measure a radial velocity $\nu = 10.9 \pm 3\mathrm{km\,s^{-1}}$ and Riedel et al. (2014) measures a trigonometric distance of 42.1 ± 5 pc, both agreeing well with our predictions, which means this object has $P_{H_k} > 99.9\%$ and $C_{H_k} < 0.1\%$ and an estimated mass of 56–74 M_{Jup}. We have performed a likelihood analysis to constrain the age of this object by comparing its absolute NIR broadband photometry to BT-Settl models. We find that the presence of Li absorption implies an age of < 80 Myr, which is consistent with the age of THA. We note that a mass of $< 65\ M_{\mathrm{Jup}}$,which would imply that this object does not burn Li at all, is only consistent with an age of < 50 Myr, and hence our present age constraint based on Li absorption remains valid. Since this object has everything needed to be considered as such, we propose it as a new 56–74 M_{Jup} bona fide BD member to the THA, making it the latest-type current bona fide member to this association.

2MASS J03552337+1133437 (2MUCD 20171) is an L5 γ BD, thus one of the latest known young dwarfs up to date. Blake et al. (2010) measured a radial velocity of 11.9 ± 0.2 $\mathrm{km\,s^{-1}}$ for this object. Faherty et al. (2013b) reported this object as a young field BD with various signs of low gravity in its NIR spectrum as well as the presence of Li absorption, proposing an age of 50–150 Myr, which is similar to the age range of the ABDMG, along with distance measurement of 8.2 ± 0.9 pc. Liu et al. (2013a) then presented a more precise measurement of its parallax of 9.1 ± 0.1 pc, that, along with its radial velocity, allowed them to propose it as a new ABDMG bona fide BD. Here we combined both parallax measurements in an error-weighted average to find a value of 9.1 ± 0.1 pc, and confirm that this object should be considered as a 13–14 M_{Jup} BD bona fide member to the ABDMG, with $P_{H_k} = 99.7\%$ and $C_{H_k} = 0.1\%$. The predicted distance and radial velocity associated with the ABDMG are 8.5 ± 0.4 pc and 12.6 ± 1.7 $\mathrm{km\,s^{-1}}$, respectively at 1.5σ and 0.4σ of the measured values (see Figure 2.10). Our analysis suggests that this object could be an unresolved binary.

2MASS J11395113–3159214 (TWA 26) is an over-luminous M9 γ dwarf with signs of low-gravity in both its optical and NIR spectra. It has a triangular-shaped H-band continuum and Witte et al. (2011) derives a low surface gravity of $\log g = 3.5$ by fitting atmosphere models to the whole NIR spectrum. Allers & Liu (2013) classify this object as VL-G. Faherty et al.

(2012) measure a distance of 28.5±3.5 pc for this object, and Weinberger et al. (2013a) measure 42.0 ± 4.5 pc. Mamajek (2005) measure a radial velocity of 11.6 ± 2 km s^{-1} and propose it as a TWA member. Here we combine both distance measurements to get 33.5 ± 15.3 pc and find that it is a 16–27 $M_{\rm Jup}$ bona fide member to TWA, with $P_{H_k} = 99.3\%$ and $C_{H_k} < 0.1\%$. It would be useful to clarify the reason why both distance measurements for this object disagree so much.

2.8.1.2 Peripheral candidates

2MASS J06085283–2753583 is an M9 γ dwarf with unusually red colors for its spectral type, Li absorption and signs of low-gravity in both its optical and NIR spectra. It displays a typical triangular-shaped H-band continuum and Allers & Liu (2013) classify it as VL-G. Rice et al. (2010) measure a radial velocity of 24.0 ± 1.0 km s^{-1}, report it as a strong candidate member to βPMG and estimate its age to be around 10 Myr based on atmospheric models fitting. Faherty et al. (2012) report a trigonometric distance of 31.3 ± 3.5 pc, and Kirkpatrick et al. (2008) estimate its age to be younger than 100 Myr based on the strength of its Li feature. Here, we find that this object is a 15–23 $M_{\rm Jup}$ BD candidate member to COL, with $P_{H_k} = 3.7\%$ and $C_{H_k} = 4.0\%$. We would thus classify this object as a peripheral COL bona fide member, rather than a member to βPMG. The reason why we find this is *solely* due to the radial velocity measurement. If we did not use radial velocity as an input parameter, our bayesian method would predict $\nu_s = 20.1 \pm 1.5$ km s^{-1} for βPMG and $\nu_s = 22.7 \pm 1.3$ km s^{-1} for COL. The latter is closer to the actual measurement, but even then it can seem surprising that the bayesian probability for the βPMG hypothesis drops that much when including it, since it is at only 2.1 σ of the predicted value for βPMG. To understand this, one must look closely at the radial velocity distribution for βPMG (see Figure 2.1) ; the distribution falls quite steeply after $\nu = 20$ km s^{-1}. In other words, the radial velocity that was measured for 2MASS J06085283–2753583 is not allowed for in our SKM model for βPMG. This large sensitivity on radial velocity is due to the fact that this object is close to the anti-apex of both βPMG and COL. The $XYZUVW$ parameters of this object are 13.1 ± 1.6 pc, -28.0 ± 2.4 pc, -34.3 ± 1.9 pc, -7.6 ± 0.7 km s^{-1}, -18.6 ± 0.8 km s^{-1}

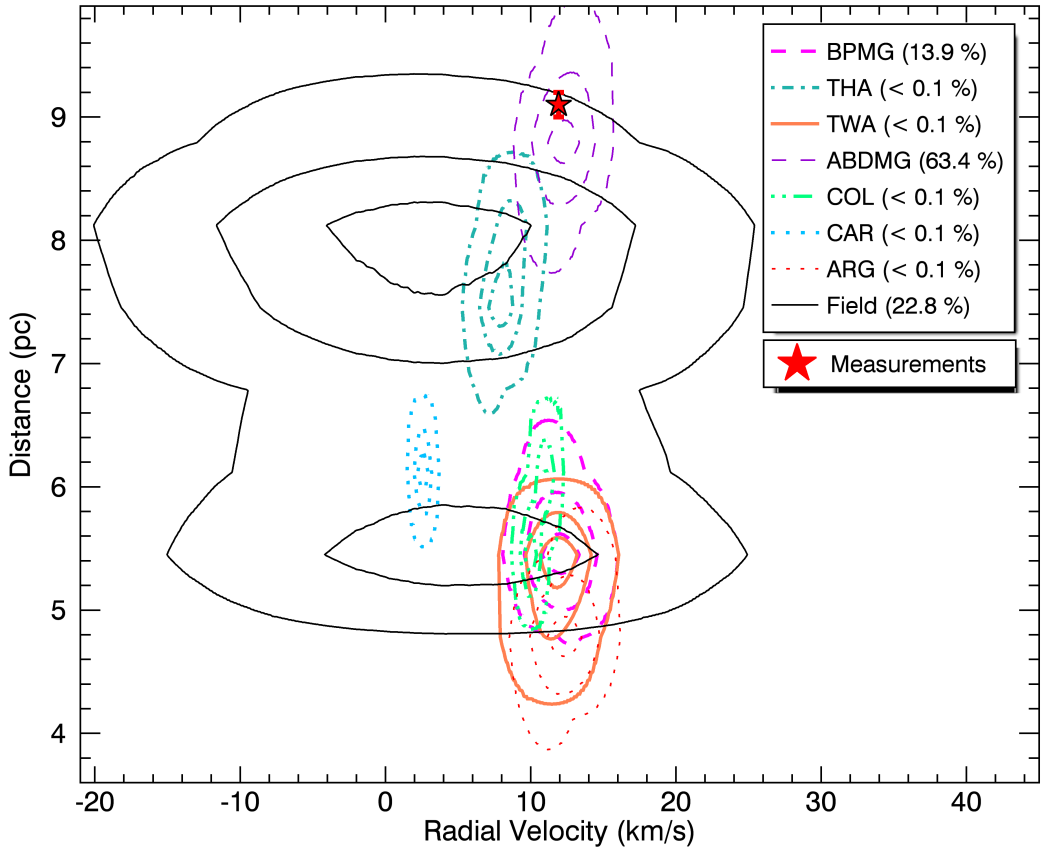

FIGURE 2.10 Probability density distributions $P(\{O_i\}, v, \varpi|H_k)$ for 2MASS J03552337+1133437 obtained from a bayesian analysis that did not use radial velocity or distance as input data, compared to the actual radial velocity and trigonometric distance measurements (red star). The three contour lines of each distribution encompass 10%, 50% and 90% of their total bayesian probability, the latter being indicated in parenthesis in the legend. We can see that the measurements agree very well with the predictions for the ABDMG hypothesis even if it did not use radial velocity or distance as input parameters. We have displayed the sum of the *single* and *binary* hypotheses PDFs for every hypothesis, which explains the bimodal shape of the field distribution. Similar figures for all candidates in Table 2.3 are available at our group's website *www.astro.umontreal.ca/~gagne*.

and -7.9 ± 0.8 km s^{-1}, respectively. Those are closer to the SKMs of βPMG than COL, which is consistent with the fact that we would classify it as a βPMG member without using the ξ_ν parameter. We conclude that the membership of this object is still ambiguous and that a better radial velocity measurement would be useful in investigating this further. COL membership could be ruled out by additional radial velocity measurements bringing it closer to 20 km s^{-1}.

2MASS J10220489+0200477 is an over-luminous M9 β dwarf with colors unusually red for its spectral type and signs of youth in its optical spectrum. Faherty et al. (2012) measure its distance to be 38 ± 16 pc, and we combine the radial velocity measurements of Schmidt et al. (2010) and West et al. (2008) into -7.9 ± 4.8 km s^{-1}. We find that this object is a 34–53 $M_{\rm Jup}$ candidate to ABDMG, albeit with a very low $P_{H_k} = 2.6\%$. This very low bayesian probability is due to the mismatch of this object's Galactic motion compared to current bona fide members of ABDMG. The $XYZUVW$ parameters for this object are -12.5 ± 5.3 pc, -23.1 ± 9.7 pc, 27.5 ± 11.6 pc, 16.1 ± 6.0 km s^{-1}, -60.3 ± 27.6 km s^{-1} and -54.2 ± 20.7 km s^{-1}, respectively. This is 51 pc and 57 km s^{-1} away from the SKM of ABDMG. The first is not problematic since it is comparable to the scatter of bona fide members, however the kinematic mismatch is highly significant. However, our Monte Carlo analysis indicates that this is associated with a low $C_{H_k} = 6.0\%$ probability of being a young field contaminant. It is thus possible that this object could be a contaminant from a source that was not considered in this work. As an alternate interpretation, it would be tempting to see this case as a tentative indication of mass segregation, however this is at odds with current evidence (Faherty et al. 2009) and a larger low-mass population would clearly be needed to assess this possibility. We also point out that a better distance and radial velocity measurements are crucial for better constraining the position of this object in the $XYZUVW$ parameter space.

2.8.1.3 Contaminants from other associations

2MASS J03393521–3525440 (LP 944–20) is an L0 dwarf with a triangular-shaped H-band continuum, Li absorption and signs of low gravity from atmospheric models fitting.

Tinney (1998) estimates its age to be 475–650 Myr. Ribas (2003) proposed it as a candidate member to the Castor moving group (CAS) (320 Myr) through a kinematic comparison with Castor members. Reid et al. (2002) measure a radial velocity of 10 ± 2 km s^{-1} where Reiners & Basri (2009) measure 7.6 ± 2.6 km s^{-1}, and Tinney (1996) measure a trigonometric distance of 5.0 ± 0.1 pc. We combine both radial velocity measurements to obtain 9.3 ± 1.7 km s^{-1}. Our bayesian analysis indicates that this object is a candidate member to ARG with $P_{H_k} = 17.5\%$, however we did not include CAS in our set of hypotheses. By performing a simpler bayesian analysis similar to that presented in Malo et al. (2013) but including the CAS hypothesis, we find that the CAS hypothesis has $P_{H_k} = 99.7\%$ whereas ARG has a negligible probability (remember those probabilities are strongly biased). This means that 2MASS J03393521–3525440 is indeed a better fit to CAS than ARG. We have used $XYZUVW$ values of -5.3 ± 12.5 pc, 4.7 ± 15.7 pc, 0.0 ± 16.3 pc, -13.3 ± 5.7 km s^{-1}, -8.5 ± 2.8 km s^{-1} and , -8.8 ± 4.5 km s^{-1} respectively for the CAS hypothesis, which were obtained from members presented in Table 1 of Barrado Y Navascués (1998).

2MASS J23134727+2117294 (NLTT 56194) is an M7.5 dwarf with X-ray emission and signs of low-gravity in its optical spectrum. Based on its X-ray emission and various spectroscopic features, Shkolnik et al. (2009) estimate its age to be between 100 and 300 Myr. Based on this age estimate and the kinematics of 2MASS J23134727+2117294, Shkolnik et al. (2012) propose that it is a candidate member to the Castor moving group, and measure a radial velocity of -1.6 ± 0.3. Here we find it is a βPMG candidate with $P_{H_k} = 22.3\%$. However, if we include the Castor hypothesis in a simpler analysis similar to that of Malo et al. (2013) without using photometry, we find that the kinematics of this object clearly better match the Castor hypothesis, with a bayesian probability $P_H > 99.9\%$, at a predicted distance of 16.8 ± 2.7 pc. We thus propose that this object is a candidate member to the Castor moving group, which would imply its mass to be between 81 and 94 $M_{\rm Jup}$. The predicted radial velocity associated with the Castor hypothesis is -0.6 ± 2.8 km s^{-1}, at only 0.4σ of the measurement.

2.8.1.4 Candidates with high probability

2MASS J00040288–6410358 is an object with signs of low gravity in its optical spectrum and NIR colors unusually red for its L1 γ spectral type. It has already been proposed as a THA candidate member by Kirkpatrick et al. (2010), in agreement with our results : we find $P_{H_k} = 99.7\%$ and $C_{H_k} = 0.5\%$. If it is actually a member to THA, it would have a mass between 13 and 14 $M_{\rm Jup}$, which would place it in the planetary-mass regime.

2MASS J00065794–6436542 is an L0 object displaying Hα emission and signs of low gravity in its optical spectrum. Here we propose it as a 21–41 $M_{\rm Jup}$ strong BD candidate member to the THA, with $P_{H_k} > 99.9\%$ and $C_{H_k} = 0.2\%$. Our analysis suggests that this object could be an unresolved binary.

2MASS J00192626+4614078 (2MUCD 10013) is an M8 dwarf with high rotational velocity, Li absorption and signs of low-gravity in its NIR spectrum. Reiners & Basri (2009) estimated its age to be less than several hundred Myr based on its Li absorption, and Allers & Liu (2013) characterized it as an Intermediate-Gravity (INT-G) dwarf. Reiners & Basri (2009) measure a radial velocity of -19.5 ± 2.0 km s^{-1} for this object. Here, we find that it is a 78–94 $M_{\rm Jup}$ LMS candidate to ABDMG, with $P_{H_k} = 88.0\%$ and $C_{H_k} = 3.9\%$. The predicted radial velocity associated with the ABDMG hypothesis is of -17.0 ± 1.4 km s^{-1}, at 1σ of the measured value.

2MASS J00325584–4405058 is an L0 γ dwarf with colors too red for its spectral type and signs of low-gravity in both its optical and NIR spectra. Allers & Liu (2013) characterize it as a Very-Low Gravity (VL-G) dwarf. Faherty et al. (2012) report and a trigonometric distance of 26.4 $\pm$ 3.3 pc for this object. Taking these measurements into account, we find that this object is a 10–12 $M_{\rm Jup}$ *planemo* candidate member to βPMG with $P_{H_k} = 91.8\%$ and $C_{H_k} = 0.2\%$.

2MASS J00374306–5846229 is another red L0 γ object with signs of low gravity in its optical spectrum. It was not previously recognized as a YMG candidate member, but here we propose it as a strong 13–15 $M_{\rm Jup}$ candidate to the THA, with $P_{H_k} = 97.3\%$ and $C_{H_k} = 0.7\%$. Our analysis suggests that this object could be an unresolved binary.

2MASS J00413538–5621127 (2MUCD 20035) is reported in Reiners et al. (2010) as a

nearby, young M8 BD with Li absorption, signs of accretion and a most probable age of 10 Myr. The authors note that its sky position and proper motion indicate that this object is a probable member of the Tucana-Horologium association. Liu et al. (2010) indicate that this object is an unresolved M6.5 + M9 binary. Here we also find that 2MASS J00413538–5621127 is a strong candidate member to THA. Furthermore its proposed age of 10 Myr agrees well with the 10–40 Myr age range for the THA. Its predicted radial velocity $\nu = 6.4 \pm 2.4$ km s^{-1} agrees relatively well with the combined measurement $\nu = 2.8 \pm 1.9$ km s^{-1} from Blake et al. (2010) and Reiners & Basri (2009), which yields $P_{H_k} > 99.9\%$ and $C_{H_k} = 0.2\%$. We estimate the masses of each component to be 14–41 $M_{\rm Jup}$ and 18–41 $M_{\rm Jup}$.

2MASS J00452143+1634446 (2MUCD 20037) is a BD with signs of low gravity in its optical spectrum, Hα emission and NIR colors unusually red for its L3.5 spectral type. We propose it as a new 13–14 $M_{\rm Jup}$ strong candidate member to the ARG. Its predicted radial velocity of $\nu = 3.4 \pm 1.3$ km s^{-1} agrees very well with the actual measurement $\nu = 3.4 \pm 0.2$ km s^{-1}, which yields $P_{H_k} > 99.9\%$ and $C_{H_k} = 1.8\%$.

2MASS J00470038+6803543 is a peculiar L7 dwarf with extremely red colors for its spectral type. Gizis et al. (2012) and Mace et al. (2013a) identify this object as possibly very dusty, over-metallic or young, which could explain its odd nature. After obtaining a NIR spectrum at a better resolution, Thompson et al. (2013) identify that this object has signs of low-gravity such as weaker-than-normal atomic lines. Here, we identify that this object is a strong candidate member to ABDMG, with $P_{H_k} = 98.2\%$ and $C_{H_k} = 2.4\%$. This object would have a very low-mass of 11–15 $M_{\rm Jup}$ if membership is confirmed.

2MASS J01033203+1935361 is an L6 β dwarf with signs of low-gravity in both its optical and NIR spectra. It has unusually red NIR colors for its spectral type and a typical triangular-shaped H-band continuum. Faherty et al. (2012) measure a trigonometric distance of 21.3 ± 3.4 pc for this object. Here, we find that it is a strong 10–11 $M_{\rm Jup}$ *planemo* candidate member to ARG, with $P_{H_k} = 76.0\%$ and $C_{H_k} = 0.1\%$.

2MASS J01174748–3403258 is an L1 dwarf whose NIR spectrum was reported by Witte et al. (2011) as fitting best with theoretical atmosphere models at a relatively low gravity of 4.5 dex. More recently, Allers & Liu (2013) report that this object has a typical triangular-

shaped H-band continuum as well as weak alkali lines, classifying it as an intermediate-gravity dwarf. Here we propose that this object is a high probability 13–14 $M_{\rm Jup}$ candidate member to the THA, with $P_{H_k} = 99.3\%$ and $C_{H_k} = 1.0\%$.

2MASS J01225093–2439505 is an M3.5 + L5 binary system in which the primary displays X-ray emission and the secondary has unusually red NIR colors for its spectral type, as well as a triangular-shaped H-band continuum. Bowler et al. (2013) report a radial velocity measurement of 9.6 $\pm$ 0.7 km s^{-1} and propose that this object could be a young candidate member to ABDMG, however we find here that it is rather a candidate member to βPMG, with $P_{H_k} = 98.2\%$ and $C_{H_k} = 3.4\%$. If we do not include the radial velocity measurement, it is a better match to ABDMG. However, the radial velocity measurement being at 2.7σ from the 15.6 $\pm$ 2.1 km s^{-1} prediction for ABDMG, but only at 0.5σ from the 10.6 $\pm$ 1.7 km s^{-1} prediction for βPMG, we conclude that it is a candidate member to βPMG rather than ABDMG. We note that our proper motion measurement arising from a cross-correlation of 2MASS and WISE ($\mu_\alpha = 89.7 \pm 7.9$ mas yr^{-1}, $\mu_\delta = -108.9 \pm 8.6$ mas yr^{-1}) is discrepant from that previously reported in UCAC4 (Zacharias et al. 2012) and PPMXL (Roeser et al. 2010; $\mu_\alpha = 89.7 \pm 7.9$ mas yr^{-1}, $\mu_\delta = -108.9 \pm 8.6$ mas yr^{-1}), resulting in a large error of 24.2 mas yr^{-1}in our adopted value for mu_α, which also favors the βPMG hypothesis over ABDMG. It would thus be useful to get a better measurement of the proper motion of this object to address the possibility that it is a member to ABDMG. We have used NIR photometry reported in Bowler et al. (2013) to estimate a mass of 5–6 $M_{\rm Jup}$ for the secondary and 67–89 $M_{\rm Jup}$ for the primary.

2MASS J01415823–4633574 is an L0 γ dwarf with several indicators of youth. Its optical and NIR spectra both display signs of low-gravity, including a triangular-shaped H-band continuum, its NIR colors are unusually red for its spectral type, it displays Hα emission and Witte et al. (2011) report that its NIR spectrum is best fitted by models with log g = 4. Kirkpatrick et al. (2006) report that this object should have an age comprised between 1 and 50 Myr, and that it could be a member either of the THA or βPMG. Here we find that this object is a very strong 14–20 $M_{\rm Jup}$ candidate member to the THA with a bayesian probability of 99.7%, associated to a field contamination probability of $C_{H_k} = 0.1\%$. Its predicted radial

velocity and distance are $\nu = 7.6 \pm 2.4$ km s^{-1} and $\varpi = 41.4 \pm 2.8$ pc if it is a member of the THA, or $\nu = 14.1 \pm 1.7$ km s^{-1} and $\varpi = 28.9 \pm 2.4$ pc if it is a member of the βPMG. The radial velocity measurement $\nu = 12 \pm 15$ from Kirkpatrick et al. (2006) is not precise enough to verify either of these two hypotheses. However, we find that this object has a significantly higher probability of being a member to the THA even if we do not take this measurement into account. Our analysis also suggests that this object could be an unresolved binary.

2MASS J02215494–5412054 and **2MASS J02251947–5837295** have both been reported as low-gravity M9 dwarfs (Reid et al. 2008b, Faherty et al. 2009), but we found no mention of them as being a candidates to any YMG. Here we propose that both objects are very strong 16–26 $M_{\rm Jup}$ and 20–32 $M_{\rm Jup}$ BD candidates to the THA with $P_{H_k} =>$ 99.9% and $C_{H_k} = 0.2\%$.

2MASS J02235464–5815067, **2MASS J02340093–6442068** and **2MASS J03231002–4631237** (2MUCD 20157) are three L0 γ dwarfs unusually red for their spectral types, with signs of low gravity in their optical spectra. Furthermore, 2MASS J03231002–4631237 shows Li absorption. Here we report that all of them are very strong 13–15 $M_{\rm Jup}$ BD candidate member to THA, with $P_{H_k} > 99.9\%$ ($C_{H_k} = 0.1\%$), $P_{H_k} = 99.9\%$ ($C_{H_k} = 0.2\%$) and $P_{H_k} = 98.4\%$ ($C_{H_k} = 1.2\%$), respectively. Our analysis suggests that both 2MASS J02235464–5815067 and 2MASS J03231002–4631237 could be unresolved binaries.

2MASS J02411151–0326587 is an L0 γ dwarf with colors too red for its spectral type, signs of low-gravity in both its optical and NIR spectra and a triangular-shaped H-band continuum. Allers & Liu (2013) categorize this as a VL-G object. Here we propose this object as a THA BD candidate, with $P_{H_k} = 79.1\%$ and $C_{H_k} = 1.1\%$, and that it would have a mass comprised between 13–14 $M_{\rm Jup}$ if it is actually a member.

2MASS J03264225–2102057 (2MUCD 10184) is an L4 dwarf with colors too red for its spectral type and Li absorption. Cruz et al. (2007) suggests that this object should be younger than 500 Myr based on the strength of its Li absorption. We find that this object is a 13–15 $M_{\rm Jup}$ BD candidate member to ABDMG, with $P_{H_k} = 98.9\%$ and $C_{H_k} = 1.3\%$. Our analysis suggests that this object could be an unresolved binary.

2MASS J03421621–6817321 (2MUCD 10204) is an L2 dwarf that was reported by

Faherty et al. (2009) as having colors too red for its spectral type. We find that even if we do not have strong indicators of youth for this object, it is still a very strong 11–13 $M_{\rm Jup}$ *planemo* candidate member to THA, with $P_{H_k} = 98.8\%$ and $C_{H_k} = 5.6\%$. Our analysis also suggests that this object could be an unresolved binary.

2MASS J03572695–4417305 is an L0 β binary system unusually red for its spectral type with subtle signs of low gravity in its unresolved optical spectrum. Bouy et al. (2003) report this object as a binary system with an angular separation of 0".098 and a position angle of 174°. Liu et al. (2010) obtained resolved spectral types of M9 and L1.5 for the two components, and estimate their age to be around 100 Myr because of their low surface gravity. Here we report this unresolved system as a very strong 14–15 $M_{\rm Jup}$ candidate member to THA, with $P_{H_k} = 99.6\%$ and $C_{H_k} = 1.2\%$.

2MASS J04210718–6306022 (2MUCD 10268) is an L5 γ dwarf with unusually red colors for its spectral type and signs of low-gravity in both its optical and NIR spectra. This object also displays Li absorption, and here we report that it is a *planemo* candidate member to ARG with $P_{H_k} = 98.1\%$ and $C_{H_k} = 8.0\%$, with a mass of 10–11 $M_{\rm Jup}$.

2MASS J04362788–4114465 is a peculiar M8 dwarf with signs of low-gravity in both its optical and NIR spectra, which Allers & Liu (2013) classify as VL-G. Here we find that this object is a very strong 32–49 $M_{\rm Jup}$ BD candidate member to COL, with $P_{H_k} = 96.0\%$ and $C_{H_k} = 9.1\%$.

2MASS J04433761+0002051 (2MUCD 10320) is an M9 γ dwarf with signs of low gravity in its optical spectrum, a high rotational velocity, NIR colors unusually red for its spectral type, and displaying Hα emission and Li absorption. Kirkpatrick et al. (2008) report that the strength of its Li absorption is compatible with an age of $<$ 100 Myr, and Schlieder et al. (2012a) proposes it as a candidate member to the ABDMG, and Reiners & Basri (2009) measure a radial velocity of 17.1 ± 3.0 km s^{-1}. This measurement agrees within 0.06σ of the predicted 17.3 ± 1.8 km s^{-1} value for the βPMG hypothesis. Here, we find that this object is probably not a member of the ABDMG, but rather a strong candidate 15–16 $M_{\rm Jup}$ BD member to the βPMG, with $P_{H_k} = 99.8\%$ and $C_{H_k} = 3.4\%$. J. Schlieder (priv. comm.) agrees with our result that this object should rather be a βPMG candidate. The reason for their claim

that this object is a candidate to ABDMG arises from their use of optical data in deriving a proper motion measurement of $\mu_\alpha = 48$ mas yr^{-1}, $\mu_\delta = -122$ mas yr^{-1}, which is at 3.3σ of the one presented here ($\mu_\alpha = 35.9 \pm 7.7$ mas yr^{-1}, $\mu_\delta = -98.0 \pm 8.2$ mas yr^{-1}). Our analysis suggests that this object could be an unresolved binary.

2MASS J05184616–2756457 (2MUCD 10381) is an unusually bright L1 γ dwarf with very red colors for its spectral type and signs of low gravity in both its optical and NIR spectra. It also shows a typical triangular-shaped H-band continuum, and Allers & Liu (2013) classify it as VL-G. Faherty et al. (2012) measure a trigonometric distance of 46.8 ± 15.0 pc. Here we report this object as a 13–22 $M_{\rm Jup}$ candidate member to COL, with $P_{H_k} = 96.2\%$ and $C_{H_k} = 0.7\%$. The predicted distance for the COL hypothesis is of 51.8 ± 5.6 pc, which is at 0.3σ from the measured value. However, it would be desirable to increase the precision of the current distance measurement, which still only has a 3σ significance. Our analysis suggests that this object could be an unresolved binary.

2MASS J05361998–1920396 (2MUCD 10397) is an L2 γ dwarf with unusually red colors for its spectral type and signs of low-gravity in its optical spectrum. This object displays a triangular-shaped H-band continuum and Allers & Liu (2013) classify it as VL-G. Faherty et al. (2012) measure a trigonometric distance of 39.0 ± 14.0 pc for this object. Here we report that it is a 11–14 $M_{\rm Jup}$ candidate member to COL, with $P_{H_k} = 95.2\%$ and $C_{H_k} = 0.7\%$. The predicted distance associated with the COL hypothesis is of 40.2 ± 3.2 pc, which is at 0.1σ from the measured value. However, it would be desirable to increase the precision of the current distance measurement, which only has a 2.8σ significance.

2MASS J12451416–4429077 (TWA 29) is an over-luminous M9.5p dwarf with Hα emission and signs of low-gravity in both its optical and NIR spectra. It has a typical triangular-shaped H-band continuum and Witte et al. (2011) derives a marginally low surface gravity of $\log g = 4.5$ by fitting atmosphere models to its NIR spectrum. It has been identified by Looper et al. (2007a) as a candidate member to the TWA, and Weinberger et al. (2013b) measure a trigonometric distance of 79.0 ± 12.9 pc. Here we also find that this object is a 17–19 $M_{\rm Jup}$ BD candidate to TWA, with $P_{H_k} = 93.3\%$ and $C_{H_k} = 0.4\%$. The predicted distance associated with the TWA hypothesis is of 74.6 ± 6.8 pc, at only 0.3σ of the measured value.

2MASS J16471580+5632057 is a peculiar L9 dwarf with colors unusually red for its spectral type. Dupuy & Liu (2012) measure a distance of 8.6 ± 2.2 pc for this object. Without making any assumption on its age, we find that it is a 4–6 $M_{\rm Jup}$ candidate to ARG, with $P_{H_k} = 26.3\%$ and $C_{H_k} = 3.3\%$. If we do not include the distance measurement, the bayesian probability is $P_{H_k} < 0.1\%$.

2MASS J20004841–7523070 (2MUCD 20845) is an M9 dwarf with signs of low gravity in its optical spectrum and NIR colors unusually red for its spectral type. Gálvez-Ortiz et al. (2010) indicate that this object could be a member of the Castor moving group, but that further spectroscopic study is needed to assess its membership. They also measure a radial velocity of 11.8 ± 1.0 km s^{-1} for this object. The Castor moving group is not considered in the results presented here because of its age older than 100 Myr, however we have performed a simpler bayesian analysis without using photometry (see Malo et al. 2013) but including the Castor hypothesis, and found that it only had a 3.1% bayesian probability (versus 72.3% for the βPMG hypothesis), associated to a predicted distance of 18.9 ± 4.4 pc. Here we rather propose it as a 18–27 $M_{\rm Jup}$ BD candidate member to the βPMG, with $P_{H_k} = 96.6\%$ and $C_{H_k} = 4.0\%$, and a predicted distance of $33.3^{+3.2}_{-2.8}$ pc. We suggest that the best way to completely rule out the Castor membership would be a measurement of its parallax. Our analysis suggests that this object could be an unresolved binary.

2MASS J21011544+1756586 (** BOY 11) is an L7.5 dwarf with unusually red colors for its spectral type and a typical triangular-shaped H-band continuum. Witte et al. (2011) estimate a marginally low surface gravity of $\log g = 4.5$ by fitting atmosphere models to its NIR spectrum. However, we consider that none of these signs of youth are strong enough to assume an age of < 1 Gyr for this object. Konopacky et al. (2010) report that this is an unresolved binary and Vrba et al. (2004) measure a distance of 33.2 ± 3.8 pc. Without making any assumption about the age of this object, we find that it is a 11–12 $M_{\rm Jup}$ *planemo* candidate member to ABDMG, with $P_{H_k} = 26.8\%$ and $C_{H_k} = 4.2\%$. Our analysis suggests that this object could be an unresolved binary.

2MASS J21140802–2251358 is a very red L7 object identified by Liu et al. (2013b) to be a *planemo* candidate member to βPMG. They report a trigonometric distance of 24.6 ± 1.4 pc

for this object. Here, we find that this object is indeed a strong 8–9 $M_{\rm Jup}$ *planemo* candidate member to the βPMG, with $P_{H_k} = 99.7\%$ and $C_{H_k} = 0.1\%$.

2MASS J21265040–8140293 is an L3 γ dwarf with unusually red colors for its spectral type and signs of low-gravity in its optical spectrum. We find that this object is a 13–14 $M_{\rm Jup}$ candidate to THA, with $P_{H_k} = 94.5\%$ and $C_{H_k} = 0.5\%$. Our analysis indicates that this object could be an unresolved binary system.

2MASS J22064498–4217208 is an L2 dwarf with Li absorption displaying unusually red colors for its spectral type. Here we find that without making any assumption on its age, it is a 18–21 $M_{\rm Jup}$ BD candidate member to ABDMG with $P_{H_k} = 95.3\%$ and $C_{H_k} = 14.1\%$.

2MASS J22443167+2043433 (2MUCD 20968) is an L6.5 lithium dwarf with signs of low gravity in its NIR spectrum, and NIR colors unusually red for its spectral type. Witte et al. (2011) suggest a value for log g = 3.5 based on atmospheric models fitting to its NIR spectrum. We found that this object is a strong candidate member to the ABDMG, with $P_{H_k} = 99.6\%$ and $C_{H_k} = 0.5\%$. We estimate a mass of 11–12 $M_{\rm Jup}$ if membership is confirmed. Our analysis suggests that this object could be an unresolved binary.

2MASS J23225299–6151275 is an L2 γ BD with signs of low gravity in its optical spectrum and NIR colors unusually red for its spectral type (Reid et al. 2008b, Cruz et al. 2009, Faherty et al. 2013b). We propose it as a new strong 12–13 $M_{\rm Jup}$ candidate to the THA, with $P_{H_k} > 99.9\%$ and $C_{H_k} = 0.3\%$. We also report that we have identified a common proper-motion primary LMS at an angular separation of 16".6: 2MASS J23225240–6151114, an M5 which has a proper motion of $\mu_\alpha = 80.2 \pm 3.7$ mas yr^{-1}, $\mu_\delta = -69.5 \pm 9.3$ mas yr^{-1}, as inferred from its 2MASS and WISE positions. This measurement is within 0.27σ and 0.37σ of the μ_α and μ_δ proper motion of the companion, respectively. The UCAC4 (Zacharias et al. 2012) proper-motion is consistent with it. If the system is at the statistical distance of 43.0 ± 2.4 pc predicted for the THA hypothesis, then the physical separation would be 714 ± 40 AU. The predicted statistical distance for the young field hypothesis is of $57.0^{+7.6}_{-9.6}$ pc, which would bring the physical separation of the system to 946^{+126}_{-159} AU. If the THA hypothesis is verified, the M5 primary would have a mass comprised between 34 and 37 $M_{\rm Jup}$, and thus the system would have a mass ratio of $q = 0.35^{+.03}_{-.05}$.

2.8.1.5 Candidates with modest probability

2MASS J00332386–1521309 is an L4 β dwarf with colors too red for its spectral type and subtle signs of low-gravity in its optical spectrum. Allers & Liu (2013) characterize its NIR spectrum as a normal Field-Gravity (FLD-G) dwarf. The only NIR gravity indicator that is not clearly consistent with FLD-G is the shape of the H-band continuum that could be triangular, however the quality of the available data is not sufficient to say more about this. We propose this object as a weak candidate to ARG, with $P_{H_k} = 31.9\%$ and $C_{H_k} = 21.8\%$. If it is actually a member of ARG, it would have a mass between 9 and 11 $M_{\rm Jup}$.

2MASS J01291221+3517580 is an unusually red L4 dwarf with Li absorption, with no clear evidence of youth. We find that, without making any assumption on its age, this object is a 9–11 $M_{\rm Jup}$ candidate member to ARG with $P_{H_k} = 7.2\%$ and $C_{H_k} = 67.1\%$.

2MASS J02530084+1652532 is an M7 dwarf for which models fitting suggest a marginally low log g $\sim$4.5 (Witte et al. 2011). Without making any assumption on its age, we find that this object is a 13–15 $M_{\rm Jup}$ BD candidate member to ARG with $P_{H_k} = 25.5\%$ and $C_{H_k} = 29.7\%$. A measurement of its radial velocity and distance, as well as a thorough analysis of its spectral properties would be needed to confirm this.

2MASS J03032042–7312300 is an L2 γ dwarf with colors too red for its spectral type and signs of low-gravity in its optical spectrum. Here, as also reported in Kirkpatrick et al. (2010), we find that this is a candidate member to THA albeit a weak one, with $P_{H_k} = 4.4\%$ and $C_{H_k} = 66.1\%$, which would make it a 12–14 $M_{\rm Jup}$ object.

2MASS J04062677–3812102 is an L0 γ dwarf with unusually red colors for its spectral type and signs of low gravity in both its optical and NIR spectra. It also displays the typical triangular-shaped H-band continuum characteristic of low-gravity. Allers & Liu (2013) classified this object as VL-G. Kirkpatrick et al. (2010) reported that the good match of this object's optical spectrum to that of 2MASS J01415823–4633574 suggests an age of $\sim$30 Myr, and that its sky location furthermore strengthens the hypothesis of this object being a member of COL. Here we find that this object effectively has a good match to the properties of COL, but we find it is quite a weak candidate member with $P_{H_k} = 2.1\%$ and $C_{H_k} = 60.7\%$.

Table 2.3. Age and Mass Estimates of Candidates

Name	SpT[d]	C_{H_k} %	P_{H_k} %	NYA	Reported Candidate[e]	Mass ($M_{\rm Jup}$)	v_{rs}[f] ($\rm km\,s^{-1}$)	d_s[f] (pc)
				Bona fide members				
J0123–6921	M7.5	< 0.1[a,b]	> 99.9	THA	···	$56-74$	9.9 ± 2.5	47.4 ± 3.2
J0355+1133	L5 γ	0.1[a,b]	99.7	ABDMG[c]	ABDMG (49)	$13-14$	12.6 ± 1.7	8.5 ± 0.4
J1139–3159	M9 γ	< 0.1[a,b]	99.3	TWA[c]	···	$16-27$	11.3 ± 2.2	46.6 ± 4.4
				Peripheral candidates				
J0608–2753	M9 γ	1.5[a,b]	3.7	COL	βPMG (66)	$16-24$	22.7 ± 1.3	42.6 ± 7.6
J1022+0200	M9 β	6.0[a,b]	2.6	ABDMG	···	$34-53$	9.6 ± 15.0	16.5 ± 1.2
				Contaminants from other associations				
J0339–3525	M9	···	99.7[g]	CAS	CAS (65)	$44-45$	14.4 ± 3.3	6.8 ± 2.6
J2313+2117	M7.5	···	95.8[g]	CAS	CAS (74)	$81-94$	-0.6 ± 2.8	16.8 ± 2.7
				Candidates with a high probability				
J0004–6410	L1 γ	0.5	99.7	THA[c]	THA (42)	$13-14$	6.8 ± 2.9	47.4 ± 3.2
J0006–6436	L0	0.2	> 99.9	THA[c]	···	$21-41$	6.5 ± 2.5	43.4 ± 2.8
J0019+4614	M8	3.9[a]	88.0	ABDMG	ABDMG (75)	$78-94$	-17.0 ± 1.4	37.4 ± 2.8
J0032–4405	L0 γ	0.2[b]	91.8	βPMG	···	$10-11$	11.6 ± 1.7	26.1 ± 2.0
J0037–5846	L0 γ	0.7	97.3	THA[c]	···	$13-15$	6.8 ± 2.5	47.8 ± 3.2
J0041-5621	M6.5+M9	0.2[a]	> 99.9	THA[c]	THA (63)	$14-41$	6.5 ± 2.4	41.8 ± 2.4
J0045+1634	L2 β	1.8[a]	99.9	ARG	···	$13-14$	3.4 ± 1.3	13.3 ± 0.8
J0047+6803	L7 p[c]	2.4	98.2	ABDMG	···	$11-15$	-20.4 ± 1.1	10.5 ± 0.8
J0103+1935	L6 β	0.1[b]	76.0	ARG	···	$10-11$	8.6 ± 2.1	15.3 ± 1.2
J0117–3403	L1[c]	1.0	99.3	THA	···	$13-14$	3.4 ± 2.1	40.6 ± 2.0
J0122–2439	M3.5+L5[d]	3.4[a]	92.8	βPMG	ABDMG (BW13)	$5-89$	10.6 ± 1.7	22.5 ± 2.8
J0141–4633	L0 γ	0.1[a]	99.7	THA[c]	THA/βPMG (42)	$14-20$	7.6 ± 2.4	41.4 ± 2.8
J0221–5412	M9	0.2	> 99.9	THA	···	$16-26$	10.2 ± 2.2	41.0 ± 2.4
J0223–5815	L0 γ	0.1	> 99.9	THA[c]	···	$14-15$	10.6 ± 2.4	43.4 ± 2.8
J0225–5837	M9	0.2	> 99.9	THA	···	$20-32$	10.7 ± 2.4	43.8 ± 2.8
J0234–6442	L0 γ	0.2	99.9	THA	THA (42)	$13-14$	10.9 ± 2.5	45.8 ± 2.8
J0241–0326	L0 γ	1.1	79.1	THA	···	$13-14$	5.1 ± 2.5	49.8 ± 3.2
J0323–4631	L0 γ	1.2	98.4	THA[c]	···	$14-15$	12.6 ± 2.4	49.4 ± 3.2
J0326–2102	L4	1.3	98.9	ABDMG[c]	···	$13-15$	23.1 ± 2.1	26.1 ± 2.0
J0342–6817	L2	5.6	98.8	THA[c]	···	$11-13$	13.1 ± 2.2	50.2 ± 3.6
J0357–4417	L0 β	1.2	99.6	THA[c]	···	$14-15$	14.2 ± 2.2	48.6 ± 3.2
J0421–6306	L5 γ	8.0	98.1	ARG	···	$10-11$	9.7 ± 2.2	16.5 ± 1.2
J0436–4114	M8 p	9.1	96.0	COL	···	$32-49$	22.0 ± 2.0	44.2 ± 6.4
J0443+0002	M9 γ	3.4[a]	99.8	βPMG[c]	ABDMG (75)	$17-19$	16.9 ± 2.0	25.7 ± 3.2
J0518–2756	L1 γ	0.7[b]	96.2	COL[c]	···	$14-22$	22.9 ± 1.7	51.8 ± 5.6

Table 2.3 — continued

Name	SpT[d]	C_{H_k} %	P_{H_k} %	NYA	Reported Candidate[e]	Mass ($M_{\rm Jup}$)	v_{rs}[f] ($\rm km\,s^{-1}$)	d_s[f] (pc)
J0536–1920	L2 γ	0.7[b]	95.2	COL	···	$12-13$	22.7 ± 1.7	40.2 ± 3.2
J1245–4429	M9.5 p	0.4[b]	93.3	TWA[c]	TWA (51)	$17-19$	9.9 ± 2.1	81.8 ± 8.4
J1647+5632	L9 p[d]	3.3[b]	26.3	ARG	···	$4-5$	-10.9 ± 3.1	14.5 ± 1.2
J2000–7523	M9	4.0[a]	96.6	βPMG[c]	CAS (26)	$19-27$	6.4 ± 2.4	32.9 ± 3.2
J2101+1756	L7.5	4.2[b]	26.8	ABDMG[c]	···	$11-12$	-19.8 ± 2.0	24.9 ± 1.6
J2114–2251	L7[d]	0.1[b]	99.7	βPMG[c]	βPMG (LI13)	$8-9$	-6.4 ± 1.7	22.1 ± 1.6
J2126–8140	L3 γ	0.5	94.5	THA[c]	···	$13-14$	8.2 ± 2.4	45.0 ± 2.8
J2206–4217	L2	14.1	95.3	ABDMG	···	$18-21$	7.6 ± 2.0	28.5 ± 1.6
J2244+2043	L6.5	0.5	99.6	ABDMG[c]	···	$11-12$	-15.5 ± 1.7	18.5 ± 1.2
J2322–6151	L2 γ	0.3	>99.9	THA	···	$12-13$	4.8 ± 2.5	43.0 ± 2.4
Candidates with a modest probability								
J0033–1521	L4 β	21.8	31.9	ARG	···	$9-11$	2.3 ± 1.3	17.3 ± 1.6
J0129+3517	L4[c]	18.4	43.5	ARG	···	$9-11$	6.4 ± 2.0	28.5 ± 3.2
J0253+3206	M7 p	29.7	25.5	βPMG	···	$13-15$	5.7 ± 2.4	35.8 ± 2.8
J0303–7312	L2 γ	66.1	4.4	THA	THA (42)	$12-14$	12.1 ± 2.7	53.0 ± 3.6
J0406–3812	L0 γ	60.7	2.1	COL	COL (42)	$12-14$	21.3 ± 3.4	69.4 ± 9.2
J0619–2903	M6	22.0	80.7	COL[c]	···	$15-23$	24.2 ± 2.0	55.8 ± 6.0
J0632–5010	L3	61.1	1.3	ABDMG	···	$10-14$	30.8 ± 1.4	10.5 ± 4.8
J0642+4101	L/T p[c]	52.0	49.5	ABDMG	···	$11-12$	0.6 ± 1.5	17.3 ± 0.8
J0652–5741	M8 β	49.7[b]	3.3	ABDMG[c]	···	$29-34$	29.2 ± 1.3	45.8 ± 5.2
J1004+5022	L3 β	29.6	32.2	ABDMG	···	$22-28$	-10.7 ± 3.5	26.1 ± 3.6
J1600–2456	M7.5p[c]	59.0	0.1	ABDMG[c]	···	$11-13$	-6.9 ± 2.0	20.5 ± 1.2
J1956–7542	L0 γ	55.3	16.6	THA[c]	···	$13-14$	6.4 ± 2.7	59.8 ± 4.4
J2148+4003	L6	36.6	48.1	ARG	···	$6-7$	-9.2 ± 1.3	4.9 ± 0.4
J2208+2921	L3 γ	53.8	10.1	βPMG	···	$9-11$	-10.6 ± 2.0	35.4 ± 3.6
J2351+3010	L5.5	62.7	47.0	ARG	···	$9-11$	-1.5 ± 1.3	20.9 ± 2.0

Table 2.3 — continued

Name	SpT[d]	C_{H_k} %	P_{H_k} %	NYA	Reported Candidate[e]	Mass ($M_{\rm Jup}$)	v_{rs}[f] ($\rm km\,s^{-1}$)	d_s[f] (pc)
Candidates with a low probability								
J0126+1428	L4 γ	76.7	3.4	βPMG	···	$7-9$	6.0 ± 4.5	38.6 ± 6.0
J0512–2949	L4.5	77.9	15.4	βPMG	···	$5-7$	19.7 ± 1.5	12.9 ± 2.0
J0712–6155	L1 β	62.8[b]	2.6	ABDMG[c]	···	$27-40$	29.0 ± 2.0	43.0 ± 6.4
J1547–2423	M9	88.0	0.1	ARG	···	$13-14$	-19.7 ± 2.2	23.3 ± 2.8
J2013–2806	M9	70.7	44.0	βPMG	···	$14-16$	-7.4 ± 2.4	44.2 ± 4.8
J2213–2136	L0 γ	80.5	3.1	βPMG	···	$12-13$	-1.9 ± 1.8	45.0 ± 3.6

[a]This result takes into account a radial velocity measurement.

[b]This result takes into account a parallax measurement.

[c]The binary hypothesis has a higher probability.

[d]Spectral types with this mention are near-infrared. Other ones are optical.

[e]Objects for which membership was already suspected. See Table 2.4 for references and abbreviations.

[f]Statistical predictions associated with the most probable NYA. For the actual measurements when available, see Table 2.4.

[g]This probability was obtained from a simpler Bayesian analysis (see Malo et al. 2013) that makes the assumption of uniform prior probabilities.

However, if we consider that this object effectively has an age of 30 Myr, the probability that it is a field contaminant would drop below $C_{H_k} < 5\%$. If it is actually a member of COL, we estimate its mass to be between 12 and 14 $M_{\rm Jup}$.

2MASS J06195260–2903592 is an M6 dwarf unusually red for its spectral type and reported as having signs of low gravity in its optical spectrum by Cruz et al. (2003). Allers & Liu (2013) estimate the age of this object to be $\sim$10 Myr because it displays a circumstellar disk (which could also explain its reddening). We find that this object is a good 15–23 $M_{\rm Jup}$ candidate member to COL, with $P_{H_k} = 80.7\%$ and $C_{H_k} = 22.0\%$. The lower-end mass estimate is more probable because of the circumstellar disk, and for the same reason C_{H_k} is probably pessimistic. Our analysis suggests that this object could be an unresolved binary.

2MASS J06322402–5010349 is an L3 dwarf with strong Li absorption. Without making

any assumption on its age, we find that it is a modest 10–14 $M_{\rm Jup}$ candidate member to ABDMG with $P_{H_k} = 1.3\%$ and $C_{H_k} = 61.1\%$. A measurement of its radial velocity and distance, as well as a thorough analysis of its spectral properties would be needed to confirm this.

2MASS J06420559+4101599 is a very peculiar object identified by Mace et al. (2013a) as an URL dwarf. It has a NIR spectrum that is badly fit by any known L or T dwarfs. It has an extremely red continuum and a classification using solely the J-band would result in a T spectral type, however this object shows no sign of CH_4, which is inconsistent with it being a T dwarf. These peculiar properties could result from a very dusty photosphere at the L/T transition, and Mace et al. (2013a) report that low-gravity or metallicity could not provide the whole explanation. They have thus classified this object as L/Tp Here we identify that without making any assertion about this object's age, it comes out as a weak candidate member to ABDMG, with $P_{H_k} = 49.5\%$ and $C_{H_k} = 52.0$. If this object turns out to be a member of ABDMG, it would have a mass of approximately 11–12 $M_{\rm Jup}$, which means that this could be a *planemo* at the L/T transition. If we could find evidence that this system is young, the probability that it is a field contaminant would also be lower. A measurement of its distance could significantly strengthen the proposition that this is a member of ABDMG. Mace et al. (2013a) report two more systems similar to this one : WISE J173859.27+614242.1 and 2MASS J07542987+7909546. We find that none of them have kinematics consistent with any of the YMGs considered here. Being able to restrict the age of 2MASS J06420559+4101599 to that of ABDMG would be of great interest in understanding the physical nature of this odd object, we thus urge that measuring its distance and radial velocity should be a priority.

2MASS J06524851–5741376 (2MUCD 10601) is an M8 β dwarf with unusually red colors for its spectral type and subtle signs of low-gravity in its optical spectrum. Chauvin et al. (2012) identifies this system as a tight binary with an angular separation of 0".23, a mass ratio of $q \sim 0.7$–0.8 and a semi-major axis of 5–6 AU. Faherty et al. (2012) measure a trigonometric distance of 32.0 ± 3.3 pc. Here we report this system as a BD binary candidate to ABDMG, with $P_{H_k} = 3.3\%$ and $C_{H_k} = 49.7\%$. The low bayesian probability is due to the fact that the predicted distance value associated with the ABDMG hypothesis is of $45.8^{+5.2}_{-4.8}$ pc, at

2.4σ of the measured value. If this system is confirmed as a member of ABDMG, the mass of each component would be approximately 21 to 33 $M_{\rm Jup}$.

2MASS J10042066+5022596 is an L3 β dwarf with unusually red colors for its spectral type, Li absorption and signs of low-gravity in both its optical and NIR spectra. It has a typical triangular-shaped H-band continuum, and Allers & Liu (2013) report it as VL-G. This object is a companion to G 196–3, a bright co-moving M3 LMS at 17".7 with a radial velocity of -0.7 ± 1.2 $\rm km\,s^{-1}$ (Shkolnik et al. 2012). Metchev et al. (2008) report an age estimate of 60 to 300 Myr for 2MASS J10042066+5022596, however McGovern et al. (2004) state that it could be younger. Here we find that it comes out as a weak 22–28 $M_{\rm Jup}$ BD candidate member to ABDMG, with $P_{H_k} = 32.2\%$ and $C_{H_k} = 29.6\%$. At the predicted distance of 26.1 ± 3.6 pc, this would mean that this object is at a physical separation of 462 ± 64 AU. Since the companion is masked by its bright primary in WISE data, we did not use WISE photometry and did not measure a proper motion from the 2MASS and WISE data for this object. As a result, we did not consider photometry at all in the bayesian analysis, which means that the true contamination rate for this object could be somewhat higher, since our Monte Carlo contamination analysis made use of the 2MASS and WISE photometry. The radial velocity of the parent star is within 0.4σ of the CAR hypothesis, which is associated with a statistical radial velocity prediction of -1.8 ± 2.8 $\rm km\,s^{-1}$. For a system of approximately 0.4 $M_\odot$at this separation, the expected variation in radial velocity is of the order of 1 $\rm km\,s^{-1}$, hence the binary nature of this object should not affect our conclusions. If we thus include this radial velocity measurement in it, the bayesian probability associated to the CAR hypothesis increases to $P_H = 97.1\%$, but still yields a high $C_{H_k} \sim 85\%$. The reason for this is that such a low radial velocity and high proper motion are unlikely to come from CAR in our SKM models (see Figure 2.1). We thus conclude that this object's membership is quite ambiguous, and that a measurement of its distance is needed to decide whether it is a candidate member to ABDMG or CAR. It is also possible that the SKM model for CAR is still not a fair representation of reality, since we know only 7 bona fide members in this YMG. Finding more members to CAR will allow to investigate this further.

2MASS J16002647–2456424 is a peculiar M7.5 dwarf with signs of low-gravity in its

NIR spectrum. We find that it is a weak 11–13 $M_{\rm Jup}$ *planemo* candidate member to ABDMG with a $P_{H_k} = 0.1\%$ and $C_{H_k} = 59.0\%$. Even if the field contamination probability seems weak for such a low bayesian probability, we stress that this result should be interpreted with caution since 2MASS J16002647–2456424 has a sky position close to the Upper Scorpius association. It is thus likely that this object is a member to Upper Scorpius, which was not considered in our analysis.

2MASS J19564700–7542270 is an L0 γ dwarf with unusually red colors for its spectral type and signs of low-gravity in its optical spectrum. We find that this object is a 13–14 $M_{\rm Jup}$ BD candidate to THA, with $P_{H_k} = 16.6\%$, $C_{H_k} = 55.3\%$, and signs that it could be an unresolved binary system.

2MASS J21481633+4003594 is an L6.5 dwarf with NIR colors unusually red for its spectral type, a triangular-shaped H-and continuum and weaker-than-normal alkali lines. Atmosphere models fitting also suggests that this is a young object with log g $\sim$4 (Witte et al. 2011). Here, we find that this object is a moderate 6–7 $M_{\rm Jup}$ *planemo* candidate to ARG, with $P_{H_k} = 48.1\%$ and $C_{H_k} = 36.6\%$.

2MASS J22081363+2921215 is an L3 γ dwarf with a triangular-shaped H-band continuum that display signs of youth in its optical spectrum. It shows Li absorption and has NIR colors unusually red for its spectral type. Here, we find that it is a moderate 9–11 $M_{\rm Jup}$ *planemo* candidate member to βPMG, with $P_{H_k} = 10.1\%$ and $C_{H_k} = 53.8\%$.

2MASS J23512200+3010540 is a peculiar L5 dwarf with unusually red NIR colors for its spectral type, as reported by Kirkpatrick et al. (2010). We find that it is a moderate 9–11 $M_{\rm Jup}$ *planemo* candidate to ARG, with $P_{H_k} = 47.0\%$ and $C_{H_k} = 62.7\%$. A measurement of its radial velocity and distance would be needed to confirm this.

2.8.1.6 Candidates not uncovered with our method

2MASS J09510459+3558098 (NLTT 22741) is an M4.5 dwarf displaying X-ray emission. Shkolnik et al. (2009) estimated its age to be comprised between 40 and 300 Myr, and then Shkolnik et al. (2009) proposed it as a candidate member to THA. Here, we find that without considering the radial velocity measurement of 10.2 ± 0.2 km s^{-1} from Shkolnik et al.

(2012), it only has a bayesian probability $P_{H_k} = 16.1\%$ for ABDMG, with a predicted radial velocity of –3.9 ± 1.8 km s^{-1}, as well as small bayesian probabilities of $P_{H_k} = 0.2\%$ for TWA and $P_{H_k} = 0.3\%$ for CAR. When the radial velocity measurement is added, bayesian probabilities fall below 0.01% for every YMG hypothesis, which is associated to a $> 99.9\%$ probability that this object is a young field contaminant. This object has an L6 co-moving companion displaying signs of youth for which Dupuy & Liu (2012) measured a distance of 62 ± 27 pc, which further weakens the hypothesis that this object is a candidate member to any YMG considered here.

2MASS J13142039+1320011 (** Law 2) is an over-luminous M7 dwarf with Hα and X-ray emission. Schlieder et al. (2012a) report that this object is a likely member of ABDMG, based on its sky position, proper motion from the LSPM catalog and parallax (Lépine & Simon 2009). However, even if our proper motion measurement agrees within 1σ to that in LSPM, we find a bayesian probability of less than $P_{H_k} = 0.1\%$ for the ABDMG hypothesis when we do not include the distance measurement. A distance of 21.3 ± 1.2 pc is predicted for the ABDMG hypothesis, which is similar to that predicted by Schlieder et al. (2012a ; 20.1 ± 1.0 pc). However, when we add the measured distance 16.4 ± 0.8 pc, the bayesian probability for all YMG hypotheses are less than 0.01%.

2.8.1.7 Discussion

Results presented here and in Malo et al. (2013) show that bayesian analysis is a powerful tool for searching for new candidate members to YMGs that are significantly spread on the sky, even without having access to radial velocity and parallax measurements. With the modified version presented here which is adapted to later-than-M5 objects, it can be now conceivable to build a credible sample of BD and *planemo* candidates to YMGs. This fraction might be even lower if there are still missing bona fide members in the A0–M0 spectral-type range. However, there are some limitations to the present method that could potentially be complemented by other methods such as traceback analysis : (1) We expect to miss a fraction of true members, which would be hard to differentiate with field contaminants unless we have measurements of their radial velocity and parallax. This is especially true for ARG, ABDMG and βPMG. (2)

Potential outlier members with $XYZUVW$ values significantly different from the locus values of their YMG, might not be uncovered by our method unless we slowly build up our SKM model by iteratively adding bona fide members with relatively low bayesian probabilities such as 2MASS J06085283–2753583. (3) Our analysis is model-dependent and thus results are vulnerable to change if the SKM or photometric models described earlier are not a good representation of reality. Several improvements could still be brought to our method, including the addition of older YMGs such as Castor and Carina-Near, and yet a better treatment of photometric sequences when we know more about broad-band photometry of young BDs (e.g., see J. Filippazzo et al., in preparation). If the IMF of YMGs is not significantly different than that from the field, one can expect that currently known members are only the tip of the iceberg, accounting for only 10% of their total population. This consideration has motivated us to initiate a systematic all-sky survey for more later-than-M5 members to YMGs in the 2MASS and WISE catalogs, which will be the subject of an upcoming paper. The very first results of this survey can be found in Gagné et al. (2013).

2.9 Summary and conclusions

We have presented several modifications to the bayesian inference method introduced by Malo et al. (2013) in order to assess the probabilities that late-type objects are members to several YMGs. In particular, we introduced the use of NIR colors and spectral types in order to calibrate the distance hypotheses for later-than-M5 objects, as well as improved our spatial and kinematic modeling of YMGs by representing their XYZ and UVW distributions as rotated ellipsoids. We have also presented a thorough contamination analysis to assess the significance of the results yielded by this method. We have then identified several LMS, BD and *planemo* candidate members to YMGs, which were already recognized for displaying various signs of youth, or for having redder-than-normal NIR colors. We also provide statistical predictions of their radial velocities and distances if they are actual members, so that these hypotheses might be tested against observation in the coming years (see, e.g., J. K. Faherty et al., in preparation). We report on 35 very strong $> M5$ candidate members to YMGs, from which 25 are assigned a membership to a YMG for the first time.

We also propose 2MASS J01231125–6921379 as a new M7.5 bona fide members to THA. We independently confirm that 2MASS J03552337+1133437 should be considered as a bona fide members to ABDMG and question the possibility that 2MASS J06085283–2753583 could be a member of COL instead of βPMG. We also report 2MASS J23225240–6151114 as an M5 common proper-motion primary to the L2 γ BD 2MASS J23225299–6151275, this system being a strong candidate member to THA. We note that 2MASS J00470038+6803543 and 2MASS J22244381–0158521, which are extremely red L dwarfs with no clear evidence of youth, are strong candidate members to ABDMG. Finally, we show that a dozen candidates unveiled here could be free-floating planetary-mass objects if their membership is confirmed. Radial velocity and parallax measurements are needed to confirm their membership. An online web tool as well as additional figures and information on YMGs can be found at our group's website *www.astro.umontreal.ca/~gagne*.

The authors would like to thank Jacqueline Faherty, Emily Rice, Adric Riedel, Philippe Delorme, Ben Oppenheimer, Céline Reylé, Sandie Bouchard, Amélie Simon and Brendan Bowler for useful comments and discussions. Thanks to Annie Robin for help with the Besançon Galactic model. We would like to address special thanks to Adric Riedel for generously sharing valuable parallax data with our team. This work was supported in part through grants from the Fond de Recherche Québécois – Nature et Technologie and the Natural Science and Engineering Research Council of Canada. This research has made use of the SIMBAD database and VizieR catalogue access tool, operated at Centre de Données astronomiques de Strasbourg (CDS), France (Ochsenbein et al. 2000). This research has benefitted from the M, L, and T dwarf compendium housed at *http://DwarfArchives.org* and maintained by Chris Gelino, Davy Kirkpatrick, and Adam Burgasser. This publication makes use of data products from the Two Micron All Sky Survey, which is a joint project of the University of Massachusetts and the Infrared Processing and Analysis Center/California Institute of Technology, funded by the National Aeronautics and Space Administration and the National Science Foundation (Skrutskie et al. 2006, Kirkpatrick et al. 2003). This publication makes use of data products from the Wide-field Infrared Survey Explorer, which is a joint project of the University of California, Los Angeles, and the Jet Propulsion Laboratory/California

Institute of Technology, funded by the National Aeronautics and Space Administration (Cutri & al 2012). This research has benefitted from the SpeX Prism Spectral Libraries, maintained by Adam Burgasser at *http://www.browndwarfs.org/spexprism*. This research has made use of the NASA/ IPAC Infrared Science Archive, which is operated by the Jet Propulsion Laboratory, California Institute of Technology, under contract with the National Aeronautics and Space Administration. We thank our anonymous referee for our initial manuscript and for several insightful comments that greatly improved the overall quality and clarity of this work.

Table 2.4. Input Sample

2MASS Designation	Opt. SpT	NIR SpT	2MASS J	2MASS H	2MASS K_s	WISE W1	WISE W2	μ_α[e] (mas yr^{-1})	μ_δ (mas yr^{-1})	$v_{\rm rad}$ (km s^{-1})	d_π (pc)	Signs of Youth[a]	Reported[g] Cand.	Other[d] Refs
Young Objects														
00034227-2822410	M7.5	M7	13.07	12.38	11.97	11.67	11.50	280.3 ± 1.5	-123.3 ± 1.7[22]	11.6 ± 1.1[74]	38.9 ± 1.2[22,74,82]	O?ITXU	···	2,23
00040288-6410358	L1γ	···	15.79	14.83	14.01	13.37	12.94	64.6 ± 8.0	-49.0 ± 17.0[42]	···	···	OR	THA[42]	25
00065794-6436542	L0	···	13.39	12.66	12.17	11.72	11.39	83.3 ± 3.6	-65.1 ± 10.2[60]	···	···	OH	···	54
00115060-1523450	···	M7.5	15.93	15.64	15.26	14.99	14.79	100.7 ± 19.0	-159.4 ± 19.4	···	···	T?M	···	6,87
00192626+4614078	M8	M8	12.60	11.94	11.50	11.26	11.00	121.3 ± 4.3	-77.7 ± 6.3[69]	-19.5 ± 2.0[63]	···	ITVL	ABDMG[75]	2,23,75
00250365+4759191	L4	···	14.84	13.67	12.90	11.74	11.57	275.0 ± 0.7	11.7 ± 0.8[22]	···	43.8 ± 1.7[82]	RL	···	16,23
00274197+0503417	M9.5	L0	16.19	15.29	14.96	14.62	14.14	10.5 ± 0.4	-0.8 ± 0.3[22]	···	72.5 ± 8.4[19]	OT	···	2,23
00325584-4405058	L0γ	L0	14.78	13.86	13.27	12.82	12.49	117.8 ± 4.3	-91.6 ± 4.3[24]	···	26.4 ± 3.3[24]	OTR	···	17,2,23,62
00332386-1521309	L4β	L1	15.29	14.21	13.41	12.80	12.48	306.3 ± 12.4	40.6 ± 8.5[11]	···	···	OR	···	17,2,23,41,62
00335534-0908247	···	M8	15.96	15.00	15.24	14.85	14.59	2.7 ± 17.0	-71.1 ± 19.8	···	···	T?M	···	6,87
00374306-5846229	L0γ	···	15.37	14.26	13.59	13.13	12.74	62.5 ± 10.2	-37.2 ± 9.4[23]	···	···	OR	···	17,25,62
00413538-5621127	M6.5+M9	···	11.96	11.32	10.86	10.61	10.36	98.1 ± 6.4	-50.1 ± 8.1[63]	2.8 ± 1.9[26,63]	···	VHLA	THA[63]	23,48
00452143+1634446	L2β	L2	13.06	12.06	11.37	10.77	10.39	374.9 ± 8.5	-27.7 ± 8.4[35]	3.3 ± 0.2[3]	···	OITRH	···	17,2,23,62,86
00470038+6803543	···	L7p	15.60	13.97	13.05	11.88	11.27	375.3 ± 2.9	-212.8 ± 9.3[31]	···	···	IR	···	2,53,78
01033203+1935361	L6β	L6	16.29	14.90	14.15	13.18	12.70	293.0 ± 4.6	27.7 ± 4.7[24]	···	21.3 ± 3.4[24]	OITR	···	2,23,56
01174748-3403258	···	L1	15.18	14.21	13.49	13.03	12.62	102.6 ± 6.9	-42.5 ± 5.6[11]	···	···	TRM	···	2,87,9
01225093-2439505	···	M3.5+L5	10.08	9.47	9.20	9.01	8.2	118.3 ± 24.2	-120.3 ± 2.9[68,88]	9.6 ± 0.7[5]	···	TXR	ABDMG ^{BW13}	···
01231125-6921379	M7.5	···	12.32	11.71	11.32	11.06	10.82	77.4 ± 2.4	-25.2 ± 9.0[69]	10.9 ± 3.0[63]	42.2 ± 4.8[67]	UL	···	23
01244599-5745379	L0γ	···	16.31	15.06	14.31	13.77	13.34	13.5 ± 18.7	35.3 ± 12.1[23]	···	···	OR	···	17,25,62
01245068-3844389	M6	M6	12.68	12.11	11.79	11.57	11.33	54.1 ± 6.0	21.0 ± 8.8	27.4 ± 6.3[77]	···	OITHL	···	2
01262109+1428057	L4γ	L2p	17.11	16.17	15.28	14.24	13.70	70.3 ± 30.8	-7.6 ± 28.7	···	···	OITR	···	2,25,30,57
01291221+3517580	···	L4	16.78	15.34	14.70	14.07	13.71	175.0 ± 9.5	-46.2 ± 11.4	···	···	RL	···	41,43
01415823-4633574	L0γ	L0p	14.83	13.88	13.10	12.55	12.17	99.8 ± 5.5	-34.0 ± 8.8[23]	12.0 ± 15.0[40]	···	OITRHM	THA/βPMG[42]	17,2,25,41,54,62,87
02212859-6831400	M8β	···	13.97	13.27	12.81	12.47	12.19	53.9 ± 4.4	13.7 ± 4.5[24]	···	39.4 ± 5.6[24]	OR	···	23,62
02215494-5412054	M9	···	13.90	13.22	12.66	12.32	11.96	107.1 ± 4.0	-16.9 ± 6.4[50]	···	···	O	···	23,62
02235464-5815067	L0γ	···	15.07	14.00	13.42	12.82	12.43	103.9 ± 4.6	-7.8 ± 10.4[23]	···	···	OR	···	17,25,62
02251947-5837295	M9	···	13.74	13.06	12.56	12.23	11.93	90.8 ± 4.0	-20.6 ± 8.9[23]	···	···	O	···	62
02292794-0053282	···	L0	16.49	15.75	15.18	14.72	14.33	17.4 ± 19.6	-35.1 ± 17.3	···	···	TR	···	2,30
02340093-6442068	L0γ	···	15.32	14.44	13.85	13.25	12.90	87.9 ± 3.9	-14.8 ± 11.2	···	···	OR	THA[42]	25,42
02364412+2240265	M6	···	10.08	9.52	9.19	8.99	8.80	-40.5 ± 21.2	-373.0 ± 14.6[45]	-3.4 ± 1.0[74]	···	OX	···	···
02411151-0326587	L0γ	L1	15.80	14.81	14.03	13.64	13.26	76.6 ± 12.8	-24.5 ± 9.7[11]	···	···	OTR	···	16,17,2,25,41
02535980+3206373	M7p	M6	13.62	12.93	12.55	12.32	12.13	89.1 ± 7.2	-98.3 ± 8.5	···	···	OR	···	15,2,41
03032042-7312300	L2γ	···	16.14	15.10	14.32	13.78	13.35	43.0 ± 2.7	2.7 ± 14.1	···	···	OR	THA[42]	25,42
03101401-2756452	L5	···	15.80	14.66	13.96	13.17	12.83	-125.1 ± 7.6	-49.3 ± 8.5[23]	···	···	VRHL	···	16,62
03231002-4631237	L0γ	···	15.39	14.32	13.70	13.07	12.66	64.3 ± 6.0	-1.3 ± 9.1[23]	···	···	ORL	···	17,62
03264225-2102057	L4	···	16.13	14.79	13.92	12.95	12.44	94.0 ± 12.2	-137.9 ± 8.7[23]	···	···	RL	···	15,16
03393521-3525440	M9	L0	10.73	10.02	9.55	9.13	8.81	324.0 ± 8.0	296.0 ± 7.0[80]	9.3 ± 1.7[61,63]	5.0 ± 0.1[80]	TLM	CAS[65]	2,23,65,81,87
03552337+1133437	L5γ	L3	14.05	12.53	11.53	10.53	9.94	218.0 ± 5.0	-626.0 ± 5.0[25]	11.9 ± 0.2[3]	9.1 ± 0.1[24,49]	OITRL	ABDMG[49]	17,2,23,62
03572695-4417305	L0β	···	14.37	13.53	12.91	12.48	12.09	64.9 ± 5.7	-8.1 ± 8.1[23]	···	···	OR	···	17,4,41,62
04062677-3812102	L0γ	L1p	16.77	15.71	15.11	14.45	14.10	9.4 ± 15.4	28.5 ± 22.5	···	···	OITR	Columba[42]	2,25,42
04210718-6306022	L5γ	···	15.56	14.28	13.45	12.56	12.14	147.5 ± 2.9	207.3 ± 7.6[23]	···	···	OIRL	···	16,17,25,42
04351455-1414468	M6δ[b]	M7	11.88	10.62	9.95	9.71	9.27	-1.9 ± 7.1	17.0 ± 7.1[23]	···	···	OIR	···	12,15,2
04362788-4114465	M8p	M9	13.10	12.43	12.05	11.74	11.46	57.2 ± 11.6	12.5 ± 7.5[23]	···	···	OI	···	16,2,41
04402325-0530082	M6	···	10.66	9.99	9.55	9.34	9.16	336.8 ± 18.4	126.2 ± 1.8[10,23,50,68]	29.3 ± 1.1[26,63,74]	9.5 ± 0.3[74]	VXRHL	HYA[26]	···
04433761+0002051	M9γ	L0	12.51	11.80	11.22	10.83	10.48	35.9 ± 7.7	-98.0 ± 8.2[23]	17.1 ± 3[63]	···	OIVRHL	ABDMG[75]	12,16,2,41,54,64,75
04465175-1116476	M5+M6	···	8.14	7.56	7.29	7.10	6.97	-149.9 ± 7.3	-41.0 ± 5.6[74]	14.9 ± 0.3[74]	18.7 ± 1.7[74]	OXU	···	···
05012406-0010452	L4γ	L3	14.98	13.71	12.96	12.05	11.52	182.4 ± 4.3	-132.7 ± 4.2[24]	···	13.1 ± 0.8[24]	OTRL	···	17,2,23,25,62
05184616-2756457	L1γ	L1	15.26	14.30	13.61	13.05	12.66	28.6 ± 4.2	-16.0 ± 4.0[24]	···	46.8 ± 15.0[24]	OITRU	···	2,23,25
05341594-0631397	M8γ	M8p	16.05	15.37	14.94	14.78	14.26	2.2 ± 19.7	-6.9 ± 20.8	···	···	OIT	···	2,42

Table 2.4 — continued

2MASS Designation	Opt. SpT	NIR SpT	2MASS J	2MASS H	2MASS K_s	WISE W1	WISE W2	μ_α[e] (mas yr^{-1})	μ_δ (mas yr^{-1})	$v_{\rm rad}$ (km s^{-1})	d_π (pc)	Signs of Youth[a]	Reported[g] Cand.	Other[d] Refs
05361998-1920396	L2 γ	L2	15.77	14.69	13.85	13.26	12.79	24.6 ± 5.3	-30.6 ± 5.0[24]	···	39.0 ± 14.0[24]	OTR	···	2,23,25
05575096-1359503	M7	M7	12.87	12.15	11.73	11.34	10.80	-10.3 ± 6.4	7.1 ± 8.1	30.3 ± 2.8[74]	···	OITXRHLA?	···	16,2,72
06052936+6049231	M5	···	9.10	8.46	8.18	7.98	7.79	289.8 ± 5.3	-787.7 ± 10.3[45]	128.5 ± 2.6[74]	···	OX	···	···
06085283-2753583	M9 γ	L0	13.60	12.90	12.37	11.98	11.62	8.9 ± 3.5	10.7 ± 3.5[24]	24.0 ± 1.0[66]	31.3 ± 3.5[24]	OITRH	βPMG[66]	15,2,23,41,54
06195260-2903592	M6	M5	15.14	14.19	13.45	13.00	12.58	7.3 ± 8.1	5.2 ± 9.4	···	···	O	···	15,2
06322402-5010349	L3	···	15.02	14.03	13.34	12.60	12.16	-100.2 ± 5.2	-4.6 ± 8.8[23]	···	···	L	···	62
06523073+4710348	L4.5	···	13.51	12.38	11.69	10.88	10.52	-133.5 ± 4.9	149.5 ± 8.1[69]	···	···	L	···	15,16,23,62
06524851-5741376	M8 β	···	13.63	12.97	12.45	12.15	11.86	0.1 ± 3.4	29.2 ± 3.3[24]	···	32.0 ± 3.3[24]	OR	···	12,23,62
06575703+6219197	M5	···	8.59	7.99	7.69	7.42	7.28	320.0 ± 5.0	-512.0 ± 5.0[45]	17.6 ± 0.6[74]	11.4 ± 0.3[45]	OXU	···	···
07123786-6155528	L1 β	···	15.30	14.39	13.67	12.99	12.63	-35.7 ± 4.9	19.1 ± 4.8[24]	···	44.0 ± 17.0[24]	ORUH	···	17
07522390+1612157	M7	M6	10.88	10.20	9.85	9.61	9.45	178.8 ± 5.2	-349.4 ± 22.6[59]	-16.5 ± 1.8[63,74]	18.4 ± 0.3[28,74]	OITXUH	···	2
08295707+2655099	L6.5	···	17.11	15.81	14.96	13.90	13.40	-88.3 ± 9.6	-44.5 ± 10.9[23]	···	···	RL	···	41
09175418+6028065	···	L5p	16.60	15.96	15.42	14.56	14.15	-163.4 ± 7.0	-81.5 ± 20.3	···	···	IR	···	27,30,57
10042066+5022596	L3 β	L3	14.83	13.65	12.78	···	···	-133.0 ± 40.0	-185.0 ± 15.0[35]	···	···	OITRL	···	15,17,2,41,55
10204406+0814234	M6	···	10.35	9.76	9.47	9.33	9.17	-244.0 ± 5.0	-6.0 ± 5.0[74]	14.1 ± 0.4[74]	37.7 ± 2.1[74]	O?XU	···	···
10220489+0200477	M9 β	M9	14.10	13.40	12.90	12.61	12.34	-156.2 ± 6.6	-429.0 ± 6.8[24]	-7.9 ± 4.8[70,85]	38.0 ± 16.0[24]	ORU	···	2,23,41,62
10224821+5825453	L1 β	L1	13.50	12.64	12.16	11.76	11.50	-814.4 ± 4.4	-729.5 ± 9.3	19.3 ± 0.1[3,71]	···	ORH	···	17,2,23,41,62
10255227+3212349	···	L7	16.86	15.59	15.07	14.37	14.06	384.3 ± 30.5	-227.0 ± 11.7[23]	···	···	IR	···	2,41
11395113-3159214	M9 γ	M9p	12.69	12.00	11.50	11.15	10.79	-78.6 ± 3.0	-24.6 ± 1.9[24,84]	11.6 ± 2[91]	33.5 ± 15.3[24,84]	OITUM	···	2,23,41,87
11544223-3400390	L0	···	14.19	13.33	12.85	12.35	12.04	-156.2 ± 6.8	12.8 ± 7.8[23]	···	···	L	···	41
12451416-4429077	M9.5p	M9	14.52	13.80	13.37	12.99	12.62	-38.4 ± 5.8	-20.8 ± 8.6[84]	···	79.0 ± 12.9[84]	OITUHM	TWA[51]	2,41,51,87
12464678+4027150	L4	···	15.09	13.94	13.28	12.57	12.20	137.8 ± 6.5	-101.0 ± 22.4[35]	···	···	RL	···	23,41
13054019-2541059	L2	L2[b]+L4[b]	13.41	12.39	11.75	11.24	10.91	-299.2 ± 1.2	-4.1 ± 1.4[22]	6.3 ± 0.4[3,71]	19.2 ± 0.7[19,22]	IVRUHL	···	32,41,47,56,69
14112131-2119503	M9	M8	12.44	11.83	11.33	11.08	10.81	-73.2 ± 7.7	-69.5 ± 8.2[10]	-0.8 ± 3.0[63]	···	IL	···	2
15065441+1321060	L3	L4	13.36	12.38	11.74	11.18	10.88	-1088.0 ± 12.0	4.0 ± 9.9[71]	-0.7 ± 0.1[3,71]	···	TRM	···	8,87
15474719-2423493	M9	L0	13.97	13.27	12.74	12.41	12.10	-133.9 ± 8.4	-127.2 ± 9.0[35]	···	···	OITR	···	2,23,62
15515237+0941148	L4 γ	L4	16.32	15.11	14.31	13.60	13.12	-69.4 ± 11.1	-55.9 ± 11.4[23]	···	···	OTR	···	2,25,30,62
15525906+2948485	L0 β	L0	13.48	12.61	12.02	11.54	11.21	-161.5 ± 8.3	-58.8 ± 9.4[35]	-18.4 ± 0.3[3,70,85]	···	OTR	···	17,2,23,62,86
15575011-2952431	M9δ	L1	16.32	15.45	14.85	14.44	14.07	-10.1 ± 15.6	-27.8 ± 19.3	···	···	OITVR	SCO[42]	2,42
16002647-2456424	···	M7.5p	15.12	14.52	14.22	13.99	13.72	-21.5 ± 11.8	-313.4 ± 13.9[20]	···	···	I	···	42
16154255+4953211	L4 γ	L3	16.79	15.33	14.31	13.20	12.62	-78.8 ± 15.6	19.4 ± 9.9[70]	···	···	OITRL	···	16,2,25,30,41,62
16170537+5516094	M5.5	···	6.60	5.99	5.76	5.64	5.43	85.3 ± 1.2	-438.5 ± 1.2[82]	-28.3 ± 0.9[73]	20.5 ± 0.4[82]	OXU	···	74
17033555-7715210	M9	···	15.21	14.40	14.02	13.69	13.33	18.9 ± 2.3	-21.3 ± 12.6	···	···	OH	···	54
17111353+2326333	L0	L1	14.50	13.67	13.06	12.58	12.23	-59.5 ± 4.5	-39.3 ± 5.0[36,70]	-0.1 ± 5.0[85]	···	TH	···	16,2,23
17195298+2630026	M5.5	···	8.23	7.64	7.35	7.20	7.01	-221.3 ± 3.2	348.9 ± 4.1[74]	-34.6 ± 0.2[74]	10.8 ± 0.3[37,74]	OXUH	···	72
17260007+1538190	L3 β	L3	15.67	14.47	13.66	13.07	12.69	-40.9 ± 7.0	-50.5 ± 7.4[35]	···	···	OITRUL	···	17,2,23,25,41,56
18212815+1414010	L4.5	L5p	13.43	12.40	11.65	10.85	10.48	233.5 ± 8.9	-236.2 ± 9.5	9.8 ± 0.8[3,42]	···	ITR	···	52
18284076+1229207	···	M7.5p	14.60	14.05	13.79	13.45	13.20	-245.5 ± 12.7	-106.0 ± 26.5[42]	···	···	TR	···	39
19223062+6610194	L1	···	14.57	13.69	13.16	12.67	12.38	93.1 ± 3.0	110.2 ± 10.5	···	···	L	···	62
19303829-1335083	M6	···	11.53	10.99	10.65	10.46	10.28	167.0 ± 5.0	359.0 ± 5.0[45,74]	-21.4 ± 0.1[74]	27.7 ± 1.2[74]	OXU	···	···
19355595-2846343	M9	M9	13.95	13.18	12.71	12.35	11.91	27.2 ± 4.8	-56.6 ± 5.1[68]	···	···	OITRH	···	2,54,62
19564700-7542270	L0 γ	···	16.15	15.04	14.23	13.69	13.25	9.0 ± 2.8	-58.8 ± 14.8	···	···	OR	···	17,25,62
20004841-7523070	M9	···	12.73	11.97	11.51	11.11	10.80	60.3 ± 1.9	-106.0 ± 10.3	11.8 ± 1.0[26]	···	OR	CAS[26]	23
20135152-2806020	M9	L0	14.24	13.46	12.94	12.52	12.16	43.0 ± 9.5	-67.6 ± 10.7	···	···	OT	···	2,41,62
20575409-0252302	L1.5	L2	13.12	12.27	11.72	11.26	10.98	1.6 ± 3.8	-86.3 ± 3.9[24]	···	14.3 ± 0.8[24]	THL	···	15,16,2,23
21011544+1756586	L7.5	L7+L8	16.85	15.86	14.89	14.10	13.56	144.0 ± 3.0	-151.0 ± 3.0[83]	···	33.2 ± 3.8[83]	TRM	···	23,87
21140802-2251358	···	L7	16.71	15.72	14.74	13.22	12.46	137.3 ± 1.3	-138.7 ± 1.4[49]	···	24.6 ± 1.4[49]	ITRM	βPMG^{LI13}	···
21265040-8140293	L3 γ	···	15.54	14.40	13.55	12.91	12.47	43.2 ± 1.3	-98.6 ± 12.8	···	···	OR	···	17,25,62
21481633+4003594	L6	L6.5p	14.15	12.78	11.77	10.74	10.23	771.6 ± 6.2	471.3 ± 8.8[23]	···	···	ITRLM	···	41,42,52,87
22064498-4217208	L2	···	15.56	14.45	13.61	12.82	12.38	125.9 ± 9.4	-179.5 ± 9.4[23]	···	···	RL	···	41

Table 2.4 — continued

2MASS Designation	Opt. SpT	NIR SpT	2MASS J	2MASS H	2MASS K_s	WISE W1	WISE W2	μ_α[e] (mas yr^{-1})	μ_δ (mas yr^{-1})	$v_{\rm rad}$ (km s^{-1})	d_π (pc)	Signs of Youth[a]	Reported[g] Cand.	Other[d] Refs
22081363+2921215	L3 γ	L3	15.80	14.79	14.15	13.35	12.89	97.6 ± 8.6	-17.1 ± 7.9^{35}	···	···	OTRL	···	17,2,23,25,41
22134491-2136079	L0 γ	L0	15.38	14.40	13.76	13.23	12.83	51.4 ± 7.4	-63.2 ± 8.6^{35}	···	···	OTR	···	16,17,2,23,25,41
22443167+2043433	L6.5	L6	16.48	15.00	14.02	12.78	12.11	242.6 ± 7.3	-219.6 ± 7.1^{35}	···	···	ITRLM	···	2,23,41,42,56,83,87
22495345+0044046	L4 γ	L3+L5[b]	16.59	15.42	14.36	13.58	13.14	81.1 ± 9.0	21.6 ± 14.0^{23}	···	···	OITRM	···	1,2,25,33,41,87
23134727+2117294	M7.5	···	11.42	10.76	10.44	10.23	10.06	256.5 ± 4.8	-28.1 ± 4.2^{45}	-1.6 ± 0.3^{74}	···	OX	CAS[74]	···
23174712-4838501	L4p	L6.5p	15.15	13.93	13.18	12.38	11.94	240.1 ± 6.2	74.2 ± 10.2	···	···	RL	···	42,62
23224684-3133231	L0 β	L2	13.58	12.79	12.32	11.97	11.71	-194.8 ± 7.4	-527.3 ± 7.5^{24}	···	17.1 ± 1.6^{24}	OIT	···	2,23
23225299-6151275	L2 γ	···	15.55	14.53	13.86	13.24	12.84	78.6 ± 4.6	-74.8 ± 11.0	···	···	OR	···	17,25,62
23591986+3241244	M5.5	···	10.45	9.79	9.56	9.43	9.27	-174.9 ± 4.0	-236.7 ± 11.2^{45}	-52.3 ± 0.2^{74}	···	OX	···	···
Potentially Young Objects														
00013044+1010146	···	M6	15.83	15.13	15.20	14.65	14.40	-71.5 ± 20.3	-93.9 ± 20.9	···	···	M	···	6,87
00125716+5059173	M6.5	···	11.41	10.82	10.52	10.30	10.14	288.1 ± 7.9	40.4 ± 8.1^{45}	3.0 ± 0.3^{74}	26.3 ± 2.1^{90}	XH	···	···
00275592+2219328	M8	M6.5+M8	10.61	9.97	9.57	9.31	9.05	403.9 ± 1.0	-165.4 ± 1.5^{22}	-16.8 ± 3.0^{63}	$14.1 \pm 0.5^{22,28}$	U	···	23
00552554+4130184	···	M8	15.81	14.96	14.98	14.44	14.22	50.6 ± 9.9	-4.8 ± 13.9	···	···	M	···	6,87
00583814-1747311	···	M6	15.94	15.74	15.47	15.01	14.86	-29.9 ± 22.5	28.1 ± 24.9	···	···	M	···	6,87
01291257+4819354	M5.5	···	10.91	10.30	10.04	9.85	9.68	212.7 ± 4.0	-22.1 ± 4.4^{45}	11.8 ± 0.4^{74}	···	X	···	···
01470204+2120242	···	M7.5Ve	15.99	15.03	15.04	14.76	14.53	19.1 ± 15.1	-20.1 ± 16.7	···	···	M	···	6,87
01490895+2956131	M9.5	···	13.45	12.58	11.98	11.56	11.31	175.7 ± 0.8	-402.1 ± 0.7^{19}	···	22.5 ± 0.4^{19}	VRH	···	23,38,61
01502711-1851360	M5.5	···	11.48	10.96	10.66	10.46	10.24	29.9 ± 16.2	-272.1 ± 9.8^{74}	20.1 ± 0.4^{74}	32.8 ± 2.7^{74}	XU	···	···
02530084+1652532	M7	···	8.39	7.88	7.59	7.32	7.06	3430.9 ± 42.3	-3813.1 ± 4.5^{68}	···	3.9 ± 0.0^{28}	M	···	87,9
03202839-0446358	···	M8.5+T6	13.26	12.53	12.13	11.80	11.45	-253.0 ± 7.7	-506.6 ± 7.0^{11}	0.6 ± 0.1^{3}	···	M	···	87,9
06590991-4746532	M6.5	M7	13.64	13.09	12.72	12.52	12.29	-79.7 ± 9.1	387.4 ± 3.2^{20}	···	···	M	···	87,9
09510459+3558098	M4.5	···	10.58	9.96	9.69	9.54	9.37	-101.0 ± 3.5	-156.9 ± 3.8^{88}	10.2 ± 0.2^{74}	···	X	THA[74]	72
12121714-2253451	···	M8	15.69	15.40	15.03	14.69	14.52	-71.9 ± 14.1	-78.4 ± 16.6	···	···	M	···	6,87
13142039+1320011	M7	···	9.75	9.18	8.79	8.56	8.34	-242.9 ± 4.9	-176.6 ± 4.9^{68}	···	16.4 ± 0.8^{46}	XUH	ABDMG[75]	18,75
14171672-0407311	···	M8	15.95	15.37	15.49	14.91	14.66	-79.0 ± 18.0	-68.7 ± 19.0	···	···	M	···	6,87
14284323+3310391	M9	···	11.99	11.23	10.74	10.43	10.17	-345.7 ± 0.4	-707.9 ± 0.4^{22}	-42.2 ± 3.3^{3}	11.0 ± 0.2^{58}	HM	···	7,87
15243203+0934386	···	M7	15.05	14.26	14.30	13.79	13.64	24.0 ± 9.6	-156.5 ± 12.4^{21}	···	···	M	···	6,87
16553529-0823401	M7	···	9.78	9.20	8.82	8.59	8.36	-808.2 ± 1.9	-869.7 ± 1.8^{14}	18.8 ± 10.0^{34}	$6.5 \pm 0.0^{14,58}$	XM	···	87,9
17364839+0220426	···	M8	15.85	15.36	14.89	14.68	14.57	-18.2 ± 20.2	0.1 ± 20.4	···	···	M	···	6,87
18244344+2937133	···	M6	15.89	15.80	15.68	15.15	14.90	-26.5 ± 19.5	88.4 ± 24.2	···	···	M	···	6,87
18320290+2030581	M5+M5	···	10.65	10.09	9.76	9.55	9.36	-45.6 ± 4.2	-205.0 ± 7.1^{45}	-18.1 ± 0.3^{74}	···	X	···	44
19165762+0509021	M8	M8	9.91	9.23	8.77	8.47	8.25	-588.8 ± 0.8	-1369.1 ± 0.8^{58}	36.0 ± 10.0^{34}	5.9 ± 0.0^{58}	XM	···	6,87
20491972-1944324	···	M7.5	12.85	12.23	11.79	11.56	11.36	186.1 ± 6.5	-262.9 ± 39.2^{10}	1.6 ± 1.0^{26}	···	RM	···	6,87
21512543-2441000	L3	···	15.75	14.57	13.65	13.06	12.74	282.0 ± 8.2	-17.6 ± 8.8^{23}	···	···	RM	···	87,9
23280459-1038452	···	L3.5	17.00	15.84	15.08	14.62	14.36	-16.2 ± 13.3	-44.6 ± 12.7^{23}	···	···	RM	···	13,87
23540928-3316266	M8.5	M8	13.05	12.36	11.88	11.61	11.39	-322.5 ± 3.4	-392.6 ± 3.1^{76}	···	22.6 ± 0.9^{76}	M	···	87,9
Red Objects														
01075242+0041563	L8	L8p	15.82	14.51	13.71	12.69	12.17	628.0 ± 7.0	91.0 ± 4.0^{83}	···	15.6 ± 1.1^{83}	R	···	23,30
01490895+2956131	M9.5	···	13.45	12.58	11.98	11.56	11.31	175.7 ± 0.8	-402.1 ± 0.7^{19}	···	22.5 ± 0.4^{19}	VRH	···	23,38,61
02062493+2640237	···	L9p	16.53	15.10	14.52	13.40	12.82	434.5 ± 7.5	-8.7 ± 6.0^{43}	···	···	R	···	53
02431371-2453298	···	T6	15.38	15.14	15.22	14.67	12.92	-287.8 ± 3.5	-207.6 ± 2.9^{22}	···	$10.7 \pm 0.3^{22,83}$	R	···	23
03421621-6817321	L2	···	16.85	15.39	14.54	13.94	13.46	65.3 ± 2.8	18.5 ± 9.1^{23}	···	···	R	···	15
05120636-2949540	L4.5	···	15.46	14.16	13.28	12.38	11.92	-16.7 ± 6.9	85.3 ± 8.0^{23}	···	···	R	···	···
06420559+4101599	···	Lp[c]	16.16	15.09	14.28	13.36	12.55	-4.8 ± 4.9	-370.5 ± 8.5	···	···	R	···	53
07542987+7909546	···	Lp[c]	16.17	15.44	14.93	14.41	13.73	294.5 ± 2.2	318.3 ± 16.0	···	···	R	···	53
08095903+4434216	···	L6	16.44	15.18	14.42	13.34	12.81	-187.0 ± 7.0	-205.8 ± 10.7^{23}	···	···	R	···	···
08583467+3256275	···	T1	16.45	15.38	14.76	14.06	13.48	-631.1 ± 9.5	47.4 ± 20.5^{70}	···	···	R	···	23
12123389+0206280	···	L1	16.13	15.00	14.19	14.03	13.89	53.2 ± 12.4	-132.1 ± 12.6^{23}	···	···	R	···	···
13243553+6358281	···	L9+T2p	15.60	14.58	14.06	13.13	12.29	-377.4 ± 3.7	-58.6 ± 10.1	···	···	R	···	23,29,30,42
13262981-0038314	L8	L5.5	16.10	15.05	14.21	13.27	12.75	-226.0 ± 8.0	-107.0 ± 6.0^{83}	···	20.0 ± 2.5^{83}	R	···	23

Table 2.4 — continued

2MASS Designation	Opt. SpT	NIR SpT	2MASS J	2MASS H	2MASS K_s	WISE W1	WISE W2	μ_α[e] (mas yr^{-1})	μ_δ (mas yr^{-1})	$v_{\rm rad}$ (km s^{-1})	d_π (pc)	Signs of Youth[a]	Reported[g] Cand.	Other[d] Refs
13313310+3407583	L0	L1p	14.33	13.40	12.89	12.55	12.32	-356.2 ± 7.6	-177.8 ± 9.3^{35}	15.4 ± 7.8^{70}	···	R	···	23,42
14153003+5724300	···	T3	16.73	15.82	15.54	14.86	13.97	48.3 ± 7.1	-347.6 ± 16.5^{23}	···	···	R	···	···
15311344+1641282	···	L1	15.58	14.54	13.80	13.28	12.89	-80.7 ± 8.7	44.4 ± 8.9^{23}	···	···	R	···	···
16471580+5632057	···	L9p	16.91	15.26	14.61	13.60	13.09	-166.0 ± 9.0	242.0 ± 8.0^{22}	···	8.6 ± 2.2^{22}	R	···	53
17385487+6142173	···	Lp[c]	16.52	16.32	15.14	17.95	17.06	45.0 ± 13.0	196.8 ± 23.2^{89}	···	···	R	···	53
17580545+4633099	···	T6.5	16.15	16.25	15.47	15.68	13.82	-16.6 ± 2.3	580.1 ± 2.3^{22}	···	14.1 ± 0.4^{82}	R	···	23
20491972-1944324	···	M7.5	12.85	12.23	11.79	11.56	11.36	186.1 ± 6.5	-262.9 ± 39.2^{10}	1.6 ± 1.0^{26}	···	RM	···	6,87
21163374-0729200	···	L6	17.20	16.20	14.98	14.61	14.33	-72.1 ± 25.2	-92.1 ± 24.7	···	···	R	···	30
21403907+3655563	···	M8p	15.61	15.07	14.68	14.71	14.47	-114.6 ± 16.6	-72.9 ± 21.7^{42}	···	···	R	···	···
21512543-2441000	L3	···	15.75	14.57	13.65	13.06	12.74	282.0 ± 8.2	-17.6 ± 8.8^{23}	···	···	RM	···	87,9
22244381-0158521	L4.5	L3.5	14.07	12.82	12.02	11.36	11.12	468.6 ± 0.5	-864.8 ± 0.6^{22}	···	11.6 ± 0.1^{22}	R	···	23
23280459-1038452	···	L3.5	17.00	15.84	15.08	14.62	14.36	-16.2 ± 13.3	-44.6 ± 12.7^{23}	···	···	RM	···	13,87
23352734+4511442	···	L9p	16.64	NaN	NaN	13.48	12.93	-242.9 ± 9.4	-288.1 ± 16.8^{79}	···	···	R	···	78
23512200+3010540	L5.5	L5p	15.85	14.57	14.02	13.22	12.86	253.2 ± 6.9	16.3 ± 7.4	···	···	R	···	42

[a] A capital letter means the object displays the associated sign of youth. O: lower-than normal equivalent width of atomic species in the optical spectrum, I: same but in the NIR spectrum, T: a triangular-shaped H-band continuum, V: high rotational velocity, X: X-ray emission, R: redder-than-normal colors for given spectral type, U: over luminous, H: Hα emission, L: Li absorption, A: signs of accretion and M: signs of low gravity from atmospheric models fitting. A question mark after any flag indicates that the result is uncertain.

[b] Uncertainty on spectral type is larger than 0.5 subtypes.

[c] Extremely red L dwarfs that defy classification (see Mace et al. 2013a).

[d] References not reported in the other columns of this table.

[e] A proper motion measurement from 2MASS and WISE was included for every object, except when high-precision proper motion was available from a parallax measurement.

[f] Objects for which membership was already suspected. The Castor (CAS) and Hyades (HYA) associations were not included in this study because they are older than 500 Myr. Upper Scorpius (USCO) was not included either because it is farther than 100 pc.

[g] Candidate membership to NYA previously reported in the literature. The reference is indicated between parentheses.

References to the table :
1: Allers et al. (2010), 2: Allers & Liu (2013), 3: Blake et al. (2010), 4: Bouy et al. (2003), 5: Bowler et al. (2013), 6: Burgasser et al. (2004), 7: Burgasser et al. (2006), 8: Burgasser et al. (2007), 9: Burgasser et al. (2008a), 10: Caballero (2007), 11: Casewell et al. (2008), 12: Chauvin et al. (2012), 13: Chiu et al. (2006), 14: Costa et al. (2005), 15: Cruz et al. (2003), 16: Cruz et al. (2007), 17: Cruz et al. (2009), 18: D'Elia et al. (2013), 19: Dahn et al. (2002), 20: Deacon & Hambly (2007), 21: Deacon et al. (2009), 22: Dupuy & Liu (2012), 23: Faherty et al. (2009), 24: Faherty et al. (2012), 25: Faherty et al. (2013b), 26: Gálvez-Ortiz et al. (2010), 27: Gálvez-Ortiz et al. (2011), 28: Gatewood & Coban (2009), 29: Geballe et al. (2002), 30: Geißler et al. (2011), 31: Gizis et al. (2012), 32: Glebocki & Gnacinski (2005), 33: Gorlova et al. (2003), 34: Gizis et al. (1997), 35: Jameson et al. (2008), 36: Jameson et al. (2008), 37: Jenkins et al. (2009), 38: Kendall et al. (2004), 39: Kirkpatrick et al. (2000), 40: Kirkpatrick et al. (2006), 41: Kirkpatrick et al. (2008), 42: Kirkpatrick et al. (2010), 43: Kirkpatrick et al. (2011), 44: Looper et al. (2008b), 45: Lépine (2005), 46: Lépine et al. (2009), 47: Liu & Leggett (2005), 48: Liu et al. (2010), 49: Liu et al. (2013a), 50: Lodieu et al. (2005), 51: Looper et al. (2007a), 52: Law et al. (2008), 53: Mace et al. (2013a), 54: Martín et al. (2010), 55: McGovern et al. (2004), 56: McLean et al. (2003), 57: Metchev et al. (2008), 58: Monet et al. (1992), 59: Monet et al. (2003), 60: Phan-Bao (2011), 61: Reid et al. (2002), 62: Reid et al. (2008b), 63: Reiners & Basri (2009), 64: Reiners & Basri (2010), 65: Ribas (2003), 66: Rice et al. (2010), 67: (Riedel et al. 2013, in prep.), 68: Roeser et al. (2010), 69: Schmidt et al. (2007), 70: Schmidt et al. (2010), 71: Seifahrt et al. (2010), 72: Shkolnik et al. (2009), 73: Shkolnik et al. (2011), 74: Shkolnik et al. (2012), 75: Schlieder et al. (2012a), 76: Subasavage et al. (2009), 77: Thackrah et al. (1997), 78: Thompson et al. (2013), 79: Thompson et al. (2013), 80: Tinney (1996), 81: Tinney (1998), 82: van Leeuwen (2007a), 83: Vrba et al. (2004), 84: Weinberger et al. (2013a), 85: West et al. (2008), 86: Wilson et al. (2003), 87: Witte et al. (2011), 88: Zacharias et al. (2012), 89: This work, 90: Dittmann et al. (2014), 91: Mamajek (2005).

Table 2.5. Bayesian Probabilities for Young and Red Candidates[a]

Name	TWA				βPMG				THA				COL				CAR				ARG				ABDMG				Young Field			
	P	P_v	P_π	$P_{v+\pi}$	P	P_v	P_π	$P_{v+\pi}$	P	P_v	P_π	$P_{v+\pi}$	P	P_v	P_π	$P_{v+\pi}$	P	P_v	P_π	$P_{v+\pi}$	P	P_v	P_π	$P_{v+\pi}$	P	P_v	P_π	$P_{v+\pi}$	P	P_v	P_π	$P_{v+\pi}$
J0001+1010	0.0	...	...	...	0.0	...	...	...	0.0	...	...	...	0.0	...	...	...	0.0	...	...	...	0.0	...	...	...	0.0	...	...	...	**0.5**	...	...	...
J0003-2822	0.0	0.0	0.0	0.0	0.1	0.0	0.0	0.0	0.0	0.0	0.0	0.0	0.0	0.0	0.0	0.0	0.0	0.0	0.0	0.0	0.0	0.0	0.0	0.0	0.0	0.0	0.0	0.0	99.9	100.0	100.0	**100.0**
J0004-6410	0.0	...	...	...	0.0	...	...	...	**99.6**[b]	...	...	...	0.0	...	...	...	0.0	...	...	...	0.0	...	...	...	0.0	...	...	...	0.3[b]	...	...	...
J0006-6436	0.0	...	...	...	0.0	...	...	...	**100.0**[b]	...	...	...	0.0	...	...	...	0.0	...	...	...	0.0	...	...	...	0.0	...	...	...	0.0	...	...	...
J0011-1523	0.0	...	...	...	0.0	...	...	...	0.0	...	...	...	0.0	...	...	...	0.0	...	...	...	0.0	...	...	...	0.0	...	...	...	0.0	...	...	...
J0012+5059	0.0	0.0	0.0	0.0	0.0	0.0	0.0	0.0	0.0	0.0	0.0	0.0	0.0	0.0	0.0	0.0	0.0	0.0	0.0	0.0	11.2	40.4	0.0	0.1	0.0	0.0	0.0	0.0	88.8	59.6	100.0	**99.9**
J0019+4614	0.0	0.0	...	...	37.9	0.0	...	...	0.0	0.0	...	...	0.0	0.0	...	...	0.0	0.0	...	...	0.0	0.0	...	...	43.2	**88.0**	...	...	18.9	12.0	...	...
J0025+4759	0.0	...	0.0	...	0.0	...	0.0	...	0.0	...	0.0	...	0.0	...	0.0	...	0.0	...	0.0	...	98.0[b]	...	0.0	...	0.0	...	0.0	...	2.0[b]	...	**100.0**	...
J0027+0503	0.0	...	0.0	...	0.0	...	0.0	...	0.0	...	0.0	...	0.0	...	0.0	...	0.0	...	0.0	...	0.0	...	0.0	...	0.0	...	0.0	...	100.0	...	**100.0**	...
J0027+2219	0.0	0.0	0.0	0.0	8.1	0.0	1.8	0.0	0.0	0.0	0.0	0.0	0.0	0.0	0.1	0.0	0.0	0.0	0.0	0.0	0.0	0.0	0.1	0.0	0.0	0.0	0.0	0.0	91.8	100.0	98.0	**100.0**
J0032-4405	0.0	...	0.0	...	0.1	...	**78.3**	...	4.8	...	0.1	...	0.0	...	0.0	...	0.0	...	0.0	...	0.0	...	0.0	...	92.3	...	13.3	...	2.8	...	8.2	...
J0033-1521	0.0	...	...	...	0.0	...	...	...	0.0	...	...	...	0.0	...	...	...	0.0	...	...	...	32.0	...	...	...	0.0	...	...	...	**68.0**	...	...	...
J0033-0908	0.0	...	...	...	0.0	...	...	...	0.0	...	...	...	0.0	...	...	...	0.0	...	...	...	0.0	...	...	...	0.0	...	...	...	**10.3**	...	...	...
J0037-5846	0.0	...	...	...	0.0	...	...	...	**97.3**[b]	...	...	...	0.0	...	...	...	0.0	...	...	...	0.0	...	...	...	0.1	...	...	...	2.6[b]	...	...	...
J0041-5621	0.0	0.0	...	...	0.0	0.0	...	...	99.8	**100.0**	...	...	0.0	0.0	...	...	0.0	0.0	...	...	0.0	0.0	...	...	0.2	0.0	...	...	0.0	0.0	...	...
J0045+1634	0.0	0.0	...	...	0.0	0.0	...	...	0.0	0.0	...	...	0.0	0.0	...	...	0.0	0.0	...	...	99.0	**99.9**	...	...	0.0	0.0	...	...	1.0[b]	0.1[b]	...	...
J0047+6803	0.0	...	...	...	8.4	...	...	...	0.0	...	...	...	0.0	...	...	...	0.0	...	...	...	0.0	...	...	...	**89.8**	...	...	...	1.7[b]	...	...	...
J0055+4130	0.0	...	...	...	0.0	...	...	...	0.0	...	...	...	0.0	...	...	...	0.0	...	...	...	0.0	...	...	...	0.0	...	...	...	**67.0**	...	...	...
J0058-1747	0.0	...	...	...	0.0	...	...	...	0.0	...	...	...	0.0	...	...	...	0.0	...	...	...	0.0	...	...	...	0.0	...	...	...	**30.1**	...	...	...
J0103+1935	0.0	...	0.0	...	0.0	...	0.0	...	0.0	...	0.0	...	0.0	...	0.0	...	0.0	...	0.0	...	46.9	...	**76.0**	...	0.0	...	0.0	...	53.1[b]	...	24.0	...
J0107+0041	0.0	...	0.0	...	0.0	...	0.0	...	0.0	...	0.0	...	0.0	...	0.0	...	0.0	...	0.0	...	0.0	...	0.0	...	0.0	...	0.0	...	26.8	...	**43.3**	...
J0117-3403	0.0	...	...	...	1.5	...	...	...	**97.0**	...	...	...	0.6	...	...	...	0.0	...	...	...	0.0	...	...	...	0.0	...	...	...	0.8[b]	...	...	...
J0122-2439	0.0	0.0	...	...	8.0	**75.1**	...	...	0.0	0.0	...	...	0.0	0.0	...	...	0.0	0.0	...	...	0.0	0.0	...	...	89.2	17.6	...	...	2.8	7.2	...	...
J0123-6921	0.0	0.0	0.0	0.0	0.0	0.0	0.0	0.0	99.9[b]	99.9[b]	99.9	**100.0**	0.0	0.0	0.0	0.0	0.0	0.0	0.0	0.0	0.0	0.0	0.0	0.0	0.0	0.0	0.0	0.0	0.1[b]	0.1[b]	0.1	0.0
J0124-5745	0.0	...	...	...	0.0	...	...	...	0.0	...	...	...	0.0	...	...	...	0.0	...	...	...	0.0	...	...	...	0.0	...	...	...	**100.0**[b]	...	...	...
J0124-3844	0.0	0.0	...	...	0.0	0.0	...	...	0.0	0.0	...	...	0.0	0.0	...	...	0.0	0.0	...	...	0.0	0.0	...	...	0.0	0.0	...	...	100.0	**100.0**	...	...
J0126+1428	0.0	...	...	...	3.2	...	...	...	0.0	...	...	...	0.1[b]	...	...	...	0.0	...	...	...	0.0	...	...	...	0.0	...	...	...	**96.6**[b]	...	...	...
J0129+3517	0.0	...	...	...	0.0	...	...	...	0.0	...	...	...	0.0	...	...	...	0.0	...	...	...	43.6	...	...	...	0.0	...	...	...	**56.4**	...	...	...
J0129+4819	0.0	0.0	...	...	0.0	0.0	...	...	0.0	0.0	...	...	0.0	0.0	...	...	0.0	0.0	...	...	15.3	0.1	...	...	0.0	0.0	...	...	84.7	**99.9**	...	...
J0141-4633	0.0	0.0	...	...	0.1	1.1	...	...	99.8[b]	**98.0**[b]	...	...	0.0	0.1[b]	...	...	0.0	0.0	...	...	0.0	0.0	...	...	0.1	0.4[b]	...	...	0.0	0.3[b]	...	...
J0147+2120	0.0	...	...	...	0.0	...	...	...	0.0	...	...	...	0.0	...	...	...	0.0	...	...	...	0.0	...	...	...	0.0	...	...	...	**77.7**	...	...	...
J0149+2956	0.0	...	0.0	...	0.0	...	0.0	...	0.0	...	0.0	...	0.0	...	0.0	...	0.0	...	0.0	...	0.0	...	0.0	...	0.0	...	0.0	...	0.6	...	**0.7**	...
J0150-1851	0.0	0.0	0.0	0.0	0.0	0.0	0.0	0.0	0.0	0.0	0.0	0.0	0.0	0.0	0.0	0.0	0.0	0.0	0.0	0.0	0.0	0.0	0.0	0.0	0.0	0.0	0.0	0.0	100.0	100.0	100.0	**100.0**
J0206+2640	0.0	...	...	...	0.0	...	...	...	0.0	...	...	...	0.0	...	...	...	0.0	...	...	...	0.0	...	...	...	0.0	...	...	...	**3.2**	...	...	...
J0221-6831	0.0	...	0.0	...	0.0	...	1.4	...	0.0	...	0.0	...	0.3[b]	...	0.0	...	0.0	...	0.0	...	0.0	...	0.0	...	0.3	...	0.2	...	99.3[b]	...	**98.4**	...
J0221-5412	0.0	...	...	...	0.0	...	...	...	**99.9**	...	...	...	0.0	...	...	...	0.0	...	...	...	0.0	...	...	...	0.1	...	...	...	0.0	...	...	...
J0223-5815	0.0	...	...	...	0.0	...	...	...	**99.7**[b]	...	...	...	0.0	...	...	...	0.0	...	...	...	0.0	...	...	...	0.2	...	...	...	0.0	...	...	...
J0225-5837	0.0	...	...	...	0.0	...	...	...	**99.9**	...	...	...	0.0	...	...	...	0.0	...	...	...	0.0	...	...	...	0.1	...	...	...	0.0	...	...	...
J0229-0053	0.0	...	...	...	0.0	...	...	...	0.0	...	...	...	0.0	...	...	...	0.0	...	...	...	0.0	...	...	...	0.0	...	...	...	**100.0**	...	...	...
J0234-6442	0.0	...	...	...	0.0	...	...	...	**99.9**	...	...	...	0.0	...	...	...	0.0	...	...	...	0.0	...	...	...	0.0	...	...	...	0.1	...	...	...
J0236+2240	0.0	0.0	...	...	0.0	0.0	...	...	0.0	0.0	...	...	0.0	0.0	...	...	0.0	0.0	...	...	0.0	0.0	...	...	0.0	0.0	...	...	100.0	**100.0**	...	...
J0241-0326	0.0	...	...	...	2.2	...	...	...	**77.5**	...	...	...	0.3	...	...	...	0.0	...	...	...	0.0	...	...	...	0.0	...	...	...	20.0[b]	...	...	...
J0243-2453	0.0	...	0.0	...	0.0	...	0.0	...	0.0	...	0.0	...	0.0	...	0.0	...	0.0	...	0.0	...	0.0	...	0.0	...	0.0	...	0.0	...	5.2[b]	...	**10.0**	...
J0253+1652	0.0	...	0.0	...	0.0	...	0.0	...	0.0	...	0.0	...	0.0	...	0.0	...	0.0	...	0.0	...	0.0	...	0.0	...	0.0	...	0.0	...	0.0	...	0.0	...
J0253+3206	0.0	...	...	...	20.7	...	...	...	0.0	...	...	...	2.9	...	...	...	0.0	...	...	...	0.0	...	...	...	1.4	...	...	...	**75.0**	...	...	...
J0303-7312	0.0	...	...	...	0.0	...	...	...	3.4	...	...	...	0.0	...	...	...	2.9[b]	...	...	...	0.0	...	...	...	0.0	...	...	...	**93.6**[b]	...	...	...
J0310-2756	0.0	...	...	...	0.0	...	...	...	0.0	...	...	...	0.0	...	...	...	0.0	...	...	...	0.0	...	...	...	0.0	...	...	...	**100.0**	...	...	...
J0320-0446	0.0	0.0	...	...	0.0	0.0	...	...	0.0	0.0	...	...	0.0	0.0	...	...	0.0	0.0	...	...	0.0	0.0	...	...	0.0	0.0	...	...	0.0	0.0	...	...
J0323-4631	0.0	...	...	...	0.2	...	...	...	**92.0**[b]	...	...	...	6.3[b]	...	...	...	0.0	...	...	...	0.0	...	...	...	0.0	...	...	...	1.4[b]	...	...	...
J0326-2102	0.0	...	...	...	1.5	...	...	...	0.0	...	...	...	0.0	...	...	...	0.0	...	...	...	0.0	...	...	...	**97.5**[b]	...	...	...	1.0[b]	...	...	...
J0339-3525	0.0	0.0	0.0	0.0	0.0	0.0	91.5	0.1	0.0	0.0	0.0	0.0	0.0	0.0	0.0	0.0	0.0	0.0	0.0	0.0	96.7	87.1	0.0	17.5	0.0	0.0	0.0	0.0	3.2[b]	12.9[b]	8.5	**82.4**
J0342-6817	0.0	...	...	...	0.0	...	...	...	**98.5**[b]	...	...	...	0.0	...	...	...	0.4[b]	...	...	...	0.0	...	...	...	0.1	...	...	...	0.7[b]	...	...	...

Table 2.5 — continued

Name	TWA				βPMG				THA				COL				CAR				ARG				ABDMG				Young Field			
	P	P_v	P_π	$P_{v+\pi}$	P	P_v	P_π	$P_{v+\pi}$	P	P_v	P_π	$P_{v+\pi}$	P	P_v	P_π	$P_{v+\pi}$	P	P_v	P_π	$P_{v+\pi}$	P	P_v	P_π	$P_{v+\pi}$	P	P_v	P_π	$P_{v+\pi}$	P	P_v	P_π	$P_{v+\pi}$
J0355+1133	0.0	0.0	0.0	0.0	12.6	15.0	0.0	0.0	0.0	0.0	0.0	0.0	0.0	0.0	0.0	0.0	0.0	0.0	0.0	0.0	0.0	0.0	0.0	0.0	64.0[b]	81.4[b]	97.0[b]	**99.7**[b]	23.4[b]	3.6[b]	3.0	0.3
J0357-4417	0.0	…	…	…	0.0	…	…	…	**99.0**	…	…	…	0.6	…	…	…	0.0	…	…	…	0.0	…	…	…	0.0	…	…	…	0.3	…	…	…
J0406-3812	0.0	…	…	…	0.0	…	…	…	0.0	…	…	…	2.9	…	…	…	0.0	…	…	…	0.0	…	…	…	0.0	…	…	…	**97.1**	…	…	…
J0421-6306	0.0	…	…	…	**49.5**	…	…	…	0.0	…	…	…	0.0	…	…	…	0.0	…	…	…	48.7	…	…	…	0.1	…	…	…	1.7[b]	…	…	…
J0435-1414	0.0	…	…	…	0.0	…	…	…	0.0	…	…	…	0.0	…	…	…	0.0	…	…	…	0.0	…	…	…	0.0	…	…	…	**100.0**[b]	…	…	…
J0436-4114	0.0	…	…	…	0.2	…	…	…	22.6[b]	…	…	…	**74.2**	…	…	…	0.1	…	…	…	0.0	…	…	…	0.0	…	…	…	3.0[b]	…	…	…
J0440-0530	0.0	0.0	0.0	0.0	0.0	0.0	0.0	0.0	0.0	0.0	0.0	0.0	0.0	0.0	0.0	0.0	0.0	0.0	0.0	0.0	0.4	0.0	0.0	0.0	0.0	0.0	0.0	0.0	99.6	100.0	100.0	**100.0**
J0443+0002	0.0	0.0	…	…	99.0[b]	**98.6**[b]	…	…	0.0	0.0	…	…	0.0	1.1[b]	…	…	0.0	0.0	…	…	0.0	0.0	…	…	0.0	0.1	…	…	1.0[b]	0.2[b]	…	…
J0446-1116	0.0	0.0	0.0	0.0	0.0	0.0	0.0	0.0	0.0	0.0	0.0	0.0	0.0	0.0	0.0	0.0	0.0	0.0	0.0	0.0	0.0	0.0	0.0	0.0	0.0	0.0	0.0	0.0	100.0[b]	100.0[b]	100.0[b]	**100.0**[b]
J0501-0010	0.0	…	0.0	…	0.3	…	0.1	…	0.0	…	0.0	…	9.9	…	2.3	…	0.0	…	0.0	…	2.9	…	0.0	…	0.0	…	0.0	…	86.9[b]	…	**97.6**	…
J0512-2949	0.0	…	…	…	17.6	…	…	…	0.0	…	…	…	0.0	…	…	…	0.0	…	…	…	0.0	…	…	…	0.0	…	…	…	**48.2**[b]	…	…	…
J0518-2756	0.0	…	0.0	…	0.1	…	0.0	…	0.0	…	0.0	…	95.1[b]	…	**96.2**[b]	…	0.0	…	0.0	…	0.0	…	0.0	…	0.0	…	0.0	…	4.8[b]	…	3.8[b]	…
J0534-0631	0.0	…	…	…	0.0	…	…	…	0.0	…	…	…	0.0	…	…	…	0.0	…	…	…	0.0	…	…	…	0.0	…	…	…	**100.0**	…	…	…
J0536-1920	0.0	…	0.0	…	0.4	…	0.1	…	0.0	…	0.0	…	95.3[b]	…	**95.1**	…	0.0	…	0.0	…	0.0	…	0.0	…	0.0	…	0.0	…	4.3[b]	…	4.8	…
J0557-1359	0.0	0.0	…	…	0.3	0.0	…	…	0.0	0.0	…	…	0.0	0.0	…	…	0.0	0.0	…	…	0.0	0.0	…	…	0.0	0.0	…	…	99.7[b]	**100.0**[b]	…	…
J0605+6049	0.0	0.0	…	…	0.0	0.0	…	…	0.0	0.0	…	…	0.0	0.0	…	…	0.0	0.0	…	…	0.0	0.0	…	…	0.0	0.0	…	…	100.0	**100.0**	…	…
J0608-2753	0.0	0.0	0.0	0.0	0.1	0.0	0.8	0.3	0.0	0.0	0.0	0.0	0.1	12.0[b]	0.0	3.4	0.0	0.0	0.0	0.0	0.0	0.0	0.0	0.0	0.0	0.0	0.0	0.0	99.8[b]	88.0[b]	99.2	**96.3**
J0619-2903	0.0	…	…	…	0.0	…	…	…	0.0	…	…	…	**82.9**[b]	…	…	…	0.0	…	…	…	0.0	…	…	…	0.0	…	…	…	17.1[b]	…	…	…
J0632-5010	0.0	…	…	…	0.0	…	…	…	0.0	…	…	…	0.0	…	…	…	0.0	…	…	…	0.0	…	…	…	1.5	…	…	…	**98.4**	…	…	…
J0642+4101	0.0	…	…	…	0.0	…	…	…	0.0	…	…	…	0.0	…	…	…	0.0	…	…	…	0.0	…	…	…	**53.0**	…	…	…	4.7	…	…	…
J0652+4710	0.0	…	…	…	0.0	…	…	…	0.0	…	…	…	0.0	…	…	…	0.0	…	…	…	0.0	…	…	…	0.0	…	…	…	**100.0**[b]	…	…	…
J0652-5741	0.0	…	0.0	…	0.0	…	0.1	…	0.0	…	0.0	…	1.9	…	0.0	…	48.5	…	0.0	…	0.0	…	0.0	…	0.0	…	3.2	…	49.6	…	**96.7**	…
J0657+6219	0.0	0.0	0.0	0.0	0.0	0.0	0.0	0.0	0.0	0.0	0.0	0.0	0.0	0.0	0.0	0.0	0.0	0.0	0.0	0.0	0.0	0.0	0.0	0.0	0.0	0.0	0.0	0.0	100.0	100.0	100.0	**100.0**
J0659-4746	0.0	…	…	…	0.0	…	…	…	0.0	…	…	…	0.0	…	…	…	0.0	…	…	…	0.0	…	…	…	0.0	…	…	…	0.0	…	…	…
J0712-6155	0.0	…	0.0	…	0.1	…	0.1[b]	…	0.0	…	0.0	…	0.0	…	0.0	…	0.0	…	1.2[b]	…	0.0	…	0.0	…	1.2	…	1.3[b]	…	98.7[b]	…	**97.4**[b]	…
J0752+1612	0.0	0.0	0.0	0.0	0.0	0.0	0.0	0.0	0.0	0.0	0.0	0.0	0.0	0.0	0.0	0.0	0.0	0.0	0.0	0.0	0.0	0.0	0.0	0.0	0.0	0.0	0.0	0.0	100.0	100.0	100.0	**100.0**
J0754+7909	0.0	…	…	…	0.0	…	…	…	0.0	…	…	…	0.0	…	…	…	0.0	…	…	…	0.0	…	…	…	0.0	…	…	…	**0.2**	…	…	…
J0809+4434	0.0	…	…	…	0.0	…	…	…	0.0	…	…	…	0.0	…	…	…	0.0	…	…	…	**28.3**	…	…	…	0.0	…	…	…	10.2	…	…	…
J0829+2655	0.0	…	…	…	0.0	…	…	…	0.0	…	…	…	0.0	…	…	…	0.0	…	…	…	2.7	…	…	…	0.0	…	…	…	**48.2**[b]	…	…	…
J0858+3256	0.0	…	…	…	0.0	…	…	…	0.0	…	…	…	0.0	…	…	…	0.0	…	…	…	0.0	…	…	…	0.0	…	…	…	**1.8**	…	…	…
J0917+6028	0.0	…	…	…	0.0	…	…	…	0.0	…	…	…	0.0	…	…	…	0.0	…	…	…	0.1[b]	…	…	…	0.0	…	…	…	**3.7**	…	…	…
J0951+3558	0.2	0.0	…	…	0.0	0.0	…	…	0.0	0.0	…	…	0.0	0.0	…	…	0.3	0.0	…	…	0.0	0.0	…	…	16.1	0.0	…	…	83.4	**100.0**	…	…
J1004+5022	0.1	…	…	…	0.0	…	…	…	0.0	…	…	…	0.0	…	…	…	0.3	…	…	…	0.0	…	…	…	31.1	…	…	…	**68.5**	…	…	…
J1020+0814	0.0	0.0	0.0	0.0	0.0	0.0	0.0	0.0	0.0	0.0	0.0	0.0	0.0	0.0	0.0	0.0	0.0	0.0	0.0	0.0	50.1	15.5	0.0	0.0	0.0	0.0	0.0	0.0	49.9	84.5	100.0	**100.0**
J1022+0200	0.0	0.0	0.1	0.0	0.0	0.0	0.0	0.0	0.0	0.0	0.0	0.0	0.0	0.0	0.0	0.0	0.0	0.0	1.0	0.0	0.0	0.0	0.0	0.0	0.0	0.0	2.1	2.5	100.0	100.0	96.8	**97.4**
J1022+5825	0.0	0.0	…	…	0.0	0.0	…	…	0.0	0.0	…	…	0.0	0.0	…	…	0.0	0.0	…	…	0.0	0.0	…	…	10.0	0.0	…	…	90.0	**100.0**	…	…
J1025+3212	0.0	…	…	…	0.0	…	…	…	0.0	…	…	…	0.0	…	…	…	0.0	…	…	…	0.0	…	…	…	0.0	…	…	…	**100.0**	…	…	…
J1139-3159	99.8[b]	99.9[b]	97.2[b]	**99.3**[b]	0.0	0.0	0.0	0.0	0.0	0.0	0.0	0.0	0.0	0.0	0.0	0.0	0.0	0.0	0.0	0.0	0.0	0.0	0.0	0.0	0.0	0.0	0.0	0.0	0.2[b]	0.1	2.8[b]	0.7[b]
J1154-3400	0.0	…	…	…	0.0	…	…	…	0.0	…	…	…	0.0	…	…	…	0.0	…	…	…	**26.2**	…	…	…	0.0	…	…	…	19.5[b]	…	…	…
J1212-2253	0.0	…	…	…	0.0	…	…	…	0.0	…	…	…	0.0	…	…	…	0.0	…	…	…	0.0	…	…	…	0.0	…	…	…	**0.3**	…	…	…
J1212+0206	0.0	…	…	…	0.0	…	…	…	0.0	…	…	…	0.0	…	…	…	0.0	…	…	…	0.0	…	…	…	0.0	…	…	…	**3.4**	…	…	…
J1245-4429	87.4[b]	…	**93.3**[b]	…	0.0	…	0.0	…	0.0	…	0.0	…	0.0	…	0.0	…	0.0	…	0.0	…	0.0	…	0.0	…	0.0	…	0.0	…	12.6[b]	…	6.7[b]	…
J1246+4027	0.0	…	…	…	0.0	…	…	…	0.0	…	…	…	0.0	…	…	…	0.0	…	…	…	0.0	…	…	…	0.0	…	…	…	**100.0**[b]	…	…	…
J1305-2541	0.0	0.0	0.0	0.0	0.0	0.0	0.0	0.0	0.0	0.0	0.0	0.0	0.0	0.0	0.0	0.0	0.0	0.0	0.0	0.0	85.9	0.0	80.3	0.0	0.0	0.0	0.0	0.0	14.1[b]	100.0[b]	19.7	**100.0**
J1314+1320	0.0	…	0.0	…	0.0	…	0.0	…	0.0	…	0.0	…	0.0	…	0.0	…	0.0	…	0.0	…	0.0	…	0.0	…	0.0	…	0.0	…	3.7	…	**17.8**	…
J1324+6358	0.0	…	…	…	0.0	…	…	…	0.0	…	…	…	0.0	…	…	…	0.0	…	…	…	0.0	…	…	…	2.4	…	…	…	**6.9**	…	…	…
J1326-0038	0.0	…	0.0	…	0.0	…	0.0	…	0.0	…	0.0	…	0.0	…	0.0	…	0.0	…	0.0	…	0.0	…	0.3	…	0.0	…	0.0	…	11.2[b]	…	**23.0**	…
J1331+3407	0.0	0.0	…	…	0.0	0.0	…	…	0.0	0.0	…	…	0.0	0.0	…	…	0.0	0.0	…	…	0.0	0.0	…	…	0.0	0.0	…	…	0.0	0.0	…	…
J1411-2119	0.0	0.1	…	…	0.0	0.0	…	…	0.0	0.0	…	…	0.0	0.0	…	…	0.0	0.0	…	…	0.0	0.0	…	…	0.0	0.0	…	…	100.0[b]	**99.9**[b]	…	…
J1415+5724	0.0	…	…	…	0.0	…	…	…	0.0	…	…	…	0.0	…	…	…	0.0	…	…	…	0.0	…	…	…	0.0	…	…	…	**1.4**	…	…	…
J1417-0407	0.0	…	…	…	0.0	…	…	…	0.0	…	…	…	0.0	…	…	…	0.0	…	…	…	0.0	…	…	…	0.0	…	…	…	**0.7**	…	…	…

Table 2.5 — continued

Name	TWA				βPMG				THA				COL				CAR				ARG				ABDMG				Young Field			
	P	P_v	P_π	$P_{v+\pi}$	P	P_v	P_π	$P_{v+\pi}$	P	P_v	P_π	$P_{v+\pi}$	P	P_v	P_π	$P_{v+\pi}$	P	P_v	P_π	$P_{v+\pi}$	P	P_v	P_π	$P_{v+\pi}$	P	P_v	P_π	$P_{v+\pi}$	P	P_v	P_π	$P_{v+\pi}$
J1428+3310	0.0	0.0	0.0	0.0	0.0	0.0	0.0	0.0	0.0	0.0	0.0	0.0	0.0	0.0	0.0	0.0	0.0	0.0	0.0	0.0	0.0	0.0	0.0	0.0	0.0	0.0	0.0	0.0	0.2	0.0	11.9	**0.1**
J1506+1321	0.0	0.0	…	…	0.0	0.0	…	…	0.0	0.0	…	…	0.0	0.0	…	…	0.0	0.0	…	…	0.3	0.0	…	…	0.0	0.0	…	…	99.7	**100.0**	…	…
J1524+0934	0.0	…	…	…	0.0	…	…	…	0.0	…	…	…	0.0	…	…	…	0.0	…	…	…	0.0	…	…	…	0.0	…	…	…	0.0	…	…	…
J1531+1641	0.0	…	…	…	0.0	…	…	…	0.0	…	…	…	0.0	…	…	…	0.0	…	…	…	0.2	…	…	…	0.0	…	…	…	**30.6**[b]	…	…	…
J1547-2423	0.0	…	…	…	0.0	…	…	…	0.0	…	…	…	0.0	…	…	…	0.0	…	…	…	0.1	…	…	…	0.0	…	…	…	**99.9**	…	…	…
J1551+0941	0.0	…	…	…	0.0	…	…	…	0.0	…	…	…	0.0	…	…	…	0.0	…	…	…	0.0	…	…	…	0.0	…	…	…	**100.0**[b]	…	…	…
J1552+2948	0.0	0.0	…	…	0.0	0.0	…	…	0.0	0.0	…	…	0.0	0.0	…	…	0.0	0.0	…	…	0.0	0.0	…	…	0.0	0.0	…	…	100.0[b]	**100.0**[b]	…	…
J1557-2952	0.0	…	…	…	0.0	…	…	…	0.0	…	…	…	0.0	…	…	…	0.0	…	…	…	0.0	…	…	…	0.0	…	…	…	**100.0**	…	…	…
J1600-2456	0.0	…	…	…	0.0	…	…	…	0.0	…	…	…	0.0	…	…	…	0.0	…	…	…	0.0	…	…	…	0.1	…	…	…	**99.9**[b]	…	…	…
J1615+4953	0.0	…	…	…	0.0	…	…	…	0.0	…	…	…	0.0	…	…	…	0.0	…	…	…	0.0	…	…	…	2.9[b]	…	…	…	**97.1**[b]	…	…	…
J1617+5516	0.0	0.0	0.0	0.0	0.0	0.0	0.0	0.0	0.0	0.0	0.0	0.0	0.0	0.0	0.0	0.0	0.0	0.0	0.0	0.0	0.0	0.0	0.0	0.0	0.0	0.0	0.0	0.0	100.0[b]	100.0[b]	100.0[b]	**100.0**[b]
J1647+5632	0.0	…	0.0	…	0.0	…	0.2	…	0.0	…	0.0	…	0.0	…	0.0	…	0.0	…	0.0	…	0.0	…	17.6	…	0.0	…	8.5	…	7.6	…	**20.9**	…
J1655-0823	0.0	0.0	0.0	0.0	0.0	0.0	0.0	0.0	0.0	0.0	0.0	0.0	0.0	0.0	0.0	0.0	0.0	0.0	0.0	0.0	0.0	0.0	0.0	0.0	0.0	0.0	0.0	0.0	0.7	0.2	31.2	**9.5**
J1703-7715	0.0	…	…	…	0.0	…	…	…	0.0	…	…	…	0.0	…	…	…	0.0	…	…	…	0.0	…	…	…	0.0	…	…	…	**100.0**	…	…	…
J1711+2326	0.0	0.0	…	…	0.0	0.0	…	…	0.0	0.0	…	…	0.0	0.0	…	…	0.0	0.0	…	…	0.0	0.0	…	…	0.0	0.0	…	…	100.0[b]	**100.0**[b]	…	…
J1719+2630	0.0	0.0	0.0	0.0	0.0	0.0	0.0	0.0	0.0	0.0	0.0	0.0	0.0	0.0	0.0	0.0	0.0	0.0	0.0	0.0	88.8	0.0	0.0	0.0	0.0	0.0	0.0	0.0	11.2	100.0	100.0	**100.0**
J1726+1538	0.0	…	…	…	0.0	…	…	…	0.0	…	…	…	0.0	…	…	…	0.0	…	…	…	0.0	…	…	…	0.0	…	…	…	**100.0**[b]	…	…	…
J1736+0220	0.0	…	…	…	0.0	…	…	…	0.0	…	…	…	0.0	…	…	…	0.0	…	…	…	0.0	…	…	…	0.0	…	…	…	**70.2**	…	…	…
J1738+6142	0.0	…	…	…	0.0	…	…	…	0.0	…	…	…	0.0	…	…	…	0.0	…	…	…	0.0	…	…	…	0.0	…	…	…	**0.3**	…	…	…
J1758+4633	0.0	…	0.0	…	0.0	…	0.0	…	0.0	…	0.0	…	0.0	…	0.0	…	0.0	…	0.0	…	0.0	…	0.0	…	0.0	…	0.0	…	3.1	…	**12.1**	…
J1821+1414	0.0	0.0	…	…	0.1	0.0	…	…	0.0	0.0	…	…	0.0	0.0	…	…	0.0	0.0	…	…	0.0	0.0	…	…	0.0	0.0	…	…	99.9	**100.0**[b]	…	…
J1824+2937	0.0	…	…	…	0.0	…	…	…	0.0	…	…	…	0.0	…	…	…	0.0	…	…	…	0.0	…	…	…	0.0	…	…	…	**2.0**	…	…	…
J1828+1229	0.0	…	…	…	0.0	…	…	…	0.0	…	…	…	0.0	…	…	…	0.0	…	…	…	0.0	…	…	…	0.0	…	…	…	**100.0**[b]	…	…	…
J1832+2030	0.0	0.0	…	…	0.0	0.0	…	…	0.0	0.0	…	…	0.0	0.0	…	…	0.0	0.0	…	…	0.0	0.0	…	…	0.0	0.0	…	…	100.0	**100.0**	…	…
J1916+0509	0.0	0.0	0.0	0.0	0.0	0.0	0.0	0.0	0.0	0.0	0.0	0.0	0.0	0.0	0.0	0.0	0.0	0.0	0.0	0.0	0.0	0.0	0.0	0.0	0.0	0.0	0.0	0.0	100.0	100.0	100.0	**100.0**
J1922+6610	0.0	…	…	…	0.0	…	…	…	0.0	…	…	…	0.0	…	…	…	0.0	…	…	…	0.0	…	…	…	0.1	…	…	…	**99.9**	…	…	…
J1930-1335	0.0	0.0	0.0	0.0	0.0	0.0	0.0	0.0	0.0	0.0	0.0	0.0	0.0	0.0	0.0	0.0	0.0	0.0	0.0	0.0	0.0	0.0	0.0	0.0	0.0	0.0	0.0	0.0	100.0	100.0	100.0	**100.0**
J1935-2846	0.0	…	…	…	9.2[b]	…	…	…	0.0	…	…	…	0.0	…	…	…	0.0	…	…	…	0.9	…	…	…	0.0	…	…	…	**89.9**[b]	…	…	…
J1956-7542	0.0	…	…	…	0.0	…	…	…	18.2[b]	…	…	…	0.0	…	…	…	0.0	…	…	…	0.1	…	…	…	0.0	…	…	…	**81.7**[b]	…	…	…
J2000-7523	0.0	0.0	…	…	73.9[b]	**96.4**[b]	…	…	0.0	0.0	…	…	0.0	0.0	…	…	0.0	0.0	…	…	23.9[b]	0.0	…	…	0.9[b]	0.1	…	…	1.3[b]	3.4[b]	…	…
J2013-2806	0.0	…	…	…	42.6	…	…	…	0.0	…	…	…	0.0	…	…	…	0.0	…	…	…	0.4	…	…	…	0.0	…	…	…	**57.0**[b]	…	…	…
J2049-1944	0.0	0.0	…	…	0.0	0.0	…	…	0.0	0.0	…	…	0.0	0.0	…	…	0.0	0.0	…	…	0.0	0.0	…	…	0.7	0.0	…	…	0.6	**0.3**	…	…
J2057-0252	0.0	…	0.0	…	0.0	…	0.0	…	0.0	…	0.0	…	0.0	…	0.0	…	0.0	…	0.0	…	0.0	…	0.0	…	0.0	…	0.0	…	100.0[b]	…	**100.0**	…
J2101+1756	0.0	…	0.0	…	0.0	…	0.0	…	0.0	…	0.0	…	0.0	…	0.0	…	0.0	…	0.0	…	0.0	…	0.0	…	49.3	…	**26.8**	…	1.7	…	4.9	…
J2114-2251	0.0	…	0.0	…	99.7[b]	…	**99.7**[b]	…	0.0	…	0.0	…	0.0	…	0.0	…	0.0	…	0.0	…	0.0	…	0.0	…	0.0	…	0.0	…	0.3[b]	…	0.3	…
J2116-0729	0.0	…	…	…	0.0	…	…	…	0.0	…	…	…	0.0	…	…	…	0.0	…	…	…	0.0	…	…	…	0.0	…	…	…	**17.3**	…	…	…
J2126-8140	0.0	…	…	…	0.0	…	…	…	**94.5**[b]	…	…	…	0.0	…	…	…	0.0	…	…	…	0.0	…	…	…	0.1	…	…	…	5.5[b]	…	…	…
J2140+3655	0.0	…	…	…	0.0	…	…	…	0.0	…	…	…	0.0	…	…	…	0.0	…	…	…	0.0	…	…	…	0.0	…	…	…	**0.1**	…	…	…
J2148+4003	0.0	…	…	…	0.0	…	…	…	0.0	…	…	…	0.0	…	…	…	0.0	…	…	…	48.0	…	…	…	0.0	…	…	…	**52.0**[b]	…	…	…
J2151-2441	0.0	…	…	…	0.0	…	…	…	0.0	…	…	…	0.0	…	…	…	0.0	…	…	…	0.7	…	…	…	0.0	…	…	…	**10.6**	…	…	…
J2206-4217	0.0	…	…	…	2.7	…	…	…	0.0	…	…	…	0.0	…	…	…	0.0	…	…	…	0.0	…	…	…	**93.1**	…	…	…	0.9[b]	…	…	…
J2208+2921	0.0	…	…	…	7.2	…	…	…	0.0	…	…	…	0.8	…	…	…	0.0	…	…	…	0.0	…	…	…	0.0	…	…	…	**92.1**[b]	…	…	…
J2213-2136	0.0	…	…	…	1.5	…	…	…	1.2	…	…	…	0.0	…	…	…	0.0	…	…	…	0.0	…	…	…	0.0	…	…	…	**97.3**[b]	…	…	…
J2224-0158	0.0	…	0.0	…	0.0	…	0.0	…	0.0	…	0.0	…	0.0	…	0.0	…	0.0	…	0.0	…	0.0	…	0.0	…	0.1	…	0.0	…	3.8	…	**1.3**	…
J2244+2043	0.0	…	…	…	0.5	…	…	…	0.0	…	…	…	0.0	…	…	…	0.0	…	…	…	0.0	…	…	…	**99.1**[b]	…	…	…	0.4	…	…	…
J2249+0044	0.0	…	…	…	0.0	…	…	…	0.0	…	…	…	0.0	…	…	…	0.0	…	…	…	0.2	…	…	…	0.0	…	…	…	**99.8**[b]	…	…	…
J2313+2117	0.0	0.0	…	…	5.1	22.3	…	…	0.0	0.0	…	…	0.0	0.0	…	…	0.0	0.0	…	…	42.3	0.0	…	…	0.0	0.0	…	…	52.7	**77.7**	…	…
J2317-4838	0.0	…	…	…	0.0	…	…	…	0.0	…	…	…	0.0	…	…	…	0.0	…	…	…	0.0	…	…	…	0.0	…	…	…	**18.7**[b]	…	…	…
J2322-3133	0.0	…	0.0	…	0.0	…	0.0	…	0.0	…	0.0	…	0.0	…	0.0	…	0.0	…	0.0	…	0.0	…	0.0	…	0.0	…	0.0	…	100.0	…	**100.0**	…
J2322-6151	0.0	…	…	…	0.0	…	…	…	**99.9**	…	…	…	0.0	…	…	…	0.0	…	…	…	0.0	…	…	…	0.0	…	…	…	0.0	…	…	…
J2328-1038	0.0	…	…	…	0.0	…	…	…	0.0	…	…	…	0.0	…	…	…	0.0	…	…	…	0.0	…	…	…	0.0	…	…	…	**60.6**[b]	…	…	…

Table 2.5 — continued

Name	TWA				βPMG				THA				COL				CAR				ARG				ABDMG				Young Field			
	P	P_v	P_π	$P_{v+\pi}$	P	P_v	P_π	$P_{v+\pi}$	P	P_v	P_π	$P_{v+\pi}$	P	P_v	P_π	$P_{v+\pi}$	P	P_v	P_π	$P_{v+\pi}$	P	P_v	P_π	$P_{v+\pi}$	P	P_v	P_π	$P_{v+\pi}$	P	P_v	P_π	$P_{v+\pi}$
J2335+4511	0.0	...	...	...	0.0	...	...	...	0.0	...	...	...	0.0	...	...	...	0.0	...	...	...	0.0	...	...	...	0.0	...	...	...	**3.4**	...	...	...
J2351+3010	0.0	...	...	...	0.0	...	...	...	0.0	...	...	...	0.0	...	...	...	0.0	...	...	...	**46.9**	...	...	...	0.0	...	...	...	8.4	...	...	...
J2354-3316	0.0	...	0.0	...	0.0	...	0.0	...	0.0	...	0.0	...	0.0	...	0.0	...	0.0	...	0.0	...	0.0	...	0.0	...	0.0	...	0.0	...	0.0	...	**0.7**	...
J2359+3241	0.0	0.0	...	...	0.0	0.0	...	...	0.0	0.0	...	...	0.0	0.0	...	...	0.0	0.0	...	...	0.0	0.0	...	...	0.0	0.0	...	...	100.0	**100.0**	...	...

[a]Bayesian Parameter without using radial velocity or parallax (P), including radial velocity information only (P_v), including parallax information only (P_π) or including radial velocity and parallax information ($P_{v+\pi}$). Parameters in red are the highest ones (not including the old field hypothesis) using all available observables. We stress the fact that one cannot directly interpret P as an actual probability.

[b]The Bayesian probability P associated to a binary hypothesis was higher.

Table 2.6. Statistical Distances and Radial Velocities[a]

Name	TWA		βPMG		THA		COL		CAR		ARG		ABDMG		Field	
	d_s	$v_{\rm rad}$	d_s	$v_{\rm rad}$	d_s	$v_{\rm rad}$	d_s	$v_{\rm rad}$	d_s	$v_{\rm rad}$	d_s	$v_{\rm rad}$	d_s	$v_{\rm rad}$	d_s	$v_{\rm rad}$
J0001+1010	15.3 ± 1.6	-12.0 ± 2.4	$63.8^{+11.6}_{-6.4}$	-5.5 ± 3.9	$55.0^{+4.0}_{-3.6}$	-2.6 ± 3.6	$84.2^{+8.0}_{-8.8}$	-4.0 ± 7.2	$60.2^{+6.0}_{-4.8}$	-5.0 ± 3.9	$83.4^{+8.0}_{-9.2}$	-6.7 ± 5.6	$87.8^{+8.0}_{-8.4}$	1.2 ± 6.5	$\mathbf{124.7^{+21.2}_{-15.2}}$	$\mathbf{-11.0 \pm 10.7}$
J0003-2822	16.1 ± 1.2	3.9 ± 1.3	$15.3^{+1.2}_{-0.8}$	6.1 ± 1.4	$18.1^{+1.2}_{-1.6}$	-5.0 ± 1.7	$18.1^{+1.2}_{-1.6}$	-2.3 ± 1.3	$19.3^{+0.4}_{-0.8}$	0.1 ± 0.4	$16.1^{+2.0}_{-1.2}$	2.2 ± 1.3	$22.1^{+0.8}_{-1.2}$	13.1 ± 2.0	$\mathbf{34.2^{+6.4}_{-4.8}}$	$\mathbf{-0.2 \pm 7.4}$
J0004-6410	$27.7^{+2.8}_{-2.4}$	6.7 ± 1.8	36.6 ± 4.0	11.6 ± 2.5	$\mathbf{47.8^{+3.6}_{-2.8}}$[b]	$\mathbf{6.8 \pm 3.1}$[b]	54.6 ± 5.6[b]	10.0 ± 3.2[b]	$55.8^{+4.8}_{-5.2}$[b]	15.6 ± 5.1[b]	$53.0^{+6.4}_{-6.0}$[b]	-0.1 ± 2.9[b]	53.0 ± 5.2[b]	20.7 ± 3.2[b]	$56.6^{+7.6}_{-9.2}$[b]	10.3 ± 8.6[b]
J0006-6436	26.5 ± 2.0	6.9 ± 1.4	30.1 ± 2.8	13.1 ± 2.0	$\mathbf{43.8^{+2.8}_{-2.4}}$[b]	$\mathbf{6.5 \pm 2.5}$[b]	45.8 ± 3.6[b]	8.5 ± 2.0[b]	$45.0^{+3.2}_{-2.8}$[b]	11.6 ± 2.0[b]	$28.1^{+3.6}_{-3.2}$	-0.1 ± 1.8	$43.8^{+3.6}_{-3.2}$[b]	20.0 ± 2.1[b]	$46.2^{+8.8}_{-7.2}$[b]	11.0 ± 8.3[b]
J0011-1523	17.7 ± 1.6	-3.7 ± 1.5	$22.1^{+1.6}_{-2.0}$	3.9 ± 1.7	32.1 ± 2.0[b]	-2.2 ± 2.5[b]	28.5 ± 2.4[b]	0.6 ± 2.5[b]	$27.3^{+2.4}_{-2.0}$[b]	1.1 ± 1.4[b]	29.3 ± 2.8[b]	1.8 ± 2.0[b]	31.7 ± 2.4[b]	7.2 ± 2.2[b]	$\mathbf{91.0^{+21.6}_{-68.1}}$	$\mathbf{-7.2 \pm 9.8}$
J0012+5059	$12.1^{+0.8}_{-1.2}$	-9.6 ± 1.5	15.3 ± 1.2	-1.8 ± 2.1	$14.5^{+0.8}_{-1.2}$	-11.9 ± 1.3	$16.9^{+0.8}_{-1.2}$	-12.1 ± 1.0	$17.7^{+1.2}_{-0.8}$	-12.1 ± 0.7	$16.5^{+1.6}_{-1.2}$	1.5 ± 1.4	14.9 ± 1.2	-21.4 ± 1.3	$\mathbf{33.3^{+8.4}_{-7.2}}$	$\mathbf{0.4 \pm 11.1}$
J0019+4614	$26.5^{+3.2}_{-2.8}$	-9.9 ± 1.7	28.9 ± 2.4	-6.7 ± 2.0	$31.7^{+2.4}_{-2.0}$	-13.5 ± 1.4	$31.3^{+2.4}_{-2.0}$	-10.3 ± 1.0	28.5 ± 1.6	-12.7 ± 0.8	32.1 ± 4.0	-4.4 ± 1.5	$\mathbf{37.4^{+2.8}_{-2.4}}$	$\mathbf{-17.0 \pm 1.4}$	$36.2^{+8.8}_{-7.2}$	-8.3 ± 10.7
J0025+4759	9.7 ± 0.8[b]	-9.6 ± 1.5[b]	$14.9^{+1.2}_{-1.6}$[b]	-0.5 ± 2.1[b]	14.9 ± 1.2[b]	-11.4 ± 1.1[b]	18.1 ± 1.2[b]	11.3 ± 0.8[b]	16.5 ± 0.8[b]	7.5 ± 0.4[b]	17.3 ± 1.6[b]	1.9 ± 1.3[b]	14.9 ± 1.2[b]	20.3 ± 1.3[b]	$\mathbf{21.7 \pm 4.0}$[b]	$\mathbf{-2.0 \pm 10.8}$[b]
J0027+0503	17.7 ± 1.6	-7.9 ± 1.3	$64.2^{+10.8}_{-8.0}$	2.9 ± 1.5	$53.0^{+4.0}_{-3.6}$	-9.3 ± 1.1	88.2 ± 8.4	-2.2 ± 0.7	$114.7^{+8.8}_{-8.4}$	-3.4 ± 0.4	$57.8^{+8.0}_{-7.6}$	-4.0 ± 1.0	$91.8^{+11.6}_{-10.0}$	-12.0 ± 1.7	$\mathbf{120.3^{+24.8}_{-19.6}}$	$\mathbf{2.7 \pm 8.0}$
J0027+2219	$12.5^{+1.2}_{-0.8}$[b]	-2.5 ± 1.5[b]	11.3 ± 0.8[b]	0.4 ± 1.7[b]	11.3 ± 0.8[b]	-9.9 ± 1.1[b]	$12.5^{+0.8}_{-0.4}$[b]	-8.2 ± 0.7[b]	$12.5^{+0.8}_{-0.4}$[b]	-7.5 ± 0.4[b]	$13.3^{+0.8}_{-1.2}$[b]	-0.6 ± 1.0[b]	13.7 ± 0.8[b]	12.7 ± 1.5[b]	$\mathbf{20.1 \pm 3.6}$[b]	$\mathbf{-5.3 \pm 9.1}$[b]
J0032-4405	23.3 ± 1.6	4.8 ± 1.3	$\mathbf{26.1 \pm 2.0}$	$\mathbf{11.6 \pm 1.5}$	$35.0^{+1.6}_{-2.0}$	5.1 ± 2.2	$31.3^{+2.4}_{-2.8}$	8.8 ± 1.4	$30.9^{+1.2}_{-1.6}$	8.9 ± 0.7	$19.7^{+2.4}_{-2.8}$	2.2 ± 1.8	$36.6^{+2.0}_{-2.4}$	17.3 ± 1.8	$41.0^{+5.6}_{-4.8}$	8.6 ± 7.4
J0033-1521	$12.9^{+1.6}_{-1.2}$	5.4 ± 1.5	$14.1^{+1.6}_{-1.2}$	6.7 ± 1.5	$14.1^{+1.6}_{-1.2}$	-11.0 ± 1.5	$12.5^{+2.0}_{-1.2}$	-4.3 ± 1.1	23.3 ± 1.2	-2.5 ± 0.7	$17.3^{+1.6}_{-2.0}$	2.3 ± 1.3	$21.7^{+2.0}_{-1.6}$	6.5 ± 2.0	$\mathbf{28.1^{+4.4}_{-4.8}}$	$\mathbf{4.3 \pm 7.4}$
J0033-0908	$20.1^{+2.0}_{-1.6}$	-6.0 ± 1.7	$56.6^{+5.6}_{-5.2}$	1.6 ± 2.8	$49.4^{+3.2}_{-2.8}$	-1.3 ± 3.2	$69.0^{+10.4}_{-6.0}$	1.2 ± 4.8	$58.2^{+5.2}_{-4.8}$	0.6 ± 2.9	$65.0^{+6.0}_{-5.6}$	-0.4 ± 3.5	$73.4^{+12.8}_{-8.0}$	9.3 ± 3.5	$\mathbf{142.3^{+24.8}_{-18.8}}$	$\mathbf{-5.1 \pm 8.7}$
J0037-5846	$29.3^{+2.8}_{-2.4}$	6.0 ± 1.5	37.4 ± 3.6	12.6 ± 2.1	$\mathbf{47.8^{+3.2}_{-2.8}}$[b]	$\mathbf{6.8 \pm 2.7}$[b]	$57.0^{+4.8}_{-4.4}$[b]	11.0 ± 2.2[b]	55.8 ± 4.4[b]	12.7 ± 2.9[b]	$50.2^{+5.6}_{-6.0}$[b]	3.6 ± 2.5[b]	$54.2^{+4.4}_{-4.8}$[b]	21.4 ± 2.5[b]	$54.6^{+7.2}_{-8.0}$[b]	10.3 ± 8.0[b]
J0041-5621	26.5 ± 2.0[b]	6.8 ± 1.4[b]	30.5 ± 2.8[b]	13.0 ± 1.8[b]	$\mathbf{41.8 \pm 2.4}$[b]	$\mathbf{6.5 \pm 2.4}$[b]	42.6 ± 3.6[b]	10.0 ± 1.7[b]	$41.8^{+2.8}_{-2.4}$[b]	11.2 ± 1.4[b]	$29.7^{+4.0}_{-3.6}$[b]	2.9 ± 2.0[b]	41.8 ± 3.6[b]	21.0 ± 2.0[b]	$48.2^{+21.2}_{-12.0}$[b]	10.3 ± 7.9[b]
J0045+1634	$9.7^{+1.6}_{-0.8}$	0.2 ± 2.0	$11.7^{+1.2}_{-0.8}$	5.5 ± 1.7	12.1 ± 0.8	-9.3 ± 1.1	13.3 ± 0.8	-7.9 ± 0.8	15.3 ± 0.8[b]	-3.3 ± 0.6[b]	$\mathbf{13.3^{+0.8}_{-1.2}}$	$\mathbf{3.4 \pm 1.3}$	$13.3^{+0.8}_{-1.2}$[b]	-13.3 ± 1.7[b]	$18.5^{+2.0}_{-2.8}$[b]	3.2 ± 8.6[b]
J0047+6803	13.3 ± 0.8[b]	-7.2 ± 1.5[b]	$9.7^{+0.4}_{-0.8}$	-7.6 ± 2.2	$8.9^{+0.8}_{-0.4}$	-16.6 ± 1.8	$9.3^{+0.4}_{-0.8}$	-12.7 ± 0.8	7.7 ± 0.4	-15.6 ± 0.7	$13.3^{+1.2}_{-0.8}$[b]	-3.6 ± 1.5[b]	$\mathbf{10.5^{+0.8}_{-0.4}}$	$\mathbf{-20.4 \pm 1.3}$	$14.1^{+0.8}_{-1.2}$[b]	-4.4 ± 11.4[b]
J0055+4130	53.0 ± 5.2	-7.5 ± 2.5	$79.8^{+7.6}_{-8.0}$	-4.1 ± 3.8	$72.2^{+6.8}_{-8.0}$	-5.8 ± 2.9	$77.4^{+6.4}_{-7.2}$	-6.9 ± 3.4	72.6 ± 6.4	-9.9 ± 3.2	$81.8^{+7.2}_{-8.0}$	2.9 ± 3.6	$87.0^{+6.8}_{-6.4}$	-17.3 ± 3.6	$\mathbf{135.5^{+26.0}_{-22.4}}$	$\mathbf{-0.4 \pm 11.6}$
J0058-1747	22.5 ± 2.0	-2.5 ± 2.2	$58.2^{+5.6}_{-5.2}$	1.3 ± 3.1	$51.0^{+3.2}_{-2.8}$	4.8 ± 3.6	$82.6^{+11.2}_{-9.6}$	20.4 ± 4.5	$63.4^{+5.6}_{-5.2}$	-2.7 ± 3.8	65.4 ± 6.0	-4.0 ± 4.5	$83.8^{+12.0}_{-10.8}$	17.7 ± 3.2	$\mathbf{163.9^{+22.0}_{-23.2}}$	$\mathbf{8.5 \pm 7.7}$
J0103+1935	11.3 ± 0.8	1.5 ± 1.8	14.1 ± 1.2	8.3 ± 1.7	15.7 ± 1.2	-8.6 ± 1.1	$14.9^{+0.8}_{-1.2}$	-6.9 ± 0.8	$16.5^{+1.2}_{-0.8}$	-0.9 ± 0.6	$\mathbf{15.3 \pm 1.2}$	$\mathbf{5.3 \pm 1.3}$	$13.7^{+1.2}_{-0.8}$	-15.2 ± 1.5	$21.3^{+4.8}_{-4.0}$	7.2 ± 8.8
J0107+0041	$7.3^{+0.8}_{-0.4}$	9.7 ± 1.5	$8.1^{+0.4}_{-0.8}$	10.6 ± 1.5	8.5 ± 0.4	-9.6 ± 1.3	6.9 ± 0.4	-7.4 ± 0.8	7.3 ± 0.4	0.8 ± 0.4	$8.9^{+0.4}_{-0.8}$	7.9 ± 1.3	$6.9^{+0.4}_{-0.8}$	-7.4 ± 1.8	$\mathbf{14.1^{+2.8}_{-2.4}}$	$\mathbf{10.2 \pm 7.9}$
J0117-3403	26.9 ± 2.4	5.8 ± 1.4	$31.7^{+3.2}_{-2.8}$	11.7 ± 1.5	$\mathbf{41.0^{+2.4}_{-2.0}}$	$\mathbf{3.6 \pm 2.1}$	41.8 ± 2.8	9.2 ± 1.5	43.0 ± 2.0	8.3 ± 1.0	$34.2^{+3.6}_{-4.0}$	6.4 ± 1.8	49.4 ± 3.6[b]	18.0 ± 2.0[b]	$53.8^{+6.8}_{-8.0}$[b]	9.2 ± 7.3[b]
J0122-2439	18.9 ± 2.0[b]	3.4 ± 2.0[b]	$\mathbf{22.9^{+2.8}_{-2.4}}$[b]	$\mathbf{10.6 \pm 1.7}$[b]	$35.4^{+2.8}_{-2.4}$[b]	4.1 ± 2.5[b]	$29.7^{+3.6}_{-3.2}$[b]	6.8 ± 2.1[b]	$26.9^{+2.4}_{-2.0}$[b]	7.8 ± 1.4[b]	27.3 ± 4.0[b]	8.2 ± 2.5[b]	$32.9^{+4.0}_{-3.2}$[b]	15.6 ± 2.1[b]	$36.6^{+14.0}_{-12.4}$[b]	7.5 ± 7.3[b]

Table 2.6 — continued

Name	TWA		βPMG		THA		COL		CAR		ARG		ABDMG		Field	
	d_s	$v_{\rm rad}$	d_s	$v_{\rm rad}$	d_s	$v_{\rm rad}$	d_s	$v_{\rm rad}$	d_s	$v_{\rm rad}$	d_s	$v_{\rm rad}$	d_s	$v_{\rm rad}$	d_s	$v_{\rm rad}$
J0123-6921	29.7 ± 2.8	9.0 ± 1.4	$33.3^{+4.0}_{-3.6}$	15.1 ± 2.0	**48.2 ± 3.2**	**9.7 ± 2.4**	$55.0^{+5.2}_{-4.8}$	12.1 ± 2.0	$53.0^{+4.4}_{-4.0}$	15.4 ± 1.7	$36.2^{+6.0}_{-5.2}$	1.2 ± 2.1	47.0 ± 4.8	22.8 ± 2.0	$55.4^{+20.8}_{-17.6}$	12.8 ± 8.4
J0124-5745	$32.1^{+3.2}_{-2.8}$	6.1 ± 2.1	$42.6^{+4.8}_{-4.4}$	6.7 ± 2.8	49.0 ± 2.8	7.9 ± 2.9	71.0 ± 6.8[b]	14.7 ± 3.5[b]	73.0 ± 6.0[b]	6.4 ± 6.2[b]	$63.0^{+6.4}_{-6.8}$[b]	-2.5 ± 3.8[b]	64.6 ± 6.8[b]	17.6 ± 3.5[b]	**$65.0^{+10.0}_{-12.0}$**[b]	**6.1 ± 8.1**[b]
J0124-3844	$30.5^{+3.2}_{-2.8}$	4.4 ± 1.5	$44.2^{+4.8}_{-4.4}$	9.3 ± 1.7	$49.8^{+3.2}_{-2.8}$	2.6 ± 2.4	$79.0^{+8.0}_{-7.2}$	12.6 ± 2.1	77.0 ± 5.2	3.2 ± 1.8	57.0 ± 6.4	1.9 ± 2.1	$77.4^{+7.2}_{-6.8}$	16.5 ± 2.2	**$91.0^{+29.6}_{-24.8}$**	**8.2 ± 7.3**
J0126+1428	26.5 ± 3.2	5.3 ± 3.9	$38.6^{+6.0}_{-4.8}$	6.4 ± 4.5	$50.2^{+4.4}_{-4.0}$[b]	1.9 ± 4.5[b]	$49.0^{+6.0}_{-5.6}$[b]	4.4 ± 6.6[b]	37.8 ± 4.0	-0.5 ± 4.1	$37.8^{+5.2}_{-4.8}$	4.8 ± 4.1	$56.2^{+6.8}_{-6.0}$[b]	5.7 ± 6.0[b]	**$62.6^{+17.6}_{-14.0}$**[b]	**5.3 ± 10.2**[b]
J0129+3517	$22.9^{+2.8}_{-2.0}$	-2.9 ± 2.2	$24.5^{+2.4}_{-2.0}$	3.6 ± 2.4	$31.3^{+2.4}_{-2.0}$	-6.4 ± 1.5	$30.5^{+2.4}_{-2.0}$	-5.0 ± 1.3	$30.1^{+2.0}_{-1.6}$	-6.0 ± 1.4	$28.5^{+2.8}_{-3.2}$	6.4 ± 2.0	32.9 ± 2.4	-12.4 ± 1.8	**$45.4^{+8.8}_{-8.4}$**	**4.0 ± 10.5**
J0129+4819	14.1 ± 1.2	-7.9 ± 1.8	18.9 ± 1.6	2.9 ± 2.2	$21.3^{+2.8}_{-2.0}$	-7.6 ± 1.1	24.5 ± 1.6	-6.5 ± 0.7	24.9 ± 1.2	-5.5 ± 0.7	$20.5^{+2.0}_{-1.6}$	6.0 ± 1.5	22.1 ± 1.6	-16.8 ± 1.3	**$40.2^{+11.6}_{-10.0}$**	**4.8 ± 11.5**
J0141-4633	26.5 ± 2.4	8.1 ± 1.4	$28.5^{+2.4}_{-2.8}$	14.1 ± 1.7	**42.2 ± 2.4**[b]	**7.6 ± 2.4**[b]	42.6 ± 3.2[b]	12.7 ± 1.5[b]	42.2 ± 2.4[b]	13.1 ± 1.4[b]	$29.3^{+2.8}_{-3.2}$	6.0 ± 2.0	42.2 ± 3.2[b]	22.8 ± 2.1[b]	$41.8^{+4.8}_{-6.4}$[b]	11.6 ± 7.4[b]
J0147+2120	31.3 ± 2.8[b]	2.0 ± 3.5[b]	$76.2^{+11.6}_{-11.2}$	4.4 ± 5.2	$66.2^{+5.6}_{-4.4}$	-0.1 ± 3.6	$71.4^{+9.2}_{-7.2}$	1.9 ± 4.8	$60.2^{+4.4}_{-4.0}$	-0.4 ± 3.9	$67.4^{+10.8}_{-6.4}$	6.5 ± 4.2	$95.8^{+8.8}_{-8.0}$	0.2 ± 6.2	**$149.5^{+26.4}_{-23.6}$**	**0.4 ± 11.9**
J0149+2956	$4.9^{+0.8}_{-0.4}$	-10.3 ± 1.7	10.5 ± 0.8	-3.2 ± 2.0	12.1 ± 0.8	-5.3 ± 1.1	$9.7^{+0.4}_{-0.8}$	0.4 ± 0.6	7.7 ± 0.4	-8.3 ± 0.4	$4.5^{+0.4}_{-0.8}$	-3.2 ± 1.1	14.9 ± 0.8	-2.6 ± 1.5	**$19.7^{+2.8}_{-3.2}$**	**-12.1 ± 10.1**
J0150-1851	$13.3^{+1.2}_{-0.8}$	-6.8 ± 1.5	$16.5^{+1.6}_{-1.2}$	8.6 ± 1.5	17.3 ± 1.2	9.9 ± 1.8	$10.5^{+1.2}_{-1.6}$	13.3 ± 1.3	$16.9^{+1.2}_{-0.8}$	5.8 ± 0.8	2.5 ± 0.4	-3.7 ± 1.1	$18.9^{+1.6}_{-1.2}$	15.9 ± 2.0	**$32.5^{+7.2}_{-6.0}$**	**2.6 ± 7.6**
J0206+2640	$4.5^{+1.6}_{-0.4}$	-4.0 ± 2.5	9.7 ± 0.8	12.8 ± 2.0	12.1 ± 0.8	-3.3 ± 1.1	12.1 ± 0.8	-1.8 ± 0.7	$11.3^{+0.8}_{-0.4}$	4.3 ± 0.7	10.9 ± 0.8	12.3 ± 1.5	11.7 ± 0.8	-11.7 ± 1.4	**$18.5^{+4.8}_{-3.2}$**	**14.8 ± 10.0**
J0221-6831	38.6 ± 3.2	9.6 ± 1.4	$42.2^{+4.4}_{-4.0}$	15.1 ± 2.0	53.8 ± 3.6	13.4 ± 2.1	$65.0^{+6.0}_{-5.6}$	15.1 ± 1.7	$72.6^{+5.6}_{-4.8}$	16.5 ± 1.4	$59.0^{+6.4}_{-6.0}$	3.4 ± 2.1	55.8 ± 5.6	26.3 ± 1.7	**$60.2^{+19.2}_{-12.0}$**	**11.6 ± 8.4**
J0221-5412	28.1 ± 2.0	11.2 ± 1.4	$28.9^{+2.8}_{-2.4}$	16.8 ± 1.7	**41.4 ± 2.4**	**10.3 ± 2.2**	39.4 ± 3.2	15.2 ± 1.4	37.8 ± 2.0	16.3 ± 1.0	28.5 ± 2.8	7.4 ± 2.1	$36.2^{+3.2}_{-2.8}$	25.9 ± 1.7	$57.0^{+10.0}_{-8.0}$[b]	15.6 ± 7.7[b]
J0223-5815	$26.5^{+2.4}_{-2.0}$	11.0 ± 1.4	$27.3^{+3.2}_{-2.8}$	16.5 ± 1.8	**43.8 ± 2.8**[b]	**10.6 ± 2.4**[b]	38.6 ± 2.8	15.4 ± 1.7	$38.2^{+2.4}_{-2.0}$	16.8 ± 1.3	31.3 ± 3.6	6.9 ± 2.4	$35.0^{+2.8}_{-3.2}$	26.0 ± 1.8	$50.2^{+6.0}_{-7.2}$[b]	14.5 ± 7.9[b]
J0225-5837	29.7 ± 2.0	10.7 ± 1.4	$30.9^{+2.8}_{-2.4}$	17.2 ± 1.8	**43.8 ± 2.8**	**10.9 ± 2.4**	$45.4^{+4.4}_{-4.0}$	15.4 ± 1.7	40.6 ± 2.8	16.9 ± 1.1	31.3 ± 2.8	6.2 ± 2.1	$39.0^{+4.0}_{-3.2}$	25.5 ± 1.8	$60.2^{+11.6}_{-9.6}$[b]	15.9 ± 8.0[b]
J0229-0053	$31.7^{+2.8}_{-2.4}$[b]	7.1 ± 2.5[b]	$53.4^{+6.0}_{-5.6}$	9.2 ± 3.8	$55.4^{+4.0}_{-3.6}$	4.8 ± 3.6	$63.0^{+6.8}_{-5.6}$	11.7 ± 4.9	$49.8^{+4.0}_{-3.6}$	5.8 ± 3.6	$57.0^{+6.0}_{-5.6}$	8.5 ± 4.2	$72.2^{+9.6}_{-8.0}$	13.3 ± 4.3	**$106.7^{+18.8}_{-15.2}$**	**3.9 ± 9.8**
J0234-6442	28.9 ± 2.4	11.0 ± 1.4	30.1 ± 3.2	17.3 ± 1.8	**46.2 ± 2.8**	**11.0 ± 2.4**	48.6 ± 4.0	15.8 ± 2.0	43.8 ± 3.6	17.3 ± 1.3	$34.6^{+6.0}_{-4.8}$	5.3 ± 2.5	41.4 ± 4.4	25.2 ± 2.0	49.0 ± 6.4	15.1 ± 8.3
J0236+2240	1.3 ± 0.4	-9.5 ± 2.0	9.7 ± 1.2	1.5 ± 2.2	$13.7^{+1.6}_{-1.2}$	-1.2 ± 1.5	9.7 ± 0.8	3.6 ± 1.0	13.3 ± 1.2	-4.3 ± 1.1	1.3 ± 0.4	-2.0 ± 1.3	$16.9^{+1.6}_{-1.2}$	3.2 ± 2.0	**$16.9^{+4.0}_{-3.6}$**	**-11.6 ± 10.5**
J0241-0326	32.1 ± 2.8	9.5 ± 2.1	$37.8^{+4.4}_{-4.0}$	14.1 ± 2.2	**50.2 ± 3.2**	**5.3 ± 2.5**	51.8 ± 4.0	11.4 ± 2.5	$45.8^{+3.2}_{-2.8}$	9.5 ± 2.1	$43.4^{+4.8}_{-4.4}$	13.1 ± 2.7	65.8 ± 5.6[b]	16.2 ± 2.9[b]	$67.8^{+9.2}_{-10.8}$[b]	12.8 ± 8.4[b]
J0243-2453	2.9 ± 0.4	-6.4 ± 1.7	3.3 ± 0.4	11.9 ± 1.5	$4.9^{+0.8}_{-1.2}$	4.0 ± 1.7	4.9 ± 0.4	10.2 ± 1.0	2.9 ± 0.4	-1.2 ± 0.4	3.3 ± 0.4	-7.8 ± 1.4	6.1 ± 0.4	24.9 ± 2.0	**$11.3^{+2.0}_{-1.6}$**	**3.3 ± 7.9**
J0253+1652	0.9 ± 0.4[b]	6.9 ± 2.0[b]	0.5 ± 0.4[b]	9.2 ± 1.8[b]	0.9 ± 0.4[b]	2.3 ± 1.1[b]	0.9 ± 0.4[b]	6.7 ± 0.6[b]	0.1 ± 0.4[b]	2.9 ± 0.4[b]	0.5 ± 0.4	6.5 ± 4.6	0.9 ± 0.4[b]	5.0 ± 1.5[b]	**$2.9^{+0.4}_{-0.8}$**	**0.8 ± 10.0**
J0253+3206	37.4 ± 2.8	6.1 ± 2.4	$35.8^{+2.8}_{-2.4}$	5.8 ± 2.5	$43.0^{+3.2}_{-2.8}$	-0.5 ± 1.7	40.2 ± 2.8	2.6 ± 1.3	39.0 ± 2.0	1.1 ± 1.4	38.6 ± 3.2	13.3 ± 2.1	48.2 ± 3.2	-2.0 ± 2.1	**$60.6^{+12.8}_{-11.2}$**	**1.9 ± 11.4**
J0303-7312	34.6 ± 3.2	11.6 ± 1.5	$40.6^{+5.2}_{-4.8}$	16.6 ± 2.4	$53.0^{+3.2}_{-3.6}$	12.3 ± 2.5	$70.2^{+7.2}_{-6.8}$[b]	16.9 ± 2.9[b]	69.8 ± 7.2[b]	18.0 ± 1.7[b]	67.8 ± 7.6[b]	3.9 ± 3.4[b]	52.2 ± 5.2	25.0 ± 2.2	**$69.4^{+10.4}_{-12.0}$**[b]	**13.8 ± 8.8**[b]
J0310-2756	3.7 ± 0.4	0.2 ± 1.8	9.7 ± 0.8	13.3 ± 1.5	$11.7^{+1.2}_{-0.8}$	6.5 ± 1.8	$11.7^{+1.2}_{-0.8}$	10.3 ± 1.1	73.8 ± 4.4[b]	-5.1 ± 2.1[b]	$8.5^{+0.8}_{-1.2}$	-8.2 ± 2.0	$12.1^{+1.6}_{-0.8}$	28.0 ± 1.8	**$29.7^{+6.4}_{-6.0}$**	**3.4 ± 8.0**
J0320-0446	2.5 ± 0.4[b]	-5.5 ± 2.4[b]	2.9 ± 0.4[b]	12.0 ± 1.7[b]	5.7 ± 0.4[b]	5.1 ± 1.4[b]	$4.5^{+0.4}_{-0.8}$[b]	9.0 ± 0.8[b]	4.5 ± 0.4[b]	-4.3 ± 0.6[b]	2.5 ± 0.4[b]	-3.6 ± 1.5[b]	$7.3^{+0.4}_{-0.8}$[b]	17.3 ± 1.8[b]	**$7.7^{+14.0}_{-0.8}$**[b]	**-3.2 ± 12.8**[b]
J0323-4631	$30.9^{+3.2}_{-2.8}$	12.1 ± 1.5	$31.3^{+4.0}_{-3.6}$	17.7 ± 1.8	**$49.4^{+3.2}_{-3.6}$**[b]	**12.7 ± 2.2**[b]	54.6 ± 5.2[b]	18.6 ± 1.8[b]	50.6 ± 3.6[b]	18.4 ± 1.3[b]	40.6 ± 3.6	10.6 ± 2.5	41.4 ± 3.6	27.8 ± 2.0	$55.4^{+6.8}_{-8.4}$[b]	15.6 ± 7.9[b]
J0326-2102	18.9 ± 1.6	8.2 ± 2.0	17.3 ± 2.0	16.3 ± 1.7	29.3 ± 2.0[b]	14.9 ± 1.8[b]	17.3 ± 1.6	17.6 ± 1.4	$24.1^{+1.6}_{-1.2}$[b]	15.6 ± 1.4[b]	14.1 ± 1.6	9.0 ± 2.2	**26.1 ± 2.0**[b]	**23.1 ± 2.1**[b]	$27.3^{+5.2}_{-4.4}$[b]	11.2 ± 8.1[b]
J0339-3525	6.9 ± 0.4	19.4 ± 2.0	6.9 ± 0.8	18.0 ± 1.5	7.3 ± 0.8	5.5 ± 2.0	1.3 ± 0.4	10.6 ± 1.1	$8.9^{+0.8}_{-0.4}$	13.5 ± 0.8	9.3 ± 0.8	15.4 ± 2.4	1.3 ± 0.4	31.2 ± 1.4	**10.5 ± 2.0**	**17.5 ± 8.0**
J0342-6817	30.9 ± 2.8	12.1 ± 1.4	$30.1^{+4.0}_{-3.6}$	17.9 ± 1.8	**50.2 ± 3.6**[b]	**13.3 ± 2.1**[b]	$55.4^{+6.4}_{-5.6}$[b]	17.6 ± 1.8[b]	$49.0^{+4.8}_{-4.0}$[b]	18.3 ± 1.1[b]	$37.8^{+5.2}_{-4.8}$	4.7 ± 2.4	$39.8^{+5.6}_{-4.8}$	26.7 ± 1.7	$56.2^{+13.6}_{-12.4}$[b]	15.4 ± 8.6[b]
J0355+1133	5.7 ± 0.4[b]	12.4 ± 2.0[b]	6.5 ± 0.4[b]	10.7 ± 2.0[b]	7.3 ± 0.4[b]	8.2 ± 1.4[b]	6.1 ± 0.4[b]	11.6 ± 0.8[b]	6.1 ± 0.4[b]	2.7 ± 0.6[b]	$5.7^{+0.8}_{-0.4}$[b]	14.2 ± 2.0[b]	**$8.5^{+0.4}_{-0.8}$**[b]	**12.3 ± 1.7**[b]	$7.7^{+0.8}_{-0.4}$[b]	3.0 ± 10.7[b]
J0357-4417	30.9 ± 2.8[b]	13.4 ± 1.7[b]	29.7 ± 3.2[b]	19.1 ± 1.7[b]	**$48.6^{+3.2}_{-2.8}$**[b]	**14.4 ± 2.1**[b]	49.0 ± 4.4[b]	20.3 ± 1.5[b]	$43.8^{+3.2}_{-2.8}$[b]	19.6 ± 1.1[b]	$39.0^{+4.8}_{-5.2}$[b]	12.6 ± 2.8[b]	$43.0^{+4.4}_{-4.8}$[b]	28.7 ± 1.8[b]	50.2 ± 6.4[b]	16.9 ± 8.1[b]
J0406-3812	$28.1^{+4.4}_{-3.2}$	14.1 ± 2.1	$36.6^{+6.8}_{-9.6}$	16.5 ± 2.8	53.4 ± 4.0	12.3 ± 3.4	$69.0^{+9.2}_{-9.6}$	21.1 ± 3.4	49.4 ± 4.4	18.7 ± 1.8	$54.2^{+6.8}_{-6.0}$	12.1 ± 4.8	$58.6^{+7.8}_{-7.2}$	24.8 ± 3.8	**$76.6^{+11.2}_{-12.8}$**	**13.4 ± 8.8**
J0421-6306	13.7 ± 1.2	16.6 ± 1.5	**11.7 ± 1.2**	**16.8 ± 1.8**	12.1 ± 1.2	18.4 ± 1.7	$10.1^{+0.8}_{-0.4}$	20.7 ± 1.3	17.7 ± 0.8	18.6 ± 0.7	16.5 ± 1.2	9.7 ± 2.2	$10.5^{+1.2}_{-0.8}$	30.5 ± 1.3	$23.7^{+5.2}_{-4.8}$[b]	14.4 ± 8.6[b]
J0435-1414	$11.3^{+1.2}_{-1.6}$[b]	17.5 ± 2.1[b]	$10.5^{+1.2}_{-1.6}$[b]	19.1 ± 1.5[b]	$75.8^{+5.2}_{-4.8}$[b]	12.7 ± 2.4[b]	$91.0^{+8.4}_{-7.6}$[b]	18.6 ± 2.8[b]	61.4 ± 3.6[b]	19.1 ± 1.4[b]	$55.4^{+6.8}_{-6.4}$	18.2 ± 3.1	$107.1^{+20.0}_{-12.0}$[b]	24.1 ± 3.4[b]	**10.5 ± 1.6**[b]	**13.1 ± 9.5**[b]
J0436-4114	28.5 ± 2.4	16.1 ± 2.0	$28.5^{+3.2}_{-2.8}$	19.4 ± 1.7	51.4 ± 4.0[b]	14.9 ± 2.4[b]	**$44.6^{+6.0}_{-5.6}$**	**22.0 ± 1.8**	37.4 ± 3.6	21.1 ± 1.4	$43.0^{+6.0}_{-5.6}$	14.4 ± 3.1	$36.6^{+6.0}_{-4.8}$	29.7 ± 1.8	$61.0^{+14.8}_{-12.0}$[b]	18.7 ± 8.7[b]
J0440-0530	$4.1^{+0.4}_{-2.8}$	15.4 ± 2.1	$4.9^{+1.2}_{-0.8}$	20.3 ± 1.5	$12.9^{+1.2}_{-0.8}$	9.9 ± 1.5	$9.7^{+0.8}_{-1.2}$	10.7 ± 1.1	$8.9^{+0.4}_{-1.2}$	21.1 ± 1.0	$6.9^{+0.8}_{-0.4}$	22.7 ± 2.2	$7.7^{+0.8}_{-1.2}$	15.6 ± 1.8	**$14.1^{+3.2}_{-2.8}$**	**24.5 ± 8.8**
J0443+0002	$26.5^{+2.8}_{-2.4}$[b]	15.5 ± 2.1[b]	**$25.7^{+3.2}_{-2.4}$**[b]	**16.9 ± 2.0**[b]	42.2 ± 3.2[b]	14.1 ± 1.8[b]	32.5 ± 2.8[b]	17.5 ± 1.5[b]	33.8 ± 2.0[b]	17.5 ± 1.3[b]	$19.7^{+2.4}_{-2.0}$	22.2 ± 2.4	$43.8^{+3.2}_{-2.8}$[b]	19.0 ± 2.2[b]	$29.3^{+6.0}_{-4.4}$[b]	9.5 ± 10.8[b]
J0446-1116	4.1 ± 0.4[b]	19.6 ± 2.2[b]	$5.7^{+1.2}_{-0.8}$[b]	18.9 ± 1.5[b]	4.5 ± 0.4[b]	8.3 ± 1.5[b]	4.9 ± 0.8[b]	4.8 ± 0.8[b]	$61.0^{+2.8}_{-4.0}$[b]	20.7 ± 1.7[b]	$0.9^{+3.6}_{-0.4}$[b]	14.1 ± 2.7[b]	$8.9^{+2.0}_{-1.6}$[b]	23.9 ± 1.8[b]	**$20.9^{+7.2}_{-5.6}$**[b]	**4.8 ± 10.4**[b]

Table 2.6 — continued

Name	TWA		βPMG		THA		COL		CAR		ARG		ABDMG		Field	
	d_s	$v_{\rm rad}$	d_s	$v_{\rm rad}$	d_s	$v_{\rm rad}$	d_s	$v_{\rm rad}$	d_s	$v_{\rm rad}$	d_s	$v_{\rm rad}$	d_s	$v_{\rm rad}$	d_s	$v_{\rm rad}$
J0501-0010	12.5 ± 1.2	12.6 ± 2.0	$8.9^{+1.6}_{-0.8}$	19.0 ± 1.7	16.1 ± 1.2	14.5 ± 1.5	$15.7^{+0.8}_{-1.2}$	20.1 ± 1.3	$14.5^{+0.4}_{-0.8}$	21.1 ± 0.8	8.5 ± 0.8	24.3 ± 2.1	$21.3^{+1.2}_{-0.8}$	16.9 ± 1.8	$\mathbf{15.7^{+3.2}_{-2.8}}$	$\mathbf{15.6 \pm 10.7}$
J0512-2949	13.7 ± 2.0	21.7 ± 2.9	12.9 ± 2.0	19.7 ± 1.5	$10.1^{+1.6}_{-1.2}$	16.3 ± 1.7	8.5 ± 0.8	14.2 ± 1.3	$41.4^{+2.0}_{-2.4}$ [b]	23.1 ± 1.4 [b]	$26.5^{+4.4}_{-3.6}$ [b]	19.4 ± 2.8 [b]	8.9 ± 0.8	31.9 ± 1.3	$\mathbf{21.7^{+4.8}_{-3.6}}$ [b]	$\mathbf{15.6 \pm 9.1}$ [b]
J0518-2756	34.6 ± 4.0 [b]	17.6 ± 2.0 [b]	$31.3^{+5.2}_{-10.4}$ [b]	20.1 ± 1.5 [b]	$59.0^{+3.6}_{-4.0}$ [b]	17.7 ± 1.8 [b]	$\mathbf{51.8 \pm 5.6}$ [b]	$\mathbf{23.1 \pm 1.4}$ [b]	47.0 ± 3.2 [b]	22.1 ± 1.1 [b]	$36.2^{+5.2}_{-4.4}$ [b]	18.6 ± 2.7 [b]	$57.4^{+4.8}_{-5.2}$ [b]	28.8 ± 1.8 [b]	$55.8^{+6.4}_{-8.4}$ [b]	16.3 ± 9.3 [b]
J0534-0631	30.5 ± 2.8 [b]	15.1 ± 2.4 [b]	$26.9^{+33.2}_{-5.6}$	18.2 ± 3.4	$83.8^{+8.0}_{-9.2}$	13.0 ± 3.8	$76.6^{+12.0}_{-11.6}$	21.3 ± 3.9	31.7 ± 2.4 [b]	20.3 ± 1.7 [b]	$22.1^{+2.8}_{-2.0}$	23.2 ± 2.7	$75.4^{+11.2}_{-10.0}$	21.8 ± 5.5	$\mathbf{131.5^{+25.2}_{-19.6}}$	$\mathbf{10.7 \pm 13.3}$
J0536-1920	28.5 ± 4.0	18.7 ± 2.1	$26.9^{+4.8}_{-4.4}$	19.8 ± 1.5	$47.4^{+3.6}_{-3.2}$	17.9 ± 1.7	$\mathbf{40.2 \pm 3.2}$	$\mathbf{22.5 \pm 1.4}$	39.0 ± 2.4	22.2 ± 1.1	$20.9^{+4.8}_{-5.2}$	23.1 ± 2.4	$47.0^{+4.0}_{-3.6}$	27.1 ± 2.0	$36.2^{+5.2}_{-6.0}$	15.1 ± 10.1
J0557-1359	$25.3^{+3.6}_{-3.2}$	20.4 ± 2.1	$26.9^{+4.8}_{-3.6}$	20.0 ± 1.5	$80.6^{+8.0}_{-8.8}$ [b]	16.5 ± 2.1 [b]	$85.0^{+10.8}_{-12.0}$ [b]	21.8 ± 2.2 [b]	$46.6^{+4.8}_{-3.6}$	22.2 ± 1.4	$27.3^{+4.8}_{-4.0}$	24.6 ± 2.2	$92.6^{+10.4}_{-8.4}$ [b]	25.7 ± 2.9 [b]	$\mathbf{44.6^{+11.6}_{-8.0}}$ [b]	$\mathbf{15.6 \pm 10.7}$ [b]
J0605+6049	5.7 ± 0.4 [b]	-3.0 ± 1.3 [b]	$5.7^{+0.8}_{-0.4}$ [b]	-4.8 ± 2.2 [b]	6.1 ± 0.4 [b]	-0.5 ± 1.5 [b]	6.9 ± 0.4 [b]	2.6 ± 0.7 [b]	5.3 ± 0.4 [b]	-2.7 ± 0.8 [b]	3.7 ± 0.4 [b]	9.2 ± 1.7 [b]	6.9 ± 0.4 [b]	-8.8 ± 1.4 [b]	$\mathbf{10.9 \pm 2.4}$	$\mathbf{2.2 \pm 12.1}$
J0608-2753	$28.9^{+3.6}_{-3.2}$	20.3 ± 1.8	$29.3^{+4.0}_{-3.6}$	20.1 ± 1.5	$59.0^{+10.0}_{-6.8}$	19.0 ± 1.7	$50.2^{+9.6}_{-7.6}$	23.2 ± 1.4	40.6 ± 3.6	24.9 ± 1.0	$37.0^{+6.4}_{-5.6}$	19.8 ± 2.4	$30.9^{+5.2}_{-4.0}$	30.9 ± 1.3	$\mathbf{38.2^{+8.0}_{-6.4}}$	$\mathbf{16.8 \pm 10.0}$
J0619-2903	$31.3^{+4.8}_{-4.4}$	19.1 ± 2.0	$34.2^{+4.8}_{-5.6}$	19.8 ± 1.7	$59.8^{+4.8}_{-4.4}$ [b]	18.0 ± 2.1 [b]	$\mathbf{55.8^{+5.6}_{-6.0}}$ [b]	$\mathbf{23.6 \pm 1.7}$ [b]	35.4 ± 4.0	24.1 ± 1.3	$54.2^{+5.6}_{-6.0}$ [b]	19.4 ± 3.1 [b]	57.0 ± 5.2 [b]	29.4 ± 2.0 [b]	57.4 ± 6.4 [b]	16.6 ± 10.1 [b]
J0632-5010	8.1 ± 0.8	17.0 ± 1.5	$9.7^{+1.6}_{-0.8}$	19.8 ± 1.5	8.9 ± 0.8	22.9 ± 1.8	$9.3^{+1.2}_{-0.8}$	20.6 ± 1.3	2.5 ± 0.4	21.5 ± 0.7	8.1 ± 0.8	14.2 ± 2.1	$10.5^{+5.2}_{-1.6}$	30.8 ± 1.3	$\mathbf{27.7^{+4.0}_{-4.8}}$	$\mathbf{10.9 \pm 9.7}$
J0642+4101	13.7 ± 0.8	8.5 ± 1.3	12.9 ± 0.8	3.9 ± 2.2	13.3 ± 0.8	4.0 ± 1.7	13.7 ± 0.8	7.4 ± 1.0	14.1 ± 0.4	7.1 ± 1.0	10.9 ± 0.8	15.8 ± 1.7	$\mathbf{17.3 \pm 0.8}$	$\mathbf{0.6 \pm 1.5}$	$17.7^{+4.4}_{-3.2}$	6.9 ± 12.8
J0652+4710	3.7 ± 0.4	5.7 ± 1.1	$4.1^{+0.8}_{-0.4}$	8.3 ± 2.1	3.3 ± 0.4	-0.1 ± 1.7	3.7 ± 0.4	-3.3 ± 0.8	0.9 ± 0.4	-7.2 ± 0.8	$3.7^{+0.4}_{-0.8}$	15.1 ± 1.5	3.3 ± 0.4	-12.1 ± 1.4	$\mathbf{15.3 \pm 2.8}$ [b]	$\mathbf{-2.3 \pm 12.2}$ [b]
J0652-5741	$45.8^{+4.4}_{-4.0}$ [b]	16.8 ± 1.5 [b]	$43.0^{+4.8}_{-4.4}$ [b]	19.1 ± 1.7 [b]	$58.6^{+5.6}_{-5.2}$ [b]	19.6 ± 1.5 [b]	$69.8^{+7.6}_{-6.8}$ [b]	21.7 ± 1.5 [b]	$59.8^{+6.0}_{-5.6}$ [b]	22.1 ± 1.0 [b]	$77.4^{+8.8}_{-8.4}$ [b]	9.0 ± 2.2 [b]	$45.8^{+5.2}_{-4.8}$ [b]	29.7 ± 1.3 [b]	$\mathbf{67.8^{+16.0}_{-12.8}}$ [b]	$\mathbf{15.6 \pm 9.4}$ [b]
J0657+6219	5.3 ± 0.4	-5.0 ± 1.3	$4.9^{+0.4}_{-0.8}$	-7.6 ± 2.1	6.5 ± 0.4	4.1 ± 1.7	$5.7^{+0.8}_{-0.4}$	5.8 ± 1.0	3.3 ± 0.4	-9.3 ± 0.7	3.3 ± 0.4	7.1 ± 1.5	$8.1^{+0.8}_{-0.4}$	-9.2 ± 1.4	$\mathbf{10.9^{+3.2}_{-2.8}}$	$\mathbf{-10.5 \pm 11.1}$
J0659-4746	$5.3^{+0.4}_{-0.8}$	19.8 ± 1.7	$6.1^{+0.8}_{-0.4}$	18.3 ± 1.7	4.9 ± 0.4	22.0 ± 1.4	4.5 ± 0.4	24.8 ± 1.1	$4.5^{+0.8}_{-0.4}$	25.2 ± 0.7	9.3 ± 0.8 [b]	14.7 ± 2.0 [b]	$4.1^{+0.4}_{-0.8}$	31.6 ± 1.1	$\mathbf{41.0^{+4.4}_{-4.0}}$	$\mathbf{22.4 \pm 9.0}$
J0712-6155	45.4 ± 6.0 [b]	16.3 ± 1.5 [b]	$37.4^{+5.6}_{-4.8}$ [b]	18.4 ± 1.8 [b]	$48.6^{+4.4}_{-4.8}$ [b]	21.7 ± 1.5 [b]	48.6 ± 5.6 [b]	20.6 ± 1.5 [b]	$61.0^{+5.2}_{-4.4}$ [b]	20.7 ± 1.1 [b]	$65.0^{+8.4}_{-6.0}$ [b]	10.7 ± 2.4 [b]	$43.0^{+6.4}_{-6.0}$ [b]	29.4 ± 1.4 [b]	$\mathbf{53.4^{+6.0}_{-8.0}}$ [b]	$\mathbf{12.3 \pm 9.7}$ [b]
J0752+1612	9.7 ± 0.8	8.1 ± 1.1	$9.3^{+0.8}_{-1.2}$	5.7 ± 2.0	6.9 ± 0.8	16.3 ± 1.7	5.7 ± 0.4	20.8 ± 1.5	10.5 ± 0.8	8.9 ± 1.3	1.7 ± 0.4	10.9 ± 1.3	12.1 ± 0.8	12.3 ± 1.8	$\mathbf{20.1^{+5.2}_{-4.0}}$	$\mathbf{-3.9 \pm 11.9}$
J0754+7909	5.3 ± 0.4	-0.2 ± 1.3	2.9 ± 0.4	-12.1 ± 2.0	2.9 ± 0.4	-7.4 ± 1.7	2.1 ± 0.4	-1.3 ± 0.8	2.5 ± 0.4	-14.4 ± 0.7	$5.3^{+0.4}_{-0.8}$	9.0 ± 1.7	2.5 ± 0.4	-19.6 ± 1.3	$\mathbf{15.3^{+2.0}_{-1.6}}$	$\mathbf{-23.1 \pm 9.1}$
J0809+4434	19.7 ± 1.6	9.6 ± 1.1	15.3 ± 1.2	5.5 ± 2.0	$13.3^{+0.8}_{-1.2}$	1.9 ± 2.0	$14.9^{+1.2}_{-0.8}$	-3.0 ± 1.1	$20.1^{+1.2}_{-0.8}$	8.8 ± 1.1	15.7 ± 1.6	15.4 ± 1.5	$23.7^{+1.2}_{-1.6}$	-5.7 ± 1.8	$\mathbf{21.3 \pm 4.4}$	$\mathbf{10.7 \pm 10.8}$
J0829+2655	35.4 ± 3.2 [b]	11.6 ± 1.5 [b]	33.8 ± 3.6 [b]	9.5 ± 2.2 [b]	16.9 ± 2.0	14.5 ± 1.8	$49.4^{+4.8}_{-4.4}$ [b]	9.6 ± 2.7 [b]	$45.0^{+3.2}_{-2.8}$ [b]	13.3 ± 2.5 [b]	28.5 ± 4.0	16.5 ± 1.8	$60.2^{+5.2}_{-4.4}$ [b]	4.8 ± 2.9 [b]	$\mathbf{39.8^{+8.4}_{-7.6}}$ [b]	$\mathbf{10.9 \pm 10.5}$ [b]
J0858+3256	5.3 ± 0.4	9.7 ± 1.0	5.7 ± 0.4	10.2 ± 1.7	2.1 ± 0.4	14.7 ± 1.8	2.1 ± 0.4	-5.0 ± 1.4	2.1 ± 0.4	9.5 ± 0.8	5.3 ± 0.4	17.9 ± 1.3	5.3 ± 0.4	-7.2 ± 1.7	$\mathbf{16.1 \pm 1.6}$	$\mathbf{24.1 \pm 8.7}$
J0917+6028	27.3 ± 2.0 [b]	4.3 ± 1.5 [b]	20.1 ± 1.6	-0.8 ± 2.1	$17.3^{+1.6}_{-1.2}$	-2.5 ± 2.2	27.7 ± 2.4 [b]	-5.3 ± 2.1 [b]	30.5 ± 2.0 [b]	0.9 ± 2.2 [b]	26.5 ± 2.4 [b]	8.6 ± 2.1 [b]	29.7 ± 2.0 [b]	-11.3 ± 2.5 [b]	$\mathbf{50.6^{+12.4}_{-30.4}}$	$\mathbf{10.5 \pm 12.3}$
J0951+3558	24.1 ± 2.0	4.4 ± 1.0	23.3 ± 2.0	-1.2 ± 1.5	15.3 ± 1.6	10.6 ± 2.1	$26.9^{+1.6}_{-2.0}$	6.2 ± 1.5	$27.3^{+0.8}_{-1.2}$	3.6 ± 0.7	14.9 ± 2.0	6.0 ± 1.1	$34.6^{+2.0}_{-1.6}$	-3.9 ± 1.8	$\mathbf{40.6^{+10.4}_{-9.6}}$	$\mathbf{5.0 \pm 9.0}$
J1004+5022	$22.1^{+2.8}_{-2.4}$ [b]	3.7 ± 3.2 [b]	17.7 ± 2.0 [b]	-4.6 ± 2.5 [b]	12.1 ± 1.2 [b]	3.7 ± 2.5 [b]	$23.7^{+3.2}_{-2.8}$ [b]	0.2 ± 3.1 [b]	$22.9^{+2.8}_{-2.4}$ [b]	-1.3 ± 2.8 [b]	$20.9^{+3.6}_{-3.2}$ [b]	4.3 ± 2.7 [b]	$26.1^{+3.6}_{-2.8}$ [b]	-10.7 ± 3.5 [b]	$\mathbf{29.7^{+10.8}_{-10.0}}$ [b]	$\mathbf{-0.8 \pm 9.5}$ [b]
J1020+0814	18.5 ± 2.0	7.2 ± 1.0	$17.3^{+1.2}_{-1.6}$	5.4 ± 1.5	8.1 ± 0.8	18.9 ± 1.4	9.3 ± 0.8	15.5 ± 1.4	18.9 ± 0.8	16.2 ± 0.7	18.9 ± 2.0	11.0 ± 1.1	14.5 ± 1.6	10.5 ± 1.8	$\mathbf{30.5^{+8.8}_{-7.6}}$	$\mathbf{12.8 \pm 9.0}$
J1022+0200	$7.3^{+0.8}_{-0.4}$	12.1 ± 1.0	$8.5^{+0.4}_{-0.8}$	5.8 ± 1.4	$6.5^{+0.4}_{-0.8}$	11.3 ± 1.4	6.5 ± 0.4	-0.4 ± 1.1	8.1 ± 0.4	7.4 ± 0.4	$5.3^{+0.4}_{-0.8}$	7.4 ± 1.0	11.3 ± 0.8	9.5 ± 1.8	$\mathbf{23.7^{+4.8}_{-3.2}}$	$\mathbf{15.1 \pm 9.1}$
J1022+5825	4.5 ± 0.4	-4.0 ± 1.1	4.5 ± 0.4	-7.1 ± 1.7	4.5 ± 0.4	-3.0 ± 2.1	4.5 ± 0.4	-5.7 ± 1.1	5.3 ± 0.4 [b]	-2.2 ± 0.6 [b]	4.1 ± 0.4	0.6 ± 1.4	5.3 ± 0.4	-15.9 ± 1.4	$\mathbf{6.5^{+8.0}_{-1.2}}$	$\mathbf{1.9 \pm 9.8}$
J1025+3212	$7.7^{+1.6}_{-0.8}$	5.5 ± 1.1	5.7 ± 0.4	-4.1 ± 1.5	4.9 ± 0.4	11.4 ± 2.0	2.5 ± 0.4	-3.4 ± 1.5	$31.3^{+4.4}_{-3.2}$ [b]	-14.7 ± 2.7 [b]	4.9 ± 0.4	3.9 ± 1.1	$8.1^{+1.6}_{-0.8}$	-3.3 ± 2.0	$\mathbf{19.7^{+2.8}_{-2.4}}$	$\mathbf{-19.4 \pm 8.3}$
J1139-3159	$\mathbf{46.6^{+4.8}_{-4.4}}$ [b]	$\mathbf{10.6 \pm 1.4}$ [b]	44.2 ± 4.0 [b]	4.8 ± 1.8 [b]	31.3 ± 2.4 [b]	13.4 ± 1.1 [b]	48.2 ± 3.2 [b]	11.4 ± 1.0 [b]	54.6 ± 2.4 [b]	13.3 ± 0.7 [b]	$47.8^{+5.6}_{-5.2}$ [b]	6.1 ± 1.1 [b]	53.4 ± 4.4 [b]	18.9 ± 1.5 [b]	$41.0^{+8.8}_{-7.2}$ [b]	6.5 ± 9.7 [b]
J1154-3400	28.5 ± 3.2	8.6 ± 1.5	29.3 ± 2.4	0.8 ± 2.1	$20.5^{+4.0}_{-2.0}$	13.3 ± 1.3	30.1 ± 2.0	13.3 ± 1.3	$34.6^{+2.0}_{-1.6}$	13.7 ± 1.3	32.9 ± 2.8	1.1 ± 1.4	29.3 ± 2.4	21.0 ± 1.5	$\mathbf{53.0^{+9.2}_{-6.8}}$ [b]	$\mathbf{2.5 \pm 9.8}$ [b]
J1212-2253	$30.1^{+2.8}_{-2.4}$ [b]	10.0 ± 1.8 [b]	29.3 ± 2.4 [b]	3.3 ± 2.5 [b]	17.7 ± 1.6	10.3 ± 1.5	31.7 ± 2.4 [b]	6.9 ± 2.1 [b]	$50.6^{+4.8}_{-4.4}$	12.3 ± 4.6	$60.2^{+6.4}_{-5.6}$	1.3 ± 3.5	$58.2^{+5.2}_{-4.8}$	9.0 ± 3.8	$\mathbf{112.7^{+13.6}_{-12.4}}$	$\mathbf{11.3 \pm 10.4}$
J1212+0206	$19.3^{+2.4}_{-1.6}$	12.6 ± 1.3	$32.1^{+4.4}_{-5.2}$	1.2 ± 1.8	$14.1^{+1.6}_{-1.2}$	6.1 ± 1.5	44.6 ± 4.8	0.1 ± 2.8	$50.6^{+4.8}_{-4.4}$	1.6 ± 1.8	14.9 ± 1.6	5.4 ± 1.1	53.8 ± 5.2	-5.3 ± 2.7	$\mathbf{54.2^{+8.8}_{-9.2}}$	$\mathbf{4.1 \pm 8.0}$
J1245-4429	$\mathbf{81.8^{+8.4}_{-7.6}}$ [b]	$\mathbf{9.6 \pm 2.0}$ [b]	71.0 ± 6.0 [b]	4.7 ± 3.1 [b]	$49.8^{+4.8}_{-5.6}$ [b]	11.2 ± 1.7 [b]	$65.8^{+4.8}_{-4.4}$ [b]	8.1 ± 2.0 [b]	$75.8^{+5.2}_{-4.8}$ [b]	13.4 ± 3.2 [b]	$79.4^{+8.0}_{-7.2}$ [b]	-3.0 ± 2.5 [b]	$80.2^{+6.8}_{-6.4}$ [b]	17.2 ± 2.1 [b]	$89.0^{+16.8}_{-14.4}$ [b]	5.7 ± 10.9 [b]
J1246+4027	17.3 ± 2.0	8.3 ± 1.3	8.9 ± 0.8	-8.2 ± 1.5	$8.1^{+0.4}_{-0.8}$	0.5 ± 2.1	$49.0^{+4.4}_{-3.6}$ [b]	-12.3 ± 2.8 [b]	$53.0^{+4.8}_{-4.0}$ [b]	-10.3 ± 2.7 [b]	$8.5^{+0.8}_{-0.4}$ [b]	6.5 ± 1.3	$45.8^{+3.6}_{-4.0}$ [b]	-25.3 ± 2.7 [b]	$\mathbf{35.0 \pm 6.4}$ [b]	$\mathbf{-10.3 \pm 7.4}$ [b]
J1305-2541	$9.7^{+1.2}_{-0.8}$	4.4 ± 1.8	$14.1^{+1.6}_{-1.2}$	-6.9 ± 1.7	$12.9^{+1.2}_{-0.8}$	8.6 ± 1.1	$16.1^{+1.2}_{-0.8}$	6.8 ± 0.7	$15.3^{+0.8}_{-1.2}$	1.2 ± 0.4	16.1 ± 1.2	-5.8 ± 1.3	14.5 ± 1.2	15.6 ± 1.4	$\mathbf{17.7^{+2.0}_{-2.4}}$	$\mathbf{-4.6 \pm 9.4}$
J1314+1320	15.3 ± 1.2 [b]	2.7 ± 1.4 [b]	13.7 ± 1.2 [b]	8.3 ± 1.4 [b]	$12.1^{+1.2}_{-0.8}$ [b]	1.1 ± 1.5 [b]	$15.7^{+1.2}_{-0.8}$ [b]	-6.9 ± 1.0 [b]	$16.9^{+0.8}_{-0.4}$ [b]	-4.4 ± 0.4 [b]	$11.7^{+1.6}_{-1.2}$ [b]	-3.7 ± 1.4 [b]	21.3 ± 1.2 [b]	-10.5 ± 2.0 [b]	$\mathbf{22.9^{+6.8}_{-5.6}}$ [b]	$\mathbf{-4.7 \pm 7.4}$ [b]
J1324+6358	12.1 ± 0.8 [b]	12.7 ± 1.5 [b]	10.9 ± 0.8 [b]	14.1 ± 1.7 [b]	$11.3^{+0.4}_{-0.8}$ [b]	-7.6 ± 2.1 [b]	$13.3^{+1.2}_{-0.8}$ [b]	-12.3 ± 1.3 [b]	$12.5^{+0.8}_{-0.4}$ [b]	-13.4 ± 0.7 [b]	$10.5^{+0.8}_{-1.2}$ [b]	-6.5 ± 1.8 [b]	12.5 ± 0.8 [b]	-24.2 ± 1.5 [b]	$\mathbf{16.1^{+2.4}_{-1.6}}$ [b]	$\mathbf{-11.9 \pm 8.1}$ [b]
J1326-0038	$19.7^{+1.6}_{-2.0}$	-5.0 ± 2.0	$16.1^{+1.6}_{-1.2}$	-7.9 ± 1.5	13.7 ± 1.2	3.7 ± 1.3	$21.3^{+1.6}_{-1.2}$	-2.0 ± 1.0	$21.7^{+0.8}_{-1.2}$	-2.9 ± 0.6	19.3 ± 2.4	-7.1 ± 1.7	26.1 ± 1.6	-3.9 ± 2.0	$\mathbf{24.9 \pm 5.2}$	$\mathbf{-4.7 \pm 8.0}$

Table 2.6 — continued

Name	TWA		βPMG		THA		COL		CAR		ARG		ABDMG		Field	
	d_s	$v_{\rm rad}$	d_s	$v_{\rm rad}$	d_s	$v_{\rm rad}$	d_s	$v_{\rm rad}$	d_s	$v_{\rm rad}$	d_s	$v_{\rm rad}$	d_s	$v_{\rm rad}$	d_s	$v_{\rm rad}$
J1331+3407	$9.7^{+1.2}_{-0.8}$	-7.5 ± 1.5	$8.5^{+0.8}_{-0.4}$	-12.1 ± 1.4	$8.9^{+0.8}_{-0.4}$	-2.6 ± 1.8	$10.5^{+0.8}_{-1.2}$	-11.2 ± 1.1	$11.7^{+0.4}_{-0.8}$	-10.2 ± 0.7	$8.1^{+0.8}_{-0.4}$	-6.0 ± 1.4	$14.1^{+1.2}_{-1.6}$	-19.8 ± 2.0	$29.3^{+4.4}_{-5.6}$	-13.0 ± 7.4
J1411-2119	42.2 ± 4.0[b]	2.0 ± 2.9[b]	$35.8^{+3.6}_{-3.2}$	-6.1 ± 2.1	30.1 ± 2.4	3.2 ± 1.4	$41.8^{+3.2}_{-2.8}$[b]	-2.3 ± 1.4[b]	43.8 ± 2.4[b]	0.4 ± 1.5[b]	$42.2^{+5.6}_{-4.8}$	-8.6 ± 2.2	$57.4^{+4.8}_{-4.0}$[b]	-0.1 ± 2.4[b]	$48.6^{+16.0}_{-9.6}$[b]	-1.3 ± 9.8[b]
J1415+5724	$9.3^{+1.2}_{-0.8}$	1.5 ± 1.4	$7.7^{+0.8}_{-0.4}$	-17.0 ± 1.7	6.5 ± 0.4	-11.9 ± 2.5	2.9 ± 0.4	-13.0 ± 1.3	6.9 ± 0.4	-12.8 ± 0.7	6.5 ± 0.4	3.3 ± 1.7	$6.9^{+0.4}_{-1.2}$	-22.7 ± 1.7	$19.7^{+2.8}_{-2.0}$	-17.9 ± 7.9
J1417-0407	$31.7^{+2.8}_{-2.4}$[b]	-0.8 ± 3.8[b]	$28.5^{+2.8}_{-2.4}$[b]	-8.8 ± 2.2[b]	18.9 ± 1.6	0.8 ± 1.8	31.7 ± 2.4[b]	-6.7 ± 2.5[b]	$32.1^{+2.4}_{-2.0}$[b]	-4.6 ± 2.1[b]	$32.5^{+3.2}_{-2.8}$[b]	-9.7 ± 2.9[b]	$61.0^{+6.0}_{-5.6}$	-9.9 ± 4.1	$132.7^{+20.4}_{-15.2}$	-3.4 ± 10.8
J1428+3310	3.3 ± 0.4	0.5 ± 1.4	2.9 ± 0.4	-14.0 ± 1.5	3.3 ± 0.4	-9.9 ± 1.7	2.1 ± 0.4	-16.6 ± 1.1	3.7 ± 0.4	-10.3 ± 0.6	2.1 ± 0.4	-1.6 ± 1.4	4.5 ± 0.4	-22.7 ± 2.0	13.7 ± 1.6	-13.8 ± 7.6
J1506+1321	3.3 ± 0.4	-22.4 ± 2.4	3.3 ± 0.4	-17.6 ± 1.7	4.1 ± 0.4	-3.7 ± 1.4	4.1 ± 0.4	-8.1 ± 0.8	4.1 ± 0.4	-16.1 ± 0.6	3.7 ± 0.4	-21.4 ± 1.8	4.1 ± 0.4	-15.6 ± 2.0	$8.9^{+2.0}_{-4.0}$	-23.4 ± 8.7
J1524+0934	11.7 ± 1.2	5.5 ± 2.2	11.7 ± 1.2	-12.4 ± 1.7	12.1 ± 1.2	-5.4 ± 1.5	16.5 ± 1.2[b]	-12.6 ± 1.3[b]	37.4 ± 2.8	-8.6 ± 1.7	8.5 ± 1.2	-0.1 ± 1.7	35.8 ± 2.8	-18.7 ± 2.4	$80.2^{+10.8}_{-8.0}$	11.7 ± 9.1
J1531+1641	28.9 ± 2.8	-19.7 ± 2.7	$22.5^{+3.2}_{-4.8}$	-17.0 ± 1.7	$18.5^{+6.8}_{-4.0}$	-3.0 ± 1.7	43.4 ± 3.2	-14.7 ± 1.8	43.4 ± 2.4	-14.7 ± 1.7	$35.4^{+3.6}_{-3.2}$	-16.5 ± 2.7	61.8 ± 4.4[b]	23.2 ± 2.7[b]	$55.0^{+8.0}_{-9.2}$[b]	-20.3 ± 8.4[b]
J1547-2423	$23.7^{+2.4}_{-2.0}$	-5.3 ± 2.7	$21.7^{+2.0}_{-1.6}$	-10.7 ± 2.1	27.3 ± 2.0	-4.0 ± 1.5	27.7 ± 2.0	-8.8 ± 1.1	$26.9^{+1.2}_{-1.6}$	-7.2 ± 1.1	$23.3^{+2.8}_{-2.0}$	-19.7 ± 2.1	$34.6^{+2.0}_{-1.6}$	-3.6 ± 2.0	$41.8^{+7.2}_{-6.0}$	-9.0 ± 11.8
J1551+0941	$31.3^{+3.2}_{-2.8}$	-12.0 ± 4.6	24.1 ± 3.6	-16.1 ± 2.0	$25.3^{+2.0}_{-4.4}$	-8.5 ± 1.8	34.2 ± 3.2	-15.9 ± 1.8	$33.3^{+2.4}_{-2.0}$	-14.7 ± 1.7	$31.7^{+4.0}_{-3.6}$	-19.4 ± 2.8	$49.0^{+4.8}_{-4.0}$[b]	-20.7 ± 2.8[b]	$50.2^{+10.4}_{-9.6}$[b]	-13.5 ± 9.3[b]
J1552+2948	$18.5^{+1.2}_{-1.6}$	-17.0 ± 2.4	$13.3^{+1.6}_{-1.2}$	-18.3 ± 1.7	$14.9^{+1.6}_{-1.2}$	-11.6 ± 1.8	$18.1^{+1.6}_{-2.0}$	-19.7 ± 1.4	$19.3^{+1.2}_{-0.8}$	-18.9 ± 1.1	$14.5^{+1.6}_{-1.2}$	-15.5 ± 2.5	22.1 ± 1.6	-26.9 ± 1.8	32.1 ± 4.0[b]	-19.1 ± 8.3[b]
J1557-2952	$49.4^{+5.2}_{-4.8}$	-2.5 ± 5.1	65.8 ± 9.6	-6.5 ± 3.6	$49.0^{+4.4}_{-3.6}$	-2.5 ± 2.9	$50.6^{+4.8}_{-4.4}$	-4.8 ± 3.1	45.4 ± 3.2	-11.6 ± 2.5	$56.2^{+8.4}_{-6.4}$	-16.5 ± 3.9	$79.0^{+7.2}_{-6.8}$	-4.1 ± 5.3	$90.2^{+16.8}_{-13.2}$	-2.9 ± 13.2
J1600-2456	12.5 ± 1.2	-11.4 ± 3.4	$12.5^{+0.8}_{-1.2}$	-8.1 ± 2.1	$14.1^{+0.8}_{-1.2}$	-1.3 ± 1.4	$12.9^{+0.8}_{-1.2}$	-5.7 ± 1.0	17.3 ± 0.8[b]	-5.5 ± 1.3[b]	11.7 ± 1.2	-13.7 ± 2.1	$20.5^{+1.2}_{-0.8}$[b]	-6.9 ± 1.8[b]	19.3 ± 2.0[b]	4.1 ± 12.1[b]
J1615+4953	$27.3^{+2.4}_{-1.6}$[b]	-17.5 ± 2.5[b]	$18.1^{+1.6}_{-2.0}$	-17.9 ± 1.8	15.7 ± 1.6	-18.4 ± 3.8	$28.5^{+3.2}_{-2.0}$[b]	-19.3 ± 1.8[b]	$27.7^{+2.0}_{-1.6}$[b]	-19.7 ± 1.8[b]	$29.7^{+3.6}_{-2.8}$[b]	-10.9 ± 2.8[b]	26.5 ± 2.4[b]	29.5 ± 1.8[b]	$27.3^{+3.2}_{-2.4}$[b]	-15.8 ± 8.4[b]
J1617+5516	$1.3^{+0.8}_{-0.4}$[b]	-4.8 ± 1.7[b]	2.1 ± 0.4[b]	-18.2 ± 1.7[b]	1.7 ± 0.4[b]	-23.2 ± 2.1[b]	0.5 ± 0.4[b]	-17.0 ± 1.3[b]	3.7 ± 0.4[b]	-11.3 ± 0.6[b]	1.3 ± 0.4[b]	2.6 ± 2.0[b]	1.7 ± 0.4[b]	-29.1 ± 1.4[b]	$12.1^{+4.8}_{-4.0}$[b]	-12.7 ± 8.6[b]
J1647+5632	$12.9^{+1.2}_{-0.8}$	-22.7 ± 1.8	11.3 ± 1.2	-17.2 ± 1.8	$8.9^{+1.2}_{-4.4}$	-21.3 ± 2.2	$9.3^{+0.8}_{-1.6}$	-21.7 ± 1.3	$13.3^{+0.4}_{-0.8}$	-22.0 ± 1.0	$14.5^{+1.2}_{-0.8}$	-13.7 ± 2.4	$9.7^{+0.8}_{-1.2}$	-31.8 ± 1.3	$22.9^{+5.2}_{-4.0}$	-18.2 ± 8.7
J1655-0823	2.9 ± 0.4	-9.5 ± 2.2	1.3 ± 0.4	-17.3 ± 1.8	3.3 ± 0.4	-11.9 ± 1.5	3.3 ± 0.4	-18.6 ± 1.4	3.3 ± 0.4	-18.3 ± 0.7	1.3 ± 0.4	-22.1 ± 2.1	4.9 ± 0.4	-14.2 ± 1.7	7.7 ± 1.2	-12.7 ± 11.8
J1703-7715	$57.0^{+4.4}_{-4.8}$	8.8 ± 1.8	$69.4^{+6.4}_{-6.0}$	6.7 ± 3.6	77.4 ± 5.6	10.0 ± 2.8	$76.2^{+7.2}_{-6.4}$	9.5 ± 2.8	$84.6^{+7.2}_{-6.8}$	16.5 ± 3.5	$93.0^{+10.4}_{-9.6}$	-4.6 ± 3.8	$86.6^{+8.4}_{-7.6}$	19.4 ± 3.2	$87.0^{+18.4}_{-14.8}$	6.1 ± 11.2
J1711+2326	$25.7^{+4.0}_{-2.8}$	-20.4 ± 2.5	$18.9^{+3.2}_{-10.0}$	-19.6 ± 1.7	$26.5^{+2.8}_{-3.2}$	-18.6 ± 2.2	26.9 ± 2.8	-22.2 ± 1.4	$30.1^{+2.0}_{-1.6}$	-22.0 ± 1.3	$20.5^{+2.4}_{-2.0}$	-20.7 ± 2.5	$39.4^{+3.2}_{-2.8}$	-27.4 ± 1.8	$52.6^{+6.8}_{-6.4}$[b]	-17.5 ± 9.5[b]
J1719+2630	3.3 ± 0.4	-26.6 ± 2.2	$3.7^{+0.8}_{-0.4}$	-20.0 ± 1.7	3.7 ± 0.4	-14.2 ± 2.7	0.5 ± 0.4	-14.4 ± 1.1	4.5 ± 0.4	-20.4 ± 1.0	$5.7^{+0.4}_{-0.8}$	-21.4 ± 2.5	0.5 ± 0.4	-31.2 ± 1.4	$11.3^{+3.6}_{-3.2}$	-23.6 ± 9.1
J1726+1538	$22.5^{+3.2}_{-2.8}$	-22.5 ± 2.5	$19.7^{+4.0}_{-4.4}$	-19.1 ± 1.7	$28.5^{+2.4}_{-2.8}$	-18.2 ± 2.7	$29.3^{+3.2}_{-2.8}$	-21.1 ± 1.5	$29.7^{+2.4}_{-2.0}$	-21.5 ± 1.5	$16.5^{+4.0}_{-2.8}$	-23.8 ± 2.2	48.2 ± 3.6[b]	25.3 ± 2.1[b]	$43.8^{+7.2}_{-8.4}$[b]	-14.7 ± 10.4[b]
J1736+0220	20.9 ± 2.0	-19.7 ± 2.9	$27.7^{+3.2}_{-2.8}$[b]	-16.2 ± 2.7[b]	$31.3^{+2.0}_{-2.4}$[b]	-12.1 ± 3.9[b]	$53.4^{+5.6}_{-5.2}$	-16.1 ± 3.8	28.1 ± 2.0[b]	18.3 ± 2.2[b]	$19.7^{+2.4}_{-2.0}$	-23.2 ± 2.5	$82.6^{+9.2}_{-10.4}$	-18.4 ± 6.0	$138.3^{+27.2}_{-22.0}$	-11.0 ± 13.7
J1738+6142	$29.7^{+1.2}_{-2.0}$	-26.4 ± 2.4	$28.5^{+1.6}_{-2.0}$	-11.2 ± 2.5	$9.7^{+0.8}_{-0.4}$	-24.6 ± 2.1	$30.9^{+2.4}_{-1.2}$	-17.6 ± 2.1	$32.1^{+3.2}_{-1.6}$	-24.8 ± 2.5	$30.9^{+2.0}_{-1.2}$	-13.7 ± 3.5	27.7 ± 2.0	-30.9 ± 1.8	$77.0^{+9.6}_{-8.0}$	-7.5 ± 9.7
J1758+4633	4.9 ± 0.4	-25.9 ± 2.0	5.3 ± 0.4	-17.7 ± 1.7	4.1 ± 0.4	-24.5 ± 1.8	3.3 ± 0.4	-24.9 ± 1.1	3.3 ± 0.4	-23.4 ± 0.7	$8.1^{+0.4}_{-0.8}$	-19.8 ± 2.2	3.7 ± 0.4	-33.3 ± 1.1	$15.7^{+3.6}_{-2.8}$	-21.0 ± 9.1
J1821+1414	3.7 ± 0.4	-28.0 ± 2.0	$4.1^{+0.4}_{-0.8}$	-19.1 ± 1.7	3.7 ± 0.4	-20.4 ± 1.7	$4.5^{+0.8}_{-0.4}$	-14.4 ± 1.4	1.3 ± 0.4	-25.2 ± 1.1	3.7 ± 0.4	-27.7 ± 1.8	$12.5^{+1.2}_{-0.8}$[b]	-28.0 ± 1.7[b]	13.3 ± 2.8[b]	-7.8 ± 11.8[b]
J1824+2937	$16.1^{+1.6}_{-2.0}$	-24.3 ± 2.4	$16.9^{+1.6}_{-2.0}$	-18.6 ± 2.1	15.3 ± 1.6	-22.0 ± 2.2	$17.7^{+2.0}_{-1.6}$	-23.1 ± 1.8	$16.1^{+1.6}_{-2.0}$	-27.6 ± 1.7	24.9 ± 2.4[b]	19.7 ± 3.2[b]	$28.5^{+3.6}_{-3.2}$[b]	-29.8 ± 2.2[b]	168.0 ± 19.2	-20.0 ± 11.8
J1828+1229	$8.5^{+0.8}_{-1.2}$	-11.6 ± 2.5	$6.5^{+0.8}_{-1.2}$	-17.7 ± 1.8	8.5 ± 0.8	-20.4 ± 2.0	6.9 ± 0.8	-24.8 ± 1.4	$7.3^{+1.2}_{-0.8}$	-24.9 ± 1.4	$4.5^{+0.8}_{-0.4}$	-16.3 ± 2.2	$13.3^{+1.2}_{-0.8}$[b]	-24.6 ± 2.0[b]	$14.5^{+1.6}_{-1.2}$[b]	-16.1 ± 11.4[b]
J1832+2030	10.1 ± 1.6[b]	22.9 ± 1.8[b]	14.1 ± 1.2[b]	-18.7 ± 1.7[b]	$12.1^{+0.8}_{-1.2}$[b]	-22.5 ± 1.8[b]	$6.9^{+0.8}_{-0.4}$[b]	-24.3 ± 1.4[b]	$8.5^{+1.2}_{-0.4}$[b]	-23.2 ± 1.0[b]	2.5 ± 0.4[b]	-20.8 ± 2.0[b]	$15.3^{+0.8}_{-1.2}$[b]	-26.7 ± 1.7[b]	$43.4^{+10.0}_{-8.8}$[b]	-3.9 ± 11.6[b]
J1916+0509	0.9 ± 0.4	-14.8 ± 1.7	0.9 ± 0.4	-14.7 ± 1.7	0.9 ± 0.4	-20.7 ± 1.7	0.9 ± 0.4	-23.5 ± 1.4	0.9 ± 0.4	-17.2 ± 1.1	0.5 ± 0.4	-14.1 ± 1.5	2.5 ± 0.4	-21.5 ± 1.7	6.5 ± 0.8	-0.4 ± 12.3
J1922+6610	$29.7^{+3.2}_{-3.6}$	-19.6 ± 1.8	22.1 ± 2.4	-14.2 ± 2.0	8.1 ± 0.8	-22.5 ± 1.7	18.1 ± 1.6	-20.0 ± 1.3	8.1 ± 0.8	-20.6 ± 0.6	35.0 ± 3.2	-15.1 ± 2.4	20.1 ± 2.0	-29.8 ± 1.3	$41.4^{+7.2}_{-5.2}$	-9.6 ± 10.0
J1930-1335	1.7 ± 0.4	-8.6 ± 1.3	2.1 ± 0.4	-13.7 ± 1.7	1.3 ± 0.4	-17.6 ± 2.5	1.3 ± 0.4[b]	-4.0 ± 1.3[b]	0.9 ± 0.4[b]	-13.8 ± 0.8[b]	2.5 ± 0.4	-15.6 ± 1.4	0.9 ± 0.4	-9.0 ± 1.7	$19.7^{+3.6}_{-2.8}$	-14.2 ± 12.1
J1935-2846	$29.3^{+2.8}_{-3.2}$	-9.2 ± 1.3	56.6 ± 5.2[b]	-8.8 ± 2.0[b]	66.2 ± 4.8[b]	8.1 ± 2.0[b]	$60.6^{+4.8}_{-4.4}$[b]	-9.0 ± 1.8[b]	55.0 ± 2.8[b]	11.6 ± 1.3[b]	$40.2^{+5.2}_{-4.8}$	-17.5 ± 1.8	$83.8^{+5.2}_{-4.8}$[b]	-5.5 ± 2.1[b]	$62.2^{+12.0}_{-9.6}$[b]	-8.1 ± 12.1[b]
J1956-7542	$35.4^{+3.6}_{-3.2}$	4.8 ± 1.8	45.8 ± 4.4	9.7 ± 2.8	59.8 ± 4.4[b]	6.5 ± 2.7[b]	60.2 ± 5.6[b]	8.9 ± 2.5[b]	61.8 ± 5.2[b]	10.6 ± 5.2[b]	$61.4^{+6.8}_{-7.2}$[b]	-3.9 ± 3.1[b]	$65.8^{+6.0}_{-5.6}$[b]	20.7 ± 3.2[b]	$64.6^{+9.2}_{-10.8}$[b]	7.9 ± 10.2[b]
J2000-7523	31.3 ± 2.8[b]	4.1 ± 1.4[b]	$33.3^{+3.2}_{-2.8}$[b]	6.4 ± 2.4[b]	43.0 ± 2.8[b]	9.7 ± 2.1[b]	35.8 ± 2.8[b]	8.5 ± 1.4[b]	$43.0^{+2.8}_{-2.4}$[b]	7.4 ± 1.7[b]	39.8 ± 4.0[b]	5.0 ± 2.1[b]	41.4 ± 3.2[b]	18.0 ± 2.0[b]	$39.0^{+8.4}_{-6.8}$[b]	3.0 ± 10.4[b]
J2013-2806	$25.3^{+3.2}_{-2.8}$	-8.6 ± 1.4	$44.2^{+4.8}_{-4.0}$	-7.4 ± 2.4	$55.8^{+4.0}_{-3.6}$[b]	-7.6 ± 2.5[b]	$47.8^{+4.4}_{-4.0}$	-10.3 ± 2.4	$41.8^{+2.8}_{-2.4}$	-11.3 ± 1.7	$39.4^{+4.4}_{-4.0}$	-16.9 ± 2.2	$65.4^{+5.2}_{-4.8}$[b]	-5.1 ± 2.9[b]	$61.4^{+11.2}_{-8.4}$[b]	-9.6 ± 11.2[b]
J2049-1944	13.3 ± 1.2	-11.7 ± 1.5	$17.3^{+3.2}_{-2.8}$	-8.8 ± 2.2	$22.1^{+4.0}_{-3.2}$	-9.5 ± 2.5	$15.7^{+2.4}_{-1.6}$	-13.5 ± 2.5	14.5 ± 1.2	-13.0 ± 1.5	$18.1^{+3.2}_{-3.6}$	-16.9 ± 2.5	21.7 ± 1.6	-8.5 ± 2.8	$28.5^{+4.4}_{-3.2}$	-18.6 ± 10.0
J2057-0252	$18.5^{+1.6}_{-2.0}$	-10.9 ± 1.0	31.7 ± 4.0	-8.8 ± 1.5	32.9 ± 2.8	-14.8 ± 2.5	$19.3^{+2.4}_{-2.0}$	-13.4 ± 1.7	37.4 ± 2.0	-11.4 ± 1.0	$11.3^{+2.8}_{-6.8}$	-9.2 ± 1.1	$49.0^{+3.6}_{-4.4}$	-15.5 ± 1.8	$22.9^{+4.8}_{-3.2}$	-4.7 ± 10.2
J2101+1756	$11.7^{+1.6}_{-2.8}$[b]	-19.3 ± 1.7[b]	18.1 ± 1.2[b]	-15.2 ± 1.5[b]	17.7 ± 1.6[b]	21.7 ± 1.4[b]	$17.3^{+1.2}_{-0.8}$[b]	-16.8 ± 1.3[b]	$13.3^{+0.8}_{-0.4}$[b]	-20.4 ± 0.6[b]	8.5 ± 0.8[b]	-14.1 ± 1.3[b]	24.9 ± 1.6[b]	22.0 ± 1.5[b]	$29.3^{+4.4}_{-3.2}$[b]	-17.0 ± 10.2[b]
J2114-2251	$19.3^{+1.6}_{-1.2}$[b]	-9.6 ± 1.0[b]	22.1 ± 1.6[b]	-6.4 ± 1.5[b]	$25.3^{+1.6}_{-2.4}$[b]	-11.4 ± 1.8[b]	$21.3^{+1.6}_{-1.2}$[b]	-8.5 ± 1.5[b]	24.5 ± 0.8[b]	15.8 ± 0.7[b]	$19.7^{+2.0}_{-1.6}$[b]	-12.0 ± 1.1[b]	$34.6^{+2.0}_{-1.6}$[b]	-2.5 ± 1.7[b]	$25.7^{+2.8}_{-3.6}$[b]	-9.3 ± 9.5[b]

Table 2.6 — continued

Name	TWA		βPMG		THA		COL		CAR		ARG		ABDMG		Field	
	d_s	$v_{\rm rad}$	d_s	$v_{\rm rad}$	d_s	$v_{\rm rad}$	d_s	$v_{\rm rad}$	d_s	$v_{\rm rad}$	d_s	$v_{\rm rad}$	d_s	$v_{\rm rad}$	d_s	$v_{\rm rad}$
J2116-0729	20.1 ± 2.0	-8.9 ± 2.2	$43.0^{+6.4}_{-6.0}$	-6.8 ± 3.6	48.2 ± 4.4	-6.1 ± 3.8	$49.8^{+7.2}_{-6.4}$	-12.6 ± 4.8	$33.8^{+3.6}_{-3.2}$	-12.1 ± 2.8	$48.2^{+7.6}_{-7.2}$	-12.6 ± 4.8	$54.6^{+6.8}_{-6.4}$ [b]	-11.0 ± 5.5 [b]	**$46.6^{+13.6}_{-11.6}$**	**2.9 ± 10.5**
J2126-8140	$27.3^{+2.8}_{-2.4}$	8.6 ± 1.5	$29.3^{+2.8}_{-3.2}$	12.4 ± 2.4	**45.0 ± 2.8** [b]	**8.3 ± 2.4** [b]	43.0 ± 3.2 [b]	9.0 ± 1.8 [b]	43.0 ± 2.8 [b]	12.7 ± 2.5 [b]	$35.8^{+5.6}_{-4.8}$ [b]	-2.0 ± 2.1 [b]	41.8 ± 3.6 [b]	20.4 ± 2.1 [b]	$39.8^{+6.4}_{-7.6}$ [b]	10.5 ± 9.7 [b]
J2140+3655	$15.3^{+1.6}_{-2.0}$	-15.6 ± 2.0	18.5 ± 2.0	-16.6 ± 2.1	57.8 ± 5.2	-8.1 ± 3.4	$101.5^{+8.8}_{-8.0}$	-15.6 ± 5.6	$60.2^{+5.6}_{-5.2}$	-12.3 ± 3.4	$101.5^{+8.8}_{-8.0}$	-6.4 ± 7.2	$77.0^{+12.4}_{-14.0}$	-14.4 ± 5.5	**$115.5^{+16.4}_{-13.2}$**	**-10.0 ± 10.8**
J2148+4003	3.7 ± 0.4	-12.7 ± 1.7	4.5 ± 0.4	-8.3 ± 1.7	3.7 ± 0.4	-22.2 ± 1.3	4.1 ± 0.4	-23.2 ± 1.0	4.1 ± 0.4	-18.2 ± 0.6	4.9 ± 0.4	-9.2 ± 1.3	3.7 ± 0.4	-29.2 ± 1.3	**$8.1^{+0.8}_{-1.2}$** [b]	**-11.6 ± 10.4** [b]
J2151-2441	$13.3^{+1.2}_{-0.8}$	-6.8 ± 1.0	15.3 ± 1.2	-6.5 ± 1.5	10.1 ± 0.8	-20.7 ± 2.0	$6.9^{+0.8}_{-3.2}$	-4.6 ± 1.7	17.7 ± 0.8	-16.5 ± 0.8	$14.9^{+1.6}_{-1.2}$	-13.5 ± 1.3	21.3 ± 1.6	2.9 ± 2.0	**$25.7^{+5.6}_{-4.8}$**	**-14.2 ± 9.3**
J2206-4217	17.7 ± 1.6	-1.5 ± 1.1	$20.9^{+2.0}_{-1.6}$	3.6 ± 1.7	27.7 ± 2.0	-1.8 ± 2.2	24.1 ± 1.6	-2.6 ± 1.7	$23.7^{+1.6}_{-1.2}$	-0.9 ± 1.0	$13.7^{+2.4}_{-2.0}$	-4.7 ± 1.3	**28.5 ± 1.6**	**7.6 ± 2.0**	$34.6^{+6.4}_{-6.0}$ [b]	-1.8 ± 8.7 [b]
J2208+2921	$21.3^{+4.0}_{-5.6}$	-15.5 ± 1.7	$35.4^{+3.6}_{-3.2}$	-10.6 ± 2.0	$35.0^{+3.2}_{-2.8}$	-20.7 ± 1.7	35.8 ± 3.2	-18.4 ± 1.7	$33.8^{+2.8}_{-2.4}$	-19.1 ± 1.4	$41.8^{+4.0}_{-4.4}$	-12.8 ± 1.8	42.6 ± 3.6	-24.5 ± 2.0	**$55.0^{+8.4}_{-9.6}$** [b]	**-13.4 ± 10.0** [b]
J2213-2136	23.7 ± 2.4	-6.1 ± 1.1	$45.0^{+3.6}_{-3.2}$	-1.9 ± 1.8	$45.4^{+2.8}_{-2.4}$	-8.6 ± 2.1	57.4 ± 4.4 [b]	7.5 ± 2.4 [b]	$47.8^{+2.4}_{-2.8}$	-7.1 ± 1.5	$42.6^{+4.4}_{-4.8}$	-7.5 ± 1.5	65.8 ± 4.0 [b]	-0.5 ± 2.7 [b]	**$62.6^{+7.2}_{-8.4}$** [b]	**-4.6 ± 8.6** [b]
J2224-0158	4.5 ± 0.4	-12.8 ± 1.3	5.3 ± 0.4	-6.5 ± 1.4	4.9 ± 0.4	-8.5 ± 1.4	4.1 ± 0.4	-0.4 ± 1.1	4.1 ± 0.4 [b]	-9.0 ± 0.4 [b]	3.7 ± 0.4	-8.5 ± 1.0	6.1 ± 0.4	-8.5 ± 1.8	**8.1 ± 1.6**	**-13.1 ± 8.8**
J2244+2043	10.9 ± 0.8	-15.9 ± 1.3	12.9 ± 0.8	-9.9 ± 1.5	12.9 ± 1.2	-14.9 ± 1.7	12.9 ± 0.8	-10.2 ± 1.0	11.3 ± 0.4	-14.8 ± 0.6	10.9 ± 0.8	-11.2 ± 1.1	**18.5 ± 1.2** [b]	**-15.5 ± 1.7** [b]	$14.9^{+1.2}_{-1.6}$	-12.1 ± 9.1
J2249+0044	$20.5^{+2.8}_{-2.4}$	-6.4 ± 1.4	$42.2^{+4.4}_{-4.0}$ [b]	-3.0 ± 2.1 [b]	$42.2^{+3.6}_{-3.2}$ [b]	-13.3 ± 4.3 [b]	$57.4^{+4.4}_{-5.6}$ [b]	-10.5 ± 2.9 [b]	$50.2^{+4.4}_{-4.0}$ [b]	-11.3 ± 2.0 [b]	$40.6^{+5.2}_{-4.4}$ [b]	-7.5 ± 2.0 [b]	$65.0^{+4.4}_{-4.0}$ [b]	-6.5 ± 3.4 [b]	**$42.6^{+11.2}_{-7.6}$** [b]	**-3.2 ± 8.6** [b]
J2313+2117	$15.3^{+1.6}_{-1.2}$	-7.8 ± 1.3	$17.3^{+1.2}_{-1.6}$	-4.0 ± 1.5	14.9 ± 1.2	-16.6 ± 1.5	$16.9^{+0.8}_{-1.2}$	-16.2 ± 1.1	19.3 ± 0.8	-14.0 ± 0.6	21.3 ± 2.0	-7.1 ± 1.0	$16.9^{+1.6}_{-1.2}$	-20.7 ± 1.5	**$29.7^{+7.6}_{-6.4}$**	**-9.5 ± 9.3**
J2317-4838	$11.3^{+2.8}_{-2.0}$	-0.6 ± 1.1	16.1 ± 1.6	0.8 ± 1.7	$8.5^{+0.8}_{-0.4}$	-4.7 ± 2.1	$6.1^{+0.8}_{-0.4}$	10.0 ± 1.4	27.7 ± 1.6 [b]	9.3 ± 1.1 [b]	12.5 ± 2.0	-9.0 ± 1.3	$14.1^{+1.6}_{-2.4}$	22.1 ± 1.7	**24.5 ± 6.0** [b]	**-2.9 ± 8.3** [b]
J2322-3133	$5.3^{+0.8}_{-0.4}$	-5.4 ± 1.0	4.9 ± 0.4	6.2 ± 1.5	4.5 ± 0.4	-2.5 ± 2.0	2.1 ± 0.4	8.8 ± 1.3	4.9 ± 0.4	5.5 ± 0.6	2.1 ± 0.4	-4.6 ± 1.0	6.1 ± 0.4	5.7 ± 1.8	**$24.1^{+3.2}_{-4.8}$**	**13.4 ± 7.6**
J2322-6151	26.9 ± 2.4	5.3 ± 1.4	$33.3^{+3.6}_{-2.8}$	11.0 ± 2.0	**43.4 ± 2.4**	**4.8 ± 2.5**	$44.2^{+3.2}_{-2.8}$	6.8 ± 2.0	$44.2^{+2.8}_{-2.4}$	8.9 ± 1.8	$34.2^{+5.6}_{-4.4}$	-0.8 ± 2.0	44.6 ± 2.8	18.2 ± 2.2	$57.0^{+7.6}_{-9.6}$ [b]	8.5 ± 8.4 [b]
J2328-1038	22.1 ± 2.0	-7.2 ± 1.4	56.6 ± 5.6	0.9 ± 2.2	49.0 ± 3.2	-4.3 ± 2.7	$76.6^{+6.8}_{-6.4}$	0.8 ± 3.9	$61.4^{+5.2}_{-4.8}$	-1.1 ± 2.4	60.6 ± 7.2	-4.1 ± 2.5	$77.8^{+6.4}_{-6.0}$	10.0 ± 3.4	**$96.2^{+18.4}_{-17.6}$** [b]	**1.8 ± 8.1** [b]
J2335+4511	0.9 ± 0.4	-16.6 ± 1.5	$2.1^{+0.4}_{-0.8}$	-10.3 ± 1.8	0.9 ± 0.4	-10.9 ± 1.1	0.9 ± 0.4	-1.9 ± 0.7	$3.3^{+0.4}_{-0.8}$	-10.9 ± 0.6	0.9 ± 0.4	-5.5 ± 1.1	1.7 ± 0.4	-20.3 ± 1.3	**$14.9^{+4.8}_{-4.4}$**	**-14.4 ± 10.5**
J2351+3010	12.1 ± 0.8	-6.9 ± 1.5	16.9 ± 1.6	-0.4 ± 1.8	14.9 ± 1.2	-13.3 ± 1.3	$18.1^{+1.6}_{-1.2}$	-13.5 ± 1.1	21.3 ± 0.8	-11.4 ± 0.7	**$20.9^{+2.0}_{-2.4}$**	**-1.5 ± 1.3**	14.9 ± 1.6	-21.0 ± 1.4	32.5 ± 6.0	-2.7 ± 9.5
J2354-3316	4.5 ± 0.4	-6.2 ± 1.0	3.7 ± 0.4	6.5 ± 1.4	3.7 ± 0.4	-3.0 ± 1.8	1.7 ± 0.4	9.7 ± 1.3	4.5 ± 0.4	4.3 ± 0.4	$2.1^{+1.2}_{-0.4}$	-5.3 ± 1.0	4.5 ± 0.4	10.7 ± 1.8	**$25.7^{+3.2}_{-2.8}$**	**15.6 ± 7.3**
J2359+3241	1.3 ± 0.4	-15.4 ± 1.7	$7.7^{+0.8}_{-2.4}$	-8.8 ± 2.1	2.1 ± 0.4 [b]	-9.7 ± 1.1 [b]	2.1 ± 0.4 [b]	-0.6 ± 0.7 [b]	6.5 ± 0.4 [b]	-9.2 ± 0.6 [b]	1.7 ± 0.4 [b]	-6.0 ± 1.0 [b]	$7.7^{+0.8}_{-1.2}$	-16.5 ± 1.4	**$23.7^{+6.0}_{-5.2}$**	**-14.5 ± 9.8**

[a] Values in red are the ones for which the hypothesis had the highest Bayesian probability (including the field hypotheses) when using all available observables.

[b] Object for which the Bayesian probability (P_{H_k}) for the binary hypothesis has a higher probability.

Chapitre 3

BANYAN. V. A SYSTEMATIC ALL-SKY SURVEY FOR NEW VERY LATE-TYPE LOW-MASS STARS AND BROWN DWARFS IN NEARBY YOUNG MOVING GROUPS

Jonathan Gagné, David Lafrenière, René Doyon, Lison Malo, and Étienne Artigau

Département de Physique and Observatoire du Mont-Mégantic, Université de Montréal, C.P. 6128 Succ. Centre-ville, Montréal, Qc H3C 3J7, Canada

Received 2014 June 28; accepted 2014 October 16

Published in *The Astrophysical Journal*,

January 2015, *Vol.* 798, *page* 73

3.1 Abstract

We present the BANYAN All-Sky Survey (BASS) catalog, consisting of 228 new late-type (M4–L6) candidate members of nearby young moving groups (YMGs) with an expected false-positive rate of $\sim$ 13%. This sample includes 79 new candidate young brown dwarfs and 22 planetary-mass objects. These candidates were identified through the first systematic all-sky survey for late-type low-mass stars and brown dwarfs in YMGs. We cross-matched the 2MASS and AllWISE catalogs outside of the galactic plane to build a sample of 98 970 potential $\geq$ M5 dwarfs in the solar neighborhood and calculated their proper motions with typical precisions of 5–15 mas yr^{-1}. We selected highly probable candidate members of several YMGs from this sample using the Bayesian Analysis for Nearby Young AssociatioNs II tool (BANYAN II). We used the most probable statistical distances inferred from BANYAN II to estimate the spectral type and mass of these candidate YMG members. We used this unique sample to show tentative signs of mass segregation in the AB Doradus moving group and the Tucana-Horologium and Columba associations. The BASS sample has already been successful in identifying several new young brown dwarfs in earlier publications, and will be of great interest in studying the initial mass function of YMGs and for the search of exoplanets by direct imaging; the input sample of potential close-by $\geq$ M5 dwarfs will be useful to study the kinematics of low-mass stars and brown dwarfs and search for new proper motion pairs.

3.2 Introduction

A few decades ago, several groups of stars sharing similar galactic space velocities have been identified in the solar neighborhood. These similar kinematics are a consequence of the young age (typically 10–200 Myr) of these groups (i.e. young moving groups; YMGs), which formed from a common origin. The closest and youngest YMGs include the TW Hydrae association (TWA; de la Reza et al. 1989, Zuckerman & Song 2004; 5 – 15 Myr; Weinberger et al. 2013a), β Pictoris (βPMG; Zuckerman et al. 2001a; 20 – 26 Myr; Mamajek & Bell 2014, Malo et al. 2014b, Binks & Jeffries 2014), Tucana-Horologium (THA; Torres et al. 2000, Zuckerman & Webb 2000; 20 – 40 Myr; Kraus et al. 2014b), Carina (CAR; 20 – 40 Myr;

Torres et al. 2008), Columba (COL; 20 – 40 Myr; Torres et al. 2008), Argus (ARG; 30 – 50 Myr; Makarov & Urban 2000) and AB Doradus (ABDMG; Zuckerman et al. 2004; 110 – 130 Myr ; Luhman et al. 2005, Barenfeld et al. 2013). Identifying these YMGs was made possible with the advent of the Hipparcos survey (Perryman et al. 1997), which provided parallax measurements for $\sim$ 120,000 bright stars. Because of its limited sensitivity and the fact that it operated at visible wavelengths, this survey mainly studied stars with spectral types earlier than $\sim$ K0. Identifying the missing later-type, low-mass members of YMGs is of great interest for multiple reasons: it would provide constraints on the low-mass end of their initial mass function (IMF) and accessible benchmarks for cool, low-pressure atmospheres, similar to those of directly imaged giant planets (e.g. Delorme et al. 2012; Faherty et al. 2013b; Liu et al. 2013b). Furthermore, direct imaging of exoplanets around these low-mass members would be facilitated by their proximity and the fact that younger planets are hotter, and thus brighter (e.g. see Bowler et al. 2012a; Bowler et al. 2012b; Delorme et al. 2013; Bowler et al. 2013; Naud et al. 2014). For these reasons, a large number of studies were aimed at finding these missing low-mass members and refine our understanding of YMGs (see Torres et al. 2003b; Weinberger et al. 2004; Torres et al. 2006; Looper et al. 2007a; Shkolnik et al. 2009; Bonnefoy et al. 2009; Lépine & Simon 2009; Schlieder et al. 2010; Looper et al. 2010a; Looper et al. 2010b; Rice et al. 2010; Rodriguez et al. 2011; Kiss et al. 2011; Schlieder et al. 2012a; Schneider et al. 2012a; Faherty et al. 2012; Shkolnik et al. 2012; Delorme et al. 2012; Schlieder et al. 2012b; Malo et al. 2013; Faherty et al. 2013b; Weinberger et al. 2013a; Moór et al. 2013; Rodriguez et al. 2013; Liu et al. 2013b; Hinkley et al. 2013; Schneider et al. 2014; Kraus et al. 2014b; Bonnefoy et al. 2014a; Gagné et al. 2014a; Malo et al. 2014a; Riedel et al. 2014; Malo et al. 2014b; Manjavacas et al. 2014; Gagné et al. 2014b; Zapatero Osorio et al. 2014; Mamajek & Bell 2014 and Gagné et al. 2014c – referred to as Chapter 2 hereafter).

The identification of later-type members of nearby YMGs is a challenging task in the absence of reliable parallax and radial velocity (RV) measurements since their members are spread on large regions of the celestial sphere. Furthermore, obtaining parallax and RV measurements for such faint targets is time-consuming. Careful pre-selection of candidates is thus essential to keep the follow-up effort to a manageable size. Efforts have already been made in

identifying late-type members in YMGs, notably by selecting X-ray or UV-bright stars (Torres et al. 2008, Rodriguez et al. 2011, Shkolnik et al. 2012) and by comparing their proper motions to those of known members with the convergent point proper motion analysis (CPA; Montes et al. 2001, Rodriguez et al. 2013). However, this method does not use all available measurements (e.g. photometry, magnitude of proper motion, RV and parallax), therefore it generally suffers from a large contamination of field stars that have proper motions similar to those of YMG members by pure chance, as well as cross-contamination between different YMG candidates. In particular, some YMGs such as COL, βPMG and TWA happen to share similar proper motion distributions as viewed from the Earth, which makes it difficult to differentiate their members using only sky position and the direction of proper motion without radial velocity measurements.

To address these problems, Malo et al. (2013) developed the Bayesian Analysis for Nearby Young AssociatioNs (BANYAN[1]), a statistical tool based on bayesian inference, to identify strong K5–M5 candidate members of YMGs primarily from a sample of X-ray bright sources. In addition to proper motion and sky position, this tool takes advantage of I_C and J photometry measurements to ensure that candidate members fall in a region of the color-magnitude diagram (CMD) consistent with other YMG members; younger low-mass stars (LMSs) and brown dwarfs (BDs) are inflated and thus brighter than field stars as they are still undergoing gravitational contraction. This approach provides a more robust set of candidates, as well as most probable distance and RV predictions. However, this study is still limited to detecting candidates with spectral types earlier than $\sim$ M5, and photometric measurements in the I_C band are required to take CMD information into account. In parallel, we presented BANYAN II[2] in Chapter 2, a new selection tool based on BANYAN that includes several improvements (e.g. a better modeling of YMGs spatial and kinematic properties and an extensive treatment of contamination and completeness), and is specifically designed to identify $>$ M5 YMG candidates, by relying on two different CMDs constructed with photometry from the Two Micron All-Sky Survey (2MASS; Skrutskie et al. 2006) and the WISE survey (Wright et al. 2010). This tool was used in Chapter 2 to identify 39 new M5–L4 candidate members

[1]Publicly available at *http://www.astro.umontreal.ca/~malo/banyan.php.*
[2]Publicly available at *http://www.astro.umontreal.ca/~gagne/banyanII.php.*

among known young field LMSs and BDs. Recently, Kraus et al. (2014b) identified 129 new K3–M6 strong candidate members of THA by carrying extensive RV measurements of targets selected for having proper motion and CMD positions similar to those of other THA members. Their results indicate that samples based on GALEX (USNO–A2.0 (VizieR catalog II/312 and Martin et al. 2005) or ROSAT (USNO–A2.0 (VizieR catalog IX/29 and Voges et al. 1999) miss candidates later than $\sim$ M2 at distances beyond $\gtrsim 40\,\mathrm{pc}$.

We present here the BANYAN All-sky Survey (BASS), which is the first all-sky, systematic survey for $\geq$ M5 LMSs and BDs in YMGs. The whole 2MASS and AllWISE (Kirkpatrick et al. 2014) catalogs outside of the galactic plane ($|b| > 15°$) were cross-matched, yielding proper motions with typical precisions of a few mas yr^{-1}. Color-quality cuts as well as the BANYAN II tool were used to select 153 high- and 21 modest-probability candidate members of YMGs, for which near-infrared (NIR) colors are consistent with $\geq$ M5 spectral types. The BASS survey has already generated a wealth of new discoveries, including a triple M5 + M5 + planetary-mass companion in THA (Delorme et al. 2013; J. Gagné et al., in preparation), an M5 + L4 host–planet system candidate member of THA (Artigau et al. 2015), a new L-type candidate member of TWA (Gagné et al. 2014a; see Chapter 4) and a new low-gravity L4 β BD candidate member of ARG (Gagné et al. 2014b; see Chapter 5). A NIR and optical spectroscopic follow-up of all candidates that will be presented here is undergoing; first results were presented in Gagné et al. (2013) and more will be presented in a subsequent paper (J. Gagné et al., accepted for publication in ApJ; see Chapter 6).

In Section 3.3, we detail our method for cross-matching the 2MASS and AllWISE catalogs, which we follow by a description of the various color-quality cuts applied, and how we use the BANYAN II tool to select candidates members of YMGs (Section 3.4). In Section 3.5, we present all information available in the literature for the BASS catalog, which we used to update the membership probability when relevant. In Section 3.6, we evaluate the recovery rate of the BASS sample for known $\geq$ M5 candidate members and bona fide members of YMGs. We then present various characteristics of the updated BASS catalog in Section 3.7. In Section 3.8, we search for new common proper motion pairs among our sample, and we tentatively investigate mass segregation in Section 3.9. Conclusion are presented in Section 3.10.

The *Low-Priority* BASS (LP-BASS) sample, consisting of objects only marginally redder than field dwarfs, is presented in Appendix, along with our full input sample of 98 970 potential close-by $\geq$ M5 dwarfs.

3.3 Cross-matching the 2MASS and AllWISE catalogs

Cross-matching the 2MASS and AllWISE catalogs ($\sim$ 470 million and $\sim$ 750 million entries respectively) without the use of significant computational resources is a challenge that must be tackled in a strategic way. Fortunately, the NASA Infrared Science Archive (IRSA[3]; Groom et al. 2010) provides useful tools to achieve this. In a first step, we have built two distinct queries for the 2MASS and AllWISE catalogs to target only potential nearby $\geq$ M5 dwarfs. We start from spectral type-color relations described in Pecaut & Mamajek (2013), Kirkpatrick et al. (2011) and Dupuy & Liu (2012) to select only targets that have NIR colors consistent with $\geq$ M5 spectral types, which we subsequently relax to include all currently known young dwarfs in the same range of spectral types (see Chapter 2 for an extensive list of known young LMSs and BDs in the field). We target only regions of the sky located more than 15 degrees away from the galactic plane, require that measurements of J, H, K_S, $W1$ and $W2$ photometry have a reasonable quality, and that no contamination or saturation flags are problematic. We also reject sources spatially resolved in 2MASS but not in AllWISE. In the Appendix, we list the requirements in the form of two Structured Query Language (SQL) statements that were used to perform all-sky IRSA queries, which correspond to[4] :

- The absolute galactic latitude $|b|$ of both 2MASS and AllWISE counterparts respect $|b| > 15$ °.
- $J > 2$, $H > 2$, $K_S > 2$, $W1 > 2$ and $W2 > 2$.
- $0.506 < J - H < 2$, $0.269 < H - K_S < 1.6$ and $0.168 < W1 - W2 < 2.5$.
- $W1 - W2 < (0.96 \cdot (W2 - W3) - 0.96)$ if $W3$ is detected with S/N > 5 and not saturated (Kirkpatrick et al. 2011).

[3] Available at *http://irsa.ipac.caltech.edu/*

[4] See the column descriptions of the 2MASS User's Guide *http://www.ipac.caltech.edu/2mass/releases/allsky/doc/sec2_2a.htm* and the AllWISE User's Guide *http://wise2.ipac.caltech.edu/docs/release/allwise/expsup/sec2_1a.html* for additional information on the keywords.

- If a 2MASS counterpart is identified in the AllWISE catalog, it must be at least at an angular distance $0\farcs3$ from the AllWISE coordinates (i.e., to reject low proper motion objects) and respect $0.153 < K_S - W1 < 2$ in addition to the 2MASS color cuts described above.
- The blue magnitude B, which is either the Johnson B_J magnitude of a Tycho 2 (Høg et al. 2000) counterpart, or the photographic blue magnitude of a USNO–A2.0 (Monet 1998) counterpart of the 2MASS object (B_M_OPT keyword) is either undetected or has $B - J \geq 4.048$.
- The red or visible VR magnitude, which is either the Johnson V_J magnitude of a Tycho 2 counterpart, or the photographic red magnitude of a USNO–A2.0 (VizieR catalog I/252) counterpart of the 2MASS object (VR_M_OPT keyword) is either undetected or has $VR - J \geq 2.63$ and $B - VR \geq 1.3$.
- At least two 2MASS bands have excellent (A) or good (B) photometric quality flags.
- No 2MASS band has a poor (D, E or F) or undetected (X or U) quality flags.
- The AllWISE photometric quality flags of the $W1$ and $W2$ bands are either excellent (A) or good (B).
- The angular distance between the object and its closest neighbor is at least $6\farcs4$ in 2MASS, to ensure that they are resolved in AllWISE.
- There are less than 0.2% of saturated pixels in the profile fitting regions of both the $W1$ and $W2$ bands in AllWISE.
- The source is detected in the $W1$ and $W2$ AllWISE bands with a statistical significance larger than 5σ.
- The reduced χ^2 of the profile fits for the $W1$ and $W2$ AllWISE bands both respect $\chi^2 < 5$.
- The 2MASS read flags do not contain 0 (no detection in any band), 6 (not detected in one band) or 9 (nominally detected in one band because of confused regions) for any band.
- The 2MASS blend flag is 1 (only one component was fit simultaneously for photometry) for all bands.

- The 2MASS contamination flag is 0 (not contaminated) for all bands.
- The 2MASS extragalactic contamination flag is 0 (resolved and not extended).
- The 2MASS minor planet flag is 0 (not associated with a known solar system object).
- The AllWISE contamination flags of the $W1$ and $W2$ bands do not correspond to potentially spurious detections (D, due to a diffraction spike; P, due to detector persistence; H, due to the scattered light of a bright nearby source; or O, due to an optical ghost caused by a nearby bright source).
- The AllWISE extended flag is either 0 (consistent with a point source) or 1 (goodness-of-fit of the profile fitting is larger than 3 in at least one band).

These queries generated two lists: 2 762 191 objects from 2MASS and 76 883 849 objects from AllWISE. To avoid obtaining very large output file sizes, we downloaded only designations, RA and DEC positions, as well as 2MASS unique identifiers at this stage (keyword CNTR in the 2MASS catalog, and TMASS_KEY in the AllWISE catalog; the IRSA team already identified 2MASS–AllWISE cross-matches within 3"). We then locally rejected all objects located in the following star-forming regions to avoid heavily reddened contaminants : Orion (5h29m < RA < 5h41m and -06°37' < DEC < -02°25'; Béjar et al. 1999), Taurus (3h50m < RA < 5h15m and 15°< DEC < 32°; Luhman 2004), Chamaeleon (10h45m < RA < 11h30m and -78°30' < DEC < -76°; Luhman 2007; Alves de Oliveira et al. 2012) and Upper Scorpius (15h35m < RA < 16h45m and -30° < DEC < -21°; Dawson et al. 2011). We subsequently counted the number of 2MASS neighbors in a 3' radius around each target in the 2MASS subset, and rejected all those with more than 71 neighbors to avoid densely populated regions. This number was chosen so that none of the known young brown dwarfs in the field and outside of the galactic plane were rejected. This cut down the number of 2MASS targets to 2 178 389. We then locally cross-matched the unique 2MASS identifiers of both catalogs to construct list A, consisting of 169 934 2MASS sources which already had an AllWISE counterpart identified in the latter catalog. The remaining unmatched 2 008 455 2MASS sources, as well as the 75 478 161 AllWISE sources with null 2MASS keys, were saved as lists B and C, respectively. AllWISE sources with non-null 2MASS entries that were not cross-matched this way were rejected, since they must have failed at least one of the 2MASS constraints

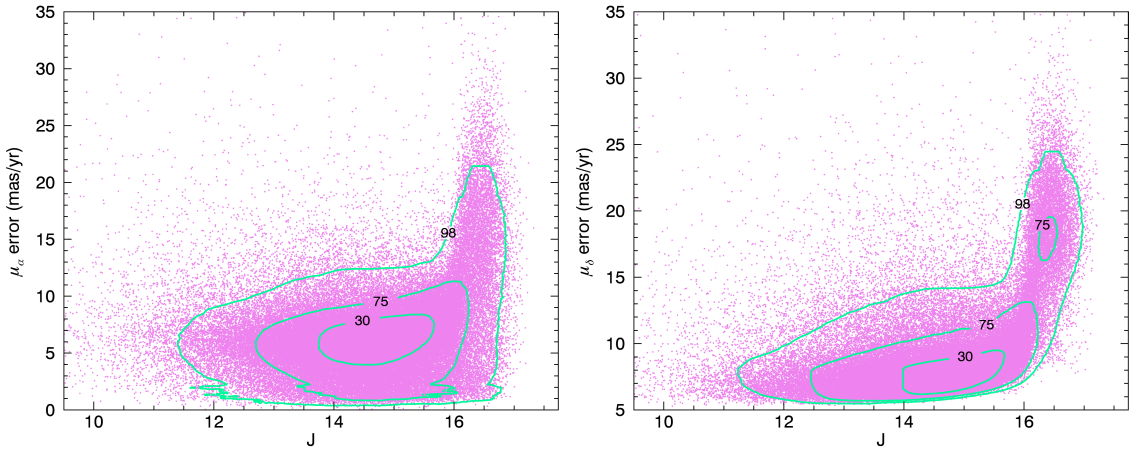

FIGURE 3.1 Proper motion precision as a function of 2MASS J magnitude in List A (pink points; see Section 3.3). Green contour lines respectively include 10%, 75% and 98% of all data points. In the case of bright objects ($J < 16$), typical precisions are 3–10 mas yr^{-1} ($\mu_\alpha \cos\delta$) and 5–10 mas yr^{-1} (μ_δ), whereas they can go down to ~ 25 mas yr^{-1} for fainter objects.

described above.

We created preliminary cross-matches by identifying the closest AllWISE entry in List C to each 2MASS entry in list B. A total of 2 001 246 of those preliminary matches were separated by distances larger than 25" (equivalent to a proper motion $> 2.2''$ yr^{-1}) or had $K_S - W1 < 0.153$ or $K_S - W1 > 2$, and were rejected. For each 2MASS component of the remaining 7 209 pairs (separated by angular distances of δ), we subsequently downloaded all AllWISE entries within δ, and verified that the closest entry with a null 2MASS_KEY corresponded to our preliminary match. We also verified that the 2MASS_KEY was not assigned to any other nearby AllWISE source. This step has rejected 767 objects. In a final step, we downloaded all 2MASS and AllWISE entries in a radius δ+3" around every AllWISE component of the 5 876 remaining pairs, and removed all IRSA-identified cross-matches. We use a search radius of δ+3" in this step to ensure that we retrieve all 2MASS–AllWISE matches in the AllWISE catalog in a radius δ, since those matches can be separated by up to 3". We then verified that the closest 2MASS entry among those objects not already cross-matched by IRSA corresponded to the 2MASS component of the preliminary pairs: this filter rejected 2 367 objects. The 3 509 pairs that survived all these selection criteria were added to List A. We then used 2MASS and AllWISE astrometry to determine proper motions for all 173 443 objects in

this supplemented List A, and rejected the 74 473 sources with a total proper motion lower than 30 mas yr^{-1}, or with a total proper motion measurement at $< 5\sigma$, to reject extragalactic contaminants and red giants.

Proper motions were calculated directly from entries in both the 2MASS and AllWISE catalogs. The right ascension (RA) and declination (DEC) entries were used for the astrometric position of both catalogs; the SIGRA and SIGDEC entries of AllWISE were used as a measurement error, and the ERR_MAJ ($\sigma_{\rm MAJ}$), ERR_MIN ($\sigma_{\rm MIN}$) and ERR_ANG (σ_θ) entries of the 2MASS catalog were projected back to errors on right ascension (σ_α) and declination (σ_δ) with :

$$\sigma_\alpha = \sqrt{(\sigma_{\rm MAJ} \sin\sigma_\theta)^2 + (\sigma_{\rm MIN} \cos\sigma_\theta)^2} \cdot \cos\delta \quad (3.1)$$

$$\sigma_\delta = \sqrt{(\sigma_{\rm MAJ} \cos\sigma_\theta)^2 + (\sigma_{\rm MIN} \sin\sigma_\theta)^2} \quad (3.2)$$

where δ is the 2MASS declination. The epochs corresponding to these astrometric measurements were taken from the JDATE and W1MJDMEAN entries in the respective catalogs. W1MJDMEAN corresponds to the mean epoch of all AllWISE exposures taken in the $W1$ band. The uncertainty on the 2MASS epoch is taken to be 30 s, as described in the 2MASS User's Guide, and the uncertainty on the AllWISE epoch is taken in a conservative way as half of the maximal distance between all exposures (from the W1MJDMAX and W1MJDMIN entries). We analytically propagated all measurement errors (astrometric and temporal) of both catalogs, assuming they were all independent, to obtain the measurement errors on our 2MASS–AllWISE proper motions. The positional accuracy of the 2MASS and AllWISE catalogs vary from $\sim 0\farcs05$ for bright sources ($J \lesssim 14$), to $0\farcs1$–$0\farcs4$ (2MASS) and $0\farcs06$–$0\farcs15$ (AllWISE) for fainter sources. The final set of 98 970 objects contains probable nearby > M5 dwarfs with measurements of proper motion above 30 mas yr^{-1}. We list this sample in the Appendix, since this sample provides a great opportunity to study the kinematics of LMSs and BDs in the solar neighborhood. In Figure 3.1, we show that typical measurement errors on proper motions are 5–10 mas yr^{-1} for bright objects ($J < 16$), or 5–25 mas yr^{-1} for fainter

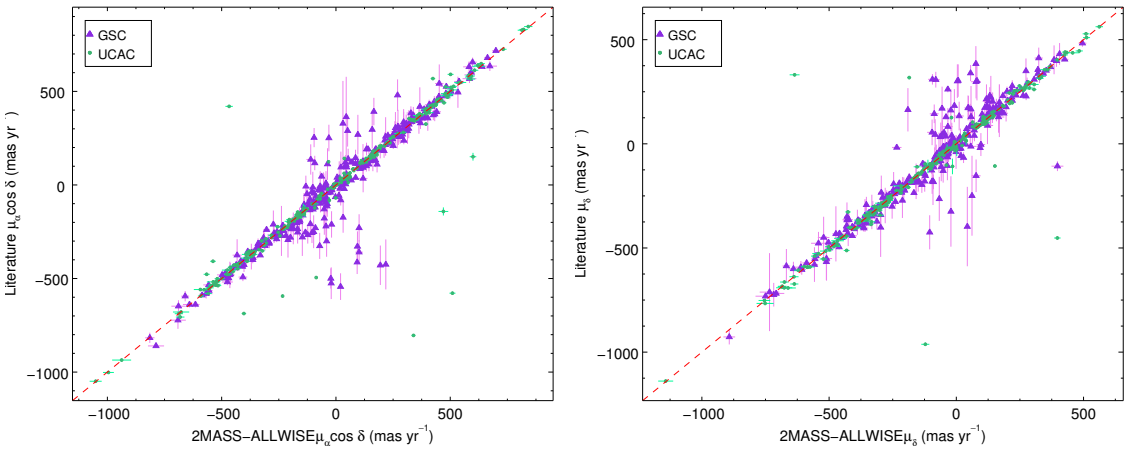

FIGURE 3.2 Comparison between proper motions determined from the 2MASS and AllWISE datasets and measurements in the literature, for a random subset of the the input sample of 98 970 objects. We only display 500 random objets per bin of $\sim 200\,\mathrm{mas\,yr^{-1}}$, to improve visibility. Measurements from the literature were obtained from the Initial Gaia Source List (VizieR catalog I/324/igsl3) which cross-matches UCAC3 (Zacharias et al. 2009; green circles) and the Guide Star Catalog (Lasker et al. 2008; purple triangles). The reduced chi-square values for $\mu_\alpha \cos\delta$ and μ_δ are 1.27 and 1.03, respectively.

objects.

We cross-matched our input sample with the Initial Gaia Source List (VizieR catalog I/324/igsl3) to obtain proper motions from the UCAC3 (VizieR catalog I/315; Zacharias et al. 2009) and the Guide Star Catalog (GSC; VizieR catalog I/305 and Lasker et al. 2008), and present in Figure 3.2 a comparison to the proper motions we derived from 2MASS–AllWISE. We find reduced χ^2 values of 1.27 and 1.03 for $\mu_\alpha \cos\delta$ and μ_δ, respectively, which indicates that our measurement errors are representative of the differences between our proper motions and those in the catalogs mentioned above. However, there are a few cases where the literature proper motions are significantly discrepant from the 2MASS–AllWISE measurements. We investigated the 25/3 873 worst cases in UCAC3 where either $\mu_\alpha \cos\delta$ or μ_δ were discrepant by more than $300\,\mathrm{mas\,yr^{-1}}$. In 24/25 cases, we found other measurements in the literature that matched the 2MASS–AllWISE measurement within a few σ (typically less than 1σ), indicating that the UCAC3 measurement might be at fault. The other case (2MASS J17274680+5200079) corresponds to a $6\farcs5$ binary which is barely above the angular resolution of AllWISE ($6\farcs1$ in the $W1$ band and $6\farcs4$ in the $W2$ band). Rodriguez et al. (2013) indicate that they observe a small

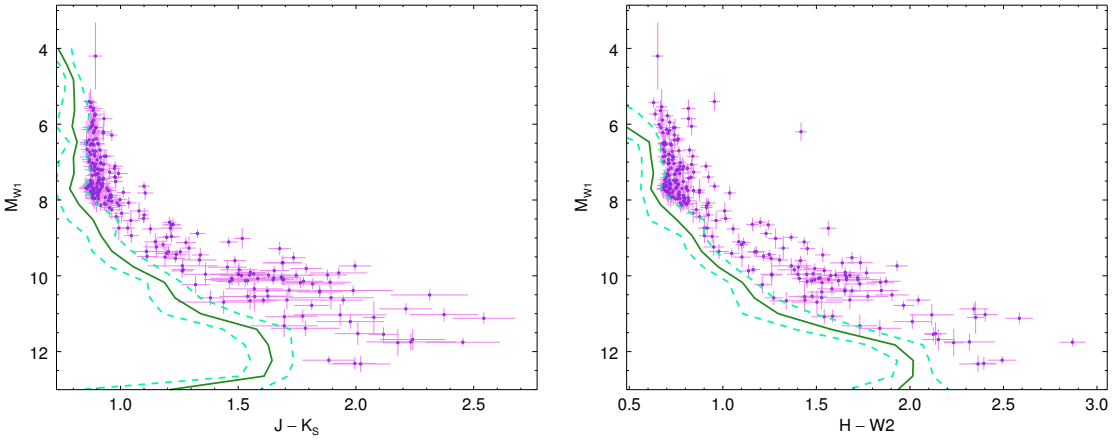

FIGURE 3.3 Positions of all objects in the BASS sample in two different CMDs (purple points), compared with the field sequence (thick green line) and its scatter (dashed green lines). We used the statistical distances of the most probable hypothesis from the BANYAN II tool to compute absolute magnitudes. The positions of all BASS candidates are consistent with them being young objects brighter and/or redder than the field sequence.

systematic distortion ($< 15\,\mathrm{mas\,yr^{-1}}$) for their $\mu_\alpha \cos\delta$ measurements from 2MASS–WISE as a function of galactic latitude. They propose a correction factor, which would increase our reduced χ^2 value to 1.27 to 1.82. This indicates that such a distortion is not clearly seen in our sample, and we thus choose not to include it in the present work. We conclude that the proper motions derived from 2MASS–AllWISE are reliable and will use only those measurements of proper motion for the remainder of this work. This will ensure that our selection criteria are more homogeneous, which will be helpful in an eventual characterization of the young population in the BASS survey.

3.4 Identification of candidate young moving group members

We used BANYAN II (Chapter 2) to compute the membership probability of all 98 970 potential close-by $\geq$ M5 dwarfs identified in the previous section (List A). The BANYAN II tool takes sky position, proper motion and 2MASS and AllWISE photometry as inputs and determines, using a naive bayesian classifier, the membership probability that an object belongs to seven YMGs (TWA, βPMG, THA, COL, CAR, ARG, ABDMG) and the field population, which constitutes our eight hypotheses. Probability Density Functions (PDFs) are computed

for every hypothesis and on each point of a regular 500×500 grid of distances and RVs spanning 0.1 to 200 pc and -35 to 35 $\mathrm{km\,s^{-1}}$ respectively, by comparing galactic positions (XYZ) and space velocities (UVW) to the spatial and kinematic model (SKM) of the respective hypotheses, as well as comparing 2MASS and AllWISE magnitudes to a photometric model. All measurement errors are propagated and considered in this comparison. SKMs of YMGs were built by fitting 3-dimensional ellipsoids, with unconstrained axes orientations, over the population of bona fide members with signs of youth as well as parallax and RV measurements (see Malo et al. 2013 and Chapter 2 for a complete list). For the field hypothesis, similar ellipsoids were fitted to synthetic objects drawn from the Besançon galactic model (A. C. Robin et al. in preparation, Robin et al. 2012) at distances of < 200 pc. The photometric model consists of an old and a young field sequence in two CMD diagrams: absolute $W1$ as a function of $H - W2$ and absolute $W1$ as a function of $J - K_S$. The positions of maxima and characteristic widths of the resulting posterior PDFs yield a statistical distance and RV prediction, assuming the object fulfills the respective hypothesis. The same PDFs are marginalized to a final probability by numerically integrating them along the whole grid. Optionally, parallax and RV measurements can be included to derive a more robust probability. In these cases, the corresponding dimension of the marginalization grid is eliminated. The Prior probabilities in the bayesian classifier are set to the respective population estimates of each hypotheses, considering the magnitude of proper motion and galactic latitude of the object. Additionally, equal-luminosity binary hypotheses for the field and all YMGs are supplemented to our set of hypotheses, where the CMDs are shifted up by 0.75 magnitudes. Objects for which the binary hypothesis has a higher probability will be flagged as potential binaries, and only the binary hypotheses will be used when we analyze known binary systems. A naive bayesian classifier implicitly considers that all input parameters are independent, which is generally not the case here. Using such an analysis with dependent input parameters will generally provide a good classification, however the bayesian probability will be biased and thus not interpretable in an absolute way (e.g. a set of candidates with a bayesian probabilities of 90% will not necessarily include a fraction of contaminants equal to 10%; Hand & Yu 2001, Russek et al. 1983). To address this, we performed in Chapter 2 a Monte Carlo analysis using all SKM

and photometric models described above to estimate the field contamination probability as a function of bayesian probability for different hypotheses. They find that bayesian probabilities are generally pessimistic, except for YMGs which are most subject to contamination (ARG, ABDMG, βPMG and COL) when no parallax measurement is included. When a parallax measurement is included, the contamination probability becomes very low ($\lesssim 20\%$ when the bayesian probability is larger than $\sim$ 10–40% depending on the YMG). These results provide a translation for the bayesian probability output by BANYAN II to an expected contamination rate. In Chapter 2, we showed that bona fide members within $< 1\sigma$ of their YMG's SKM all have a bayesian probability $> 95\%$ associated with a membership to their respective YMG, whereas peripheral (1–2.5σ) bona fide members have a bayesian probability between 10–95%. For more details about the BANYAN II tool, the reader is referred to Chapter 2.

After applying BANYAN II to our input sample (list A), we rejected all objects with a bayesian probability $< 10\%$ of being a member to a YMG, or with an estimated contamination rate $> 50\%$. At this point we are left with 983 candidates. We used statistical distances of the most probable hypotheses to place all candidates in the two CMDs described above, and rejected all candidates that did not have NIR colors at least 1σ redder than the field sequence. These filters cut down the candidate list to 273 objects. Another set of 275 candidates located to the right of the field sequence by an amount less than 1σ were used to build the low-priority BASS catalog (LP-BASS) which is discussed in the Appendix of this paper. The AllWISE catalog includes WISE observations that were performed in its warm phase, hence in some cases, the measurement of $W1$ or $W2$ can be saturated. To avoid overlooking such saturated targets, we repeated all steps described above using the WISE catalog instead of AllWISE, and supplemented our sample with the additional 26 objects uncovered this way (96 in the case of LP-BASS). We subsequently used the IRSA dust extinction tool[5] to remove 9 objects displaying extinction larger than 0.4 mag, potentially corresponding to distant contaminants reddened by interstellar matter in our line of sight. Another 3 objects listed in the the *2MASS extended sources* catalog (VizieR catalog VII/233/xsc) were rejected. In a final step, we visually inspected all SDSS, DSS, 2MASS and AllWISE acquisition images to flag any object

[5] Available at *http://irsa.ipac.caltech.edu/applications/DUST/*

Table 3.1. Expected Completeness of the BASS Survey.

YMG Name	$\|b\| \leq 15°$	$\mu \leq$ 30 mas yr^{-1}	SFRs[a]	Any Filter	Contam. $\geq 50\%$	Expected Completeness
ARG	42.1%	0.5%	0.6%	42.6%	89.6%	6.0%
COL	15.7%	23.4%	1.8%	36.4%	59.7%	25.6%
βPMG	25.2%	0.8%	3.4%	28.3%	60.0%	28.7%
ABDMG	20.7%	1.1%	1.6%	22.8%	59.6%	31.2%
CAR	41.2%	2.7%	0.1%	42.9%	9.9%	51.4%
TWA	19.7%	0.4%	0%	20.0%	10.3%	71.8%
THA	$< 0.1\%$	$< 0.1\%$	0%	$< 0.1\%$	10.0%	90.0%

[a]Expected fraction of members aligned with Orion, Taurus, Chamaeleon and Upper Scorpius (see Section 3.3).

[b]Filters on position and proper motion are not independent.

with a suspicious shape or evidence of interstellar absorption in the surrounding $5'$. No such occurrence was found, which indicates the filters described above were efficient in preventing such contaminating objects. The resulting BASS catalog is presented in Table 3.2. We divide the sample in two sections: those with a contamination probability lower than 15% are grouped in a *High Probability* section, whereas those with a contamination probability between 15–50% are grouped in the *Modest Probability* section.

In Table 3.1, we present the fraction of members in each moving group that would fail our galactic plane and proper motion filters, assuming that our SKM models are accurate. We obtained these quantities by drawing a million synthetic objects from a gaussian random distribution represented by each SKM and assessing what fraction fails each filter. We used the estimated recovery rate of the BANYAN II tool for each YMG (see Chapter 2) corresponding to our tolerated field contamination of $< 50\%$ and combined all these sources of incompleteness to estimate that the BASS sample is complete at the 6–90% level in the range of spectral types considered here, depending on the YMG in question. The YMGs that would benefit the most from a search within the galactic plane are ARG and CAR, and to a lesser extent βPMG, ABDMG and TWA. However, such a survey would present a significant challenge for two reasons ; (1) a cross-match between the 2MASS and AllWISE catalogs would require the use of powerful algorithms because of crowded regions; and (2) a new free parameter would have

to be added to the analysis, describing the effect of reddening by interstellar medium on the CMD sequence of field stars (e.g. this effect could be represented by a reddening vector of unknown amplitude in both CMDs that are used in the BANYAN II tool). We note that even if those two hurdles would be overcome, we expect the field contamination to remain very high within the galactic plane, unless the survey benefits from RV and parallax measurements for a large number of objects. The only YMG which is significantly affected by our low proper motion cut is COL. Since this filter serves the main purpose of rejecting distant extragalactic and red giant contaminants, starting from a sample of targets with distance measurements would allow relaxing this filter and accessing to a larger number of COL candidates. The final major obstacle to identify efficiently a large number of candidate members of ARG, COL, βPMG and ABDMG is the low recovery rate intrinsic to a naive bayesian classifier in the situation where no information is known on the RV and distance of the input sample. It could be expected that adopting a more complex method, which could for example take account of the dependency of input parameters, would help to draw the most possible information from a sample without RV and distance measurements. However, Hand & Yu (2001) suggest otherwise by demonstrating that a naive bayesian classifier performs much better than could be expect in these conditions. This would leave only three foreseeable options to attack this aspect of our survey completeness; (1) allow for significantly more contaminants in our sample and perform an extensive spectroscopic follow-up; (2) start from a sample that includes RV and parallax measurements; or (3) identify new readily-accessible observables, such as new filters in color-color diagrams, that could distinguish YMG members from field interlopers.

3.5 A literature search for additional information

We searched for any additional information in the literature for all candidates in Table 3.2 using the SIMBAD and VizieR web tools. We found 122 objects for which at least one of RV, parallax, spectral type, signs of youth or any other relevant information was available, including 60 known candidates or bona fide members of the YMGs considered here. There are only 4 known bona fide members included in those: 2MASS J00452143+1634446 (ARG; Zapatero Osorio et al. 2014 and Section 3.5.2) 2MASS J01231125–6921379 (THA;

Table 3.2. All-Sky Search for > M5 Candidates in Young Moving Groups.

2MASS Designation	Estim. SpT	2MASS J	2MASS H	2MASS K_S	AllWISE $W1$	AllWISE $W2$	$\mu_\alpha \cos\delta$ (mas yr^{-1})	μ_δ (mas yr^{-1})	Member-ship	Prob. (%)	Cont. (%)
Candidates with a High Probability											
00011217+1535355	L3.2	15.52	14.51	13.71	12.97	12.54	139.6 ± 7.8	-183.5 ± 11.8	ABDMG	79.1	1.6
00040288-6410358	L2.5	15.79	14.83	14.01	13.41	12.96	77.7 ± 3.0	-56.1 ± 8.4	THA[a]	99.9	< 0.1
00041589-8747254	M5.7	12.90	12.20	11.86	11.65	11.41	77.3 ± 2.0	-29.9 ± 9.2	THA	55.4	< 0.1
00065794-6436542	M6.9	13.39	12.66	12.17	11.74	11.42	92.7 ± 3.1	-71.0 ± 7.3	THA[a]	99.9	< 0.1
00111532-3756553	M5.7	12.15	11.60	11.22	11.02	10.79	105.7 ± 5.0	-77.4 ± 7.4	THA	80.2	< 0.1
00182834-6703130	M9.6	15.46	14.48	13.71	13.19	12.80	83.6 ± 2.9	-65.0 ± 9.3	THA[a]	99.8	< 0.1
00191296-6226005	M9.7	15.64	14.62	13.96	13.38	12.96	66.1 ± 2.9	-50.6 ± 8.4	THA	99.5	< 0.1
00212774-6351081	M4.0	11.02	10.48	10.11	9.91	9.66	83.0 ± 2.9	-57.6 ± 7.2	THA	99.8	< 0.1
00235732-5531435	M4.5	11.11	10.55	10.24	10.07	9.87	92.3 ± 3.4	-67.7 ± 7.4	THA[a]	99.5	< 0.1
00305785-6550058[b]	M2.1	9.82	9.24	8.95	8.79	8.61	70.3 ± 2.9	-51.9 ± 8.7	THA	99.1	< 0.1
00325584-4405058	M9.5	14.78	13.86	13.27	12.84	12.52	125.9 ± 4.9	-79.4 ± 6.9	THA	82.0	7.0
00344300-4102266	L2.4	15.71	14.81	14.08	13.52	13.12	96.9 ± 5.1	-51.8 ± 7.0	THA	96.1	< 0.1
00354313+0233137	M4.8	10.52	9.93	9.54	9.32	9.12	153.8 ± 8.7	-185.3 ± 9.0	ABDMG[a]	88.2	1.4
00374306-5846229	M9.2	15.37	14.26	13.59	13.15	12.77	81.7 ± 3.2	-40.0 ± 6.9	THA[a]	99.8	< 0.1
00413538-5621127	M5.3	11.96	11.32	10.86	10.63	10.37	110.0 ± 3.6	-55.9 ± 6.6	THA[a]	99.5	< 0.1
00452143+1634446	L2.4	13.06	12.06	11.37	10.78	10.40	367.0 ± 11.7	-47.7 ± 9.9	ARG	94.7	4.5
00514081-5913320	M4.5	11.28	10.70	10.40	10.21	9.99	92.6 ± 3.1	-48.5 ± 8.2	THA	99.8	< 0.1
00525451-6624501	L0.3	15.67	14.69	13.98	13.35	12.95	74.9 ± 2.4	-10.2 ± 6.9	ABDMG[a]	11.8	< 0.1
01033563-5515561	M3.4	10.16	9.58	9.24	9.05	8.80	111.6 ± 3.6	-43.8 ± 8.1	THA[a]	99.3	< 0.1
01075572-6030194	M5.3	11.84	11.25	10.97	10.76	10.56	105.0 ± 3.4	-33.9 ± 7.4	THA	99.6	< 0.1
01134031-5939346	M3.3	9.95	9.34	9.06	8.90	8.70	99.4 ± 3.7	-25.2 ± 9.8	THA[a]	99.3	< 0.1
01174748-3403258	M9.6	15.18	14.21	13.49	13.05	12.64	108.5 ± 5.5	-58.9 ± 6.3	THA	98.8	< 0.1
01180670-6258591	M4.9	11.53	10.96	10.64	10.44	10.22	95.4 ± 3.0	-49.0 ± 6.7	THA	99.3	< 0.1
01205114-5200349	L2.5	15.64	14.66	13.75	13.23	12.82	101.9 ± 4.0	-47.0 ± 6.8	THA[a]	99.9	< 0.1
01231125-6921379	M5.3	12.32	11.71	11.32	11.07	10.83	89.9 ± 2.3	-26.3 ± 6.7	THA[a]	99.9	< 0.1
01243060-3355014	M5.2	10.56	10.01	9.68	9.48	9.29	164.2 ± 5.5	-140.9 ± 6.5	ABDMG	88.4	1.5
01265327-5505506[b]	M4.5	12.04	11.48	11.09	10.90	10.64	96.8 ± 4.5	-37.6 ± 9.2	THA	99.8	< 0.1
01294256-0823580[b]	M2.5	10.65	10.09	9.77	9.55	9.33	100.7 ± 8.4	-56.4 ± 9.0	BPMG	71.6	< 0.1
01320814-6023536	M4.5	11.42	10.84	10.52	10.33	10.13	89.2 ± 3.0	-23.5 ± 8.2	THA	99.8	< 0.1
01344601-5707564	M5.3	12.07	11.52	11.16	10.98	10.75	98.6 ± 3.4	-29.3 ± 7.3	THA	99.8	< 0.1
01372781-4558261	M4.6	11.11	10.54	10.19	9.99	9.76	117.9 ± 4.3	-40.3 ± 6.3	THA	98.6	< 0.1
01393605-6455456	M5.4	12.58	11.99	11.58	11.42	11.19	80.6 ± 2.6	-6.0 ± 6.7	THA	88.9	< 0.1
01415823-4633574	M9.0	14.83	13.88	13.10	12.58	12.19	111.2 ± 4.3	-45.7 ± 6.5	THA[a]	99.9	< 0.1
01443191-4604318	M5.3	11.88	11.30	10.98	10.75	10.49	102.8 ± 5.0	-42.2 ± 7.1	THA	99.6	< 0.1
01484859-5201158	M4.0	10.87	10.35	9.99	9.81	9.58	104.2 ± 3.7	-28.9 ± 6.4	THA[a]	99.8	< 0.1
01504543-5716488	M5.3	12.16	11.56	11.28	11.04	10.80	100.4 ± 3.3	-27.2 ± 6.5	THA	99.9	< 0.1
01531463-6744181	L2.7	16.41	15.11	14.42	13.73	13.26	82.0 ± 2.7	-21.3 ± 9.4	THA[a]	99.9	< 0.1
01532494-6833226	M3.9	11.07	10.49	10.18	10.00	9.77	93.4 ± 2.6	-16.7 ± 7.3	THA[a]	99.9	< 0.1
02004709-5105206	L5.9	16.41	14.94	13.87	12.89	12.36	171.3 ± 5.4	-75.5 ± 10.0	ABDMG[a]	99.1	0.7
02013900-5948345	M5.3	11.78	11.19	10.87	10.68	10.48	118.7 ± 3.5	-49.4 ± 7.3	THA	33.1	< 0.1
Candidates with a Modest Probability											
00160844-0043021	L4.0	16.33	15.23	14.54	13.84	13.39	138.3 ± 9.9	-33.7 ± 14.2	BPMG	18.8	36.4
00192626+4614078	M5.9	12.60	11.94	11.50	11.28	11.02	119.6 ± 6.1	-82.5 ± 6.9	ABDMG	53.3	17.5
00274534-0806046	M5.3	11.57	10.97	10.61	10.41	10.18	111.5 ± 7.0	-59.9 ± 6.7	BPMG	45.6	35.1
00390342+1330170	M5.1	10.94	10.37	10.06	9.84	9.65	109.8 ± 6.8	-96.5 ± 7.0	BPMG	57.9	15.3
00464841+0715177	M8.2	13.89	13.18	12.55	12.09	11.64	97.0 ± 9.2	-60.3 ± 7.3	BPMG[a]	78.5	28.4
00581143-5653326	L6.1	16.78	15.55	14.55	13.76	13.24	197.4 ± 6.2	46.0 ± 12.2	ARG	80.4	32.9
01033203+1935361	L6.2	16.29	14.90	14.15	13.18	12.70	303.0 ± 13.4	16.6 ± 7.2	ARG	31.7	16.9
01525534-6329301	M4.7	10.17	9.60	9.26	9.06	8.84	130.0 ± 3.5	7.0 ± 6.4	BPMG	71.4	22.1
02534448-7959133	M5.4	11.34	10.74	10.38	10.18	9.97	81.7 ± 2.2	90.3 ± 9.3	BPMG	71.8	24.9
03390160-2434059	M3.7	10.90	10.34	9.97	9.72	9.52	56.3 ± 5.7	-12.7 ± 6.0	COL	60.5	32.9

[a]The binary hypothesis is more probable than the single hypothesis (see Section 3.4).

[b]Object from the WISE catalog rather than AllWISE.

This table is available in its entirety at *http://dx.doi.org/10.6084/m9.figshare.1207880*. The complete table has 263 rows (239 high probability candidates and 24 modest probability candidates).

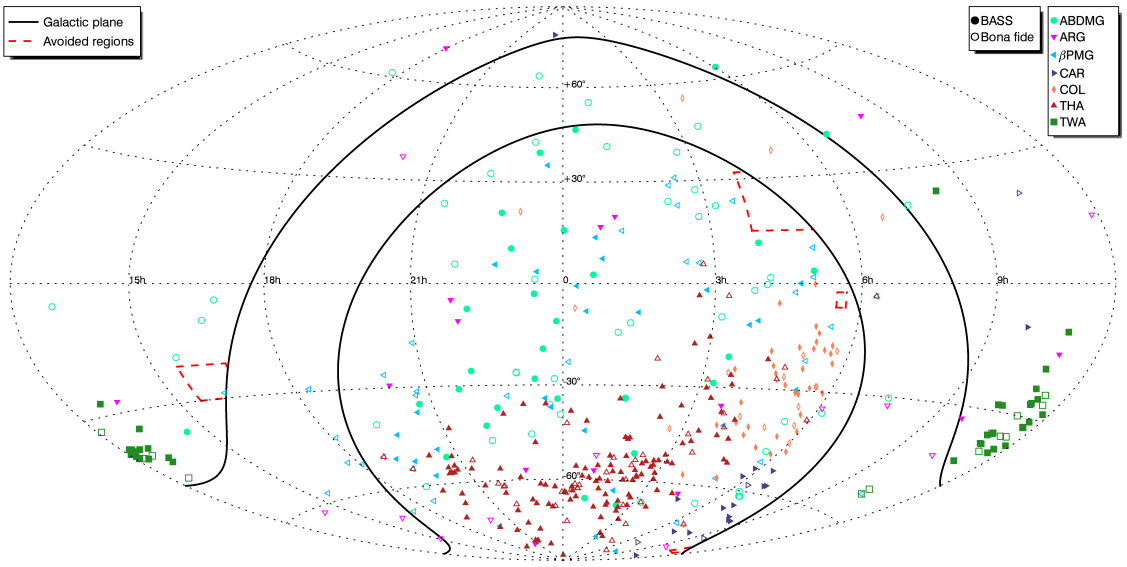

FIGURE 3.4 Sky position of all BASS candidates (filled symbols), compared with currently known bona fide members (open symbols) of each YMG considered here. Thick black lines delimit the galactic plane within ±15° of galactic latitude, and the dahsed red lines delimit regions that were avoided in our search for YMG candidates (see Section 3.3).

Chapter 2), GJ 2022 (ABDMG; Riedel 2012a, Shkolnik et al. 2012 and Riedel et al. 2014), 2MASS J03552337+1133437 (ABDMG; Faherty et al. 2013b, Liu et al. 2013a). We list these 59 objects in Table 3.3, with an updated bayesian probability in light of these additional measurements. In Figure 3.5, we compare the BANYAN II statistical predictions for the RV and distance to measurements found in the literature, and show that the reduced χ^2 values are 1.32 and 0.84, respectively. This indicates that errors on statistical predictions are representative of the scatter observed here.

3.5.1 Estimates of spectral types

We used 2MASS and AllWISE J, H, K_S, $W1$ and $W2$ magnitudes with the statistical distance associated to the most probable hypothesis from BANYAN II to assign a tentative spectral type to all candidates identified here. We used the *Database of Ultracool Parallaxes*[6] (Dupuy & Liu 2012) to compare the position of each candidate with the corresponding spectral type – magnitude sequence (spanning the M5–T9 range) and derived a PDF in each case as a

[6] Available at *http://www.cfa.harvard.edu/~tdupuy/plx/Database_of_Ultracool_Parallaxes.html*

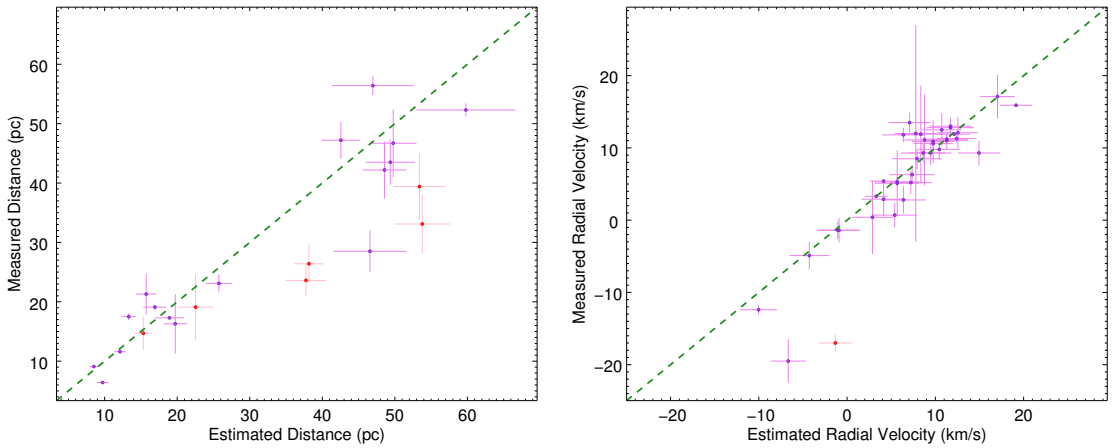

FIGURE 3.5 Comparison of statistical RV and distance predictions from BANYAN II to measurements found in the literature. The dashed green line has a unit slope and intersects with the origin. Measurements which corroborated the most probable hypothesis are displayed in purple, whereas those favoring a different YMG are displayed in red. Measurements which are significantly discrepant and thus rejecting possible YMG memberships are not displayed here.

function of spectral type. We then combined these PDFs in a likelihood analysis, and used the maximal position of the final PDF to assign a most probable spectral type to each object. In Figure 3.6, we compare our spectral type estimates to measurements available in the literature and show that these estimates are reliable to within ~ 2.5 subtypes.

We note a clear trend where we tend to underestimate spectral types for $<$M5 objects and overestimate those of $>$L5 objects. We used a linear fit to characterize this systematic trend and obtain a correction for our estimated spectral types:

$$\mathrm{SpT}_{\mathrm{corr}} = 1.64 + 0.81 \cdot \mathrm{SpT}_{\mathrm{estim}}, \tag{3.3}$$

where 0 corresponds to the M0 spectral type. We used this equation to correct all estimated spectral types listed in Tables 3.2 and 3.5. Before the correction, the reduced χ^2 value for our estimated spectral types is 2.51, and the estimated–measured spectral type differences display a standard deviation of 1.1 subtypes. After the correction, the reduced χ^2 and standard deviation become 1.0 and 0.8 subtypes, respectively.

In Figure 3.7, we use spectral type measurements when available or estimates of spectral

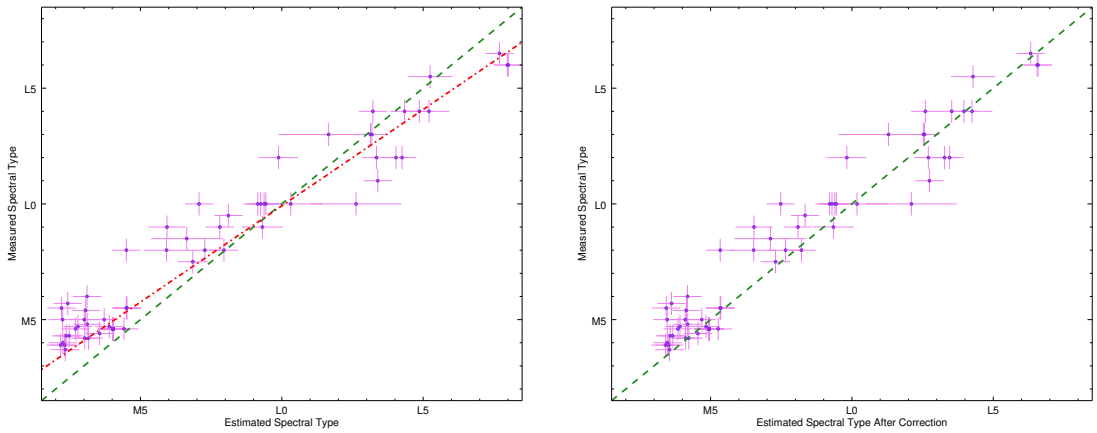

(a) Before Correction (b) After Correction

FIGURE 3.6 Estimated spectral types obtained from 2MASS and AllWISE photometry as well as statistical distances from BANYAN II, compared with measurements available in the literature from optical or NIR spectroscopy. The dashed green line has a unit slope and intersects with the origin. Our estimates are reliable within ~ 1.5 subtype in the M5–L6 range, but tend to overestimate (underestimate) later (earlier) spectral types. To account for this effect, we adjusted a linear correction to the estimated spectral types (red dashed line; top panel). Corrected estimations of spectral types are displayed in the bottom panel.

types otherwise to compare the BASS sample with current bona fide members in YMGs. This Figure clearly demonstrates that a significant fraction of the BASS candidates have a later spectral type than most known members of YMGs, which outlines that we are entering a yet poorly explored mass regime of the YMG population.

3.5.2 Comments on individual objects

In this Section, we present comments on individual objects which deserve further discussion. All those already discussed in Chapter 2 (see the Reference column in Table 3.3) will not be discussed here, unless new information is available.

2MASS J00390342+1330170 has been identified by Schlieder et al. (2012a) as a candidate member of ABDMG with X-ray and near-UV emission indicative of a young, early-M dwarf, however they do not estimate a spectral type. We find that this object has a bayesian probability of 84.3% and 7.5% for βPMG and ABDMG, respectively. We thus assign it as a candidate member of βPMG, but we note that there is an expected $\sim$ 10% contamination

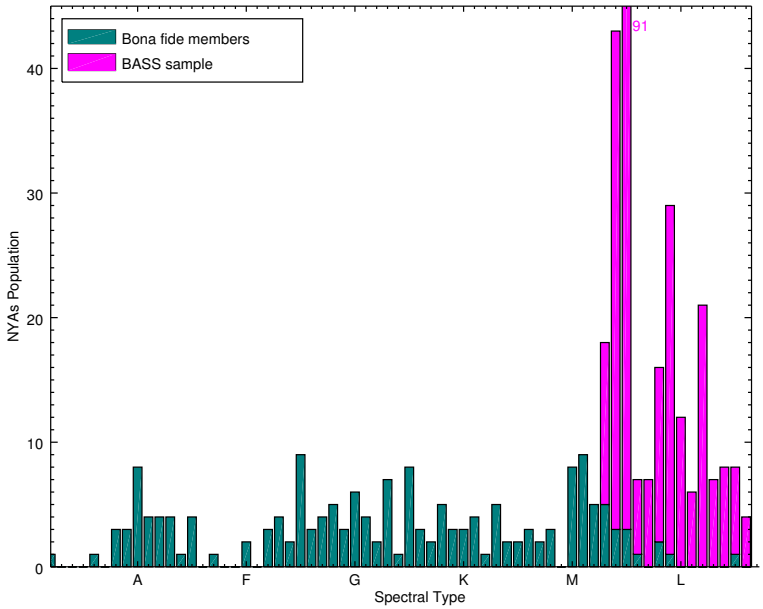

FIGURE 3.7 Estimated spectral types (violet bars) for the BASS sample, compared with the current bona fide population of all YMGs considered here (green bars). The M5 spectral bin has a value of 91: the vertical range has been shortened for clarity. The BASS sample targets YMG candidates in a range of spectral types which is yet largely unexplored.

rate from ABDMG to βPMG for such a result (see Chapter 2).

2MASS J00452143+1634446 was reported in Chapter 2 as a candidate member of ARG with unusually red NIR colors for its L2 spectral type. Blake et al. (2010) measured a RV of 3.4 ± 0.2 km s^{-1}, and Zapatero Osorio et al. (2014) measured a trigonometric distance of 17.5 ± 0.6, pc, which bring the bayesian probability of the ARG membership hypothesis to 98.0%. Zapatero Osorio et al. (2014) also derived an isochronal age of 10–100 Myr and detected lithium in its atmosphere. As noted by Zapatero Osorio et al. (2014), all evidence points towards a membership to ARG, hence we propose that this $\sim 15\,M_{\rm Jup}$ object is a bona fide member of this association.

2MASS J01033563–5515561 was first identified as a highly probable candidate to THA in early versions of the BASS sample. Delorme et al. (2013) used high contrast imaging to search for low-mass companions around BASS candidates and demonstrated that this object is in fact an M5+M5, $0\farcs26$ tight binary harboring a 12–14 $M_{\rm Jup}$ substellar companion at a separation of $1\farcs78$. They note that the NIR colors of the companion are indicative of a

young L-type object, which is consistent with the THA membership. Subsequently, Kraus et al. (2014b) and Malo et al. (2014a) independently measured RVs of 4.0 ± 2.0 km s^{-1} and 7.3 ± 2.6 km s^{-1} respectively, whereas the latter independently identifies it as a candidate member of THA. We combined both RV measurements to obtain RV $= 5.2 \pm 1.6$ km s^{-1}. Riedel et al. (2014) measured a trigonometric distance of 47.2 ± 3.1 pc, in good agreement with our statistical distance of 42.3 ± 3 pc (which is at 1.1σ from the measurement). Without using any RV measurement, they argue that its kinematics are more consistent with CAR rather than THA. They also use empirical isochrones for YMGs to show that the system is over-luminous for THA or CAR even when binarity is taken into account, which could mean that it is possibly younger, or an even higher-order multiple system. When not using the RV measurement in BANYAN II, we obtain a bayesian probability of 98.9%, 0.7% and $2 \cdot 10^{-7}$ for THA, ABDMG and CAR, respectively. The statistical RVs associated to these hypotheses are respectively 7.2 ± 2.5 km s^{-1}, 10.8 ± 1.8 km s^{-1} and 14.0 ± 2.0 km s^{-1}. Both the measured RVs are consistent with the THA hypothesis (at 0.7σ) and not consistent with CAR (at 3.0σ), which strengthens the THA hypothesis even more. Once we include the RV measurement, the THA hypothesis clearly dominates with a bayesian probability of 99.9% for THA and $2 \cdot 10^{-10}$ for CAR. We thus suggest that this system is a bona fide member of THA, since it has all measurements needed to be considered as such (i.e. complete $XYZUVW$ kinematics and signs of youth). This system will be discussed in more details in a subsequent paper (J. Gagné et al., in preparation).

2MASS J01243060–3355014 (GJ 2022 B) was identified by Jao et al. (2003) as a co-moving companion to the tight $1\farcs8$ M4+M4 binary GJ 2202 AC. Shkolnik et al. (2009) used the X-ray emission and low K I EW of the latter to constrain its age between 40–300 Myr, and Shkolnik et al. (2012) measured a trigonometric distance of 25.1 ± 1.0 pc and a RV of 18.3 ± 1.5 km s^{-1} for GJ 2022 B. They use this information to identify this object as a new bona fide member of ABDMG. Riedel et al. (2014) subsequently measured a trigonometric distance of 25.8 ± 1.4 pc; we combined both distance measurements in an error-weighted average to obtain 25.3 ± 0.8 pc. We find that the ABDMG membership, distance and RV measurements are all consistent with our results from BANYAN II; the predicted RV of 18.3 ± 2.0 km s^{-1}

is consistent with the measurement, and the statistical distance of 26.1 ± 1.6 pc is at $< 1\sigma$ of the combined distance measurements. Including youth, RV, distance and spectral types in our analysis yields a membership probability of 99.98% for the ABDMG hypothesis, associated with a field contamination probability of $< 0.1\%$. This is consistent with the conclusions of Shkolnik et al. (2012) and Riedel et al. (2014) that this system is a bona fide member of ABDMG. We note that Shkolnik et al. (2012) refer to the wide companion as GJ 2022 C, whereas Jao et al. (2003) and Riedel et al. (2014) refer to it as GJ 2022 B. We adopt the latter to preserve historical nomenclature, as proposed by Riedel et al. (2014).

2MASS J01303563–4445411 was identified as an M9 dwarf by Reid et al. (2008a) and Faherty et al. (2009). Subsequently, Dhital et al. (2011) resolved this system as an M9+L6 pair with a $3\farcs2$ separation. They note that the companion displays red colors for its spectral type, at 1.7σ of the field L6 BDs, but the primary has normal NIR colors for its spectral type, which could be an indication that the companion has an unusually dusty atmosphere. They show that the optical spectrum of the primary does not display Hα or Li, which indicates a minimal age of 250 Myr. Furthermore, a resolved NIR spectrum of the L6 companion does not display typical signs of youth such as a triangular H-band continuum. We thus conclude that this system must be a false positive in our analysis, despite its 90.6% bayesian probability of being a member of THA, since its age is not consistent with any YMG in the solar neighborhood.

2MASS J02212859–6831400 has been identified as an M8 dwarf by Reid et al. (2008a), and Faherty et al. (2009) indicate that it is unusually red and for its spectral type and displays signs of low-gravity. Faherty et al. (2012) measured a trigonometric distance of 39.4 ± 5.6 pc. This object was not considered as a strong candidate member of any YMG in Chapter 2, but here we find it as a candidate member of ABDMG with a bayesian probability of 40.8% and a contamination probability of $< 0.1\%$. This discrepancy is due to the 2MASS–AllWISE proper motion, which is at 2.2σ or $5.0\,\mathrm{mas\,yr^{-1}}$ ($\mu_\alpha \cos\delta$) and 1.7σ (μ_δ) or $9.1\,\mathrm{mas\,yr^{-1}}$ of the proper motion used in the analysis presented in Chapter 2 (which was measured by Faherty et al. 2012). We visually inspected the 2MASS and AllWISE Atlas images and found that our cross-match between both catalogs is unambiguous, however it is possible that this candidate is a false positive in our analysis. A measurement of RV will be necessary to better constrain

the membership of this object.

2MASS J02401209–5305527 was reported as an M9.5 BD by Martín et al. (2010). They measured the equivalent width (EW) of the Na I doublet at 8170–8200 Å to be EW = 5.5 ± 0.8 Å. It is well known that low-gravity objects have a low Na I EW, however no classification scheme using this measurement extends to such a late spectral type. We note that this EW is low compared with other M9.5 BDs in their sample, for which Na I EWs range from 5.9 to 9.7 Å with an average and standard deviation of 7.3 and 1.3 Å respectively. However, it is higher than the Na I EW of low-gravity field BDs in their sample (2MASS J04433761+0002051, 3.6 ± 0.8 Å; and 2MASS J06085283–2753583, 5.0 ± 0.7 Å). NIR spectroscopy would be useful to clarify the age of 2MASS J02401209–5305527.

2MASS J03014892–5903021 and **2MASS J03252938–4312299** have both been identified as M9 dwarfs by Reid et al. (2008a). Martín et al. (2010) measured the equivalent width of their 8170–8200 Å Na I doublets and find 4.5 ± 0.8 Å and 5.1 ± 0.8 Å, respectively. They also revised the spectral type of 2MASS J03252938–4312299 to M8.5. In a similar way to 2MASS J02401209–5305527, they have not flagged either objects as low-gravity, but both display the lowest Na I EW of all objects of their respective spectral types, except for Upper Scorpius candidates. NIR spectroscopy would be useful in clearly identifying potential signs of low-gravity in these objects.

2MASS J03393521–3525440 (LP 944–20) was identified as an M9 dwarf by Leggett et al. (2001). They used their lithium detection to constrain its age below 1 Gyr. Allers & Liu (2013) updated its spectral classification to an intermediate gravity L0β; Reid et al. (2002) and Reiners & Basri (2009) measured a RV which we combined in Chapter 2 to obtain $9.3 \pm 1.7\,\mathrm{km\,s^{-1}}$; Dieterich et al. (2014) measured a trigonometric distance of 6.41 ± 0.04 pc. In Chapter 2, we used a previous parallax measurement from Tinney (1996); 5.0 ± 0.1 pc) with the BANYAN II tool to derive a bayesian probability of 17.5% that this is a member of ARG. However, Ribas (2003) indicated that it is a candidate member to the purported ~ 200 Myr old Castor moving group (CAS; Barrado Y Navascués 1998). They thus use an alternate bayesian analysis similar to BANYAN I (Malo et al. 2013) but including a SKM of CAS built from members reported by Barrado Y Navascués (1998) and find a significantly larger

bayesian probability for CAS (99.7%). More recently, Mamajek et al. (2013) used updated distance and RV measurements of the original CAS members to demonstrate that they are too far apart in velocity space to be a part of a moving group of common origin. They thus argue that CAS likely a dynamical stream rather than a moving group, which is in line with the results of Mamajek (2012), Monnier et al. (2012) and Zuckerman et al. (2013). The difference in UVW space between LP 944–20 and ARG is considerable ($9.7\,\mathrm{km\,s^{-1}}$) and comparable to its distance to Fomalhaut ($13.5\,\mathrm{km\,s^{-1}}$). We conclude that LP 944–20 is likely a contaminant in our analysis, which could possibly be explained by the fact that our SKM model of field stars, derived from the Besançon galactic model (Robin et al. 2014; Robin et al. 2012), does not explicitly include such dynamical streams that could act as an additional source of contamination.

2MASS J05002100+0330501 was identified as an L4 dwarf by Reid et al. (2008a) and Blake et al. (2010) measured a RV of $15.9 \pm 0.2\,\mathrm{km\,s^{-1}}$, from which we obtain a 62.8% membership probability associated with ABDMG. However, Reid et al. (2008a) specified that this object displays no notable peculiarities and would be a good spectral standard. While NIR spectroscopy could unambiguously rule out low-gravity, it is likely that this object is a field contaminant in our analysis.

2MASS J05012406–0010452 has been identified by Reid et al. (2008a) as an L4 BD with signs of low-gravity in its optical spectrum. Cruz et al. (2009) updated its classification to L4 γ using its optical spectrum, and Allers & Liu (2013) classified it as L3 γ using NIR spectroscopy. Faherty et al. (2012) measured a trigonometric distance of $13.1 \pm 0.8\,\mathrm{pc}$. In Chapter 2, we considered this object and found no obvious candidacy to any YMG considered here. However, we find that it has a 64.7% bayesian probability of being a member of COL, associated with a 2.3% contamination probability. The discrepancy between this result and that presented in Chapter 2 is due to the μ_δ proper motion measurement from 2MASS–AllWISE, which is at 2.8σ of the value they used (which was measured by Faherty et al. 2012). We visually inspected the 2MASS and AllWISE Atlas images and found that our cross-match between both catalogs is unambiguous. Much like the case of 2MASS J02212859–6831400, a RV measurement will be needed to better constrain the membership of this object,

but it is plausible that this object is a false-positive in our analysis.

2MASS J10584787–1548172 (DENIS–P J1058.7–1548) has been identified as an L3 dwarf by Geballe et al. (2002) and Dahn et al. (2002) measured a trigonometric distance of 17.3 ± 0.3 pc, from which we obtain a 93.1% membership probability to ARG. Reid et al. (2008a) measured Hα emission in its optical spectrum, but reported no further peculiarities. Schneider et al. (2014) subsequently measured the gravity-sensitive $H_2(K)$ in its NIR spectrum and obtain a value of 1.021, which is consistent with a field L3 dwarf. It is thus likely that this object is a field contaminant in our analysis.

2MASS J12474428–3816464 has been identified in Chapter 4 as a low-gravity M9 γ candidate member of TWA, as part of the initial follow-up of the BASS survey. They note that its kinematics are discrepant with TWA albeit its low probability of being a field contaminant: its kinematics would match with TWA if it was placed further away, however this would make it over-luminous compared to young BDs of the same spectral type and age. It could be expected that this is a contaminant from the Lower-Centaurus-Crux region (LCC; ∼10–20 Myr; de Zeeuw et al. 1999) of the Scorpius-Centaurus complex, but its distance ($\sim$ 120 pc) would also make it over-luminous. It is possible that this object could be an unresolved binary and located further away, between TWA and LCC: this is reminiscent of TWA 29 and TWA 31, and might strengthen the proposition of Song et al. (2003; see also Schneider et al. 2012a) that TWA could actually be part of the LCC.

2MASS J14252798–3650229 has been identified as an L5 BD by Faherty et al. (2009). Including RV and trigonometric distance measurements from Blake et al. (2010) and Riedel et al. (2014) respectively, we find a 99.6% probability that this object is a member of ABDMG, with 0.1% contamination probability. Only signs of youth need to be confirmed before we can consider this object a bona fide member of ABDMG, however we note that its has NIR colors $J - K_S = 1.94$, at 1σ redder than field L5 dwarfs, which could be an indication of youth.

2MASS J17571539+7042011 (LP 44–162) has been identified as an M7.5 dwarf by Gizis et al. (2000). Tanner et al. 2010 and Terrien et al. 2012 measured its radial velocity, which we combine in an error-weighted mean to obtain $-12.4 \pm 0.6\,\mathrm{km\,s^{-1}}$. Lépine et al. (2009) measured a trigonometric distance of 19.1 ± 0.4 pc and report that it is significantly over-luminous

compared to dwarfs of the same colors, and propose that it might be an unresolved multiple. We find a bayesian probability of 91.0% that this is a member of ARG. However, Deshpande et al. (2012) obtained high-resolution NIR spectroscopy and report pseudo-equivalent widths of K I lines in the J band which are consistent with M7.5 field dwarfs (Allers & Liu 2013). It is thus plausible that this object is a false positive in our analysis, despite its high probability.

SIMP J21543454–1055308 has been independently discovered in the SIMP survey for field BDs (Artigau et al. 2009; J. Robert et al., in preparation). A NIR spectroscopic follow-up revealed that this object is a low-gravity L4 β BD with an estimated mass of $10 \pm 0.5\,M_{\rm Jup}$, well into the planetary regime, if it is a member of ARG as suspected (Chapter 5).

2MASS J23225384+7847386 has been identified as an M5 proper motion companion to V 368 Cep and LSPM J2322+7847 by Makarov et al. (2007). Using the X-ray luminosity of V 368 Cep as well as an isochrone analysis on all three components, they estimated an age of ~ 50 Myr for the system. Using the RV measurement from Kharchenko et al. (2007), and combined trigonometric distances measurements from Kharchenko et al. (2007) and Dittmann et al. (2014), we find that this object has a 29.7% probability of being a member of CAR, with a contamination probability of 1.0%. The estimated age of this system is consistent with that of CAR, which makes it a compelling candidate member, even if its bayesian probability is somewhat low. This low probability is a consequence of its galactic position $XYZ = (-8.7 \pm 2.5, 16.1 \pm 4.6, 5.5 \pm 1.6)$ pc, at 2.5σ of our spatial model for CAR. We note however that its kinematics are a very good match to CAR with $UVW = (-10.1 \pm 5.2, -23.5 \pm 2.9, -6.3 \pm 1.0)$, at only 0.5σ of our kinematic model. This could be an indication that CAR is in fact spatially larger than our present model, which would not be surprising since it was built from the only 7 currently known bona fide members. We thus suggest that 2MASS J23225384+7847386 is probably a member in CAR, and that we might be currently missing more objects like this one as a result of our spatial and kinematic model for this association being too narrowly confined. Finding additional objects like this one will be needed to better constrain the SKM of CAR. Montes et al. (2001) suggested that V 368 Cep is a member of the Pleiades moving group (PMG; also called the Local Association), however we find that its kinematics are much more consistent with those of CAR, at only $1.5\,{\rm km\,s^{-1}}$ of our dynamical model, compared to

a difference of $5.5\,\mathrm{km\,s^{-1}}$ with the kinematics of the PMG (Montes et al. 2001). Famaey et al. (2005) demonstrated that the PMG is likely a dynamical stream with a large spread in age rather than a coeval moving group, hence the age constraint acts as a further indication that a membership to CAR is more likely.

3.6 Recovery of known candidates and members of young moving groups

In this Section, we assess the fraction of known $\geq$ M5 candidate members of YMGs that are recovered in the BASS and LP-BASS catalogs. We identified a total of 98 candidate members of the YMGs considered here in the literature (Schlieder et al. 2012b; Shkolnik et al. 2012; Malo et al. 2013; Rodriguez et al. 2013; Chapter 2; Kraus et al. 2014b and references therein). We do not include low-probability candidates from Chapter 2 here, since they have a contamination probability of $>50\%$ by definition, which ensures that they are not listed in the BASS catalog. We find that a total of 55/98 of all these candidates are recovered in BASS (see Table 3.3), whereas 8 others are recovered in LP-BASS (see the Appendix), hence making up for 64% of currently known candidate members. All 35 candidates not recovered here are listed in Table 3.4, along with a list of the filters which caused them to be rejected. We note that 17 of those 36 candidates were missed only because they were cut from our input sample because of quality filters (i.e. low galactic latitude, low proper motion, large number of 2MASS neighbors, poor 2MASS or AllWISE photometric quality or NIR colors too blue), whereas 18 were missed at least because of a low bayesian probability, high contamination probability or position in a CMD diagram derived from its statistical distance. Considering only the known candidate members that were part of our input search sample, the BASS and LP-BASS catalogs thus recover 68% of them.

Table 3.3. Candidates With Additional Information in the Literature.

2MASS Name	Measured SpT[a]	Signs of Youth[b]	RV ($km\,s^{-1}$)	Trig. Dist. (pc)	Multiplicity[c]	Known Membership	Updated Membership	Updated Prob. (%)
00011217+1535355	L4:[51]	...	...	...	...	...	ABDMG	77.8
00040288-6410358	L1γ[49]	OR[49]	...	...	...	THA[49,31]	THA	> 99.9
00065794-6436542	M9:[82]	OH[72]	...	...	...	THA[31]	THA	> 99.9
00160844-0043021	L5.5[51]	...	...	...	...	...	BPMG	19.1
00192626+4614078	M8[94]	LH[83,94]	-19.5 ± 3.0[83]	...	...	ABDMG[92,31]	ABDMG	92.1
00212774-6351081	M5.5[50]	...	...	...	...	...	THA	99.8
00235732-5531435	M4.1[53]	...	5.3 ± 0.7[53]	...	...	THA[53]	THA	99.8
00325584-4405058	L0γ[16,71]	OITRH[16,71]	...	26.4 ± 3.3[28]	...	BPMG[31]	BPMG	97.7
00354313+0233137	M5+M6[55]	...	...	...	AB[55]	...	ABDMG	88.4
00374306-5846229	L0γ[82,16]	OR[16]	...	...	...	THA[31]	THA	99.9
00390342+1330170	...	XN[92]	...	...	...	ABDMG[92]	BPMG	91.9
00413538-5621127	M6.5+M9[94]	VHLA[90]	2.8 ± 1.9[83,34,31]	...	AB[94]	THA[31]	THA	> 99.9
00452143+1634446	L2β[82,16]	OITRH[16]	3.3 ± 0.2[4]	17.5 ± 0.6[114]	...	ARG[31]	ARG	98.0
00464841+0715177	M9[82,118]	...	...	...	...	...	BPMG	77.0
00514081-5913320	M4.4[53]	...	6.3 ± 1.3[53]	...	...	THA[53]	THA	99.9
01033203+1935361	L6β[28,119]	OITR[27,28]	...	21.3 ± 3.4[28]	...	ARG[31]	ARG	78.2
01033563-5515561	M5.5[19,53]	OHU[19,89]	5.2 ± 1.6[68,53]	47.2 ± 3.1[89]	AB[19]	THA;CAR[19,89]	THA	99.9
01134031-5939346	M5.0[53]	...	11.9 ± 6.7[53]	...	...	THA[53]	THA	99.7
01174748-3403258	L1β[14,2]	TRM[7,112,2]	...	...	...	THA[31]	THA	99.6
01180670-6258591	M5.1[53]	L[53]	9.3 ± 1.3[53]	...	...	THA[53]	THA	> 99.9
01231125-6921379	M8[94]	UL[83]	10.9 ± 3.0[83]	42.2 ± 4.8[87]	...	THA[31d]	THA	> 99.9
01243060-3355014	M4.5[89]	OU[89]	18.3 ± 0.5[100]	25.3 ± 0.8[100,89]	C[106]	ABDMG[88,100d]	ABDMG	> 99.9
01294256-0823580	M5[81]	...	...	...	...	...	BPMG	66.2
01344601-5707564	M4.9[53]	L[53]	11.1 ± 6.3[53]	...	...	THA[53]	THA	99.8
01372781-4558261	M5.0[53]	L[53]	13.5 ± 1.4[53]	...	...	THA[53]	THA	97.8
01415823-4633574	L0γ[120,16]	OITRHM[120,16]	12.0 ± 15.0[53]	...	...	THA[31]	THA	99.5
01443191-4604318	M5.5[76]	...	...	...	...	...	THA	99.1

Table 3.3 — continued

2MASS Name	Measured SpT[a]	Signs of Youth[b]	RV ($km\,s^{-1}$)	Trig. Dist. (pc)	Multiplicity[c]	Known Membership	Updated Membership	Updated Prob. (%)
01504543-5716488	M5.5[53]	L[53]	9.3 ± 1.7[53]	···	···	THA[53]	THA	> 99.9
01531463-6744181	L2:[82]	···	···	···	···	···	THA	99.9
01532494-6833226	M5.1[90,53]	N[90]	9.8 ± 1.4[53]	···	···	THA[90,53]	THA	> 99.9
02153328-5627175	M5.4[90,53]	LN[53]	11.3 ± 5.7[53]	···	···	THA[90,53]	THA	99.8
02180960-6657524	M4.5[53]	L[53]	11.0 ± 1.2[53]	···	···	THA[53]	THA	> 99.9
02192210-3925225	M4.9[53]	L[53]	10.6 ± 0.7[53]	···	···	THA[53]	THA	> 99.9
02212859-6831400	M8:[82]	OR[27]	···	39.4 ± 5.6[28]	···	···	ABDMG	40.8
02215494-5412054	M8β[82,27]	OR[16]	···	···	···	THA[31]	THA	99.8
02235464-5815067	L0 γ[82,27]	OR[82]	···	···	···	THA[31]	THA	> 99.9
02251947-5837295	M9[82,27]	O[82]	···	···	···	THA[31]	THA	99.9
02294869-6906044	M4.6[53]	L[53]	13.0 ± 1.2[53]	···	···	THA[53]	THA	> 99.9
02321934-5746117	M4.4[90,53]	···	11.2 ± 0.7[53]	···	···	THA[53]	THA	> 99.9
02340093-6442068	L0 γ[29]	OR[29]	···	···	···	THA[49,31]	THA	99.8
02401209-5305527	M9.5[72]	···	···	···	···	···	THA	99.9
02411151-0326587	L0 γ[64,15,16,48]	OTR[15,16,2]	···	46.7 ± 5.7[114]	···	THA[31]	THA	98.3
02435103-5432194	M9[82]	···	···	···	···	···	THA	99.9
02501167-0151295	···	···	···	33.1 ± 4.9[107]	···	···	BPMG	88.3
02523550-7831183	M4.4[53]	···	12.8 ± 1.3[53]	···	···	THA[53]	THA	98.6
02534448-7959133	M5.5[76]	H[56]	···	···	···	···	BPMG	50.1
03014892-5903021	M9[82,72]	···	···	···	···	···	THA	99.9
03032042-7312300	L2 γ[49]	OR[49]	···	···	···	THA[49,31]	THA	78.2
03050556-5317182	M5.4[90,53]	N[90]	12.1 ± 2.2[53]	···	···	THA[90,53]	THA	99.9
03093877-3014352	M4.7[53]	L[53]	12.5 ± 2.3[53]	···	···	THA[53]	THA	99.9
03114544-4719501	M4.3[90,53]	N[90]	11.3 ± 0.5[53]	···	···	THA[90,53]	THA	> 99.9
03152363-5342539	M5.2[90]	N[90]	···	···	···	THA[90]	THA	99.9
03164512-2848521	L0:[14]	···	···	···	···	···	ABDMG	77.2
03231002-4631237	L0 γ[82,27]	ORL[16]	···	···	···	THA[31]	THA	99.7

Table 3.3 — continued

2MASS Name	Measured SpT[a]	Signs of Youth[b]	RV ($km\,s^{-1}$)	Trig. Dist. (pc)	Multiplicity[c]	Known Membership	Updated Membership	Updated Prob. (%)
03252938-4312299	M9[82,72]	...	...	...	...	...	THA	78.9
03264225-2102057	L4[15]	ORL[15]	...	...	...	ABDMG[31]	ABDMG	98.9
03363144-2619578	M5.7[90]	N[90]	...	43.5 ± 3.8[89]	...	THA[90]	THA	99.9
03390160-2434059	M5.9[90]	N	...	...	...	COL[90]	COL	77.8
03393521-3525440	L0β[2,44,27]	TLM[27,112,2]	9.3 ± 1.7[83,77]	6.41 ± 0.04[22]	...	CAS[86,31]	ARG	87.6
03421621-6817321	L2:[15]	R[27]	...	...	...	THA[31]	THA	99.7
03550477-1032415	M8.5[14,27]	...	...	...	...	...	BPMG	39.5
03552337+1133437	L5 γ[82,27]	OITRL[16]	11.9 ± 0.2[4]	9.1 ± 0.1[61,28]	AB[3]	ABDMG[61,31d]	ABDMG	99.7
03572695-4417305	M9 β+L1.5β[60]	OR[16]	...	...	AB[60]	THA[31]	THA	99.9
03582255-4116060	L5[82,27]	...	...	...	...	...	BPMG	36.8
04174743-2129191	M8[15,27]	...	...	...	...	...	THA	57.7
04210718-6306022	L5 γ[82,27]	OIRL[15]	...	...	...	ARG;BPMG[31]	ARG	97.7
04362788-4114465	M8 γ[15,2]	OITR[15.2]	...	...	...	COL[31]	COL	97.6
04433761+0002051	M9 γ[15,2]	OITVRHL[27,72,31,2]	17.1 ± 3.0[83]	...	...	BPMG[31,92]	BPMG	99.8
04532647-1751543	L3:[14]	...	...	...	...	...	COL	95.8
04533604-2835349	...	...	22.5 ± 6.7[52]	...	...	...	COL	87.6
05002100+0330501	L3 γ[82,27]	...	15.9 ± 0.2[4]	...	...	...	ABDMG	62.8
05012406-0010452	L3 γ[82,16,2]	OTRL[27]	...	14.7 ± 2.8[28,114]	...	FIELD[31]	CAR	97.7
05120636-2949540	L4:[14]	R[48]	...	...	...	BPMG[31]	BPMG	33.8
05181131-3101529	M6.5[12]	...	...	...	...	...	COL	93.7
05361998-1920396	L2 γ[29]	OITR[29,2]	...	39.0 ± 14.0[28]	...	COL[31]	COL	96.6
06022216+6336391	L1:[82]	...	...	...	...	...	ABDMG	26.1
06420559+4101599	L/Tp[65]	R[65]	...	...	...	ABDMG[31]	ABDMG	38.4
06524851-5741376	M8β[82,27]	OR[82,27]	...	32.0 ± 3.3[28]	AB[10]	ABDMG[31]	CAR	87.9
08095903+4434216	L6[51,116]	...	...	...	...	...	ARG	30.7
09455843-3253299	M4.5[85]	X[85]	...	...	...	...	ARG	89.2

Table 3.3 — continued

2MASS Name	Measured SpT[a]	Signs of Youth[b]	RV ($km\,s^{-1}$)	Trig. Dist. (pc)	Multiplicity[c]	Known Membership	Updated Membership	Updated Prob. (%)
09532126-1014205	L0[15]	...	...	...	...	...	CAR	63.7
10284580-2830374	M5[96]	...	...	...	...	TWA[96]	TWA	96.3
10582800-1046304	M4[91]	...	...	...	...	...	TWA	4.3
10584787-1548172	L3[36]	...	...	17.3 ± 0.3[18]	...	...	ARG	93.1
11020983-3430355	M8.5 γ[28,116]	...	...	56.4 ± 1.6[104]	...	TWA[116]	TWA	99.8
11393382-3040002	M4.7[96]	...	...	...	...	TWA[96]	TWA	99.0
11395113-3159214	M8 γ[38,82,2]	OITRM[38,112]	11.2 ± 2.0[69]	28.5 ± 3.5[28]	...	TWA[38,69d]	TWA	99.8
12073346-3932539	M8[48]	ORL[48,17,2]	...	52.3 ± 1.1[24]	Ab[10]	TWA[38,69d]	TWA	99.6
12074836-3900043	L1γ[32]	OITR[32]	...	...	...	TWA[32]	TWA	99.7
12474428-3816464	M9γ[32]	ITR[32]	...	...	...	TWA[32]	TWA	47.1
13262009-2729370	L5[38,82]	...	...	...	...	...	ARG	23.3
14252798-3650229	L5[51,82]	...	5.4 ± 0.3[4]	11.6 ± 0.1[22]	...	...	ABDMG	99.6
17571539+7042011	M7.5[37]	U[57]	-12.4 ± 0.6[103,20]	19.1 ± 0.4[57]	...	...	ARG	91.0
19564700-7542270	L0γ[15]	OR[90]	...	...	...	THA[31]	THA	85.2
20004841-7523070	M9[94]	OR[90]	11.8 ± 1.0[34]	...	...	CAS;BPMG[34,31]	BPMG	98.2
20111744-2917584	M5.5[81]	...	...	...	...	...	ARG	49.3
20224803-5645567	M5.5[12]	...	...	...	...	...	THA	59.2
20291446-5456116	M4.3[53]	...	-1.4 ± 1.2[53]	...	...	THA[53]	THA	71.4
20330186-4903105	...	...	...	16.3 ± 5.0[89]	...	...	BPMG	99.1
20334670-3733443	M5[81]	...	...	...	...	...	BPMG	80.0
20414283-3506442	L2:[15]	...	...	...	...	...	ABDMG	14.4
20423672-5425263	M4.0[53]	...	-1.4 ± 1.7[53]	...	...	THA[53]	THA	94.8
21083826-4244540	M4.4[53]	...	-4.9 ± 1.9[53]	...	...	THA[53]	THA	84.4
21265040-8140293	L3γ[82]	OR[90]	...	...	...	THA[31]	THA	85.1
21420580-3101162	L2[58,27,8]	...	...	...	...	...	ABDMG	12.6
21490499-6413039	M4.5[85,53]	X[85]	0.4 ± 5.1[53]	...	...	THA[53]	THA	99.7
21543454-1055308	L4β[33]	ITR[33]	...	...	...	ARG[33]	ARG	58.6

Table 3.3 — continued

2MASS Name	Measured SpT[a]	Signs of Youth[b]	RV ($km\,s^{-1}$)	Trig. Dist. (pc)	Multiplicity[c]	Known Membership	Updated Membership	Updated Prob. (%)
22060961-0723353	M5.5[78]	···	···	···	···	···	ABDMG	82.1
22064498-4217208	L2[14]	R[14]	···	···	···	ABDMG[31]	ABDMG	95.2
22244102-7724036	M4.2[53]	···	8.5 ± 1.4[53]	···	···	THA[53]	THA	99.2
22400144+0532162	···	···	···	23.6 ± 2.7[23]	···	···	BPMG	79.0
22443167+2043433	L6γ[82,2]	ITRLM[90]	···	···	···	ABDMG[31]	ABDMG	99.8
22444835-6650032	M4.8[53]	L[53]	0.7 ± 1.7[53]	···	···	THA[53]	THA	99.7
22583200+1014589	···	···	···	23.1 ± 1.4[23]	···	···	ABDMG	98.3
23130558-6127077	M4.5[53]	L[53]	2.9 ± 2.3[53]	···	···	THA[53]	THA	99.8
23225240-6151114	M5[31]	···	···	···	A[31]	THA[31]	THA	98.7
23225299-6151275	L2 γ[82]	OR[16]	···	···	B[31]	THA[31]	THA	> 99.9
23225384+7847386	M5[66]	UC[66]	-17.0 ± 1.3[46]	19.1 ± 5.5[66,23]	B[66]	Pleiades[74]	CAR	29.7
23255604-0259508	L3[8]	···	···	···	···	···	ABDMG	29.8
23392527+3507165	L3.5[82,8]	···	···	···	···	···	BPMG	10.6
23424333-6224564	M4.3[53]	···	5.1 ± 4.6[53]	···	···	THA[53]	THA	99.6
23520507-1100435	M7[14,58,15]	···	···	···	···	···	ABDMG	42.0

[a]The β and γ symbols stand for low-gravity and very low-gravity, p stands for peculiar, and a semi-colon indicates an uncertain spectral type.

[b]A capital letter means the object displays the associated sign of youth. O: lower-than normal equivalent width of atomic species in the optical spectrum, I: same but in the NIR spectrum, T: a triangular-shaped H-band continuum, V: high rotational velocity, X: X-ray emission, R: redder-than-normal colors for given spectral type, U: over luminous, H: Hα emission, L: Li absorption, A: signs of accretion, M: signs of low gravity from atmospheric models fitting, N: bright NUV emission and C: Companion to a young star. A question mark following a flag indicates that the result is uncertain.

[c]AB: Unresolved binary, B or C: Resolved companion.

[d]Bona fide member.

References to the table :

(1) Allen et al. 2007; (2) Allers & Liu 2013; (3) Bernat et al. 2010; (4) Blake et al. 2010; (5) Bochanski et al. 2005; (6) Boyer et al. 2011; (7) Burgasser et al. 2008a; (8) Burgasser et al. 2010; (9) Caballero 2007; (10) Chauvin et al. 2012; (11) Costa et al. 2005; (12) Crifo et al. 2005; (13) Cruz & Reid 2002; (14) Cruz et al. 2003; (15) Cruz et al. 2007; (16) Cruz et al. 2009; (17) da Silva et al. 2009; (18) Dahn et al. 2002; (19) Delorme et al. 2013; (20) Terrien et al. 2012; (21) Dhital et al. 2011; (22) Dieterich et al. 2014; (23) Dittmann et al. 2014; (24) Ducourant et al. 2008; (25) Dupuy & Liu 2012; (26) Finder Charts; (27) Faherty et al. 2009; (28) Faherty et al. 2012; (29) Faherty et al. 2013b; (30) Forveille et al. 2005; (31) Gagné et al. 2014c; (32) Gagné et al. 2014a; (33) Gagné et al. 2014b; (34) Gálvez-Ortiz et al. 2010; (35) Gatewood & Coban 2009; (36) Geballe et al. 2002; (37) Gizis et al. 2000; (38) Gizis 2002; (39) Gould & Chanamé 2004; (40) Guenther & Wuchterl 2003; (41) Gizis et al. 1997; (42) Hearty et al. 1999; (43) Janson et al. 2012; (44) Jenkins et al. 2009; (45) Kendall et al. 2007a; (46) Kharchenko et al. 2007; (47) Khovritchev et al. 2013; (48) Kirkpatrick et al. 2008; (49) Kirkpatrick et al. 2010; (50) Kirkpatrick et al. 2011; (51) Knapp et al. 2004; (52) Kordopatis et al. 2013; (53) Kraus et al. 2014b; (54) Lane et al. 2011; (55) Law et al. 2008; (56) Lee et al. 2010; (57) Lépine & Simon 2009; (58) Liebert & Gizis 2006; (59) Liu et al. 2008; (60) Liu et al. 2010; (61) Liu et al. 2013a; (62) Liu et al. 2013b; (63) Looper et al. 2007a; (64) Luhman et al. 2009; (65) Mace et al. 2013a; (66) Makarov 2007; (67) Malo et al. 2013; (68) Malo et al. 2014a; (69) Mamajek 2005; (70) Mann et al. 2013b; (71) Marocco et al. 2013; (72) Martín et al. 2010; (73) Mason et al. 2001; (74) Montes et al. 2001; (75) Newton et al. 2014; (76) Phan-Bao & Bessell 2006; (77) Reid et al. 2002; (78) Reid et al. 2003; (79) Reid et al. 2004; (80) Reid et al. 2006; (81) Reid et al. 2007; (82) Reid et al. 2008b; (83) Reiners & Basri 2009; (84) Reylé et al. 2006; (85) Riaz et al. 2006; (86) Ribas 2003; (87) A. R. Riedel et al., in preparation; (88) Riedel 2012a; (89) Riedel et al. 2014; (90) Rodriguez et al. 2013; (91) Rojas-Ayala et al. 2012; (92) Schlieder et al. 2012a; (93) Schlieder et al. 2012b; (94) Schmidt et al. 2007; (95) Schmidt et al. 2010; (96) Schneider et al. 2012b; (97) Schneider et al. 2014; (98) Seifahrt et al. 2010; (99) Shkolnik et al. 2009; (100) Shkolnik et al. 2012; (101) Zwitter et al. 2008; (102) Subasavage et al. 2005; (103) Tanner et al. 2010; (104) Teixeira et al. 2008; (105) Bonnefoy et al. 2009; (106) Thé & Staller 1974; (107) Tinney 1996; (108) Tinney 1996; (109) van Leeuwen 2007a; (110) Vrba et al. 2004; (111) West et al. 2008; (112) Witte et al. 2011; (113) Zacharias et al. 2012; (114) Zapatero Osorio et al. 2014; (115) Nidever et al. 2002; (116) Scholz et al. 2005; (117) Chiu et al. 2006; (118) Wilson et al. 2003; (119) Kirkpatrick et al. 2000; (120) Kirkpatrick et al. 2006.

3.7 The updated BASS sample

We present in Table 3.5 a complete list of the BASS sample, which contains only objects respecting all criteria mentioned in Sections 3.3–3.4 after taking account of all information available in the literature. We list in this table all the contamination probability of all objects, obtained from the Monte Carlo analysis described in Section 3.4, as well as statistical estimates for their distance and RV. We refer to this list as the BASS sample for the remainder of this work. We used the individual contamination probability of all candidate members to estimate an average contamination fraction from field stars of 2.4% and 29.5% for the high probability and modest probability samples, respectively. These estimates of contamination do not take account of possible cross-contamination between the YMGs considered here, or other, older nearby associations not considered, e.g. Carina-Near ($\sim$ 200 Myr; Zuckerman et al. 2006), the Ursa Major moving ($\sim$ 500 Myr; King et al. 2003) and the Hercules-Lyrae moving group ($\sim$ 250 Myr; Eisenbeiss et al. 2013). Another way to assess a minimal contamination rate is to count the fraction of candidates with RV, distance or spectra in the literature which were rejected from these measurements. This estimate yields a larger contamination rate of 12.6% (11/87) for the high probability candidates. Small number statistics prevent an accurate estimation for the low-probability candidates: only 37 had such measurements in the literature, from which 4 were rejected. We rather choose to scale the observed 12.6% contamination fraction of the high-probability sample with the ratio of predicted contamination fractions of both samples to estimate a more reliable expected contamination fraction of $\sim$ 71% for the modest probability BASS sample.

In Figures 3.14–3.20, we compare proper motions and sky positions of the BASS sample with currently known bona fide members of YMGs; it can be seen that, as expected, trajectories of candidates in the BASS sample projected on the celestial sphere are consistent with known bona fide members. In Figure 3.3, we use the statistical distances from BANYAN II to display the position of candidates of the BASS sample in two color-magnitude diagrams: absolute $W1$ as a function of $H - W2$, and absolute $W1$ as a function of $J - K_S$. These two CMDs are used as observable in the BANYAN II tool as they are useful to distinguish young $>$ M5 dwarfs from their field counterparts. In Figures 3.21–3.27, we compare the statistical

Table 3.4. Known YMG Candidate Members not Recovered in BASS.

2MASS Designation	Measured SpT[a]	Known Candidacy	Reason for Rejection[b]
00332386-1521309	L4 β	ARG[31]	$HW2_{CMD}$
00470038+6803543	L7p	ABDMG[31]	b, $2M_{\#}$
01112542+1526214	M5+M6	βPMG[67]	$W1_{SAT}$
01291221+3517580	L4	ARG[31]	$HW2_{CMD}$
01424687-5126469	M6.5	COL[90]	$J-H$, $2M_{PH}$, $\sigma\mu$, μ, P, C
02535980+3206373	M7p	βPMG[31]	$HW2_{CMD}$, P
03214475-3309494	M5.8	COL[90]	$V-J$, $2M_{PH}$, P, C
03244305-2733230	M5.5	COL[90]	K_S-W1, μ, P, C
03350208+2342356	M8.5	βPMG[100]	$W1_{SAT}$, $W2_{SAT}$, C
04062677-3812102	L0 γ	COL[31]	P, C
05184616-2756457	L1 γ	COL[31]	μ
06195260-2903592	M6	COL[31]	μ
06322402-5010349	L3	ABDMG[31]	$HW2_{CMD}$, $\sigma\mu$, C
07285117-3015527	M5	ABDMG[100]	b, $W1_{SAT}$, $2M_{\#}$
09445422-1220544	M5	ARG[67]	$W1-W2$, $W1_{SAT}$
10042066+5022596	L3 β	ABDMG[31]	$W1_{SAT}$, P, C
10172689-5354265	M5	βPMG[105]	b, $J-H$, $W1_{SAT}$, $2M_{\#}$
11321831-3019518	M5	TWA[67]	$H-K_S$, K_S-W1
11324116-2652090	M5	TWA[69]	$H-K_S$, K_S-W1, $2M_{CC}$, $W1_{SAT}$, W_{CC}
12242443-5339088	M5	βPMG[67]	b, K_S-W1, $HW2_{CMD}$, $2M_{\#}$
12451416-4429077	M9.5p	TWA[31]	$2M_{\#}$
13142039+1320011	M7	ABDMG[93]	P
16002647-2456424	M7.5p	ABDMG[31]	JK_{CMD}, $HW2_{CMD}$, USco, $2M_{\#}$, P, C
16471580+5632057	L9p	ARG[31]	P, C
17410280-4642218	L7p	βPMG;ABDMG[97]	b, $2M_{CC}$, $2M_{\#}$
18450097-1409053	M5	ARG[67]	b, $W1-W2$, $2M_{CC}$, $2M_{PROX}$, $W1_{SAT}$, $W2_{SAT}$, $2M_{\#}$, P
21011544+1756586	L7.5	ABDMG[31]	$2M_{PH}$, $2M_{CC}$, $2M_{\#}$
21103096-2710513	M5	βPMG[67]	$WISE$
21140802-2251358	L7	βPMG[62]	$2M_{PH}$
21354554-4218343	M5.2	THA[53]	$B-V$, P, C
21374019+0137137	M5	βPMG[93]	$H-K_S$, $W1_{SAT}$
21481633+4003594	L6	ARG[31]	b, $2M_{\#}$
22081363+2921215	L3 γ	βPMG[31]	P, C
23204705-6723209	M5	THA[67]	$V-J$, $2M_{PH}$, $2M_{CC}$, $\sigma\mu$
23512200+3010540	L5.5	ARG[31]	$B-J$, χ^2_{W1}, $2M_{BL}$, $HW2_{CMD}$

[a]Measured in the NIR unless symbol otherwise specified.

[b]This column contains codes corresponding to the filters that rejected an object from the BASS catalog; (1) $WISE$ – No entry in the WISE and AllWISE catalogs, (2) b – Absolute Galactic latitude is too low, (3) $B-V$ color is too blue, (4) $B-J$ color is too blue, (5) $V-J$ color is too blue, (6) $J-H$ color is too blue, (7) $H-K_S$ color is too blue, (8) K_S-W1 color is too blue, (9) $W1-W2$ color is too blue, (10) χ^2_{W1} – the reduced χ^2 from the adjusted profile in the $W1$ band is too large, (11) $2M_{PH}$ – 2MASS photometric quality is too low, (12) $2M_{BL}$ – A blend flag is suspicious in 2MASS, (13) $2M_{CC}$ – A contamination flag is suspicious in 2MASS, (14) $2M_{PROX}$ – A close-by 2MASS source is unresolved in AllWISE, (15) $W1_{SAT}$ – $W1$ magnitude is saturated, (16) $W2_{SAT}$ – $W2$ magnitude is saturated, W_{CC} – A contamination flag is suspicious in AllWISE, (17) JK_{CMD} – The object falls to the left of the M_{W1} versus $J-K_S$ field sequence using its statistical distance, (18) $HW2_{CMD}$ – The object falls to the left of the M_{W1} versus $H-W2$ field sequence using its statistical distance, (19) Usco – The object is too close to Upper Scorpius, (20) $2M_{\#}$ – The object has too many immediate neighbours in 2MASS, (21) $\sigma\mu$ – the 2MASS–AllWISE proper motion is not precise enough, (22) μ – The proper motion is too low, (23) P – The Bayesian probability is too low, (24) C – The contamination probability is too high. See Sections 3.3–3.4 for detailed descriptions of these respective filters.

References to this table are identical to those of Table 3.3.

Table 3.5. The Complete BASS Catalog.

2MASS Designation	Spectral Type[a]	Probable Membership	Bayesian Prob. (%)	Contamination Prob. (%)	Estimated Mass Range ($M_{\rm Jup}$)	Statistical Distance (pc)	Statistical RV ($\rm km\,s^{-1}$)
Candidates with a High Probability							
00011217+1535355	L4:	ABDMG	77.8	1.8	$17.5^{+0.8}_{-1.1}$	27.3 ± 1.6	-6.5 ± 2.0
00040288-6410358	L1 γ	THA	> 99.9	< 0.1	12.8 ± 0.3	45.0 ± 2.4	6.5 ± 2.5
00041589-8747254	(M5.7)	THA	55.4	< 0.1	$60.9^{+8.8}_{-7.1}$	51.8 ± 3.6	11.3 ± 2.2
00065794-6436542	M9:	THA	> 99.9	< 0.1	$20.5^{+1.1}_{-13.9}$	41.4 ± 2.4	6.2 ± 2.4
00111532-3756553	(M5.7)	THA	80.2	< 0.1	$60.6^{+8.6}_{-6.7}$	$38.2^{+2.0}_{-2.4}$	1.5 ± 2.2
00182834-6703130	(M9.6)	THA	99.8	< 0.1	13.3 ± 0.3	$43.8^{+2.8}_{-2.4}$	6.9 ± 2.5
00191296-6226005	(M9.7)	THA	99.5	< 0.1	$13.3^{+0.3}_{-0.4}$	$46.6^{+2.4}_{-2.8}$	6.7 ± 2.5
00192626+4614078	M8	ABDMG	92.1	4.1	$87.1^{+8.5}_{-8.6}$	37.8 ± 3.2	-19.5 ± 3.0
00212774-6351081	M5.5	THA	99.8	< 0.1	$158.3^{+19.9}_{-18.5}$	$44.2^{+2.8}_{-2.4}$	6.8 ± 2.4
00235732-5531435	M4.1	THA	99.8	< 0.1	$133.1^{+17.4}_{-14.6}$	41.4 ± 2.4	5.3 ± 0.7
00305785-6550058	(M3.3)	THA	99.1	< 0.1	$392.6^{+49.2}_{-44.1}$	$47.0^{+2.8}_{-3.2}$	7.4 ± 2.5
00325584-4405058	L0 γ	BPMG	97.7	0.2	12.2 ± 0.3	26.4 ± 3.3	11.2 ± 1.7
00344300-4102266	(L2.4)	THA	96.1	< 0.1	12.8 ± 0.3	42.2 ± 2.4	2.6 ± 2.2
00354313+0233137	M5+M6	ABDMG	88.4	1.5	$191.9^{+13.9}_{-11.8}$	26.9 ± 1.6	1.3 ± 2.0
00374306-5846229	L0 γ	THA	99.9	< 0.1	$13.9^{+0.4}_{-0.3}$	46.6 ± 2.8	6.8 ± 2.4
00390342+1330170	(M5.1)	BPMG	91.9	11.3	$88.2^{+5.7}_{-5.4}$	$29.7^{+2.4}_{-2.8}$	0.1 ± 1.7
00413538-5621127	M6.5+M9	THA	> 99.9	< 0.1	$78.6^{+10.2}_{-9.6}$	$39.8^{+2.0}_{-2.4}$	2.8 ± 1.9
00452143+1634446	L2 β	ARG	98.0	0.1	$14.7^{+0.3}_{-0.1}$	17.5 ± 0.6	3.3 ± 0.2
00514081-5913320	M4.4	THA	99.9	< 0.1	$128.9^{+16.9}_{-14.5}$	$43.4^{+2.4}_{-2.8}$	6.3 ± 1.3
00525451-6624501	(L0.3)	ABDMG	11.8	< 0.1	$31.0^{+2.0}_{-2.4}$	55.0 ± 4.8	23.8 ± 1.8
01033203+1935361	L6 β	ARG	78.2	0.2	10.4 ± 0.4	21.3 ± 3.4	8.6 ± 2.2
01033563-5515561	M5.5	THA	99.9	< 0.1	$320.6^{+40.2}_{-37.4}$	47.2 ± 3.1	5.2 ± 1.6
01075572-6030194	(M5.3)	THA	99.6	< 0.1	$85.7^{+11.1}_{-8.9}$	42.2 ± 2.4	8.2 ± 2.4
01134031-5939346	M5.0	THA	99.7	< 0.1	$207.8^{+2.6}_{-1.3}$	43.0 ± 3.2	11.9 ± 6.7
01174748-3403258	L1 β	THA	99.6	< 0.1	13.5 ± 0.3	39.0 ± 2.0	4.7 ± 2.1
01180670-6258591	M5.1	THA	> 99.9	< 0.1	$105.1^{+13.7}_{-11.7}$	$42.2^{+2.4}_{-2.8}$	9.3 ± 1.3
01205114-5200349	(L2.5)	THA	99.9	< 0.1	12.8 ± 0.3	41.0 ± 2.4	7.6 ± 2.2
01231125-6921379	M8	THA	> 99.9	< 0.1	$65.2^{+9.6}_{-8.6}$	42.2 ± 4.8	10.9 ± 3.0
01243060-3355014	M4.5	ABDMG	> 99.9	0.1	$167.6^{+14.6}_{-13.4}$	25.3 ± 0.8	18.3 ± 0.5
01265327-5505506	(M5.3)	THA	99.8	< 0.1	$77.2^{+10.5}_{-8.8}$	$42.6^{+2.4}_{-2.8}$	8.2 ± 2.4
01294256-0823580	M5	BPMG	66.2	< 0.1	$122.9^{+8.4}_{-8.8}$	32.5 ± 3.2	9.2 ± 1.7
01320814-6023536	(M4.5)	THA	99.8	< 0.1	$126.0^{+16.3}_{-14.1}$	45.4 ± 2.8	9.2 ± 2.4
01344601-5707564	M4.9	THA	99.8	< 0.1	$76.2^{+10.5}_{-8.8}$	$43.4^{+2.8}_{-3.2}$	11.1 ± 6.3
Candidates with a Modest Probability							
00160844-0043021	L5.5	BPMG	19.1	36.1	9.6 ± 0.3	$30.9^{+2.8}_{-3.2}$	3.3 ± 1.8
00274534-0806046	(M5.3)	BPMG	45.6	35.1	66.9 ± 4.2	32.1 ± 2.8	4.4 ± 1.5
00464841+0715177	M9	BPMG	77.0	26.9	$15.0^{+0.1}_{-0.3}$	$33.8^{+2.8}_{-3.2}$	3.2 ± 1.7
00581143-5653326	(L6.1)	ARG	80.4	32.9	$10.3^{+0.7}_{-0.3}$	$25.3^{+2.8}_{-2.4}$	2.6 ± 2.0
01525534-6329301	(M4.7)	BPMG	71.4	22.1	$107.6^{+6.8}_{-7.8}$	23.7 ± 2.4	14.7 ± 1.7
02534448-7959133	M5.5	BPMG	50.1	30.9	66.9 ± 4.9	$28.9^{+2.8}_{-3.2}$	12.0 ± 2.1
03390160-2434059	M5.9	COL	77.8	31.9	$204.7^{+6.6}_{-3.5}$	$59.4^{+5.6}_{-6.0}$	18.6 ± 1.8
03473987-4114014	(M5.3)	COL	38.0	45.4	$77.2^{+11.0}_{-10.5}$	$71.0^{+8.8}_{-8.0}$	19.7 ± 1.7
03510460-5701469	(M5.1)	COL	17.6	47.4	$88.3^{+12.0}_{-11.7}$	$68.6^{+8.8}_{-8.0}$	19.1 ± 1.7
03550477-1032415	M8.5	BPMG	39.5	38.5	$26.4^{+3.5}_{-4.2}$	$35.0^{+4.4}_{-4.8}$	17.7 ± 1.8

[a]Spectral types in parentheses were estimated from 2MASS–AllWISE colors (see Section 3.5.1).

[b]The binary hypothesis is more probable than the single hypothesis (see Section 3.4).

This table is available in its entirety at *http://dx.doi.org/10.6084/m9.figshare.1207880*. The complete table has 252 rows.

predictions for galactic positions (XYZ) and space velocities (UVW) of all BASS candidates with those of currently known bona fide members of YMGs, as well as the 1.557σ contours of the SKM ellipsoids used in BANYAN II. We use 1.557σ as the 3-dimensional analog to 1σ in one dimension in the sense that it encompasses 68% of objects drawn from a gaussian random PDF.

3.7.1 Mass estimates

We used the YMG age and statistical distance associated to the most probable hypothesis from BANYAN II and the AMES-Cond isochrones (Baraffe et al. 2003) in combination with the CIFIST2011 BT-Settl atmosphere models (Allard et al. 2013; Rajpurohit et al. 2013) to estimate the mass of all candidates presented here. A uniform distribution spanning the age range of each YMG was used to compare their absolute J, H, K_S, $W1$ and $W2$ magnitudes with model isochrones in a maximum likelihood analysis. Mass estimates are listed in Table 3.5. The BASS sample comprises 79 new candidate young BDs and 22 candidate planetary-mass objects.

3.8 A search for new common proper motion pairs

Since the 2MASS and AllWISE catalogs provide a fast way to determine proper motions for a large number of targets, we performed a search for common proper motion objects around all candidates in the BASS sample. We used the BANYAN II statistical distance of each candidate to define a projected separation radius of 10,000 AU within which we have searched for any other object with a proper motion respecting the criteria of Lépine & Bongiorno (2007), albeit with a more conservative filter on allowed proper motion difference. This requires that the separation $\Delta\theta$ (measured in arc seconds) and the proper motion difference $\Delta\mu$ (measured in $\mathrm{mas\,yr^{-1}}$) obey the following equations :

$$\begin{aligned} \Delta\theta\ \Delta\mu &< 1,000 \cdot (\mu/150)^{3.8}, \\ \Delta\mu &< 50. \end{aligned} \tag{3.4}$$

These criteria should ensure that the majority of genuine proper motion pairs are recovered, with a minimal amount of contamination from chance alignments. This search allowed us to find 5 new common proper motion pairs and recover 10 which were already known in the literature. Those already known are :

- 2MASS J00451358+0015509* (M3.8) and 2MASS J00451098+0015117 (HD 4271); F8; Newton et al. 2014)
- 2MASS J01243060–3355014* (GJ 2022 B; M4.5) and 2MASS J01242767–3355086 (GJ 2022 AC; M5+M5; Thé & Staller 1974)
- 2MASS J02033222+0648588* (estimated M4.5) and 2MASS J02032589+0648008 (estimated early-M; Zacharias et al. 2012)
- 2MASS J02420204–5359147* (M4.6) and 2MASS J02420404–5359000 (estimated early-M; (Zacharias et al. 2012))
- 2MASS J03114240–1537183* (LP 722–14; estimated M5.0) and 2MASS J03114269–1537327 (LP 722–15; estimated M2.2; Luyten 1977)
- 2MASS J03283911–1537333* (GJ 3229 B; M3.5) and 2MASS J03283893–1537171 (GJ 3228 A; M3.5; Gliese & Jahreiß 1991)
- 2MASS J03505949+1414017* (M5) and 2MASS J03510078+1413398 (M4; Mason et al. 2001)
- 2MASS J21440795+1704372* (G 126–30; M4.5) and 2MASS J21440900+1703348 (G 126–31; M4; Mason et al. 2001)
- 2MASS J23225240–6151114* (M5) and 2MASS J23225299–6151275* (L2 γ; Chapter 2)
- 2MASS J23102196–0748531* (M5) and 2MASS J23102471–0748432 (HIP 114424; K0; Mann et al. 2014)

We identified components present in the BASS or LP-BASS catalogs with an asterisk. Any potentially useful information from these matches were already taken into account in Section 3.5. We discuss the new potential common proper motion pairs below :

2MASS J04353042–6449570 from BASS (estimated M8.4 with $J = 15.27$) seems to be co-moving with 2MASS J04352709–6450042 ($J = 15.16$) at an angular separation of $22\farcs4$ and a proper motion difference of 0.4 mas yr^{-1} (0.05σ) with respect to a total proper motion

of 53.2 mas yr^{-1}. However, we note that 2MASS J04352709–6450042 is only 0.11 magnitudes brighter in the J band, and yet its NIR colors are significantly bluer : it has $J-K_S = 0.42$ and $H-W2 = 0.02$, versus $J-K_S = 1.34$ and $H-W2 = 1.30$ for the BASS candidate. These very blue colors would be indicative of a spectral type earlier than M, which is not consistent with it being at the same distance from the primary, even if the latter was a multiple system. For this reason, BANYAN II rejects it as a probable candidate member of CAR, but if we do not include photometry, then its bayesian probability for CAR is 31.4%, with a contamination probability of 21.9%. We conclude nonetheless that the secondary is most probably not a member of CAR and that this system is possibly a chance alignment, since otherwise it would be hard to reconcile the very different colors and the similar apparent J magnitudes of its components. We note that Lépine & Bongiorno (2007) used their common proper motion criteria only on stars with $\mu > 150$ mas yr^{-1} hence it is possible that it does not perform as well on this system which has only $\mu = 53.2$ mas yr^{-1}.

2MASS J05121347+0131539 (NLTT 14667) from LP-BASS (estimated M4.9 with $J = 10.36$) seems to be co-moving with 2MASS J05121170+0131154 ($J = 16.39$) at an angular separation of $46\farcs8$ and a proper motion difference of 28.6 mas yr^{-1} (0.9σ) with respect to a total proper motion of 212.4 mas yr^{-1}. The contrast is significant with $\Delta J = 6.03$, which would point to a late-T spectral type for the secondary if it is at the same distance than the primary. However, we note that the secondary is most probably a contaminating object, since an extended PSF is visible within 10" of its 2MASS position in the red DSS filter.

2MASS J14415883–1649008 (WT 2090) from LP-BASS (M4.5 with $J = 10.23$) is co-moving with 2MASS J14415908–1653133 (Wolf 1501; M3 with $J = 9.35$) at an angular separation of $252\farcs5$ and a proper motion difference of 3.8 mas yr^{-1} (0.3σ) with respect to a total proper motion of 290.3 mas yr^{-1}. Kirkpatrick et al. (2010) obtained a NIR spectral type of M3 for Wolf 1501. We note that the contrast ratio $\Delta J = 0.88$ is large for their respective spectral types of M3 and M4.5. Both objects are weak candidate members of ABDMG, with respective bayesian probabilities of 5.4% and 3.8% and contamination probabilities of 23.4% and 26.9%.

2MASS J21500933+0558102 from LP-BASS (estimated M4.9 with $J = 10.66$) is co-

moving with 2MASS J21501011+0558137 from LP-BASS (estimated M4.9 with $J = 10.74$) at an angular separation of 12" and a proper motion difference of 21.9 mas yr^{-1} (0.8σ) with respect to a total proper motion of 146.9 mas yr^{-1}. Their contrast ratio is relatively small with $\Delta J = 0.08$, which is consistent with their similar estimated spectral types. The direction of their 2MASS–AllWISE proper motions is slightly different, which favors ARG for the primary and βPMG for the secondary. However, both have a somewhat ambiguous membership between ARG and βPMG; the primary has respective bayesian probabilities of 8.0% and 15.6%, whereas the secondary has 16.6% and 3.0%. We thus regard this system as an ambiguous, low-probability candidate member of βPMG and ARG.

2MASS J23133055–5352079 from LP-BASS (estimated M5.7 with $J = 12.08$) is comoving with 2MASS J23133024–5351389 (HD 219046; $J = 8.59$) at an angular separation of $29\farcs1$ and a proper motion difference of 17.0 mas yr^{-1} (1.5σ). The contrast ratio is consistent with the latter component being a K-type star. We find no additional information in the literature for this system.

3.9 A preliminary investigation of mass segregation

According to the virial theorem, it is expected that all components of a gravitationally bound astrophysical system will end up with the same average kinetic energy after relaxing to the equilibrium state. Hence, lower-mass members of associations of stars are expected to have a larger velocity than their higher-mass siblings; this effect is called mass segregation. It has already been demonstrated for globular clusters (Hasan & Hasan 2011; Olczak et al. 2011; Pang et al. 2013), however no signs of mass segregation have yet been identified for YMGs. The BASS catalog provides a unique sample on which to test for this effect, since it potentially contains the latest-type, lowest-mass members known to all YMGs.

Instead of relying on mass estimates which are dependent on physical hypotheses inherent to evolutionary models, we use statistical distance predictions from BANYAN II to obtain absolute $W1$ magnitudes for all high probability candidates in the BASS sample. Since members of YMGs are expected to be coeval, their absolute $W1$ magnitude should depend on their mass in a monotonic way, thus providing a more direct way to bring out mass segregation.

The AllWISE $W1$-band is preferred to 2MASS bands since it is less affected by clouds in the atmospheres of BDs, which could introduce errors in the absolute magnitude–mass relation. Since the UVW separation to the center of mass of a given YMG is directly related to the kinetic energy of a member with respect to the YMG, it is expected that mass segregation would cause fainter (less massive) objects to be more scattered in the UVW space (i.e. dynamical mass segregation). As a consequence of this, one would also expect that they be more scattered spatially at a given moment in the XYZ space (i.e. spatial mass segregation).

Allison et al. (2009b) devised a quantitative way to assess mass segregation in associations of stars, which is more sensitive than a simple visual characterization, and more importantly does not dependent on the geometry of the members' distribution. They base this characterization on the principle of *Minimum Spanning Trees* (MSTs). For a given distribution of coordinates (e.g. RA and DEC in a bi-dimensional space which is most often used in the case of open clusters), a MST is the shortest network of straight lines that connects all individual points without creating any loop. A mass segregation ratio (MSR) is then defined as :

$$\Lambda_{\rm MSR} = \frac{< l_{\rm norm} >}{l_{\rm massive}} \pm \frac{\sigma_{\rm norm}}{l_{\rm massive}}, \tag{3.5}$$

where $l_{\rm massive}$ is the total length of the MST of the N most massive stars in an association, and $< l_{\rm norm} >$ and $\sigma_{\rm norm}$ are respectively the average and standard deviation of a set of Monte Carlo simulations in which the MST network length is determined for a set of N stars randomly selected from the sample. If mass segregation is present, it is expected that $\Lambda_{\rm MSR}$ will have a value above unity. On the other hand, a value below unity would indicate that massive stars are more scattered than other members. We performed this analysis in both the the XYZ and UVW 3-dimensional spaces, using the algorithm described by Cartwright & Whitworth (2004) to build MSTs. We determined the MSR for values of N spanning 3 to the total number of stars in each YMG, using 100 random subsets in each Monte Carlo simulation. We show resulting MSTs for the full set of N high bona fide members and high probability BASS candidates of each YMG in Figures 3.8–3.9. We sorted stars according to

their increasing absolute $W1$ magnitudes instead of decreasing mass when we determined $\Lambda_{\rm MSR}$, for the reasons mentioned above. This was done for only bona fide members in a first step, and then for bona fide members and all high probability candidates of the BASS catalog taken together.

We show in Figures 3.10–3.11 the resulting MSRs as a function of N for only bona fide members of each YMG. A MSR larger than one indicates that massive stars are more concentrated towards the center of the distribution, whereas a MSR smaller than one indicates the inverse situation. In most cases with a large statistical significance, the MSR ratio is above unity, which is expected from the physical considerations mentioned above. ABDMG is the only case where both the maximal spatial and dynamical mass segregation are present at $> 2\sigma$, with 2.5σ and 2.4σ, respectively. βPMG displays a spatial mass segregation at 2.4σ and COL displays a dynamical mass segregation at 2.9σ. In some cases (βPMG, TWA and THA), an inverse spatial or dynamical mass segregation is apparent between 1σ and 2σ, but never at a larger statistical significance. The inclusion of high priority BASS candidates in this analysis (see Figures 3.12–3.13) generally increases the significance of the previous results, the only exception being COL. As a consequence, ABDMG, THA and COL display both a maximal dynamical and spatial mass segregation at 2–4σ in this situation. Spatial segregation is also apparent for ARG and BPMG at 3.2σ and 3.4σ, respectively. We note that in most cases which are statistically significant, mass segregation only starts appearing at masses lower than 0.3–0.5 $M_{\odot}$. However, we stress that a follow-up of the BASS sample must be completed before cases other than ABDMG can be considered as significant. We add that even in the case of ABDMG, securing more members will be necessary to increase the statistical significance of this tentative result.

Our analysis does not take account of two effects that could bias our results; (1) the selection criteria imposed to the BASS survey; and (2) the effect of unresolved binaries. To investigate the former effect, we performed a Monte Carlo simulation in which we have drawn a million synthetic objects from each SKM, and rebuilt 500 times the MST corresponding to a random subset of 100 synthetic objects. We repeated this with and without applying the selection filters described in Section 3.3 to assess whether they have any systematic effect on

the length of the MST. Any such systematic bias will only affect BASS candidates, which all have masses lower than currently known bona fide members. Hence, if this bias systematically shrinks the MST length, we will have underestimated mass segregation in the analysis described above, and vice versa. We found that our selection bias did not significantly affect the dynamical mass segregation: in all cases, they decreased the length of the dynamical MST with a statistical significance between 0 and 0.1σ. However, the spatial mass segregation was affected by our selection filters: in all cases, the average length of the MST has also decreased, with statistical significances of $\sim 1.5\sigma$ (ABDMG), $\sim 1.8\sigma$ (ARG and TWA), $\sim 2.2\sigma$ (CAR), $\sim 2.8\sigma$ (βPMG) and $\sim 3\sigma$ (COL; THA was unaffected). We have thus likely underestimated any positive spatial mass segregation in our analysis, as well as overestimated any negative spatial mass segregation. Since all of the statistically significant spatial mass segregation ratios obtained here are positive (less massive objects are more spread out), this does not change the conclusions of our analysis, except that we might generally underestimate the statistical significance of these conclusions.

Since we did not account of known and unknown unresolved binaries in our analysis and because the $W1$ flux of an object always falls rapidly when decreasing its mass, we will have systematically overestimated the total mass of unresolved systems. However, there is no apparent reason that would cause the fraction of multiple systems in a given YMG to correlate with $XYZUVW$. Hence, the effect of ignoring unresolved systems will be the same as overestimating the mass and luminosity of a random subset of members that we considered isolated. This addition of noise will thus tend to draw the MSR closer to unity, as well as increase the measurement error on the MSR. As a consequence, this simplification will has made us less sensitive to the detection of any mass segregation, whether it be positive or negative.

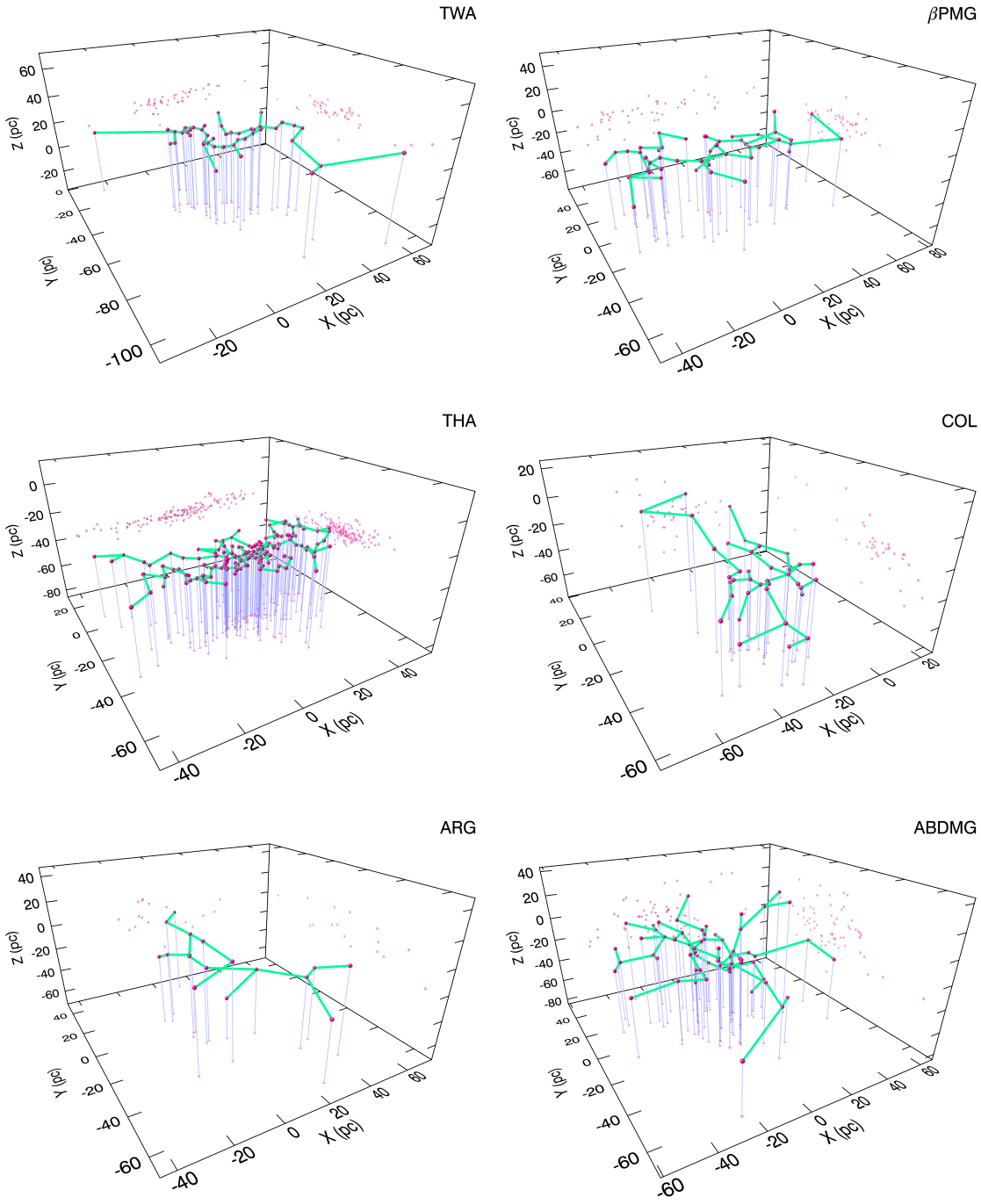

FIGURE 3.8 Minimum spanning trees (MSTs; green lines) in XYZ space for bona fide members and high probability BASS candidates (red points and their projections). Blue lines link each data point to its projection on the XZ plane for clarity. The total length of the MSTs for the brightest subsets of objects, compared with a random subset, is a useful diagnosis to determine the presence of mass segregation.

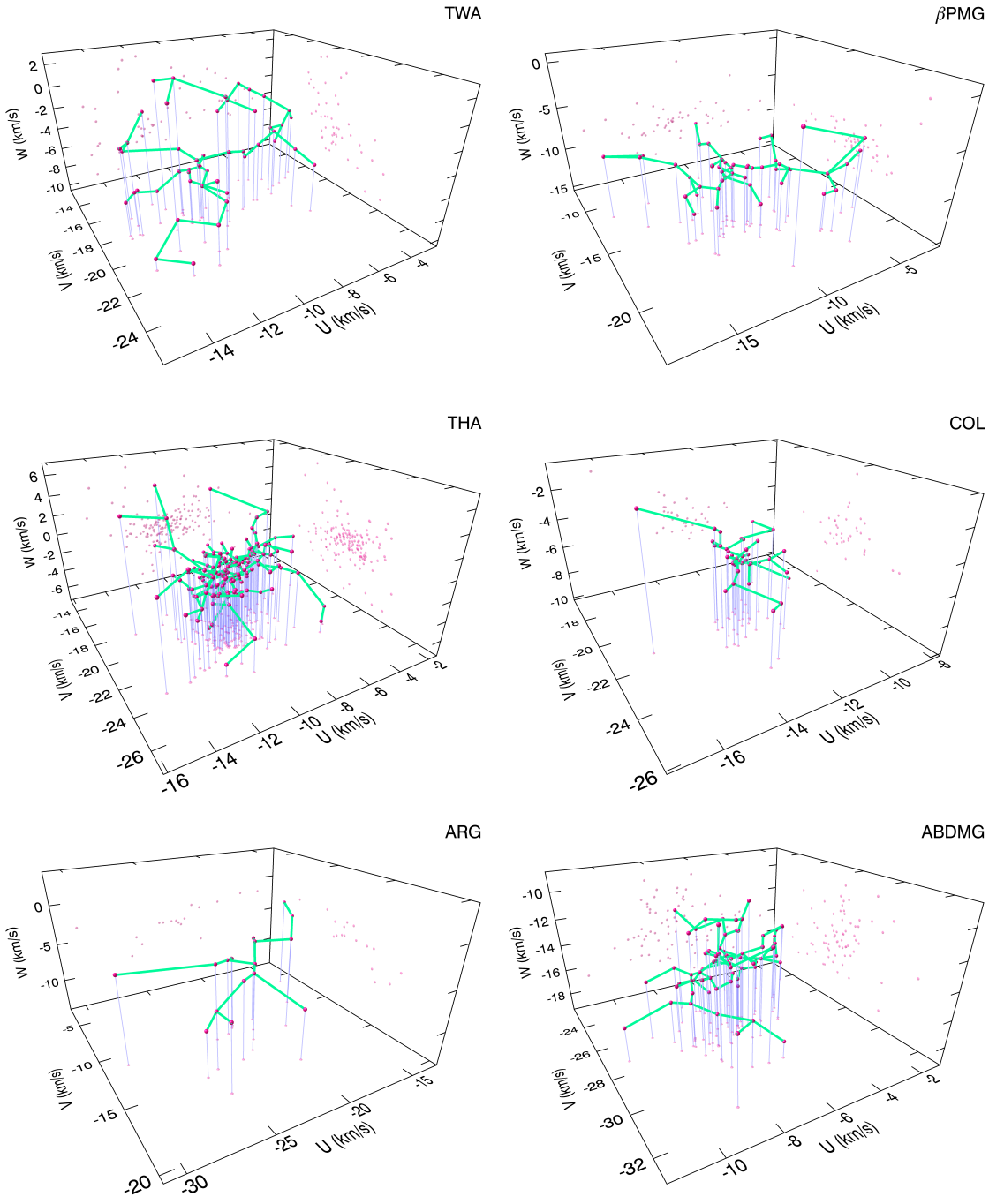

FIGURE 3.9 Minimum spanning trees (MSTs; green lines) in UVW space for bona fide members and high probability BASS candidates (red points and their projections). Blue lines link each data point to its projection on the UV plane for clarity. The total length of the MSTs for the brightest subsets of objects, compared with a random subset, is a useful diagnosis to determine the presence of mass segregation.

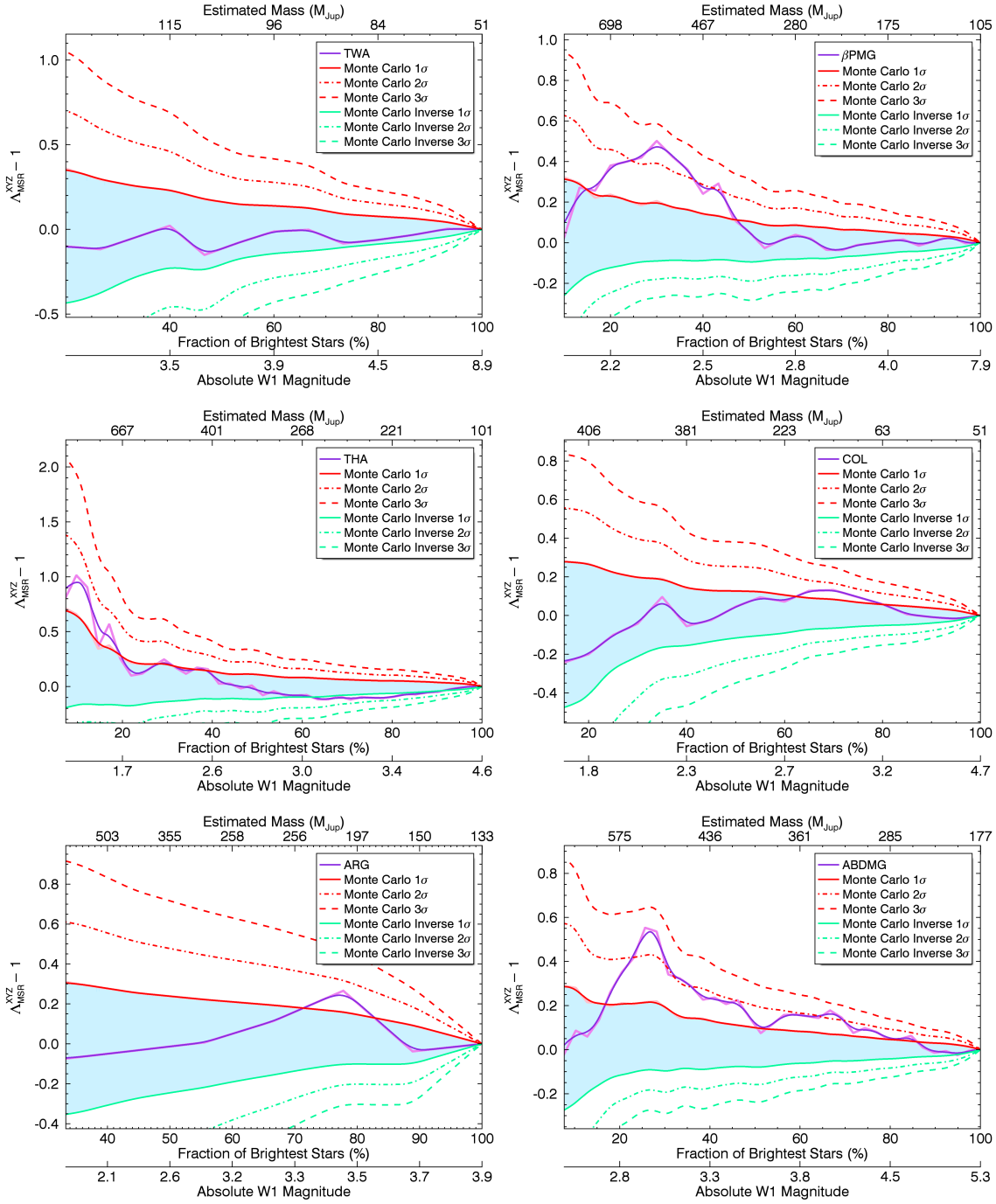

FIGURE 3.10 Spatial mass segregation ratios (MSRs) for bona fide members of YMGs considered here except CAR, as a function of the population fraction of brightest stars that were used in the calculation. Purple curves represent the departure of the MSR from unity, whereas red curves represent results of the Monte Carlo simulation where random stars were chosen instead of the brightest ones. Green curves delimit the region below which the MSR would be smaller than unity with statistical significance (i.e. least massive stars more concentrated towards the center). A MSR (purple curve) located inside the pale blue region indicates no significant difference between the scatter of the brightest or faintest objects. Darker, thick lines represent smoothed versions of the light-colored lines. The segregation mass ratio of CAR does not significantly depart from unity for any value of N.

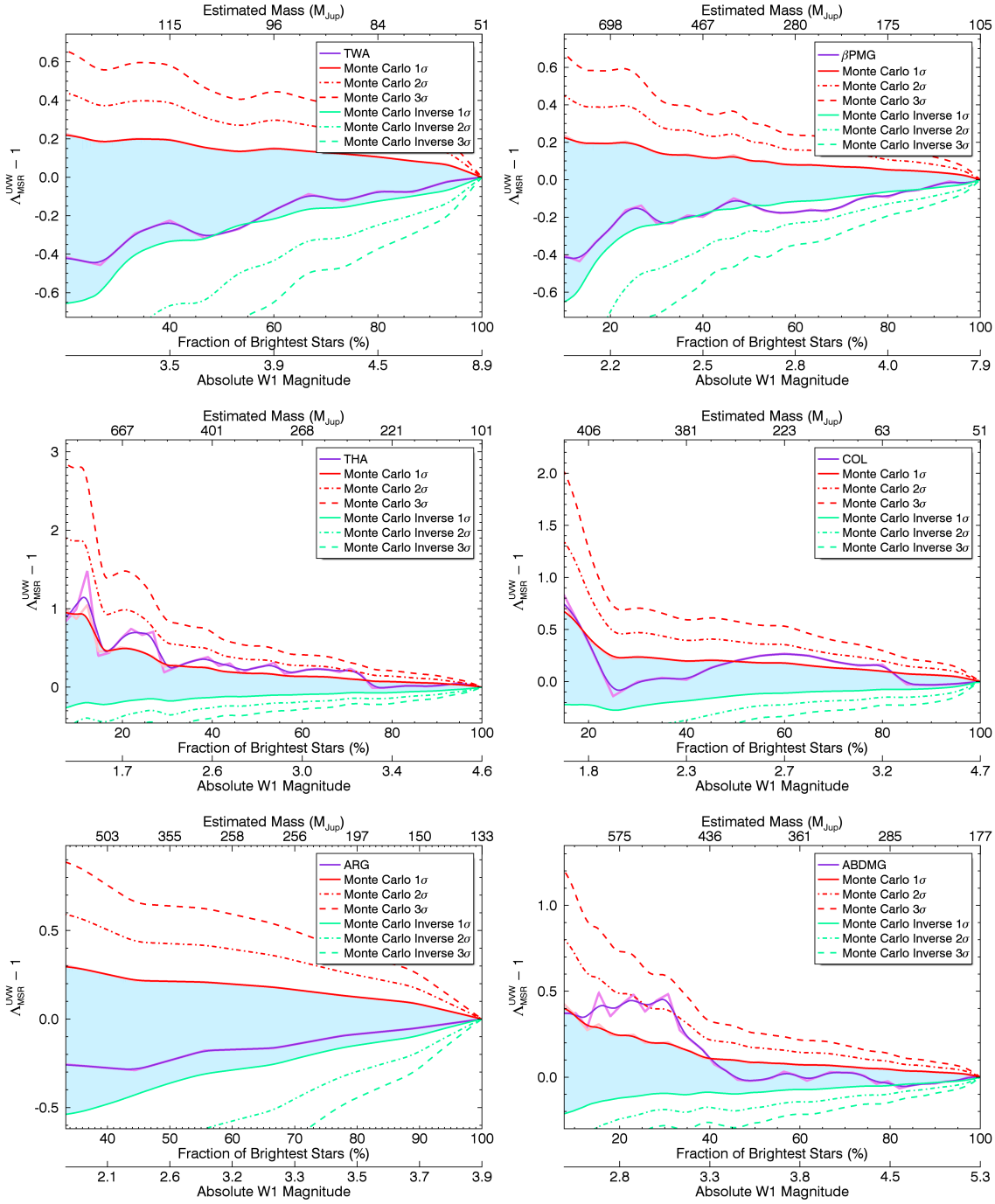

FIGURE 3.11 Same as Figure 3.10 for dynamical mass segregation.

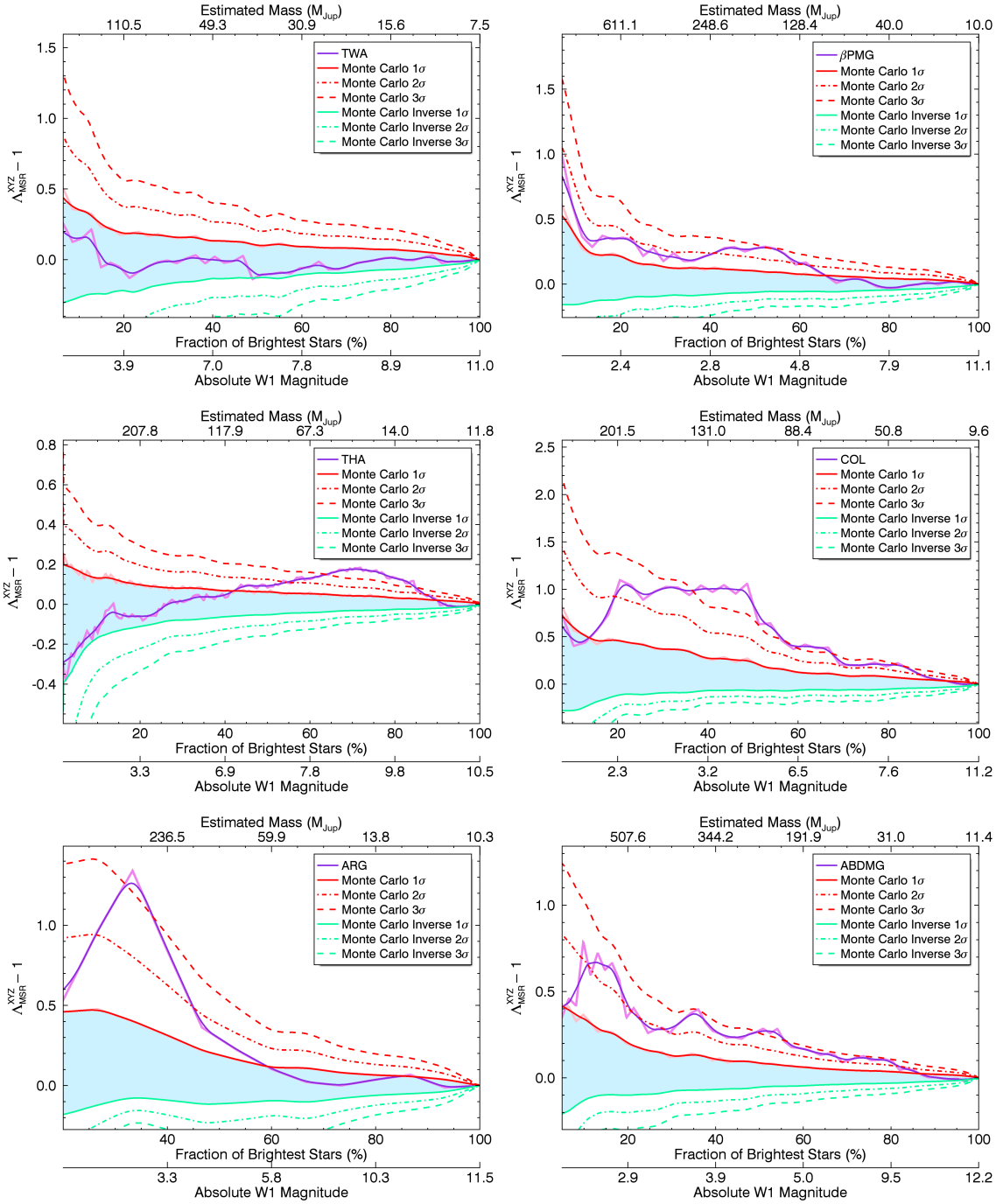

FIGURE 3.12 Same as Figure 3.10 with high probability BASS candidates added to the set of bona fide members.

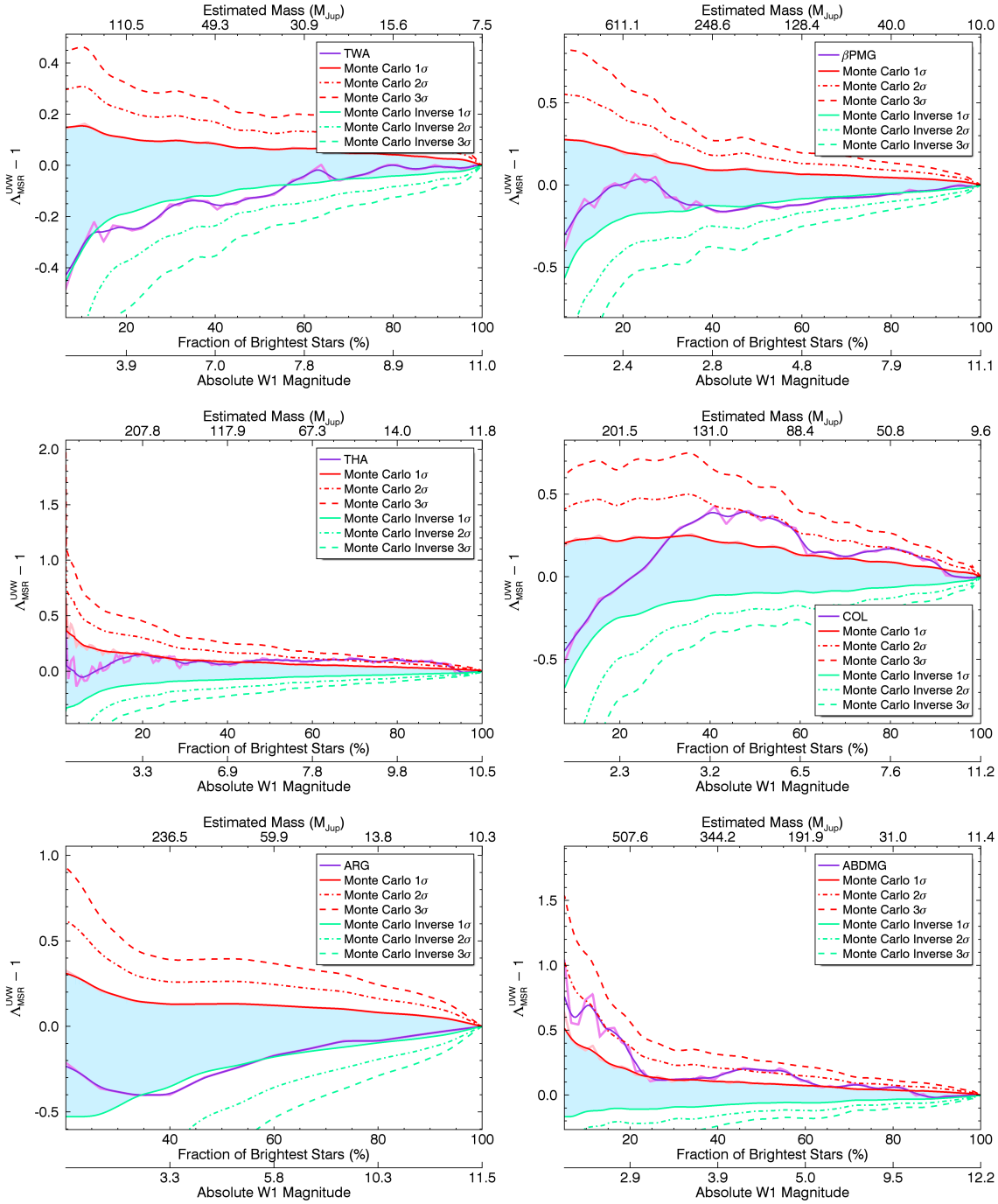

FIGURE 3.13 Same as Figure 3.11 with high probability BASS candidates added to the set of bona fide members.

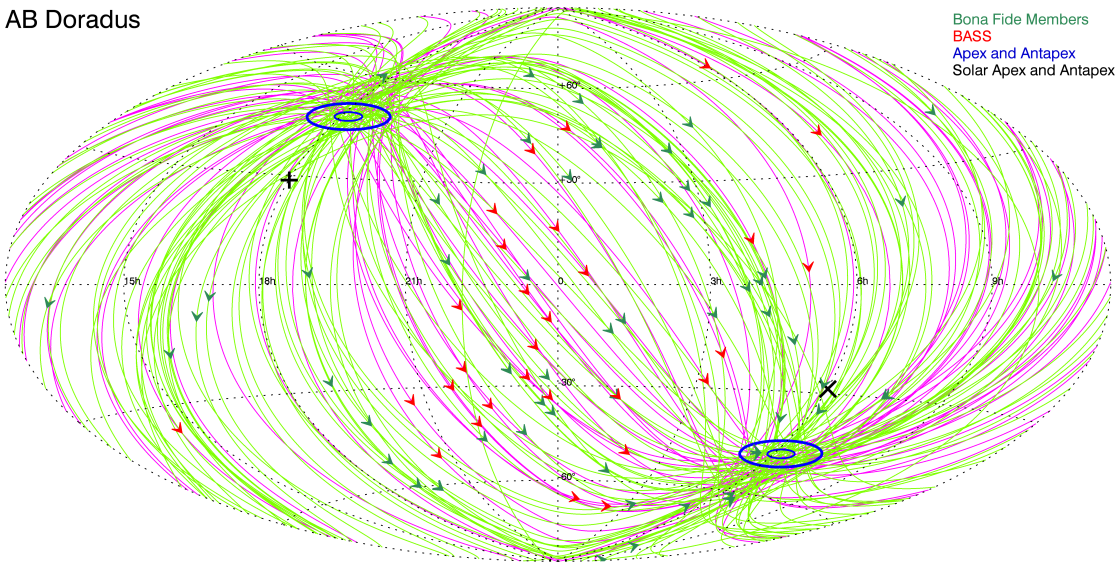

FIGURE 3.14 Proper motion as a function of sky position for candidate members of AB Doradus in the BASS Catalog (red arrows and lines), compared with currently known bona fide members (light green; see Chapter 2). The proper motions of candidate members and bona fide members all converge to the apex and antapex of ABDMG (blue circles), which is a well known property of YMGs.

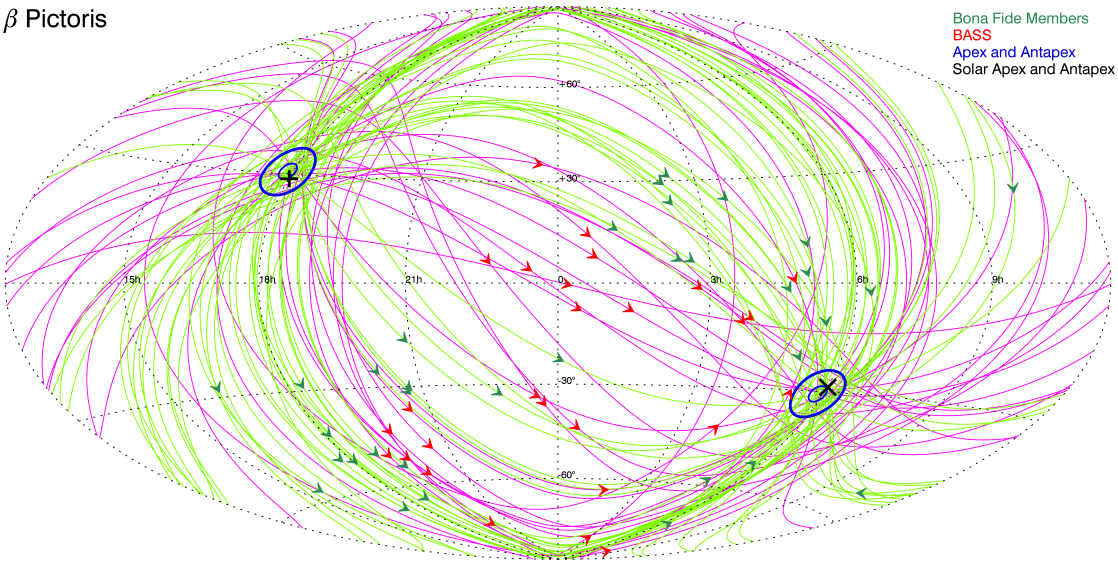

FIGURE 3.15 Proper motion as a function of sky position for BASS candidate members and bona fide members of βPMG. Colors and symbols are defined in the same way as in Figure 3.14

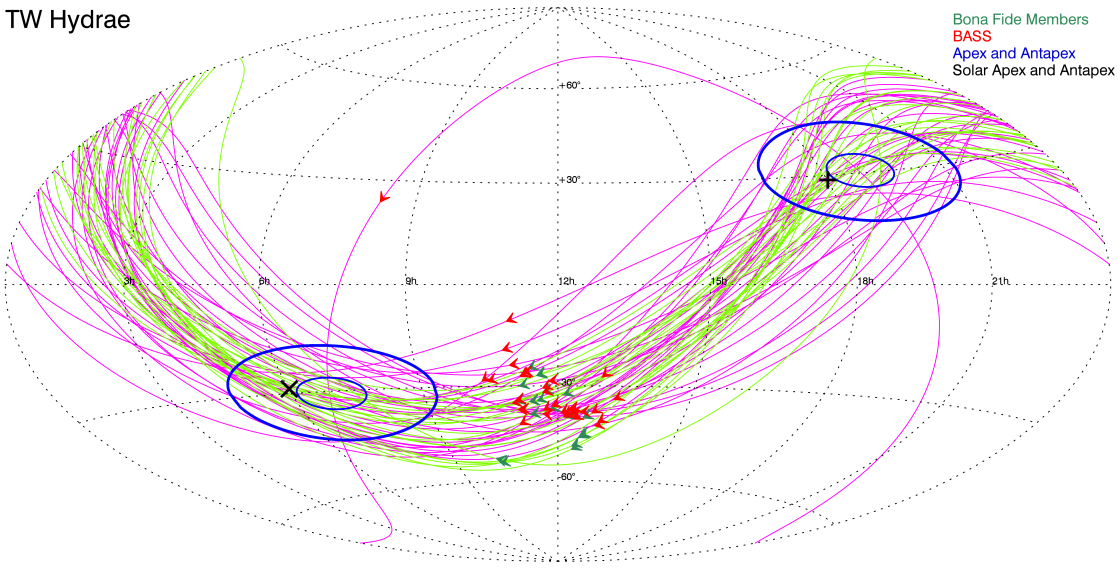

FIGURE 3.16 Proper motion as a function of sky position for BASS candidate members and bona fide members of TWA. Colors and symbols are defined in the same way as in Figure 3.14

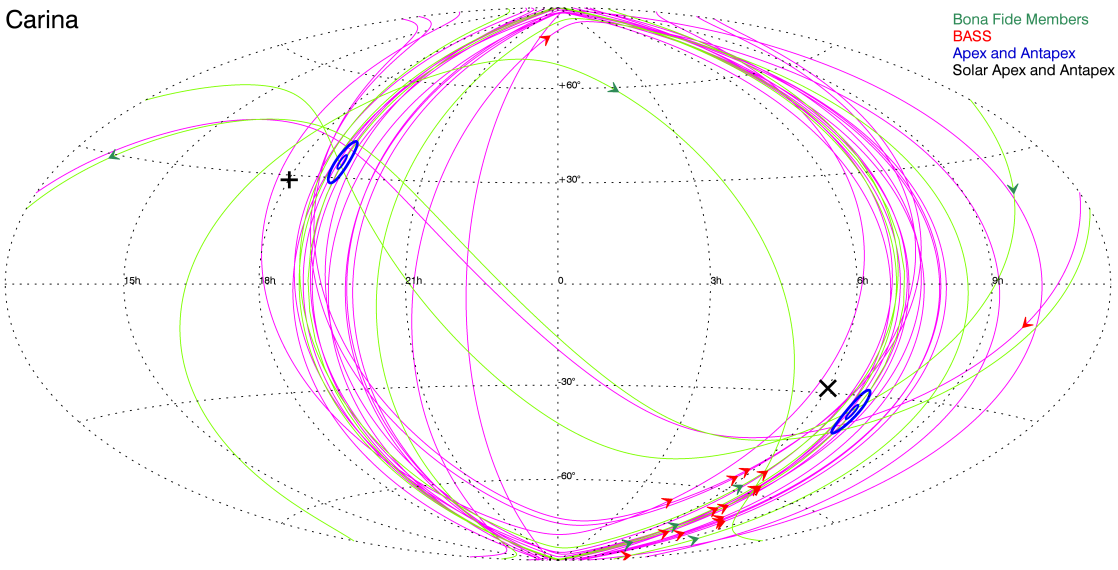

FIGURE 3.17 Proper motion as a function of sky position for BASS candidate members and bona fide members of CAR. Colors and symbols are defined in the same way as in Figure 3.14

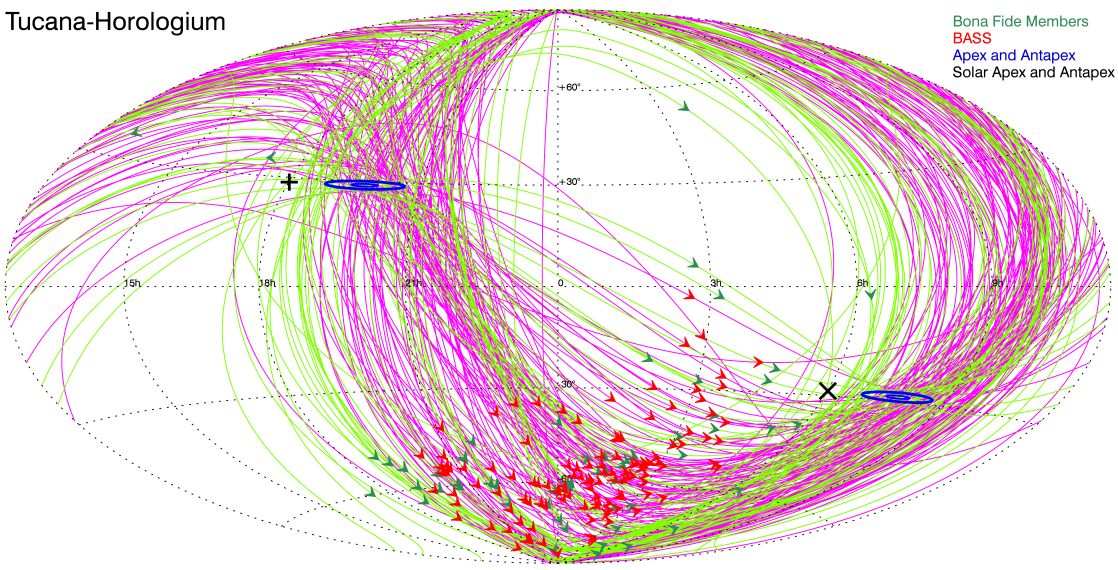

FIGURE 3.18 Proper motion as a function of sky position for BASS candidate members and bona fide members of THA. Colors and symbols are defined in the same way as in Figure 3.14

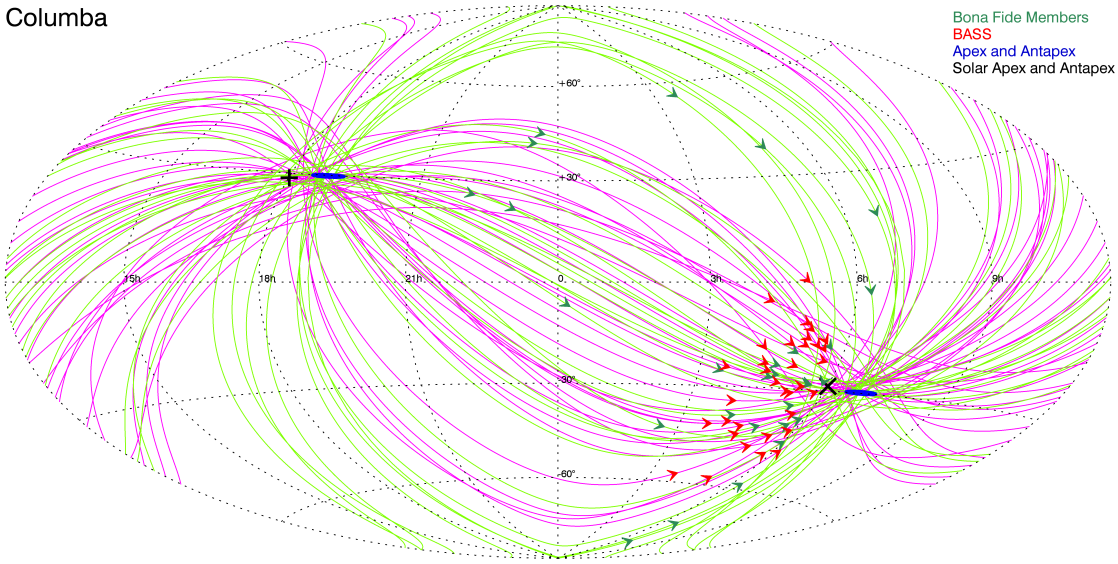

FIGURE 3.19 Proper motion as a function of sky position for BASS candidate members and bona fide members of COL. Colors and symbols are defined in the same way as in Figure 3.14

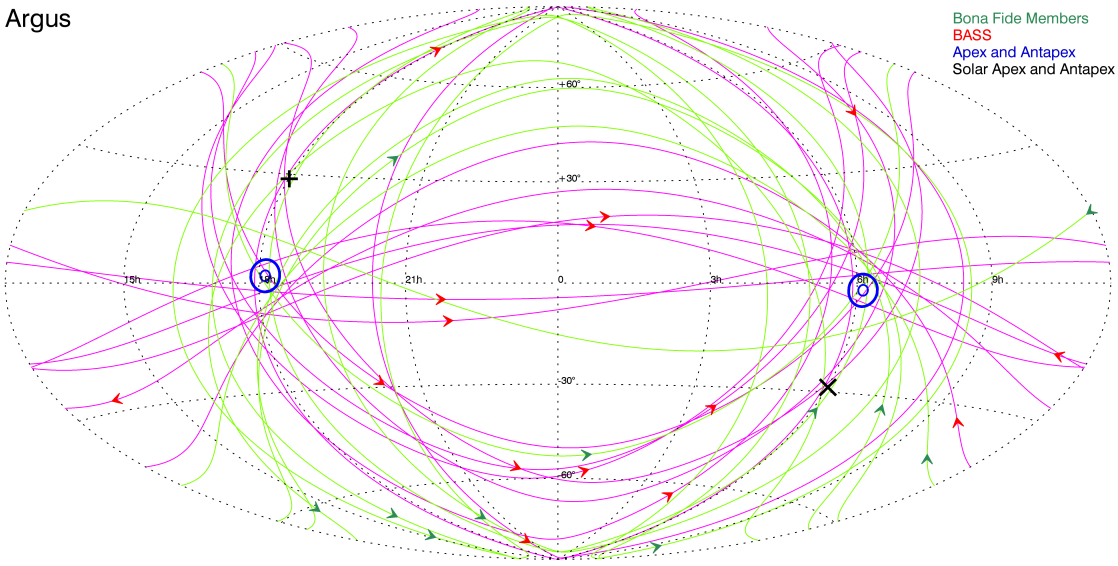

FIGURE 3.20 Proper motion as a function of sky position for BASS candidate members and bona fide members of ARG. Colors and symbols are defined in the same way as in Figure 3.14

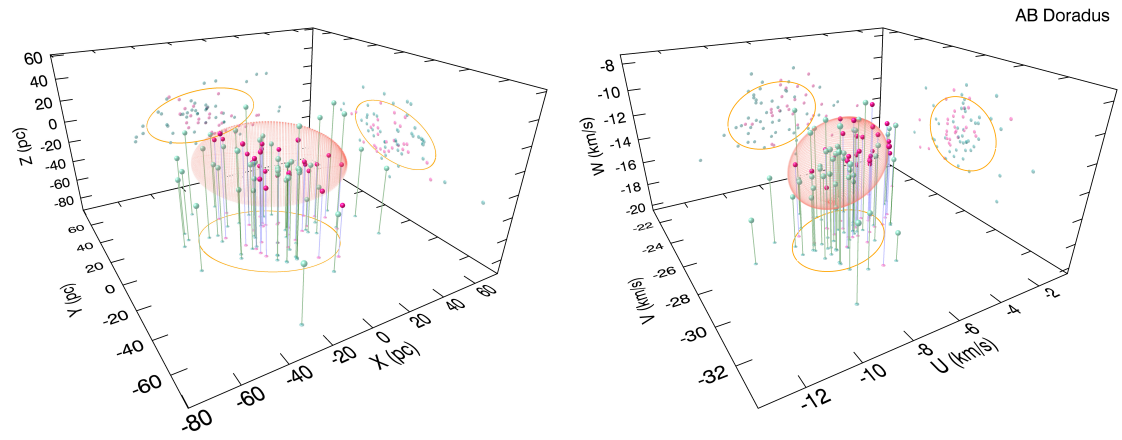

(a) XYZ (b) UVW

FIGURE 3.21 Most probable galactic positions XYZ and space velocities UVW based on BANYAN II statistical distances and RVs for all BASS candidate members in ABDMG (red points), compared with bona fide members (green points), as well as the spatial and kinematic ellipsoid models used in BANYAN II (orange ellipsoids; see Chapter 2 for more details). All points and models are projected on the three normal planes for a better clarity.

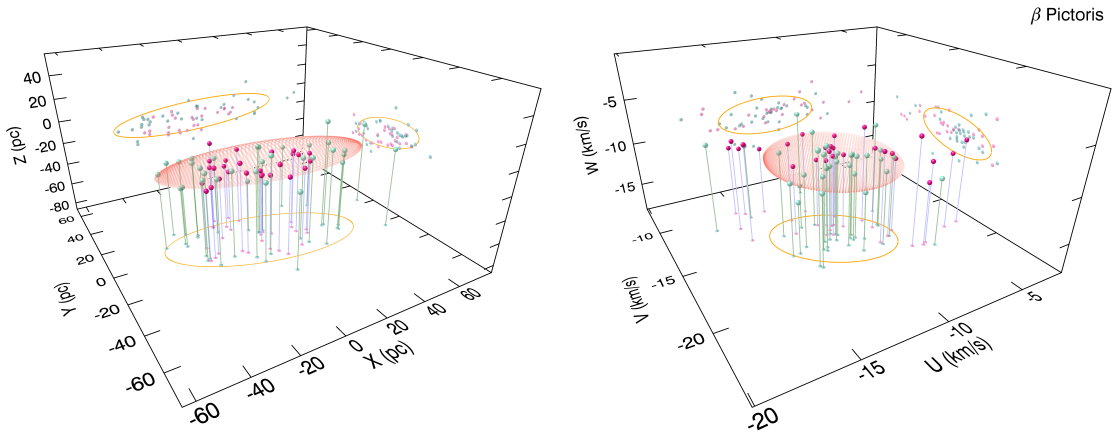

(a) XYZ (b) UVW

FIGURE 3.22 Most probable galactic positions XYZ and space velocities UVW based on BANYAN II statistical distances and RVs for all BASS candidate members in βPMG compared with bona fide members. Colors and symbols are defined in the same way as in Figure 3.21.

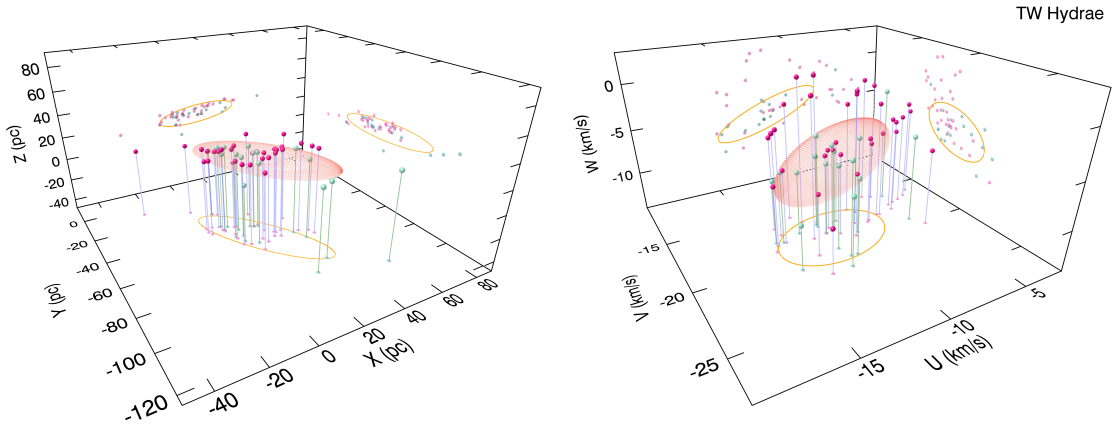

(a) XYZ (b) UVW

FIGURE 3.23 Most probable galactic positions XYZ and space velocities UVW based on BANYAN II statistical distances and RVs for all BASS candidate members in TWA compared with bona fide members. Colors and symbols are defined in the same way as in Figure 3.21. We note that a fraction of BASS candidates have kinematics slightly discrepant with those of TWA. It is possible that contamination from the Lower-Centaurus-Crux causes this (i.e. Schneider et al. 2012a), however a follow-up of these candidates will be needed to confirm this.

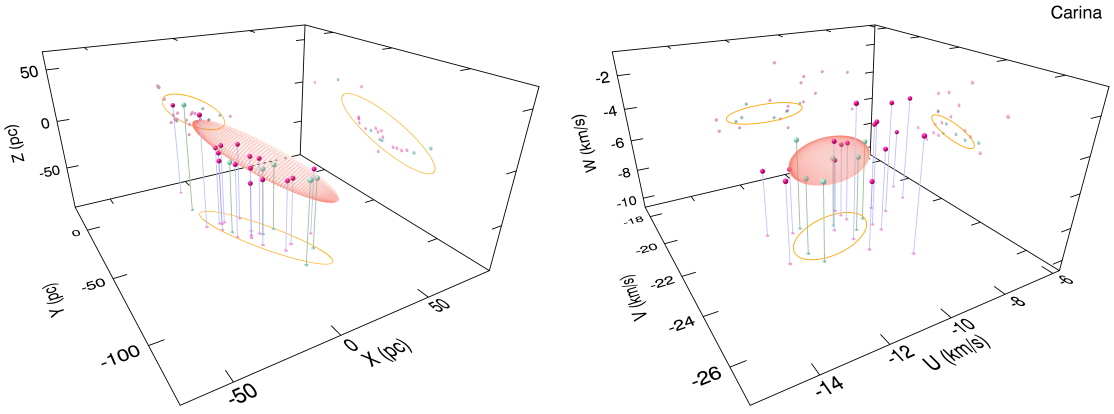

(a) XYZ (b) UVW

FIGURE 3.24 Most probable galactic positions XYZ and space velocities UVW based on BANYAN II statistical distances and RVs for all BASS candidate members in CAR compared with bona fide members. Colors and symbols are defined in the same way as in Figure 3.21. We note that the SKMs presented here (orange ellipsoids) are based on only 7 bona fide members, and they are thus most probably incomplete (see Chapter 2 for a discussion). It can be seen that BASS candidates preferentially fall in a region slightly outside of the kinematic model, which potentially points out to an overlooked region of CAR members in the kinematic space.

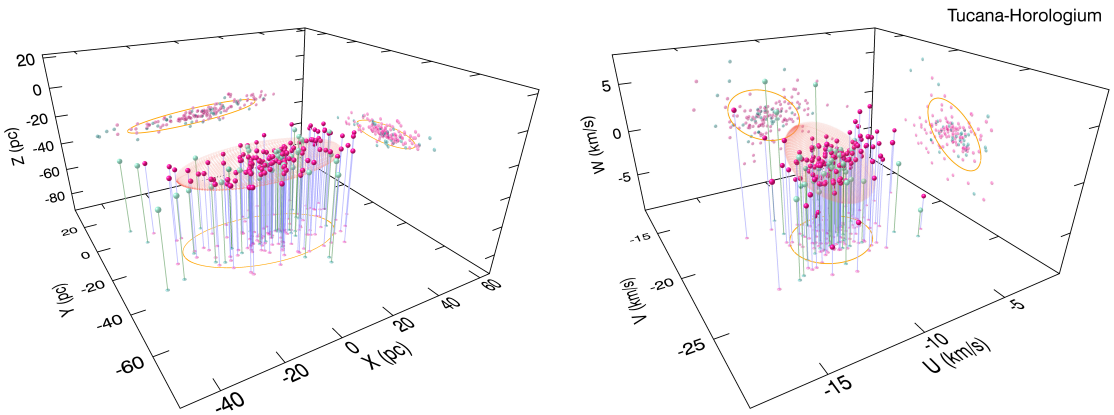

(a) XYZ (b) UVW

FIGURE 3.25 Most probable galactic positions XYZ and space velocities UVW based on BANYAN II statistical distances and RVs for all BASS candidate members in THA compared with bona fide members. Colors and symbols are defined in the same way as in Figure 3.21. As noted by Kraus et al. (2014b), the spatial distribution of THA is significantly thinner in the Z direction and thus forms a plane in the XYZ space.

3.10 Summary and conclusions

We used the 2MASS and AllWISE surveys to perform the first systematic all-sky survey for $\geq$ M5 candidate members of YMGs. We identified a total of 275 M4–L7 candidate members, from which 153 are new strong candidates with an expected overall contamination of 13% from field stars, from which 79 are expected to be brown dwarfs, and 22 are expected to be planetary-mass objects. We searched for all additional information available in the literature for the BASS sample to update membership probability, and show that we recover 60% of known $\geq$ M5 candidates to YMGs, whereas most of the remaining 40% were missed due to the quality filters used to minimize false-positives. Three new common proper motion pairs were discovered among low-probability candidates. We finally used this unique sample to tentatively identify signs of mass segregation in YMGs. We find marginal evidence for mass segregation in ABDMG even when considering only bona fide members, and this result extends to THA and COL when high probability BASS candidates are taken into account. The BASS sample will open the door to the identification of BD members of YMGs, and has already proved extremely fruitful from a number of discoveries previously published. Extensive NIR and optical spectroscopic follow-ups are ongoing and have already enabled the discovery of several new young BDs which will be presented in upcoming papers. Complementary data can be found at our group's website *http://www.astro.umontreal.ca/mbderg* and *http://www.astro.umontreal.ca/~gagne*, and the BANYAN II web tool is publicly available at *http://www.astro.umontreal.ca/~gagne/banyanII.php*.

We thank the anonymous referee of this Paper, which provided us with valuable comments that significantly increased the quality of this work. The authors would also like to thank Kelle Cruz, Jacqueline K. Faherty, Philippe Delorme, Adric Riedel, Loïc Albert, Rebecca Oppenheimer, Eric Mamajek, Brendan Bowler, David Blank, Amélie Simon and Jonathan Foster for useful comments and discussions and Adric Riedel for sharing data. This work was supported in part through grants from the the Fond de Recherche Québécois - Nature et Technologie and the Natural Science and Engineering Research Council of Canada. This research has benefitted from the SpeX Prism Spectral Libraries, maintained by Adam Burgasser at *http://pono.ucsd.edu/~adam/browndwarfs/spexprism*, and the *Database of Ultracool Paral-*

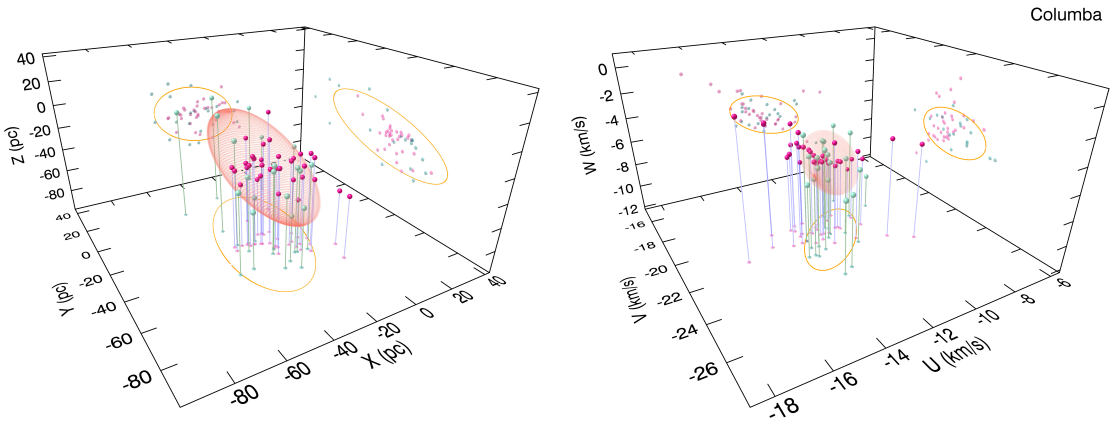

(a) XYZ (b) UVW

FIGURE 3.26 Most probable galactic positions XYZ and space velocities UVW based on BANYAN II statistical distances and RVs for all BASS candidate members in COL compared with bona fide members. Colors and symbols are defined in the same way as in Figure 3.21.

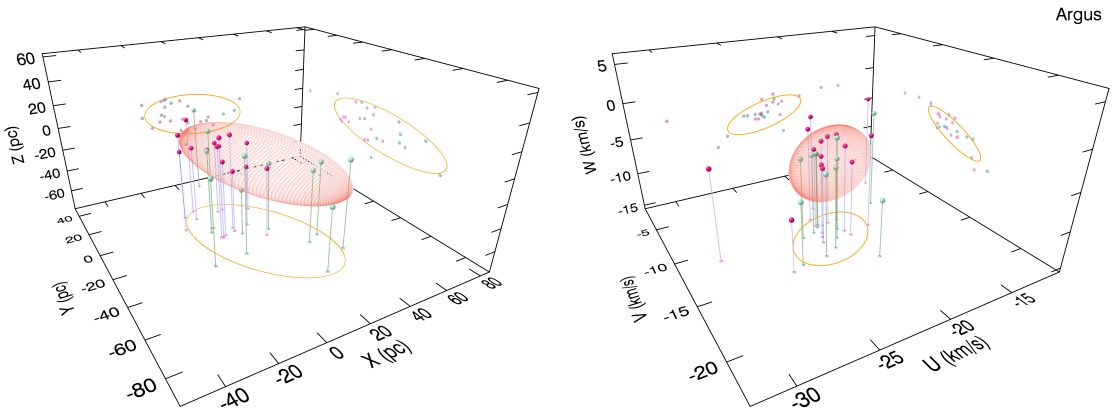

(a) XYZ (b) UVW

FIGURE 3.27 Most probable galactic positions XYZ and space velocities UVW based on BANYAN II statistical distances and RVs for all BASS candidate members in ARG compared with bona fide members. Colors and symbols are defined in the same way as in Figure 3.21.

laxes at *http://www.cfa.harvard.edu/~tdupuy/plx/Database_of_Ultracool_Parallaxes.html*. This research made use of; the SIMBAD database and VizieR catalog access tools, operated at Centre de Données astronomiques de Strasbourg, France (Ochsenbein et al. 2000); data products from the Two Micron All Sky Survey, which is a joint project of the University of Massachusetts and the Infrared Processing and Analysis Center (IPAC)/California Institute of Technology (Caltech), funded by the National Aeronautics and Space Administration (NASA) and the National Science Foundation (Skrutskie et al. 2006); data products from the Wide-field Infrared Survey Explorer, which is a joint project of the University of California, Los Angeles, and the Jet Propulsion Laboratory (JPL)/Caltech, funded by NASA (Wright et al. 2010); the NASA/IPAC Infrared Science Archive, which is operated by the JPL, Caltech, under contract with NASA; the M, L, and T dwarf compendium housed at *http://DwarfArchives.org* and maintained by Chris Gelino, Davy Kirkpatrick, and Adam Burgasser.

3.A The input sample of nearby potential > M5 dwarfs

We present in Table 3.6 the complete sample of 98 970 potential > M5, nearby objects in which we searched for candidate members to YMGs, which will might prove useful to study the kinematics of such red objects. This table includes all observables that were fed to BANYAN II to determine the bayesian probability: 2MASS and AllWISE magnitudes, sky position and proper motion determined from the 2MASS–AllWISE cross-match. This list was built from the selection criteria described in Section 3.3, which produced the two following SQL statements that we used to query the 2MASS and AllWISE all-sky catalogs, respectively, on the IRSA service :

- 2MASS :

```
(GLAT > 15 OR GLAT < -15) AND (J_M-H_M) >= 0.506 AND (J_M-H_M) < 2  AND (H_M-K_M)
    >= 0.269 AND (H_M-K_M) < 1.6 AND (NOT rd_flg LIKE '%0%') AND (NOT rd_flg LIKE '
    %6%') AND (NOT rd_flg LIKE '%9%') AND bl_flg = '111' AND cc_flg = '000' AND
    gal_contam = '0' AND J_M > 2 AND H_M > 2 AND K_M > 2 AND (NOT ph_qual LIKE '%D%
    ') AND (NOT ph_qual LIKE '%E%') AND (NOT ph_qual LIKE '%F%') AND (NOT ph_qual
    LIKE '%X%') AND (NOT ph_qual LIKE '%U%') AND (NOT ph_qual LIKE '%CC%') AND (NOT
     ph_qual='CAC') AND (NOT ph_qual='CBC') AND PROX > 6.4 AND mp_flg = '0' AND (
    b_m_opt is null OR (b_m_opt - J_M) >= 4.048) AND (vr_m_opt is null OR (vr_m_opt
     - J_M) >= 2.63) AND (b_m_opt is null OR vr_m_opt is null OR (b_m_opt -
    vr_m_opt) >= 1.3)
```

- AllWISE :

```
(GLAT > 15 OR GLAT < -15) AND (W1MPRO - W2MPRO) >= 0.168 AND (W1MPRO - W2MPRO) <
    2.5 AND ( W3SNR < 5 OR (NOT W3SAT = 0) OR ( (W1MPRO - W2MPRO) > (0.96*(W2MPRO -
     W3MPRO)-0.96) ) ) AND (cc_flags NOT LIKE '_D__' AND cc_flags NOT LIKE 'D___'
    AND cc_flags NOT LIKE '_O__' AND cc_flags NOT LIKE 'O___' AND cc_flags NOT LIKE
     '_P__' AND cc_flags NOT LIKE 'P___' AND cc_flags NOT LIKE '_H__' AND cc_flags
    NOT LIKE 'H___') AND (EXT_FLG = '0' OR EXT_FLG = '1') AND W1SNR > 5 AND W2SNR >
     5 AND W1RCHI2 < 5 AND W2RCHI2 < 5 AND W1MPRO > 2 AND W2MPRO > 2 AND W1SAT <
    0.002 AND W2SAT < 0.002 AND (PH_QUAL LIKE 'AA%' OR PH_QUAL LIKE 'AB%' OR
    PH_QUAL LIKE 'BA%' OR PH_QUAL LIKE 'BB%') AND (tmass_key is null OR (R_2MASS >=
     0.3 AND (j_m_2MASS - h_m_2MASS) >= 0.506 AND (j_m_2MASS - h_m_2MASS) < 2 AND (
    h_m_2MASS - k_m_2MASS) >= 0.269 AND (h_m_2MASS - k_m_2MASS) < 1.6 AND (
    k_m_2MASS - w1mpro) >= 0.153 AND (k_m_2MASS - w1mpro) < 2))
```

Table 3.6. All-Sky input sample of nearby, potential > M5 objects.

2MASS				AllWISE			μ_α	μ_δ
Designation	J	H	K_S	Designation	$W1$	$W2$	(mas yr^{-1})	(mas yr^{-1})
00000027-1534494	10.47 ± 0.02	9.90 ± 0.02	9.63 ± 0.02	000000.46-153448.4	9.40 ± 0.02	9.22 ± 0.02	240.5 ± 9.3	87.4 ± 7.4
00000058-2621542	12.83 ± 0.02	12.27 ± 0.02	11.98 ± 0.02	000000.60-262154.9	11.78 ± 0.02	11.59 ± 0.02	27.2 ± 5.2	-63.1 ± 6.2
00000160-7721530	15.66 ± 0.08	15.09 ± 0.09	14.76 ± 0.13	000002.10-772152.6	14.33 ± 0.03	14.06 ± 0.04	151.6 ± 3.8	32.9 ± 10.0
00000296+2541349	13.34 ± 0.02	12.82 ± 0.02	12.51 ± 0.03	000002.98+254134.4	12.29 ± 0.02	12.09 ± 0.02	29.0 ± 5.2	-40.4 ± 6.1
00000497+3740328	15.66 ± 0.05	15.15 ± 0.08	14.82 ± 0.10	000004.96+374033.4	14.57 ± 0.03	14.32 ± 0.05	-16.0 ± 6.7	56.3 ± 9.6
00000540-5418547	14.23 ± 0.03	13.70 ± 0.04	13.39 ± 0.04	000005.29-541855.4	13.20 ± 0.02	13.03 ± 0.03	-85.2 ± 3.7	-64.8 ± 8.5
00000717+0525209	15.22 ± 0.04	14.65 ± 0.05	14.36 ± 0.09	000007.15+052519.6	13.96 ± 0.03	13.74 ± 0.04	-34.9 ± 8.3	-127.0 ± 9.5
00000814+2356328	13.99 ± 0.03	13.42 ± 0.04	13.13 ± 0.03	000008.18+235632.8	12.97 ± 0.02	12.79 ± 0.03	60.0 ± 6.6	-3.2 ± 15.1
00001033+8627328	15.48 ± 0.05	14.95 ± 0.07	14.66 ± 0.09	000010.99+862732.8	14.40 ± 0.03	14.23 ± 0.03	56.4 ± 1.4	6.7 ± 11.6
00001103+3838315	15.98 ± 0.08	15.44 ± 0.10	15.00 ± 0.13	000011.02+383831.0	14.84 ± 0.03	14.66 ± 0.06	-7.2 ± 7.4	-49.5 ± 10.0
00001151+3757013	15.79 ± 0.06	15.02 ± 0.07	14.50 ± 0.07	000011.55+375700.6	14.25 ± 0.03	13.95 ± 0.04	46.1 ± 6.3	-65.6 ± 8.5
00001296-5406573	14.46 ± 0.04	13.86 ± 0.04	13.58 ± 0.05	000013.02-540657.4	13.41 ± 0.02	13.23 ± 0.03	43.2 ± 3.3	-9.8 ± 10.1
00001365+0714139	14.42 ± 0.03	13.91 ± 0.04	13.54 ± 0.04	000013.70+071413.6	13.31 ± 0.03	13.06 ± 0.03	61.9 ± 7.8	-23.5 ± 7.8
00001474+0526070	12.79 ± 0.02	12.23 ± 0.02	11.96 ± 0.02	000014.75+052606.4	11.80 ± 0.02	11.63 ± 0.02	8.5 ± 7.1	-55.4 ± 8.0
00001550-0756442	15.17 ± 0.04	14.58 ± 0.05	14.23 ± 0.06	000015.58-075644.9	14.07 ± 0.03	13.80 ± 0.04	96.6 ± 7.5	-54.4 ± 8.7
00001635-1933581	12.03 ± 0.02	11.50 ± 0.02	11.21 ± 0.02	000016.31-193357.6	11.05 ± 0.02	10.84 ± 0.02	-56.0 ± 6.1	45.8 ± 6.5
00001662-4155289	14.88 ± 0.03	14.27 ± 0.03	13.96 ± 0.07	000016.61-415530.6	13.66 ± 0.03	13.46 ± 0.03	-8.5 ± 4.6	-155.1 ± 8.5
00001717+3245124	14.47 ± 0.04	13.89 ± 0.04	13.61 ± 0.05	000017.14+324512.1	13.45 ± 0.03	13.21 ± 0.03	-29.2 ± 5.0	-26.9 ± 6.5
00001823-1303230	15.15 ± 0.05	14.62 ± 0.06	14.32 ± 0.06	000018.26-130322.5	13.94 ± 0.03	13.70 ± 0.04	32.5 ± 6.7	41.2 ± 8.3
00001886-4544588	13.42 ± 0.02	12.85 ± 0.02	12.56 ± 0.03	000018.90-454458.7	12.40 ± 0.02	12.23 ± 0.02	42.9 ± 4.2	9.2 ± 7.3
00001909-7156506	13.72 ± 0.02	13.13 ± 0.03	12.86 ± 0.04	000019.06-715651.1	12.68 ± 0.02	12.46 ± 0.02	-11.2 ± 1.4	-51.2 ± 7.7
00001952-2556359	14.25 ± 0.03	13.68 ± 0.03	13.36 ± 0.03	000019.54-255636.2	13.15 ± 0.02	12.93 ± 0.03	19.0 ± 6.5	-33.7 ± 7.5
00001980+0122099	15.21 ± 0.04	14.68 ± 0.07	14.33 ± 0.07	000019.87+012210.1	14.08 ± 0.03	13.91 ± 0.05	95.0 ± 9.5	28.1 ± 10.0
00002020-3227308	13.95 ± 0.03	13.39 ± 0.04	13.08 ± 0.04	000020.27-322730.8	12.81 ± 0.02	12.62 ± 0.03	73.4 ± 5.1	-0.8 ± 6.3
00002094+0656062	14.95 ± 0.03	14.44 ± 0.06	14.15 ± 0.06	000020.98+065606.2	13.90 ± 0.03	13.68 ± 0.04	49.8 ± 8.3	0.4 ± 8.2
00002101+2826405	13.94 ± 0.03	13.31 ± 0.03	13.02 ± 0.03	000021.04+282640.5	12.83 ± 0.02	12.65 ± 0.03	38.1 ± 6.1	-1.0 ± 6.9
00002116+3611427	14.92 ± 0.04	14.24 ± 0.04	13.87 ± 0.05	000021.19+361142.6	13.69 ± 0.03	13.50 ± 0.03	35.1 ± 6.1	-9.6 ± 8.6
00002267-1629461	14.81 ± 0.04	14.27 ± 0.04	13.90 ± 0.04	000022.72-162946.1	13.74 ± 0.03	13.53 ± 0.03	62.5 ± 7.0	0.1 ± 7.3
00002451-5335478	16.64 ± 0.13	15.70 ± 0.12	15.24 ± 0.16	000024.57-533547.6	15.00 ± 0.03	14.74 ± 0.05	53.1 ± 8.5	16.1 ± 19.7
00002503-6709515	14.78 ± 0.04	14.15 ± 0.05	13.81 ± 0.06	000025.15-670951.3	13.64 ± 0.03	13.44 ± 0.03	68.2 ± 2.5	13.2 ± 7.9
00002565-0119161	14.91 ± 0.04	14.32 ± 0.05	14.00 ± 0.07	000025.62-011916.4	13.83 ± 0.03	13.61 ± 0.04	-40.8 ± 8.2	-30.8 ± 9.6
00002583-1846013	12.49 ± 0.02	11.95 ± 0.02	11.67 ± 0.02	000025.98-184600.9	11.49 ± 0.02	11.30 ± 0.02	182.9 ± 7.2	35.5 ± 6.4
00002614-6127416	12.89 ± 0.02	12.32 ± 0.03	12.01 ± 0.02	000026.36-612742.1	11.79 ± 0.02	11.61 ± 0.02	158.2 ± 4.7	-52.9 ± 8.1
00002645+4234117	13.89 ± 0.02	13.31 ± 0.02	12.98 ± 0.03	000026.49+423411.8	12.82 ± 0.02	12.65 ± 0.03	36.9 ± 4.2	9.2 ± 6.9
00002652-0838401	14.53 ± 0.03	13.96 ± 0.04	13.63 ± 0.04	000026.57-083840.0	13.39 ± 0.03	13.15 ± 0.03	65.4 ± 6.6	8.5 ± 6.6
00002748-1429437	14.56 ± 0.02	14.01 ± 0.02	13.55 ± 0.04	000027.51-142943.9	13.17 ± 0.02	12.99 ± 0.03	37.2 ± 6.2	-18.4 ± 6.5
00002855+3810535	16.06 ± 0.08	15.44 ± 0.10	15.17 ± 0.14	000028.63+381053.5	14.94 ± 0.03	14.65 ± 0.06	92.0 ± 8.9	2.1 ± 13.3
00002856+2241264	15.63 ± 0.06	15.10 ± 0.11	14.70 ± 0.09	000028.59+224126.6	14.49 ± 0.03	14.23 ± 0.05	50.3 ± 8.5	11.9 ± 11.7
00002867-1245153	13.20 ± 0.02	12.44 ± 0.02	11.97 ± 0.02	000028.55-124516.4	11.71 ± 0.02	11.50 ± 0.02	-156.4 ± 6.7	-95.2 ± 7.8

This table is available in its entirety at *http://dx.doi.org/10.6084/m9.figshare.1207880*. The complete table has 98 970 rows.

3.B The *LP-BASS* catalog of marginally red candidates

We present here the *Low-Priority* BASS (LP-BASS) sample, consisting of all candidates which were rejected from the BASS sample because they were less than 1σ redder than the field in the M_{W1} versus $J - K_S$ and M_{W1} versus $H - W2$ CMD diagrams as indicated by the statistical distance of their most probable BANYAN II membership. However, we still only include candidates which are redder than the field sequence. Using the same method as described in the Paper, we estimate contamination fractions of $\sim 26\%$ and $\sim 80\%$ in the high and modest-probability LP-BASS samples. We thus discourage the use of this for statistical studies or time-consuming follow-ups. However, since the spread in the NIR colors of young objects in the two CMD mentioned above are large, we expect that a fraction of young objects will be rejected by our conservative filter which requires candidates to be $> 1\sigma$ redder than the field. It is thus likely that this sample will contain a considerable fraction of true members of YMGs. Candidate members in the LP-BASS are also being following spectroscopically to identify signs of youth, albeit with a lower priority. Results will be presented in subsequent papers.

In Table 3.7, we show all measurements in the literature which are useful in constraining the membership of the LP-BASS candidate members. We use these measurements to refine results from BANYAN II, and report the final probability and most probable YMG for all LP-BASS objects in Table 3.8.

We note that 2MASS J00455663+3347109 (G 132–25) had three distinct trigonometric distance measurements in the literature with one being very discrepant : Reid & Cruz (2002) report 68.0 ± 18.5 pc from the Yale catalog (van Altena et al. 1995), Khovritchev et al. (2013) measure 20.1 ± 2.1 pc, and Dittmann et al. (2014) measure 17.4 ± 1.3 pc. We thus consulted the Yale catalog directly to verify the measurement. Sky coordinates are reported as of 1900 in the catalog; we thus used the precess IDL routine from the IDL Astronomy Users Library[7] to precess the coordinates of G 132–25 back to this epoch. We find RA=00h40m32.625s, DEC=33°14′21.″78. The closest entry in the Yale catalog is that of LP 294–2, at a distance of 4′. Since LP 294–2 has a distinct 2MASS counterpart (2MASS J00461297+3350108), we

[7]Available at *http://idlastro.gsfc.nasa.gov/*

conclude the most probable explanation is that the trigonometric distance of LP 294–2 has been misattributed to G 132–25 in Reid & Cruz (2002). We thus rejected this measurement and combined the two others to obtain 18.1 $\pm$ 1.3 pc in Table 3.7.

Table 3.7. LP-BASS Candidates With Additional Information in the Literature.

2MASS Designation	Measured SpT[a]	Signs of Youth[b]	RV ($km\,s^{-1}$)	Trig. Dist. (pc)	Multiplicity[c]	Known Membership	Updated Membership	Updated Prob. (%)
00165057-7122387	...	...	-3.4 ± 3.0[54]	...	...	...	THA	36.6
00192753-3620153	M5.5[12]	...	...	...	...	...	THA	11.5
00281434-3227556	M5[85]	...	...	...	...	...	BPMG	30.4
00303013-1450333	L7[14,47]	...	...	26.7 ± 3.2[110]	...	...	ARG	24.1
00425349-6117384	M4.2[53]	...	6.9 ± 1.0[53]	...	...	THA[53]	THA	99.9
00455663+3347109	M4.5+M5.5[55]	...	...	18.1 ± 1.3[47,23]	AB[55]	...	ARG	89.7
00551459+4511019	...	...	...	35.8 ± 3.3[23]	...	...	ABDMG	19.3
00584253-0651239	L0[14,48,27]	...	...	29.6 ± 3.5[71]	...	...	BPMG	88.6
01000219-6156270	M6[12]	...	...	...	...	...	THA	99.1
01044008+1129485	...	N[92]	...	...	...	ABDMG[92]	BPMG	76.5
01234181-3833496	M4.5[78]	...	18.4 ± 6.3[101]	...	...	...	BPMG	0.6
01253196-6646023	M4.2[53]	...	7.1 ± 5.1[53]	...	...	THA[53]	THA	99.7
01275875-6032243	M4.2[90,53]	N	9.1 ± 2.5[53]	...	...	THA[90,53]	THA	> 99.9
01283025-4921094	M4.1[53]	...	6.5 ± 5.7[53]	...	...	THA[53]	THA	99.3
01375879-5645447	M3.9[53]	...	8.5 ± 0.6[53]	...	...	THA[53]	THA	99.9
01534955+4427284	...	...	...	20.2 ± 1.2[23]	...	...	ARG	98.5
02001992-6614017	M4.3[90,53]	N	11.8 ± 1.1[53]	...	...	THA[90,53]	THA	> 99.9
02025788-3136262	M4.0[90]	N	...	...	...	FIELD[90]	COL	40.7
02030658-5545420	M4.5[90]	N	...	...	...	ABDMG[90]	THA	99.9
02033222+0648588	...	...	...	...	C[113]	ABDMG[92]	BPMG	64.5
02123372-6049185	M6.5[34]	...	13.1 ± 0.2[34]	...	...	...	THA	94.8
02190228+2352550	M3.6[99]	X[99]	15.7 ± 0.7[100]	20.6 ± 0.8[23]	...	...	ARG	72.2
02294569-5541496	M4.8[53]	L[53]	11.5 ± 1.0[53]	...	...	THA[53]	THA	> 99.9
02341866-5128462	M4.3[53]	...	10.9 ± 0.9[53]	...	...	THA[53]	THA	> 99.9
02351494+0247534	...	...	...	17.8 ± 1.0[23]	...	...	BPMG	77.6
02383255-7528065	M4.1[53]	...	12.3 ± 0.6[53]	...	...	THA[53]	THA	98.9
02412721-3049149	M4.7[90,53]	ON[90]	18.2 ± 1.1[53]	...	...	THA[90,53]	BPMG	88.3
02420204-5359147	M4.6[90,53]	N	11.5 ± 2.3[53]	...	...	THA[90,53]	THA	> 99.9
02591904-5122341	M5.4[53]	L[53]	11.0 ± 2.3[53]	...	...	THA[53]	THA	> 99.9
03090022-4924513	M4.5[84]	...	...	...	...	...	ARG	18.8
03104941-3616471	M4.3[90,53]	N	13.8 ± 1.6[53]	...	...	THA[90,53]	THA	> 99.9
03341065-2130343	M6[14]	...	19.0 ± 0.8[34]	...	...	IC 2391?[34]	BPMG	22.9
03370359-1758079	L4.5[1]	...	...	...	...	...	ARG	11.6
03561624-3915219	M5.0[90,53]	N	16.7 ± 0.7[53]	...	...	THA[90,53]	THA	99.9
04032484+0824508	...	X[92]	...	...	...	ABDMG[92]	BPMG	96.7
04054799-1515399	M8[45]	...	...	...	...	...	THA	70.1
04111790-0556489	M9[111]	...	20.1 ± 5.0[111]	...	...	...	COL	20.6
04133609-4413325	M3.9[90,53]	N	16.4 ± 1.4[53]	...	...	THA[90,53]	THA	99.6
04231498-1533245	...	...	...	22.4 ± 1.0[23]	AB[26]	...	BPMG	93.3
04390494-0959012	M6[13]	...	...	...	...	...	ABDMG	15.4
04475779-5035200	M4.0[53]	...	18.6 ± 0.9[53]	...	...	THA[53]	COL	72.0
05195412-0723359	M4+M4.5[85,43]	X[85]	...	...	AB[43]	...	COL	89.7

Table 3.7 — continued

2MASS Designation	Measured SpT[a]	Signs of Youth[b]	RV ($km\,s^{-1}$)	Trig. Dist. (pc)	Multiplicity[c]	Known Membership	Updated Membership	Updated Prob. (%)
06142994-6318559	...	...	...	...	Ab[73]	...	ARG	89.0
06313103-8811365	M5[102]	...	...	...	...	...	ARG	28.1
07135309-6545115	...	...	...	...	AB[26]	...	CAR	91.5
07140394+3702459	M8[94,82,27]	...	...	12.5 ± 0.7[23]	...	...	ARG	74.9
07355465+3333459	M4.5[78]	...	...	32.4 ± 2.5[23]	...	...	ABDMG	26.2
10023100-2814280	M4+M6[80]	...	...	...	AB[43]	...	CAR	93.7
10134260-2759586	M5[38]	...	...	...	...	TWA[38]	CAR	43.5
10451718-2607249	M8[38,82,27]	...	...	...	...	...	ABDMG	18.2
15031325-2840134	M5[78]	...	...	...	...	...	ABDMG	4.3
20042845-3356105	M4.5[85]	X[85]	...	...	...	...	BPMG	93.8
21144103-4339531	...	...	2.7 ± 0.3[34]	...	...	CAS[34]	ABDMG	74.5
21272613-4215183	M8[82]	...	-7.6 ± 0.3[34]	34.6 ± 7.5[108]	...	Pleiades[34]	BPMG	82.5
21380269-5744583	M3.7[53]	...	-0.5 ± 1.3[53]	...	...	THA[53]	THA	98.7
21414678-2704542	M4.5[78]	...	...	...	...	...	ABDMG	45.7
22021125-1109461	M6.5[77]	...	-9.4 ± 1.0[40]	...	...	...	ABDMG	84.9
22043859-1832204	M4.5[5]	...	-7.2 ± 3.8[52]	...	...	...	BPMG	26.3
22294830-4858285	M4.5[80]	...	...	...	...	...	BPMG	21.1
22302626-0142063	M4[5]	...	...	...	...	...	ABDMG	14.6
22541103+1606546	M4[42]	...	...	30.2 ± 1.3[23]	...	...	ARG	68.8
23261182+1700082	M4.5+M6[43]	...	...	...	AB[43]	...	BPMG	66.8
23301129-0237227	M6[81]	...	...	...	...	...	BPMG	42.8
23310161-0406193	M8+L3[9]	...	-12.86 ± 0.09[9,115]	26.1 ± 0.4[109]	AB[9]	...	ABDMG	0.5
23524562-5229593	M4.6[53]	L[53]	3.1 ± 0.7[53]	...	...	THA[53]	THA	99.9

[a]The β and γ symbols stand for low-gravity and very low-gravity, p stands for peculiar, and a semi-colon indicates an uncertain spectral type.

[b]A capital letter means the object displays the associated sign of youth. O: lower-than normal equivalent width of atomic species in the optical spectrum, I: same but in the NIR spectrum, T: a triangular-shaped H-band continuum, V: high rotational velocity, X: X-ray emission, R: redder-than-normal colors for given spectral type, U: over luminous, H: Hα emission, L: Li absorption, A: signs of accretion, M: signs of low gravity from atmospheric models fitting, N: bright NUV emission and C: Companion to a young star. A question mark following a flag indicates that the result is uncertain.

[c]AB: Unresolved binary, B or C: Resolved companion.

References to this table are identical to those of Table 3.3.

Table 3.8. The Complete LP-BASS Catalog.

2MASS Designation	Spectral Type[a]	Probable Membership	Bayesian Prob. (%)	Contamination Prob. (%)	Estimated Mass Range ($M_{\rm Jup}$)	Statistical Distance (pc)	Statistical RV ($\rm km\,s^{-1}$)
Candidates with a High Probability							
00081980-2559449	(M5.8)	ABDMG	60.1	5.3	$87.1^{+8.2}_{-7.8}$	$36.2^{+2.4}_{-2.0}$	10.0 ± 2.0
00091768+0603461	(M5.2)	ABDMG	36.6	2.4	$156.3^{+14.4}_{-12.8}$	25.3 ± 1.6	-2.0 ± 2.0
00165057-7122387	(M5.7)	THA	36.6	< 0.1	$57.7^{+8.1}_{-6.3}$	47.4 ± 3.2	-3.4 ± 3.0
00165242-7640540	(M5.3)	THA	31.8	< 0.1	$85.0^{+11.1}_{-8.9}$	$45.4^{+3.2}_{-2.8}$	6.4 ± 2.4
00200551-5359372	(M6.2)	THA	98.9	< 0.1	$36.2^{+9.3}_{-6.7}$	$39.8^{+2.4}_{-2.0}$	5.3 ± 2.4
00303013-1450333	L7	ARG	24.1	2.6	$10.4^{+0.6}_{-0.4}$	26.7 ± 3.2	4.3 ± 2.0
00381489-6403529	(M8.6)	THA	99.7	< 0.1	$15.3^{+0.7}_{-6.1}$	44.2 ± 2.4	7.5 ± 2.4
00425349-6117384	M4.2	THA	99.9	< 0.1	$123.0^{+15.6}_{-13.1}$	42.6 ± 2.4	6.9 ± 1.0
00455663+3347109	M4.5	ARG	89.7	0.1	$86.4^{+8.4}_{-7.7}$	18.1 ± 1.3	4.3 ± 1.4
00474453+4159428	(M3.7)	BPMG	49.0	14.4	$169.0^{+10.5}_{-11.0}$	30.5 ± 2.8	-3.2 ± 2.2
00485254-6526330	(M3.3)	THA	84.9	< 0.1	$207.2^{+3.3}_{-1.7}$	50.2 ± 3.2	8.5 ± 2.5
00514561-6227073	(M5.7)	THA	99.8	< 0.1	$54.7^{+7.7}_{-6.1}$	$43.4^{+2.8}_{-2.4}$	7.6 ± 2.4
00530909+0511387	(M5.1)	ABDMG	24.9	4.8	$168.7^{+16.0}_{-15.7}$	32.1 ± 2.8	1.8 ± 2.4
00551459+4511019	(M5.3)	ABDMG	19.3	3.3	$141.1^{+13.9}_{-13.5}$	35.8 ± 3.3	-14.4 ± 2.2
00575326-1028004	(M5.3)	ABDMG	15.6	12.3	$122.3^{+12.4}_{-11.3}$	38.6 ± 2.4	8.5 ± 2.0
00583298-0547135	(M5.7)	BPMG	10.8	< 0.1	$54.2^{+3.9}_{-4.6}$	36.6 ± 4.0	5.5 ± 1.8
00584253-0651239	L0	BPMG	88.6	0.3	34.8 ± 2.1	29.6 ± 3.5	6.7 ± 2.0
01000219-6156270	M6	THA	99.1	< 0.1	$48.3^{+7.4}_{-5.9}$	41.4 ± 2.4	7.8 ± 2.4
01075893-3255427	(M5.2)	THA	52.1	< 0.1	$90.6^{+11.6}_{-9.2}$	41.8 ± 2.4	1.9 ± 2.1
01121205+0541262	(M5.3)	ABDMG	24.1	4.7	$134.3^{+13.1}_{-12.1}$	30.9 ± 2.4	3.2 ± 2.2
01144953-7813430	(M5.0)	THA	52.2	< 0.1	$96.3^{+12.7}_{-10.6}$	$51.8^{+3.6}_{-3.2}$	12.4 ± 2.1
01190749-4943305	(M5.7)	THA	77.2	< 0.1	$52.5^{+7.5}_{-5.7}$	$37.4^{+2.4}_{-2.0}$	6.7 ± 2.2
01225371-4952175	(M5.3)	THA	82.8	< 0.1	$75.5^{+10.3}_{-7.9}$	35.8 ± 2.0	7.4 ± 2.2
01253196-6646023	M4.2	THA	99.7	< 0.1	$172.1^{+21.9}_{-19.2}$	46.2 ± 3.2	7.1 ± 5.1
01275875-6032243	M4.2	THA	> 99.9	< 0.1	$147.8^{+19.2}_{-16.0}$	43.8 ± 2.8	9.1 ± 2.5
01283025-4921094	M4.1	THA	99.3	< 0.1	$189.5^{+16.6}_{-13.8}$	43.0 ± 2.8	6.5 ± 5.7
01321248-0910029	(M6.3)	THA	20.8	< 0.1	$36.3^{+8.8}_{-6.0}$	$45.8^{+3.2}_{-2.8}$	0.6 ± 2.1
01375150+0727458	(M6.8)	ABDMG	53.7	8.1	$66.0^{+6.3}_{-5.9}$	39.0 ± 2.8	4.6 ± 2.2
01375879-5645447	M3.9	THA	99.9	< 0.1	$198.6^{+10.0}_{-7.7}$	$43.4^{+2.4}_{-2.8}$	8.5 ± 0.6
01422579-6504120	(M5.4)	THA	99.7	< 0.1	$68.1^{+9.8}_{-7.1}$	46.2 ± 2.8	10.2 ± 2.2
01534955+4427284	(M5.3)	ARG	98.5	0.1	$86.8^{+8.2}_{-7.2}$	20.2 ± 1.2	7.4 ± 1.8
02001992-6614017	M4.3	THA	> 99.9	< 0.1	$182.4^{+21.2}_{-17.8}$	43.8 ± 2.8	11.8 ± 1.1
02015072-0726581	(M3.9)	THA	87.0	< 0.1	$163.2^{+20.9}_{-18.1}$	$43.8^{+3.2}_{-2.8}$	3.6 ± 2.1
Candidates with a Modest Probability							
00085614-2813211	(L8.9)	BPMG	21.5	21.8	6.1 ± 0.1	16.1 ± 1.2	5.8 ± 1.5
00102936-0746487	(M6.2)	ABDMG	18.2	19.9	$74.3^{+7.0}_{-6.6}$	$43.8^{+3.2}_{-2.8}$	3.3 ± 2.1
00192753-3620153	M5.5	THA	11.5	43.0	$60.3^{+8.6}_{-6.8}$	$37.8^{+2.0}_{-2.4}$	0.9 ± 2.2
00193193-0554404	(M5.0)	BPMG	30.8	44.2	$89.9^{+6.4}_{-6.1}$	$33.8^{+3.6}_{-3.2}$	3.2 ± 1.7
00281434-3227556	M5	BPMG	30.4	45.7	$168.7^{+10.6}_{-11.1}$	$32.1^{+2.8}_{-3.2}$	8.1 ± 1.5
00324451+2744454	(M5.0)	BPMG	17.4	36.0	93.9 ± 5.6	35.8 ± 3.2	-3.6 ± 2.0
00465095+3822416	(M5.5)	ARG	15.8	28.2	$77.3^{+7.9}_{-8.2}$	$33.8^{+3.2}_{-3.6}$	2.3 ± 1.7
00473149-1424425	(M4.8)	BPMG	54.3	34.2	$100.0^{+5.7}_{-6.3}$	30.9 ± 2.8	6.9 ± 1.5
00584590+2430511	(M5.8)	BPMG	24.8	27.3	46.8 ± 2.6	31.3 ± 2.8	2.2 ± 2.1
01012488-2412472	(M6.0)	BPMG	12.1	30.2	$41.5^{+2.8}_{-2.5}$	23.3 ± 2.0	9.3 ± 1.5

[a]Spectral types in parentheses were estimated from 2MASS–AllWISE colors (see Section 3.5.1).

[b]The binary hypothesis is more probable than the single hypothesis (see Section 3.4).

This table is available in its entirety at *http://dx.doi.org/10.6084/m9.figshare.1207880*. The complete table has 249 rows.

Chapitre 4

THE COOLEST ISOLATED BROWN DWARF CANDIDATE MEMBER OF TWA

Jonathan Gagné[1], Jacqueline K. Faherty[2,3,4], Kelle Cruz[5,6], David Lafrenière[1], René Doyon[1], Lison Malo[1], Étienne Artigau[1]

[1] *Département de Physique and Observatoire du Mont-Mégantic, Université de Montréal, C.P. 6128 Succ. Centre-ville, Montréal, Qc H3C 3J7, Canada*

[2] *Department of Terrestrial Magnetism, Carnegie Institution of Washington, Washington, DC 20015, USA*

[3] *Departamento de Astronomía, Universidad de Chile, Cerro Calán, Las Condes, Chile*

[4] *Hubble Fellow*

[5] *Department of Astrophysics, American Museum of Natural History, Central Park West at 79th Street, New York, NY 10034*

[6] *Department of Physics & Astronomy, Hunter College, 695 Park Avenue, New York, NY 10065, USA*

Received 2014 February 7; accepted 2014 March 12

Published in *The Astrophysical Journal Letters*,

April 2014, *Vol.* 785, *page* L14

4.1 Abstract

We present two new late-type brown dwarf candidate members of the TW Hydrae association (TWA) : 2MASS J12074836–3900043 and 2MASS J12474428–3816464, which were found as part of the BANYAN all-sky survey (BASS) for brown dwarf members to nearby young associations. We obtained near-infrared (NIR) spectroscopy for both objects (NIR spectral types are respectively L1 and M9), as well as optical spectroscopy for J1207–3900 (optical spectral type is L0 γ), and show that both display clear signs of low-gravity, and thus youth. We use the BANYAN II bayesian inference tool to show that both objects are candidate members to TWA with a very low probability of being field contaminants, although the kinematics of J1247–3816 seem slightly at odds with that of other TWA members. J1207–3900 is currently the latest-type and the only isolated L-type candidate member of TWA. Measuring the distance and radial velocity of both objects is still required to claim them as bona fide members. Such late-type objects are predicted to have masses down to 11–15 $M_{\rm Jup}$ at the age of TWA, which makes them compelling targets to study atmospheric properties in a regime similar to that of currently known imaged extrasolar planets.

4.2 Introduction

The known population of brown dwarfs (BDs) has significantly increased in the last decades due to all-sky near-infrared (NIR) surveys such as 2MASS and WISE (Skrutskie et al. 2006, Wright et al. 2010). The acumulation of a large number of BDs allowed for a better understanding of the underlying physics in their atmospheres, which went along with the development of increasingly more realistic atmosphere models (Baraffe et al. 2003, Saumon & Marley 2008, Morley et al. 2012, Allard et al. 2013) and empirical spectral classification schemes (Kirkpatrick et al. 1991, Cushing et al. 2005, Burgasser et al. 2006, Cruz et al. 2009, Allers & Liu 2013). These tools allowed in turn the identification of peculiar BDs, most of which are now recognized as having atypical metallicity or surface gravity.

Low surface gravity BDs are thought to be younger than several hundred million years since they have not yet reached their equilibrium radii (Burrows et al. 2001). The youngest

and latest-type of these objects are believed to have cool, low-pressure atmospheres similar to those of currently known imaged gaseous giant exoplanets, but only a few of those are known in the solar neighborhood (e.g. 2MASS J03552337+1133437; Faherty et al. 2013b; PSO J318.5338-22.8603; Liu et al. 2013b; CFBDSIR 2149-0403; Delorme et al. 2012). Hence, atmosphere models for such physical conditions are still subject to poor empirical constraints (e.g. the behavior of dust in these low-pressure environments). While the luminosity, equivalent width of atomic lines, and shape of the continuum can be used to identify young brown dwarfs, there is no evidence yet that those can be used to narrowly constrain ages (Allers & Liu 2013). Therefore, assembling an an age-calibrated sample identified by kinematics could potentially help addressing this in an empirical way. Given their relative proximity, nearby, young moving groups (YMGs) such as TW Hydrae (TWA; Zuckerman & Song 2004) are perfect test benches for such empirical calibrations. The search for late-type objects in YMGs has been the subject of many efforts (Zuckerman & Song 2004; Looper et al. 2007a; Torres et al. 2008; Malo et al. 2013), however their late-type ($>$M5) population is poorly constrained. To address this further, we developed Bayesian Analysis for Nearby Young AssociatioNs II (BANYAN II) in Chapter 2, a tool based on Malo et al. (2013) that uses naive bayesian inference to identify late-type candidate members to such YMGs from their sky position, proper motion and photometry. Using this new tool, our team has initiated the BANYAN all-sky survey (BASS) that generated hundreds of $>$M5 candidate members to YMGs from the 2MASS and WISE surveys, using both catalogues as a baseline for a proper motion measurement. The current status of this project is described in more detail in Gagné et al. (2013).

Here, we present two of the potential latest-type and lowest-mass objects that were identified as candidate members to TWA from this all-sky survey : 2MASS J12474428–3816464 (M9; called J1247–3816 hereafter) and 2MASS J12074836–3900043 (L1; called J1207–3900 hereafter), with NIR spectral types M9 and L1, respectively. We present NIR SpeX spectroscopy for the two objects, as well as optical MagE spectroscopy for J1207–3900 in Section 4.4.1. In Section ,4.4.2, we show evidence that both have a low surface gravity, and we use the BANYAN II tool in Section 4.4.3 to show that both objects are likely members of TWA with

a small probability of being young field contaminants, but that J1247–3816 seems to display slightly discrepant kinematics.

4.3 Spectroscopy

4.3.1 NIR spectroscopy

We have obtained SpeX (Rayner et al. 2003) NIR spectroscopy for J1207–3900 and J1247–3816 at the IRTF telescope on May 10 2013. Observations were obtained under a typical seeing of 0".6. We used the prism disperser with the 0".8 slit for both objects, yielding a resolution $R \sim 95$ over 0.8 to 2.5 μm. Four exposures of 200 s for J1207–3900 and 180 s for J1247–3816 were sufficient to reach signal-to-noise (S/N) per resolution element $\sim$240 for both objects. We have subsequently obtained an R $\sim$ 750 spectrum for J1207–3900 in the cross-dispersed mode with the 0".8 slit on May 14 2013 to be able to measure the equivalent width of several atomic lines and better constrain its low-gravity using the approach of Allers & Liu (2013; see Section 4.4.2). Ten exposures of 200 s yielded a S/N per resolution element $\sim$65. Individual exposures were reduced by subtracting dithered sequences along the slit, extracting both traces and correcting for

telluric absorption with A0-type standards, using the SpeXtool Interactive Data Language (IDL) package (Cushing et al. 2004; Vacca et al. 2003). The NIR spectra for both objects are displayed in Figure 4.1.

4.3.2 Optical spectroscopy

In addition to the NIR spectroscopy described in the previous section, we have obtained optical spectroscopy for J1207–3900 on May 14 2013 with MagE at the Magellan telescope to compare it with standard optical spectra of low-gravity BDs (Cruz et al. 2009). We used the 0".7 slit and 2800 s of exposure to obtain a R $\sim$ 5800 spectrum in the 5500–10300 Å range with a S/N per resolution element $\sim$ 16. Individual exposures were reduced in a similar manner than described in the previous section by using the MASE IDL package (Bochanski et al.

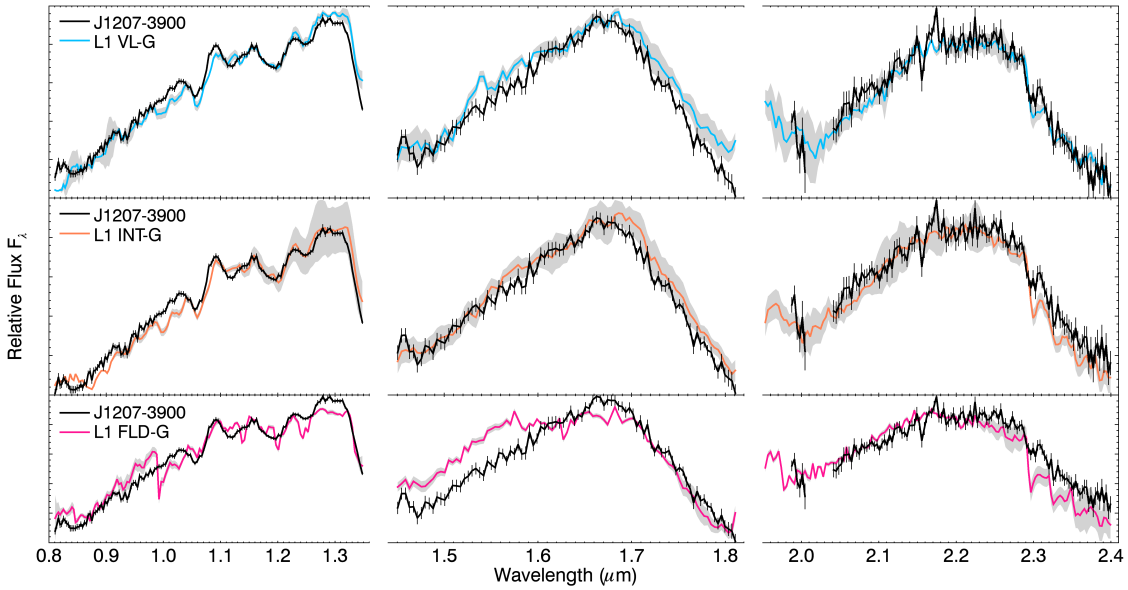

(a) 2MASS J12074836-3900043

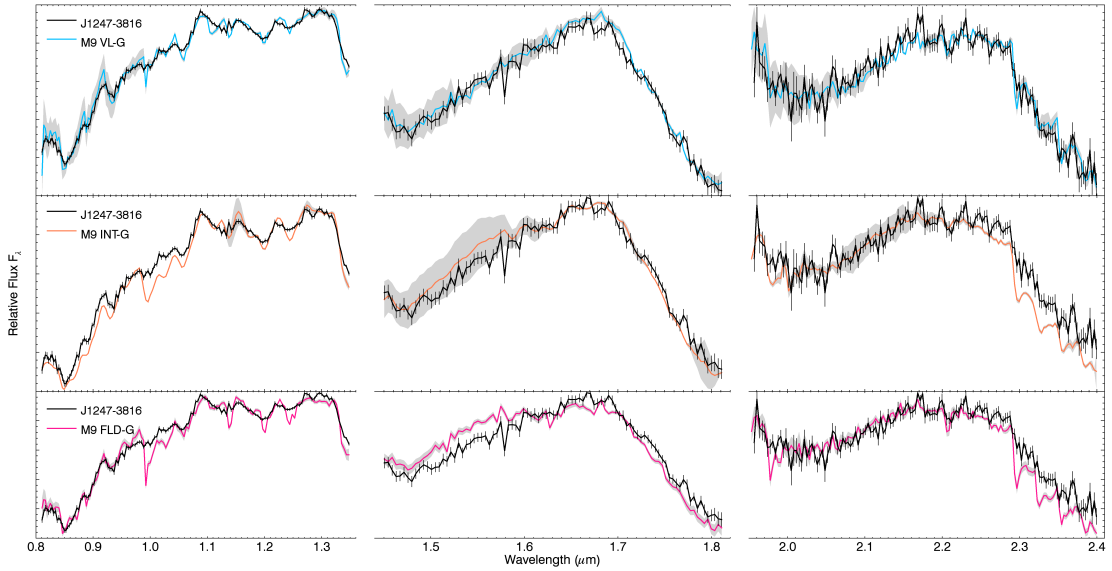

(b) 2MASS J12474428-3816464

FIGURE 4.1 Comparison of the NIR spectra of J1207–3900 (a) and J1247–3816 (b; black lines) with L1 and M9 spectroscopic templates (colored lines; as described in Section 4.4.1), respectively. Each band was normalized individually. The grey shaded region represents the scatter between individual objects that were used to create the templates and the black vertical lines represent the measurement errors on each bin of the candidates' spectra. In the case of J1247–3816, a better match is clearly achieved with the very low gravity template, whereas J1207–3900 is well fit by both the VL-G and INT-G templates which are quite similar themselves.

Table 4.1. Properties of the New Candidates

Property	J1207–3900	J1247–3816
R.A.	12:07:48.362	12:47:44.290
Decl.	-39:00:04.40	-38:16:46.40
μ_α (mas yr^{-1})	-57.2 ± 7.9	-33.2 ± 7.1
μ_δ (mas yr^{-1})	-24.8 ± 10.5	-16.6 ± 9.5
I (DENIS)	···	17.85 ± 0.16
J (2MASS)	15.50 ± 0.06	14.79 ± 0.03
H (2MASS)	14.61 ± 0.05	14.10 ± 0.04
K_S (2MASS)	14.04 ± 0.06	13.57 ± 0.04
$W1$ (WISE)	13.63 ± 0.03[a]	13.11 ± 0.02
$W2$ (WISE)	13.22 ± 0.03	12.52 ± 0.03
$W3$ (WISE)	> 13.20	10.95 ± 0.08
$W4$ (WISE)	> 9.20	8.84 ± 0.29[b]
Optical Spectral type	L0 $\pm$ 0.5 γ	···
NIR Spectral type	L1 $\pm$ 1 VL-G	M9 $\pm$ 0.5 VL-G
TWA d_s[c](pc)	60.2 ± 5.2	63.8 ± 6.4
TWA v_s[c](km s^{-1})	9.7 ± 1.7	9.6 ± 1.7
$Field$ d_s[c](pc)	63.0 ± 10.4	55.4 ± 11.6
$Field$ v_s[c](km s^{-1})	6.7 ± 10.2	4.0 ± 10.4

[a]Possibly contaminated by a diffraction spike.

[b]Possibly contaminated by a nearby source.

[c]Statistical predictions from the BANYAN II tool. See Section 4.4.3 for more information.

2009). The optical spectrum of J1207–3900 is presented in Figure 4.2[1].

4.4 Results and discussion

4.4.1 Spectral classification

We used the method of K. Cruz et al. (in preparation)[2] to median-combine all NIR spectra from Allers & Liu (2013) by spectral type to create individual NIR spectroscopic templates for intermediate-gravity (INT-G) objects in the M8–L3 range, as well as very low gravity (VL-G) objects in the M6–L4 range. We used objects that were classified as having a normal surface gravity, as well as medium-resolution spectra from the SpeX Prism library to build field NIR templates in the M5–L9 range. We then assigned spectral types to both objects by visually comparing their spectra band-by-band with those composite spectroscopic templates (see Figure 4.1). We find that the M9 VL-G template is clearly the best match to J1247–3816 and that the L1 INT-G and L1 VL-G templates are equally good matches to J1207–3900. We

[1]All spectra presented here for J1207–3900 and J1247–3816 can be found at *www.astro.umontreal.ca/~gagne*.

[2]see also the 2012 Cool Stars 17 poster Cruz & Núñez 2012

have visually assigned uncertainties of ± 0.5 and ± 1 subtypes, respectively. If we restrict our comparison to field NIR standards only, we also find that M9 and L1 spectral types are the best matches, however we would have assigned larger uncertainties to them. We also directly compared the spectra of the two candidates to the latest currently known TWA members and candidates (TWA 28, M8.5 candidate; TWA 26, M9 member; and TWA 29, M9.5 candidate; see Mamajek 2005 and Looper et al. 2007a) to confirm our results. Since there are no known L0–L4 objects in TWA, we could only verify that J1207–3900 has redder *J*- and *H*-band slopes than TWA 29, which is consistent with it being later-type.

We have subsequently compared the MagE optical spectrum to several field and young M8 to L5 optical templates (Stauffer et al. 2003; Gizis & Reid 2005; Burgasser & McElwain 2006; Reid et al. 2008a) to find that the best match are LHS 2924 (a field M9), KPNO-Tau 4 (a young M9.5 BD in the Taurus star forming region; 1–10 Myr; Briceño et al. 2002) and 2MASS 0141-4633 (a young L0 γ candidate member to the 10–40 Myr Tucana-Horologium association; Kirkpatrick et al. 2006, Paper II). The continuum redwards of 8500 Å matches 2MASS 0141-4633 better, however J1207–3900 clearly shows a VO band at 7450 Å which is deeper than that of 2MASS 0141-4633, and similar to that of KPNO-Tau 4. This is consistent with J1207–3900 having a similar spectral type than 2MASS 0141-4633 while being slightly younger. We thus assign it an optical classification of L0 γ (see Figure 4.2).

4.4.2 Signs of low gravity

We used the NIR gravity classification scheme described in Allers & Liu (2013 ; based on of the gravity-sensitive equivalent widths of K I, Na I and continuum features) to analyze the NIR spectra presented here and find that, based on a comparison to other objects of the same spectral types, both objects are clearly VL-G objects (see Figure 4.3), as was expected from the visual comparison with low gravity dwarfs. The MagE spectrum of J1207–3900 was subsequently used in deriving various gravity-dependent indices described in Cruz et al. (2009; e.g. K-a, K-b, Na-a, Na-b), which also point towards a low surface gravity. We used the IRSA dust extinction tool[3] to verify that both objects are not significantly reddened by interstellar

[3]available at *http://irsa.ipac.caltech.edu/applications/DUST/*

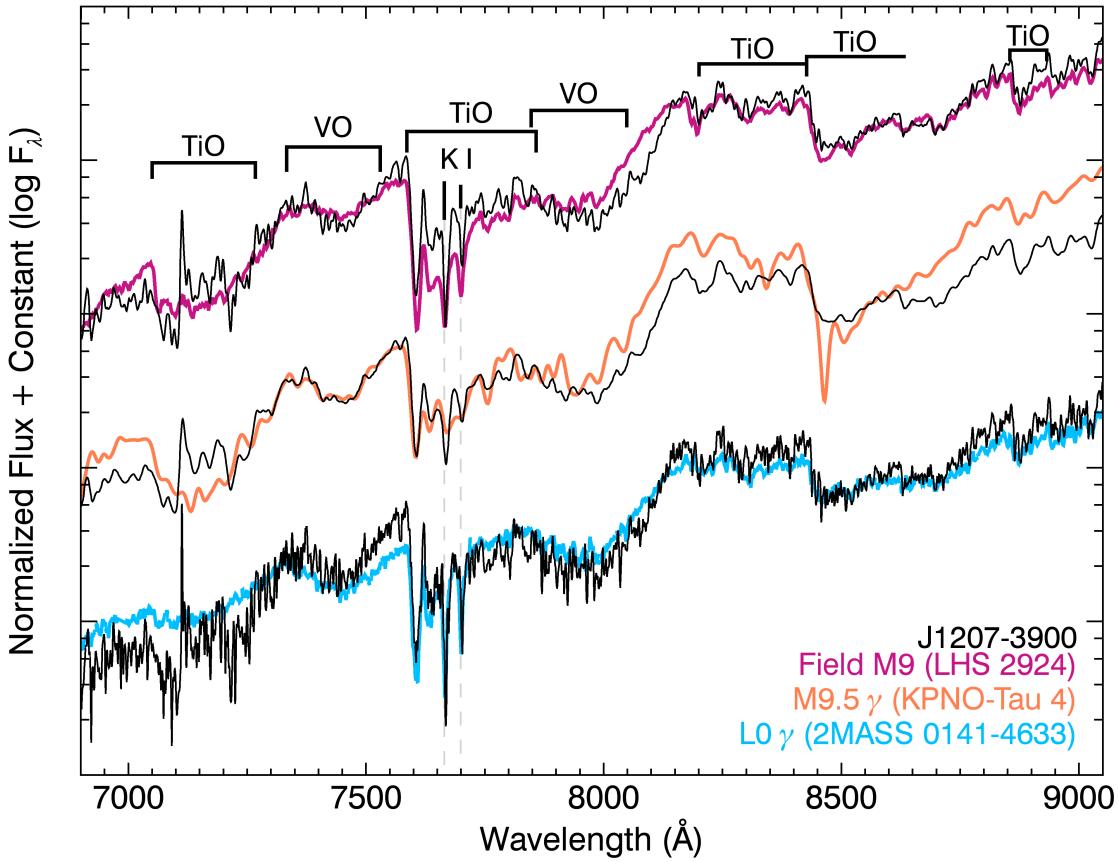

FIGURE 4.2 Optical MagE spectrum of J1207–3900, compared to known field and young late M standards (Stauffer et al. 2003; Gizis & Reid 2005; Burgasser & McElwain 2006; Reid et al. 2008a). All spectra were normalized to their median between 7000 and 9000 Å. It can be seen that the VO band at 7450 Å is deeper than that of field dwarfs in J1207–3900, which is a telltale sign of youth.

dust along the line of sight, which could potentially mimic some signatures of low gravity. We find that J1207–3900 and J1247–3816 respectively lie in regions of the sky where the E(B-V) extinction is low at 0.0687 ± 0.0035 mag and 0.0492 ± 0.0014 mag, using a 5′ search radius (Schlafly & Finkbeiner 2011).

4.4.3 TWA membership

We have applied the BANYAN II tool described in Paper II to assess the probability that both objects considered here are members of YMGs. We used their sky position, proper

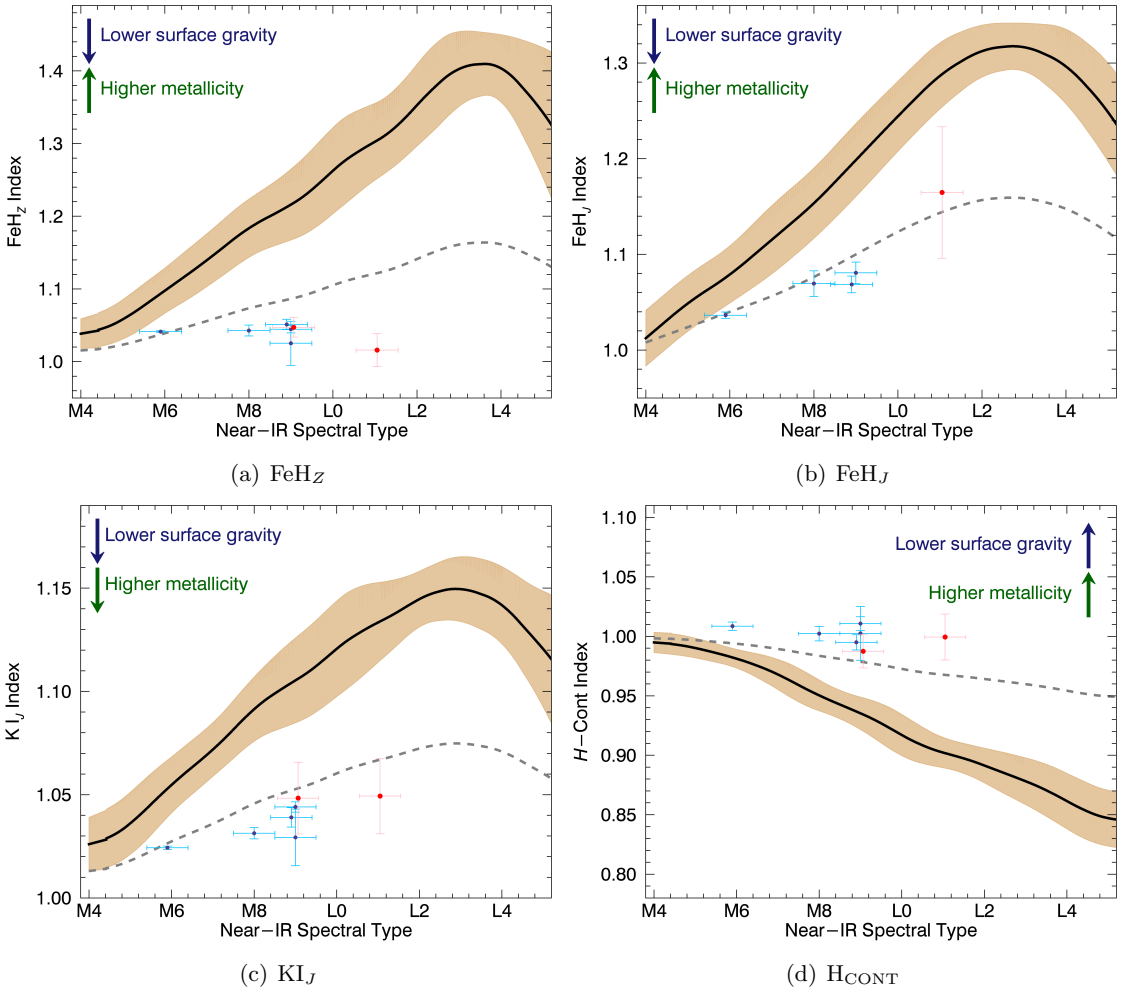

(a) FeH$_Z$ (b) FeH$_J$

(c) KI$_J$ (d) H$_{\mathrm{CONT}}$

FIGURE 4.3 Spectral indices as defined by Allers & Liu (2013) for J1207–3900 and J1247–3816 (red dots), compared to known TWA members (blue dots), the field sequence (thick, black line) and its scatter (beige shaded region). The dotted line represents the delimitation between intermediate (INT-G) gravity and very low gravity (VL-G) regimes. Both candidates have spectral indices consistent with TWA members. Spectral types were offset by small (<0.15) random subtypes so that vertical error bars can be distinguished. All indices displayed here for J1207–3900 and J1247–3816 were measured using the SpeX prism spectra, except for the FeH$_J$ index which was measured with the cross-dispersed spectrum. The spectra of known TWA members in this figure are those of TWA 22 A (M5) and TWA 34 (M6) obtained respectively from Bonnefoy et al. (2009) and J. Gagné et al. (accepted for publication in ApJ; see Chapter 6), as well as TWA 27 A (M8), TWA 26 (M9), TWA 28 (M8) and TWA 29 (M9) obtained from Allers & Liu (2013).

motion, spectral types as well as 2MASS and WISE photometry as input observables in this analysis, which are then compared to the spatial and kinematic models of each hypothesis considered (TWA, β Pictoris, Tucana-Horologium, Columba, Carina, Argus, AB Doradus and the field) using a naive bayesian classifier. The spatial and kinematic models are built by fitting the spatial XYZ and UVW distribution of known bona fide members or synthetic objects from the Besançon Galactic model (A. C. Robin et al., in preparataion ; Robin et al. 2012) with 3D ellipsoids that are free to rotate along any axes. Following our conclusion that both systems are low gravity dwarfs, we have assumed conservatively that they are younger than 1 Gyr in the construction of the field hypothesis. Using this tool, we find that J1207–3900 and J1247–3816 are both candidate members to TWA with bayesian probabilities of 99.7% and 19.9%, respectively. In an ideal case where quantities input in BANYAN II are strictly independent, the bayesian probability should represent the best estimate of the probability that a given star be a member of a given YMG, taking into account all available evidence (i.e. data input in the bayesian inference tool). However, as described in Paper II, the bayesian probabilities determined this way are biased when quantities fed to BANYAN II (which consists of a *naive bayesian classifier*) are not strictly independent, which is generally the case in our analysis. A Monte Carlo analysis was thus performed to estimate the unbiased probability that a given object is a field contaminant based on its bayesian probability. Here, we applied this analysis and found very low field contamination probabilities of 0.004% and 0.006%, respectively (meaning that our present bayesian probabilities are pessimistic). In Table 4.1 we show the radial velocities v_s and distances d_s predicted by Banyan II, according to the hypotheses that they are actual members to TWA or the field. These estimates were shown by Paper II to be accurate to 8 % and 1.6 $\mathrm{km\,s^{-1}}$, respectively, when membership is confirmed.

We have compared our results to those of BANYAN I (without using photometry as an observable, see Malo et al. 2013), as well as the convergent point analysis (CPA, see Rodriguez et al. 2013). In the case of J1207–3900, BANYAN I yields a membership probability of 99.94% for TWA and 0.06% for the field with predictions [$v_s = 9.78 \pm 2.2\,\mathrm{km\,s^{-1}}$, $d_s = 54.0 \pm 5.6\,\mathrm{pc}$] for TWA, whereas the CPA yields a 91.6% probability for TWA, 100.0% probability for

β Pictoris and 81.1% probability for Columba with respective predictions of [$v_s = 6.8\,\mathrm{km\,s^{-1}}$, $d_s = 69.6\,\mathrm{pc}$], [$v_s = 5.7\,\mathrm{km\,s^{-1}}$, $d_s = 67.7\,\mathrm{pc}$] and [$v_s = 12.7\,\mathrm{km\,s^{-1}}$, $d_s = 79.3\,\mathrm{pc}$]. Probabilities from BANYAN I are generally higher than those of BANYAN II because prior probabilities were set to unity in their analysis, whereas prior probabilities in BANYAN II are smaller to reflect the smaller populations of YMGs compared to that of the field. Furthermore, we stress the fact that even BANYAN II probabilities as low as $P_{H_k} \sim 20\%$ for any YMG must be considered as potentially significant, since such values are often found for several known bona fide YMG members that lie 1–2.5σ away from the spatial and kinematic locus of bona fide members (see Paper II). Probabilities yielded by the CPA are determined individually for each YMG, which means that the total probability can be larger than 100%. Thus, both versions of BANYAN agree very well, but the CPA would place J1207–3900 as an ambiguous candidate between β Pictoris, TWA and Columba. We do not consider that J1207–3900 is a viable candidate to β Pictoris or Columba, since it has been shown by Paper II that such cross-contamination from those two associations to TWA are lower than 3%, even for low probability TWA candidates. The CPA tool does not consider spatial information or the magnitude of proper motion, and thus often cannot differentiate between a few YMG hypotheses without a radial velocity measurement, especially when their convergent points are close one to another on the celestial sphere, which is the case for TWA, β Pictoris and Columba.

In the case of J1247–3816, BANYAN I yields a membership probability of 87.59% for TWA and 12.41% for the field, with predictions of [$v_s = 7.25 \pm 2.57\,\mathrm{km\,s^{-1}}$, $d_s = 55.5 \pm 5.9\,\mathrm{pc}$] for TWA, and the CPA yields 99.3% for TWA, 98.7% for β Pictoris and 96.0% for Columba, with respective predictions of [$v_s = 4.0\,\mathrm{km\,s^{-1}}$, $d_s = 120.7\,\mathrm{pc}$], [$v_s = 3.1\,\mathrm{km\,s^{-1}}$, $d_s = 117.0\,\mathrm{pc}$] and [$v_s = 9.5\,\mathrm{km\,s^{-1}}$, $d_s = 141.0\,\mathrm{pc}$]. We note that the relatively smaller probabilities yielded by BANYAN as well as the very large predicted distances from the CPA can both be seen as a consequence of the fact that J1247–3816 has a slightly deviant proper motion compared to TWA members at this sky position. Effectively, the most probable scenario yielded by BANYAN II places this object at a Galactic position and space velocity $XYZUVW$ of respectively : 30.9 ± 3.1 pc, -49.1 ± 4.9 pc, 26.5 ± 2.7 pc, -2.7 ± 2.2 $\mathrm{km\,s^{-1}}$, -14.5 ± 2.1 $\mathrm{km\,s^{-1}}$ and -0.7 ± 2.7 $\mathrm{km\,s^{-1}}$, at respectively 1.5σ and 3.0σ from the spatial and kinematic models

used in BANYAN II. The CPA tool, which is purely kinematic, places J1247–3816 at a larger distance so that it ends up with kinematics closer to those of TWA (at 0.7σ of the same kinematic model).

Schneider et al. (2012a) point out that the Lower-Centaurus-Crux (LCC) complex is a possible source of contamination for TWA, however it is located at ~ 120 pc (further than typical TWA members at ~ 50 pc). Most probable distances derived from BANYAN II for both the TWA and field hypotheses place place J1207–3900 and J1247–3816 at distances of ~ 60 pc either for TWA or the field hypothesis, which is not compatible with them being at such a large distance. We conclude that J1207–3900 should be considered as the first isolated L dwarf candidate member to TWA, whereas the membership of J1247–3816 is more ambiguous. Radial velocity and parallax would further constrain their memberships.

We have compared these same distance estimates yielded by BANYAN II as well as 2MASS and WISE NIR photometry to the AMES-Cond isochrones (Baraffe et al. 2003) in combination with CIFIST2011 BT-SETTL atmosphere models (Allard et al. 2013 ; Rajpurohit et al. 2013) in a likelihood analysis, while assuming the age of TWA (8–12 Myr), to estimate the masses of both components. We find that J1207–3900 is thus a candidate 11–13 $M_{\rm Jup}$ BD and J1247–3816 is a candidate 14–15 $M_{\rm Jup}$ BD.

Both new candidates presented here bring the opportunity of extending the population of TWA members redward in a color-magnitude diagram, up into the L dwarfs regime. In Figure 4.4, we show a NIR color-magnitude diagram comparing current TWA members in the literature to field stars and new TWA candidates. In the cases where a trigonometric distance is not available (e.g. for both candidates presented here), we used BANYAN II to produce a statistical distance estimate corresponding to the kinematics of TWA and used it to compute a statistical absolute magnitude. It can be seen the TWA sequence is shifted towards redder colors (for late-type objects) and brighter absolute magnitudes (for early-type objects) compared to the field sequence, which is consistent with current evidence on the atmospheric properties of young systems (Faherty et al. 2012 ; Liu et al. 2013a). J1207–3900 and J1247–3816 are similarly redder to the field dwarfs sequence, and extend the TWA sequence.

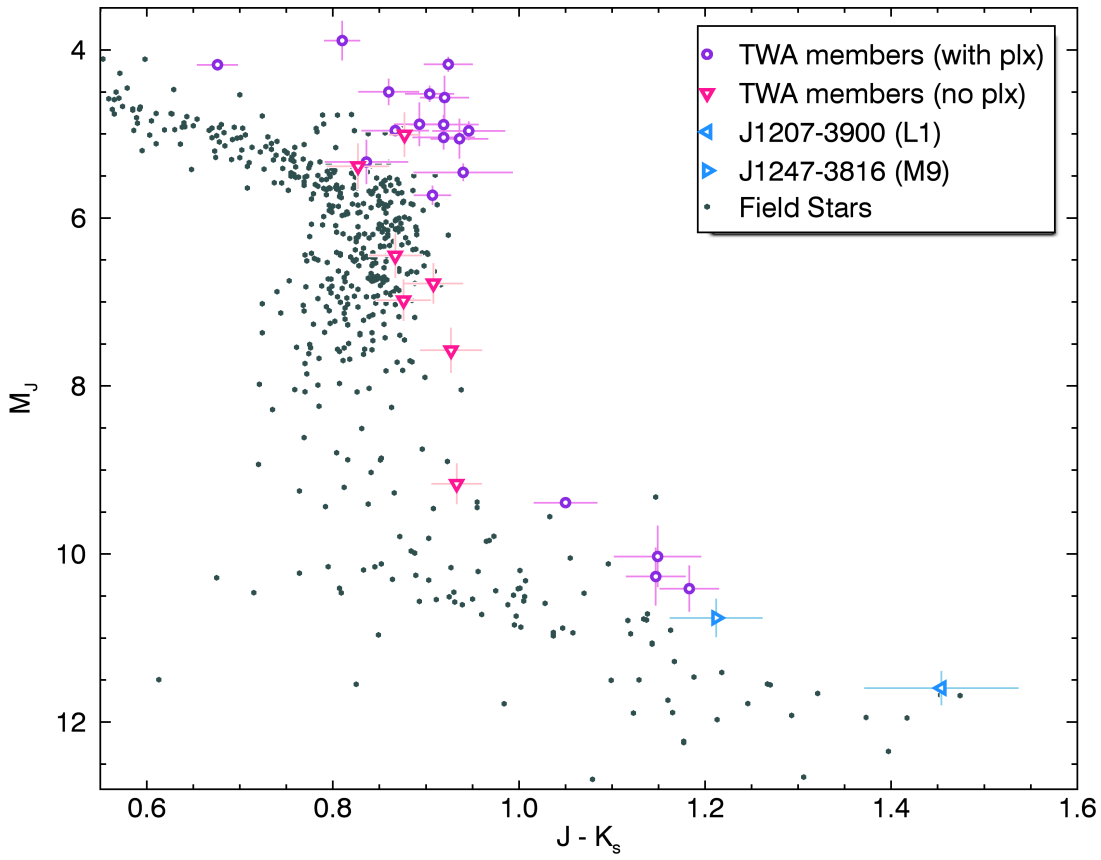

FIGURE 4.4 Color-magnitude sequence for all known primary TWA members and field stars from the CNS3 catalog (Gliese & Jahreiß 1991) and Trent Dupuy's *Database of Ultracool Parallaxes* (black dots, Dupuy & Liu 2012). We used parallax measurements for TWA candidates when they were available (pink downside triangles ;van Leeuwen 2007a ; Teixeira et al. 2008 ; Weinberger et al. 2013a ; Ducourant et al. 2014), or otherwise statistical predictions from BANYAN II (purple circles). J1247–3816 (right-pointing blue triangle) and J1207–3900 (left-pointing blue triangle) also rely on distance predictions from BANYAN II, and appear as an extension of the TWA sequence into the L dwarfs regime.

4.5 Concluding remarks

The two new candidates to TWA presented here were discovered as part of BASS, an all-sky survey for late-type low-mass stars (LMSs) and BDs in YMGs based on the 2MASS and WISE catalogs. This survey has already identified other young objects such as 2MASS J01033563-5515561 ABb (see Delorme et al. 2013), and several hundreds of $>$ M5 candidates identified in the same way are currently being followed and results will be published in an upcoming paper (see Gagné et al. 2013 for more information).

We thank our anonymous referee for a thorough and useful revision of this work. We thank Katelyn Allers and Mickaël Bonnefoy for sharing data and David Rodriguez as well as Michael Liu for useful discussions. This work was supported in part through grants from the Fond de Recherche Québécois – Nature et Technologie and the Natural Science and Engineering Research Council of Canada. This research has benefitted from the SpeX Prism Spectral Libraries, maintained by Adam Burgasser at *http://pono.ucsd.edu/~adam/browndwarfs/spexprism*, and the *Database of Ultracool Parallaxes* at *http://www.cfa.harvard.edu/~tdupuy/plx/Database_of_Ultracool_Parallaxes.html*. This research made use of ; the SIMBAD database and VizieR catalogue access tool, operated at Centre de Données astronomiques de Strasbourg, France (Ochsenbein et al. 2000) ; data products from the Two Micron All Sky Survey, which is a joint project of the University of Massachusetts and the Infrared Processing and Analysis Center (IPAC)/California Institute of Technology (Caltech), funded by the National Aeronautics and Space Administration (NASA) and the National Science Foundation (Skrutskie et al. 2006) ; data products from the Wide-field Infrared Survey Explorer, which is a joint project of the University of California, Los Angeles, and the Jet Propulsion Laboratory (JPL)/Caltech, funded by NASA (Wright et al. 2010) ; the NASA/IPAC Infrared Science Archive, which is operated by the JPL, Caltech, under contract with NASA ; the Infrared Telescope Facility, which is operated by the University of Hawaii under Cooperative Agreement NNX-08AE38A with NASA, Science Mission Directorate, Planetary Astronomy Program. This paper includes data gathered with the 6.5 meter Magellan Telescopes located at Las Campanas Observatory, Chile (CNTAC program CN2013A-135).

Chapitre 5

SIMP J2154–1055: A NEW LOW-GRAVITY L4 β BROWN DWARF CANDIDATE MEMBER OF THE ARGUS ASSOCIATION

Jonathan Gagné[1], David Lafrenière[1], René Doyon[1], Étienne Artigau[1], Lison Malo[1,2], Jasmin Robert[1] and Daniel Nadeau[1]

[1] *Département de Physique and Observatoire du Mont-Mégantic, Université de Montréal, C.P. 6128 Succ. Centre-ville, Montréal, Qc H3C 3J7, Canada*

[2] *Canada-France-Hawaii Telescope, 65-1238 Mamalahoa Hwy, Kamuela, HI 96743, USA*

Received 2014 June 2; accepted 2014 July 18

Published in *The Astrophysical Journal Letters*,
August 2014, *Vol.* 792, *page* L17

5.1 Abstract

We present SIMP J21543454–1055308, a new L4 β brown dwarf identified in the *Sondage Infrarouge de Mouvement Propre* survey that displays signs of low gravity in its near-infrared spectrum. Using the Bayesian Analysis for Nearby Young AssociatioNs II (BANYAN II), we show that it is a candidate member of the Argus association, albeit with a 21% probability that it is a contaminant from the field. Measurements of radial velocity and parallax will be needed to verify its membership. If it is a member of Argus (age 30–50 Myr), then this object would have a planetary mass of $10 \pm 0.5\ M_{\rm Jup}$.

5.2 Introduction

In the last decade, several brown dwarfs (BDs) in the field have been identified as displaying low-gravity features attributable to youth (Kirkpatrick et al. 2008; Cruz et al. 2009; Allers & Liu 2013; Liu et al. 2013b; Gagné et al. 2014a – see Chapter 4). One could expect that a fraction of those young objects are unrecognized members of kinematic associations. However, the lack of parallax or radial velocity measurements for those objects prevents us from directly assessing their kinematics, which makes the identification of BD members to nearby young associations very hard. Identifying such BDs of known age would provide benchmarks to study the atmospheres of very low-mass BDs that are known to have features similar to those of the few directly imaged giant exoplanets known today (e.g., Chauvin et al. 2004; Marois et al. 2008; Lafrenière et al. 2008; Lagrange et al. 2009; Bowler et al. 2013; Rameau et al. 2013; Kuzuhara et al. 2013; Currie et al. 2014; Naud et al. 2014). In order to address this, we developed in Chapter 2 the Bayesian Analysis for Nearby Young AssociatioNs II tool (BANYAN II), a statistical analysis based on BANYAN I (Malo et al. 2013) that uses a naive bayesian classifier to identify low-mass star and BD candidates to membership in nearby young associations, even in the absence of radial velocity and parallax measurements.

SIMP J21543454–1055308 (SIMP J2154–1055 hereafter) is a new low-gravity BD that we discovered as part of the *Sondage Infrarouge de Mouvement Propre* (SIMP). We briefly describe the SIMP survey in Section 5.3, and then present a spectroscopic follow-up of

SIMP J2154–1055 in Section 5.4. In Section 5.5, we show evidence that this BD displays signs of low gravity, by comparing its near-infrared (NIR) spectrum with low-gravity standards and by using the gravity classification scheme of Allers & Liu (2013). We finally use the BANYAN II tool to show that this young BD is a candidate Argus association member (Section 5.6).

5.3 The SIMP survey

The SIMP survey (Artigau et al. 2009) has been initiated in 2006 to identify new nearby BDs from their red optical-to-NIR colors and high proper motions, by obtaining a second J-band epoch for 30% of the sky (mostly in the Southern Hemisphere), 5–8 yr after the Two Micron All Sky Survey (2MASS; Skrutskie et al. 2006). This was achieved by using the CPAPIR camera (Artigau et al. 2004) on both the CTIO 1.5 m telescope and the Observatoire du Mont-Mégantic 1.6 m telescope. The SIMP survey typically reached an astrometric precision of $0\farcs15$ and a photometric depth of $J = 17$. Any source in the SIMP survey that satisfied at least one of three filters based on proper motion (μ) and $I - J$ color was selected for a spectroscopic follow-up: (1) $\mu > 100\,\mathrm{mas\,yr^{-1}}$ and detected in I with $I - J > 3.5$; (2) $\mu > 100\,\mathrm{mas\,yr^{-1}}$ and not detected in I such that $I - J > 3$; or (3) $\mu > 200\,\mathrm{mas\,yr^{-1}}$ and not detected in I. I magnitudes were selected either from the *SuperCOSMOS Sky Survey* (SSS; Hambly et al. 2001), the Sloan Digital Sky Survey (SDSS; York et al. 2000), or the Catalina Sky Survey (CSS; Larson et al. 1998), as available and in this order of preference. These criteria were designed to reject close-by M-type dwarfs as well as distant objects. A large number of new BD candidates have been identified this way, from which more than a hundred have been followed with NIR spectroscopy and confirmed as new M5–T3 very low-mass stars and BDs, most of them having spectral types later than L0. Among those, we have identified SIMP J2154–1055, an L4 β BD displaying signs of low-gravity. A few other SIMP discoveries have been highlighted in Artigau et al. (2006) and Artigau et al. (2011), whereas remaining discoveries will be presented in an upcoming paper (J. Robert et al., in preparation).

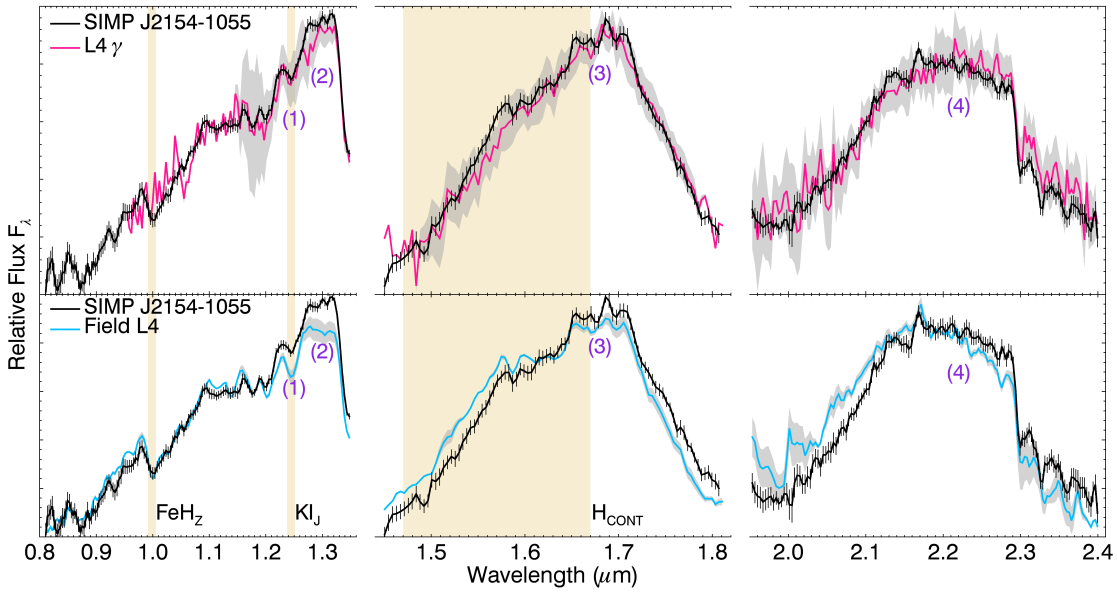

FIGURE 5.1 NIR spectrum of SIMP J2154–1055, compared with field (blue) and very low-gravity (red) template spectra of the same spectral type. Each band was normalized individually. We classify this object as L4 β using the classification scheme of Allers & Liu (2013; Section 5.5), however we do not currently have access to any L4 β BD to build a template and compare it with SIMP J2154–1055. The gray shaded region represents the scatter of the individual objects used to create the templates and the black vertical lines represent the measurement uncertainty on each bin of the observed spectrum. Beige shaded regions correspond to the locations of gravity-sensitive spectral indices defined by Allers & Liu (2013). The global continuum shape of this new BD is a better match to the L4 γ template, despite its H-band continuum that seems to be an intermediate case between the two templates, which is consistent with our classification. We denote regions useful to differentiate between the field and low-gravity templates with purple numbers (Section 5.5).

5.4 Spectroscopic follow-up

The NIR spectrum of SIMP J2154–1055 presented here was obtained on 2008 September 16 at the IRTF (program number 2008B054), using SpeX in the prism mode with the 0.″5 slit ($R \sim 150$), covering the 0.8–2.5 μm range. The source was moved along the slit in an ABBA pattern, with a total of 10 exposures of 180 s to achieve a signal-to-noise ratio of $\sim$180 per resolution element. Raw exposures were reduced and combined using the SpeXtool package (Cushing et al. 2004), and telluric corrections were applied in a standard way (Vacca et al. 2003), using the A-type star HD 202990 observed immediately before the target and at a similar airmass.

5.5 Signs of low gravity

The NIR spectrum of SIMP J2154–1055 was visually compared with various NIR spectral templates to assign it a spectral type and identify peculiar features, following the method of K. Cruz et al. (in preparation; see also Cruz & Núñez 2012). Field templates were built for all spectral types in the M5–T8 range by median-combining high-quality spectra that showed no peculiarities nor signs of unresolved binarity in the DwarfArchives.[1] Low-gravity templates were built from known L0 γ–L4 γ BDs that were classified as low-gravity objects in the optical or the NIR (Cruz et al. 2009; Allers & Liu 2013; K. Cruz et al., in preparation). This comparison showed that SIMP J2154–1055 matches the L4 templates better than any other spectral types. Furthermore, the L4 γ template is a better match than the field L4. The key spectral regions that differentiate between those two templates are; (1) the depth of the KI_J feature at $\sim$1.25 μm; (2) the level of the red end of the J band ($\sim$1.3 μm); (3) the triangular shape of the H band (1.5–1.8 μm); and (4) the slope of the K band plateau (2.15–2.3 μm). We show a comparison of SIMP J2154–1055 with the L4 and L4 γ templates in Figure 5.1, with those four regions identified. The L4 and L4 γ templates were built using five and two distinct spectra respectively.

Allers & Liu (2013) developed an NIR classification scheme to determine spectral types in a way that should not be sensitive to surface gravity, using visual classification supplemented by the H_2O indices, and then determined a gravity class using various spectroscopic indices sensitive to surface gravity. Objects for which most low-gravity indices are strong are classified as very low-gravity (VL-G) objects, and those having only a few indices as intermediate-gravity (INT-G) objects. Those without significant signs of youth are classified as field gravity. We have used this scheme to classify SIMP J2154–1055, with the exception that we used solely visual classification to determine its spectral type. Results are presented in Table 5.1, as well as in Figure 5.2. We find it is classified as an INT-G BD. Allers & Liu (2013) indicate that their INT-G and VL-G classifications respectively correspond to the β and γ classifications defined for optical spectra by Cruz et al. (2009). For this reason, we adopt L4 β as the NIR spectral type of SIMP J2154–1055. Obtaining a higher-resolution NIR spectrum for this object

[1] *http://dwarfarchives.org*

Table 5.1. Properties of SIMP J2154–1055

Property	Value
R.A.	21:54:34.54
Decl.	–10:55:30.8
$\mu_\alpha \cos\delta$ (mas yr^{-1})[a]	169.2 ± 8.6
μ_δ (mas yr^{-1})[a]	-1.6 ± 8.8
I (CSS)[b]	21.63 ± 0.06
J (2MASS)	16.44 ± 0.12
H (2MASS)	15.07 ± 0.08
K_S (2MASS)	14.20 ± 0.07
$W1$ (AllWISE)	13.36 ± 0.03
$W2$ (AllWISE)	12.91 ± 0.03
$W3$ (AllWISE)	12.54 ± 0.53
$W4$ (AllWISE)	> 9.05
NIR spectral type	L4 $\pm 0.5\,\beta$
Gravity score[c]	*1021*
Gravity class[c]	INT-G
Estimated mass ($M_{\rm Jup}$)	10–11

[a]Proper motion from 2MASS, AllWISE, SIMP and *DENIS*.

[b]Combined measurement from 34 epochs.

[c]See Allers & Liu (2013). Scores of *0*, *1* or *2* mean high, medium and low gravity, respectively. The four numbers are based on FeH, VO, K I and the H-band continuum shape, respectively.

would be useful in verifying that its alkali line equivalent widths are effectively weaker than normal. SIMP J2154–1055 is detected in the AllWISE (Kirkpatrick et al. 2014) $W3$ channel, but does not display signs of infrared excess. We also show that it displays the reddest $J - K_s$ NIR color of all currently known L4 dwarfs (Figure 5.3), an effect likely attributed to thicker clouds in its photosphere. It is suspected that low gravity (youth) can cause such thicker clouds (Burgasser et al. 2008b).

5.6 Argus membership

We used the BANYAN II tool (Chapter 2) to verify if SIMP J2154–1055 is a candidate member of nearby young associations. We used the 2MASS and AllWISE astrometry, as well as data from the DEep Near Infrared Survey of the Southern Sky (*DENIS*; Epchtein 1998) and measurements obtained with CPAPIR through the SIMP survey to calculate its proper motion (Table 5.1). We find that SIMP J2154–1055 has a 83.8% probability of being a member of the Argus association (30–50 Myr; Torres et al. 2008). The Argus association of stars was

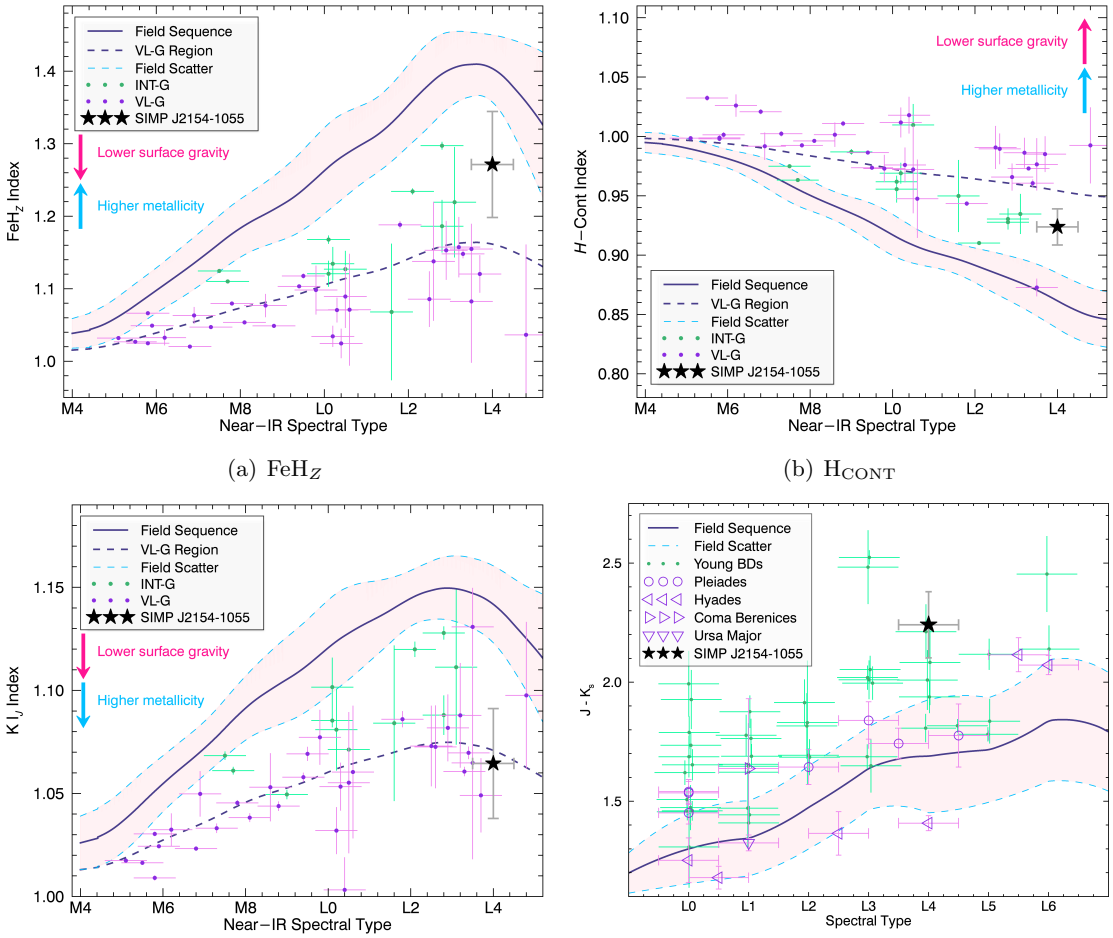

(a) FeH_Z (b) $\mathrm{H}_{\mathrm{CONT}}$

(c) KI_J (d) $J - K_S$

FIGURE 5.2 Panels (a)-(c): Gravity-sensitive spectroscopic indices for SIMP J2154–1055 (black star) compared with the field dwarf sequence (dark blue line) and its associated scatter (pink shaded region delimited by dashed pale blue lines). The dashed dark blue line delimits the intermediate-gravity and very low-gravity regimes. All objects classified as INT-G and VL-G in Allers & Liu (2013) are also displayed as green and purple dots, respectively.

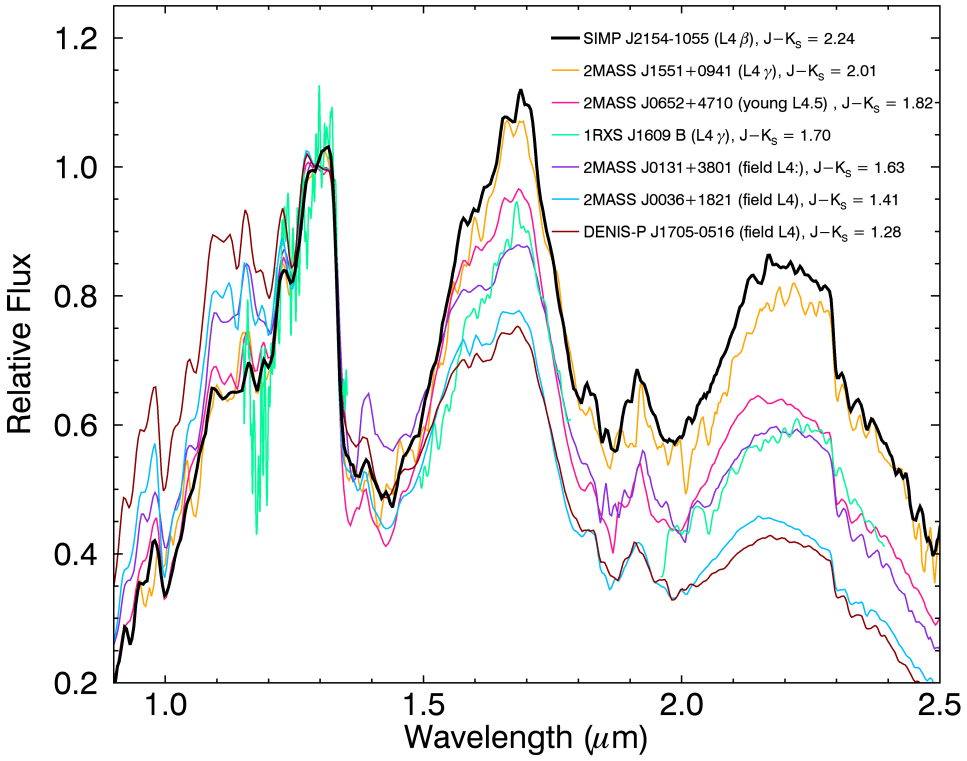

FIGURE 5.3 NIR spectrum of SIMP J2154–1055 (L4 β) compared with other known L4 BDs (Reid et al. 2000; Cruz et al. 2003; Kendall et al. 2004; Cruz et al. 2007; Reid et al. 2008a; Burgasser et al. 2008a; Lafrenière et al. 2008; Lafrenière et al. 2010; Burgasser et al. 2010; Allers & Liu 2013). Although it is classified as INT-G, it is the reddest L4 BD yet identified. All spectra are normalized to their median in the 1.27–1.33 μm range.

first identified by Makarov & Urban (2000), which proposed that the open cluster IC 2391 was a part of it. Torres et al. (2003a) used the method of convergent point proper motion to show that both associations shared common kinematics, thus confirming this hypothesis. This association currently has 11 known A0–M5 bona fide members (Malo et al. 2013), from which the latest-type is the nearby star AP Col (Riedel et al. 2011). In Chapter 2, we also proposed three low-gravity L-type BDs as candidate members to this association. Since the probability for the Argus membership of SIMP J2154–1055 is derived from a naive bayesian classifier, it is expected to be biased when using dependent measurements as input observables (such as is the case here, see detail in Chapter 2). Hence, we used the Monte Carlo contamination analysis presented in Chapter 2 to obtain a probability of 20.5% that SIMP J2154–1055 is a young false-positive from the field. In the present case, the contamination and membership

probabilities are almost exactly complementary, but this is not true in general.

In Figure 5.4, we show the proper motion of SIMP J2154–1055 compared with those of known bona fide members in Argus. Since members are spread across a large portion of the sky, the direction of their proper motion can be different, however it is expected that the great circles corresponding to the motion of all members of a given moving group will pass close to the group's apex and antapex. The proper motion of SIMP J2154–1055 thus seems consistent with a membership to Argus, since its great circle is closer to the apex than 6/11 bona fide members. Its very red $J - K_S$ colors (Figures 5.2 and 5.3) are also consistent with this interpretation. The BANYAN II tool allows us to predict that this object should have a distance of $22.1^{+2.8}_{-2.4}$ pc and a radial velocity of $-13.0 \pm 1.4\,\mathrm{km\,s^{-1}}$ if it is a member of Argus, or a distance of $23.7^{+6.4}_{-5.2}$ pc and a radial velocity of $-8.9 \pm 9.1\,\mathrm{km\,s^{-1}}$ if it is a field object. Using its 2MASS and AllWISE apparent magnitudes, statistical distance, AMES-Cond isochrones (Baraffe et al. 2003) and CIFIST2011 BT-Settl atmosphere models (Allard et al. 2013) we determined that, at the age of Argus (30–50 Myr; Torres et al. 2008), SIMP J2154–1055 has a predicted mass of 10–11 M_{Jup}. Measurements of radial velocity and parallax will be needed to assert its membership.

5.7 Conclusions

We present the discovery of a new young L4 β BD, identified as part of the SIMP survey. We classify it as intermediate-gravity BD following the NIR gravity classification scheme of Allers & Liu (2013). We determine that it has an 84% probability of being an Argus member. We estimate that if it is a member of the Argus association with an adopted age of 30–50 Myr, its mass would be $10 \pm 0.5\,M_{\mathrm{Jup}}$, in the planetary-mass regime. Adding this object to the currently known late-type low-mass stars and BDs will help shape our understanding of the properties of low-gravity, low-pressure atmospheres reminiscent of those of giant, gaseous exoplanets. The data presented in this Letter can be downloaded at our group's Web site[2].

The authors would like to thank the anonymous referee for its suggestions, as well as Kelle Cruz and Jacqueline Faherty for useful comments and discussions and the sharing of spectro-

[2] *http://www.astro.umontreal.ca/~gagne*

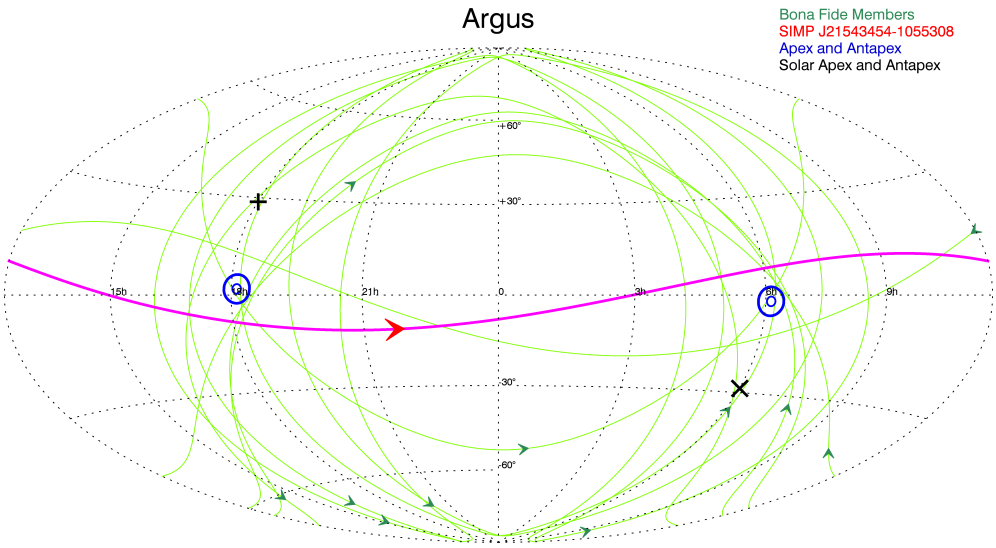

FIGURE 5.4 Position and proper motion (red arrow) of SIMP J2154–1055 with its associated projected great circle on the celestial sphere (pink line), as compared with bona fide members in the Argus association (green lines and arrows). It can be seen that the proper motion of SIMP J2154–1055 is consistent with other bona fide members: its projected great circle falls closer to Argus' apex and antapex (blue circles) than 6 out of 11 known members. The solar motion's apex and antapex are displayed with a black plus sign and cross, respectively.

scopic templates. We thank Katelyn Allers for the sharing of several low-gravity spectra. This work was supported in part through grants from the Fonds de Recherche Québécois - Nature et Technologie and the Natural Science and Engineering Research Council of Canada. This research has benefited from the SpeX Prism Spectral Libraries, maintained by Adam Burgasser at *http://pono.ucsd.edu/ adam/browndwarfs/spexprism*, as well as the M, L, T and Y dwarf compendium housed at DwarfArchives.org. This research made use of; the SIMBAD database and VizieR catalogue access tool, operated at the Centre de Données astronomiques de Strasbourg, France; data products from the 2MASS, which is a joint project of the University of Massachusetts and the Infrared Processing and Analysis Center (IPAC)/California Institute of Technology (Caltech), funded by the National Aeronautics and Space Administration (NASA) and the National Science Foundation (Skrutskie et al. 2006); data products from the *Wide-field Infrared Survey Explorer*, which is a joint project of the University of California, Los Angeles, and the Jet Propulsion Laboratory (JPL)/Caltech, funded by NASA (Wright et al. 2010); the NASA/IPAC Infrared Science Archive, which is operated by JPL, Caltech,

under contract with NASA; the Infrared Telescope Facility (IRTF), which is operated by the University of Hawaii under Cooperative Agreement NNX-08AE38A with NASA, Science Mission Directorate, Planetary Astronomy Program; and of tools provided by Astrometry.net. This publication uses observations obtained at IRTF through program number 2008B054. The authors recognize and acknowledge the very significant cultural role and reverence that the summit of Mauna Kea has always had within the indigenous Hawaiian community. We are most fortunate to have the opportunity to conduct observations from this mountain.

Chapitre 6

BANYAN. VII. A NEW POPULATION OF YOUNG SUBSTELLAR CANDIDATE MEMBERS OF NEARBY MOVING GROUPS FROM THE BASS SURVEY

Jonathan Gagné[1], Jacqueline K. Faherty[2,3,4], Kelle L. Cruz[3,5], David Lafrenière[1], René Doyon[1], Lison Malo[6,1], Adam J. Burgasser[7], Marie-Eve Naud[1], Étienne Artigau[1], Sandie Bouchard[1], John E. Gizis[8], and Loïc Albert[1]

[1] *Institut de Recherche sur les Exoplanètes (iREx), Université de Montréal, Département de Physique, C.P. 6128 Succ. Centre-ville, Montréal, QC H3C 3J7, Canada.*

[2] *DTM, Carnegie Institution of Washington, Washington, DC 20015, USA*

[3] *Department of Astrophysics, American Museum of Natural History, Central Park West at 79th Street, New York, NY 10024.*

[4] *Hubble Fellow*

[5] *Department of Physics & Astronomy, Hunter College, 695 Park Avenue, NY 10065, USA.*

[6] *Canada-France-Hawaii Telescope, 65-1238 Mamalahoa Hwy, Kamuela, HI 96743, USA*

[7] *Center for Astrophysics and Space Sciences, University of California, San Diego, 9500 Gilman Dr., Mail Code 0424, La Jolla, CA 92093, USA*

[8] *Department of Physics and Astronomy, University of Delaware, 104 The Green, Newark, DE 19716, USA*

Received 2015 April 15; accepted 2015 June 25

Accepted for publication in *The Astrophysical Journal Supplement Series*

6.1 Abstract

We present the results of a near-infrared (NIR) spectroscopic follow-up survey of 182 M4–L7 low-mass stars and brown dwarfs (BDs) from the *BANYAN All-Sky Survey* (*BASS*) for candidate members of nearby, young moving groups (YMGs). We confirm signs of low-gravity for 42 new BD discoveries with estimated masses between 8–75 $M_{\rm Jup}$ and identify previously unrecognized signs of low gravity for 24 known BDs. We refine the fraction of low-gravity dwarfs in the high-probability *BASS* sample to $\sim$82%. We use this unique sample of 66 young BDs, supplemented with 22 young BDs from the literature, to construct new empirical NIR absolute magnitude and color sequences for low-gravity BDs. We show that low-resolution NIR spectroscopy alone cannot differentiate between the ages of YMGs younger than $\sim$120 Myr, and that the BT-Settl atmosphere models do not reproduce well the dust clouds in field or low-gravity L-type dwarfs. We obtain a spectroscopic confirmation of low-gravity for 2MASS J14252798–3650229, which is a new $\sim$27 $M_{\rm Jup}$, L4 γ bona fide member of AB Doradus. We identify a total of 19 new low-gravity candidate members of YMGs with estimated masses below 13 $M_{\rm Jup}$, seven of which have kinematically estimated distances within 40 pc. These objects will be valuable benchmarks for a detailed atmospheric characterization of planetary-mass objects with the next generation of instruments. We find 16 strong candidate members of the Tucana-Horologium association with estimated masses between 12.5–14 $M_{\rm Jup}$, a regime where our study was particularly sensitive. This would indicate that for this association there is at least one isolated object in this mass range for every $17.5^{+6.6}_{-5.0}$ main-sequence stellar member, a number significantly higher than expected based on standard log-normal initial mass function, however in the absence of radial velocity and parallax measurements for all of them, it is likely that this over-density is caused by a number of young interlopers from other associations.

6.2 Introduction

Young moving groups (YMGs) consist of stars that formed recently ($\lesssim$120 Myr) from a molecular cloud and that are too young to have experienced significant gravitational per-

turbations from their environment. The members of YMGs share similar galactic velocities within a few $\mathrm{km\,s^{-1}}$. The closest and youngest moving groups include the TW Hydrae association (TWA; 5–15 Myr; de la Reza et al. 1989; Kastner et al. 1997; Zuckerman & Song 2004; Weinberger et al. 2013a), β Pictoris (βPMG; 20–26 Myr; Zuckerman et al. 2001a; Malo et al. 2014b; Binks & Jeffries 2014), Tucana-Horologium (THA; 20–40 Myr; Torres et al. 2000; Zuckerman & Webb 2000; Zuckerman et al. 2001b; Kraus et al. 2014b), Carina (CAR; 20–40 Myr; Torres et al. 2008), Columba (COL; 20–40 Myr; Torres et al. 2008), Argus (ARG; 30–50 Myr; Makarov & Urban 2000) and AB Doradus (ABDMG; 110–130 Myr; Zuckerman et al. 2004; Luhman et al. 2005; Barenfeld et al. 2013). The YMGs are ideal laboratories to measure fundamental properties of star formation such as the initial mass function (IMF) because their members are coeval. This is of particular interest in the case of very low-mass stars and substellar-mass objects (spectral types $\geq$ M5) since these populations are still poorly characterized. The massive, bright population of YMGs has already been explored, thanks to the *Hipparcos* survey (Perryman et al. 1997). However, fainter members are hard to identify mainly because of the lack of radial velocity (RV) and trigonometric distance measurements that are necessary to obtain their spacial velocities and galactic positions. Several efforts have been made to identify the very low-mass members of YMGs (Kiss et al. 2011; Schlieder et al. 2012b; Shkolnik et al. 2012; Faherty et al. 2012, 2013b; Rodriguez et al. 2013; Liu et al. 2013b; Malo et al. 2014a; Kraus et al. 2014b; Riedel et al. 2014; Murphy & Lawson 2015); however, as of today it is likely that most of them still remain to be identified.

The Bayesian Analysis for Nearby Young AssociatioNs tool[1] (BANYAN; Malo et al. 2013), which is based on naive Bayesian inference, identified promising candidate members of YMGs among a sample of low-mass stars that do not have prior RV or parallax measurements. The BANYAN II tool[2] (Gagné et al. 2014c; Chapter 2 hereafter) was subsequently developed to identify substellar candidate members with a similar but improved algorithm. BANYAN II is an expansion on BANYAN I that is focused on very-low mass stars and brown dwarfs (BDs) with spectral types $\geq$ M5. The *BANYAN All-Sky Survey* (*BASS*; Gagné et al. 2015; Chapter 3 hereafter) was initiated by our team to search for the elusive late-type ($\geq$ M5)

[1]Publicly available at *http://www.astro.umontreal.ca/~malo/banyan.php*
[2]Publicly available at *http://www.astro.umontreal.ca/~gagne/banyanII.php*

members of YMGs, using the BANYAN II tool on an all-sky cross-match of the *Two Micron All-Sky Survey* (*2MASS*; Skrutskie et al. 2006) with the *AllWISE* survey (Kirkpatrick et al. 2014). The *AllWISE* survey is based on a combination of the cryogenic phase of the *Wide-Field Survey Explorer mission* (*WISE*; Wright et al. 2010) and the *Near-Earth Object WISE* (*NEOWISE*; Mainzer et al. 2011) post-cryogenic phase.

We present here the results of a near-infrared (NIR) spectroscopic follow-up survey of substellar candidate members of YMGs identified in *BASS*. In Section 6.3, we summarize *BASS* and the method that we used to build the sample of candidate members from a cross-match of *2MASS* and *AllWISE*. We detail our NIR spectroscopic follow-up and its motivation in Section 6.4. In Section 6.5, we present our method to assign a spectral and gravity classification. We present the resulting spectral types and updated YMG membership probability for our sample in Section 6.6. In Section 6.7, we use new discoveries presented here and other known low-gravity BDs and low-mass stars to build empirical photometric sequences, and we then investigate the physical properties of young BDs. We summarize and conclude in Section 6.8.

6.3 The *BASS* survey

BASS is a systematic all-sky search for later-than-M5 candidate members to nearby YMGs that was the focus of an earlier publication (Chapter 3). In this work, we undertake a spectroscopic follow-up of the *BASS* sample, which we briefly summarize in this section. We refer the reader to Chapter 3 for an extensive description of the *BASS* survey.

We cross-matched the *2MASS* and *AllWISE* catalogs outside of the galactic plane and crowded regions ($\geq$ 2.5 objects per square arcminute) using a cross-match radius of 25" and applied several color, catalog confusion and photometric quality cuts to produce a starting sample of 98 970 targets with NIR colors consistent with a spectral type later than M5 and a proper motion measurement larger than 30 mas yr^{-1} at a statistical significance larger than 5σ (see Chapter 3 for the detailed cross-matching algorithm and selection criteria). Astrometry provided in the *2MASS* and *AllWISE* catalogs as well as the mean epochs of observation for both surveys (*JD* keyword in *2MASS*; *W1MJDMEAN* keyword in *AllWISE*) were used to calculate proper motions. We used *W1MJDMAX* - *W1MJDMIN* as a conservative measure-

ment error on the *AllWISE* astrometric epoch, which typically corresponds to ~ 6 months to one year, compared to a ~ 11 yr baseline between *2MASS* and *AllWISE*. This uncertainty as well as those on astrometric measurements themselves were propagated to the proper motion measurement errors, as described in Chapter 3. We obtain a typical proper motion precision of 5–15 mas yr^{-1}.

We used the BANYAN II tool to select only objects that have a Bayesian probability $> 10\%$ of belonging to any YMG considered here (this threshold ensures that known bona fide members are recovered; see Chapter 3). The BANYAN II tool takes the sky position, proper motion and J, H, K_S, *W1* and *W2* photometry as input quantities. It then uses a naive Bayesian classifier to compare those measurements with spatial and kinematic models (SKMs) of YMGs, as well as with old and young color-magnitude diagram (CMD) sequences in both $M_{W1}(J-K_S)$ and $M_{W1}(H-W2)$ spaces. Those CMD sequences were chosen because they were found as the most efficient independent sequences to distinguish between young and field M6–L4 dwarfs. Probabilities generated from a naive Bayesian classifier can be biased when the input parameters are not independent (which is the case here); however, the relative ranking of hypotheses for a given object overcomes this bias (Hand & Yu 2001).

It is known that there is a large scatter in the NIR colors of young BDs even though they are redder than field dwarfs on average (e.g. Faherty et al. 2012). The inclusion of the CMD sequences described above in BANYAN II will systematically bias our sample towards red NIR colors, and decrease our sample completeness for YMG members that are not especially red. However, this effect is likely less important than the color criteria that were applied in selecting the 98 970 objects that were input to BANYAN II. Furthermore, a total of only two independent photometric observables (corresponding to the color-magnitude diagrams) are used in BANYAN II, compared to four kinematics observables when no RV or parallax is available; the relative weight of kinematics is thus twice that of photometry in the calculation of probabilities. Parallax motion was not accounted for in our proper motion measurements or in the BANYAN II tool; the maximal relative importance of this effect will become as large as our typical *2MASS–AllWISE* proper motion precision only for objects closer than ~ 10 pc (considering the 11 yr baseline between *2MASS* and *AllWISE*). This correction will properly

be accounted for in a future version of the BANYAN II tool.

We performed a Monte Carlo simulation based on the Besançon galactic model (A. C. Robin et al. in preparation, Robin et al. 2012) and the SKMs of YMGs to obtain a field contamination probability for each individual target in our sample, which allows for a more absolute interpretation in terms of the expected contamination fraction. We used the results of this simulation to reject any candidate member with a $> 50\%$ probability of being a field contaminant. Note that the contamination probability from this Monte Carlo analysis is not necessarily complementary with the YMG Bayesian probability (see Chapter 3 for more detail). We refer the reader to Chapter 3 for an extensive description of all filters that were used to build the *BASS* sample (e.g., minimal proper motion, color and quality filters, etc.).

There are three distinct samples that are referred to in this Paper: (1) *PRE-BASS* consists of targets that were initially selected as potential members and followed up with spectroscopy, but that were later rejected as we modified our selection criteria to decrease the fraction of contaminants; (2) *Low-Priority BASS* (*LP-BASS*) consists of targets that have NIR colors only slightly redder than field dwarfs; and (3) *BASS* is the final sample presented in Chapter 3 that contains targets at least 1σ redder than field dwarfs and that has a lower fraction of contaminants. As discussed in Chapter 3, the statistical distance associated with the most probable YMG of a candidate member can be used to place it in two CMDs (M_{W1} versus $J - K_S$ and $H - W2$) and compare its position to known field and young BDs and low-mass stars.

Table 6.1. Observing log.

2MASS Designation	J	Observing Date (UT)	Telescope	Instrument	Slit Width (")	R	Tot. Exp. Time (s)	Num. Exp.
Candidate Members from *BASS* or *LP-BASS*								
00011217+1535355	15.52	2014 Aug 06	Magellan	FIRE	0.6	450	720	6
00065794-6436542	13.39	2014 Jan 16	Gemini-South	Flamingos-2	0.72	500	840	4
00182834-6703130	15.46	2013 Sep 28	Gemini-South	Flamingos-2	0.72	500	2000	8
00191296-6226005	15.64	2013 Oct 29	Gemini-South	Flamingos-2	0.72	500	6200	20
00192626+4614078	12.60	2012 Oct 26	IRTF	SpeX	0.8	750	1200	8
00274534-0806046	11.57	2013 Oct 02	Gemini-South	Flamingos-2	0.72	500	240	8
00344300-4102266	15.71	2014 Oct 12	Gemini-South	Flamingos-2	0.72	500	8575	35
00381489-6403529	14.52	2014 May 31	Gemini-South	Flamingos-2	0.72	500	2080	8
00390342+1330170 AB	10.94	2013 Jul 31	IRTF	SpeX	0.8	750	900	6
00413538-5621127	11.96	2013 Nov 25 & 2014 Jan 21	Gemini-South	Flamingos-2	0.72	500	360	12
00464841+0715177	13.89	2013 Aug 11	IRTF	SpeX	0.8	750	1600	8
00514561-6227073	12.58	2014 Jan 16	Gemini-South	Flamingos-2	0.72	500	1680	8
00584253-0651239	14.31	2013 Aug 11	IRTF	SpeX	0.8	750	1600	8
01205114-5200349	15.64	2013 Sep 27	Gemini-South	Flamingos-2	0.72	500	6200	20
01265327-5505506	12.04	2014 Jan 21	Gemini-South	Flamingos-2	0.72	500	240	8
01294256-0823580	10.65	2013 Oct 02	Gemini-South	Flamingos-2	0.72	500	240	8
01344601-5707564	12.07	2013 Nov 25	Gemini-South	Flamingos-2	0.72	500	240	8
01484859-5201158	10.87	2013 Oct 02	Gemini-South	Flamingos-2	0.72	500	240	8
01531463-6744181	16.41	2013 Apr 21	Magellan	FIRE	0.6	6000	1500	2
02103857-3015313	15.07	2013 Dec 16	Gemini-South	Flamingos-2	0.72	500	1680	8
02265658-5327032	15.40	2013 Oct 02	Gemini-South	Flamingos-2	0.72	500	2400	8
02282694+0218331	12.12	2013 Oct 18	Gemini-South	Flamingos-2	0.72	500	240	8
02404759-4253377	12.20	2013 Oct 28	Gemini-South	Flamingos-2	0.72	500	240	8
02410564-5511466	15.39	2014 Dec 10, 12 & 15	Gemini-South	Flamingos-2	0.72	500	10605	42
02441019-3548036	15.34	2013 Oct 19	Gemini-South	Flamingos-2	0.72	500	5280	16
02501167-0151295	12.89	2014 Aug 02 & 03	Gemini-South	Flamingos-2	0.72	500	2920	16
02534448-7959133	11.34	2013 Oct 27	Gemini-South	Flamingos-2	0.72	500	240	8
02583123-1520536	15.91	2013 Dec 12	Magellan	FIRE	0.6	6000	1310	2
03093877-3014352	11.58	2013 Oct 19	Gemini-South	Flamingos-2	0.72	500	240	8
03132588-2447246	12.53	2013 Dec 16	Gemini-South	Flamingos-2	0.72	500	240	8
03182597-3708118	13.37	2013 Oct 28	Gemini-South	Flamingos-2	0.72	500	1680	8
03204919-3313400	12.54	2013 Oct 15	Gemini-South	Flamingos-2	0.72	500	240	8
03224622-7940595	12.22	2013 Oct 19	Gemini-South	Flamingos-2	0.72	500	240	8
03264225-2102057	16.13	2007 Nov 13	IRTF	SpeX	0.5	150	180	6
03333313-3215181	13.17	2013 Aug 11	IRTF	SpeX	0.8	750	1200	8
03363144-2619578	10.68	2012 Feb 05	IRTF	SpeX	0.8	750	600	4
03370359-1758079	15.62	2011 Dec 08	IRTF	SpeX	0.5	150	1440	8
03370362-3709236	12.75	2013 Aug 11	IRTF	SpeX	0.8	750	1200	8
03390160-2434059	10.90	2012 Feb 05	IRTF	SpeX	0.8	750	600	4
03420931-2904317	15.92	2013 Apr 21	Magellan	FIRE	0.6	6000	1204	2
03550477-1032415	13.08	2013 Oct 20	Gemini-South	Flamingos-2	0.72	500	1680	8
03552337+1133437	14.05	2013 Feb 16	IRTF	SpeX	0.8	750	1440	8
03582255-4116060	15.85	2011 Dec 08	IRTF	SpeX	0.5	150	1440	8
04185879-4507413	16.16	2014 Dec 10 & 15	Gemini-South	Flamingos-2	0.72	500	7820	31
04231498-1533245	12.54	2014 Sep 16	Gemini-South	Flamingos-2	0.72	500	3240	27
04400972-5126544	15.69	2013 Oct 27	Gemini-South	Flamingos-2	0.72	500	5600	20
04433761+0002051	12.51	2012 Feb 05	IRTF	SpeX	0.8	750	600	4
04532647-1751543	15.14	2012 Feb 05	IRTF	SpeX	0.8	750	1800	12
04584239-3002061	13.50	2015 Feb 03	IRTF	SpeX	0.8	90	800	16
05002100+0330501	13.67	2015 Feb 02	IRTF	SpeX	0.8	750	1000	4
05012406-0010452	14.98	2013 Feb 16	IRTF	SpeX	0.8	750	2880	16
05104958-1843548	15.35	2015 Feb 03	IRTF	SpeX	0.8	90	2000	10
05123569-3041067	11.90	2013 Oct 08 & 20	Gemini-South	Flamingos-2	0.72	500	480	16
05181131-3101529	11.88	2012 Feb 05	IRTF	SpeX	0.8	750	600	4
05264316-1824315	12.36	2013 Feb 19	IRTF	SpeX	0.8	750	800	4
05361998-1920396	15.77	2012 Oct 26	IRTF	SpeX	0.8	750	150	1
06022216+6336391	14.27	2008 Jan 08	IRTF	SpeX	0.6	120	540	6
06272161-5308428	16.39	2015 Jan 23	Gemini-South	Flamingos-2	0.72	500	4800	16
07140394+3702459	11.98	2015 Feb 03	IRTF	SpeX	0.8	90	300	8

Table 6.1 — continued

2MASS Designation	J	Observing Date (UT)	Telescope	Instrument	Slit Width (")	R	Tot. Exp. Time (s)	Num. Exp.
08095903+4434216	16.44	2008 Jan 12	IRTF	SpeX	0.6	120	1500	10
09532126-1014205	13.47	2014 Jan 22	IRTF	SpeX	0.8	750	2000	8
10212570-2830427	16.91	2015 Feb 13 & 26	Gemini-South	Flamingos-2	0.72	500	6300	21
10284580-2830374	10.95	2012 May 12	IRTF	SpeX	0.8	750	1200	8
10455263-2819303	12.82	2012 May 12	IRTF	SpeX	0.8	750	1200	8
10513331-1916530	14.69	2014 Jan 22	IRTF	SpeX	0.8	750	4000	16
11064461-3715115	14.49	2012 May 12	IRTF	SpeX	0.8	750	2400	16
11271382-3735076	16.47	2015 Feb 09	Magellan	FIRE	0.6	450	480	4
11480096-2836488	16.11	2015 Feb 13	Gemini-South	Flamingos-2	0.72	500	4800	16
12073346-3932539	12.99	2012 May 12	IRTF	SpeX	0.8	95	1200	8
12074836-3900043	15.49	2013 May 10	IRTF	SpeX	0.8	750	800	4
12214223-4012050	16.47	2015 Feb 08	Magellan	FIRE	0.6	450	1080	9
12310489-3801065	14.68	2015 Feb 08	Magellan	FIRE	0.6	450	240	2
12474428-3816464	14.78	2013 May 10	IRTF	SpeX	0.8	750	720	4
12535039-4211215	16.00	2015 Feb 09	Magellan	FIRE	0.6	450	480	4
12563961-2718455	16.42	2014 May 12	Magellan	FIRE	0.6	6000	1800	2
12574463-3635431	14.57	2014 Aug 03	Gemini-South	Flamingos-2	0.72	500	7595	31
12574941-4111373	13.02	2014 Feb 14	Gemini-South	Flamingos-2	0.72	500	400	8
13262009-2729370	15.85	2009 Jun 30	IRTF	SpeX	0.6	120	1200	8
14252798-3650229	13.75	2010 Jul 07	IRTF	SpeX	0.6	120	720	6
19350976-6200473	16.25	2014 Jul 21 & Aug 03	Gemini-South	Flamingos-2	0.72	500	6060	24
19395435-5216468	14.66	2014 Jun 18	Magellan	FIRE	0.6	450	360	4
20004841-7523070	12.73	2014 Aug 04	Gemini-South	Flamingos-2	0.72	500	1920	16
20113196-5048112	16.42	2014 Jun 18	Magellan	FIRE	0.6	450	480	4
20224803-5645567	11.76	2013 Oct 09	Gemini-South	Flamingos-2	0.72	500	240	8
20282203-5637024	13.84	2014 May 28	Gemini-South	Flamingos-2	0.72	500	800	8
20334670-3733443	10.85	2013 Oct 09	Gemini-South	Flamingos-2	0.72	500	240	8
20414283-3506442	14.89	2014 May 28	Gemini-South	Flamingos-2	0.72	500	2480	8
20484222-5127435	15.38	2014 Jun 02	Gemini-South	Flamingos-2	0.72	500	6000	24
20505221-3639552	13.00	2014 Jul 29	Gemini-South	Flamingos-2	0.72	500	7560	42
21121598-8128452	10.67	2013 Oct 20	Gemini-South	Flamingos-2	0.72	500	240	8
21144103-4339531	13.02	2013 Aug 20	IRTF	SpeX	0.8	750	1500	10
21490499-6413039	10.35	2013 Oct 30	Gemini-South	Flamingos-2	0.72	500	240	8
21543454-1055308	16.44	2008 Sep 17	IRTF	SpeX	0.5	120	1800	10
21544859-7459134	14.29	2013 Oct 28	Gemini-South	Flamingos-2	0.72	500	2400	8
22021125-1109461	12.36	2013 Aug 11	IRTF	SpeX	0.8	750	1950	13
22025794-5605087	14.36	2014 Jun 02	Gemini-South	Flamingos-2	0.72	500	1360	8
22064498-4217208	15.56	2013 Aug 01	IRTF	SpeX	0.8	750	450	3
22191486-6828018	13.92	2014 Jul 21 & Aug 02	Gemini-South	Flamingos-2	0.72	500	6240	24
22351658-3844154	15.18	2013 Sep 27	Gemini-South	Flamingos-2	0.72	500	4480	16
22353560-5906306	14.28	2014 Jul 10	Gemini-South	Flamingos-2	0.72	500	640	4
22400144+0532162	11.72	2013 Aug 20	IRTF	SpeX	0.8	750	1500	10
22444835-6650032	11.03	2013 Oct 30	Gemini-South	Flamingos-2	0.72	500	240	8
22511530-6811216	12.10	2013 Oct 28	Gemini-South	Flamingos-2	0.72	500	240	8
23102196-0748531	11.60	2013 Jul 31	IRTF	SpeX	0.8	750	900	6
23130558-6127077	10.93	2013 Oct 21	Gemini-South	Flamingos-2	0.72	500	240	8
23143092-5405313	11.50	2013 Oct 21	Gemini-South	Flamingos-2	0.72	500	240	8
23155665-4747315	16.08	2014 Jun 19	Magellan	FIRE	0.6	450	600	5
23225240-6151114	11.53	2013 Oct 20	Gemini-South	Flamingos-2	0.72	500	240	8
23225299-6151275	15.55	2013 Oct 21	Gemini-South	Flamingos-2	0.72	500	1680	8
23255604-0259508	15.96	2013 Aug 01	IRTF	SpeX	0.8	750	450	3
23270843+3858234	11.74	2013 Jul 31	IRTF	SpeX	0.8	750	1200	8
23290437+0329113	11.11	2012 Oct 26	IRTF	SpeX	0.8	95	800	8
23310161-0406193	12.94	2014 Jul 21 & Aug 02	Gemini-South	Flamingos-2	0.72	500	1920	16
23353085-1908389	11.51	2013 Jul 31	IRTF	SpeX	0.8	750	900	6
23355015-3401477	11.64	2013 Oct 28	Gemini-South	Flamingos-2	0.72	500	240	8
23360735-3541489	14.65	2014 Jul 10	Gemini-South	Flamingos-2	0.72	500	760	4
23433470-3646021	16.57	2014 Jun 19	Magellan	FIRE	0.6	450	480	4
23520507-1100435	12.84	2010 Jul 07	IRTF	SpeX	0.6	120	540	12
23532556-1844402 AB	11.24	2012 Oct 26	IRTF	SpeX	0.8	750	1040	13

Table 6.1 — continued

2MASS Designation	J	Observing Date (UT)	Telescope	Instrument	Slit Width (")	R	Tot. Exp. Time (s)	Num. Exp.
Candidate Members from *PRE-BASS*								
00020382+0408129 AB	10.40	2013 Jul 31	IRTF	SpeX	0.8	750	1200	8
00045753-1709369	11.00	2013 Nov 25	Gemini-South	Flamingos-2	0.72	500	240	8
00171571-3219539	10.64	2013 Nov 25	Gemini-South	Flamingos-2	0.72	500	240	8
00174858-0316334	13.23	2013 Aug 11	IRTF	SpeX	0.8	750	1200	8
00210589-4244433	13.52	2013 Aug 01	IRTF	SpeX	0.8	750	1200	8
00425923+1142104	14.75	2013 Aug 11	IRTF	SpeX	0.8	750	3200	16
00461551+0252004	14.40	2013 Aug 01	IRTF	SpeX	0.8	750	1800	12
01035369-2805518 AB	11.66	2012 Oct 26	IRTF	SpeX	0.8	750	1200	8
02590146-4232204	12.24	2013 Oct 02	Gemini-South	Flamingos-2	0.72	500	240	8
03005033-5459267	12.42	2013 Nov 25	Gemini-South	Flamingos-2	0.72	500	240	8
03111547+0106307	10.68	2013 Oct 19	Gemini-South	Flamingos-2	0.72	500	240	8
03140344+1603056	12.53	2013 Feb 16	IRTF	SpeX	0.8	750	1200	8
03263956-0617586	12.96	2013 Feb 18	IRTF	SpeX	0.8	750	1500	6
03350208+2342356	12.25	2012 Feb 05	IRTF	SpeX	0.8	750	600	4
03442859+0716100 AB	12.72	2012 Oct 26	IRTF	SpeX	0.8	750	1200	8
04044052+2616275 AB	12.65	2012 Oct 26	IRTF	SpeX	0.8	750	1200	8
04070752+1546457	15.48	2012 Feb 05	IRTF	SpeX	0.8	750	3600	12
04173836-1140256	11.75	2013 Dec 04	Gemini-South	Flamingos-2	0.72	500	240	8
04281061+1839021	13.38	2012 Oct 26	IRTF	SpeX	0.8	750	1200	8
04402583-1820414	12.65	2013 Dec 16	Gemini-South	Flamingos-2	0.72	500	480	8
04493288+1607226	14.27	2012 Feb 05	IRTF	SpeX	0.8	750	600	4
05071137+1430013 AB	10.57	2013 Feb 16	IRTF	SpeX	0.8	750	600	4
05201794+0511521	13.04	2012 Oct 26	IRTF	SpeX	0.8	750	1200	8
05243009+0640349	11.98	2013 Feb 19	IRTF	SpeX	0.8	750	800	4
05271676+0007526 AB	12.17	2013 Feb 16	IRTF	SpeX	0.8	750	1200	8
05370704-0623170	15.70	2013 Oct 21	Gemini-South	Flamingos-2	0.72	500	1680	8
05402325-0906326	14.59	2013 Oct 19 & 21	Gemini-South	Flamingos-2	0.72	500	3120	24
05404919-0923192	11.31	2014 Jan 16	Gemini-South	Flamingos-2	0.72	500	240	8
05410983-0737392	13.46	2013 Feb 19	IRTF	SpeX	0.8	750	600	4
05415929-0217020	13.22	2013 Dec 23	Gemini-South	Flamingos-2	0.72	500	240	8
05431887+6422528	13.57	2008 Jan 09	IRTF	SpeX	0.6	120	360	4
05451198-0121021	13.83	2013 Nov 24 & Dec 26	Gemini-South	Flamingos-2	0.72	500	3360	16
05484454-2942551	10.56	2013 Feb 18	IRTF	SpeX	0.8	750	150	1
06021735-1413467	14.34	2013 Feb 19	IRTF	SpeX	0.8	750	1000	4
06353541-6234059	12.42	2013 Oct 20	Gemini-South	Flamingos-2	0.72	500	240	8
06494706-3823284	11.65	2013 Nov 02 & 20	Gemini-South	Flamingos-2	0.72	500	120	4
07083261-4701475	14.16	2013 Oct 29	Gemini-South	Flamingos-2	0.72	500	1680	8
07200325-0846499	10.63	2014 Jan 22	IRTF	SpeX	0.8	750	480	8
07202582-5617224	12.88	2013 Oct 21	Gemini-South	Flamingos-2	0.72	500	1680	8
07525247-7947386	12.83	2013 Oct 28 & 2014 Jan 17	Gemini-South	Flamingos-2	0.72	500	2520	12
07583046+1530004	10.43	2012 Oct 26	IRTF	SpeX	0.8	750	800	4
07583098+1530146 AB	9.97	2012 Oct 26	IRTF	SpeX	0.8	750	800	4
08034469+0827000	11.83	2013 Feb 15	IRTF	SpeX	0.8	750	900	6
08045433-6346180	9.93	2013 Nov 02	Gemini-South	Flamingos-2	0.72	500	240	8
08055944+2505028 AB	11.53	2013 Feb 16	IRTF	SpeX	0.8	750	900	6
08141769+0253199	11.52	2012 Oct 26	IRTF	SpeX	0.8	750	800	4
08194309-7401232	10.06	2013 Oct 20 & 25	Gemini-South	Flamingos-2	0.72	500	240	8
08194351-0450071	14.82	2014 Jan 17	Gemini-South	Flamingos-2	0.72	500	1680	8
08204440-7514571	16.59	2013 Apr 21	Magellan	FIRE	0.6	6000	1500	2
08254335-0029110	15.45	2013 Apr 21	Magellan	FIRE	0.6	6000	1310	2
08255896+0340198	10.01	2013 Feb 18	IRTF	SpeX	0.8	750	300	2
08540240-3051366	9.01	2013 Nov 20	Gemini-South	Flamingos-2	0.72	500	240	8
08561384-1342242	13.60	2012 May 12	IRTF	SpeX	0.8	750	1200	8
09104094-7552528	13.62	2014 Feb 07	Gemini-South	Flamingos-2	0.72	500	560	8
09451445-7753150	13.89	2014 Feb 15	Gemini-South	Flamingos-2	0.72	500	800	8
09510459+3558098	10.58	2013 Feb 18	IRTF	SpeX	0.8	750	300	2
10051641+1703264	11.13	2013 Feb 16	IRTF	SpeX	0.8	750	600	4
10130718-1706349 AB	12.79	2013 Feb 16	IRTF	SpeX	0.8	750	1200	8
10352029-2058382	11.66	2014 Jan 22	IRTF	SpeX	0.8	750	600	4

Table 6.1 — continued

2MASS Designation	J	Observing Date (UT)	Telescope	Instrument	Slit Width (")	R	Tot. Exp. Time (s)	Num. Exp.
11014673-7735144	15.97	2014 Feb 16	Gemini-South	Flamingos-2	0.72	500	8320	32
11083081+6830169	13.12	2009 Mar 04	Palomar	TripleSpec	1.0	2700	1200	4
11195251-3917150	13.13	2014 Jan 22	IRTF	SpeX	0.8	95	1200	8
11335700-7807240	13.20	2014 Feb 15	Gemini-South	Flamingos-2	0.72	500	400	8
11532691-3015414	12.31	2014 Jan 22	IRTF	SpeX	0.8	750	900	6
11544223-3400390	14.19	2008 Jan 09	IRTF	SpeX	0.6	120	480	4
11560224-4043248	16.00	2014 Feb 17	Gemini-South	Flamingos-2	0.72	500	8000	32
12002750-3405371	9.61	2014 Mar 17	Gemini-South	Flamingos-2	0.72	500	1600	32
12042529-2806364	16.11	2014 Mar 17 & 20	Gemini-South	Flamingos-2	0.72	500	16000	64
12212770+0257198	13.17	2014 Feb 14	Gemini-South	Flamingos-2	0.72	500	400	8
12265135-3316124	10.69	2012 May 12	IRTF	SpeX	0.8	750	1200	8
12271545-0636458	14.19	2014 Feb 14	Gemini-South	Flamingos-2	0.72	500	1040	8
12492353-2035592	9.32	2014 Feb 16	Gemini-South	Flamingos-2	0.72	500	400	8
12521062-3415091	11.65	2013 May 27	Gemini-North	GNIRS	0.675	800	120	4
13015465-1510223	14.54	2013 Aug 20	IRTF	SpeX	0.8	750	1500	6
13252237+0600290	12.25	2012 May 12	IRTF	SpeX	0.8	750	1200	8
13582164-0046262	10.81	2012 May 12	IRTF	SpeX	0.8	750	1200	8
14112131-2119503	12.44	2012 May 12	IRTF	SpeX	0.8	750	1200	8
15104786-2818174	12.84	2014 Feb 14	Gemini-South	Flamingos-2	0.72	500	360	8
15291017+6312539	11.64	2013 Aug 20	IRTF	SpeX	0.8	750	800	8
15424676-3358082	17.02	2014 Jun 01	Gemini-South	Flamingos-2	0.72	500	16000	64
15470557-1626303 AB	13.86	2013 Aug 11	IRTF	SpeX	0.8	750	1800	12
16210134-2346554	15.16	2013 Aug 20	IRTF	SpeX	0.8	750	2400	12
16221255-2346418	10.90	2013 Aug 11	IRTF	SpeX	0.8	750	2400	12
16232017-2353248	13.38	2012 May 12	IRTF	SpeX	0.8	750	1200	8
16251377-2358021	13.75	2013 May 17	Gemini-North	GNIRS	0.675	800	360	4
16272178-2411060	13.98	2013 May 17	Gemini-North	GNIRS	0.675	800	360	4
16330142-2425083	16.16	2013 Aug 11	IRTF	SpeX	0.8	95	1200	8
16422788-1942350	15.23	2014 Jun 18	Magellan	FIRE	0.6	450	480	4
17065487-1314396	14.52	2013 Aug 20	IRTF	SpeX	0.8	750	2400	12
18393308+2952164	11.01	2013 Aug 11	IRTF	SpeX	0.8	750	600	4
18460473+5246027 AB	11.03	2013 Aug 11	IRTF	SpeX	0.8	750	300	2
18462188-5706040	15.06	2014 May 28	Gemini-South	Flamingos-2	0.72	500	1680	8
19033113-3723302	13.41	2013 Sep 28	Gemini-South	Flamingos-2	0.72	500	1680	8
19480544+5944412 AB	11.49	2013 Aug 20	IRTF	SpeX	0.8	750	600	4
20025265-1316418	14.48	2013 Aug 11	IRTF	SpeX	0.8	750	1600	8
20050639-6258034	11.75	2013 Oct 20	Gemini-South	Flamingos-2	0.72	500	240	8
20385687-4118285	11.66	2013 Nov 26	Gemini-South	Flamingos-2	0.72	500	240	8
20391314-1126531	13.79	2013 Aug 01	IRTF	SpeX	0.8	750	1200	8
20482880-3255434	14.71	2013 Aug 11	IRTF	SpeX	0.8	750	2800	14
21272613-4215183	13.32	2008 Jul 14	IRTF	SpeX	0.6	120	240	4
21342814-1840298	11.04	2013 Oct 09	Gemini-South	Flamingos-2	0.72	500	240	8
21484123-4736506	10.97	2013 Oct 20	Gemini-South	Flamingos-2	0.72	500	240	8
22062157-6116284	16.61	2014 May 15	Magellan	FIRE	0.6	450	240	2
22444905-3045535	14.65	2013 Aug 01	IRTF	SpeX	0.8	750	450	3
22573768-5041516	14.96	2014 Jul 17	Gemini-South	Flamingos-2	0.72	500	5280	16
23231347-0244360	13.58	2008 Nov 03	IRTF	SpeX	0.6	120	720	8
23453903+0055137	13.77	2008 Jul 14	IRTF	SpeX	0.6	120	270	6

All candidate members that were placed blueward of the field sequence in any of the two CMDs were rejected from *BASS* and *LP-BASS*. Those that were not at least 1σ redder than both field sequences were grouped into the *LP-BASS* sample, which is expected to be more contaminated by field objects and young M dwarfs with spectral types earlier than M5. We note that the *PRE-BASS* sample does not necessarily consist of erroneous YMG candidate members; however, it likely suffers from a higher contamination rate from field interlopers or members of moving groups not considered in BANYAN II.

6.4 Observations

Because of their recent formation, young, low-mass objects have inflated radii compared to their field counterparts and are warmer for a given mass. As a consequence, they have a lower surface gravity at a given temperature (and spectral type). It is well known that these low-gravity dwarfs display weaker alkali and molecular absorption lines (K I at 7665 & 7669 Å in the optical and 1.17 & 1.25 μm in the NIR; Na I at 8183 & 8195 Å in the optical and 1.14 & 2.21 μm in the NIR; Rb I at 7800 & 7948 Å; Cs I at 8521 & 8943 Å; FeH at 8692 Å in the optical and 0.99, 1.20 & 1.55 μm in the NIR; TiO at 8432 Å; and CrH at 8611 Å). This is due to a lower-pressure in their photosphere, which is a direct consequence of their lower surface gravity. Collision-induced absorption (CIA) of the H_2 molecule is also decreased in this lower pressure environment, causing a flatter K-band plateau at 2.18–2.28 μm (see the $H_2(K)$ index of Canty et al. 2013), leaving the effect of water vapor to become apparent from the triangular-shaped continuum of the H band (Lucas et al. 2001; Kirkpatrick et al. 2006; Allers et al. 2007; Rice et al. 2010; see the H-cont index of Allers & Liu 2013). Furthermore, VO condensate clouds get thicker in the external layers of low-pressure atmospheres, causing deeper absorption bands at 7300-7550 and 7850–8000 Å in the optical and 1.06 μm in the NIR (These effects are discussed in more detail by Gorlova et al. 2003; McGovern et al. 2004; Kirkpatrick et al. 2006, 2008; Cruz et al. 2009; Allers & Liu 2013 and Canty et al. 2013). Gravity-sensitive features were initially identified by comparing the optical spectra of M-type giants and M-type dwarfs (Kleinmann & Hall 1986; Joyce et al. 1998), and it was later demonstrated that the same features could be used to identify young, inflated M-type

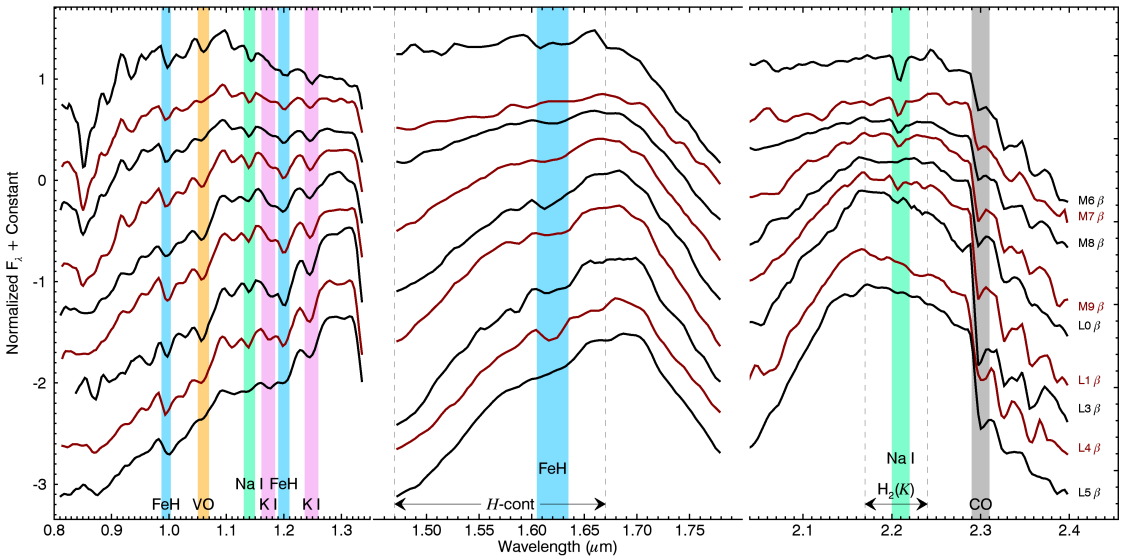

(a) Intermediate-Gravity (β) Templates

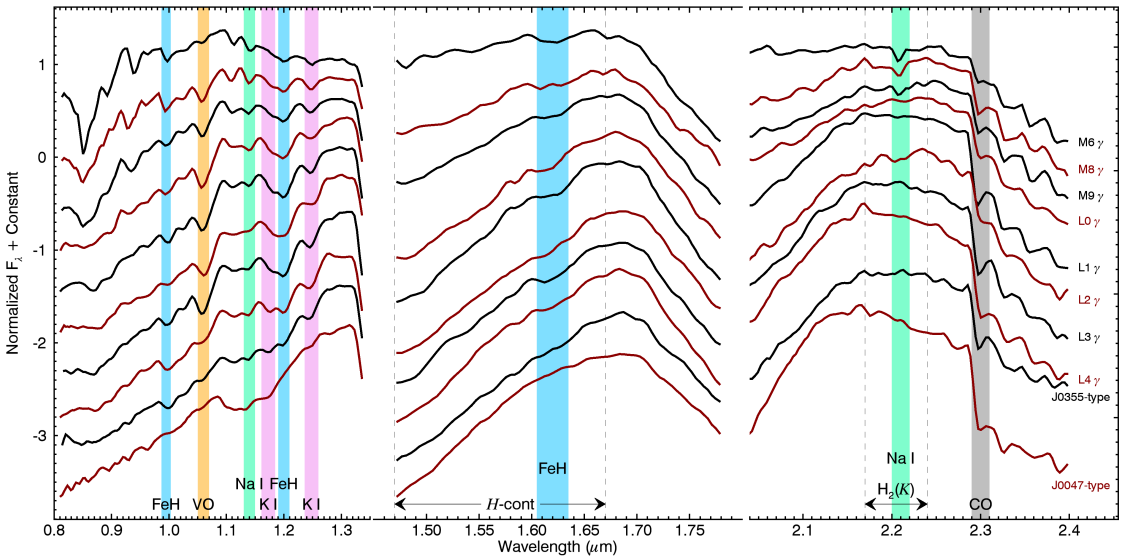

(b) Very Low-Gravity (γ) Templates

FIGURE 6.1 NIR spectra of intermediate-gravity (Panel a) and very low-gravity (Panel b) templates constructed as described in the text (black and red solid lines). All spectra were normalized to their median across the full wavelength range in each band and shifted vertically for comparison purposes. All spectra were resampled at the same resolution ($R \sim 120$). The colored regions correspond to the gravity-sensitive features identified at the bottom of the Figure.

dwarfs by observing members of star-forming regions (Martín et al. 1996; Luhman et al. 1997; Slesnick et al. 2004; Lucas et al. 2001; Allers et al. 2007; Lodieu et al. 2008).

A number of low-gravity features (CIA effects of H_2 on the continuum, weaker FeH absorption and stronger VO absorption) can be measured in low-mass stars and BDs with spectral types later than M6 using low-resolution ($R \sim 75$) NIR spectroscopy, providing an efficient way of identifying field interlopers in a set of YMG candidates. A higher spectral resolution ($R \sim 1000$) allows for a more robust determination of low gravity features through the measurement of the pseudo-equivalent width (EW) of the atomic lines listed above. We thus obtained low-resolution NIR spectra of 241 candidate YMG members from the *BASS*, *LP-BASS* and *PRE-BASS* samples. We describe in this section all observations and the individual instrumental configurations that were used. A description of individual observations is included in Table 6.1.

6.4.1 FIRE at Magellan

We obtained NIR spectroscopy for 17 targets with the Folded-port InfraRed Echellette (FIRE; Simcoe et al. 2008, 2013) at the Magellan Telescopes in April and December 2013, as well as May, June, August and September 2014 and February 2015. We used both the cross-dispersed and high-throughput prism modes to obtain respective resolving powers $R \sim 450$ (prism mode) and $R \sim 6000$ (echelle mode) across the 0.8–2.45 μm range. Total exposure times ranged from 200 s to 1800 s, depending on source brightness, instrument configuration and weather conditions. This allowed us to obtain a typical S/N > 100 per resolution element. Science targets were observed in an ABBA pattern along the slit, and a standard A0-type star was observed immediately before or after each of them at a similar airmass to ensure a proper telluric correction. We obtained ThAr (prism mode) or NeNeAr (echellette mode) lamp exposures between every science target to perform wavelength calibration, as well as high- and low-illumination flat fields that were combined to obtain a flat-field image with a large S/N across all orders while avoiding saturation. We reduced all data using the Interactive Data Language (IDL) pipeline FIREHOSE, which is based on the MASE (Bochanski et al.

2009) and SpeXTool (Vacca et al. 2003; Cushing et al. 2004) packages. We supplemented the list of Ar atomic lines with those listed in Norlén (1973) to allow a more robust wavelength solution in the K band in the case of prism data.

The six echellette spectra that we obtained here have a sufficient resolution to measure radial velocities down to a precision down to a few $\mathrm{km\,s^{-1}}$. These measurements will be presented in a future publication along with a significant number of additional FIRE echellette spectra.

6.4.2 SpeX at IRTF

We obtained NIR spectroscopy with SpeX (Rayner et al. 2003) at the IRTF telescope for 118 targets from 2007 to 2015. We used the cross-dispersed and prism modes with slits of $0\farcs6$, $0\farcs8$ and $1\farcs0$ depending on the seeing to obtain resolving powers ranging from $R \sim 75$ to $R \sim 750$ over the 0.8–2.45 μm range. We used ABBA nodding patterns along the slit with typical exposure times of 60 s to 250 s which yielded typical S/N > 100 per resolution element. A standard early A-type star was observed immediately before or after every science target at a similar airmass to ensure a proper telluric correction. Several high-S/N quartz lamp and Ar lamp exposures were obtained immediately after every target to ensure a proper wavelength calibration and flat field correction. The data were reduced with the IDL SpeXTool package (Vacca et al. 2003; Cushing et al. 2004).

6.4.3 Flamingos-2 at Gemini-South

We used Flamingos-2 (Eikenberry et al. 2004) at Gemini-South to obtain NIR spectroscopy for 101 targets from 2013 to 2015. We observed each target with both the *JH* and *HK* low resolution grisms and the $0\farcs72$ slit to obtain a resolving power of $R \sim 500$ over 0.9–2.4 μm. Targets were observed in an ABBA pattern along the slit, with total exposure times ranging from 120 s to 3400 s, to obtain S/N > 80 per resolution element. Standard A0 to A6-type stars were observed immediately before or after every science target at a similar airmass to ensure a proper telluric correction. Several high-S/N quartz lamp and Ar lamp exposures were obtained immediately after every telluric standard star to ensure a proper wavelength calibration and

flat field correction. Dark exposures were obtained at the end of each night, using similar exposure times than all of the science and calibration data to ensure a proper correction of the dark current. A numbers of observations were split between a few nights when observing conditions changed before the required S/N could be obtained.

We used a custom IDL pipeline to apply dark current subtraction and flat field calibrations, correct the trace curvature, optimally extract the spectrum (Horne 1986) and perform a wavelength calibration using the Ar lamp observations. A dark current subtraction is usually not needed when data is reduced in $A - B$ pairs, like is the case here; however, we found that applying this correction improved the quality of the data. This is likely due to the large exposure times that were used for some targets, which resulted in a large contribution from the dark current that must be corrected both in the data and flat field exposures before applying the flat field correction. A low-pass filter was applied to the flat field exposures to avoid contaminating data with scattered light. We observed that the spectral dispersion (and thus wavelength solution) generally varied from one exposure to another; the wavelength solutions obtained from the Ar calibrations are hence only approximate.

To address this problem, we used several telluric absorption features in the raw spectra of the science and telluric observations to refine individual wavelength solutions. The JH and HK blocking filters also caused significant fringing in the data (up to $\sim 7\%$). We corrected this by adjusting a sinusoid fringing solution to the low frequencies of the raw spectra. We found that a complete fringing solution (which includes finesse as an additional parameter) did not improve the results; we thus chose the simpler sinusoid approach to have a more robust algorithm.

The extracted science and telluric spectra were combined and telluric-corrected using a modified version of the SpeXtool package adapted for Flamingos-2. We observed that the slope of the continuum in the overlapping region of both observing modes (in the H band) varied in a systematic way at the edge of the detector. Hence, we removed these regions before combining the spectra. A few objects for which we obtained Flamingos-2 data (e.g. 2MASS J07083261–4701475, 2MASS 20414283–3506442 and 2MASS J12042529–2806364) turned out to be field dwarfs that closely match literature SpeX-prism spectra of other known objects of the same

spectral type: this is an indication that the systematics mentioned above were accurately corrected.

6.4.4 GNIRS at Gemini-North

We used GNIRS at Gemini-North to obtain NIR spectroscopy for three targets in 2013. We used the $32\,\mathrm{l\,mm^{-1}}$ grating centered at $1.65\,\mu$m in the cross-dispersed mode with the $0\farcs675$ slit to achieve a resolving power of $R \sim 750$ over 0.9–2.45 μm. We nodded exposures along the slit in ABBA patterns with total exposure times ranging from 120 s to 360 s to reach S/N > 100 per resolution element. A0-type telluric standard stars were observed immediately before or after science targets at a similar airmass to ensure a proper telluric correction. Several high-S/N quartz lamp and Ar lamp exposures were obtained immediately after every target to ensure a proper wavelength calibration and flat field correction. The data were reduced with the XDGNIRS IRAF package provided by Gemini.

6.4.5 TripleSpec at Hale

We used TripleSpec (Herter et al. 2008) at the Palomar Observatory 5 m Hale Telescope to obtain NIR spectroscopy for one target in the cross-dispersed mode with the $1\farcs0$ slit, yielding a resolving power $R \sim 3\,800$ over 1.0–2.45 μm. We observed the science target in 4-position ABBA nodding pattern along the slit with a total exposure time of 1200 s to reach a S/N > 100 per resolution element. High-S/N quartz lamp and NeAr lamp exposures were obtained to ensure a proper wavelength calibration and flat field correction. We reduced the data using an adapted version of SpeXtool (see Section 6.4.2).

6.5 Spectral and low-gravity classification

We describe in this section the method that we used to assign spectral types to our new observations. Our typing scheme consists of two distinct dimensions : the first dimension consists of the usual spectral subtypes and is mostly sensitive to $T_{\rm eff}$. The second dimension, introduced by Kirkpatrick (2005) and Kirkpatrick et al. (2006), aims at characterizing the surface gravity with the use of a greek-letter suffix. Field-gravity dwarfs are designated with

the α suffix or no suffix, intermediate-gravity dwarfs with the β suffix, and very low-gravity dwarfs with the γ suffix. The δ suffix was also introduced by Kirkpatrick et al. (2006) to designate objects with an even younger age (typically less than a few Myrs) and lower surface gravity than those associated to the γ suffix.

Optical spectral standards were used to classify NIR spectra of field K7–M9 spectral types. We used the NIR data of GJ 820 B (K7), Gl 229 A (M1), Gl 411 (M2), Gl 213 (M4), Gl 51 (M5), Gl 406 (M6), GJ 644 C (M7), GJ 752 B (M8) and LHS 2924 (M9) as field-gravity spectral standards for these respective spectral types. These standards were identified from the list maintained by Eric Mamajek[3] (Boeshaar, P. C. 1976; Kirkpatrick et al. 1991; Pecaut & Mamajek 2013) and their spectra were downloaded from the IRTF spectral library[4]. We did not use any of the suggested K8, K9, M0 and M3-type standards, since none of them were available in the IRTF spectral library.

While NIR L dwarfs spectral standards have been identified by Kirkpatrick et al. (2010), we have opted to use optically-anchored NIR spectral average templates for classifying field L0–L9 dwarfs. Templates are constructed by median-combining all spectra of a given optical spectral type and gravity class. These templates were provided by K. Cruz and their creation will be discussed in detail and be made public as part of a forthcoming paper (Cruz et al. in preparation). The spectral morphology of these templates is consistent with the Kirkpatrick et al. (2010) spectral standards but since they are an average of many objects, they also reflect the diversity of spectral morphologies present in each spectral type.

Spectral standards have been determined for low-gravity M and L dwarfs by Allers & Liu (2013), but we opted to use spectral average templates in this case too, for the reasons mentioned above. We generated M6–M9 γ templates with data published in Allers & Liu (2013) and sent to us directly by the authors. These templates are available at the Montreal Spectral Library[5]. The optically-anchored L0 β, L1 β and L0–L4 γ templates were provided by K. Cruz. They will be discussed in detail and be made public as part of a forthcoming paper et al. (Cruz et al. in preparation).

[3] *http://www.pas.rochester.edu/~emamajek/spt/*

[4] Maintained by Michael C. Cushing and available at *http://irtfweb.ifa.hawaii.edu/~spex/IRTF_Spectral_Library/*.

[5] *www.astro.umontreal.ca/~gagne/MSL.php*

Table 6.2. An extended sequence of low-gravity dwarfs.

Name	Spectral Type
USco J160603.75–221930.0	L0 δ
USco J160727.82–223904.0	L0 δ
USco J160737.99–224247.0	L0 δ
USco J160818.43–223225.0	L0 δ
USco J160828.47–231510.4	L0 δ
USco J160843.44–224516.0	L0: δ
USco J160918.69–222923.7	L0 δ
USco J161228.95–215936.1	L0 δ
USco J161441.68–235105.9	L0 δ
USco J163919.15–253409.9	L0 δ
CD–35 2722 B	L3 β
2MASS J01531463–6744181	L3 β
2MASS J17260007+1538190	L3 β
2MASS J00011217+1535355	L4 β
2MASS J05120636–2949540	L5 β
2MASS J23174712–4838501	L5 β
2MASS J03264225-2102057	L5 β/γ
SIMP J21543454–1055308	L5 β/γ
2MASS J03552337+1133437	*J0355-type* (L3–L6 γ)
2MASS J16154255+4953211	*J0355-type* (L3–L6 γ)
2MASS J23433470–3646021	*J0355-type* (L3–L6 γ)
WISEP J004701.06+680352.1	*J2244-type* (L6–L8 γ)
2MASS J22443167+2043433	*J2244-type* (L6–L8 γ)
PSO J318.5338–22.8603	*J2244-type* (L6–L8 γ)

Note. — All spectral types are from this work and are based on NIR spectra. A : symbol indicates that the spectral type is based on low signal-to-noise data and is uncertain (± 1), and a :: symbol that it is very uncertain (± 2 subtypes); pec indicates peculiar features; β and γ respectively indicate intermediate gravity and very low gravity.

All template, standard, and target spectra were re-sampled to the same resolution and wavelength grid as SpeX prism observations with the $0\farcs6$ slit ($R \sim 120$). Following the method of Cruz & Núñez (2012), the spectra were normalized in three sections in order to minimize the effect of large NIR color variations within a given spectral type. The spectra were broken into three sections: 0.80–1.35 μm, 1.40–1.80 μm and 1.95–2.40 μm, roughly corresponding to the zJ, H, and K bands.

In a first step to estimating a spectral type, we categorized our 245 new spectra with the spectral template and standard grid described above. There were 11 objects, however, that did not have a good visual match to any standard or template in the grid; this number excludes the early-type contaminants which are discussed later in this work. We collected additional low-gravity brown dwarf spectra in the literature to identify 19 more objects that do not

match our standards.

We performed a visual analysis of all of the unclassifiable spectra and identified enough objects with similar spectral morphologies to create tentative new spectral types and templates for L0 δ, L3 β, L4 β and L5 β. The objects that were used in the creation of these templates are listed in Table 6.2. We list the revised spectral types that we obtain for other spectra from the literature in Table 6.3. We note that our L3 β template includes 2MASS J17260007+1538190, which was suggested by Allers & Liu (2013) as a tentative template for the L3 β spectral type.

We could not build a template for the L2 β spectral type, as the only objects that were confirmed as L2 β from optical data have either very low signal-to-noise (S/N) ratios in the NIR or no NIR data. As we gather more high-S/N spectra of low-gravity L dwarfs, we expect to fill this gap.

The L0 δ template was built from eight candidate members of Upper Scorpius (Lodieu et al. 2008) and one candidate member of βPMG (2MASS 00464841+0715177) that are similar to the L0 γ template except that their H band is even more triangular and their K band has a redder continuum. It is also notable that the H_2O-dependent slope of the L0 δ at 1.7–1.8 μm is slightly steeper than what is seen in any other L-type template.

There are two sets of objects with similar spectra, each with three targets, that we identified via our visual analysis; however, we are unable to confidently assign them a spectral type that fits into our grid of templates. For the purposes of this paper, we label these objects as *J0355-type* and *J2244-type*. One set is composed of 2MASS J03552337+1133437, 2MASS J16154255+4953211 and 2MASS J23433470–3646021. Their spectra are similar to the L4 γ template except that they have a shallower CO band at 2.3 μm. The other set is composed of 2MASS J00470038+6803543, PSO J318.5338–22.8603 and 2MASS J22443167+2043433. Their spectra display a significantly redder continuum than our templates, which might be indicative of a later spectral type. We note that two objects have previous classifications based on the index-based scheme of Allers & Liu (2013): 2MASS J00470038+6803543 was classified as an intermediate-gravity L7 dwarf by Gizis et al. (2015) and PSO J318.5338–22.8603 was classified as a very low-gravity L7 dwarf by Liu et al. (2013b). We listed these two sets of objects as well in Table 6.2.

Table 6.3. Revised NIR spectral types from the literature.

Name	Spectral Type[a]				
	Optical	Ref.	NIR	Ref.	Adopted
Low-gravity dwarfs					
2MASS J21324036+1029494	···		L4.5:	1	L4: β/γ
2MASS J14482563+1031590	L4:	2	L3.5	3	L5: β
WISE J174102.78–464225.5	···		L7::	4	L5:–L7: γ
G 196–3 B	L3 β	5	L3 γ	6	L2–L4 γ
2MASS J00303013–1450333	L7	7	L4.5::	8	L4–L6 β
2MASS J20025073–0521524	L6	9	L7::	10	L5–L7 γ
Red brown dwarfs with no clear signs of low gravity					
2MASS J08354256-0819237	L5	11	L5	12	L4 pec[b]
2MASS J18212815+1414010	L4.5 pec	13	L5 pec	14	L4 pec
2MASS J21512543–2441000	L3	9	···		L4 pec
2MASS J01033203+1935361	L6 β	7,15	L6 β	6	L6 pec
2MASS J01075242+0041563	L8	16	L8 pec	17	L7 pec[b]
2MASS J08251968+2115521	L7.5	7	L6	18	L7 pec[b]
2MASS J08575849+5708514	L8	5	L8 $\pm$ 1	19	L8–L9 pec

[a]All revised spectral types are from this work and are based on NIR spectra.

[b]Candidate member of the $\sim$625 Myr-old Hyades association (Bannister & Jameson 2007).

Note. — References to this Table :
(1) Chiu et al. 2006; (2) Reid et al. 2008a; (3) Wilson et al. 2003; (4) Schneider et al. 2014; (5) Kirkpatrick et al. 2008; (6) Allers & Liu 2013; (7) Kirkpatrick et al. 2000; (8) Burgasser et al. 2010; (9) Cruz et al. 2007; (10) Bardalez Gagliuffi et al. 2014; (11) Cruz et al. 2003; (12) Marocco et al. 2013; (13) Looper et al. 2008b; (14) Kirkpatrick et al. 2010; (15) Faherty et al. 2012; (16) Hawley et al. 2002; (17) Geissler et al. 2011; (18) Knapp et al. 2004; (19) Geballe et al. 2002.

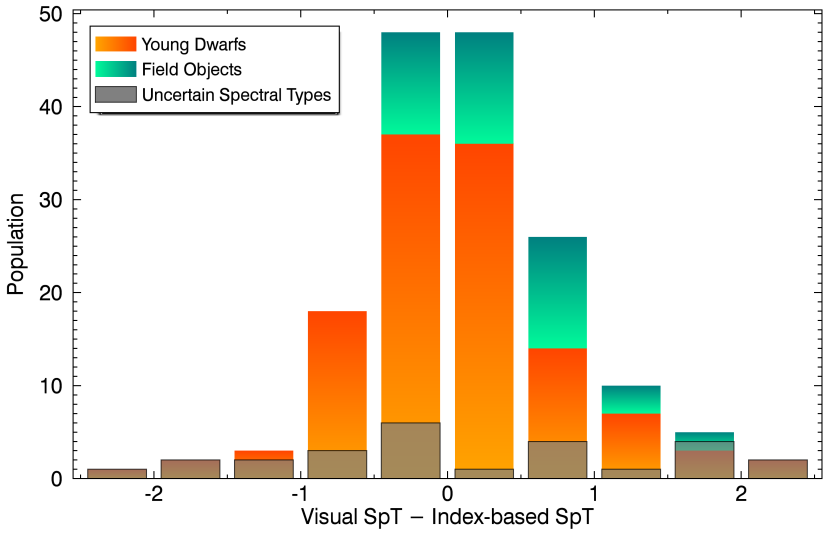

FIGURE 6.2 Distribution of the differences between our visual and index-based spectral classifications, for young dwarfs and field objects. Spectral types generally agree within one subtype, with a standard deviation of 0.7 subtypes and a reduced χ^2 value of 0.8. This is indicative that our measurement errors are representative of the observed differences between the two methods. It can also be seen that most of the outliers in the distribution correspond to objects with uncertain spectral types (i.e., measurement errors of one subtype or more.)

We adopt a conservative estimate of L3–L6 γ for the spectral type range of the *J0355-type*. The spectral features of the *J2244-type* are indicative of a spectral type in the range L6–L8 γ range. For both of these new spectral types, we refrain from assigning them a more precise location in the spectral sequence until more data are available at these late low-gravity types. It is unclear at this stage whether *J0355-type* and *J2244-type* objects are peculiar or a simple extension of low-gravity brown dwarfs at spectral types later than L5. A larger number of late-type, low-gravity L dwarfs will need to be identified before we can assess this. Our set of low-gravity templates is displayed in Figure 6.1.

We used the index-based classification method of Allers & Liu (2013) to corroborate our visual classification. This method consists of measuring the slope of H_2O continuum features to assign a spectral type, and a combination of several gravity-sensitive spectroscopic indices to assign a gravity class. We found that spectral types obtained from the template grid system described above generally agree with index-based spectral types within one subtype (Figure 6.2). The standard deviation between the two methods for the 163 non-peculiar objects

that we categorized is of 0.7 subtypes, with a reduced χ^2 value of 0.8. A reduced $\chi^2 \approx 1$ indicates that measurement errors are representative of the discrepancies. The reduced χ^2 is given by $1/(N-1) \cdot \sum y/\sigma_y$, where N is the number of objects, y is the spectral type discrepancy and σ_y is the quadrature sum of the index-based and visual-based spectral type measurement errors. All cases discrepant by more than 1.5 spectral types correspond to low-S/N data, except for 2MASS J21420580–3101162 that gets L1.5±0.3 from the index-based method and L3 from the visual-based method. This object does not display signs of youth or significantly peculiar features, but it has a slightly redder slope at 1.7–1.8 μm. It unclear what is the cause of this discrepancy.

We used optical data to assign an adopted spectral type using a template-based visual classification method (Cruz et al. 2009) only for the 4 objects for which no NIR data were available. In all other cases, our adopted spectral types are based on NIR data only. Our NIR spectral types based on a visual comparison with templates show a standard deviation of 0.9 subtype with respect to optical spectral types in the literature, and the reduced χ^2 of the differences is 1.5, hence slightly larger than what would be expected given the uncertainties. If we compare optical spectral types to the index-based spectral types of Allers & Liu (2013), we obtain a slightly larger standard deviation (1.1 subtype) and reduced χ^2 (2.4). This is indicative that our visual-based classification method is more consistent with spectral types based on optical data that were reported in the literature. This should be expected, as our templates are anchored on optical data. In both cases, we observe no systematic bias (the mean of the differences is smaller than 0.1 subtype). Several objects that deserve further discussion are presented in detail in the Appendix.

We note that the index-based field-gravity, intermediate-gravity and very low-gravity classes defined by Allers & Liu (2013) were built to correspond to the optical α, β and γ classes, which is what we observe in 143/176 (81%) of the cases. Some of the discrepancies arise for objects near the spectral type thresholds where the method of Allers & Liu (2013) stops being applicable ($\lesssim$M6 or $\gtrsim$L6) or for data with a lower S/N. The δ gravity class does not have an equivalent in the index-based classification of Allers & Liu (2013), but we note that all three of the young dwarfs that we categorized as δ are assigned with the

maximal index-based gravity score (2222). It does not seem that this maximal index-based gravity score always translates as a δ visual classification though, as there are four additional objects in our sample that obtained the score 2222 but that we visually categorized as γ (2MASS J00182834–6703130; L0 γ, 2MASS J01205114–5200349; L1 γ; 2MASS J20113196–5048112; L3 γ; 2MASS J22351658–3844154; L1.5 γ; all are THA candidate members). For consistency within this work, we have adopted the visual spectral types in the remaining sections, but we list all visual and index-based spectral types in Table 6.4. We note that this choice does not affect the conclusions presented in this work.

6.6 Results

In Figure 6.3, we present the NIR spectra of several new intermediate (β) and very-low (γ) gravity dwarfs discovered in this work, as well as known dwarfs for which we have obtained new data. Several objects that were uncovered as candidate members of YMGs in *BASS* had NIR or optical spectroscopy readily available in the SpeX Prism Spectral Libraries or the RIZzo Ultracool Spectral Library[6] with no discussion of low gravity in the literature; we included them in our present analysis and the resulting spectral classification is listed in Table 6.4 along with the new discoveries.

There are some cases where the BANYAN II tool yields ambiguous candidate membership to more than one association (i.e., at least a second moving group shares 10% of the total YMG Bayesian probabilities). In all such cases, we list in Table 6.4 all plausible YMGs with their relative share of the total YMG probability (i.e., excluding the field probability). An extensive RV and parallax follow-up will be required before more can be said on their YMG membership.

We have identified seven objects (Table 6.4) that display signs of low gravity, but for which additional information was inconsistent with membership to any of the YMGs presented here (e.g., RV and distance measurements or the effect of interstellar extinction affecting the NIR spectrum which is not consistent with ages older than $\sim$5 Myr). It is possible that these

[6]Kirkpatrick et al. (2000); Cruz et al. (2003, 2007); Kirkpatrick et al. (2008); Reid et al. (2008a); Cruz et al. (2009); Kirkpatrick et al. (2010); see *http://www.astro.umontreal.ca/~gagne/rizzo*

objects belong to YMGs or star-forming regions that are not considered here, that their RV or parallax measurements are affected by an unresolved binary companion (see the Appendix for a detailed discussion), or that other physical properties such as enhanced dust mimics a lower gravity.

In Figure 6.4, we show a histogram of all previously known low-gravity dwarfs along with new discoveries or confirmations of low gravity that are presented here. It might seem surprising that we did not identify any new low-gravity L2 dwarfs, however this is likely the effect of small number statistics and the fact that we still lack a template for the L2 β spectral type, e.g., some low-S/N low-gravity objects presently typed as L1: and L3: might turn out to be L2 dwarfs when more data becomes available. We anticipate our visual-based low-gravity classification scheme to improve as more data is obtained. If we account for the measurement errors on our spectral types using gaussian probability density functions (which softens the gap at L2) and use Poisson statistics to assess the significance of this lack of L2 dwarfs, we find that the differences between the number of known low-gravity L1, L2 and L3 dwarfs is insignificant (at the level of 0.2σ).

In Figures 6.5 and 6.6, we compare all new low-gravity confirmations with the field and low-gravity sequences defined by Allers & Liu (2013). The individual values for these gravity-sensitive spectroscopic indices are listed in Table 6.5. There are 7 objects in our sample that did not have a discussion of low gravity in the literature and for which optical spectra were available in the Ultracool RIZzo Spectral Library. We used them to revise their spectral types and measure gravity-sensitive optical indices defined by Kirkpatrick et al. (1999) and Cruz et al. (2009). These results, based on optical data only, are presented in Table 6.6. The new spectroscopic observations presented here (95 from *BASS*, 26 from *LP-BASS* and 120 from *PRE-BASS*) allowed us to uncover a total of 108 new M6–L5 low-gravity dwarfs, doubling the number of such known objects (98 before this work).

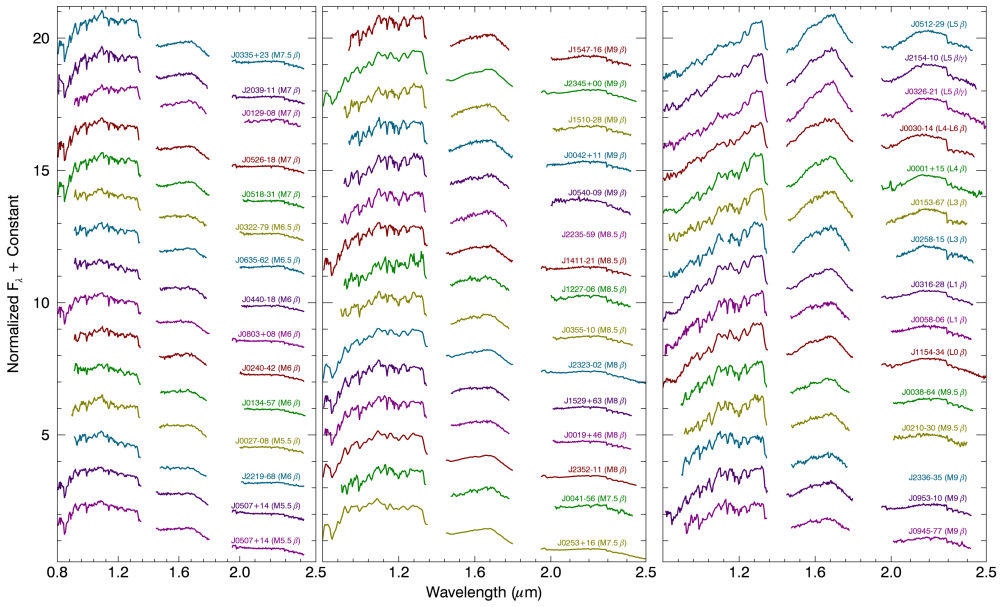

(a) Intermediate-gravity (β) dwarfs

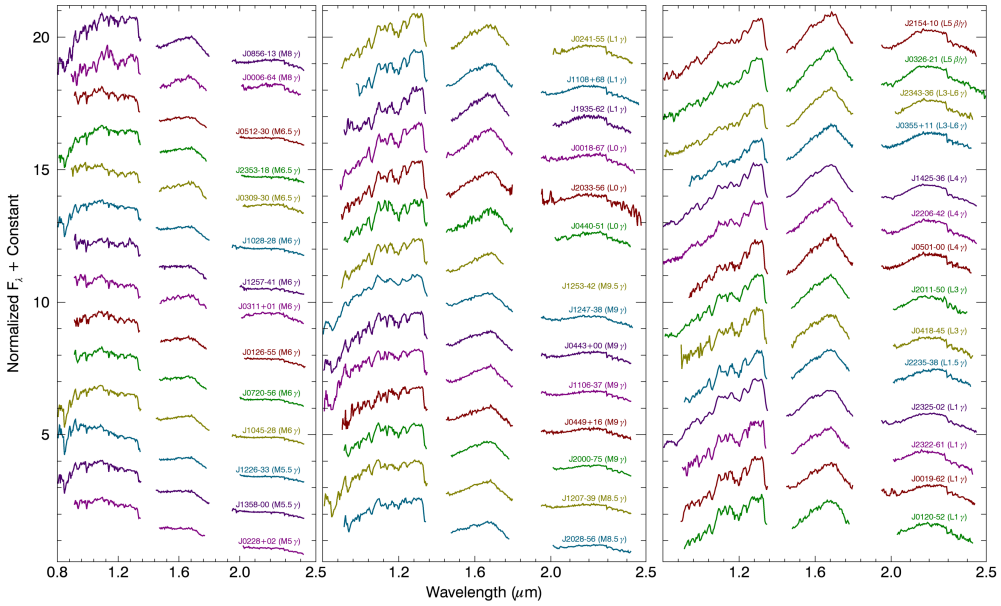

(b) Very low-gravity (γ) dwarfs

FIGURE 6.3 NIR spectra of all new observations and objects for which spectral types were revised in this work. All spectra were re-sampled to a spectral resolution of $R \sim 120$ and a dispersion relation identical to SpeX observations in the prism mode with the 0.″6 slit. We used alternating colors for visibility.

Table 6.4. Spectral Classification, Low Gravity and YMG membership.

2MASS		Spectral Type[a]						Ind. Gravity[b]		YMG Membership					Source
Designation	J	Lit. Opt.	Ref.	Lit. NIR	Ref.	H_2O Ind.	Adopted	Class	Score	Lit.	Ref.	Updated *BASS*[c]	B_P (%)[d]	C_P (%)[e]	Catalog
Bona fide members															
03350208+2342356	12.25	M8.5	29	M7 VL-G	30	M7.3	M7.5 β	INT-G	1n21	BPMG	31	BPMG	84.2	3.9	*PRE-BASS*
03552337+1133437	14.05	L5 γ	32	L3 VL-G	30	L2.3	L3–L6 γ	VL-G	2122	ABDMG	33	ABDMG	99.5	1.1	*BASS*
14252798–3650229	13.75	L3:	15	L5	52	L3.1	L4 γ	INT-G	11?1	···		ABDMG	99.9	0.1	*BASS*
Low-gravity candidate members															
00011217+1535355	15.52	···		L4:	1	L3.7	L4 β	INT-G	1211	···		ABDMG	97.4	1.1	*BASS*
00065794–6436542	13.39	L0	4	···		M7.4	M8 γ	INT-G	1n12	THA	5	THA	> 99.9	< 0.1	*BASS*
00182834–6703130	15.46	···		···		L0.4	L0 γ	VL-G	2222	···		THA	99.9	< 0.1	*BASS*
00191296–6226005	15.64	···		···		L1.0	L1 γ	VL-G	1212	···		THA	99.7	< 0.1	*BASS*
00192626+4614078	12.60	M8	7	···		M7.4	M8 β	INT-G	1n12	ABDMG	8	ABDMG	92.1	4.0	*BASS*
00274534–0806046	11.57	···		···		M5.7	M5.5 β	INT-G	nn1n	···		BPMG	85.2	26.3	*BASS*[f]
00303013–1450333	16.28	L7	7,11	L4.5::	9	L3.2	L4–L6 β	VL-G	2n21	···		ARG	26.5	2.6	*LP-BASS*
00344300–4102266	15.71	···		···		L1.5	L1: β	VL-G	2121	···		THA	98.7	< 0.1	*BASS*
00381489–6403529	14.52	···		···		M8.2	M9.5 β	INT-G	1n12	···		THA	99.9	< 0.1	*LP-BASS*
00413538–5621127	11.96	M6.5 + M9	13	···		M7.9	M7.5 β u	VL-G	0n22	THA	14	THA	99.9	< 0.1	*BASS*
00425923+1142104	14.75	···		···		M9.8	M9 β	INT-G	0n11	···		ABDMG(66);BPMG(33)	19.6	53.1	*PRE-BASS*
00464841+0715177	13.89	L0::	15	···		L0.9	L0 δ	VL-G	2222	···		BPMG	89.3	25.1	*BASS*[f]
00514561–6227073	12.58	···		···		M7.4	M5.5: β	INT-G	nn1n	···		THA	> 99.9	< 0.1	*LP-BASS*
00584253–0651239	14.31	L0	11	L1	16	L0.6	L1 β	INT-G	11?1	···		ABDMG(66);BPMG(33)	96.5	0.3	*LP-BASS*
01205114–5200349	15.64	···		···		L1.4	L1 γ	VL-G	2222	···		THA	> 99.9	< 0.1	*BASS*
01265327–5505506	12.04	···		···		M6.2	M6 γ	FLD-G	0n20	···		THA	> 99.9	< 0.1	*BASS*
01294256–0823580	10.65	M5	6	···		M6.1	M7 β	VL-G	2n22	···		BPMG	95.9	18.9	*BASS*
01344601–5707564	12.07	M4.5	20	···		M5.8	M6 β	VL-G	2n20	THA	20	THA	> 99.9	< 0.1	*BASS*
01484859–5201158	10.87	···		···		M5.0	M5 β	INT-G	nn1n	···		THA	> 99.9	< 0.1	*BASS*
01531463–6744181	16.41	L2:	15	···		L2.9	L3 β	VL-G	2211	···		THA	> 99.9	< 0.1	*BASS*
02103857–3015313	15.07	···		···		M8.4	M9.5 β	INT-G	1n12	···		THA	99.9	< 0.1	*BASS*
02265658–5327032	15.40	···		···		L0.5	L0: γ	VL-G	2221	···		THA	> 99.9	< 0.1	*BASS*
02282694+0218331	12.12	···		···		M5.3	M5 γ	VL-G	nn2n	···		THA(68);BPMG(29)	89.9	< 0.1	*LP-BASS*
02404759–4253377	12.20	···		···		M6.1	M6 β	INT-G	1n02	···		THA	99.9	< 0.1	*LP-BASS*
02410564–5511466	15.39	···		···		L1.6	L1 γ	VL-G	1221	···		THA	> 99.9	< 0.1	*BASS*
02501167–0151295	12.89	···		···		M7.3	M7: β	VL-G	1n22	···		BPMG	92.9	1.1	*BASS*
02583123–1520536	15.91	···		···		L3.0	L3 β	INT-G	1111	···		THA	88.9	< 0.1	*BASS*
02590146–4232204	12.24	···		···		M5	M5 γ	VL-G	nn2n	COL	24	COL	8.6	62.5	*PRE-BASS*
03093877–3014352	11.58	M4.5	20	···		M6.7	M6.5 γ	VL-G	2n20	THA	20	THA	> 99.9	< 0.1	*BASS*
03111547+0106307	10.68	M5.5	17	···		M7.6	M6: γ	FLD-G	0n20	···		BPMG(55);THA(45)	79.0	15.7	*PRE-BASS*
03164512–2848521	14.58	L0:	7	L1	19	L1.7	L1 β	INT-G	1101	···		ABDMG	96.9	3.2	*BASS*
03182597–3708118	13.37	···		···		M5.7	M6: γ	VL-G	2n1n	···		COL(62);THA(38)	75.5	39.2	*LP-BASS*[f]
03224622–7940595	12.22	···		···		M6.3	M6.5 β	INT-G	2n10	···		THA	80.9	< 0.1	*BASS*
03264225–2102057	16.13	L4	28	···		L4.1	L5 β/γ	FLD-G	0n01	···		ABDMG	98.8	1.1	*BASS*

Table 6.4 — continued

2MASS		Spectral Type[a]							Ind. Gravity[b]		YMG Membership					Source
Designation	J	Lit. Opt.	Ref.	Lit. NIR	Ref.	H_2O Ind.	Adopted		Class	Score	Lit.	Ref.	Updated *BASS*[c]	B_P (%)[d]	C_P (%)[e]	Catalog
03363144–2619578	10.68	M5.5	24	···		M5.8	M5.5 β		INT-G	nn1n	THA;COL	24	THA	99.9	< 0.1	*BASS*
03390160–2434059	10.90	M6	24	···		M4.8	M5 β		INT-G	nn1n	COL	24	COL(53);THA(35);BPMG(12)	73.9	32.3	*BASS*[f]
03420931–2904317	15.92	···		···		L1.0	L0: β		VL-G	122n	···		THA	99.7	< 0.1	*BASS*
03421621–6817321	16.85	L2:	28	···		···	L4 γ o		···	···	THA	5	THA	99.8	< 0.1	*BASS*
03550477–1032415	13.08	M8.5	7	···		M8.7	M8.5 β		INT-G	1n21	···		THA(76);COL(24)	93.8	< 0.1	*BASS*[f]
04185879–4507413	16.16	···		···		L2.8	L3 γ		VL-G	2211	···		THA	92.7	< 0.1	*BASS*
04400972–5126544	15.69	···		···		M8.4	L0: γ		VL-G	1212	···		THA(73);COL(23)	86.7	< 0.1	*BASS*
04402583–1820414	12.65	···		···		M6.1	M6 β		INT-G	1n20	···		COL(71);BPMG(28)	13.0	31.7	*PRE-BASS*
04433761+0002051	12.51	M9 γ	28	L0 VL-G	30	M9.9	M9 γ		INT-G	1n21	BPMG	5,12	BPMG	99.8	2.8	*BASS*
04493288+1607226	14.27	···		···		M9.0	M9 γ		VL-G	2n22	···		BPMG	1.6	98.2	*PRE-BASS*
05012406–0010452	14.98	L4 γ	32	L3 VL-G	30	L3.1	L4 γ		VL-G	1212	···		COL(74);CAR(26)	65.9	2.4	*BASS*
05071137+1430013 A	10.57	···		···		M5.6	M5.5 β		INT-G	nn1n	BPMG	12	BPMG	28.5	84.9	*PRE-BASS*
05071137+1430013 B	10.57	···		···		M5.2	M5.5 β		INT-G	nn1n	BPMG	12	BPMG	28.5	84.9	*PRE-BASS*
05120636–2949540	15.46	L4.5	7,35	L4.5::	19	L3.8	L5 β		INT-G	1n01	BPMG	5	BPMG	57.0	37.9	*BASS*[f]
05123569–3041067	11.90	···		···		M6.8	M6.5 γ		FLD-G	0n20	···		COL	96.4	11.5	*BASS*
05181131–3101529	11.88	M6.5	2	···		M7.1	M7 β		VL-G	1n22	···		COL	96.2	8.8	*BASS*
05264316–1824315	12.36	···		···		M6.2	M7 β		VL-G	1n22	···		COL	93.5	12.8	*BASS*
05361998–1920396	15.77	L2 γ	28	L2 VL-G	30	L2.8	L2 γ		INT-G	2111	COL	5	COL	97.6	7.4	*BASS*
05402325–0906326	14.59	···		···		M8.0	M9 β		INT-G	1n11	···		COL	72.0	16.1	*PRE-BASS*
06272161–5308428	16.39	···		···		L0.1	L0: β/γ		INT-G	1012	···		CAR	87.2	9.1	*BASS*
06322402–5010349	15.02	L3	15	···		···	L3 β o		···	···	ABDMG	5	ABDMG	29.5	76.7	*PRE-BASS*
06494706–3823284	11.65	···		···		M4.2	M5 γ		···	nn2n	···		CAR(85);COL(15)	38.8	41.1	*PRE-BASS*
07140394+3702459	11.98	M8	15	···		M7.5	M7.5 β		INT-G	1n10	···		ARG	88.9	0.5	*LP-BASS*
07202582–5617224	12.88	···		···		M5.9	M6 γ		INT-G	1n21	···		BPMG	29.3	73.1	*PRE-BASS*
07525247–7947386	12.83	···		···		M6.1	M5: γ		VL-G	nn2n	···		CAR	97.1	2.5	*PRE-BASS*
08034469+0827000	11.83	···		···		M5.7	M6 β		INT-G	1n02	···		ABDMG	91.2	5.2	*PRE-BASS*
08194309–7401232	10.06	···		···		M5.0	M4.5		···	···	···		CAR	99.3	1.6	*PRE-BASS*
08561384–1342242	13.60	···		···		M8.6	M8 γ		INT-G	1n11	···		TWA	4.9	< 0.1	*PRE-BASS*
09451445–7753150	13.89	···		···		M8.2	M9 β		INT-G	1n21	···		CAR	90.4	2.8	*PRE-BASS*
09532126–1014205	13.47	L0	28	···		M9.9	M9 β		INT-G	1n11	···		TWA(91);CAR(9)	81.2	< 0.1	*BASS*
10212570–2830427	16.91	···		···		L2.5	L4: β/γ		INT-G	1012	···		TWA	92.4	< 0.1	*BASS*
10284580–2830374	10.95	M5	45	···		M5.7	M6 γ		VL-G	2n22	TWA	45	TWA	97.5	< 0.1	*BASS*
10455263–2819303	12.82	···		···		M6.1	M6 γ		VL-G	1n22	···		TWA	65.0	< 0.1	*LP-BASS*
11064461–3715115	14.49	···		···		M9.4	M9 γ		VL-G	2n22	···		TWA	94.6	< 0.1	*BASS*
11083081+6830169	13.12	L1	28,46	···		L2.0	L1 γ		INT-G	1211	···		CAR	6.0	89.9	*PRE-BASS*
11271382–3735076	16.47	···		···		L0.6	L0 δ		VL-G	2222	···		TWA	92.5	< 0.1	*LP-BASS*
11480096–2836488	16.11	···		···		M9.7	L1: β		INT-G	0112	···		TWA	68.9	< 0.1	*BASS*
11544223–3400390	14.19	L0	35	L0.5	19	L0.8	L0 β		INT-G	110?	···		ARG	55.6	46.4	*PRE-BASS*
12073346–3932539	12.99	M8 pec	49	M8 VL-G	30	M9.0	M8.5 γ		VL-G	2n22	TWA	49	TWA	99.9	< 0.1	*BASS*
12074836–3900043	15.49	L0 γ	50	L1 VL-G	50	L1.3	L1 δ		VL-G	2222	TWA	50	TWA	99.7	< 0.1	*BASS*
12265135–3316124	10.69	M5	51	···		M5.7	M5.5 γ		VL-G	nn2n	TWA	51	TWA	95.3	< 0.1	*PRE-BASS*
12271545–0636458	14.19	M9	7	···		M8.1	M8.5 β		INT-G	2n10	···		TWA	1.5	0.6	*PRE-BASS*

Table 6.4 — continued

2MASS		Spectral Type[a]							Ind. Gravity[b]		YMG Membership					Source
Designation	J	Lit.	Opt.	Ref.	Lit. NIR	Ref.	H_2O Ind.	Adopted	Class	Score	Lit.	Ref.	Updated *BASS*[c]	B_P (%)[d]	C_P (%)[e]	Catalog
12474428–3816464	14.78	···			M9 VL-G	50	M8.7	M9 γ	VL-G	2n22	TWA	50	TWA	46.6	< 0.1	*BASS*
12535039–4211215	16.00	···			···		L0.3	M9.5 γ	VL-G	2n22	···		TWA	59.3	0.0	*BASS*
12563961–2718455	16.42	···			···		L4.3	L3: β	VL-G	2021	···		TWA	15.9	< 0.1	*BASS*
12574463–3635431	14.57	···			···		M6.6	M6:: γ	···	···	···		TWA	25.6	< 0.1	*LP-BASS*
12574941–4111373	13.02	···			···		M5.9	M6 γ	VL-G	2n20	···		TWA	67.2	< 0.1	*BASS*
15104786–2818174	12.84	M8		49	···		M9.3	M9 β	INT-G	2n11	···		ARG	59.1	60.2	*PRE-BASS*
15291017+6312539	11.64	···			···		M7.8	M8 β	INT-G	1n10	···		ABDMG	24.6	79.2	*PRE-BASS*
15470557–1626303 A	13.86	···			···		M9.6	M9 β	INT-G	0n11	···		ABDMG	10.6	63.4	*PRE-BASS*
15470557–1626303 B	13.86	···			···		···	M5::	VL-G	nn2n	···		ABDMG	10.6	63.4	*PRE-BASS*
19350976–6200473	16.25	···			···		L1.0	L1 γ	VL-G	2212	···		THA	20.8	0.2	*BASS*
20004841–7523070	12.73	M9		25	···		M9.2	M9 γ	VL-G	2n22	CAS;BPMG	5,54	BPMG(69);ARG(28)	99.1	13.0	*BASS*
20113196–5048112	16.42	···			···		L2.4	L3 γ	VL-G	2222	···		THA	42.6	< 0.1	*BASS*
20224803–5645567	11.76	M5.5		2	···		M5.5	M5.5 β	INT-G	nn1n	···		THA	86.2	< 0.1	*BASS*
20282203–5637024	13.84	···			···		M8.0	M8.5 γ	VL-G	2n22	···		THA	44.3	< 0.1	*BASS*
20334473–5635338	15.72	···			···		L1.2	L0 γ	VL-G	1221	···		THA	93.4	< 0.1	*BASS*
20334670–3733443	10.85	M5		6	···		M6.6	M6: β	INT-G	1n10	···		BPMG	97.4	10.8	*BASS*[f]
20391314–1126531	13.79	M8		7	···		M7.4	M7 β	INT-G	0n11	Pleiades	54	ABDMG	2.2	46.6	*PRE-BASS*
20505221–3639552	13.00	···			···		M5.2	M5 β	INT-G	nn1n	···		ARG(66);BPMG(34)	85.9	47.9	*LP-BASS*[f]
21121598–8128452	10.67	···			···		M5.5	M5.5 β	INT-G	nn1n	···		THA	44.6	< 0.1	*BASS*
21324036+1029494	16.59	···			L4.5:	39	L2.0	L4: β	FLD-G	00?1	···		ARG	30.8	61.6	*PRE-BASS*
21490499–6413039	10.35	M4.5		42	···		M4.1	M4.5	···	···	THA	20	THA	99.7	< 0.1	*BASS*
21543454–1055308	16.44	···			L4 INT-G	56	L3.7	L5 β/γ	INT-G	0n11	ARG	56	ARG	83.8	25.1	*BASS*[f]
21544859–7459134	14.29	···			···		M9.8	M9.5: β	VL-G	2n2n	···		THA	99.4	< 0.1	*BASS*
21572060+8340575	13.97	L0		15	···		···	M9 γ o	···	···	···		ABDMG	30.8	62.9	*PRE-BASS*
22025794–5605087	14.36	···			···		M6.2	M9: γ	VL-G	1n22	···		THA	98.4	< 0.1	*BASS*
22064498–4217208	15.56	L2		11	···		L1.9	L3 γ	VL-G	2?12	ABDMG	5	ABDMG	99.2	1.1	*BASS*
22064498–4217208	15.56	L2		11	···		L1.0	L3 γ	VL-G	1222	ABDMG	5	ABDMG	99.2	1.1	*BASS*
22191486–6828018	13.92	···			···		M6.0	M6 β	VL-G	1n22	···		THA	28.3	< 0.1	*LP-BASS*
22351658–3844154	15.18	···			···		L1.4	L1.5 γ	VL-G	2222	···		THA	96.2	< 0.1	*BASS*
22353560–5906306	14.28	···			···		M8.6	M8.5 β	INT-G	1n11	···		THA	99.8	< 0.1	*BASS*
22444835–6650032	11.03	M5		20	···		M5.1	M5 γ	VL-G	nn2n	THA	20	THA	99.8	< 0.1	*BASS*
22511530–6811216	12.10	···			···		M7.4	M5: γ	VL-G	nn2n	···		THA	99.9	< 0.1	*BASS*
23130558–6127077	10.93	M4.5		20	···		M5.2	M5 β	INT-G	nn1n	THA	20	THA	99.9	< 0.1	*BASS*
23143092–5405313	11.50	···			···		M5.0	M5 β	INT-G	nn1n	···		THA	99.6	< 0.1	*LP-BASS*
23225240–6151114	11.53	M5		5	···		M5.2	M5 γ	INT-G	nn1n	THA	5	THA	99.9	< 0.1	*BASS*
23225299–6151275	15.55	L2 γ		32	L2	57	L1.8	L1 γ	VL-G	1221	THA	5	THA	> 99.9	< 0.1	*BASS*
23231347–0244360	13.58	M8.5		28	···		M7.7	M8 β	INT-G	1n?1	···		BPMG	30.6	54.4	*PRE-BASS*
23255604–0259508	15.96	L3:		9	L3	9	L1.3	L1 γ	INT-G	1111	···		ABDMG	73.4	12.3	*BASS*[f]
23255604–0259508	15.96	L3:		9	L3	9	L2.8	L1 γ	INT-G	0121	···		ABDMG	73.4	12.3	*BASS*[f]
23353085–1908389	11.51	···			···		M5.4	M5 β	INT-G	nn1n	···		ABDMG(86);BPMG(13)	84.8	9.2	*BASS*[f]
23355015–3401477	11.64	···			···		M5.1	M6: γ	VL-G	2n1n	···		BPMG	76.8	31.1	*BASS*[f]
23360735–3541489	14.65	···			···		M8.6	M9 β	VL-G	1n22	···		ABDMG(60);THA(39)	50.8	30.3	*BASS*
23433470–3646021	16.57	···			···		L3.7	L3–L6 γ	VL-G	2012	···		ABDMG(46);BPMG(38);THA(16)	68.9	4.8	*BASS*

Table 6.4 — continued

2MASS		Spectral Type[a]							Ind. Gravity[b]		YMG Membership					Source
Designation	J	Lit.	Opt.	Ref.	Lit. NIR	Ref.	H_2O Ind.	Adopted	Class	Score	Lit.	Ref.	Updated *BASS*[c]	B_P (%)[d]	C_P (%)[e]	Catalog
23520507–1100435	12.84	M7		28	···		M7.6	M8 β	INT-G	1n11	···		ABDMG	90.6	4.0	*BASS*
23532556–1844402 A	11.24	···			···		M5.8	M6.5 γ	VL-G	0n22	···		THA(46);BPMG(34);ABDMG(20)	61.4	< 0.1	*LP-BASS*
23532556–1844402 B	11.24	···			···		M5.2	M4.5 pec	···	···	···		THA(46);BPMG(34);ABDMG(20)	61.4	< 0.1	*LP-BASS*
Candidate members with no constraint on surface gravity																
00020382+0408129 A	10.40	···			···		···	M3	···	···	···		ABDMG	99.6	0.7	*PRE-BASS*
00020382+0408129 B	10.40	···			···		···	M3	···	···	···		ABDMG	99.6	0.7	*PRE-BASS*
00171571–3219539	10.64	M4.5		6	···		M4.3	M4	···	···	···		BPMG(56);ARG(44)	83.0	17.6	*PRE-BASS*
00390342+1330170 A	10.94	···			···		M5.8	M4 pec	···	···	ABDMG	12	BPMG(92);ABDMG(8)	91.9	11.2	*BASS*
00390342+1330170 B	10.94	···			···		M6.0	M5 pec	···	···	ABDMG	12	BPMG(92);ABDMG(8)	91.9	11.2	*BASS*
01035369–2805518 A	11.66	M4.5		17	···		M4.8	M4	···	···	···		ABDMG	83.2	3.5	*PRE-BASS*
01035369–2805518 B	11.66	···			···		M4.9	M4	···	···	···		ABDMG	83.2	3.5	*PRE-BASS*
03132588–2447246	12.53	···			···		M4.8	M5.5: pec	···	···	···		BPMG(47);THA(49)	97.8	< 0.1	*LP-BASS*
03442859+0716100 A	12.72	···			···		···	M4	···	···	···		BPMG	27.5	85.1	*PRE-BASS*
03442859+0716100 B	12.72	···			···		M4.1	M4.5	···	···	···		BPMG	27.5	85.1	*PRE-BASS*
03582255–4116060	15.85	L5		28	···		L5.4	L6 pec	···	nnn?	···		BPMG	67.1	16.6	*BASS*[f]
04173836–1140256	11.75	···			···		···	M2:	···	···	···		ARG(76);BPMG(24)	12.4	92.9	*PRE-BASS*
04231498–1533245	12.54	···			···		M4.7	M4: pec	···	···	···		BPMG	95.4	1.3	*LP-BASS*
05104958–1843548	15.35	···			···		L2.5	L2: β?	INT-G	1?1?	···		COL	68.6	6.6	*LP-BASS*
05201794+0511521	13.04	···			···		···	K0	···	···	···		COL(51);BPMG(49)	9.0	62.5	*PRE-BASS*
05484454–2942551	10.56	···			···		M4.2	M4::	···	···	···		COL(56);BPMG(43)	62.4	24.0	*PRE-BASS*
06021735–1413467	14.34	···			···		···	$<$ K0	···	···	···		COL	81.8	25.3	*PRE-BASS*
07583046+1530004	10.43	M4.5		38	···		···	M4	···	···	···		TWA(45);ARG(39);ABDMG(16)	35.7	< 0.1	*PRE-BASS*
07583098+1530146 A	9.97	M3.5		38	···		M4.2	M4.5	···	···	···		ARG(69);TWA(31)	47.7	41.2	*PRE-BASS*
07583098+1530146 B	9.97	M3.5		38	···		M4.3	M4.5	···	···	···		ARG(69);TWA(31)	47.7	41.2	*PRE-BASS*
08045433–6346180	9.93	···			···		···	$<$ M2	···	···	···		CAR	98.8	1.8	*PRE-BASS*
08095903+4434216	16.44	···			L6	39	L5.4	L6 pec(red)	INT-G	nnn1	···		ARG	80.7	27.4	*BASS*[f]
08540240–3051366	9.01	M4		42	···		···	M4	···	···	···		BPMG	89.1	23.6	*PRE-BASS*
09104094–7552528	13.62	···			···		···	$<$ K0	···	···	···		ARG(59);CAR(28);BPMG(10)	69.9	73.8	*PRE-BASS*
09510459+3558098	10.58	M4.5		44	···		···	M5:	···	···	···		ABDMG	18.9	31.1	*PRE-BASS*
11195251–3917150	13.13	···			···		···	M3	···	···	···		TWA	99.8	< 0.1	*PRE-BASS*
11532691–3015414	12.31	···			···		M4.7	M4.5	···	···	···		TWA(84);ARG(16)	6.1	< 0.1	*PRE-BASS*
12002750–3405371	9.61	···			···		···	M4	···	···	···		TWA	97.7	< 0.1	*PRE-BASS*
12492353–2035592	9.32	···			···		···	M2	···	···	···		TWA	3.6	< 0.1	*PRE-BASS*
13262009–2729370	15.85	L5		49	L6.5:	19	L5.9	L7	···	nnnn	···		ARG	85.5	18.7	*BASS*[f]
19480544+5944412 A	11.49	···			···		M4.2	M4	···	···	···		ARG(86);ABDMG(14)	16.8	69.6	*PRE-BASS*
19480544+5944412 B	11.49	···			···		M4.2	M4.5	···	···	···		ARG(86);ABDMG(14)	16.8	69.6	*PRE-BASS*
23102196–0748531	11.60	···			···		M5.0	M5	···	···	···		BPMG(61);ABDMG(39)	96.9	8.3	*LP-BASS*
23290437+0329113	11.11	···			···		M5.2	M5.5 pec	···	···	···		BPMG	67.5	30.0	*BASS*[f]

Table 6.4 — continued

2MASS		Spectral Type[a]						Ind. Gravity[b]		YMG Membership					Source
Designation	J	Lit. Opt.	Ref.	Lit. NIR	Ref.	H_2O Ind.	Adopted	Class	Score	Lit.	Ref.	Updated *BASS*[c]	B_P (%)[d]	C_P (%)[e]	Catalog
Field contaminants															
00045753–1709369	11.00	M5.5	2	M5.5	3	M5.6	M6	FLD-G	0n00	···		Field	···	···	*PRE-BASS*
00193927–3724392	15.52	L3:	9	L3.5:	9	L2.2	L3	INT-G	10?1	···		Field	···	···	*PRE-BASS*
00210589–4244433	13.52	M9.5	10	···		M9.8	L0.5	FLD-G	000?	···		Field	···	···	*PRE-BASS*
00461551+0252004	14.40	···		···		M9.7	L0 pec	FLD-G	1000	···		Field	···	···	*PRE-BASS*
01291221+3517580	16.78	L4	18	L4.5	19	L3.0	L3.5	FLD-G	?010	ARG	5	Field	···	···	*PRE-BASS*
01550354+0950003	14.82	L5	15	L5:	9	L3.2	L4	INT-G	101?	···		Field	65.3	23.7	*PRE-BASS*
02441019–3548036	15.34	···		···		L0.8	L2 pec	FLD-G	1000	···		Field	···	···	*BASS*
02534448–7959133	11.34	M5.5	23	···		M7.1	M6 pec	FLD-G	0n10	···		Field	···	···	*BASS*[f]
03005033–5459267	12.42	···		···		M5.5	M5	FLD-G	nn0n	···		Field	···	···	*PRE-BASS*
03140344+1603056	12.53	L0	15,25	···		M9.3	M9 pec	FLD-G	0n00	UMA	26	UMA	···	···	*PRE-BASS*
03204919–3313400	12.54	···		···		M8.7	M5.5:	FLD-G	nn0n	···		Field	···	···	*BASS*
03263956–0617586	12.96	M5	27	···		M5.0	M5	FLD-G	nn0n	···		Field	···	···	*PRE-BASS*
03333313–3215181	13.17	···		···		M6.3	M6.5	FLD-G	0n10	···		Field	···	···	*LP-BASS*
03370359–1758079	15.62	L4.5	11	···		L4.3	L4	FLD-G	1000	···		Field	···	···	*LP-BASS*[f]
03370362–3709236	12.75	···		···		M5.8	M5.5	FLD-G	nn0n	···		Field	···	···	*LP-BASS*
04070752+1546457	15.48	L3.5	15	L3.5	22	L3.0	L3	FLD-G	2100	···		Field	···	···	*PRE-BASS*
04532647–1751543	15.14	L3:	7	···		L2.5	L3	INT-G	1110	···		Field	96.5	8.0	*BASS*
04584239–3002061	13.50	···		···		M6.1	M6.5	FLD-G	0n00	···		Field	···	···	*LP-BASS*
05002100+0330501	13.67	L4	15	L4	34	L4.2	L4 pec	FLD-G	0000	···		Field	···	···	*BASS*
05431887+6422528	13.57	L1	15	L2	36	L1.9	L2	INT-G	1110	···		Field	···	···	*PRE-BASS*
06022216+6336391	14.27	L1:	15	L1.5	19	L1.7	L2	FLD-G	1??0	···		Field	···	···	*BASS*
07083261–4701475	14.16	···		···		M8.8	M8.5	FLD-G	0n00	···		Field	···	···	*PRE-BASS*
07200325–0846499	10.63	M9:	37	···		M9.8	L0 pec	FLD-G	1000	···		Field	···	···	*PRE-BASS*
08055944+2505028 A	11.53	···		···		M4.3	M4	···	···	···		Field	···	···	*PRE-BASS*
08055944+2505028 B	11.53	···		···		M5.2	M5	FLD-G	nn0n	···		Field	···	···	*PRE-BASS*
08141769+0253199	11.52	···		···		M5.2	M5	FLD-G	nn0n	···		Field	···	···	*PRE-BASS*
08194351–0450071	14.82	···		···		L0.7	L1: pec	FLD-G	010n	···		Field	···	···	*PRE-BASS*
08204440–7514571	16.59	···		···		L2.8	L3.5	INT-G	101?	···		Field	···	···	*PRE-BASS*
08254335–0029110	15.45	···		···		L0.3	L0.5	FLD-G	1010	···		Field	···	···	*PRE-BASS*
08255896+0340198	10.01	···		···		···	M3	···	···	···		Field	···	···	*PRE-BASS*
08503593+1057156	16.47	L6+L6	40,41	···		L6.2	L7 pec(red) u	FLD-G	nnn0	···		Field	···	···	*PRE-BASS*
08511627+1817302	16.57	···		L4.5:	39	L4.4	L5:	FLD-G	0n00	···		Field	···	···	*PRE-BASS*
08575849+5708514	15.04	L8	35	L8:	43	L7.1	L8 pec	···	···	···		Field	···	···	*PRE-BASS*
10051641+1703264	11.13	···		···		M4.9	M5	FLD-G	nn0n	···		Field	···	···	*PRE-BASS*
10130718–1706349 A	12.79	···		···		M5.1	M5 pec	FLD-G	nn0n	···		Field	···	···	*PRE-BASS*
10130718–1706349 B	12.79	···		···		M5.1	M5 pec	FLD-G	nn0n	···		Field	···	···	*PRE-BASS*
10352029–2058382	11.66	···		···		M5.5	M5.5	FLD-G	nn0n	···		Field	···	···	*PRE-BASS*
10513331–1916530	14.69	···		···		L0.3	M9 pec	FLD-G	0n00	···		Field	···	···	*BASS*

Table 6.4 — continued

2MASS		Spectral Type[a]						Ind. Gravity[b]		YMG Membership					Source
Designation	J	Lit. Opt.	Ref.	Lit. NIR	Ref.	H_2O Ind.	Adopted	Class	Score	Lit.	Ref.	Updated *BASS*[c]	B_P (%)[d]	C_P (%)[e]	Catalog
10584787–1548172	14.15	L3	18	L3	1	L2.2	L3	FLD-G	0000	···		Field	···	···	*BASS*
11335700–7807240	13.20	M8	47	···		M6.2	M6: pec	FLD-G	0n01	···		Field	···	···	*PRE-BASS*
11555389+0559577	15.66	L0	48	L7.5	1	L6.8	L6–L8 pec	FLD-G	nnn0	···		Field	···	···	*PRE-BASS*
12042529–2806364	16.11	···		···		M9.7	L0.5	FLD-G	0010	···		Field	···	···	*PRE-BASS*
12212770+0257198	13.17	L0	15	···		M9.7	M9 pec	FLD-G	1n00	···		Field	···	···	*PRE-BASS*
12310489–3801065	14.68	···		···		M8.0	M8 pec	FLD-G	0n10	···		Field	···	···	*BASS*
12521062–3415091	11.65	···		···		M5.2	M5.5	FLD-G	nn0n	···		Field	···	···	*PRE-BASS*
13015465–1510223	14.54	L1	15	···		M9.6	L1.5:	FLD-G	0001	···		Field	···	···	*PRE-BASS*
13252237+0600290	12.25	···		···		···	< M0	···	···	···		Field	···	···	*PRE-BASS*
17065487–1314396	14.52	···		···		L5.0	L5 pec	FLD-G	0n00	···		Field	···	···	*PRE-BASS*
18393308+2952164	11.01	M6.5	53	···		M6.9	M7	FLD-G	0n00	···		Field	···	···	*PRE-BASS*
18462188–5706040	15.06	···		···		L0.2	L1:	INT-G	2020	···		Field	···	···	*PRE-BASS*
19395435–5216468	14.66	···		···		M9.7	L1	INT-G	1021	···		Field	···	···	*BASS*
20025265–1316418	14.48	···		···		M8.9	M8.5	FLD-G	0n00	···		Field	···	···	*PRE-BASS*
20050639–6258034	11.75	···		···		M4.3	M5	FLD-G	nn0n	···		Field	···	···	*PRE-BASS*
20414283–3506442	14.89	L2:	28	L2	19	L0.7	L2	FLD-G	1010	···		Field	···	···	*BASS*[f]
20482880–3255434	14.71	···		···		M9.4	M9	FLD-G	0n00	···		Field	···	···	*PRE-BASS*
20484222–5127435	15.38	···		···		L1.9	L2 pec	FLD-G	10?0	···		Field	···	···	*BASS*
20484222–5127435	15.38	···		···		L0.7	L2 pec	FLD-G	1001	···		Field	···	···	*BASS*
21144103–4339531	13.02	···		···		M9.0	M7.5 pec	FLD-G	0n00	CAS	54	Field	···	···	*LP-BASS*
21272613–4215183	13.32	M7.5	15	M8	19	M8.5	M8	FLD-G	0n00	Pleiades	54	Field	···	···	*PRE-BASS*
21342814–1840298	11.04	···		···		···	M3: pec	···	···	···		Field	···	···	*PRE-BASS*
21420580–3101162	15.84	L3	55	L2	9	L1.5	L3	FLD-G	10?0	···		Field	···	···	*BASS*[f]
21484123–4736506	10.97	···		···		M4.4	M5	FLD-G	nn0n	···		Field	···	···	*PRE-BASS*
22021125–1109461	12.36	M6.5	29	···		M7.2	M7	FLD-G	0n00	···		Field	···	···	*LP-BASS*
22062157–6116284	16.61	···		···		L1.0	L0: pec	FLD-G	1020	···		Field	···	···	*PRE-BASS*
22400144+0532162	11.72	···		···		M5.7	M6 pec	FLD-G	0n02	···		Field	···	···	*BASS*
22444905–3045535	14.65	···		···		L0.2	M9 pec	FLD-G	0n00	···		Field	···	···	*PRE-BASS*
23155665–4747315	16.08	···		···		L5.2	L3 pec	FLD-G	1010	···		Field	···	···	*BASS*
23270843+3858234	11.74	···		···		M6.3	M5.5 pec	FLD-G	nn0n	···		Field	···	···	*BASS*[f]
23310161–0406193	12.94	M8 + L3	58	···		M8.4	M8 pec u	FLD-G	1n00	···		Field	···	···	*LP-BASS*
23392527+3507165	15.36	L3.5	15	L4.5	9	L3.0	L4 pec	FLD-G	1020	···		Field	···	···	*BASS*
23512200+3010540	12.47	L5.5	59	L5 p(red)	59	L3.9	L5 pec	FLD-G	0n01	ARG	5	Field	92.8	5.8	*PRE-BASS*
Young contaminants															
02530084+1652532	8.39	M6.5	21	M7	22	M7.4	M7.5 β	INT-G	1n12	ARG	5	Field	···	···	*PRE-BASS*
05243009+0640349	11.98	···		···		M5.5	M5.5 β	INT-G	nn1n	···		Field	···	···	*PRE-BASS*
06353541–6234059	12.42	···		···		M6.3	M6.5 β	INT-G	0n12	···		Field	···	···	*PRE-BASS*
13582164–0046262	10.81	···		···		M5.5	M5.5 γ	VL-G	nn2n	···		Field	···	···	*PRE-BASS*
14112131–2119503	12.44	M9	7	M9	52	M8.7	M8.5 β	INT-G	1n10	···		Field	···	···	*PRE-BASS*

Table 6.4 — continued

2MASS		Spectral Type[a]						Ind. Gravity[b]		YMG Membership						Source
Designation	J	Lit. Opt.	Ref.	Lit. NIR	Ref.	H_2O Ind.	Adopted	Class	Score	Lit.	Ref.	Updated	*BASS*[c]	B_P (%)[d]	C_P (%)[e]	Catalog
20385687–4118285	11.66	···		···		M5.2	M5 β	INT-G	nn1n	···		Field		···	···	*PRE-BASS*
23453903+0055137	13.77	M9	15	···		M9.7	M9 β	INT-G	1n11	···		Field		···	···	*PRE-BASS*
Reddened contaminants																
00174858–0316334	13.23	···		···		M8.2	M7 β	···	···	···		Field		···	···	*PRE-BASS*
04044052+2616275 A	12.65	···		···		···	< M0	···	···	···		TAU?		···	···	*PRE-BASS*
04044052+2616275 B	12.65	···		···		···	< M0	···	···	···		TAU?		···	···	*PRE-BASS*
04281061+1839021	13.38	···		···		···	< M3	···	···	···		TAU?		···	···	*PRE-BASS*
05271676+0007526 A	12.17	···		···		···	M0	···	···	···		OMC		···	···	*PRE-BASS*
05271676+0007526 B	12.17	···		···		···	M3	···	···	···		OMC		···	···	*PRE-BASS*
05370704–0623170	15.70	···		···		···	< M0	···	···	···		OMC?		···	···	*PRE-BASS*
05404919–0923192	11.31	···		···		···	< M0	···	···	···		Field		···	···	*PRE-BASS*
05410983–0737392	13.46	···		···		···	< M0	···	···	···		Field		···	···	*PRE-BASS*
05415929–0217020	13.22	···		···		···	< M0	···	···	···		Field		···	···	*PRE-BASS*
05451198–0121021	13.83	···		···		···	< M0	···	···	···		Field		···	···	*PRE-BASS*
11014673–7735144	15.97	···		···		M4.2	< M5:	···	···	···		CHA?		···	···	*PRE-BASS*
11560224–4043248	16.00	···		···		···	< M5	···	···	···		Field		···	···	*PRE-BASS*
12214223–4012050	16.47	···		···		···	< M0	···	···	···		Field		···	···	*BASS*
15424676–3358082	17.02	···		···		···	< K0	···	···	···		Lupus?		···	···	*PRE-BASS*
16210134–2346554	15.16	···		···		···	< M5	···	···	···		SCC?		···	···	*PRE-BASS*
16210134–2346554	15.16	···		···		···	< M5	···	···	···		SCC?		···	···	*PRE-BASS*
16221255–2346418	10.90	···		···		···	< M5	···	···	···		SCC?		···	···	*PRE-BASS*
16232017–2353248	13.38	···		···		M7.0	M5 β	···	···	···		SCC?		···	···	*PRE-BASS*
16251377–2358021	13.75	···		···		···	< M0	···	···	···		ρOPH?		···	···	*PRE-BASS*
16272178–2411060	13.98	···		···		···	< M0	···	···	···		ρOPH?		···	···	*PRE-BASS*
16330142–2425083	16.16	···		···		···	< M5	···	···	···		SCC?		···	···	*PRE-BASS*
16422788–1942350	15.23	···		···		···	< M5	···	···	···		SCC?		···	···	*PRE-BASS*

Table 6.4 — continued

2MASS		Spectral Type[a]						Ind. Gravity[b]		YMG Membership					Source
Designation	J	Lit. Opt.	Ref.	Lit. NIR	Ref.	H_2O Ind.	Adopted	Class	Score	Lit.	Ref.	Updated *BASS*[c]	B_P (%)[d]	C_P (%)[e]	Catalog
18460473+5246027 A	11.03	···		···		···	K0	···	···	···		Field	···	···	*PRE-BASS*
18460473+5246027 B	11.03	···		···		···	K0	···	···	···		Field	···	···	*PRE-BASS*
19033113–3723302	13.41	···		···		···	$<$ M0	···	···	···		Field	···	···	*PRE-BASS*
22573768–5041516	14.96	···		···		···	$<$ M5	···	···	···		Field	···	···	*PRE-BASS*

[a]All spectral types determined in this work (fourth column) are based on NIR spectra, except those with the o suffix, which are based on optical data. A semi-colon in the optical and NIR spectral types indicates that the subtype is uncertain ($\pm$ 1), and a double semi-colon indicates that the subtype is very uncertain ($\pm$ 2 subtypes or more); pec indicates peculiar features; β and γ respectively indicate intermediate gravity and very low gravity, determined from a visual classification.

[b]The index-based gravity classes and scores are defined by Allers & Liu (2013) and based on the FeH and VO features, alkali lines depth and the H-band continuum shape, respectively. We used our adopted spectral subtypes in their calculation. A score value of 0 indicates field gravity, 1 indicates intermediate gravity and 2 indicates a very low gravity. A score of n indicates that no conclusion can be drawn either because the spectroscopic indicator in question is not sensitive to gravity at this spectral type or because the data does not cover the wavelength of this index. A question mark indicates that the quality of the data is not good enough to draw any conclusion (i.e., the measurement is consistent with low gravity, but the measurement error bar overlaps with the field sequence). The final gravity score is taken as the median of these individual gravity scores, ignoring n or ? scores and taking the average of the two central values when an even number of scores is used.

[c]Results reported in the *BASS* survey paper (Paper V), updated using data presented here.

[d]Bayesian probability for membership in a YMG.

[e]The probability that this object is a field contaminant, based on a Monte Carlo analysis and the Besançon galactic model (see text and Chapter 2).

[f]Low-probability Sample.

Note. — References to this Table :
(1) Knapp et al. 2004; (2) Crifo et al. 2005; (3) Deshpande et al. 2012; (4) Martín et al. 2010; (5) Gagné et al. 2014c; (6) Reid et al. 2007; (7) Cruz et al. 2003; (8) Schlieder et al. 2012b; (9) Burgasser et al. 2010; (10) Basri 2000; (11) Kirkpatrick et al. 2000; (12) Schlieder et al. 2012a; (13) Reiners & Basri 2010; (14) Reiners & Basri 2009; (15) Reid et al. 2008a; (16) Marocco et al. 2013; (17) Bochanski et al. 2005; (18) Kirkpatrick et al. 1999; (19) Bardalez Gagliuffi et al. 2014; (20) Kraus et al. 2014b; (21) Teegarden et al. 2003; (22) Burgasser et al. 2008a; (23) Phan-Bao & Bessell 2006; (24) Rodriguez et al. 2013; (25) Schmidt et al. 2007; (26) Seifahrt et al. 2010; (27) West et al. 2008; (28) Cruz et al. 2007; (29) Reid et al. 2002; (30) Allers & Liu 2013; (31) Shkolnik et al. 2012; (32) Cruz et al. 2009; (33) Liu et al. 2013a; (34) Bardalez Gagliuffi et al. 2014; (35) Kirkpatrick et al. 2008; (36) Kirkpatrick et al. 2014; (37) Scholz 2014; (38) Gizis et al. 1997; (39) Chiu et al. 2006; (40) Faherty et al. 2011; (41) Dupuy & Liu 2012; (42) Riaz et al. 2006; (43) Geballe et al. 2002; (44) Shkolnik et al. 2009; (45) Schneider et al. 2012a; (46) Gizis et al. 2000; (47) Luhman 2007; (48) Schmidt et al. 2010; (49) Gizis 2002; (50) Gagné et al. 2014a; (51) Rodriguez et al. 2011; (52) Kendall et al. 2004; (53) Reid et al. 2003; (54) Gálvez-Ortiz et al. 2010; (55) Liebert & Gizis 2006; (56) Gagné et al. 2014b; (57) Manjavacas et al. 2014; (58) Caballero 2007; (59) Kirkpatrick et al. 2010.

Table 6.5. Equivalent Widths and Spectral Indices.

2MASS Designation	Spectral Type	Equivalent Widths (Å)					Spectral Indices (Allers & Liu 2013)				
		Na(1.138 μm)	K(1.169 μm)	K(1.177 μm)	K(1.244 μm)	K(1.253 μm)	FeH_Z	VO_Z	FeH_J	KI_J	H–cont
Intermediate-gravity (β)											
00011217+1535355	L4 β	7.3 ± 1.0	5.7 ± 1.0	7.0 ± 1.3	···	2.9 ± 1.4	1.22 ± 0.01	1.17 ± 0.01	1.24 ± 0.01	1.13 ± 0.01	0.92 ± 0.01
00274534–0806046	M5.5 β	4.1 ± 0.7	1.3 ± 0.7	2.7 ± 0.9	0.6 ± 0.6	1.5 ± 0.6	1.06 ± 0.01	1.01 ± 0.01	1.04 ± 0.01	1.03 ± 0.01	0.97 ± 0.01
00303013–1450333	L4–L6 β	···	···	···	···	···	1.10 ± 0.03	1.03 ± 0.02	···	1.06 ± 0.02	0.92 ± 0.01
00344300–4102266	L1: β	7.5 ± 1.5	6.0 ± 1.6	5.5 ± 1.6	2.9 ± 2.1	3.6 ± 1.6	1.18 ± 0.01	1.14 ± 0.01	1.15 ± 0.02	1.09 ± 0.01	0.96 ± 0.01
00381489–6403529	M9.5 β	8.3 ± 1.4	4.1 ± 1.0	5.2 ± 1.3	3.6 ± 1.9	2.8 ± 1.2	1.12 ± 0.01	1.19 ± 0.01	1.18 ± 0.01	1.07 ± 0.01	1.01 ± 0.01
00425923+1142104	M9 β	10.2 ± 1.4	4.1 ± 1.3	6.5 ± 1.7	3.0 ± 1.0	3.4 ± 1.3	1.17 ± 0.01	1.10 ± 0.01	1.16 ± 0.02	1.08 ± 0.01	0.95 ± 0.01
00514561–6227073	M5.5: β	5.1 ± 1.2	2.0 ± 0.9	2.5 ± 0.8	5.1 ± 1.3	2.3 ± 0.7	1.07 ± 0.01	1.03 ± 0.01	1.06 ± 0.01	1.01 ± 0.01	···
00584253–0651239	L1 β	12.0 ± 1.4	6.7 ± 1.6	8.7 ± 1.8	2.5 ± 1.5	5.6 ± 1.3	1.23 ± 0.01	1.16 ± 0.01	1.19 ± 0.02	1.10 ± 0.01	0.93 ± 0.01
01294256–0823580	M7 β	3.7 ± 1.0	0.3 ± 0.5	2.5 ± 0.7	1.6 ± 1.2	1.8 ± 0.6	1.04 ± 0.01	1.00 ± 0.01	1.04 ± 0.01	1.03 ± 0.01	1.03 ± 0.01
01531463–6744181	L3 β	8.6 ± 0.2	5.6 ± 0.2	6.7 ± 0.2	3.2 ± 0.2	4.5 ± 0.2	1.14 ± 0.01	1.20 ± 0.01	1.19 ± 0.01	1.09 ± 0.01	0.92 ± 0.01
02103857–3015313	M9.5 β	7.5 ± 1.9	4.3 ± 1.4	5.7 ± 1.5	2.6 ± 1.9	4.1 ± 1.4	1.15 ± 0.01	1.25 ± 0.01	1.20 ± 0.01	1.08 ± 0.01	1.00 ± 0.01
02404759–4253377	M6 β	6.1 ± 0.9	1.2 ± 0.5	3.2 ± 0.9	1.6 ± 1.2	2.6 ± 0.7	1.05 ± 0.01	1.02 ± 0.01	1.07 ± 0.01	1.04 ± 0.01	1.00 ± 0.01
02501167–0151295	M7: β	7.2 ± 1.3	0.5 ± 1.1	···	6.7 ± 1.6	···	1.06 ± 0.01	0.99 ± 0.01	1.13 ± 0.01	1.05 ± 0.01	1.02 ± 0.01
02530084+1652532	M7.5 β	···	···	···	···	···	1.07 ± 0.01	1.02 ± 0.01	···	1.05 ± 0.01	1.00 ± 0.01
03164512–2848521	L1 β	···	···	···	···	···	1.16 ± 0.01	1.18 ± 0.03	···	1.12 ± 0.02	0.95 ± 0.01
03224622–7940595	M6.5 β	5.1 ± 1.0	1.9 ± 0.6	1.3 ± 0.7	0.2 ± 0.8	1.9 ± 0.7	1.06 ± 0.01	0.99 ± 0.01	1.03 ± 0.01	1.04 ± 0.01	0.98 ± 0.01
03550477–1032415	M8.5 β	8.8 ± 1.2	3.2 ± 0.9	3.0 ± 1.2	3.7 ± 1.3	3.6 ± 1.0	1.11 ± 0.01	1.07 ± 0.01	1.15 ± 0.01	1.06 ± 0.01	0.97 ± 0.01
04402583–1820414	M6 β	6.5 ± 1.2	-0.1 ± 0.9	2.0 ± 0.9	···	1.4 ± 0.8	1.05 ± 0.01	1.02 ± 0.01	1.09 ± 0.01	1.06 ± 0.01	0.99 ± 0.01
05071137+1430013 A	M5.5 β	4.9 ± 0.9	1.4 ± 0.7	1.9 ± 0.8	···	1.3 ± 0.6	1.06 ± 0.01	1.01 ± 0.01	1.04 ± 0.01	1.04 ± 0.01	1.00 ± 0.01
05071137+1430013 B	M5.5 β	4.2 ± 1.0	1.3 ± 0.7	2.0 ± 0.8	1.3 ± 0.9	1.8 ± 0.6	1.05 ± 0.01	1.00 ± 0.01	1.02 ± 0.01	1.03 ± 0.01	1.01 ± 0.01
05120636–2949540	L5 β	···	···	···	···	···	1.21 ± 0.04	1.09 ± 0.02	···	1.10 ± 0.02	0.91 ± 0.02
05181131–3101529	M7 β	7.0 ± 0.9	1.7 ± 0.7	3.0 ± 0.9	1.7 ± 0.7	1.8 ± 0.6	1.08 ± 0.01	1.04 ± 0.01	1.08 ± 0.01	1.05 ± 0.01	1.00 ± 0.01
05243009+0640349	M5.5 β	4.8 ± 0.7	0.9 ± 0.5	2.0 ± 0.6	1.2 ± 0.4	1.3 ± 0.4	1.06 ± 0.01	1.00 ± 0.01	1.05 ± 0.01	1.03 ± 0.01	1.00 ± 0.01
05264316–1824315	M7 β	7.1 ± 1.0	1.8 ± 0.6	3.5 ± 0.9	2.0 ± 0.6	2.1 ± 0.6	1.09 ± 0.01	1.02 ± 0.01	1.08 ± 0.01	1.04 ± 0.01	1.00 ± 0.01
05402325–0906326	M9 β	10.0 ± 1.4	5.0 ± 1.4	5.2 ± 1.7	2.5 ± 2.6	4.4 ± 1.6	1.16 ± 0.01	1.11 ± 0.01	1.16 ± 0.02	1.09 ± 0.01	0.97 ± 0.01
06353541–6234059	M6.5 β	6.3 ± 1.2	2.2 ± 0.8	2.8 ± 0.9	0.4 ± 1.0	2.0 ± 0.8	1.07 ± 0.01	1.01 ± 0.01	1.05 ± 0.01	1.05 ± 0.01	1.01 ± 0.01
08034469+0827000	M6 β	8.8 ± 1.1	2.1 ± 0.7	3.3 ± 1.0	2.4 ± 0.6	2.0 ± 0.6	1.06 ± 0.01	1.00 ± 0.01	1.05 ± 0.01	1.04 ± 0.01	1.00 ± 0.01
09451445–7753150	M9 β	10.5 ± 1.7	2.8 ± 1.2	4.1 ± 1.6	2.6 ± 2.0	3.6 ± 1.4	1.14 ± 0.01	1.06 ± 0.01	1.11 ± 0.01	1.08 ± 0.01	0.97 ± 0.01
09532126–1014205	M9 β	8.1 ± 1.0	4.6 ± 1.2	6.4 ± 1.5	2.8 ± 1.1	4.0 ± 1.1	1.13 ± 0.01	1.22 ± 0.01	1.16 ± 0.01	1.08 ± 0.01	0.96 ± 0.01
11544223–3400390	L0 β	···	···	···	···	···	1.16 ± 0.02	1.19 ± 0.02	···	1.11 ± 0.02	0.94 ± 0.01
12271545–0636458	M8.5 β	12.1 ± 2.3	6.8 ± 1.6	8.2 ± 2.0	2.0 ± 2.2	1.8 ± 2.1	1.04 ± 0.01	0.99 ± 0.01	1.10 ± 0.01	1.11 ± 0.01	0.95 ± 0.01
12563961–2718455	L3: β	12.8 ± 0.1	1.3 ± 0.2	3.5 ± 0.1	1.9 ± 0.2	2.7 ± 0.1	1.16 ± 0.01	0.97 ± 0.01	1.30 ± 0.01	1.07 ± 0.01	0.91 ± 0.01
15104786–2818174	M9 β	8.3 ± 1.4	3.4 ± 1.0	4.7 ± 1.4	2.8 ± 1.7	3.6 ± 1.1	1.05 ± 0.01	1.11 ± 0.01	1.11 ± 0.01	1.08 ± 0.01	0.95 ± 0.01
15291017+6312539	M8 β	8.9 ± 1.2	3.2 ± 0.9	4.7 ± 1.4	2.0 ± 0.8	3.4 ± 0.8	1.11 ± 0.01	1.05 ± 0.01	1.11 ± 0.01	1.06 ± 0.01	0.95 ± 0.01
15470557–1626303 A	M9 β	9.5 ± 1.3	4.6 ± 1.5	6.9 ± 1.6	3.0 ± 1.2	4.8 ± 1.2	1.18 ± 0.01	1.11 ± 0.01	1.16 ± 0.01	1.10 ± 0.01	0.95 ± 0.01
20224803–5645567	M5.5 β	5.5 ± 0.9	0.1 ± 0.6	1.3 ± 1.0	2.2 ± 1.9	1.2 ± 0.7	1.09 ± 0.01	1.02 ± 0.01	1.05 ± 0.01	1.03 ± 0.01	1.01 ± 0.01
20334670–3733443	M6: β	4.1 ± 0.9	1.7 ± 0.6	2.7 ± 0.8	5.6 ± 1.2	1.7 ± 0.5	1.06 ± 0.01	1.01 ± 0.01	1.10 ± 0.01	1.02 ± 0.01	0.99 ± 0.01
20391314–1126531	M7 β	9.5 ± 1.2	2.9 ± 1.0	4.2 ± 1.3	1.8 ± 0.9	3.3 ± 0.9	1.11 ± 0.01	1.05 ± 0.01	1.10 ± 0.01	1.06 ± 0.01	0.99 ± 0.01
21121598–8128452	M5.5 β	5.3 ± 1.0	0.7 ± 0.6	1.3 ± 0.8	1.8 ± 1.0	1.7 ± 0.5	1.06 ± 0.01	1.01 ± 0.01	1.05 ± 0.01	1.02 ± 0.01	1.00 ± 0.01
21324036+1029494	L4: β	···	···	···	···	···	···	1.02 ± 0.05	···	1.09 ± 0.04	0.92 ± 0.02

Table 6.5 — continued

2MASS Designation	Spectral Type	Equivalent Widths (Å)					Spectral Indices (Allers & Liu 2013)				
		Na(1.138 μm)	K(1.169 μm)	K(1.177 μm)	K(1.244 μm)	K(1.253 μm)	FeH_Z	VO_Z	FeH_J	KI_J	H–cont
21544859–7459134	M9.5: β	10.0 ± 1.7	3.8 ± 1.2	2.0 ± 1.3	···	···	0.98 ± 0.01	1.11 ± 0.01	1.09 ± 0.03	···	···
22191486–6828018	M6 β	6.5 ± 1.3	1.5 ± 0.5	2.1 ± 0.9	1.6 ± 1.2	1.7 ± 0.7	1.05 ± 0.01	1.03 ± 0.01	1.06 ± 0.01	1.05 ± 0.01	1.01 ± 0.01
22353560–5906306	M8.5 β	7.2 ± 1.4	3.5 ± 1.0	5.6 ± 1.5	2.2 ± 1.9	2.7 ± 1.2	1.14 ± 0.01	1.16 ± 0.01	1.16 ± 0.02	1.06 ± 0.01	0.97 ± 0.01
23231347–0244360	M8 β	···	···	···	···	···	1.09 ± 0.01	1.05 ± 0.01	···	1.07 ± 0.01	0.98 ± 0.01
23360735–3541489	M9 β	9.4 ± 1.3	4.1 ± 1.2	6.3 ± 1.8	2.8 ± 2.0	3.0 ± 1.4	1.13 ± 0.01	1.12 ± 0.01	1.17 ± 0.01	1.07 ± 0.01	0.99 ± 0.01
23453903+0055137	M9 β	···	···	···	···	···	1.12 ± 0.01	1.11 ± 0.01	···	1.07 ± 0.01	0.97 ± 0.01
23520507–1100435	M8 β	···	···	···	···	···	1.11 ± 0.01	1.05 ± 0.01	···	1.07 ± 0.01	0.98 ± 0.01
Very low-gravity (γ or δ)											
00182834–6703130	L0 γ	6.1 ± 1.0	3.8 ± 1.2	4.0 ± 1.6	1.3 ± 1.3	1.4 ± 1.1	1.06 ± 0.01	1.34 ± 0.02	1.09 ± 0.02	1.03 ± 0.01	1.02 ± 0.01
00191296–6226005	L1 γ	8.8 ± 1.5	5.7 ± 1.4	5.6 ± 1.6	4.2 ± 2.1	3.8 ± 1.6	1.13 ± 0.01	1.29 ± 0.01	1.18 ± 0.02	1.11 ± 0.01	1.00 ± 0.01
00464841+0715177	L0 δ	7.5 ± 1.0	3.3 ± 1.1	3.5 ± 1.3	2.4 ± 1.0	1.7 ± 0.9	1.06 ± 0.01	1.27 ± 0.01	1.12 ± 0.01	1.05 ± 0.01	0.98 ± 0.01
01205114–5200349	L1 γ	5.1 ± 1.1	5.2 ± 1.4	6.5 ± 1.7	4.6 ± 2.1	2.7 ± 1.3	1.13 ± 0.01	1.27 ± 0.01	1.14 ± 0.01	1.08 ± 0.01	1.01 ± 0.01
01265327–5505506	M6 γ	7.3 ± 1.6	-0.4 ± 0.4	0.8 ± 0.6	1.2 ± 0.9	1.1 ± 0.6	1.07 ± 0.01	1.01 ± 0.01	1.05 ± 0.01	1.05 ± 0.01	0.98 ± 0.01
02265658–5327032	L0 γ	6.6 ± 1.4	3.8 ± 1.4	4.8 ± 1.4	3.2 ± 1.5	2.7 ± 1.1	1.07 ± 0.01	1.30 ± 0.01	1.13 ± 0.01	1.06 ± 0.01	0.93 ± 0.01
02410564–5511466	L1 γ	5.1 ± 1.1	5.0 ± 1.3	5.7 ± 1.5	3.5 ± 1.8	3.6 ± 1.4	1.19 ± 0.01	1.26 ± 0.01	1.15 ± 0.01	1.10 ± 0.01	0.97 ± 0.01
03264225–2102057	L5 β/γ	···	···	···	···	···	1.28 ± 0.11	1.08 ± 0.04	···	1.12 ± 0.02	0.94 ± 0.02
04185879–4507413	L3 γ	7.7 ± 2.5	6.6 ± 2.0	8.8 ± 2.1	5.7 ± 3.0	4.5 ± 1.9	1.08 ± 0.01	1.31 ± 0.01	1.18 ± 0.02	1.08 ± 0.01	0.94 ± 0.01
04400972–5126544	L0 γ	9.2 ± 1.6	4.9 ± 1.1	5.2 ± 1.5	0.5 ± 1.5	2.5 ± 1.2	1.11 ± 0.01	1.30 ± 0.01	1.20 ± 0.01	1.09 ± 0.01	1.05 ± 0.01
04493288+1607226	M9 γ	10.6 ± 1.3	4.2 ± 1.5	3.9 ± 1.4	3.1 ± 1.4	2.9 ± 1.1	1.07 ± 0.01	1.16 ± 0.01	1.10 ± 0.04	1.05 ± 0.01	1.00 ± 0.01
05123569–3041067	M6.5 γ	5.9 ± 1.0	0.8 ± 0.4	1.7 ± 0.8	4.0 ± 1.6	0.4 ± 0.6	1.07 ± 0.01	1.02 ± 0.01	1.05 ± 0.01	1.02 ± 0.01	0.98 ± 0.01
07202582–5617224	M6 γ	5.4 ± 0.8	0.9 ± 0.6	1.8 ± 0.8	2.1 ± 1.1	2.0 ± 0.6	1.05 ± 0.01	1.00 ± 0.01	1.05 ± 0.01	1.04 ± 0.01	0.99 ± 0.01
08561384–1342242	M8 γ	7.6 ± 1.1	1.6 ± 1.0	3.9 ± 1.2	2.5 ± 0.9	2.9 ± 0.9	1.12 ± 0.01	1.12 ± 0.01	1.12 ± 0.01	1.06 ± 0.01	0.98 ± 0.01
10284580–2830374	M6 γ	3.9 ± 0.6	0.3 ± 0.3	1.5 ± 0.4	1.0 ± 0.3	0.6 ± 0.3	1.04 ± 0.01	1.00 ± 0.01	1.04 ± 0.01	1.02 ± 0.01	1.01 ± 0.01
10455263–2819303	M6 γ	4.2 ± 0.7	0.8 ± 0.4	1.5 ± 0.5	1.1 ± 0.3	1.0 ± 0.3	1.05 ± 0.01	1.01 ± 0.01	1.05 ± 0.01	1.03 ± 0.01	1.01 ± 0.01
11064461–3715115	M9 γ	6.3 ± 1.0	0.7 ± 0.7	2.1 ± 0.9	1.7 ± 0.7	1.4 ± 0.7	1.06 ± 0.01	1.14 ± 0.01	1.04 ± 0.01	1.05 ± 0.01	1.02 ± 0.01
11083081+6830169	L1 γ	9.5 ± 1.2	6.2 ± 1.2	7.2 ± 1.4	5.2 ± 1.1	4.8 ± 1.0	1.30 ± 0.01	1.28 ± 0.01	1.14 ± 0.02	1.11 ± 0.01	0.95 ± 0.01
12074836–3900043	L1 δ	···	···	···	···	···	1.02 ± 0.02	1.26 ± 0.02	···	1.05 ± 0.02	1.00 ± 0.02
12474428–3816464	M9 γ	···	···	···	···	···	1.05 ± 0.01	1.10 ± 0.01	···	1.05 ± 0.02	0.99 ± 0.01
12574941–4111373	M6 γ	8.0 ± 1.4	0.0 ± 0.6	1.8 ± 0.8	0.6 ± 0.8	1.9 ± 0.6	1.03 ± 0.01	1.01 ± 0.01	1.03 ± 0.01	1.06 ± 0.01	0.99 ± 0.01
13582164–0046262	M5.5 γ	6.6 ± 0.9	1.0 ± 0.6	2.6 ± 0.8	1.4 ± 0.4	1.4 ± 0.5	1.07 ± 0.01	1.00 ± 0.01	1.05 ± 0.01	1.03 ± 0.01	0.99 ± 0.01
14252798–3650229	L4 γ	···	···	···	···	···	1.22 ± 0.02	1.11 ± 0.01	···	1.11 ± 0.02	0.94 ± 0.01
19350976–6200473	L1 γ	5.9 ± 2.0	4.9 ± 2.0	5.9 ± 1.7	0.8 ± 3.8	4.2 ± 1.9	1.11 ± 0.01	1.35 ± 0.01	1.09 ± 0.01	1.09 ± 0.01	1.01 ± 0.01
20113196–5048112	L3 γ	5.4 ± 1.5	1.3 ± 1.4	0.5 ± 1.5	···	1.2 ± 1.3	1.15 ± 0.01	1.31 ± 0.01	1.13 ± 0.02	1.05 ± 0.01	0.98 ± 0.01
20282203–5637024	M8.5 γ	4.5 ± 0.7	1.1 ± 0.7	2.8 ± 0.9	2.2 ± 1.0	1.3 ± 0.7	1.02 ± 0.01	1.12 ± 0.01	1.10 ± 0.01	1.00 ± 0.01	1.01 ± 0.01
20334473–5635338	L0 γ	5.7 ± 1.2	5.1 ± 1.3	5.8 ± 1.4	2.9 ± 2.1	2.7 ± 1.6	1.14 ± 0.01	1.27 ± 0.01	1.16 ± 0.02	1.09 ± 0.01	0.96 ± 0.01
21543454–1055308	L5 β/γ	···	···	···	···	···	1.27 ± 0.04	1.04 ± 0.03	···	1.06 ± 0.02	0.92 ± 0.01
22025794–5605087	M9: γ	9.5 ± 1.6	3.9 ± 1.2	7.0 ± 1.6	2.9 ± 2.4	2.4 ± 1.3	1.12 ± 0.01	1.13 ± 0.01	1.12 ± 0.02	1.05 ± 0.01	1.02 ± 0.01
22064498–4217208	L4 γ	···	···	···	···	···	1.11 ± 0.03	1.09 ± 0.04	···	1.08 ± 0.02	0.97 ± 0.01
22351658–3844154	L1.5 γ	5.5 ± 1.0	4.1 ± 1.3	4.9 ± 1.3	1.1 ± 1.5	2.0 ± 1.0	1.05 ± 0.01	1.31 ± 0.02	1.11 ± 0.01	1.04 ± 0.01	0.97 ± 0.01
23255604–0259508	L1 γ	···	···	···	···	···	1.16 ± 0.01	1.16 ± 0.01	···	1.07 ± 0.02	0.93 ± 0.01
23433470–3646021	L3–L6 γ	8.1 ± 1.4	6.0 ± 1.1	6.6 ± 1.1	0.5 ± 1.6	2.9 ± 1.2	1.24 ± 0.01	1.03 ± 0.01	1.13 ± 0.02	1.07 ± 0.01	0.97 ± 0.01
23532556–1844402 A	M6.5 γ	6.0 ± 1.0	0.9 ± 0.8	1.7 ± 1.0	1.4 ± 1.0	1.8 ± 0.7	1.07 ± 0.01	1.01 ± 0.01	1.07 ± 0.01	1.03 ± 0.01	1.00 ± 0.01

Table 6.6. Revised Optical Spectral Types and Spectral Indices.

2MASS Designation	Opt. type	Spectral Indices										
		K-a	K-b	Na-a	Na-b	VO-a	Cs-a	Cs-b	TiO-b	Rb-a	Rb-b	FeH-a	CrH-a
03164512–2848521	L1 β	3.27 ± 0.36^{a}	2.90 ± 0.38	0.975 ± 0.053^{a}	0.988 ± 0.059^{a}	1.244 ± 0.095^{a}	1.125 ± 0.036	1.071 ± 0.050	1.374 ± 0.061^{a}	1.214 ± 0.075^{b}	1.089 ± 0.080^{a}	1.254 ± 0.043^{a}	1.196 ± 0.045^{a}
03264225–2102057	L5 β	4.23 ± 0.94^{a}	8.80 ± 3.04^{a}	1.023 ± 0.037^{a}	1.064 ± 0.046^{a}	0.993 ± 0.030^{a}	1.44 ± 0.10^{b}	1.249 ± 0.071	1.058 ± 0.022^{a}	1.34 ± 0.19^{a}	1.83 ± 0.27	1.345 ± 0.053	1.701 ± 0.065^{a}
03421621–6817321	L4 γ	3.99 ± 0.61^{a}	3.23 ± 0.46^{a}	0.946 ± 0.031^{a}	1.026 ± 0.035^{a}	0.930 ± 0.054	1.011 ± 0.028^{a}	1.123 ± 0.049^{b}	0.873 ± 0.056^{a}	1.164 ± 0.088^{a}	1.281 ± 0.066^{a}	1.102 ± 0.038^{a}	1.284 ± 0.047^{a}
06322402–5010349	L3 β	7.83 ± 1.53^{a}	5.81 ± 1.29^{b}	1.034 ± 0.022^{a}	1.079 ± 0.036^{a}	1.059 ± 0.031^{a}	1.276 ± 0.066	1.020 ± 0.033^{a}	1.081 ± 0.020^{a}	1.316 ± 0.099^{b}	1.328 ± 0.078^{b}	1.214 ± 0.023^{a}	1.555 ± 0.028^{a}
11083081+6830169	L1 γ	6.1 ± 1.7^{a}	2.97 ± 0.72^{a}	0.909 ± 0.065^{a}	1.04 ± 0.12^{a}	1.20 ± 0.10^{a}	1.091 ± 0.085^{b}	0.970 ± 0.037^{a}	1.240 ± 0.051^{a}	1.32 ± 0.14	1.24 ± 0.12	1.067 ± 0.064^{a}	1.324 ± 0.070^{a}
11544223–3400390	L0 β	3.48 ± 0.38^{a}	2.43 ± 0.25^{a}	1.098 ± 0.048^{b}	1.120 ± 0.054^{a}	1.218 ± 0.025^{b}	1.106 ± 0.024^{b}	1.072 ± 0.027	1.504 ± 0.030^{a}	1.113 ± 0.036^{b}	1.144 ± 0.030^{b}	1.135 ± 0.017^{a}	1.171 ± 0.011
21572060+8340575	M9 γ	2.33 ± 0.23^{a}	1.54 ± 0.14^{a}	0.920 ± 0.037^{a}	0.943 ± 0.048^{a}	1.33 ± 0.14^{a}	1.081 ± 0.040^{b}	1.047 ± 0.041^{b}	1.61 ± 0.10^{a}	1.090 ± 0.085	0.797 ± 0.068^{a}	0.888 ± 0.035^{a}	0.990 ± 0.034^{a}

[a] This index is consistent with a low gravity at this spectral type.

[b] This index is marginally consistent with a low gravity at this spectral type (the measurement is consistent with a low gravity but its error bars overlap with the field population).

In addition to several new candidate members of YMGs, we report here that 2MASS J14252798–3650229 (DENIS-P J142527.97-365023.4) is a new low-mass BD bona fide member of ABDMG. This object was identified by Kendall et al. (2004) as an L5 dwarf with an estimated spectrophotometric distance of ~ 10 pc. Blake et al. (2010) measured an RV of $5.37 \pm 0.25\,\mathrm{km\,s^{-1}}$ and Dieterich et al. (2014) measured a trigonometric distance of 11.57 ± 0.11 pc. We reported in Chapter 3 that the galactic position and space velocities of this object are a very good match to ABDMG (Figure 6.7), suggesting that it would be a new bona fide member if low gravity would be confirmed. They also indicated that its NIR colors are redder than those of field dwarfs of the same spectral type, which hints at low gravity. The low gravity is indeed readily apparent in the new SpeX prism spectrum that we obtained for this object (Figure 6.8): both a visual comparison and the index-based classification of Allers & Liu (2013) indicate that this object is an L4 γ dwarf. We conclude that 2MASS J14252798–3650229 is a new bona fide member of ABDMG, making it the second latest-type confirmed member of this moving group after the L7 β member WISEP J004701.06+680352.1. At the age of ABDMG, 2MASS J14252798–3650229 has an estimated mass of $26.6^{+0.3}_{-1.0}\,M_{\rm Jup}$.

6.6.1 Updated YMG membership

It is possible to use the spectral type information as well as the youth of candidate members determined from the spectroscopic follow-up presented here as additional inputs in BANYAN II to refine estimates of distance, RV and YMG membership and contamination probabilities. Spectral types are used to assess if the absolute $W1$ magnitude of a target is consistent with its spectral type at the statistical distance that corresponds to a given YMG membership (using distinct sequences for field and low-gravity dwarfs; see Chapter 3), whereas prior knowledge of youth reduces the number of potential contaminants from the field and thus improves the probability that the object belongs to a YMG. We reject all objects with spectral types $\geq$ M5 that display no signs of low gravity (17 in *BASS*, 7 in *LP-BASS* and 41 in *PRE-BASS*), since this implies an age older than the Pleiades (~ 120 Myr; Cruz et al. 2009; Allers & Liu 2013) and is not consistent with membership to any YMG considered here. These updated results are listed in Table 6.4, and individual objects of interest are discussed

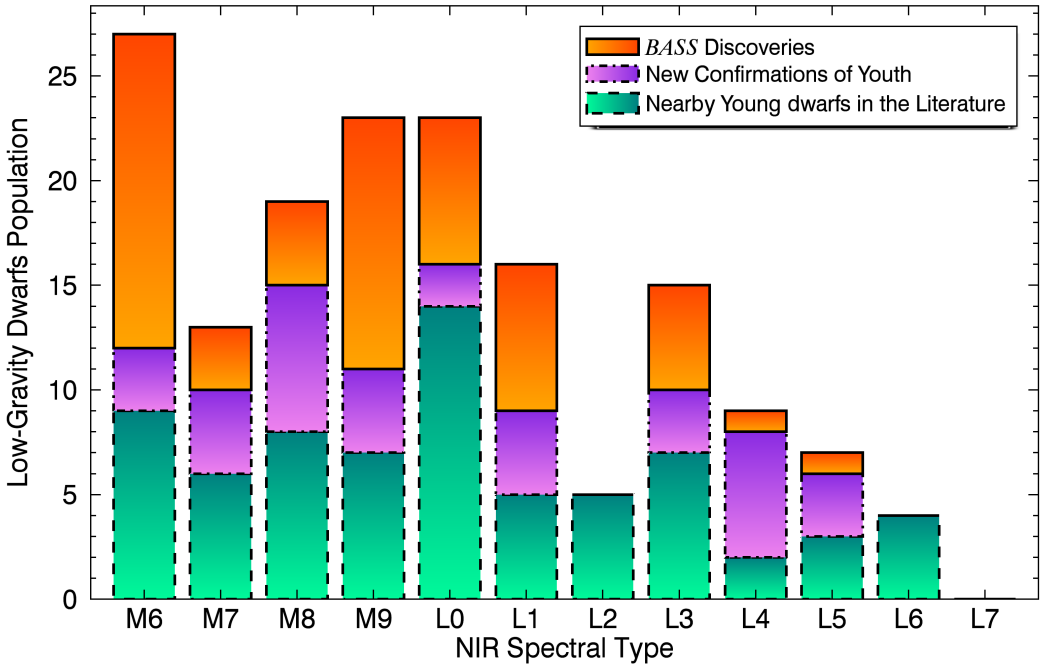

FIGURE 6.4 NIR Spectral type histogram of all known low-gravity dwarfs and those presented in this work. Green bars delimited by dashed lines represent the known population prior to *BASS*, purple bars delimited by dash-dotted lines represent known dwarfs for which low-gravity features were identified here for the first time, and orange bars delimited by solid lines represent new discoveries from *BASS*. The *BASS* survey has contributed significantly in increasing the number of known low-gravity M6–L5 dwarfs.

in the Appendix.

6.6.2 X-ray luminosity

We followed up several objects that turned out to have spectral types earlier than expected, some of them ($\leq$ M5) to the point where current NIR and optical index-based methods are unable to determine whether they are likely young or field objects. In this section, we take advantage of the ROSAT bright and faint source catalogs (Voges et al. 1999, 2000; VizieR catalogs *IX/10A* and *IX/29*) to assess whether these objects are young candidate members of YMGs or field interlopers.

Malo et al. (2014a) demonstrated that the distribution of absolute X-ray luminosity for M0–M5 dwarf members of ABDMG and βPMG is significantly distinct from that of field M0–M5 dwarfs. In particular, they showed that βPMG members are $\sim$4 times more X-ray

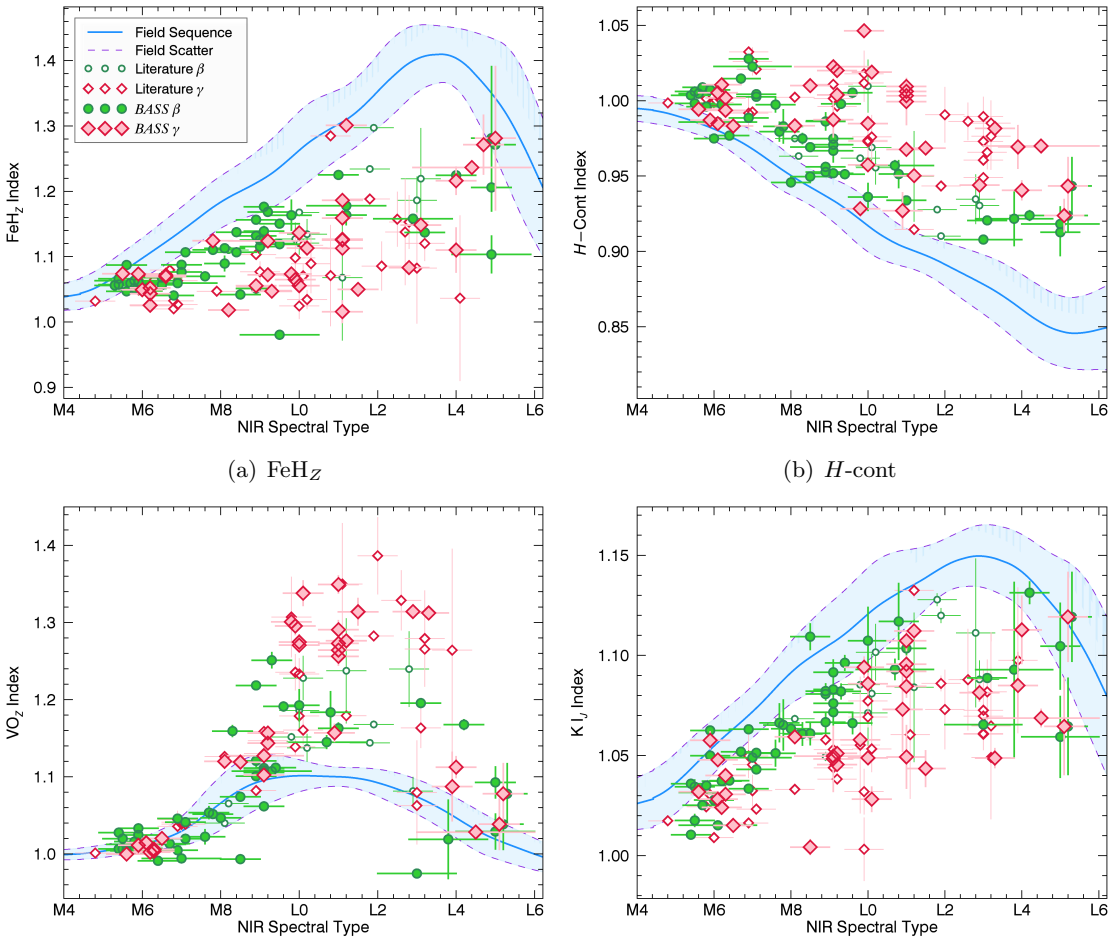

(a) FeH_Z (b) H-cont

(c) VO_Z (d) KI_J

FIGURE 6.5 Low-resolution ($\mathrm{R} \gtrsim 75$) gravity-sensitive NIR indices defined by Allers & Liu (2013) for all intermediate-gravity (green circles) and very low-gravity (red diamonds) dwarfs from the *BASS* sample. This sample consists mainly of new discoveries and known dwarfs with a new low-gravity classification. Previously known intermediate-gravity and low-gravity dwarfs from the samples of Allers & Liu (2013) and Manjavacas et al. (2014) are displayed as smaller, open symbols. The thick, blue line and the pale blue region delimited by dashed, purple lines represent the field sequence and its scatter. Random offsets smaller than 0.25 subtypes have been added to the spectral types for clarity. It is readily apparent that low-gravity dwarfs of the same spectral type can display a different set of low-gravity features, which is why a classification based on multiple gravity-sensitive indices is necessary (Allers & Liu 2013).

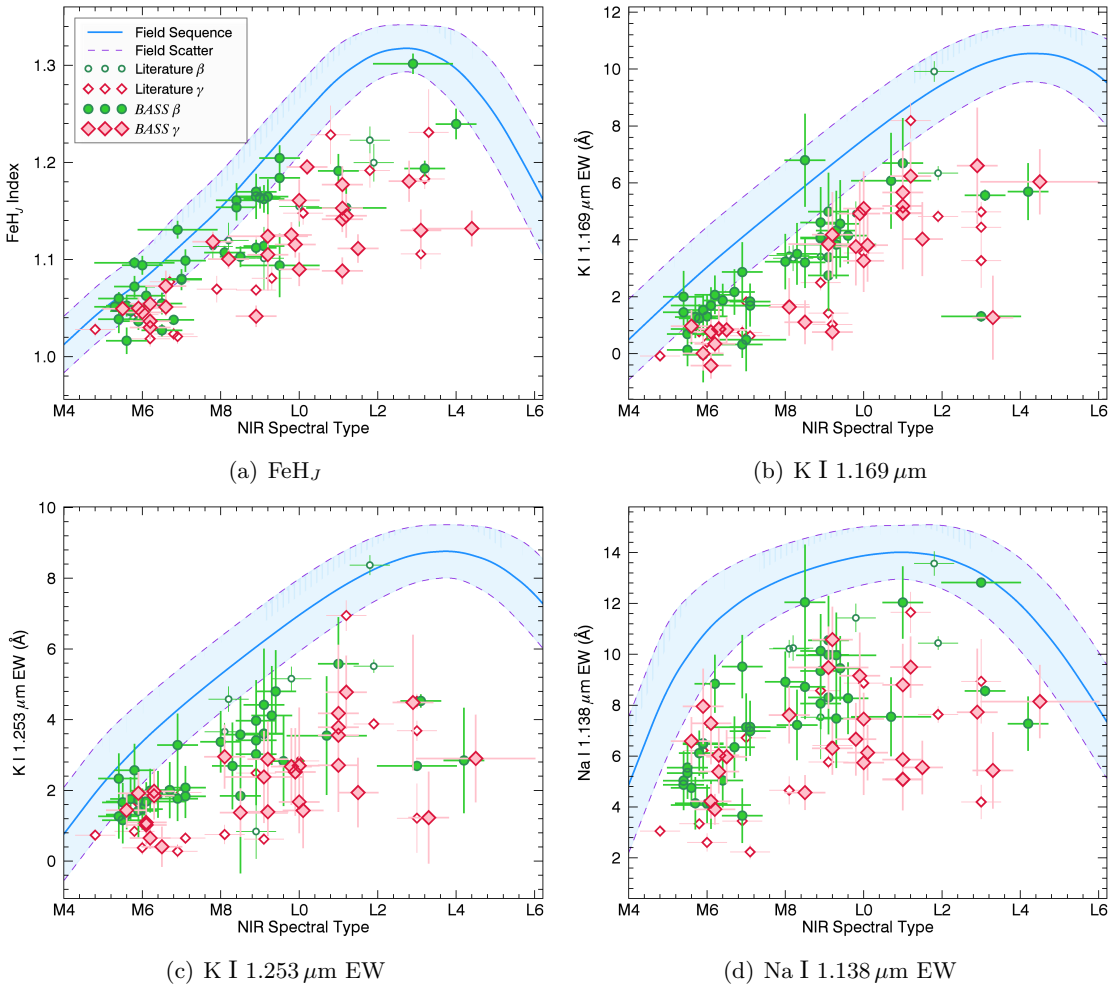

(a) FeH$_J$

(b) K I 1.169 μm

(c) K I 1.253 μm EW

(d) Na I 1.138 μm EW

FIGURE 6.6 Moderate-resolution (R $\gtrsim$ 750) gravity-sensitive NIR indices defined by Allers & Liu (2013) for all intermediate-gravity and very low-gravity dwarfs from the *BASS* sample. Symbols and color coding are identical to those of Figure 6.5. Lower-gravity dwarfs display weaker alkali and FeH absorption features, which results in lower Na I and K I EWs and a lower FeH$_J$ index.

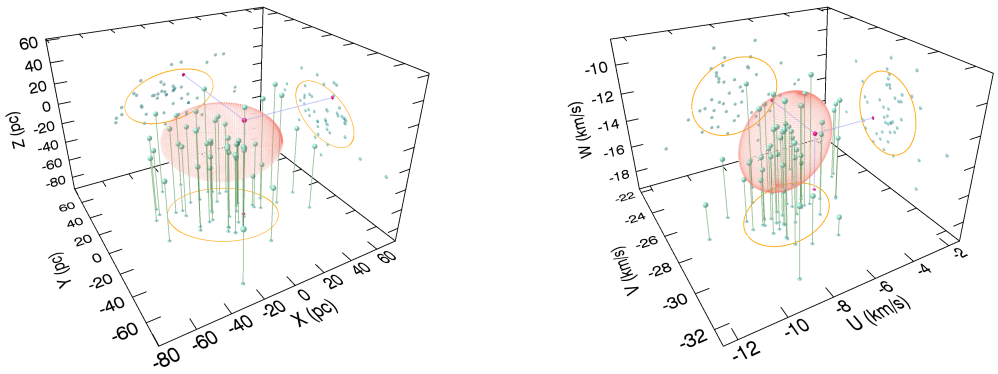

(a) Galactic position (b) Space velocity

FIGURE 6.7 Galactic position XYZ and space velocity UVW of the new AB Doradus bona fide member 2MASS J14252798–3650229 (red point and its projections), compared with other bona fide members of ABDMG (green points and their vertical projections on the XY and UV planes) and the SKM models of ABDMG (as defined in Chapter 2; orange ellipsoid and its projections).

luminous than ABDMG members, a factor that goes up to $\gtrsim$40 when instead compared with field dwarfs. We investigated whether any of our M0–M5 candidate members listed in Table 6.4 display X-ray emission by cross-matching their *2MASS* position with the ROSAT catalogs with a 15" search radius. We computed the absolute X-ray luminosity for all X-ray sources recovered this way, using trigonometric distances when possible or kinematic distances otherwise.

We have identified ROSAT entries for only three objects: 2MASS J08540240–3051366 (M4 candidate member of βPMG; $\log L_X = 28.4 \pm 0.3$) has a low X-ray luminosity compared with M3–M5 members of ABDMG or βPMG (both have $\log L_X \approx 28.5 - 29.5$) and could thus be a field interloper ($\log L_X \approx 27 - 28.5$; see Figures 7 and 8 of Malo et al. 2014a). 2MASS J08194309–7401232 (M4.5 candidate member of COL; $\log L_X = 29.3 \pm 0.4$) and 2MASS J21490499–6413039 (M4.5 candidate member of THA; $\log L_X = 29.3 \pm 0.3$) both have X-ray luminosities consistent with an age similar or younger than that of ABDMG, making them likely members of their respective moving groups. We note that 2MASS J21490499–6413039 has already been reported as a candidate member of THA by Kraus et al. 2014b, who measured its RV and found it to be consistent with other THA members. Objects that

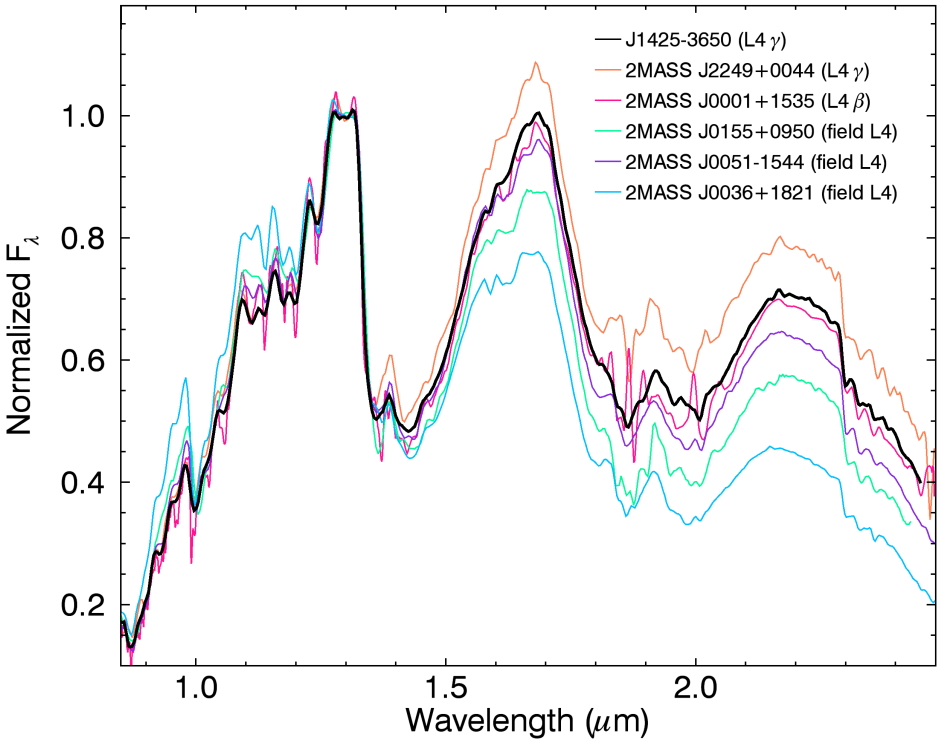

FIGURE 6.8 NIR spectrum of the new L4 γ ABDMG bona fide member 2MASS J14252798–3650229 (thick black line), compared with various field and low-gravity L4 BDs. All spectra were degraded to a resolution of $R \sim 120$ and normalized at their median value in the $\sim$1.27–1.33 μm range. The H-band continuum of 2MASS J14252798–3650229 has a typical triangular shape and its global slope is particularly red, which are both telltale signs of low gravity.

do not have a ROSAT counterpart do not necessarily have a low absolute X-ray luminosity, but might be too distant or located outside of the regions covered by the ROSAT survey.

Using the ROSAT bright catalog detection limit of 0.1 ct/s in the 0.1–2.4 keV energy band and assuming a hardness ratio $HR1 \approx 0$, we can only put an upper limit of $\log L_X = 28 - 29.8$ on the remaining targets, which is generally not sufficient to reject any more candidate members. Only 3/41 of these targets (2MASS J05484454–2942551, 2MASS J06494706–3823284 and 2MASS J07583098+1530146 AB) have $\log L_X < 28.5$, potentially making them less interesting candidate members. It should be noted however that one of these three objects (2MASS J06494706–3823284) has weak Na I absorption consistent with a very low surface gravity. This demonstrates how the absence from the ROSAT catalog is not a strong enough constraint to reject any of our M0–M5 candidate members. Kraus et al. (2014b) has demons-

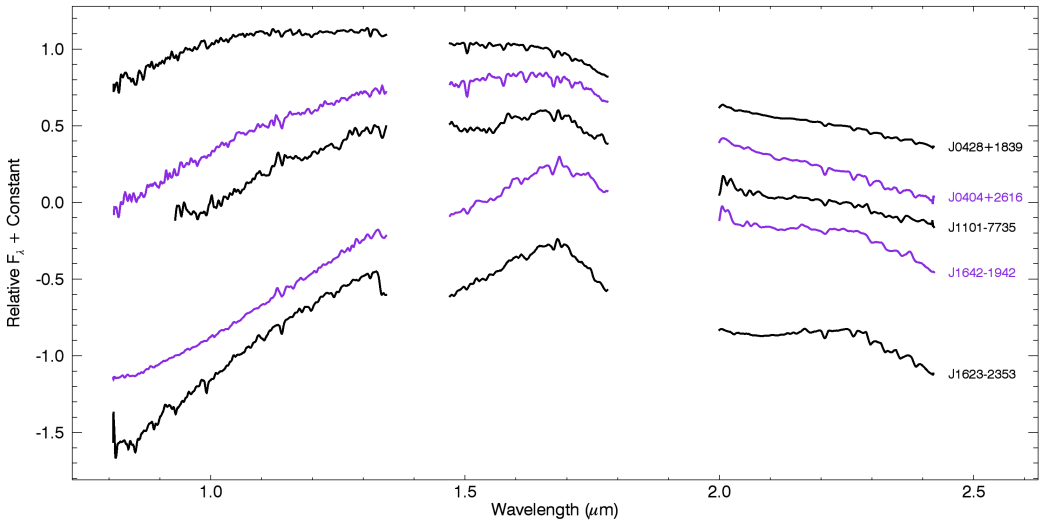

FIGURE 6.9 NIR spectra of typical contaminants in the *PRE-BASS* sample. Resolution was degraded in the same way as described in Figure 6.1. All spectra were normalized to their median across the full wavelength range and shifted vertically for comparison purposes. The contaminants presented in this figure likely correspond to background K- and M-type stars reddened by interstellar dust. We used alternating colors for visibility.

trated that surveys for M-type moving group members based on either X-ray or UV-bright samples are incomplete because of the sky coverage and detection limits of current X-ray and UV catalogs.

6.6.3 Sources of contamination

In Chapter 2, we demonstrated that a fraction of candidate members identified by the BANYAN II tool are expected to be field interlopers, especially if no prior knowledge is available on age. This fraction of contaminants is dependent on the YMG considered: ARG, ABDMG and βPMG are expected to be the most contaminated, mostly due to their proximity and their overlap with the galactic plane. Counting the fraction of low-gravity dwarfs in the spectroscopic follow-up presented here allows us to estimate minimal contamination rates of 18% and 33% in the *BASS* and *LP-BASS* samples, respectively. These values are slightly larger than the estimates that we derived in Chapter 3 (12.6% for *BASS* and 26% for *LP-BASS*). The most likely explanation is that the kinematic distribution of field BDs is not perfectly reproduced by the Besançon galactic model, on which our previous estimates were based.

The reason why these updated estimates correspond to a minimal contamination fraction is that some low-gravity dwarfs in our candidate sample could still be contaminants from associations not considered in BANYAN II, e.g., the Ursa Majoris moving group (UMA; $\sim$300 Myr; Zuckerman & Song 2004), the Hercules-Lyrae moving group (250 Myr; Eisenbeiss et al. 2013), the ϵ Chamaeleontis association (also called Cha-Near; $\sim$10 Myr; Zuckerman & Song 2004), the Octans association (30–40 Myr; Torres et al. 2008; Murphy & Lawson 2015) and the Carina-Near moving group (200 Myr; Zuckerman et al. 2006). Measurements of RV and trigonometric distance will be helpful to identify such contaminants. Besides field-gravity $\geq$M5 dwarfs, we identified other kinds of contaminants in our sample of candidates, based on our new NIR spectroscopy. We uncovered a number of objects with spectral types earlier than M5 (4 in *BASS*, 4 in *LP-BASS* and 28 in *PRE-BASS*), for which there is no known reliable low-gravity indicators in the NIR. In addition to those, we uncovered 27 contaminants mostly in the *PRE-BASS* sample (only one was found in *BASS*) that correspond to K- and M-type low-mass stars reddened by interstellar dust in the line of sight (Figure 6.9). A number of these are likely located in star-forming regions, such as ρ Ophiucus (ρOPH), the Scorpius-Centaurus Complex (SCC) and Taurus-Aurigae (TAU; Elias 1978). These objects were all rejected from the *BASS* sample, mainly because (1) we avoided star-forming regions in the final survey; and (2) the extragalactic WISE color filter defined by Kirkpatrick et al. (2011) and the *2MASS* crowding filter defined in Chapter 3 efficiently rejected them.

6.7 Discussion

6.7.1 Updated color-magnitude sequences for young low-mass stars and brown dwarfs

We complemented the list of all spectroscopically confirmed $\geq$ L0 dwarfs as of February 2014 (Mace 2014) and the DwarfArchives online library[7] with more recent discoveries, measurements of photometry in the literature and additional NIR photometry from a cross-match with *2MASS* and *WISE*, in order to build an up-to-date sequence of field dwarfs. This list

[7] *http://dwarfarchives.org*

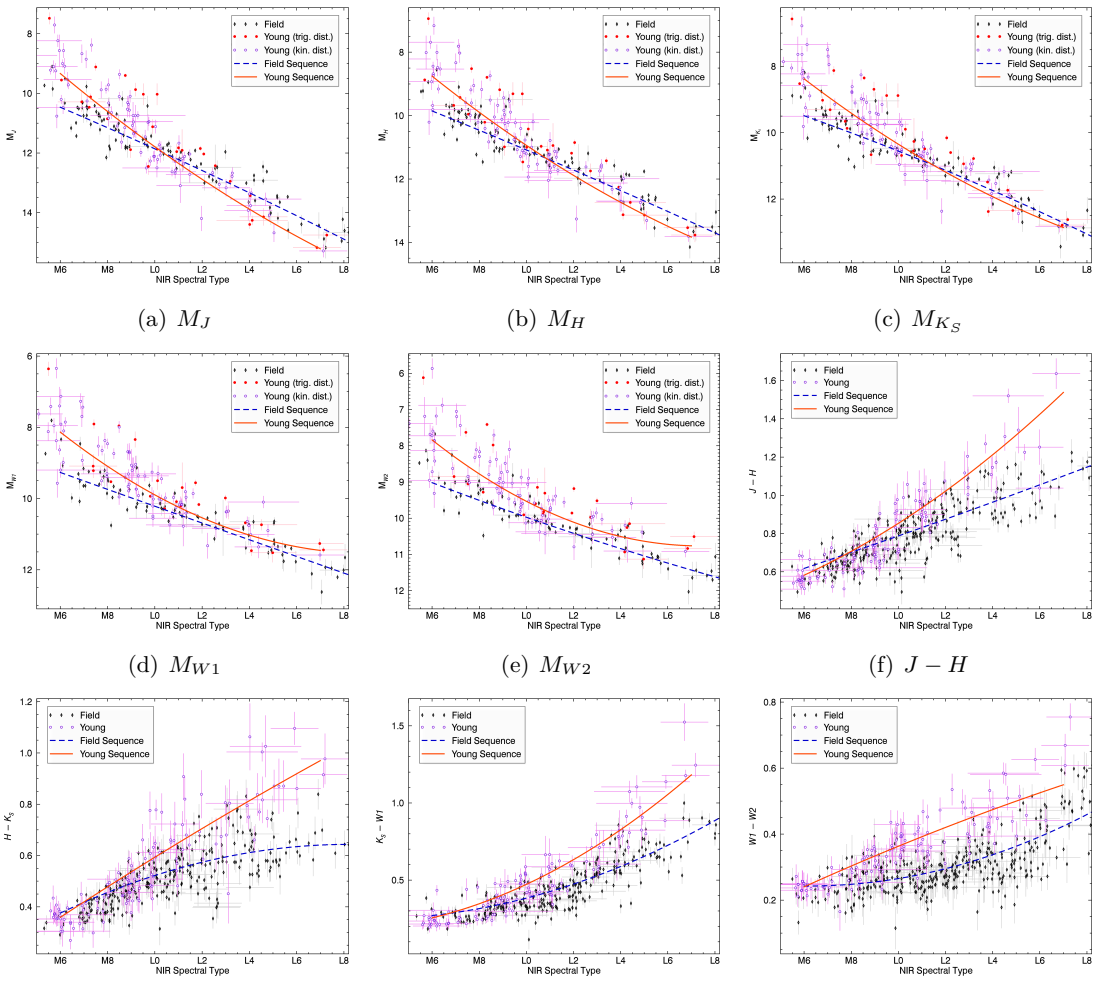

(a) M_J (b) M_H (c) M_{K_S}

(d) M_{W1} (e) M_{W2} (f) $J-H$

(g) $H-K_S$ (h) K_S-W1 (i) $W1-W2$

FIGURE 6.10 Absolute magnitude–NIR spectral type and color–NIR spectral type sequences for field (black diamonds) and young dwarfs (red dots when trigonometric distances were used, or purple circles when kinematic distances were used), as well as polynomial sequences (blue and orange lines, respectively) defined in Table 6.7. We used the kinematic distances obtained from the BANYAN II tool (without photometry as input) to include low-gravity candidate members of YMGs that do not have a trigonometric distance measurement. Young dwarfs are generally brighter because of their inflated radii; however, thicker/higher dust clouds compete with this effect at spectral types L0–L7. Low-gravity L dwarfs are systematically redder than their field counterparts because of thicker/higher dust clouds in their photosphere.

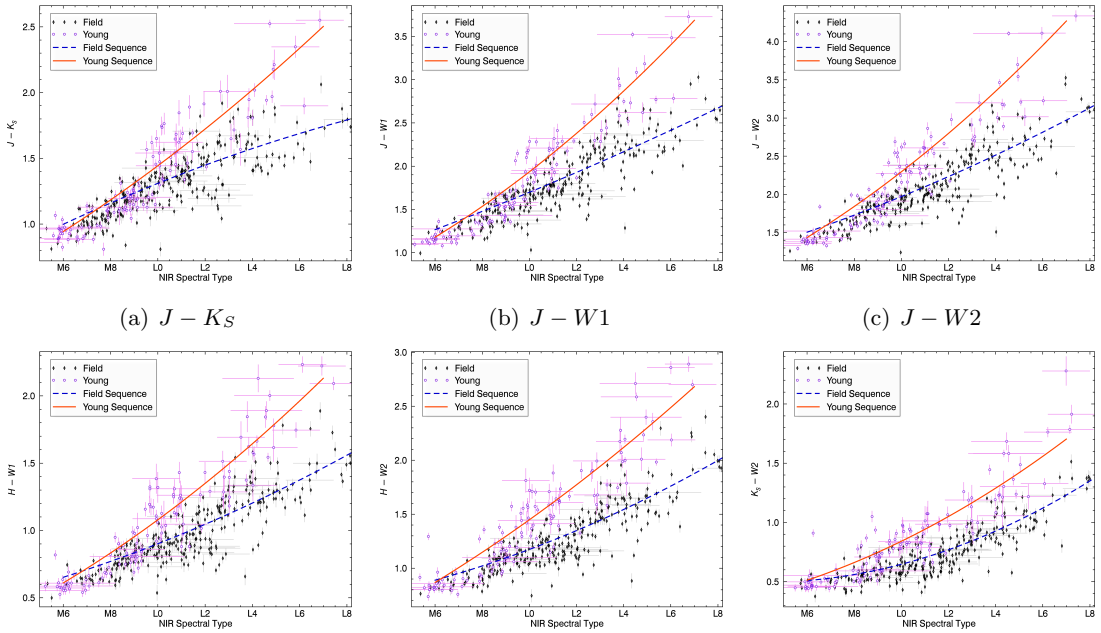

(a) $J - K_S$ (b) $J - W1$ (c) $J - W2$

(d) $H - W1$ (e) $H - W2$ (f) $K_S - W2$

FIGURE 6.11 Additional color–NIR spectral type sequences for young and field dwarfs as well as polynomial sequences defined in Table 6.7. The color scheme is identical to that of Figure 6.10 except that all young dwarfs are displayed with purple circles.

currently contains >1800 published $\geq$ L0 low-mass stars and BDs[8]. We compiled a similar list of >8700 M6–M9 low-mass stars and BDs[9]. These two lists of dwarfs contain photometric data from articles referenced throughout the present work[10]. In Figures 6.10 and 6.11, we compare our updated population of known young low-mass stars and BDs to the field sequence in various spectral type-color and spectral type-absolute magnitude diagrams. We used data from the two aforementioned lists to build the photometric sequences. In the case of YMG candidate members that do not have a trigonometric distance measurement, we used the statistical distance from BANYAN II, associated with the most probable YMG hypothesis. In

[8]Publicly available at *www.astro.umontreal.ca/~gagne/listLTYs.php*

[9]Publicly available at *www.astro.umontreal.ca/~gagne/listMs.php*

[10]In addition to the following references: Andrei et al. (2011); Artigau et al. (2010); Beichman et al. (2014); Burgasser et al. (2006); Burningham et al. (2008, 2013); Castro et al. (2013); Costa et al. (2005, 2006); Cushing et al. (2011); Deacon et al. (2014); Delorme et al. (2008a,b); Dieterich et al. (2014); Faherty et al. (2013b); Hawley et al. (2002); Kendall et al. (2007b,a); Kirkpatrick et al. (2012); Leggett et al. (2000, 2002, 2009, 2010, 2013, 2015); Lodieu et al. (2005, 2007); Looper et al. (2007b,a); Lucas et al. (2010); Mace et al. (2013b,a); Marocco et al. (2010); Marsh et al. (2013); Monet et al. (1992); Pérez-Garrido et al. (2014); Phan Bao et al. (2008); Pinfield et al. (2008); Strauss et al. (1999); Thompson et al. (2013); Tinney et al. (2003, 2014); van Leeuwen (2007b); Warren et al. (2007); Wilson et al. (2003); Zapatero Osorio et al. (2014); and van Altena et al. (1995)

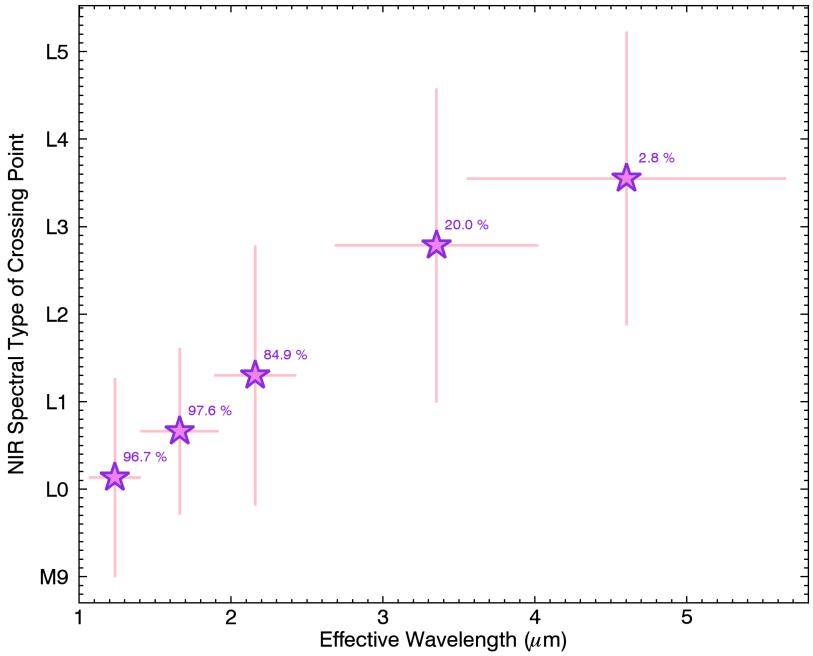

FIGURE 6.12 Spectral type at which the young and field absolute magnitude polynomial sequences cross (see Figure 6.10), as a function of the effective wavelength in which each sequence is defined. Young dwarfs are systematically brighter than their field counterparts because of their inflated radii; however, dust clouds are thicker in the high atmosphere of young L dwarfs, which counter-balances this effect and causes the young sequence to cross the field sequence. The fraction of Monte Carlo steps where the sequences crossed is indicated next to a given data point; see text for more detail. Dust clouds are more opaque in the J band ($\sim 1.2\,\mu$m), hence the crossing point for this sequence happens at earlier spectral types. At longer wavelengths ($\sim 4.5\,\mu$m), dust clouds do not have as much effect. This causes the sequences to cross less often and when they do, they cross at later spectral types.

each case, we calculated the error-weighted median sequence in bins of 1 subtype and adjusted a polynomial relation by minimizing the χ^2 value. We list in Table 6.7 the coefficients of these polynomial fits as well as the respective standard deviation of the data with respect to the best fit. We note that our field sequences are slightly redder than those derived from samples based on the Sloan Digital Sky Survey (*SDSS*; York et al. 2000) such as those presented by West et al. (2008) and Schmidt et al. (2015). This is true because *SDSS*-based surveys rely directly on spectra and are thus un-biased, whereas other surveys based on *2MASS* and/or *WISE* (e.g., Cruz et al. 2003; Reid et al. 2008a; Kirkpatrick et al. 2011) perform a spectroscopic follow-up only on targets that were pre-selected from color cuts, which makes them

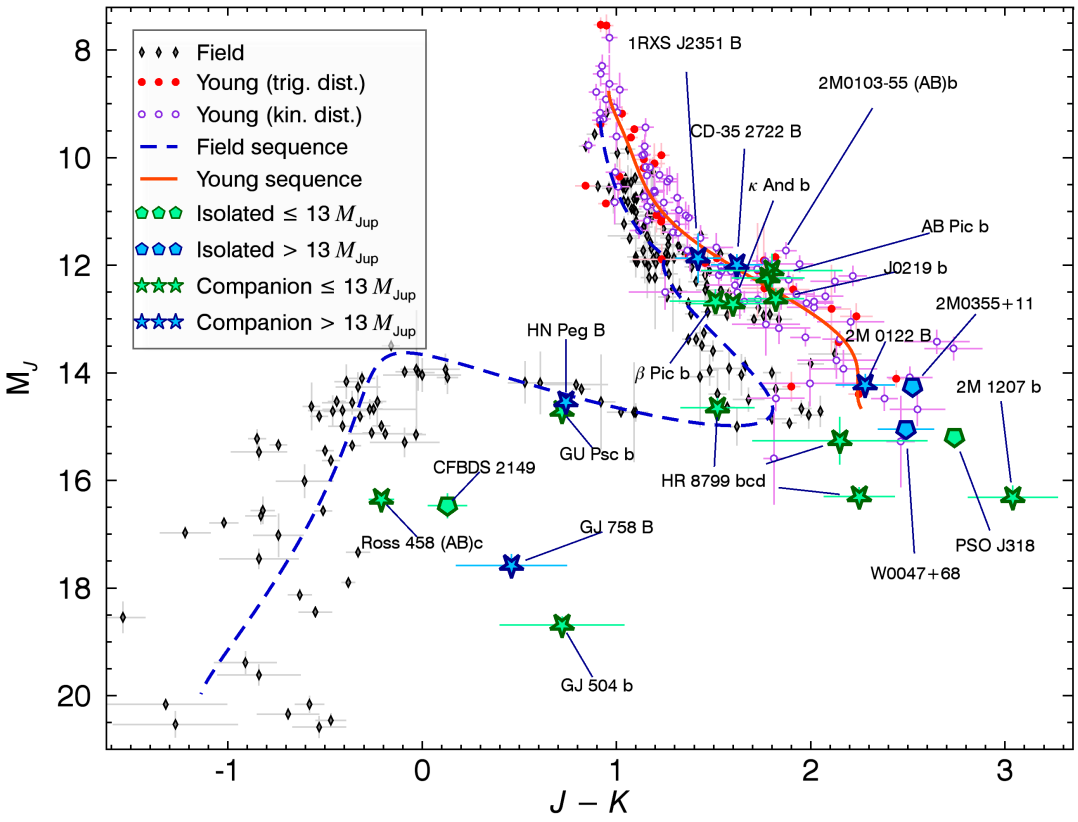

FIGURE 6.13 NIR CMD for young (red dots when trigonometric distances were used, or purple circles when kinematic distances were used) and field (black diamonds) low-mass stars and BDs. The young and field sequences are displayed with the dashed blue line and the solid orange-red line, respectively (see text for more detail). The young sequence is systematically shifted compared to field dwarfs because of the combined effect of larger radii and thicker/-higher clouds. Blue stars indicate the positions of known low-mass BDs and directly imaged exoplanets (Thalmann et al. 2009; Janson et al. 2011; Delorme et al. 2013; Kuzuhara et al. 2013; Skemer et al. 2012; Biller et al. 2013; Bonnefoy et al. 2014b; Males et al. 2014; Bowler et al. 2013; Luhman et al. 2009; Carson et al. 2013; Chauvin et al. 2005; Marocco et al. 2014; Naud et al. 2014; Marois et al. 2008; Chauvin et al. 2004; Goldman et al. 2010; Lagrange et al. 2010; Delorme et al. 2012; Goto et al. 2002; Luhman et al. 2007; Bowler et al. 2014; Wahhaj et al. 2011; Currie et al. 2014; Kraus et al. 2014a; Artigau et al. 2015; and references therein).

biased towards detecting red objects more easily. Since *2MASS*- and *WISE*-based surveys dominating the population of L dwarfs identified in the literature, our field sequences are consequently redder than those based on *SDSS* samples. This effect is also demonstrated in Figure 3 of Schmidt et al. (2010).

The radii of young low-mass stars and BDs are inflated compared with old objects of the same spectral type. For this reason, it could be expected that young absolute magnitude sequences fall above the field sequences across all spectral types. However, starting at spectral type $\sim$L0, dust clouds form in the photosphere of BDs. Young BDs have a lower atmospheric pressure, which allows the formation of thick clouds higher in their atmosphere (Kirkpatrick et al. 2006; Looper et al. 2008b). As a result, a fraction of the NIR light at $\sim$0.5–3 μm gets redirected to longer wavelengths, causing young BDs to display similar absolute J magnitudes to those of field BDs around spectral type $\sim$L0, as well as absolute J magnitudes even fainter than those of field dwarfs at later spectral types (Faherty et al. 2012, 2013b; Liu et al. 2013a; Zapatero Osorio et al. 2014). We could expect that this effect will eventually cease around spectral type T, where dust clouds fall below the photosphere. This has yet to be demonstrated, because there is only a very small number of young T dwarfs currently known (e.g., Delorme et al. 2012; Naud et al. 2014). In Figure 6.12, we show the spectral type at which the young and field sequences cross as a function of spectral band. Horizontal error bars represent the effective width of the photometric filters and vertical error bars are drawn from a 10 000-step Monte Carlo simulation, introducing noise in the data that is representative of photometric uncertainties and repeating the polynomial fit every time. Cases where the sequences do not cross are not included in the calculation of the median and standard deviation of the crossing points. We note that the fraction of Monte Carlo steps where the sequences cross significantly decreases at increasing wavelengths. This is explained by the fact that the photometric sequences become gradually disjointed in the spectral range considered; it is thus possible that in reality the sequences generally cross at spectral types $\geq$L7 (or not at all) in the $W1$ and $W2$ bands. This figure shows a clear correlation which indicates that flux is redistributed out to longer wavelengths in low-gravity dwarfs, a likely effect of the dust clouds (J. K. Faherty et al., in preparation). This is a known effect which

is in part due to the larger opacity from the H_2O, CO and H_2 molecules at wavelengths larger than $\sim 1\,\mu$m that are masking the effects of clouds (Ackerman & Marley 2001). The BT-Settl isochrones (Allard et al. 2013; Baraffe et al. 2003) do not reproduce this effect, as the young (≤ 100 Myr) and old (≥ 1 Gyr) isochrones do not cross in neither of the J, H or K_S bands over the range of effective temperatures that correspond to the M and L spectral types ($\sim$1300–3000 K; Stephens et al. 2009).

In Figure 6.13, we show a M_J versus $J-K$ CMD in the Mauna Kea Observatories NIR filter system (MKO; Simons & Tokunaga 2002) for low-gravity and field dwarfs. When MKO photometry was not available, we used *2MASS* photometry with the conversion relations of Stephens & Leggett (2004; L and T dwarfs) and Leggett et al. (2006; M dwarfs). The combined effects of redder colors due to thicker/higher clouds (Marley et al. 2002) and brighter absolute J magnitude due to inflated radii cause a systematic shift of the low-gravity sequence to the right compared to the field sequence. This Figure brings into evidence the fact that the currently known population of young BDs does not reach a color reversal similar to the L/T transition of field dwarfs (at $J-K \sim 1.8$ and $M_J \sim 14.5$), corresponding to the temperature at which dust clouds fall below the photosphere (Barman et al. 2011a; Dupuy & Liu 2012; Faherty et al. 2012, 2013b; Bonnefoy et al. 2013; Liu et al. 2013a; Zapatero Osorio et al. 2014; Males et al. 2014). We chose this parameter space because a significant amount of data is available in these filters and it is very efficient in displaying this color reversal. It can be expected that a color reversal would eventually be reached for young dwarfs around the T spectral type, corresponding to cooler temperatures than the currently known population. The coolest known directly imaged young exoplanets and low-mass BDs (blue stars in Figure 6.13) tentatively hint at such a color reversal.

Since $J-K$ and M_J are generally correlated for a given spectral type, the $(J-K)$–spectral type and M_J–spectral type relations listed in Table 6.7 are not the best representation for the low-gravity and field sequences in this CMD diagram. In the case of the young sequence, the absence of a color reversal allowed us to simply fit a polynomial sequence to the young dwarfs directly in the M_J–$(J-K)$ space; however, the field sequence cannot be represented by a simple polynomial relation across the M6–T9 range. We used a Markov Chain Monte

Carlo algorithm to construct a parametrized polynomial sequence that fits the field sequence across its complete spectral range. We started from a parametrized equation obtained from the combination of the $J-K$ and M_J polynomial relations described in Table 6.7, and allowed the eight coefficients of each dimension to vary such that the sequence minimizes the quadrature sum of the bi-dimensional distance of all individual field dwarf positions in the CMD diagram relative to their error bars. This results in a parametrized sequence that describes $J-K$ and M_J as a function of the parametric variable λ. Larger values of λ correspond to later spectral types on average, but no relation between λ and spectral types can be provided as the field sequence is a parametric equation that does not assign a λ value to individual data points. We obtain:

$$\begin{aligned}(M_J)_{\rm Young} = & \ 1.61\times10^{3} - 8.92\times10^{2}\ (J-K) \\ & +2.04\times10^{2}\ (J-K)^2 - 2.46\times10^{1}\ (J-K)^3 \\ & +1.65\ (J-K)^4 - 5.87\times10^{-2}\ (J-K)^5 \\ & +8.59\times10^{-4}\ (J-K)^6 \end{aligned} \tag{6.1}$$

$$\begin{aligned}(J-K)_{\rm Field} = & \ 1.98\times10^{1} - 1.55\times10^{1}\ \lambda \\ & +5.09\ \lambda^2 - 8.76\times10^{-1}\ \lambda^3 \\ & +8.68\times10^{-2}\ \lambda^4 - 5.12\times10^{-3}\ \lambda^5 \\ & +1.76\times10^{-4}\ \lambda^6 - 3.27\times10^{-6}\ \lambda^7 \\ & +2.53\times10^{-8}\ \lambda^8 \end{aligned} \tag{6.2}$$

$$
\begin{aligned}
(M_J)_{\rm Field} = & -5.61 \times 10^1 + 3.73 \times 10^1 \ \lambda \\
& -8.45 \ \lambda^2 + 1.04 \ \lambda^3 \\
& -7.64 \times 10^{-2} \ \lambda^4 + 3.56 \times 10^{-3} \ \lambda^5 \\
& -1.06 \times 10^{-4} \ \lambda^6 + 1.84 \times 10^{-6} \ \lambda^7 \\
& -1.43 \times 10^{-8} \ \lambda^8
\end{aligned} \tag{6.3}
$$

where the young sequence is valid in the range $8.8 \leq M_J \leq 14.7$ and the field sequence is valid in the range $4.5 \leq \lambda \leq 28.5$ (i.e., $J \geq -1.1$ and $9.3 \leq M_J \leq 19.9$).

We note that the NIR colors of young BDs discovered in the BASS and LP-BASS surveys are likely affected by a form of the confirmation bias, in the sense that we specifically looked for red objects in our survey (see Chapter 3). Hence, this new photometric data should not be taken as additional evidence that young BDs are redder than field BDs. Reinforcing this result would require looking for signs of low gravity in a sample of BDs that were selected independently of their photometric colors. Directly imaged young planets and brown dwarf companions do not suffer from this potential bias however, and their colors seem consistent with those of isolated young BDs Chauvin et al. 2004, 2005; Barman et al. 2011a; Bonnefoy et al. 2013; Delorme et al. 2013; Bowler et al. 2013; Currie et al. 2014. This might be an indication that our confirmation bias is not significant.

6.7.2 An updated investigation on the age dependence of spectroscopic indices

Since they are the only BDs with a well calibrated age, members of YMGs provide the exciting opportunity of creating a spectroscopic age calibration applicable to all young BDs. Using Pleiades members and the fact that known low-gravity BDs were located away from star-forming regions, Kirkpatrick et al. (2008) and Cruz et al. (2009) estimated that the very low-gravity (γ) and intermediate gravity (β) classifications likely correspond to $\sim$10 Myr and $\sim$100 Myr, respectively. Allers & Liu (2013) extended this investigation by using a restrained sample of 25 M6–L5 dwarf members of young associations. They found that very

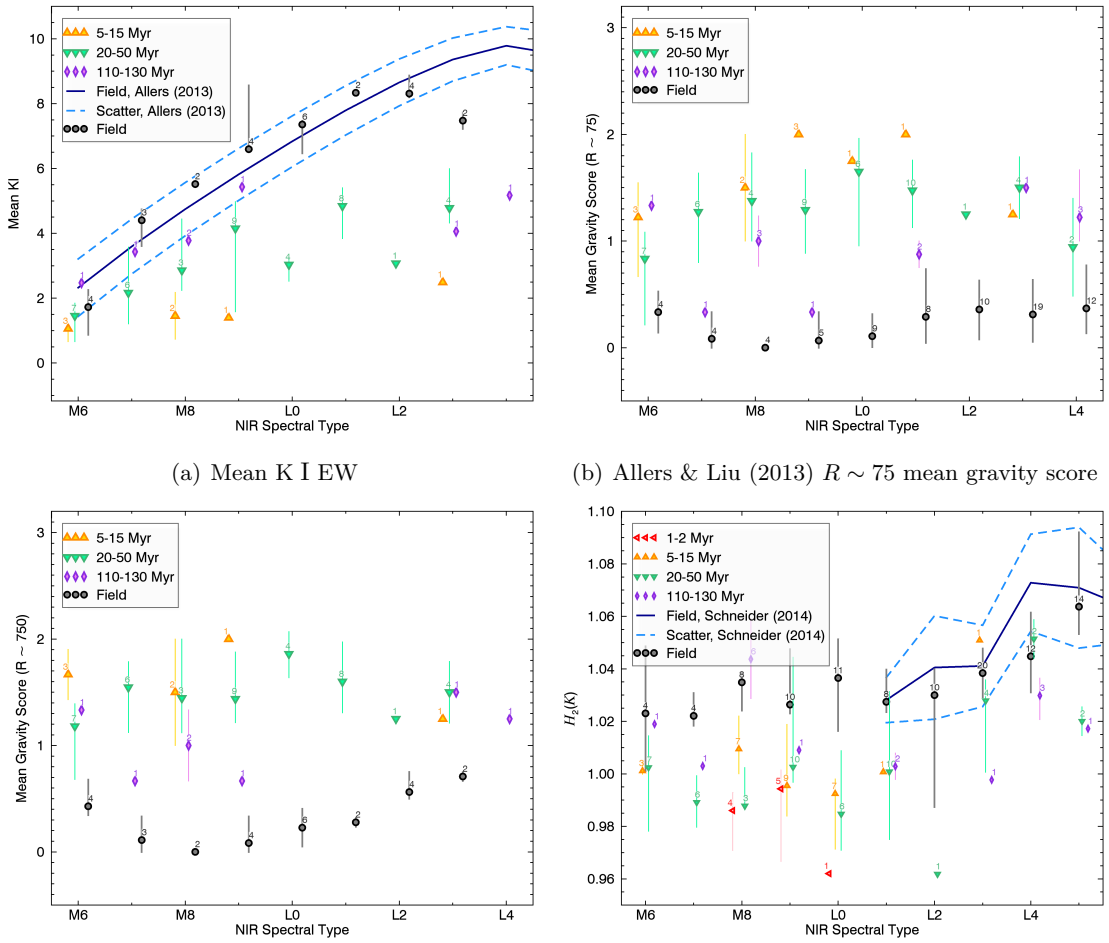

(a) Mean K I EW

(b) Allers & Liu (2013) $R \sim 75$ mean gravity score

(c) Allers & Liu (2013) $R \sim 750$ mean gravity score

(d) Canty et al. (2013) $H_2(K)$

FIGURE 6.14 Spectroscopic indices versus NIR spectral type for YMG candidates of distinct ages in our sample, binned by spectral type (see legends for color coding). We find that the mean EW of J-band K I and the mean gravity score defined by Allers & Liu (2013) seems to correlate with age. However, we do not see a clear correlation in the case of the $H_2(K)$ index in the 1–130 Myr range.

low-gravity (γ) and intermediate-gravity (β) dwarfs likely correspond to ages of $\sim$10–30 Myr and $\lesssim$200 Myr; however, they note that BDs with ages older than $\sim$30 Myr, such as the $\sim$120 Myr ABDMG member 2MASS J03552337+1133437, can display very strong signs of low-gravity that correspond to the very low gravity (γ) classification.

We used our updated sample of low-gravity candidate members of YMGs to investigate this further. We inspected various spectroscopic index–spectral type relations of candidate members of different YMGs to identify any systematic correlation with age. We assigned the age of the most probable YMG to our candidates, while rejecting any candidate with ambiguous membership (Table 6.4). We found that the strongest correlations with age in the $\sim$10–130 Myr range resulted from: (1) the mean value of the EW of the three K I doublets at 1.169 μm, 1.177 μm and 1.253 μm; and (2) the mean gravity score defined by Allers & Liu (2013). The resulting sequences are presented in Figure 6.14. Even though they do correlate with age on average, the scatter is too large to allow a precise determination of the age of an individual system from spectroscopic indices alone. We find that the $H_2(K)$ index defined by Canty et al. (2013) does not seem to correlate significantly with age in the 1–130 Myr range. Our results seem to be in contradiction with the findings of Canty et al. (2013) that the $H_2(K)$ index is sufficient to differentiate between objects from populations of $\sim$1–2 Myr, $\sim$3–10 Myr and field dwarfs in the M8–L0 range: we observe an overlap of the typical values for $H_2(K)$ in populations of $\sim$1–2 Myr and $\sim$5–15 Myr. However, our results are consistent with $H_2(K)$ being a good gravity-sensitive index, as it discriminates between the field population and $\lesssim$100 Myr dwarfs for spectral types in the M6–L1 range, or $\lesssim$130 Myr for L2–L6. It is possible that interlopers from other young associations not considered in BANYAN II contaminate our sample, which would introduce noise in these relations. A full RV and parallax follow-up of the candidates presented here will be needed to assess this.

6.7.3 Model comparison

We used our sample of 86 new low-gravity M6–L5 dwarfs supplemented with 39 low-gravity and 131 field M6–L9 dwarfs from Allers & Liu (2013) and the SpeX Prism Spectral Libraries to investigate the physical properties of our sample of young dwarfs, using BT-Settl

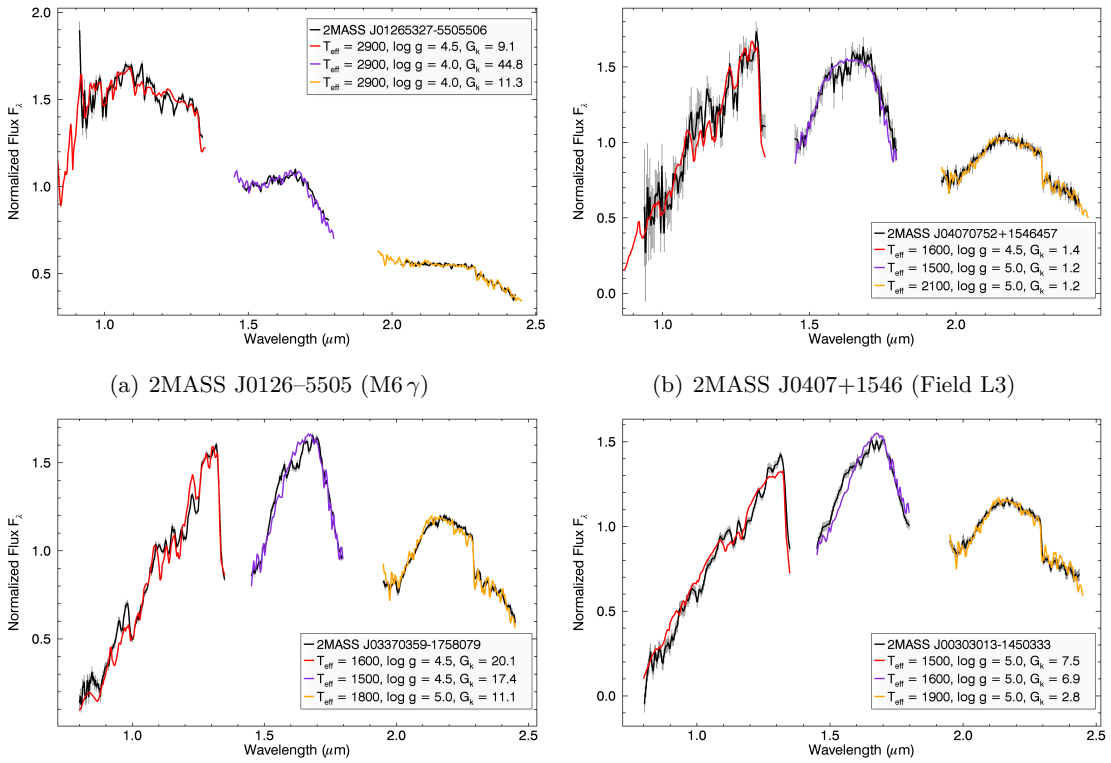

(a) 2MASS J0126–5505 (M6 γ)

(b) 2MASS J0407+1546 (Field L3)

(c) 2MASS J0337–1758 (Field L4)

(d) 2MASS J0030–1450 (L4–L6 β)

FIGURE 6.15 Best-fitting BT-Settl atmosphere models for typical field and low-gravity BDs (thick, black line and gray error bars). The zJ (red line), H (purple line) and K (yellow line) dilution factors were adjusted separately so that the goodness-of-fit is optimized (see text). We observe that BT-Settl models are generally unable to reproduce the zJ bands or the H-band dip at $\sim 1.6\,\mu$m that is due to FeH absorption.

atmosphere models (Allard et al. 2013; Baraffe et al. 2003). In Section 6.7.3.1, we focus on effective temperatures and surface gravities obtained from a comparison of our NIR spectra with atmosphere models. In Section 6.7.3.2, we focus on the mass and radii that are obtained from a comparison of our photometry with evolution models.

6.7.3.1 BT-Settl atmosphere models

Manjavacas et al. (2014) used BT-Settl atmosphere models to determine the physical parameters of seven young L dwarfs and found that (1) low-gravity L0–L3 dwarfs fit models with similar temperatures of $\sim 1800\,$K; (2) the continuum shape of the H band is not well reproduced by solar-metallicity models; (3) the 1.1–2.5 μm range in the zJ bands is not well re-

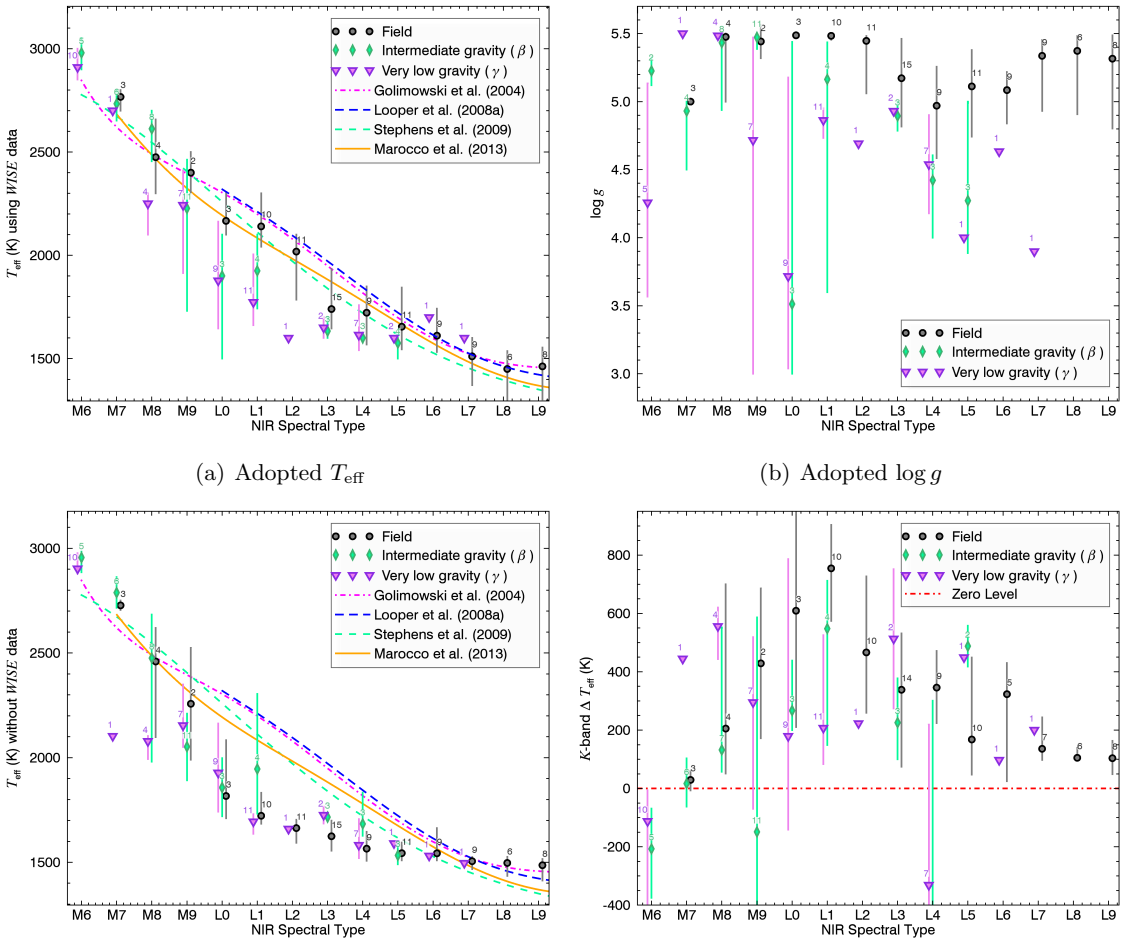

(a) Adopted $T_{\rm eff}$

(b) Adopted $\log g$

(c) JH-band $T_{\rm eff}$

(d) K-band $T_{\rm eff}$ bias

FIGURE 6.16 Panel a: Adopted effective temperature ($T_{\rm eff}$) derived by simultaneously fitting atmosphere models to full JHK spectra and *WISE* photometry as a function of spectral type for our sample of field and low-gravity dwarfs, binned by spectral type. The number of data points that were included in each bin is displayed above each symbol. Field dwarfs are represented with black circles, intermediate gravity dwarfs (β) with green diamonds and very low-gravity dwarfs (γ) with purple downside triangles. We added small systematic offsets in the spectral types of very low-gravity and field dwarfs for visibility. The solid orange line, green dashed line and fuchsia dash-dotted lines represent $T_{\rm eff}$–spectral type relations from Marocco et al. (2013); Golimowski et al. (2004); Looper et al. (2008a) and Stephens et al. (2009), respectively. Panel b: Adopted surface gravity ($\log g$) as a function of spectral type for our sample of field and low-gravity dwarfs, binned by spectral type. The color coding is similar to that of Panel a. Panel c: Effective temperature, derived by fitting atmosphere models to individual zJ- and H-bands only without *WISE* photometry, as a function of spectral type for our sample of field and low-gravity dwarfs, binned by spectral type. Color-coding is identical to Panel a. Panel d: Difference in the derived effective temperature from the K-band model fitting from that obtained by individual zJ- and H-bands model fitting (all without using *WISE* photometry), binned by spectral type. Color-coding is identical to Panel a and the red dot-dashed lines marks $\Delta T_{\rm eff} = 0$.

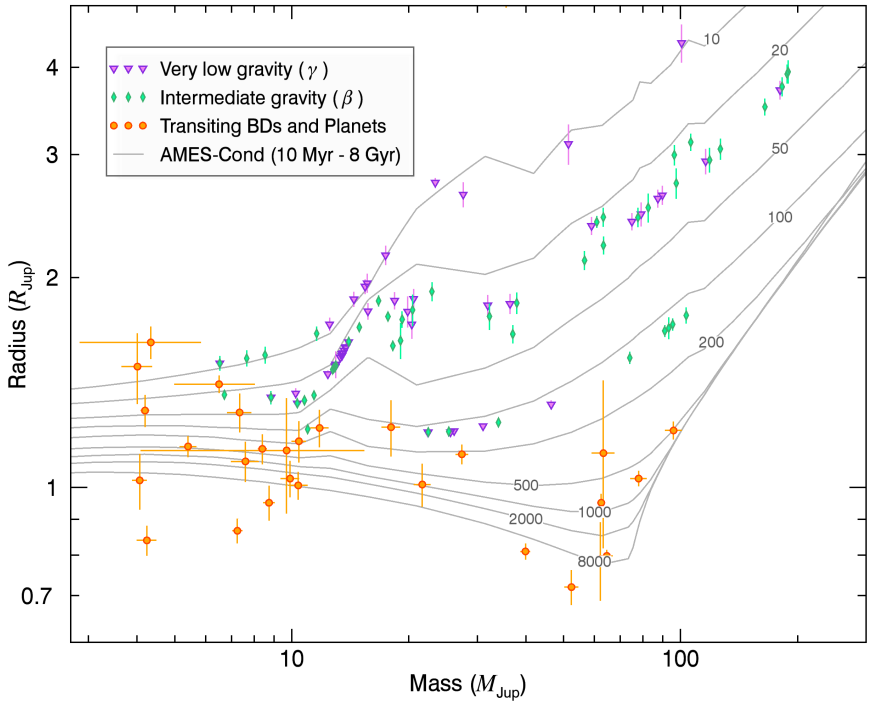

(a) Mass versus Radius

FIGURE 6.17 Radius as a function of mass for intermediate-gravity (green diamonds) and very low-gravity (purple downside triangles) candidate members of YMGs, derived from the BT-Settl models, compared with exoplanets and BD companions that benefit from transit and RV data (orange circles). Isochrones of various ages (gray lines; 10 Myr to 8 Gyr) were added for comparison. Transit and RV data were obtained from Stassun et al. (2006); Sahu et al. (2006); Deleuil et al. (2008); Winn et al. (2008); Buchhave et al. (2010); Southworth (2010); Bouchy et al. (2011b); Tingley et al. (2011); Bouchy et al. (2011a); Bakos et al. (2011); Buchhave et al. (2011); Deleuil et al. (2012); Siverd et al. (2012); Cappetta et al. (2012); Triaud et al. (2013); Díaz et al. (2013); Hébrard et al. (2013); Moutou et al. (2013); Blecic et al. (2013); Parviainen et al. (2014); Díaz et al. (2014); Shporer et al. (2014); Littlefair et al. (2014); Montet et al. (2014); and Quinn et al. (2014).

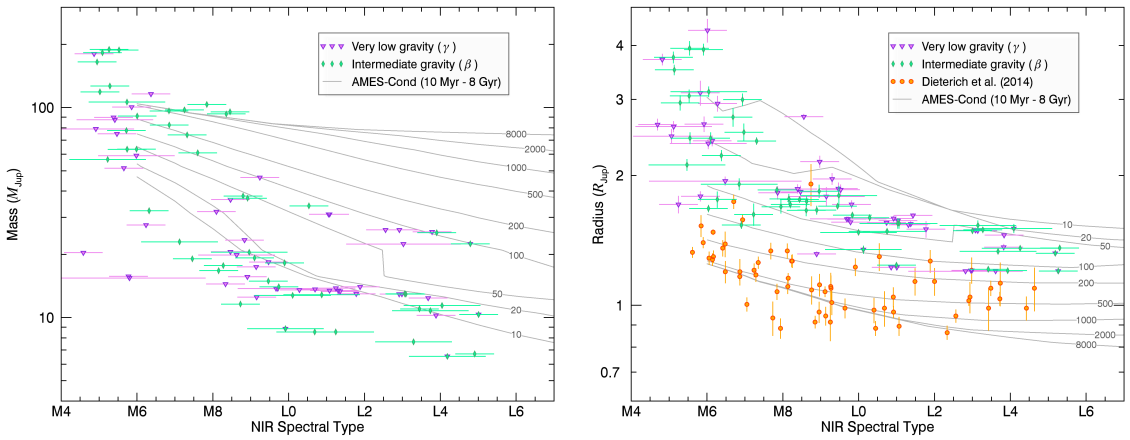

(a) Mass versus NIR Spectral Type

(b) Radius versus NIR Spectral Type

FIGURE 6.18 Panel a: Mass as a function of spectral type for intermediate-gravity (green diamonds) and very low-gravity (purple downside triangles) candidate members of YMGs, compared with BT-Settl isochrones (gray lines; 10 Myr to 8 Gyr) from which the masses were derived. The isochrones were mapped on the spectral type dimension by converting effective temperatures to spectral types using the polynomial relation of Stephens et al. (2009). Panel b: Radius as a function of spectral type for intermediate-gravity (green diamonds) and very low-gravity (purple downside triangles) candidate members of YMGs, compared with radii measurements from Dieterich et al. (2014; orange circles). BT-Settl isochrones of various ages (gray lines; 10 Myr to 8 Gyr), which were used to derive our radii, were added for comparison. They were mapped on the spectral type dimension by converting effective temperatures to spectral types using the polynomial relation of Stephens et al. (2009).

produced by models; and (4) the global continuum slope is not well reproduced by atmosphere models for L dwarfs.

We used a method similar to that of Cushing et al. (2008) and Naud et al. (2014) to identify the best fitting solar-metallicity CIFIST2011 BT-Settl atmosphere model for our observed spectra, on a grid of effective temperature and surface gravity ranging from $T_{\rm eff}$ = 500–5000 K and $\log g$ = 3.0–5.5 dex with a grid spacing of 100 K and 0.5 dex, respectively. We computed the goodness-of-fit ($G_{k,j}$; Cushing et al. 2008) in each case.

Cushing et al. (2008) demonstrated that $T_{\rm eff}$ can only be recovered efficiently by performing such a model fitting on a very large spectral range in the case of field L1–L8 dwarfs; however, while fitting a single model spectrum in this way allows recovering a good $T_{\rm eff}$ estimate, it does not reproduce well the general slope and the features in individual spectral bands. Since gravity-sensitive spectral features are generally narrow, this method will not yield good estimates of $\log g$. We have thus performed our model fitting in two different steps : (1) by fitting one single BT-Settl spectrum to the full 0.8–5 μm range (*WISE* $W1$ and $W2$ magnitudes were added as additional data to our spectra in order to do this); and (2) by fitting one BT-Settl spectrum to each one of the zJ, H and K spectral bands. The first method allowed us to obtain an estimate of $T_{\rm eff}$, while the second one allowed us to obtain an estimate of $\log g$ for each object in our sample.

In order to append the *WISE* photometric data to an observed NIR spectrum, we compute the synthetic J, H and K_S *2MASS* magnitudes of the spectrum and determine the three corresponding normalization factors. We then use the median of these factors to bring back the two *WISE* photometric data points to the same scale as the observed spectrum. The dilution factor is treated as a free parameter in our analysis so that no estimate nor measurement of distance is needed in the model fitting. We thus choose the dilution factor that minimizes $G_{k,j}$ for each fitted model. We do so in an analytical way to decrease computing time. We thus define the goodness-of-fit as :

$$G_{k,j} = \sum_{i=1}^{N} W_{i,j} \left(\frac{F_{obs,i,j} - D_{k,j} F_{k,i,j}}{\sigma_{obs,i,j}} \right)^2, \tag{6.4}$$

$$\text{where } D_{k,j} = \frac{\sum_{i=1}^{N} W_{i,j} \frac{F_{obs,i,j} F_{k,i,j}}{\sigma^2_{obs,i,j}}}{\sum_{i=1}^{N} W_{i,j} \frac{F^2_{k,i,j}}{\sigma^2_{obs,i,j}}}, \tag{6.5}$$

$$W_{i,j} = \frac{\left. \frac{\mathrm{d} \ln \lambda}{\mathrm{dx}} \right|_{x=x_{i,j}}}{\sum_{i'=1}^{N} \left. \frac{\mathrm{d} \ln \lambda}{\mathrm{dx}} \right|_{x=x_{i',j}}}, \tag{6.6}$$

where $x_{i,j}$ is the pixel number (i.e., the spectral position), j is the index of the spectral band (i.e., zJ, H or K, applicable only when we fit by individual bands), k is the atmosphere model index (each value of k corresponds to a given combination of $T_{\rm eff}$ and $\log g$), N is the total number of pixels in the fitting range, λ is the wavelength (μm), $W_{i,j}$ are the normalized weight factors, $D_{k,j}$ is the dilution factor that minimizes $G_{k,j}$, $F_{obs,i,j}$ and $\sigma_{obs,i,j}$ are the observed spectrum and its measurement error, and $F_{k,i,j}$ is an atmosphere model. The weights are chosen to ensure that equal wavelength ranges in log space equally contribute to the goodness-of-fit. For example, a broadband photometric measurement or one pixel of a low-dispersion spectroscopic order would be given a larger weight than one pixel of a high-dispersion spectroscopic order as it covers a larger wavelength range. Cushing et al. (2008) introduced this weighting method except that it was not done in log space; Naud et al. (2014) noted that the log space provides a more physically meaningful scale (i.e. using the log space prevents a bias that would be caused by working in wavelength space rather than frequency space).

We calculated errors on the adjusted parameters a_l (i.e., $T_{\rm eff}$ and $\log g$) from Wolberg (2006; p.50) :

$$\sigma_{a_l,k,j} = \sqrt{\frac{N}{N-2} G_{k,j} \; C^{-1}_{l,l,k,j}} \text{ with} \tag{6.7}$$

$$C_{l,m,k,j} = \sum_{i=1}^{N} W_{i,j} \frac{\partial}{\partial a_l} \left(D_{k,j} F_{k,i,j} \right) \frac{\partial}{\partial a_m} \left(D_{k,j} F_{k,i,j} \right), \tag{6.8}$$

where $C_{l,m,k,j}$ are elements of the correlation matrix. Equation (6.7) and the equivalent expression of Wolberg (2006) differ by a factor $\sqrt{N}$ to compensate for our use of normalized weights in Equation (6.4). These error estimates do not take into account any systematic error in either our observations or the BT-Settl atmosphere models, and are thus only based on the variation of the goodness-of-fit with respect to each parameter. We show a few typical examples of per-band model fitting in Figure 6.15.

As noted by Manjavacas et al. (2014), we find that the BT-Settl models generally fail to accurately reproduce the zJ-bands spectra of L dwarfs, especially at wavelengths smaller than $\sim 1\,\mu$m; the general slope seems to be in agreement, but a high-gravity solution is almost always preferred for all L dwarfs. Moreover, the FeH absorption features at $\sim 1.6\,\mu$m are not present at all in the atmosphere models, which could be explained by missing opacity sources in the synthetic models. For this reason, we have only kept results from the H and K bands to determine $\log g$. The adopted $\log g$ value is thus determined from the weighted mean of the values obtained from the H-band and K-band fitting, where the weights are set to the total values of $W_{i,j}$ (see Equation 6.6) within the fitting range divided by the inverse square of the individual measurement errors. This corresponds to the optimal weights that account both for the measurement error and the wavelength range used in the fitting process. Both the measurements and errors were rounded to the nearest half-integer and to the nearest factor of 100 K in the case of $\log g$ and $T_{\rm eff}$, respectively. We imposed a floor on measurement errors that correspond to the grid size of our BT-Settl models, i.e. 0.5 and 100 K for $\log g$ and $T_{\rm eff}$.

Our adopted $T_{\rm eff}$ and $\log g$ values are listed in Table 6.8 for our complete sample of low-gravity and field dwarfs. In Figures 6.16(a), we show the spectral type–$T_{\rm eff}$ sequence that we obtain, compared to various sequences from the literature (Stephens et al. 2009; Golimowski et al. 2004; Marocco et al. 2013). We find $T_{\rm eff}$ values that are consistent with the literature across the full range of spectral types, except for low-gravity objects which seem to be systematically cooler. This might be an additional indication that low-gravity brown dwarfs have cooler effective temperatures compared with field brown dwarfs of the same spectral types, an effect that was previously demonstrated for the young, directly-imaged BD and exoplanet companions HD 203030 B, TWA 27 b, HR 8799 b and β Pictoris b (Metchev

& Hillenbrand 2006; Barman et al. 2011a,b; Males et al. 2014), as well as for young brown dwarfs (Faherty et al. 2012; Liu et al. 2013b; J. Filippazzo et al., submitted to ApJ).

In Figure 6.16(b), we show the spectral type–$\log g$ sequence that we obtain for low-gravity and field dwarfs. The $\log g$ values that we derive for our low-gravity sample are systematically lower than those of our field sample, as expected. However, we observe a large scatter in the $\log g$ values of low-gravity dwarfs, although they are lower on average. This indicates that the model fitting method that we described above might not be very efficient in recovering low-gravity dwarfs in an ensemble of NIR spectra. Additionally, we derive slightly lower $\log g$ values for field dwarfs with spectral types M7 and L3–L6, indicating that the false positive rate might be larger when identifying low-gravity dwarfs based solely on model fitting in this range of spectral types. Our results also tentatively indicate that M7 dwarfs are systematically better fit by low-gravity atmosphere models, however this is based on only three objects and is thus possibly an effect of small number statistics.

We tried to reproduce the results of Cushing et al. (2008) showing that fitting individual bands yield systematically offset $T_{\rm eff}$ values, and to extend this result to our full M6–L9 range as well as to low-gravity dwarfs. In Figure 6.16(c), we show the spectral type–$T_{\rm eff}$ sequence that we obtain if we combine the zJ- and H-band measurements in a weighted mean (using similar weights than described above for $\log g$). We show that the systematic offsets in $T_{\rm eff}$ values derived with this method are significant in the M9–L5 range, and independent of surface gravity. In Figure 6.16(d), we compare the difference of $T_{\rm eff}$ values obtained from zJ- and H-band fitting to those obtained from the K-band fitting only. We show that $T_{\rm eff}$ values derived from the K-band only are systematically warmer in the M9–L5 range. The values of $T_{\rm eff}$ obtained from K-band fitting only are thus closer to those presented in Figure 6.16(a), except that the scatter is much larger. These results confirm the findings of Cushing et al. (2008), while extending them to earlier spectral types (down to M9) and seem to indicate that the zJ and H bands are the most likely cause of the systematic offset in $T_{\rm eff}$.

It will be interesting to investigate whether fixing the $T_{\rm eff}$ value using a large spectral coverage, and subsequently determining the best $\log g$ value using wavelength regions significantly smaller than a spectral band that are known to be gravity-sensitive, might provide a better

way to determine accurate $\log g$ values for L dwarfs. This will be the subject of a future work, along with repeating this analysis with future generations of BT-Settl atmosphere models that include a more realistic treatment of dust clouds (see Manjavacas et al. 2014 for a discussion on this topic).

6.7.3.2 Evolution models

We estimated the physical parameters (mass, radius, $T_{\rm eff}$, $\log g$) of all low-gravity candidate members presented here from a comparison of their absolute *2MASS* and *WISE* photometry with isochrones from CIFIST2011 BT-Settl models using a likelihood analysis. The age range of the most probable host YMG was used in each case, and statistical distances from BANYAN II are used when a trigonometric distance is not available. These models do not account for magnetic fields and assume a hot-start formation (large initial entropy). Both effects could cause a systematic underestimation of mass (Stassun et al. 2012; Marleau & Cumming 2014; Malo et al. 2014b). However, it has been demonstrated that BD masses derived from evolution models are systematically too large when compared to dynamical mass measurements (Lane et al. 2001; Bouy et al. 2004; Dupuy et al. 2009a,b,c, 2010; Konopacky et al. 2010; Dupuy et al. 2014, 2015). This seems in contradiction with what would be expected from the model limitations described above; instead, it is likely that the cooling rate of BDs is slowed down by atmospheric clouds, an effect that is not taken into account in current evolution models (Dupuy et al. 2015).

The resulting physical parameters are presented in Table 6.8. This allowed us to compile a total of 25 objects with an estimated mass in the planetary regime ($< 13\,M_{\rm Jup}$); they are individually discussed in the Appendix. These objects are all likely located within 10–60 pc and will constitute a sample of choice for a detailed study of the connection between the physical properties of BDs and giant, gaseous exoplanets, e.g. using the James Webb Space Telescope (Gardner et al. 2006).

In Figure 6.18, we compare the masses and radii estimated for the objects in our sample with those of other known exoplanets and young BDs, as well as with BD radii measured by Dieterich et al. (2014). We show that our sample overlaps with the regime of giant, gaseous

exoplanets. Our sample displays inflated radii and lower masses than field dwarfs, for given spectral types, which is expected for young, low-gravity low-mass stars and BDs.

6.7.4 Space density at the deuterium-burning limit

Late-type members of YMGs provide the opportunity of measuring the low-mass end of the IMF which is still poorly constrained. The *BASS* survey is still not complete enough to construct individual IMFs for the YMGs under study, but we can already put constraints on the population of objects near the planetary-mass boundary where our survey is particularly sensitive.

We display in Figure 6.19 a histogram of the estimated masses of all objects in our sample. We also display in this Figure a probability density function (PDF) that represents a continuous analog of the histogram which is independent on the binning and that includes individual measurement errors. This PDF is obtained by normalizing the integral of each individual mass estimation PDF to unity and summing them over the full sample. In the case of absolute $W1$ magnitudes, the PDFs that correspond to individual measurements were taken as normalized gaussian distributions with a characteristic width that corresponds to the measurement error.

There are 15 objects in our sample of THA candidates that have estimated masses in the 12.5–14 $M_{\rm Jup}$ range, which corresponds to the planetary-mass limit. This peak-shaped distribution of estimated masses for the THA candidate members uncovered here is the combined effect of a selection bias (we observed the latest-type objects first) and the distance distribution of THA members ($\sim$30–70 pc; Chapter 2), as 12/15 of these objects are likely located within 50 pc. Furthermore, we have identified a larger number of THA candidates compared to other YMGs, because its members are more easily identified in an all-sky search–the slightly larger distance of THA ensures that its members have a narrower distribution in space position and proper motion. The relatively large number of 12.5–14 $M_{\rm Jup}$ objects compared to objects in the 5–10 $M_{\rm Jup}$ or 15–75 $M_{\rm Jup}$ ranges is thus a selection effect.

Since our sample is biased on recovering objects more efficiently in the 12.5–14 $M_{\rm Jup}$ range, it remains useful to assess the space density of such objects. We will concentrate on the THA

candidate members for this as they provide a larger sample. Assuming that we have uncovered all of the 12.5–14 $M_{\rm Jup}$ candidate members of THA in *BASS* within 50 pc (accounting for 65.6% of the expected population according to our SKM model for THA) and correcting for the expected completeness of BASS for this association (90%; Chapter 3), we can expect that there are a total number of $20.3^{+6.8}_{-5.1}$ objects in THA that lie within this range of masses. The error was estimated assuming that the objects were drawn from a Poisson distribution, and they thus account for small number statistics.

Assuming that the population of 1.00–1.26 $M_{\odot}$ stars is complete in THA ($N = 14^{+4.3}_{-3.3}$ using Poisson statistics, see Figure 8 of Kraus et al. 2014b) and adjusting a fiducial log-normal IMF peaking at 0.25 $M_{\odot}$with a width $\sigma = 0.5$ dex (Jeffries 2012), we can expect a total of 356^{+61}_{-47} main-sequence stars in THA ($> 75\,M_{\rm Jup}$) and only $0.56^{+0.17}_{-0.13}$ objects in the 12.5–14 $M_{\rm Jup}$ range (the ratio of 12.5–14 $M_{\rm Jup}$ to 1.00–1.26 $M_{\odot}$ objects derived from that IMF is 0.04). We thus seem to be uncovering at least $36.4^{+16.6}_{-12.5}$ times too many objects in this mass range, compared to the predictions of a typical log-normal IMF anchored on the 1.00–1.26 $M_{\odot}$ population of THA.

It is possible that this is a consequence of a fault in the evolution models rather than a true over-population. For example, one could argue that the models fail to reproduce the effects of clouds which have a larger impact on the spectra of less massive, cooler objects. This could lead us to misinterpret the masses of our 15 low-gravity THA candidates, assigning them 12.5–14 $M_{\rm Jup}$ while their true masses span a larger range. If this effect alone is to explain the over-population, the true range of masses for our 15 objects would have to be extended by 190% in log space, which would mean that their true masses would span 4.5–39 $M_{\rm Jup}$. This effect is thus unlikely to be the lone explanation of this over-population. It is also possible that the current age estimate of THA is wrong–e.g., βPMG, Upper Scorpius, AB Doradus and the Pleiades have recently been found to be slightly older than previously thought (Luhman et al. 2005; Pecaut et al. 2012; Malo et al. 2014b; Binks & Jeffries 2014; Mamajek & Bell 2014). If it turns out that this is also the case for THA, our estimated masses would need to be shifted to larger values. As an example, doubling the age of THA would shift the estimated mass of a member from $\sim 13\,M_{\rm Jup}$ to $\sim 20\,M_{\rm Jup}$. This effect alone would thus be insufficient to

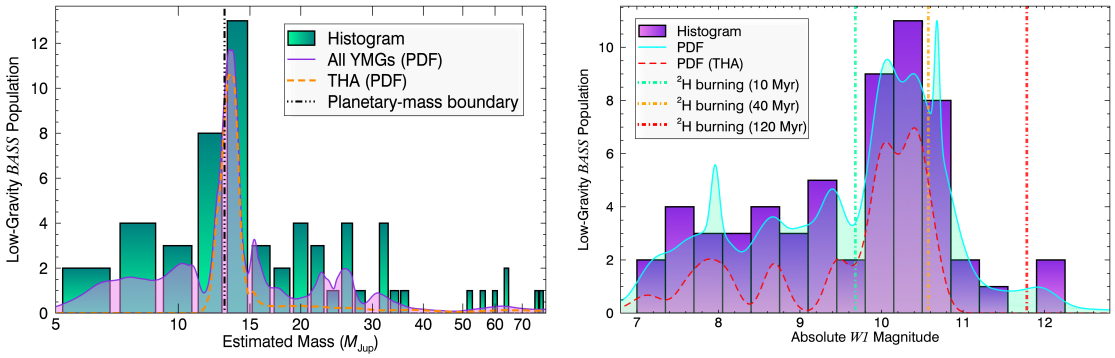

(a) Estimated Mass (b) Absolute $W1$ Magnitude

FIGURE 6.19 Panel a: Histogram of estimated masses (green bars) for low-gravity dwarfs in the *BASS* sample, obtained from a comparison of NIR photometry and trigonometric or kinematic distances with BT-Settl–CIFIST2011 synthetic models. The continuous PDFs of different subsets of the candidates are indicated with different lines (see legend). They were obtained by combining the individual mass estimation PDFs directly, and they thus provide a histogram-like continuous distribution that include measurement errors and are independent of the binning. Panel b: Histogram of absolute *WISE* M_{W1} magnitude of low-gravity dwarfs in the *BASS* sample (purple bars), obtained from trigonometric or kinematic distances. The thick aqua distribution is a continuous distribution that does not include binning and takes account of measurement uncertainties, and was built in the same way as that of Panel a. The most limiting aspect of our survey is the inclusion in the *2MASS* catalog, with a limiting magnitude around $J \sim 16$–17. The absence of a strong over-density is not in contradiction with Panel a, because our sample is composed of objects at different ages (~ 12–120 Myr), hence a given mass can correspond to a different temperature and absolute magnitude. The green, yellow and red vertical dashed lines correspond to the absolute $W1$ magnitudes of a 10, 40 and 120 Myr object, respectively.

explain the large number of 12.5–14 MJup THA candidates that we found. A similar shift of our estimated masses could be caused by systematics in evolution models (see our discussion in Section 6.7.3.2), although it is difficult to estimate the magnitude of this effect at this time. Dupuy et al. (2015) has shown that masses from evolution model are likely under-estimated for dusty BDs at the L/T transition; it could be expected that the same effect is important in young L dwarfs. This would further accentuate the discrepancy between our observations and the predictions from a typical IMF.

Bowler et al. (2013) noted that the age–absolute luminosity model sequences of $\sim 13\,M_{\rm Jup}$ and $\sim 25\,M_{\rm Jup}$ objects at different young ages overlap; such a pile-up in the isochrones could cause a degeneracy in our estimated masses and cause our method to mis-interpret true $\sim 25\,M_{\rm Jup}$ objects as planetary-mass objects. However, there are several observations that

make this explanation unlikely: (1) The likelihood method with which we estimate masses not only generates a measurement and error bars, but it also provides a continuous PDF for each individual mass estimate. If this effect is important, we would thus be able to observe double-peaked individual measurement PDFs, as well as a peak at $\sim 25\,M_{\rm Jup}$ in the PDF displayed in Figure 6.19. Note that even if present, this effect would not introduce a second peak in the histogram, since it was constructed from the most probable values of the estimated masses only. (2) While the young age–absolute luminosity isochrones overlap at different masses, this effect is much more subtle in the individual J, H, K_S, $W1$ and $W2$ age–absolute magnitude isochrones. Furthermore, the slight overlap happens at slightly different ages and masses in the different filters, and allows to lift the degeneracy between $\sim 13\,M_{\rm Jup}$ and $\sim 25\,M_{\rm Jup}$ objects. This likely explains why we do not observe dual-valued mass estimate PDFs. (3) Performing a Monte Carlo analysis in which 20 and 40 Myr isochrones are used to estimate the masses of a population of 20 000 synthetic objects with true masses uniformly distributed between 4 and $80\,M_{\rm Jup}$ produces no over-density of estimated masses in the 12–$14.5\,M_{\rm Jup}$ range. The absolute J, H, K_S, $W1$ and $W2$ magnitudes of these synthetic objects are obtained from the model isochrones themselves, hence this Monte Carlo analysis cannot be used to investigate systematics in the model cooling tracks. Instead, it only addresses the potential problem of overlapping isochrones that could produce degenerate mass estimates.

As a consequence of these observations, it does not appear that overlapping isochrones are the cause of the large population of 12–$14.5\,M_{\rm Jup}$ THA candidates in our sample. We note that it is however possible that a fraction of these THA candidate members are contaminants in our analysis (i.e., young interlopers from other moving groups or associations, considered in BANYAN II or not) despite their high Bayesian probability and the low expected contamination rate in this particular YMG. It will be necessary to measure the RVs and parallaxes for all 12 objects discussed here to assess this, but at this stage it seems that this effect would be the most likely explanation for this over-density. For example, only 5/12 of these objects would need to be interlopers in order for the over-density to become a 1σ result.

If we assume that the over-density is real, it would mean that there is at least one isolated dwarf in the 12.5–$14\,M_{\rm Jup}$ range for every $17.5^{+6.6}_{-5.0}$ main-sequence star in THA. Comparing

with the space density of main-sequence stars in the solar neighborhood (9.3×10^{-2} stars pc^{-3}; Chabrier 2005) and assuming that the ratio we observed in THA is valid in the field, this would amount to a field density of $5.3^{+3.8}_{-2.9} \times 10^{-3}$ dwarfs pc^{-3} in the 12.5–14 $M_{\rm Jup}$ range in THA. At ages older than 2.5 Gyr, they will all have temperatures below 450 K that correspond to spectral types later than Y0, and will thus be hard to locate due to their extreme faintness (Cushing et al. 2011; Kirkpatrick et al. 2011; Luhman 2014; Beamín et al. 2014). This is significantly larger than the lower limit measured by Kirkpatrick et al. (2011) that corresponds to at least one $\geq$Y0 dwarf for every 78 main-sequence star (or 1.2×10^{-3} dwarfs pc^{-3}), especially when considering that the population of field $\geq$Y0 dwarfs is also probably composed of objects that span a large range of ages and thus masses. Kirkpatrick et al. (2011) noted that their measurement is only a gross underestimation on the space density of Y-type dwarfs due to several biases. We note however that the IMF of YMGs might be different than that of the field, which could be yet another cause for this difference.

A less likely scenario is that our results could be an indication that we are approaching an up-turn in the IMF of isolated objects in THA with masses below the deuterium-burning limit: such an up-turn has already been hinted at by micro-lensing surveys in the galactic plane that measure $1.8^{+1.7}_{-0.8}$ Jupiter-mass object for every main-sequence star (corresponding to space density of $1.7^{+1.6}_{-0.7} \times 10^{-1}$ objects pc^{-3}; Sumi et al. 2011). Measurements of RV and distance for the complete set of YMG candidates in *BASS* will be crucial to assess whether the observed over-density holds, and discovering YMG candidate members at even lower masses will provide a strong constraint on whether there is an up-turn in the IMF of YMGs.

6.8 Summary and Conclusions

We presented a NIR spectroscopic follow-up of 241 candidate members of YMGs identified through the *BASS*, *LP-BASS* and *PRE-BASS* samples. This allowed us to identify 108 new low-gravity M5–L5 candidate members of YMGs with estimated masses spanning the range of 7–189 $M_{\rm Jup}$. Thirty-seven of these objects were previously known in the literature, but no signs of low gravity had been reported for them before this work. We complemented this unique sample with 22 low-gravity dwarfs from the literature to (1) build color–spectral type

and absolute magnitude–spectral type sequences for field and young dwarfs; (2) show that some gravity-sensitive indices correlate with age in the 10–200 Myr regime, albeit with a large scatter, such that low-resolution NIR spectroscopy does not allow a strong constraint on the age of an individual object; (3) we discuss some limitations of the current BT-Settl models, mainly their improper treatment of dust clouds in L-type dwarfs of all ages; and (4) show that we find an unexpectedly large number of isolated objects with estimated planetary masses in the Tucana-Horologium association, which might be caused by young interlopers from other moving groups. This study represents one of the first steps towards bridging the gap in our knowledge of the the space density of the lowest-mass BDs ($\sim 13\,M_{\rm Jup}$; Kirkpatrick et al. 2011) and potential isolated giant planets that were ejected from their stellar system ($\sim 1\,M_{\rm Jup}$; Sumi et al. 2011). Additional figures, data and information on this work can be found on the website *www.astro.umontreal.ca/~gagne* and in the Montreal Spectral Library, which is located at *www.astro.umontreal.ca/~gagne/MSL.php*.

The authors would like to thank the anonymous referee who suggested to improve BANYAN II with the inclusion of parallax motion and significantly helped to improve the quality of this paper, as well as make it more concise and clear. We would like to thank Robert Simcoe, Philippe Delorme, Michael C. Cushing, Rebecca Oppenheimer, Amélie Simon, Gilles Fontaine, Sergio B. Dieterich, Benjamin M. Zuckerman, André-Nicolas Chené, Sarah Jane Schmidt, Simon Coudé, Daniella C. Bardalez Gagliuffi and Jonathan B. Foster for useful comments and discussions. We thank Katelyn N. Allers, Michael C. Liu, Federico Marocco and Brendan P. Bowler for sharing data. We also thank all observatory staff and observers who helped us in this quest - Bernard Malenfant, Ghislain Turcotte, Pierre-Luc Lévesque, Alberto Pastén, Rachel Mason, Stuart Ryder, Rubén Díaz, Stéphanie Côté, John P. Blakeslee, Mischa Schirmer, Andrew McNichols, Dave Griep, Brian Cabreira, Tony Matulonis, German Gimeno, Steve Margheim, Percy L. Gomez, René Rutten, Bernadette Rodgers, Tim J. Davidge, Jaehyon Rhee Jay, Inger Jørgensen, Thomas L. Hayward, Andrew Cardwell, Blair C. Conn, Eleazar Rodrigo Carrasco Damele, David A. Krogsrud, Eduardo Marin, Erich Wenderoth, Fredrik T. Rantakyro, Joanna E. Thomas-Osip, Pablo Patricio Candia, Pascale Hibon, Cláudia Winge, Benoit Neichel, Peter Pessev, Matthew B. Bayliss and Anne Sweet. This

work was supported in part through grants from the Fond de Recherche Québécois - Nature et Technologie and the Natural Science and Engineering Research Council of Canada. This research has benefited from the SpeX Prism Spectral Libraries, maintained by Adam Burgasser at *http://pono.ucsd.edu/~adam/browndwarfs/spexprism*, as well as the M, L, T and Y dwarf compendium housed at *http://DwarfArchives.org* and maintained by Chris Gelino, Davy Kirkpatrick, and Adam Burgasser, whose server was funded by a NASA Small Research Grant, administered by the American Astronomical Society. This research made use of: the SIMBAD database and VizieR catalog access tool, operated at the Centre de Données astronomiques de Strasbourg, France (Ochsenbein et al. 2000); data products from the Two Micron All Sky Survey (*2MASS*; Skrutskie et al. 2006; Kirkpatrick et al. 2003), which is a joint project of the University of Massachusetts and the Infrared Processing and Analysis Center (IPAC)/California Institute of Technology (Caltech), funded by the National Aeronautics and Space Administration (NASA) and the National Science Foundation (Skrutskie et al. 2006); the Extrasolar Planets Encyclopaedia (*exoplanet.eu*), which was developed and is maintained by the exoplanet TEAM; data products from the *Wide-field Infrared Survey Explorer* (*WISE*; Wright et al. 2010), which is a joint project of the University of California, Los Angeles, and the Jet Propulsion Laboratory (JPL)/Caltech, funded by NASA; the NASA/IPAC Infrared Science Archive (IRSA), which is operated by JPL, Caltech, under contract with NASA; the Infrared Telescope Facility (IRTF), which is operated by the University of Hawaii under Cooperative Agreement NNX-08AE38A with NASA, Science Mission Directorate, Planetary Astronomy Program; the Database of Ultracool Parallaxes maintained by Trent Dupuy (Dupuy & Liu 2012); the Hale 5 m telescope at Palomar Observatory, which received funding from the Rockefeller Foundation; and of tools provided by Astrometry.net. This paper includes data gathered with the 6.5 meter Magellan Telescopes located at Las Campanas Observatory, Chile (CNTAC program CN2013A-135). Based on observations obtained at the Gemini Observatory through programs number GN-2013A-Q-118, GS-2013B-Q-79, GS-2014A-Q-55, GS-2014B-Q-72, GS-2014B-Q-47 and GS-2015A-Q-60. The Gemini Observatory is operated by the Association of Universities for Research in Astronomy, Inc., under a cooperative agreement with the National Science Foundation (NSF) on behalf of the Gemini

partnership: the NSF (United States), the National Research Council (Canada), CONICYT (Chile), the Australian Research Council (Australia), Ministério da Ciência, Tecnologia e Inovação (Brazil) and Ministerio de Ciencia, Tecnología e Innovación Productiva (Argentina). All data were acquired through the Canadian Astronomy Data Center and part of it was processed using the Gemini IRAF package. This material is based upon work supported by AURA through the National Science Foundation under AURA Cooperative Agreement AST 0132798 as amended. This publication uses observations obtained at IRTF through programs number 2007B023, 2007B070, 2008A050, 2008B054, 2009A055, 2010A045, 2011B071, 2012A097, 2012B015, 2013A040, 2013A055, 2013B025, 2014B026 and 2015A026. The authors recognize and acknowledge the very significant cultural role and reverence that the summit of Mauna Kea has always had within the indigenous Hawaiian community. We are most fortunate to have the opportunity to conduct observations from this mountain.

Table 6.7. Polynomial coefficients for spectral type-magnitude and spectral type-color diagrams.

Sequence Name	Field Sequence				Young Sequence			
	c_0	c_1	c_2	σ	c_0	c_1	c_2	σ
M_J	8.53 $\pm 3.07e-1$	$3.08e-1$ $\pm 5.66e-2$	$2.56e-3$ $\pm 2.42e-3$	0.66	4.97 $\pm 5.65e-1$	$7.96e-1$ $\pm 1.02e-1$	$-1.14e-2$ $\pm 4.35e-3$	1.16
M_H	8.11 $\pm 2.86e-1$	$2.81e-1$ $\pm 5.23e-2$	$1.65e-3$ $\pm 2.24e-3$	0.63	4.76 $\pm 5.04e-1$	$7.37e-1$ $\pm 8.81e-2$	$-1.20e-2$ $\pm 3.60e-3$	0.72
M_{K_S}	8.12 $\pm 2.74e-1$	$2.05e-1$ $\pm 5.02e-2$	$3.86e-3$ $\pm 2.19e-3$	0.60	4.69 $\pm 4.74e-1$	$6.88e-1$ $\pm 8.16e-2$	$-1.22e-2$ $\pm 3.28e-3$	0.56
M_{W1}	7.84 $\pm 2.94e-1$	$2.40e-1$ $\pm 5.07e-2$	$-1.92e-4$ $\pm 2.10e-3$	0.55	4.30 $\pm 4.83e-1$	$7.57e-1$ $\pm 8.27e-2$	$-1.98e-2$ $\pm 3.35e-3$	0.57
M_{W2}	7.43 $\pm 2.96e-1$	$2.82e-1$ $\pm 5.14e-2$	$-2.73e-3$ $\pm 2.16e-3$	0.56	3.95 $\pm 5.02e-1$	$7.84e-1$ $\pm 8.69e-2$	$-2.25e-2$ $\pm 3.60e-3$	0.42
$J-H$	$3.83e-1$ $\pm 2.95e-2$	$3.83e-2$ $\pm 5.75e-3$	$2.29e-4$ $\pm 2.57e-4$	0.09	$3.39e-1$ $\pm 7.39e-2$	$2.43e-2$ $\pm 1.62e-2$	$2.72e-3$ $\pm 8.33e-4$	0.09
$H-K_S$	$3.92e-2$ $\pm 2.43e-2$	$6.68e-2$ $\pm 4.95e-3$	$-1.85e-3$ $\pm 2.34e-4$	0.08	$-1.83e-2$ $\pm 5.34e-2$	$6.55e-2$ $\pm 1.13e-2$	$-4.31e-4$ $\pm 5.41e-4$	0.07
K_S-W1	$2.87e-1$ $\pm 3.36e-2$	$-2.05e-2$ $\pm 6.36e-3$	$2.99e-3$ $\pm 2.87e-4$	0.08	$1.85e-1$ $\pm 7.56e-2$	$-1.40e-2$ $\pm 1.60e-2$	$4.27e-3$ $\pm 8.09e-4$	0.08
$W1-W2$	$3.00e-1$ $\pm 2.15e-2$	$-1.91e-2$ $\pm 4.07e-3$	$1.55e-3$ $\pm 1.87e-4$	0.05	$3.32e-2$ $\pm 3.59e-2$	$3.68e-2$ $\pm 7.75e-3$	$-3.77e-4$ $\pm 3.95e-4$	0.07
$J-K_S$	$4.48e-1$ $\pm 4.55e-2$	$9.91e-2$ $\pm 9.02e-3$	$-1.34e-3$ $\pm 4.14e-4$	0.14	$3.35e-1$ $\pm 1.04e-1$	$8.71e-2$ $\pm 2.23e-2$	$2.38e-3$ $\pm 1.11e-3$	0.13
$J-W1$	$6.75e-1$ $\pm 6.73e-2$	$9.25e-2$ $\pm 1.31e-2$	$1.02e-3$ $\pm 6.01e-4$	0.19	$3.80e-1$ $\pm 1.07e-1$	$9.97e-2$ $\pm 2.35e-2$	$5.57e-3$ $\pm 1.16e-3$	0.21
$J-W2$	$9.85e-1$ $\pm 5.99e-2$	$7.04e-2$ $\pm 1.15e-2$	$2.73e-3$ $\pm 5.04e-4$	0.22	$5.12e-1$ $\pm 1.36e-1$	$1.18e-1$ $\pm 2.84e-2$	$6.09e-3$ $\pm 1.35e-3$	0.23
$H-W1$	$3.69e-1$ $\pm 4.50e-2$	$3.81e-2$ $\pm 8.90e-3$	$1.54e-3$ $\pm 4.17e-4$	0.14	$8.67e-2$ $\pm 9.00e-2$	$6.93e-2$ $\pm 1.93e-2$	$3.00e-3$ $\pm 9.62e-4$	0.13
$H-W2$	$6.30e-1$ $\pm 4.10e-2$	$2.64e-2$ $\pm 7.96e-3$	$2.76e-3$ $\pm 3.61e-4$	0.18	$1.68e-1$ $\pm 1.30e-1$	$9.99e-2$ $\pm 2.74e-2$	$2.82e-3$ $\pm 1.36e-3$	0.15
K_S-W2	$5.80e-1$ $\pm 3.78e-2$	$-3.93e-2$ $\pm 6.86e-3$	$4.56e-3$ $\pm 2.92e-4$	0.13	$2.41e-1$ $\pm 1.11e-1$	$2.29e-2$ $\pm 2.34e-2$	$3.71e-3$ $\pm 1.18e-3$	0.11

Note. — All abscissa are spectral types $S_{\rm type}$, expressed in decimal value, where zero is M0, ten is L0, etc. A given sequence respects the equation $y = \sum_{i=0}^{N} c_i S_{\rm type}^i$. The scatter of the data with respect to a best-fitting sequence is given by σ. All sequences are valid in the M6–L8 range.

Table 6.8. Physical Parameters.

2MASS Designation	Spectral Type	YMG Age (Myr)	Estimated from isochrones[a]		Estimated from SED fitting	
			Mass ($M_{\rm Jup}$)	Radius ($R_{\rm Jup}$)	$T_{\rm eff}$ (K)[b]	$\log g$[c]
Field objects						
02535980+3206373	M6	···	···	···	···	5.5 ± 0.5
07522390+1612157	M6	···	···	···	···	5.5 ± 0.5
00335534-0908247	M7	···	···	···	···	4.5 ± 1.0
18393308+2952164	M7	···	···	···	2800 ± 200	5.0 ± 1.0
22021125-1109461	M7	···	···	···	2800 ± 200	5.0 ± 1.0
16553529-0823401	M7	···	···	···	2700 ± 100	5.0 ± 0.5
00115060-1523450	M7	···	···	···	···	5.0 ± 0.5
21144103-4339531	M7.5 pec	···	···	···	···	5.5 ± 0.5
23540957-3316220	M8	···	···	···	···	5.5 ± 0.5
21272613-4215183	M8	···	···	···	2300 ± 200	5.5 ± 0.5
23520481-2208032	M8	···	···	···	···	5.5 ± 0.5
00552554+4130184	M8	···	···	···	···	5.5 ± 0.5
17364839+0220426	M8	···	···	···	···	5.0 ± 1.0
23310161-0406193	M8 β	···	···	···	2700 ± 200	5.0 ± 1.0
20025265-1316418	M8.5	···	···	···	2300 ± 200	5.5 ± 0.5
12531308+2728028	M8.5	···	···	···	···	5.0 ± 1.0
07083261-4701475	M8.5	···	···	···	2700 ± 200	5.5 ± 0.5
22444905-3045535	M9 pec	···	···	···	2300 ± 200	5.5 ± 0.5
12212770+0257198	M9 pec	···	···	···	2300 ± 200	5.5 ± 0.5
14284323+3310391	M9	···	···	···	2500 ± 200	5.0 ± 0.5
03140344+1603056	M9 pec	~ 500	$71.2^{+3.6}_{-3.7}$	1.06 ± 0.02	2300 ± 200	5.5 ± 0.5
10513331-1916530	M9 pec	···	···	···	2100 ± 300	5.5 ± 0.5
12212770+0257198	M9 pec	···	···	···	2600 ± 200	5.5 ± 0.5
20482880-3255434	M9	···	···	···	2300 ± 200	5.5 ± 0.5
10473109-1815574	L0	···	···	···	···	5.5 ± 0.5
17312974+2721233	L0	···	···	···	···	5.5 ± 0.5
02281101+2537380	L0	···	···	···	2100 ± 400	5.5 ± 0.5
00461551+0252004	L0 pec	···	···	···	2300 ± 200	5.5 ± 0.5
22062157-6116284	L0: pec	···	···	···	2100 ± 200	5.5 ± 0.5
07200325-0846499	L0 pec	···	···	···	2300 ± 200	5.5 ± 0.5
23515044-2537367	L0.5	···	···	···	2600 ± 200	5.0 ± 0.5
08254335-0029110	L0.5	···	···	···	2100 ± 200	5.5 ± 0.5
21073169-0307337	L0.5	···	···	···	2300 ± 200	5.5 ± 0.5
02441019-3548036	L1 pec	···	···	···	1700 ± 100	4.5 ± 0.5
10484281+0111580	L1	···	···	···	2100 ± 300	5.5 ± 0.5
00332386-1521309	L1	···	···	···	···	5.5 ± 0.5
20343769+0827009	L1	···	···	···	2100 ± 300	5.5 ± 0.5
18071593+5015316	L1	···	···	···	2100 ± 300	5.5 ± 0.5
02081833+2542533	L1	···	···	···	2100 ± 200	5.5 ± 0.5
18071593+5015316	L1	···	···	···	···	5.5 ± 0.5
17054834-0516462	L1	···	···	···	2300 ± 200	5.5 ± 0.5
03454316+2540233	L1	···	···	···	2300 ± 200	5.5 ± 0.5
14392836+1929149	L1	···	···	···	2300 ± 100	5.5 ± 0.5
16452211-1319516	L1.5	···	···	···	2100 ± 300	5.5 ± 0.5
16532970+6231364	L1.5	···	···	···	1900 ± 200	5.5 ± 0.5
13015465-1510223	L1.5	···	···	···	2100 ± 300	5.5 ± 0.5
20575409-0252302	L2	···	···	···	2100 ± 200	5.5 ± 0.5
20360316+1051295	L2	···	···	···	2100 ± 200	5.0 ± 0.5
22425317+2542573	L2 pec	···	···	···	1700 ± 100	5.5 ± 0.5
20282035+0052265	L2	···	···	···	2100 ± 200	5.5 ± 0.5
02055138-0759253	L2	···	···	···	2100 ± 200	5.0 ± 0.5
08472872-1532372	L2	···	···	···	2100 ± 200	5.5 ± 0.5
02415367-1241069	L2	···	···	···	2100 ± 200	5.5 ± 0.5
06022216+6336391	L2	···	···	···	2100 ± 200	5.5 ± 0.5
05431887+6422528	L2	···	···	···	2100 ± 200	5.5 ± 0.5
14313029+1436599	L2	···	···	···	···	5.5 ± 0.5
20484222-5127435	L2 pec	···	···	···	1900 ± 100	5.5 ± 0.5
20414283-3506442	L2	···	···	···	1700 ± 100	5.5 ± 0.5

Table 6.8 — continued

2MASS Designation	Spectral Type	YMG Age (Myr)	Estimated from isochrones[a]		Estimated from SED fitting	
			Mass ($M_{\rm Jup}$)	Radius ($R_{\rm Jup}$)	$T_{\rm eff}$ (K)[b]	$\log g$[c]
21041491-1037369	L2	···	···	···	1900 ± 100	5.5 ± 0.5
11463449+2230527	L2.5	···	···	···	1800 ± 100	5.0 ± 0.5
04532647-1751543	L3	···	···	···	2100 ± 100	5.0 ± 0.5
10584787-1548172	L3	···	···	···	1900 ± 100	5.0 ± 0.5
21420580-3101162	L3	···	···	···	1800 ± 100	5.0 ± 0.5
04070752+1546457	L3	···	···	···	···	5.0 ± 0.5
23155665-4747315	L3 pec	···	···	···	1800 ± 100	5.0 ± 0.5
21420580-3101162	L3	···	···	···	1800 ± 100	5.5 ± 0.5
04070752+1546457	L3	···	···	···	···	5.0 ± 0.5
10584787-1548172	L3	···	···	···	1900 ± 100	5.0 ± 0.5
13571237+1428398	L3	···	···	···	1700 ± 100	5.5 ± 0.5
11000965+4957470	L3	···	···	···	1700 ± 100	5.0 ± 0.5
08234818+2428577	L3	···	···	···	1700 ± 100	5.5 ± 0.5
08204440-7514571	L3.5	···	···	···	1700 ± 100	4.5 ± 0.5
00165953-4056541	L3.5	···	···	···	1600 ± 100	5.0 ± 0.5
22244381-0158521	L3.5	···	···	···	1600 ± 100	5.0 ± 0.5
14482563+1031590	L3.5	···	···	···	1600 ± 100	4.5 ± 0.5
00193927-3724392	L3.5:	···	···	···	1700 ± 100	5.0 ± 0.5
01291221+3517580	L3.5	···	···	···	1600 ± 100	5.0 ± 0.5
18212815+1414010	L4 pec	···	···	···	1600 ± 100	4.5 ± 0.5
01550354+0950003	L4	···	···	···	1800 ± 100	4.5 ± 0.5
03370359-1758079	L4	···	···	···	1500 ± 100	4.5 ± 0.5
23392527+3507165	L4 pec	···	···	···	1800 ± 100	5.0 ± 0.5
00361617+1821104	L4	···	···	···	1900 ± 100	5.0 ± 0.5
00511078-1544169	L4	···	···	···	1600 ± 100	4.5 ± 0.5
02050344+1251422	L4 pec	···	···	···	1600 ± 100	5.0 ± 0.5
06523073+4710348	L4	···	···	···	1600 ± 100	4.5 ± 0.5
08014056+4628498	L4: pec	···	···	···	1500 ± 100	5.0 ± 0.5
08354256-0819237	L4 pec	···	···	···	1800 ± 100	5.0 ± 0.5
11040127+1959217	L4	···	···	···	1900 ± 100	5.0 ± 0.5
12392727+5515371	L4 pec	···	···	···	1600 ± 100	4.5 ± 0.5
15065441+1321060	L4	···	···	···	1800 ± 100	5.5 ± 0.5
21512543-2441000	L4 pec	···	···	···	1600 ± 100	5.0 ± 0.5
00043484-4044058	L4.5	···	···	···	1600 ± 100	5.0 ± 0.5
14283132+5923354	L4.5	···	···	···	1800 ± 100	5.0 ± 0.5
02082363+2737400	L5	···	···	···	1600 ± 100	5.0 ± 0.5
06244595-4521548	L5	···	···	···	1500 ± 100	5.0 ± 0.5
09054654+5623117	L5	···	···	···	1700 ± 100	4.5 ± 0.5
17065487-1314396	L5 pec	···	···	···	1900 ± 100	5.0 ± 0.5
08511627+1817302	L5:	···	···	···	1500 ± 100	4.5 ± 0.5
08350622+1953050	L5	···	···	···	1600 ± 100	5.0 ± 0.5
00282091+2249050	L5	···	···	···	···	5.0 ± 0.5
15261405+2043414	L5	···	···	···	1600 ± 100	5.0 ± 0.5
01443536-0716142	L5 pec	···	···	···	1600 ± 100	5.0 ± 0.5
02052940-1159296	L5.5	···	···	···	1500 ± 100	5.5 ± 0.5
15074769-1627386	L5.5	···	···	···	1900 ± 100	5.0 ± 0.5
17461199+5034036	L5.5	···	···	···	1900 ± 100	5.0 ± 0.5
13262981-0038314	L5.5	···	···	···	1600 ± 100	5.5 ± 0.5
17502484-0016151	L5.5	···	···	···	1800 ± 100	4.5 ± 0.5
06540564+6528051	L6	···	···	···	1800 ± 100	5.0 ± 0.5
08095903+4434216	L6 pec	30–50	8.1 ± 0.8	$1.31^{+0.01}_{-0.03}$	1600 ± 100	4.5 ± 0.5
15150083+4847416	L6	···	···	···	1600 ± 100	5.0 ± 0.5
21011544+1756586	L6	···	···	···	1500 ± 100	4.5 ± 0.5
16335933-0640552	L6	···	···	···	1500 ± 100	5.0 ± 0.5
01033203+1935361	L6 pec	···	···	···	1600 ± 100	4.5 ± 0.5
09153413+0422045	L6	···	···	···	1600 ± 100	5.5 ± 0.5
04390101-2353083	L6 pec	···	···	···	1600 ± 100	5.0 ± 0.5
03582255-4116060	L6 pec	20–26	8.2 ± 0.6	1.37 ± 0.01	1600 ± 100	4.5 ± 0.5
23512200+3010540	L6 pec	···	···	···	1600 ± 100	5.0 ± 0.5
10101480-0406499	L6	···	···	···	1600 ± 100	5.0 ± 0.5

Table 6.8 — continued

2MASS Designation	Spectral Type	YMG Age (Myr)	Estimated from isochrones[a]		Estimated from SED fitting	
			Mass ($M_{\rm Jup}$)	Radius ($R_{\rm Jup}$)	$T_{\rm eff}$ (K)[b]	$\log g$[c]
21321145+1341584	L6	···	···	···	1500 ± 100	5.5 ± 0.5
12281523-1547342	L6	···	···	···	1700 ± 100	5.0 ± 0.5
07171626+5705430	L6.5	···	···	···	1700 ± 100	5.0 ± 0.5
10433508+1213149	L7	···	···	···	1500 ± 100	5.5 ± 0.5
23254530+4251488	L7	···	···	···	1200 ± 100	5.5 ± 0.5
08503593+1057156	L7 pec u	···	···	···	1600 ± 100	4.5 ± 0.5
14002320+4338222	L7	···	···	···	1600 ± 100	5.5 ± 0.5
08251968+2115521	L7 pec	···	···	···	1500 ± 200	5.0 ± 0.5
16303054+4344032	L7	···	···	···	1500 ± 100	5.0 ± 0.5
03185403-3421292	L7	···	···	···	1600 ± 100	5.0 ± 0.5
01075242+0041563	L7 pec	···	···	···	···	4.5 ± 0.5
10440942+0429376	L7	···	···	···	1600 ± 100	5.5 ± 0.5
22521073-1730134	L7.5	···	···	···	1500 ± 100	5.5 ± 0.5
15150607+4436483	L7.5	···	···	···	1500 ± 100	5.0 ± 0.5
09293364+3429527	L7.5	···	···	···	1600 ± 100	4.5 ± 0.5
15232263+3014562	L8	···	···	···	1500 ± 100	5.5 ± 0.5
10365305-3441380	L8	···	···	···	1600 ± 200	5.5 ± 0.5
10430758+2225236	L8 pec	···	···	···	1600 ± 100	4.5 ± 0.5
00325937+1410371	L8	···	···	···	1400 ± 100	5.5 ± 0.5
16322911+1904407	L8	···	···	···	1500 ± 100	5.0 ± 0.5
12195156+3128497	L8	···	···	···	1200 ± 100	4.5 ± 0.5
08575849+5708514	L8 pec	···	···	···	1600 ± 200	4.5 ± 0.5
10071185+1930563	L8	···	···	···	1500 ± 100	5.0 ± 0.5
15400942+3742316	L9	···	···	···	1600 ± 100	5.0 ± 0.5
09083803+5032088	L9	···	···	···	1600 ± 100	5.5 ± 0.5
20431769-1551031	L9	···	···	···	1500 ± 100	5.5 ± 0.5
08300825+4828482	L9	···	···	···	1400 ± 100	4.5 ± 0.5
02550357-4700509	L9	···	···	···	1500 ± 100	5.5 ± 0.5
03105986+1648155	L9	···	···	···	1500 ± 100	5.0 ± 0.5
03284265+2302051	L9.5	···	···	···	1400 ± 100	5.5 ± 0.5
08523490+4720359	L9.5	···	···	···	1200 ± 100	5.5 ± 0.5
08583467+3256275	T1	···	···	···	1400 ± 100	5.0 ± 0.5
Low-gravity objects						
05071137+1430013 B	M5.5 β	20–26	$176.8^{+17.7}_{-17.9}$	$4.00^{+0.21}_{-0.22}$	···	4.0 ± 1.5
03363144-2619578	M5.5 β	20–40	$189.1^{+14.1}_{-17.2}$	3.94 ± 0.14	···	5.0 ± 1.0
05071137+1430013 A	M5.5 β	20–26	$176.8^{+17.7}_{-17.9}$	$4.00^{+0.21}_{-0.22}$	···	5.0 ± 1.5
22191486-6828018	M6 β	20–40	$32.2^{+6.2}_{-9.3}$	$1.76^{+0.10}_{-0.05}$	3100 ± 300	4.5 ± 1.5
02404759-4253377	M6 β	20–40	$63.3^{+7.3}_{-9.1}$	$2.22^{+0.07}_{-0.06}$	2900 ± 200	4.0 ± 1.5
04402583-1820414	M6 β	20–40	···	···	3000 ± 200	4.5 ± 1.5
08034469+0827000	M6 β	110–130	$91.0^{+4.1}_{-4.0}$	1.68 ± 0.03	3000 ± 100	5.5 ± 0.5
03182597-3708118	M6: γ	20–40	···	···	3000 ± 400	4.5 ± 2.0
10284580-2830374	M6 γ	5–15	$100.6^{+23.9}_{-27.5}$	$4.33^{+0.29}_{-0.24}$	2800 ± 300	4.0 ± 1.5
10455263-2819303	M6 γ	5–15	$27.6^{+9.6}_{-5.2}$	$2.63^{+0.11}_{-0.09}$	2900 ± 100	5.0 ± 1.0
07202582-5617224	M6 γ	20–26	$15.7^{+2.3}_{-0.7}$	$1.79^{+0.05}_{-0.04}$	2900 ± 200	5.0 ± 1.0
20334670-3733443	M6: γ	20–26	$106.2^{+8.0}_{-6.9}$	3.12 ± 0.08	2800 ± 200	4.5 ± 1.5
01265327-5505506	M6 γ	20–40	$75.0^{+8.7}_{-10.2}$	2.40 ± 0.06	2900 ± 200	4.0 ± 1.5
12574941-4111373	M6 γ	5–15	$51.5^{+12.4}_{-17.1}$	$3.11^{+0.26}_{-0.14}$	2900 ± 200	5.0 ± 1.0
23355015-3401477	M6: γ	20–26	59.0 ± 5.1	$2.37^{+0.07}_{-0.06}$	3000 ± 300	4.0 ± 1.5
03111547+0106307	M6 γ	20–40	···	···	3000 ± 200	3.5 ± 0.5
06353541-6234059	M6.5 β	···	···	···	2900 ± 300	3.5 ± 1.5
03093877-3014352	M6.5 γ	20–40	$116.0^{+13.2}_{-14.8}$	$2.93^{+0.13}_{-0.11}$	···	3.5 ± 1.0
05123569-3041067	M6.5 γ	···	···	···	2900 ± 200	4.0 ± 2.0
02501167-0151295	M7: β	20–26	$22.9^{+5.4}_{-4.6}$	$1.91^{+0.06}_{-0.05}$	2800 ± 200	4.5 ± 1.0
20391314-1126531	M7 β	110–130	$74.0^{+3.6}_{-3.4}$	1.53 ± 0.03	2600 ± 200	5.0 ± 1.0
05181131-3101529	M7 β	20–40	$97.5^{+14.3}_{-13.6}$	$2.73^{+0.14}_{-0.12}$	2800 ± 100	3.5 ± 1.5
05264316-1824315	M7 β	20–40	$82.5^{+11.4}_{-11.5}$	$2.52^{+0.12}_{-0.11}$	2800 ± 100	5.0 ± 1.0

Table 6.8 — continued

2MASS Designation	Spectral Type	YMG Age (Myr)	Estimated from isochrones[a]		Estimated from SED fitting	
			Mass ($M_{\rm Jup}$)	Radius ($R_{\rm Jup}$)	$T_{\rm eff}$ (K)[b]	$\log g$[c]
01294256-0823580	M7 β	20–26	$96.3^{+7.3}_{-7.1}$	$2.99^{+0.09}_{-0.10}$	2700 ± 300	3.5 ± 1.5
03350208+2342356	M7.5 β	20–26	$60.9^{+4.0}_{-4.4}$	2.40 ± 0.04	···	5.0 ± 1.0
00413538-5621127	M7.5 γ u	20–40	···	···	2700 ± 200	5.5 ± 0.5
23231347-0244360	M8 β	20–26	$16.7^{+4.0}_{-0.8}$	1.85 ± 0.03	2600 ± 200	4.5 ± 1.0
00192626+4614078	M8 β	110–130	$103.4^{+7.4}_{-6.5}$	1.76 ± 0.04	2700 ± 200	5.0 ± 1.0
23520507-1100435	M8 β	110–130	95.4 ± 4.3	1.71 ± 0.03	2600 ± 200	5.0 ± 0.5
15291017+6312539	M8 β	110–130	$93.2^{+7.9}_{-7.2}$	1.69 ± 0.06	2700 ± 200	5.0 ± 1.0
08561384-1342242	M8 γ	5–15	$14.4^{+0.8}_{-1.4}$	1.86 ± 0.04	2300 ± 200	5.5 ± 0.5
00065794-6436542	M8 γ	20–40	$31.9^{+8.7}_{-9.5}$	$1.82^{+0.07}_{-0.05}$	2100 ± 300	5.5 ± 0.5
22353560-5906306	M8.5 β	20–40	$17.7^{+6.0}_{-2.4}$	1.76 ± 0.02	2300 ± 200	5.5 ± 0.5
03550477-1032415	M8.5 β	20–40	···	···	2700 ± 200	5.5 ± 0.5
14112131-2119503	M8.5 β	···	···	···	2600 ± 200	5.0 ± 1.0
12073346-3932539	M8.5 γ	5–15	$23.4^{+2.5}_{-1.0}$	$2.73^{+0.03}_{-0.04}$	2300 ± 200	5.5 ± 0.5
20282203-5637024	M8.5 γ	20–40	$36.4^{+6.9}_{-9.7}$	$1.83^{+0.07}_{-0.05}$	2300 ± 200	5.5 ± 0.5
05402325-0906326	M9 β	20–40	$19.2^{+5.1}_{-3.6}$	$1.74^{+0.03}_{-0.06}$	2600 ± 200	5.0 ± 1.5
15104786-2818174	M9 β	30–50	$37.0^{+4.4}_{-4.8}$	$1.66^{+0.05}_{-0.04}$	2600 ± 200	5.5 ± 0.5
15474719-2423493	M9 β	30–50	12.9 ± 0.3	1.06 ± 0.01	···	5.5 ± 0.5
15470557-1626303 A	M9 β	110–130	···	···	2300 ± 100	5.5 ± 0.5
23360735-3541489	M9 β	20–130	···	···	2300 ± 200	5.5 ± 0.5
09451445-7753150	M9 β	20–40	$37.9^{+6.3}_{-8.8}$	$1.84^{+0.07}_{-0.05}$	2600 ± 200	4.5 ± 1.5
09532126-1014205	M9 β	5–40	···	···	1800 ± 100	5.5 ± 0.5
00425923+1142104	M9 β	20–130	···	···	2300 ± 100	5.5 ± 0.5
23453903+0055137	M9 β	···	···	···	2300 ± 200	5.5 ± 0.5
04493288+1607226	M9 γ	20–26	$18.4^{+5.5}_{-2.2}$	$1.85^{+0.05}_{-0.04}$	2300 ± 200	5.5 ± 0.5
22025794-5605087	M9: γ	20–40	$19.9^{+6.5}_{-3.9}$	$1.79^{+0.02}_{-0.16}$	2600 ± 200	5.5 ± 0.5
00274197+0503417	M9 γ	···	···	···	···	3.0 ± 0.5
11395113-3159214	M9 γ	5–15	$19.3^{+1.4}_{-1.0}$	$0.99^{+0.02}_{-0.01}$	2300 ± 100	3.0 ± 0.5
12474428-3816464	M9 γ	5–15	$17.4^{+0.8}_{-0.9}$	2.15 ± 0.06	2100 ± 300	5.5 ± 0.5
20004841-7523070	M9 γ	20–50	···	···	2300 ± 200	5.5 ± 0.5
11064461-3715115	M9 γ	5–15	$15.6^{+0.7}_{-1.1}$	$1.96^{+0.06}_{-0.05}$	2300 ± 100	3.0 ± 0.5
19355595-2846343	M9 γ	···	···	···	···	3.0 ± 0.5
04433761+0002051	M9 γ	20–26	$20.6^{+5.9}_{-3.8}$	$1.86^{+0.06}_{-0.05}$	1800 ± 100	5.5 ± 0.5
00381489-6403529	M9.5 β	20–40	$14.9^{+5.1}_{-0.4}$	1.70 ± 0.02	1700 ± 100	5.5 ± 0.5
21544859-7459134	M9.5: β	20–40	$20.4^{+6.5}_{-4.5}$	$1.80^{+0.02}_{-0.16}$	2300 ± 300	5.5 ± 0.5
02103857-3015313	M9.5 β	20–40	$14.0^{+0.4}_{-0.3}$	1.62 ± 0.02	1700 ± 100	5.5 ± 0.5
12535039-4211215	M9.5 γ	5–15	$12.5^{+1.2}_{-2.0}$	$1.71^{+0.04}_{-0.03}$	···	4.5 ± 0.5
15525906+2948485	L0 β	···	···	···	···	3.0 ± 0.5
11544223-3400390	L0 β	30–50	$18.2^{+3.5}_{-3.6}$	$1.60^{+0.02}_{-0.03}$	2100 ± 200	5.5 ± 0.5
00325584-4405058	L0 β	20–26	11.7 ± 0.6	1.00 ± 0.01	···	5.5 ± 0.5
03420931-2904317	L0: β	20–40	12.7 ± 0.4	1.48 ± 0.02	2100 ± 200	3.0 ± 0.5
06272161-5308428	L0: β/ γ	20–40	$8.8^{+1.0}_{-1.1}$	1.35 ± 0.03	1500 ± 100	5.5 ± 0.5
12451416-4429077	L0 γ	5–15	$18.4^{+1.4}_{-1.3}$	$1.24^{+0.03}_{-0.02}$	2300 ± 200	3.0 ± 0.5
00182834-6703130	L0 γ	20–40	$13.7^{+0.4}_{-0.3}$	1.58 ± 0.02	1700 ± 100	5.0 ± 0.5
04400972-5126544	L0 γ	20–40	···	···	1700 ± 100	4.5 ± 0.5
20334473-5635338	L0 γ	20–40	$13.6^{+0.3}_{-0.4}$	1.56 ± 0.02	2100 ± 200	3.0 ± 0.5
01415823-4633574	L0 γ	20–40	$14.7^{+5.7}_{-0.4}$	1.16 ± 0.01	1700 ± 100	5.0 ± 0.5
02292794-0053282	L0 γ	···	···	···	···	5.5 ± 0.5
02411151-0326587	L0 γ	20–40	$13.1^{+0.3}_{-0.4}$	1.04 ± 0.02	···	5.0 ± 0.5
06191291-5803156 b	L0 γ	20–40	$12.8^{+0.4}_{-0.3}$	1.03 ± 0.01	···	3.0 ± 1.0
22134491-2136079	L0 γ	20–26	13.5 ± 0.3	1.09 ± 0.01	···	5.0 ± 0.5
00464841+0715177	L0 δ	20–26	$15.4^{+0.5}_{-0.3}$	$1.79^{+0.03}_{-0.02}$	2100 ± 100	5.5 ± 0.5
06085283-2753583	L0 δ	20–40	$19.8^{+3.9}_{-4.2}$	1.20 ± 0.02	···	3.0 ± 0.5
20135152-2806020	L0 δ	20–26	$15.7^{+1.5}_{-0.6}$	1.10 ± 0.02	···	3.0 ± 0.5
02265658-5327032	L0 δ	20–40	13.7 ± 0.3	1.59 ± 0.02	1700 ± 100	4.5 ± 0.5
11271382-3735076	L0 δ	5–15	$9.2^{+1.4}_{-1.7}$	$1.56^{+0.05}_{-0.03}$	2100 ± 200	4.5 ± 0.5

Table 6.8 — continued

2MASS Designation	Spectral Type	YMG Age (Myr)	Estimated from isochrones[a]		Estimated from SED fitting	
			Mass ($M_{\rm Jup}$)	Radius ($R_{\rm Jup}$)	$T_{\rm eff}$ (K)[b]	$\log g$[c]
00344300-4102266	L1: β	20–40	12.8 ± 0.4	1.48 ± 0.01	1700 ± 100	5.5 ± 0.5
11480096-2836488	L1: β	5–15	$8.5^{+1.4}_{-1.6}$	$1.55^{+0.04}_{-0.03}$	1800 ± 100	3.5 ± 0.5
03164512-2848521	L1 β	110–130	$34.0^{+1.6}_{-1.5}$	1.24 ± 0.01	2100 ± 200	5.5 ± 0.5
00584253-0651239	L1 β	20–130	...	...	2100 ± 200	5.5 ± 0.5
19350976-6200473	L1 γ	20–40	$13.5^{+0.3}_{-0.4}$	1.54 ± 0.02	2100 ± 200	4.5 ± 0.5
23225299-6151275	L1 γ	20–40	13.6 ± 0.3	1.56 ± 0.02	1700 ± 100	5.0 ± 0.5
23255604-0259508	L1 γ	110–130	$31.0^{+1.4}_{-1.2}$	1.22 ± 0.01	1800 ± 100	5.0 ± 0.5
02410564-5511466	L1 γ	20–40	13.6 ± 0.3	1.57 ± 0.02	1700 ± 100	5.0 ± 0.5
01205114-5200349	L1 γ	20–40	13.3 ± 0.3	1.54 ± 0.02	1700 ± 100	5.0 ± 0.5
01174748-3403258	L1 γ	20–40	13.6 ± 0.3	1.09 ± 0.01	1800 ± 100	5.0 ± 0.5
04062677-3812102	L1: γ	20–40	$11.7^{+0.7}_{-1.1}$	$0.98^{+0.03}_{-0.02}$	...	4.5 ± 0.5
05184616-2756457	L1 γ	20–40	$15.3^{+6.7}_{-1.5}$	1.11 ± 0.05	...	5.0 ± 0.5
00191296-6226005	L1 γ	20–40	13.8 ± 0.3	1.59 ± 0.02	1600 ± 100	5.0 ± 0.5
11083081+6830169	L1 γ	20–40	13.5 ± 0.3	1.55 ± 0.01	1700 ± 100	5.0 ± 0.5
12074836-3900043	L1 δ	5–15	$12.1^{+1.4}_{-2.0}$	1.69 ± 0.04	2100 ± 100	5.0 ± 0.5
22351658-3844154	L1.5 γ	20–40	$14.0^{+0.4}_{-0.3}$	1.62 ± 0.02	1600 ± 100	5.0 ± 0.5
06023045+3910592	L2 β	...	...	...	...	5.0 ± 0.5
00452143+1634446	L2 γ	30–50	14.7 ± 0.3	1.14 ± 0.01	...	5.0 ± 0.5
05361998-1920396	L2 γ	20–40	13.0 ± 0.9	$1.50^{+0.07}_{-0.06}$	1600 ± 200	4.5 ± 0.5
02583123-1520536	L3 β	20–40	$13.0^{+0.3}_{-0.4}$	$1.50^{+0.02}_{-0.01}$	1700 ± 100	5.0 ± 0.5
12563961-2718455	L3: β	5–15	$7.7^{+1.4}_{-1.5}$	$1.53^{+0.04}_{-0.03}$	1600 ± 100	4.5 ± 0.5
01531463-6744181	L3 β	20–40	$12.9^{+0.3}_{-0.5}$	1.49 ± 0.02	1600 ± 100	5.0 ± 0.5
17260007+1538190	L3 γ	...	...	...	...	4.5 ± 0.5
04185879-4507413	L3 γ	20–40	$12.9^{+0.3}_{-0.4}$	1.49 ± 0.02	1600 ± 100	5.0 ± 0.5
22081363+2921215	L3 γ	20–26	$12.9^{+0.3}_{-0.1}$	1.14 ± 0.01	...	4.5 ± 0.5
20113196-5048112	L3 γ	20–40	12.9 ± 0.4	1.49 ± 0.02	...	5.0 ± 0.5
10042066+5022596	L3: γ	20–40	12.5 ± 0.4	1.54 ± 0.07	...	4.0 ± 0.5
15515237+0941148	L3: γ	...	...	...	...	3.5 ± 0.5
00011217+1535355	L4 β	110–130	25.3 ± 1.0	1.20 ± 0.01	1600 ± 100	4.5 ± 0.5
21324036+1029494	L4: β	30–50	11.4 ± 0.4	1.36 ± 0.01	1600 ± 100	4.0 ± 0.5
10212570-2830427	L4: β/γ	5–15	$6.5^{+1.3}_{-1.2}$	$1.51^{+0.04}_{-0.03}$	1600 ± 200	5.0 ± 1.0
22064498-4217208	L4 γ	110–130	26.1 ± 1.0	1.21 ± 0.01	1800 ± 100	5.0 ± 0.5
05012406-0010452	L4 γ	20–40	$10.2^{+0.8}_{-1.0}$	1.36 ± 0.02	1600 ± 100	4.0 ± 0.5
22495345+0044046	L4 γ	...	...	...	1700 ± 100	4.5 ± 0.5
14252798-3650229	L4 γ	110–130	$26.6^{+0.3}_{-1.0}$	1.20 ± 0.01	1600 ± 100	5.0 ± 0.5
03552337+1133437	L3–L6 γ	110–130	$22.4^{+0.9}_{-1.0}$	1.20 ± 0.01	1500 ± 100	4.5 ± 0.5
23433470-3646021	L3–L6 γ	20–130	...	...	1500 ± 100	4.0 ± 0.5
16154255+4953211	L3–L6 γ	...	...	...	...	4.0 ± 0.5
05120636-2949540	L5 β	20–26	$6.7^{+1.0}_{-0.9}$	1.36 ± 0.01	1600 ± 100	4.0 ± 0.5
23174712-4838501	L5 β	...	...	...	...	4.5 ± 0.5
00303013-1450333	L4–L6 β	30–50	$10.8^{+0.4}_{-0.6}$	1.33 ± 0.01	1500 ± 100	5.0 ± 0.5
21543454-1055308	L5 β/γ	30–50	$10.3^{+0.5}_{-0.7}$	1.32 ± 0.01	1600 ± 100	4.0 ± 0.5
03264225-2102057	L5 β/γ	110–130	$22.4^{+1.0}_{-1.1}$	1.20 ± 0.01	1600 ± 100	...
20025073-0521524	L5–L7 γ	...	...	...	1700 ± 100	4.5 ± 0.5
17410280-4642218	L5:–L7: γ	...	...	...	...	3.5 ± 0.5
00470038+6803543	L6–L8 γ	...	...	...	...	4.0 ± 0.5
22443167+2043433	L6–L8 γ	110–130	12.0 ± 0.1	0.86 ± 0.01	...	4.0 ± 0.5
21140802-2251358	L6–L8 γ	20–26	9.0 ± 0.3	1.00 ± 0.01	...	4.0 ± 0.5

[a]Estimated masses and radii were derived from a comparison of the trigonometric or statistical distances, the age of the most probable YMG membership and the *2MASS* and *WISE* photometry with AMES-Cond evolutionary models (see the text for a detailed explanation).

[b]Values obtained from the modified model fitting that uses *WISE* $W1$, $W2$ photometry as well as NIR spectra in the J, H and K bands.

[c]Values obtained from a weighted mean of H-band and K-band $\log g$ (see text for more information).

Table 6.9. Potential isolated planetary-mass objects.

2MASS Designation	Ref.	Spectral Type	Source Sample	Moving Group	Estimated Mass ($M_{\rm Jup}$)	Distance[a] (pc)
00303013–1450333	1	L4–L6 β	*LP-BASS*	ARG	$10.8^{+0.4}_{-0.6}$	26.72 ± 3.21[b]
00344300–4102266	2	L1: β	*BASS*	THA	12.8 ± 0.4	41.2 ± 2.4
01531463–6744181	3	L3 β	*BASS*	THA	$12.9^{+0.3}_{-0.5}$	47.0 ± 3.2
03420931–2904317	2	L0: β	*BASS*	THA	12.7 ± 0.4	$48.2^{+3.6}_{-3.2}$
03421621–6817321	4	L4 γ	*BASS*	THA	12.4 ± 0.5	48.6 ± 3.6
04185879–4507413	2	L3 γ	*BASS*	THA	$12.9^{+0.3}_{-0.4}$	$49.8^{+4.0}_{-3.6}$
05012406–0010452	3	L4 γ	*BASS*	COL,CAR	$10.2^{+0.8}_{-1.0}$	14.7 ± 2.8[b]
05120636–2949540	5	L5 β	*BASS*	BPMG	$6.7^{+1.0}_{-0.9}$	$10.9^{+4.4}_{-4.0}$
06272161–5308428	2	L0: β/γ	*BASS*	CAR	$8.8^{+1.0}_{-1.1}$	$24.1^{+2.4}_{-2.0}$
06322402–5010349	3	L3 β	*PRE-BASS*	ABDMG	$11.0^{+0.5}_{-0.6}$	$7.7^{+3.2}_{-2.8}$
10212570–2830427	2	L4: β/γ	*BASS*	TWA	$6.5^{+1.3}_{-1.2}$	42.6 ± 5.6
11271382–3735076	2	L0 δ	*LP-BASS*	TWA	$9.2^{+1.4}_{-1.7}$	$62.2^{+8.8}_{-8.0}$
11480096–2836488	2	L1: β	*BASS*	TWA	$8.5^{+1.4}_{-1.6}$	47.8 ± 5.6
12074836–3900043	6	L1 δ	*BASS*	TWA	$12.1^{+1.4}_{-2.0}$	$58.2^{+6.8}_{-6.4}$
12271545–0636458	5	M8.5 β	*PRE-BASS*	TWA	$11.6^{+1.4}_{-1.9}$	32.5 ± 3.2
12535039–4211215	2	M9.5 γ	*BASS*	TWA	$12.5^{+1.2}_{-2.0}$	$81.0^{+7.6}_{-7.2}$
12563961–2718455	2	L3: β	*BASS*	TWA	$7.7^{+1.4}_{-1.5}$	44.6 ± 5.2
20113196–5048112	2	L3 γ	*BASS*	THA	12.9 ± 0.4	$53.4^{+4.0}_{-3.6}$
21324036+1029494	7	L4: β	*PRE-BASS*	ARG	11.4 ± 0.4	34.2 ± 4.8
21543454–1055308	8	L5 β/γ	*BASS*	ARG	$10.3^{+0.5}_{-0.7}$	22.5 ± 2.8

[a]Kinematic distances estimated from moving group membership unless noted.

[b]Trigonometric distance.

Note. — References to this Table :
(1) Kirkpatrick et al. 2000; (2) This paper; (3) Reid et al. 2008a; (4) Cruz et al. 2007; (5) Cruz et al. 2003; (6) Gagné et al. 2014a; (7) Chiu et al. 2006; (8) Gagné et al. 2014b.

6.A Discussions on individual objects from the BASS NIR follow-up

Several objects presented here deserve a detailed discussion, either because they display peculiar features, or were reported in the literature as candidate members of other YMGs. Additionally, optical spectra were available in the literature for some objects discussed here, and can serve as an independent assessment of low surface gravity.

6.A.1 Potential planetary-mass low-gravity candidate members of YMGs

We list in Table 6.9 twenty potential isolated planetary-mass objects in our sample, ten of which were discovered as part of this work. A few of these objects deserving further discussion

are listed below.

2MASS J05012406–0010452 was discovered by Reid et al. (2008a) as an L4 dwarf in the optical, and was categorized as a low-gravity L4 γ by Cruz et al. (2009), using its optical spectrum. Allers & Liu (2013) categorized it as a very-low gravity L3 dwarf in the NIR, whereas we categorize it as an L4 γ dwarf. Faherty et al. (2012) measured a trigonometric distance of 13.1 ± 0.8 pc. We recovered this object in *BASS* as an ambiguous candidate member of Columba or Carina with respective Bayesian probabilities of 49% and 17%, taking the trigonometric distance measurement of Faherty et al. (2012) into account. If this object is a member of either COL or CAR (both YMGs are coeval at 20–40 Myr), it has an estimated mass of $10.2^{+0.8}_{-1.0}\,M_{\rm Jup}$. Zapatero Osorio et al. (2014) independently measured a trigonometric distance of 19.6 ± 1.4 pc, which is discrepant with that of Faherty et al. (2012) at the 5σ level. The reason for this large discrepancy is unclear; the measurement of Faherty et al. (2012) used a smaller number of epochs (11 versus 21); however, they were spread across a larger temporal coverage (3 yr versus 2 yr). If we adopt the distance measurement of Zapatero Osorio et al. (2014), the CAR membership probability becomes negligible and that of COL becomes considerably smaller (7.2%), although we also calculate a low field contamination probability (1.3%). It will be necessary to better constrain the distance of this object to assess whether it is a viable candidate member of COL or CAR. Obtaining an RV measurement would also be useful for this.

2MASS J05120636–2949540 has been identified as an L4.5 dwarf in the optical by Cruz et al. (2003); Kirkpatrick et al. (2008), and Bardalez Gagliuffi et al. (2014) obtained a NIR spectrum to categorize it as an L4.5 $\pm$2 dwarf. In Chapter 2, we determined that this object is a low-probability candidate member of βPMG. We used the NIR spectrum of Bardalez Gagliuffi et al. (2014) to revisit its spectral classification: we find that this object is a very good match to our L5 β template; however, the method of Allers & Liu (2013) assigns it an intermediate gravity. We note that the VO_Z index is significantly larger than that of field L5 dwarfs, but Allers & Liu (2013) only use this index within the L0–L4 spectral types, as later-type low-gravity dwarfs in their sample displayed similar VO absorption than that of field dwarfs of the same spectral types. However, only one low-gravity L5 dwarf was

available at the time, hence it is possible that the VO_Z index remains useful to discriminate low-gravity L5 dwarfs. For this reason, we adopt the L5 β spectral type. Due to its low-gravity features, this object is preserved as a candidate member of βPMG. This object has one of the lowest estimated masses among the YMG candidates presented here, with $6.7^{+1.0}_{-0.9}\,M_{\rm Jup}$. Its statistical distance associated with membership to βPMG is $10.9^{+4.4}_{-4.0}$ pc, which makes it a valuable benchmark to study the atmosphere of planetary-mass objects.

2MASS J12074836–3900043 (2MASS J1207–3900) was discovered as a candidate member of TWA in *BASS*. Its discovery and NIR spectroscopic follow-up have been presented in Gagné et al. (2014a; see Chapter 4). They reported an optical spectral type L0 γ and a NIR spectral type L1 γ. Here we used the spectra of several low-gravity candidate members of Upper Scorpius obtained by Lodieu et al. (2008) to define tentative templates for the spectral type L0 δ, which likely correspond to objects younger than $\sim$15–20 Myr and have an even more triangular H-band continuum than the L0 γ type. Given that both the optical and NIR spectra of 2MASS J1207–3900 are peculiar even in comparison to the best template matches (L0 γ and L1 γ respectively) and that its H band continuum is more triangular than any β or γ template, we revised its spectral classification by comparing it to Upper Scorpius candidate members. We find that the best match is the L0 δ template; however, 2MASS J1207–3900 displays features that are attributable to a later spectral type (redder slopes at 1.2–1.35 μm and 1.5–1.6 μm). We thus suggest a tentative spectral type of L1 δ for this object, but identifying other similar objects will be necessary to confirm this. If it is a member of TWA (5–15 Myr), this object has an estimated mass of $12.1^{+1.4}_{-2.0}\,M_{\rm Jup}$ and a statistical distance of $58.2^{+6.8}_{-6.4}$ pc.

2MASS J12271545–0636458 was identified as an M9 dwarf by Cruz et al. (2003) using optical spectroscopy. We identified it as a candidate member of TWA in *PRE-BASS*, and NIR spectroscopy allowed us to categorize it as a low-gravity M8.5 β dwarf. It was initially rejected from the *BASS* sample because of its low Bayesian probability, which is in part due to the fact that its kinematic distance of 32.5 ± 3.2 pc if it is a member of TWA does not match its spectrophotometric distance (63.2 ± 11.4 pc). The latter estimate would place 2MASS J12271545–0636458 at the far-end of the TWA members ($\sim$40–62 pc; Chapter 2; Weinberger et al. 2013a; Ducourant et al. 2014). This is reminiscent of 2MASS J12474428–

3816464, TWA 29 and TWA 31, which are young and seem to be located between TWA and SCC in terms of distance (Song et al. 2003; Schneider et al. 2012a; Chapters 4 and 3). Measurements of distance and RV will be useful to assess whether this is a true member of TWA despite its small Bayesian probability. If it is a true member of TWA (5–15 Myr) located at its statistical distance, this object has an estimated mass of $11.6^{+1.4}_{-1.9}\,M_{\rm Jup}$.

2MASS J12563961–2718455 was identified in *PRE-BASS* as a low-probability candidate member of TWA. NIR spectroscopy revealed that this object is a low-gravity L3±1 β dwarf. The probability that this object belongs to TWA is lower than 20%, but the field contamination probability is also very low at $<0.1\%$. This usually points out to either an incomplete SKM for the YMG or to contamination from a source not taken into account in BANYAN II. The most likely a priori explanation would be that this object is a contaminant from SCC (located at $\sim$100–150 pc; Sartori et al. 2003); however, the spectrophotometric distance of 2MASS J12563961–2718455 (43.1 ± 3 pc) is not consistent with this hypothesis, even when its low gravity is taken into account. Using its *2MASS* and *WISE* photometry and comparing it with other known low-gravity L4 dwarfs, we can rule out a distance larger than 48.5 pc at a 95% confidence level, assuming this object is not an unresolved multiple system. We can hence conclude that as long as this object is not extremely peculiar for a low-gravity L4 dwarf or a multiple system composed of four equal-luminosity components, it cannot be a member of SCC. The statistical distance from BANYAN II which is associated to the TWA hypothesis ($46.2^{+4.8}_{-4.4}$ pc) is similar to those of bona fide members of TWA ($\sim$40–62 pc; Chapter 2; Weinberger et al. 2013a; Ducourant et al. 2014), hence this case is different from those of 2MASS J12271545-0636458, 2MASS J12474428–3816464, TWA 29 and TWA 31, which are young and seem to be located between TWA and SCC in terms of distance (Song et al. 2003; Schneider et al. 2012a; Chapters 4 and 3). Obtaining a distance measurement for this object will be helpful to assess whether it is a member of TWA. Assuming an age of 5–15 Myr and comparing its statistical distance from BANYAN II with BT-Settl *2MASS* and *WISE* isochrones, the estimated mass of this object is $7.7^{+1.4}_{-1.5}\,M_{\rm Jup}$, amongst the lowest of all candidate YMG members reported here. Its statistical distance associated with membership to TWA is 44.6 ± 5.2 pc.

2MASS J21324036+1029494 was discovered as an L4.5 ±1 dwarf by Chiu et al. (2006) using low-S/N NIR spectroscopy. We identified it as a candidate member of ARG from *PRE-BASS*. The NIR spectrum obtained by Chiu et al. (2006) is available in the SpeX PRISM Spectral Libraries, we thus retrieved it to assess whether it is a low-gravity dwarf. We categorize this object as an L4:β dwarf. Its H-cont index (Allers & Liu 2013) is consistent with low-gravity objects; however, the quality of the data is not sufficient to assess whether its FeH_Z and KI_J indices are consistent with this. Obtaining a better-quality and higher-resolution NIR spectrum will be useful to confirm the spectral type of this object. If it is a member of ARG (30–50 Myr), this object has an estimated mass of $11.4 \pm 0.4\,M_{\rm Jup}$ and a statistical distance of 34.2 ± 4.8 pc.

6.A.2 Low-gravity candidate members of YMGs

2MASS J00413538–5621127 (DENIS-P J00041353–562112) has been identified as a candidate nearby, red dwarf by Phan-Bao et al. (2001), and spectroscopically confirmed by Schmidt et al. (2007) as an active M8 dwarf. Using high resolution optical spectroscopy, Reiners (2009) revised its spectral type to M7.5 and showed evidence that it displays Li and signatures of active accretion, which indicates that it is a young, $\sim$10 Myr BD. Based on its position, proper motion and RV, they suggest that it could be a member of THA, or an ejected member of βPMG, which would make it the first accreting BD discovered in either of these associations. Liu et al. (2010) reported that it is a binary with estimated spectral types of M6.5 ±1 and M8 from photometry. In Chapter 2, we corroborated that it is a high-probability candidate member of THA, with estimated masses of 14–41 $M_{\rm Jup}$ and 18–41 $M_{\rm Jup}$ for the individual components. This object was retrieved in *BASS* as a high-probability candidate of THA. We obtained NIR spectroscopy for the unresolved system, and categorize it as a very low-gravity M7.5 γ BD system, which is consistent with its young age.

2MASS J02590146–4232204 was identified by Rodriguez et al. (2013) as a candidate member of COL with infrared excess indicative of the presence of a circumstellar disk host. We independently identified this object as a candidate member of COL in *PRE-BASS*; however, it was subsequently rejected from *BASS* because of its low membership probability and the

fact that its *WISE* colors did not survive the extragalactic filter defined by Kirkpatrick et al. (2011), which is likely a consequence of its infrared excess. NIR spectroscopy allowed us to categorize it as an M5 γ dwarf. This is consistent with the results of Rodriguez et al. (2013), who reported that this object displays weak Na I absorption that is indicative of a low surface gravity. Including the RV measurement of $15.3 \pm 1.5\,\mathrm{km\,s^{-1}}$ from Rodriguez et al. (2013), we find that this object is a low-probability candidate member of COL: this conclusion differs from that of Rodriguez et al. (2013), which found that 2MASS J02590146–4232204 is a candidate member of THA. Obtaining a trigonometric distance will be useful to assess whether this object is a member of COL or THA.

2MASS J03264225–2102057 has been identified as an L4 dwarf with Li absorption by Cruz et al. (2007). Using the DUSTY evolution models (Chabrier et al. 2000), the presence of Li and the spectrophotometric absolute magnitude of this object, they determined that it should be younger than 500 Myr and less massive than $50\,M_{\mathrm{Jup}}$. We identified this object as a highly probable L5 β/γ candidate member of ABDMG in *PRE-BASS*. Dahn et al. (2002) measured a trigonometric distance of 32.3 ± 1.6 pc that is consistent with membership to ABDMG. The presence of low-gravity feature in its optical and NIR and optical spectra puts a slightly stronger constraint on the age of 2MASS J03264225–2102057, since it is expected that gravity-sensitive spectral indices remain useful only up to $\sim$200 Myr (Cruz et al. 2009; Allers & Liu 2013). We therefore categorize this object as a low-gravity L5 β/γ dwarf. An RV measurement is needed before it can be assessed whether this object is a bona fide member of ABDMG.

2MASS J04493288+1607226 was identified in *PRE-BASS* as a candidate member of βPMG, but was rejected from the *BASS* sample because of its proximity with TAU. NIR spectroscopy revealed that it is a low-gravity M9 γ dwarf. We estimate a distance of 54.9 ± 10.0 pc for this object by comparison with other low-gravity dwarfs. A distance larger than 82 pc can be excluded at a 99% confidence level, which is incompatible with membership to TAU (140 ± 20 pc; Torres et al. 2007) unless it is an unresolved multiple with at least 3 individual equal-luminosity components. This scenario is unlikely, especially considering that the NIR spectrum of 2MASS J04493288+1607226 is not reddened. We thus preserve this

object as a candidate member of βPMG.

2MASS J11083081+6830169 has been discovered by Gizis et al. (2000) as an L1 dwarf in the optical with Hα emission. We recovered this object in *BASS* as a candidate member of ABDMG, and Gizis (2002) identified it as a candidate member of TWA. The RV of $-9.8 \pm 0.1\,\mathrm{km\,s^{-1}}$ measured by Blake et al. (2010) does not match the predicted RV of $-18.9 \pm 1.5\,\mathrm{km\,s^{-1}}$ for membership to ABDMG. It closely matches that of the CAR hypothesis (-9.7 ± 0.8), but it still obtains a very low Bayesian probability of being a member of CAR. Its statistical distance ($15.3 \pm 0.8\,\mathrm{pc}$) places it right into the locus of known young L dwarfs in both an M_{W1} versus $J - K_S$ and M_{W1} versus $H - W2$ CMDs. This distance places it at only $0.27\,\mathrm{km\,s^{-1}}$ of the CAR bona fide member HIP 33737 in UVW space, and at 17.2 pc of the CAR bona fide member GJ 2079 in XYZ space. We show in Figure 6.20 its $XYZUVW$ position at its most probable distance: it seems that this object has a most probable position that is consistent with bona fide members of CAR, but our SKM fails to represent this. It can be expected that our SKM of CAR is not accurate because it was derived from a small number of bona fide members. Furthermore, both the NIR spectrum that we obtained and the optical spectrum from the RIZzo spectral library display clear signs of low-gravity and allowed us to categorize it as an L1 γ dwarf, which is consistent with membership to a YMG. A measurement of this object's trigonometric distance will be useful to assess whether or not it is a member of CAR, but we note that it is likely a member despite its low Bayesian membership probability.

2MASS J12265135–3316124 (TWA 32) has been identified by Shkolnik et al. (2011) as an UV-bright M6.5 low-mass star. They measured strong Hα emission and Li absorption, as well as an RV of $7.15 \pm 0.26\,\mathrm{km\,s^{-1}}$. They used this information as well as a photometric distance ($53 \pm 5\,\mathrm{pc}$) to identify it as a new member of TWA, and they noted that it is a 656.1 ± 0.4 mas visual binary with near-equal luminosity. Rodriguez et al. (2011) independently discovered this object and measured strong Hα and He I emission at 5876 Å and 6678 Å, as well as strong Li absorption. They argued that the Hα full width at 10% of $270\,\mathrm{km\,s^{-1}}$ is consistent with this object being a classical T Tauri star. They measured an RV of $14.8 \pm 3\,\mathrm{km\,s^{-1}}$ and note that its UVW space velocity is consistent with TWA and SCC. We recovered this object

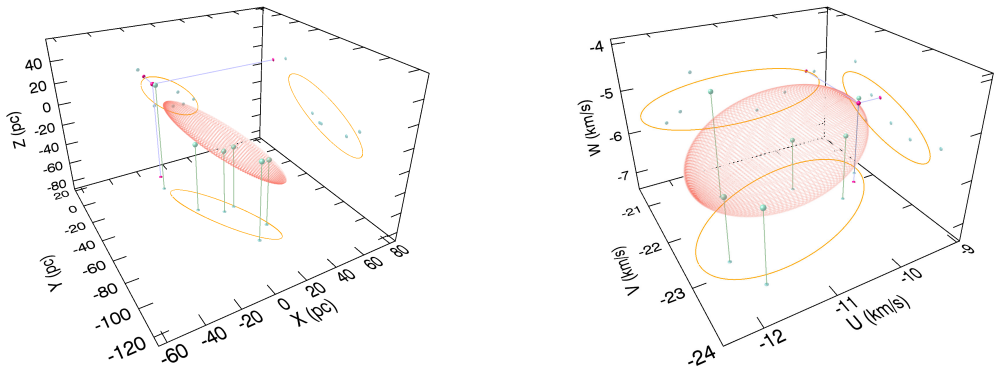

(a) Galactic position (b) Space velocity

FIGURE 6.20 Predicted galactic position XYZ and space velocity UVW of the CAR candidate member 2MASS J11083081+6830169 (red point and its projections) using its statistical distance from BANYAN II, compared with bona fide members of CAR (green points and their vertical projections on the XY and UV planes) and the SKM models of CAR (as defined in Chapter 2; orange ellipsoid and its projections).

in *PRE-BASS* as a candidate member of TWA, and obtained NIR spectroscopy that allowed us to assign it a spectral type of M5.5 γ. At this spectral type, only the weaker Na I absorption is a useful low-gravity indicator. We adopted the RV measurement of Shkolnik et al. (2011) which is more precise, and, like them, found that this object is a strong candidate member of TWA. The BANYAN II statistical distance corresponding to the TWA hypothesis is $61.8^{+6.4}_{-6.0}$ pc, which is consistent with the photometric estimate of Shkolnik et al. (2011) that takes its binary nature into account. The SKMs of BANYAN II do not take SCC into account, which includes the Lower Centaurus Crux (LCC) and the Upper Centaurus Lupus (UCL) regions, hence our result does not preclude membership to SCC. The space velocity UVW for this object is $(-8.6 \pm 1.4, -15.7 \pm 1.1, -3.4 \pm 1.1)$ km s^{-1} (Shkolnik et al. 2011), at 4.6 km s^{-1} from the kinematic center of TWA (Chapter 2), 4.6 km s^{-1} from that of UCL and 4.2 km s^{-1} from that of LCC (Sartori et al. 2003). Its kinematics are thus consistent with SCC and TWA; however, its photometric distance is not consistent with the distance of this complex ($\sim$100–150 pc; Sartori et al. 2003), whereas it is consistent with that of TWA members ($\sim$40–62 pc; Chapter 2; Weinberger et al. 2013a; Ducourant et al. 2014). We conclude that TWA 32 is a likely member of TWA, unless it is a multiple system composed of at least three equal-

luminosity components. A trigonometric distance measurement will be useful to assess this.

2MASS J20391314–1126531 was discovered as an M9 dwarf by Cruz et al. (2003) using optical spectroscopy. Gálvez-Ortiz et al. (2010) reported that it is a candidate member of the Pleiades stream. Famaey et al. (2005) demonstrated that the Pleiades stream is not a moving group but rather a dynamical stream of stars without a common origin. We identified 2MASS J20391314–1126531 as a candidate member of ABDMG as part of *PRE-BASS* and obtained NIR spectroscopy which revealed that this is a low-gravity M7 β dwarf. The RV of $-18.0 \pm 2\,\mathrm{km\,s^{-1}}$ that was measured by Gálvez-Ortiz et al. (2010) is consistent with a membership to ABDMG, and the fact that it has a low gravity indicates that it might not be a contaminant from the Pleiades stream. A measurement of its distance will be needed to assess this.

6.A.3 Candidate members of YMGs with no age constraint

2MASS J03582255–4116060 has been discovered by Cruz et al. (2007) as an L5 BD in the optical. We identified it as a low-probability candidate member of βPMG as part of *BASS*. $R \sim 75$ NIR spectroscopy allowed us to categorize it as a peculiar L6 dwarf. Its continuum is redder and its H band is slightly more triangular than our field L6 template, however it is unclear at this time if these effects are due to a low gravity or not. Obtaining a higher-resolution spectrum would be useful to assess this. If we assume an age of 20–26 Myr and the BANYAN II statistical distance associated with the βPMG hypothesis (18.1 ± 3.2 pc) and compare its *2MASS* and *WISE* photometry with the BT-Settl isochrones, we find that this object has one of the lowest estimated mass of all candidate YMG members reported here, with $8.2 \pm 0.6\,M_{\mathrm{Jup}}$.

2MASS J08095903+4434216 was identified by Knapp et al. (2004) and confirmed by Chiu et al. (2006) as an L6 dwarf. In Chapter 3, we identified it as a candidate member of ARG as part of *BASS*. We used its NIR spectrum to revise its spectral type to L6 pec (red) from a visual comparison with field and low-gravity templates. This object has a red continuum and red NIR colors for its spectral type, with $J - K_S = 2.02$ and $J - W2 = 3.63$, compared with median values of $J - K_S = 1.7 \pm 0.3$ and $J - W2 = 2.9 \pm 0.4$ for field L6 dwarfs (Figure 6.11).

The low-resolution gravity classification scheme of Allers & Liu (2013) categorizes it as an intermediate-gravity L5.4 dwarf due to its H–cont, KI_J and FeH_Z indices. However, it is visually a better match to the field L6 template than the field L5 template, albeit it displays a slightly redder continuum. Adopting a spectral type of L6, only the H–cont index remains useful and categorizes it as an intermediate-gravity dwarf, but this index alone does not reject the possibility that this object is a dusty dwarf in the field. Schneider et al. (2014) demonstrated that the $H_2(K)$ index defined by Canty et al. (2013) seems to be gravity-sensitive up to at least L8; we obtain a value of $H_2(K) = 1.056 \pm 0.008$ for 2MASS J08095903+4434216, which is slightly lower than the typical values for field L6 dwarfs (1.06 ± 0.01; see Figure 6.14(d) of this work and Figure 10 of Schneider et al. 2014). It is unclear at this time if this object is a low-gravity L6 dwarf; a higher resolution ($R \gtrsim 750$) NIR spectrum will be useful to confirm if this object is a very low-mass, very late-type candidate member of ARG, or more massive and dusty field interloper. At the age of ARG (30–50 Myr), this object would have one of the lowest estimated masses amongst all YMG candidates presented here, with $8.1 \pm 0.8\,M_{\rm Jup}$. Its statistical distance associated with membership to ARG is 15.3 ± 2.0 pc.

2MASS J23512200+3010540 was discovered by Kirkpatrick et al. (2010) as L5.5 dwarf in the optical, and as an unusually red L5.5 dwarf in the NIR. In Chapter 2, we identified this object as a candidate member of ARG, and it was recovered as such in *PRE-BASS*. We used its NIR spectrum to categorize it as a peculiar L5 dwarf. Only the H–cont index is indicative of a possible young gravity; it is thus a likely scenario that this object is a dusty field interloper. Obtaining a higher-resolution spectrum would be useful to assess this. If it is a member of ARG (30–50 Myr), this object has an estimated mass of $10.0^{+0.6}_{-0.7}\,M_{\rm Jup}$ and a statistical distance of 20.5 ± 2.0 pc.

6.A.4 Interlopers from the field or other regions

2MASS J00174858-0316334 was identified as a candidate member of ABDMG as part of *PRE-BASS*. NIR spectroscopy revealed that this is a reddened low-gravity M7 β dwarf. We de-reddened its spectrum using the *fm_unred.pro* IDL routine based on the extinction law of Fitzpatrick (1999) and visually compared it with our M7 β template to determine that its

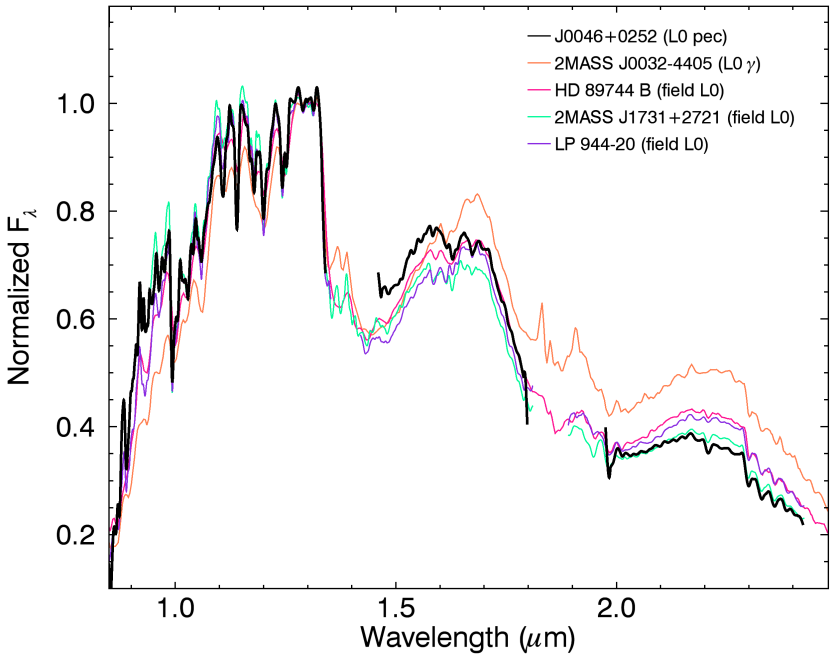

FIGURE 6.21 NIR spectrum of the peculiar L0 dwarf 2MASS J00461551+0252004 that was recovered as a candidate member of ABDMG in *PRE-BASS*. The H-band bump at 1.57 μm could be a hint of an unresolved T-type companion.

total extinction is $A(V) = 2.5$. We used the parametrization of Fitzpatrick (1999) with a total-to-selective extinction of $R(V) = 3.1$. This reddening is unlikely caused by interstellar dust, since this object is far from the galactic plane ($b = -64.8°$) and has a spectro-photometric distance of only 65.1 ± 11.5 pc (low gravity was considered in this estimate). It can be expected that this object is still embedded in its formation material, which indicates that it is not a member of ABDMG, but rather a member of another young star-forming region that might not be known. It would be interesting to investigate whether other very young objects can be found in its vicinity.

2MASS J00461551+0252004 was identified as a candidate member of ABDMG in *PRE-BASS*. NIR spectroscopy revealed that it is a peculiar L0 dwarf with no indication of low gravity. The H-band bump at 1.57 μm is significantly stronger than that of field dwarfs, which could hint at an unresolved T-type component (Figure 6.21); however, the spectral indices constructed by Bardalez Gagliuffi et al. (2014) do not categorize it as a likely L-type + T-type binary. The cause of its peculiar properties is thus unclear.

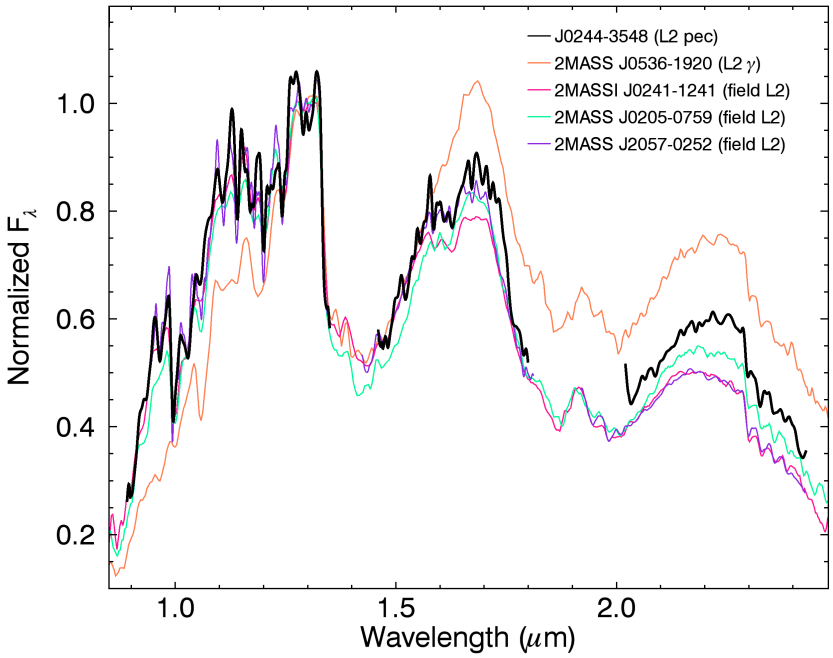

FIGURE 6.22 NIR spectrum of the peculiar L1 dwarf 2MASS J02441019–3548036 that was recovered as a candidate member of THA in *BASS*. Its NIR continuum is redder than usual and the shape of its H band is peculiar. This could be explained by a dusty atmosphere; however, this object is likely older than the YMGs considered here.

2MASS J02441019–3548036 was discovered as candidate member of THA in *BASS*. NIR spectroscopy ($R \sim 750$) reveals that it is an L2 dwarf that lacks the weaker alkali lines or stronger VO absorption that are typical of low-gravity dwarfs. However, its continuum is unusually red for an L2 dwarf and the shape of its H band is unusual (Figure 6.22). This could be explained by an unusually dusty atmosphere or an unresolved later-type companion; however, the classification of Bardalez Gagliuffi et al. (2014) based on various spectral indices does not categorize it as a candidate binary. We reject it as a candidate member of THA, as the weaker-than-usual alkali lines are not consistent with a young age even if this object is dusty or multiple.

2MASS J02530084+1652532 (Teegarden's star) was discovered by Teegarden et al. (2003) as a nearby (2.43 ± 0.54 pc) M6.5 dwarf; Henry et al. (2006) refined its distance measurement to 3.85 ± 0.01 pc. Witte et al. (2011) identified this object as a potential low-gravity dwarf from atmosphere model fitting, and we identified it as a candidate member of ARG

in Chapter 2, but its distance is not consistent with this possibility. We obtained the NIR spectrum of Burgasser et al. (2012) from the SpeX PRISM spectral library and categorized it as an M7.5 β dwarf. The classification scheme of Allers & Liu (2013) assigns it an intermediate gravity, which is consistent with our visual comparison. This is due to a low FeH_Z index (1.0699 ± 0.0040), a low KI_J index (1.0511 ± 0.0065) and a high H-cont index (0.9974 ± 0.0049) compared with field M7.5 dwarfs. This object has a relatively blue *2MASS* $J - K_S$ color (0.809 ± 0.053) for an M7.5 dwarf (Figure 6.11(a)), which is not expected for a low-gravity dwarf. We used the NIR spectrum to measure its synthetic NIR colors and obtained $J - K_S = 0.869 \pm 0.077$ (assuming a 5% uncertainty in the *2MASS* photometric zero points), which places it closer to the locus of low-gravity and field M7 dwarfs, albeit still on the blue end. Its *WISE* $W1-W2$ color (0.265 ± 0.034) is consistent with field and low-gravity M7.5 dwarfs (Figure 6.10(i)). Obtaining a higher-resolution NIR spectrum will be useful to assess whether alkali lines are weaker than usual, which would confirm if this object has a low gravity or not. Another explanation could be that this object is an unresolved binary. If Teegarden's star is young, it could be a member of a YMG that is not considered here, and it would thus be interesting to measure its RV. It is worthwhile mentioning that this object would be the nearest low-gravity dwarf if this is confirmed, a record currently held by LP 944–20 (an L0 β at 6.41 ± 0.04 pc that is a candidate member of the Castor stream; Leggett et al. 2001; Allers & Liu 2013; Dieterich et al. 2014; Barrado Y Navascués 1998).

2MASS J03140344+1603056 was identified by Schmidt et al. (2007) as an L0 dwarf with Hα emission. Seifahrt et al. (2010) measured its RV and used its kinematics to assign it as a candidate member of UMA. We initially identified this object as a low-probability candidate member of βPMG in *PRE-BASS*, but was later rejected because of its large contamination probability, as well as its position on a M_{W1} versus $H - W2$ diagram that is not consistent with young BDs at the most probable statistical distances obtained from BANYAN II. A NIR follow-up allowed us to categorize it as a peculiar M9 dwarf with no apparent sign of low gravity from the classification scheme of Allers & Liu (2013) or a visual comparison with spectroscopic standards. However, it is unclear at what exact age signs of low-gravity stop being apparent in moderate-resolution NIR spectra, and Allers & Liu (2013) suggest that

this might take place around $\sim$200 Myr. We thus reject any possible membership with the younger moving groups considered here, but our data is insufficient to corroborate its possible membership to UMA.

2MASS J04070752+1546457 has been identified as an L3.5 dwarf by Reid et al. (2008a) from optical spectroscopy. We identified this BD as an ambiguous candidate member of βPMG and COL as part of *PRE-BASS*, but we subsequently rejected it because of its alignment with TAU. NIR spectroscopy allowed us to categorize it as field L3 BD. It displays marginal signs of low-gravity (weaker FeH and slightly weaker alkali line widths); however, all other features as well as a visual comparison with spectroscopic standards are consistent with a field L3 BD. It could be interesting to investigate whether this object has a peculiar metallicity or a slightly young age ($\sim$200 to a few hundred Myrs), but it is most probably not a member of any YMG considered here.

2MASS J05243009+0640349 has been identified as a potential member of βPMG in *PRE-BASS*. It has been subsequently excluded from *BASS* because of its low Bayesian probability, but its NIR spectrum allowed us to categorize it as a low-gravity M5.5 β. The only useful sign of low gravity for this spectral type is the weaker Na I absorption. This object has a low galactic latitude ($b = -15.92°$) and is located within the Orion II super bubble (Gatley et al. 1974) at only 10.′6 of the Ori C 11 core (see Figure 12b of Wood et al. 1994; the B1950 coordinates of this object are 05h21m48.67s, +06°37′54.″5). These clouds are located at significantly larger distances ($\sim$400–500 pc; Schlafly et al. 2014) compared to the YMGs considered here. Using the absolute *2MASS* and *WISE* photometry of known young M5.5 dwarfs, we estimate a spectrophotometric distance of 42.0 ± 7.7 pc for 2MASS J05243009+0640349 and exclude a distance larger than 63 pc at a 99% confidence level, assuming it is not a multiple system. This discrepancy, supplemented with the fact that its spectrum does not seem reddened by interstellar dust, makes it unlikely that this object is a member of the Orion Molecular Complex (OMC) even though it is clearly young. Even when its youth is taken into account, this object has a very low probability of being a member of βPMG. It will be useful to obtain a distance and RV measurement to investigate whether this object is a member of another YMG that is not considered here.

2MASS J05271676+0007526 has been identified as a potential member of βPMG in *PRE-BASS*. Its low Bayesian probability as well as color filters ($H-K_S > 0.269$ and $VR-J \geq 2.63$; Chapter 2) excluded it from the *BASS* sample. This object has a low galactic latitude ($b = -18.57°$) and is located in the vicinity of the OMC (Gatley et al. 1974; Schlafly et al. 2014). Acquisition images obtained with SpeX revealed that this is a $2\farcs4$ visual binary. We obtained resolved NIR spectroscopy and determined that both components are reddened early M dwarfs. We de-reddened both spectra using the *fm_unred.pro* IDL routine based on the extinction law of Fitzpatrick (1999) and visually compared the results with NIR spectroscopic standards to determine the best matching spectral types and total extinction $A(V)$, using the parametrization of Fitzpatrick (1999) with a total-to-selective extinction of $R(V) = 3.1$. We find a best match of $A(V) = 0.93$ with spectral types M0 + M3. We note that the H-band continuum of both objects has a rounded triangular shape, which is only seen at those spectral types for very young ($\lesssim 5$ Myr) objects. This system is thus likely very young and still embedded in its formation material. Using the *2MASS J* magnitude of the unresolved system with the young absolute magnitude-spectral type sequences of Malo et al. (2013), we estimate a distance of ~ 450 pc. We conclude that this system is a probable very young low-mass star member of OMC.

2MASS J08503593+1057156 (2MASS J0850+1057) was first identified from the *2MASS* survey as an L6 BD by Kirkpatrick et al. (1999). Subsequently, Reid et al. (2001) and Bouy et al. (2008) identified and confirmed that this object is a $0\farcs16$ binary system, and Burgasser et al. (2011) used a template fitting method constrained by the flux ratio of its individual components to assign them spectral types of L7 and L6. They noted the surprising fact that the brighter primary component is the one that gets assigned a later spectral type. They argue that this could be explained either by youth or the latest-type component being an unresolved binary. Faherty et al. (2011) subsequently identified the NLTT 20346 M5+M6 binary system as a very wide (~ 7700 AU) co-moving companion to 2MASS J0850+1057. They assign an age estimate of 250–450 Myr for NLTT 20346 based on X-ray luminosity, but they note that this estimate is discrepant with that based on Hα emission (6.3 ± 1.0 Gyr and 6.5 ± 1.0 Gyr for its respective components). They measure a systemic RV of 26 ± 9 km s^{-1} for NLTT 20346, and a

trigonometric distance of 29 ± 7 pc for 2MASS J0850+1057. They note that this latter measurement is not precise enough to discriminate between two previous inconsistent measurements in the literature (38 ± 6 pc from Vrba et al. 2004 and 25.6 ± 2.3 pc from Dahn et al. 2002). Using their proper motion measurement of $\mu_\alpha = -144 \pm 6\,\mathrm{mas\,yr^{-1}}$and $\mu_\delta = -38 \pm 6\,\mathrm{mas\,yr^{-1}}$, they argued that a faint background contaminant was blended at the epochs used for previous distance measurements, which could explain the discrepancy.

Dupuy & Liu (2012) independently measured a proper motion of $-144.2 \pm 0.6\,\mathrm{mas\,yr^{-1}}$, $\mu_\delta = -12.6 \pm 0.6\,\mathrm{mas\,yr^{-1}}$ and a distance of 33.2 ± 0.9 pc for 2MASS J0850+1057. They also refined the photometry of its resolved components, and used these new measurements to draw different conclusions than those outlined above. First, they used a similar analysis to that of Burgasser et al. (2011) with their updated photometry to argue that the spectral types of the components are rather L6.5 $\pm$1 and L8.5 $\pm$1, with the fainter component now associated with the later spectral type. This conclusion does away with the need to invoke youth or any additional component, which was previously based on flux reversal (Burgasser et al. 2011). They thus argued that 2MASS J0850+1057 is a BD system displaying no notable peculiarity. Furthermore, they use their new proper motion measurement at 6.7σ from that of NLTT 20346 with the criterion of Lépine & Bongiorno (2007) to argue that the two systems are likely random alignments, and thus not gravitationally linked.

We measure a proper motion of $-141.1 \pm 7.7\,\mathrm{mas\,yr^{-1}}$ and $\mu_\delta = -13.1 \pm 9.5\,\mathrm{mas\,yr^{-1}}$, based on *2MASS* and *ALLWISE*. The μ_α component is consistent with both measurements, whereas the μ_δ component is at 2.2σ and 0.05σ respectively from the measurements of Faherty et al. (2011) and Dupuy & Liu (2012). Our measurement thus favors the later one, but our precision is $\sim$ 16 times lower. We find that even if both components seem to display no peculiarity in their relative fluxes, the unresolved system seems to be unusually red for its absolute magnitude (Figure 6.23). This could be explained either by additional unresolved later-type components, or the presence of thicker/higher clouds in their atmosphere compared to field BDs. We used the $R \sim 120$ NIR spectrum for the unresolved BD system to assign a spectral type of L7. For such a late spectral type, the only features known to be gravity-sensitive in a low-resolution NIR spectrum are the H-cont index of Allers & Liu (2013)

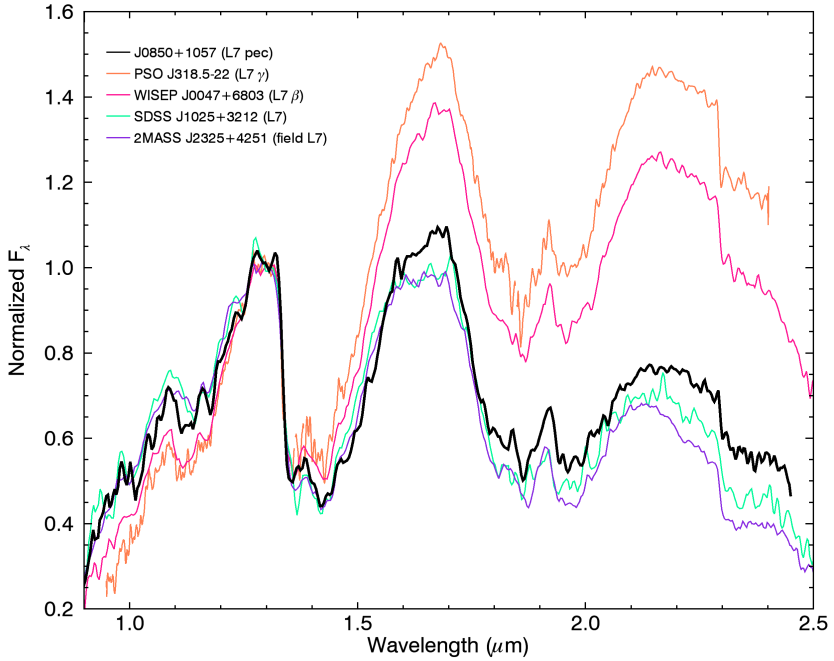

FIGURE 6.23 NIR spectrum of the peculiar L7 dwarf 2MASS J0850+1057 that was recovered as a candidate member of ARG in *BASS*. This system is a binary with resolved spectral types of L6.5 ±1 and L8.5 ±1 estimated from photometry. The NIR continuum of 2MASS J0850+1057 is redder than field L7 dwarfs which is likely an effect of its binary nature, and its kinematics are not consistent with those of ARG.

and the $H_2(K)$ index of Canty et al. (2013). We find values of H-cont $= 0.872 \pm 0.025$ and $H_2(K) = 1.055 \pm 0.014$, both being only marginally consistent with a low surface gravity. The parallax and proper motion measurements of Dupuy & Liu (2012) preclude a possible membership to ARG; however, obtaining a higher-resolution NIR spectrum for this system would be interesting to assess whether it displays signs of low surface gravity. If this system is younger than $\sim$200 Myr, the individual mass of each component would be well below the deuterium burning limit, which would make it a remarkable benchmark system to understand the properties of planetary-mass objects.

2MASS J08575849+5708514 has been discovered by Geballe et al. (2002) as an L8 ±1 BD. Stephens et al. (2009) used atmosphere model fitting to determine that this object is unusually cloudy and seems to have a low surface gravity ($\log g = 4.5$). Using our visual comparison with spectral templates, we categorize this object as a peculiar L8 dwarf (Figure 6.24). No indices from Allers & Liu (2013) are gravity-sensitive for such a late spectral

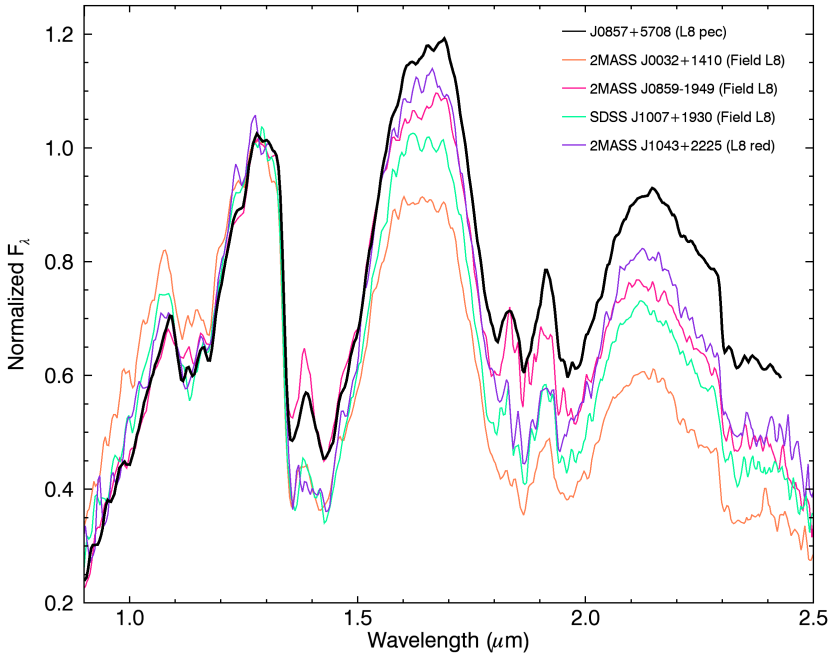

FIGURE 6.24 NIR spectrum of the peculiar L8 dwarf 2MASS J08575849+5708514 that was recovered as a candidate member of ARG in *BASS*. Its red NIR continuum could be an indication of a low surface gravity, but an RV measurement that was obtained from low-S/N data is not consistent with membership to ARG.

type, but the $H_2(K)$ index defined by Canty et al. (2013) seem to remain useful (Schneider et al. 2014). We find a weaker $H_2(K)$ value (1.102 ± 0.006) compared with typical field L8 dwarfs (1.12 ± 0.02), which could be an indication of a lower surface gravity. We identified this object as a highly probable candidate member of ARG in *BASS*, with an estimated mass of $8.5 \pm 0.8\,M_{\rm Jup}$ and an estimated distance of 8.9 ± 1.2 pc. However, Schmidt et al. (2010) measured an RV of -123.5 ± 20.0 km s^{-1}, which is not consistent with membership to ARG or even with the kinematics of any young BD in the solar neighborhood. This large RV thus seems contradictory with its unusually red colors and tentative indications of a lower surface gravity, but it was measured from a low-signal optical spectrum. It is likely that this object is not a young member of ARG but rather an interloping cloudy object from the field. However, obtaining an RV measurement from higher-S/N data will be useful to assess this.

2MASS J11335700–7807240 was identified by Luhman (2007) in the optical as an M8 dwarf in a search for new members of the Chamaeleon I (CHA) star-forming region. They

rejected it because it lacks low-gravity indications in its optical spectrum. We independently recovered this object in *PRE-BASS* as a candidate member of CAR and obtained a NIR spectrum. We categorize this object as a peculiar M6±1 dwarf; its H band is more triangular and the slope of its K band is bluer. This could be indicative of a low surface gravity, but it lacks all the other usual signatures: only the 1.253 μm K I line is slightly weaker than that of field M6 dwarfs. All other K I lines, the Na I doublet and FeH absorption are all consistent with a field M6 dwarf : the classification scheme of Allers & Liu (2013) thus categorizes this object as a field-gravity M6 dwarf. It is unclear what is the source of the peculiar features in this object's NIR spectrum. It is possible that the triangular-shaped H band could be caused by dust in its photosphere (Allers & Liu 2013), but this would be unusual at such an early spectral type, and neither its $J - K_S$ color (1.01 ± 0.04) or its $J - W2$ color (1.53 ± 0.04) are redder than those of field M6 dwarfs, which would be unexpected for a dusty object. We thus categorize this object as a peculiar M6 dwarf and reject it as a candidate member of CAR.

2MASS J11555389+0559577 was discovered by Knapp et al. (2004) as an L7.5 dwarf using NIR spectroscopy. We recovered this object in *PRE-BASS* as a candidate member of ARG. Faherty et al. (2012) measured a trigonometric distance of 17.27 ± 3.04 pc and Schmidt et al. (2010) used a low-quality optical spectrum from SDSS to categorize it as an L0 dwarf and measure an RV of $136.8 \pm 20.0\,\mathrm{km\,s^{-1}}$. If we include only the trigonometric measurement, it remains a modest candidate of ARG; however, the RV measurement is not consistent with this, nor with the kinematics of nearby, young dwarfs (Faherty et al. 2009), much like the case of 2MASS J08575849+5708514. We retrieved the NIR spectrum of this object from the SpeX PRISM Libraries and categorize it as a peculiar L6–L8 dwarf. It lacks the triangular-shaped H-band continuum that would be expected for a young object (H-cont $= 0.8230 \pm 0.0087$), and its NIR colors are consistent with those of field dwarfs. We measured the gravity-sensitive $H_2(K)$ index defined by Canty et al. (2013) and find a value of 1.0862 ± 0.0085, which is consistent with field L6–L7 dwarfs (Schneider et al. 2014). Higher-resolution NIR spectroscopy as well as an RV measurement derived from a high signal-to-noise spectrum would be needed to completely rule out low gravity, but it is very likely that this object is a regular BD; we thus reject it as a candidate member of ARG.

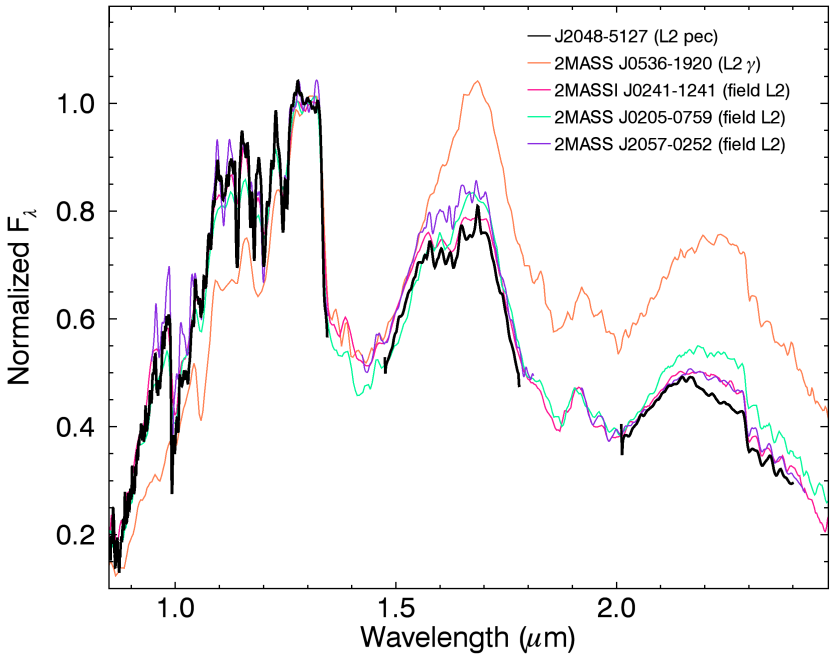

FIGURE 6.25 NIR spectrum of the peculiar L2 dwarf 2MASS J20484222–5127435 that was recovered as a candidate member of THA in *BASS*. It lacks indications of a low surface gravity and is thus not a likely member of THA. Its K band is peculiar, as it resembles those of later-type L dwarfs.

2MASS J20484222–5127435 was identified as a candidate member of THA as part of *BASS*. NIR spectroscopy revealed that its J and H bands are similar to a field L2 dwarf, but its K band is significantly different, and similar to the K band of field L5 dwarfs (Figure 6.25). This object is thus unlikely young and we reject it as a candidate member of THA; however, it is unclear what is the cause of its peculiar K band. It would be worthwhile investigating whether this is an early-L / mid-L binary from high-resolution imaging or an RV follow-up.

2MASS J22062157–6116284 has been identified as a candidate member of THA in *PRE-BASS*. We obtained NIR spectroscopy and categorized it as a peculiar L0 ±1 dwarf because its H-band flux at $\sim 1.57\,\mu$m is stronger than usual (Figure 6.26). This could indicate the presence of an unresolved T-type component; however, the index-based scheme of Bardalez Gagliuffi et al. (2014) indicates that this scenario is unlikely.

2MASS J23155665–4747315 has been identified as a candidate member of THA in *BASS*. We obtained NIR spectroscopy and categorized it as a peculiar L3 dwarf; its J band

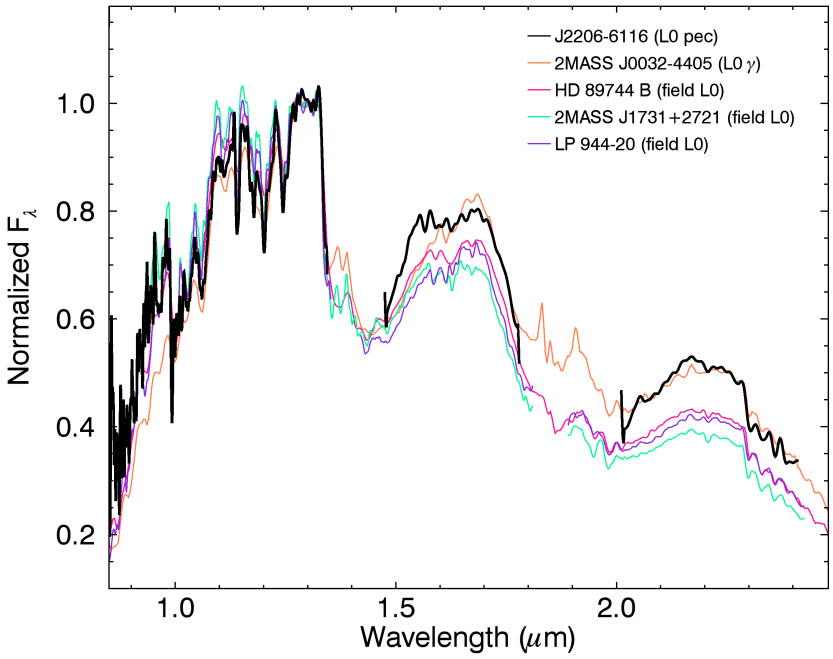

FIGURE 6.26 NIR spectrum of the peculiar L2 dwarf 2MASS J22062157–6116284 that was recovered as a candidate member of THA in *PRE-BASS*. It lacks indications of a low surface gravity and is thus not a likely member of THA. Furthermore, its H-band bump at $\sim 1.57\,\mu$m is stronger than usual.

is similar to an L3 dwarf albeit with stronger FeH absorption, and its H and K bands are similar to our field L5 template (Figure 6.27).

2MASS J23310161–0406193 (Koenigstuhl 3 BC) was discovered by Gizis et al. (2000) as an M9 dwarf in the optical, and Gizis et al. (2003) demonstrated that it is an M8 + L3, $0\farcs58$ binary system. Caballero (2007) discovered that this system is a very wide $451\farcs8$ comoving system to the F8 star HR 8931 (HD 221356). Koenigstuhl 3 BC was identified as a candidate member of ABDMG in *LP-BASS*, but measurements of RV and distance for the co-moving star HR 8931 ($-12.86 \pm 0.09\,\mathrm{km\,s^{-1}}$ and $26.12 \pm 0.37\,\mathrm{pc}$; Nidever et al. 2002; van Leeuwen 2007b) preclude a possible membership to all YMGs considered here. We categorize its unresolved spectrum as a peculiar M8 dwarf; our best-matching NIR template is M8 γ, however it presents several differences with it and lacks several low-gravity indications such as weaker alkali lines. We thus conclude that the peculiar nature of this spectrum is likely related to its binary nature, which further rules out a possible membership to ABDMG.

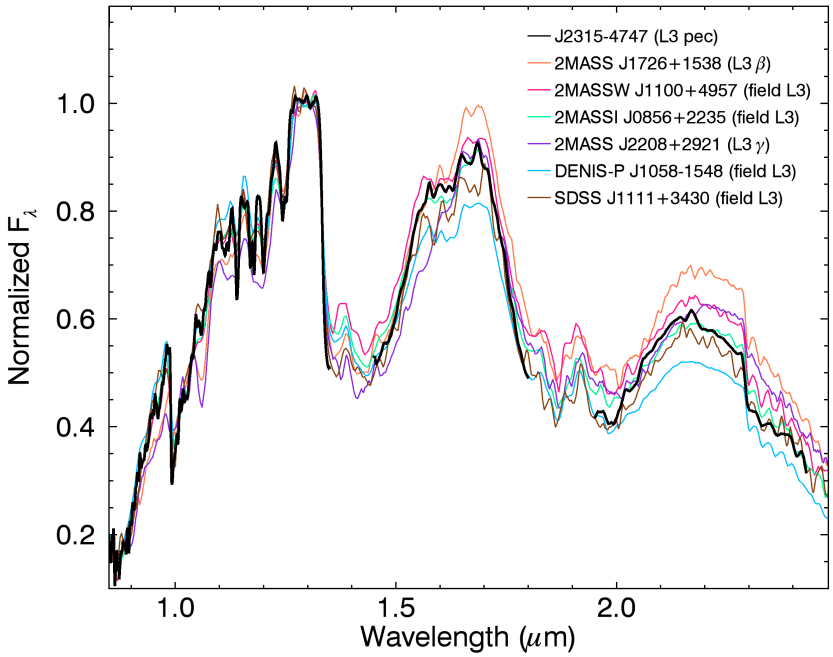

FIGURE 6.27 NIR spectrum of the peculiar L3 dwarf 2MASS J23155665–4747315 that was recovered as a candidate member of THA in *BASS*. It lacks indications of a low surface gravity and is thus not a likely member of THA. Its J band is similar to a field L3 dwarf with stronger FeH absorption, and its H and K bands are consistent with a later spectral type.

2MASS J23392527+3507165 has been discovered as an L3.5 BD in the optical by Reid et al. (2008a), and Burgasser et al. (2010) categorized it as an L4.5 BD in the NIR. We recovered this object as a candidate member of βPMG in *BASS*. We used its NIR spectral type to categorize it as a peculiar L4 BD that has a stronger H-band peak at $\sim 1.57\,\mu$m (Figure 6.28). However, it is unlikely that this object is young as it lacks the usual low-gravity indications. We thus reject it as a candidate member of βPMG. The peculiar H-band feature described above can be an effect of an unresolved T-type companion; however, the index-based scheme of Bardalez Gagliuffi et al. (2014) indicates that this scenario is unlikely.

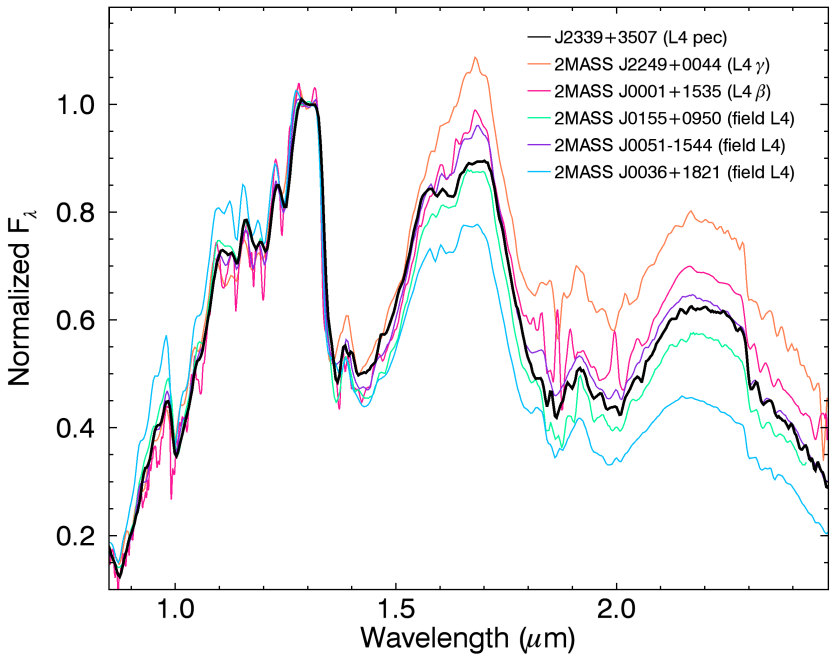

FIGURE 6.28 NIR spectrum of the peculiar L4 dwarf 2MASS J23392527+3507165 that was recovered as a candidate member of βPMG in *BASS*. It lacks indications of a low surface gravity and is thus not a likely member of βPMG. Furthermore, its H-band bump at $\sim 1.57\,\mu$m is stronger than usual.

Chapitre 7

Conclusion (*Français*)

Les travaux de cette thèse sont concentrés sur l'identification et la caractérisation de la population des naines brunes et étoiles de faible masse membres des associations cinématiques jeunes (AJs) du voisinage solaire. L'intérêt principal de ces travaux porte sur l'identification de naines brunes jeunes dont la masse et les propriétés physiques s'apparentent à celles des exoplanètes géantes gazeuses détectées principalement par l'imagerie directe à haute gamme dynamique. Ils visent aussi à identifier la population aux faibles masses des AJs afin de permettre une éventuelle caractérisation détaillée de leur fonction de masse initiale (FMI) aux masses substellaires.

7.1 L'outil BANYAN II

La première partie de cette thèse a été dédiée au développement d'un algorithme permettant d'identifier les candidates membres d'AJs aux très faibles masses ($\lesssim 0.11\,M_{\odot}$ ou $\lesssim 115\,M_{\rm Jup}$) correspondant aux types spectraux M5 ou plus tardifs. Cet algorithme, nommé BANYAN II, prend en entrée plusieurs observables dont la position céleste, le mouvement propre et les magnitudes infrarouges dans les bandes J, H, K_S, $W1$ et $W2$. Celui-ci compare alors les coordonnées $XYZUVW$ de l'objet avec les AJs du voisinage solaire et avec un modèle des étoiles du champ dans la Galaxie en supposant un ensemble de distances et vitesses radiales. Cette comparaison est effectuée par inférence bayésienne et résulte en une distribution de densité de probabilités pour chaque hypothèse, en fonction de la vitesse radiale

et de la distance. Ces deux paramètres, lorsqu'inconnus, sont alors marginalisés en intégrant la distribution de densité de probabilités sur tout le domaine, afin d'obtenir une probabilité d'appartenance à chacune des hypothèses.

Cet outil, inspiré de BANYAN I (Malo et al. 2013, 2014a), inclut plusieurs modifications et améliorations importantes. En particulier, deux diagrammes couleur–magnitude en longueurs d'onde infrarouges sont utilisés pour cibler les objets jeunes aux couleurs très rouges, une conséquence des nuages de poussière plus épais dans leur haute atmosphère. En comparaison, BANYAN I utilisait un seul diagramme couleur–magnitude dans les longueurs d'onde visibles et proche-infrarouges, limitant ainsi son utilisation aux objets de types spectraux plus précoces que M5. De plus, les modèles spatiaux (XYZ) et cinématiques (UVW) décrivant les AJs ont été rendus plus généraux en les décrivant par des ellipsoïdes gaussiennes dont les axes principaux peuvent tourner librement dans l'espace. Finalement, les probabilités *a priori* utilisées dans le théorème de Bayes ont été rendues plus réalistes, et une analyse extensive du taux de faux-positifs et de faux-négatifs a été effectuée via une méthode Monte Carlo. Avant d'établir les modèles cinématiques d'AJs utilisés dans notre analyse, nous avons mis à jour la compilation des membres des AJs du voisinage solaire présentée par Malo et al. (2013), en y ajoutant 16 nouveaux membres identifiés par Shkolnik et al. (2012) et Weinberger et al. (2013a).

Nous avons utilisé BANYAN II pour identifier 25 nouvelles candidates $\geq$ M5 aux AJs du voisinage solaire parmi une liste de 158 naines brunes et étoiles de faible masse jeunes connues dans la littérature. L'une de ces prédictions a depuis été confirmée par une autre équipe via la mesures de vitesse radiale et parallaxe d'une candidate (Gizis et al. 2015). Un suivi similaire est en cours pour plusieurs autres candidates (J. K. Faherty et al., en préparation). Nous avons mis l'outil BANYAN II à disposition du public via une page web[1], laquelle a été visitée à plus de 4 000 reprises par des utilisateurs de 23 pays à ce jour.

[1] http://www.astro.umontreal.ca/~gagne/banyanII.php

7.2 Le sondage BASS

Forts de l'outil BANYAN II, nous avons ensuite initié le sondage *BANYAN All-Sky Survey* (BASS), lequel a permis d'identifier 228 nouvelles candidates membres d'AJs du voisinage solaire de types spectraux M4–L6. Dans un premier temps, nous avons dressé une liste de 98 970 objets potentiellement plus tardifs que M4 du voisinage solaire et mesuré leur mouvement propre à l'aide d'une corrélation croisée des catalogues 2MASS et WISE. Nous avons validé notre méthode en corrélant ces 228 candidates avec les informations disponibles dans la littérature, ce qui nous a permis de rejeter ou confirmer certaines candidates ainsi que d'estimer un taux de faux-positifs de 13%. Cette analyse nous a permis d'identifier le système 2MASS J01033563–5515561 (AB)b comme nouveau membre bona fide de l'association Tucana-Horologium. Ce système comprend une étoile binaire de type spectral M5+M5 et un compagnon de 12–14 $M_{\rm Jup}$ à une séparation orbitale projetée de $\sim$84 AU.

Le sondage BASS nous a permis de dresser une liste de 275 candidates additionnelles dont les couleurs proche-infrarouges sont seulement marginalement plus rouges que la séquence à l'âge du champ (le catalogue *Low-Priority BASS*, ou LP-BASS, présenté en détail à l'Annexe 3.B). Il est attendu que cette liste contienne également des membres réels d'AJs, cependant son taux de faux-positif est plus haut et estimé à 26%.

Nous avons utilisé cet ensemble de nouvelles candidates membres d'AJs pour identifier les premiers signes de ségrégation de masse (voir Section 1.1.4) dans les associations AB Doradus, Tucana-Horologium et Columba. Pour ce faire, nous avons utilisé la méthode des *Minimum Spanning Trees* (MSTs; Borůvka 1926; Barrow et al. 1985; Cartwright & Whitworth 2004; Allison et al. 2009b), celle-ci ayant déjà été appliquée avec succès pour mesurer la ségrégation de masse dans les amas ouverts (p.ex., Allison et al. 2009a; Hasan & Hasan 2011; Olczak et al. 2011; Pang et al. 2013), mais jamais dans le cas des AJs du voisinage solaire.

Le sondage BASS inclut aussi une liste de 98 970 objets potentiellement plus tardifs que M4 du voisinage solaire qui ont servi d'échantillon de départ. Cette liste sera particulièrement utile pour la recherche d'exoplanètes autour d'étoiles M tardives via la vélocimétrie infrarouge de haute précision et la méthode du transit, notamment pour la mission *Transiting Exoplanet Survey Satellite* (TESS) qui sondera plus de 500 000 étoiles distribuées sur toute la sphère

céleste. De plus, cet échantillon sera utile pour la recherche de nouvelles naines brunes vieilles du voisinage solaire.

7.3 La découverte et la caractérisation de nouvelles naines brunes jeunes

La troisième partie de la thèse (Chapitre 6) a porté sur le suivi spectroscopique proche-infrarouge de 240 membres candidates membres d'AJs du voisinage solaire identifiées dans le cadre de cette thèse. Ces candidates proviennent à la fois des catalogues BASS, LP-BASS et de versions préliminaires du catalogue BASS. Ce suivi nous a permis d'identifier 110 nouvelles étoiles de faible masse et naines brunes jeunes de types spectraux M5–L5, lesquelles sont probablement membres des associations en question. Ces nouvelles découvertes nous ont permis de définir pour la première fois des spectres de référence pour les types spectraux L3 β, L4 β et L5 β, lesquels sont ancrés dans la classification en longueurs d'onde visibles définie par Kirkpatrick et al. (2008); Cruz et al. (2009), tout en étant cohérents avec la méthode décrite par Allers & Liu (2013). Ces découvertes nous ont permis de préciser le taux de faux-positifs de l'échantillon BASS à 20%, ce qui est légèrement plus élevé que la première estimation présentée au Chapitre 3 (13%), mais qui représente un grand progrès par rapport aux méthodes précédentes. Avant la publication de cet article, seulement 66 candidates membres d'AJs de types spectraux $\geq$ M5 étaient connues (Song et al. 2003; Allers et al. 2009; Looper et al. 2007a; Riedel et al. 2014; Gizis 2002; Mamajek 2005; Looper et al. 2010a; Reiners & Basri 2009; Teixeira et al. 2009; Bowler et al. 2013; Shkolnik et al. 2012; Kirkpatrick et al. 2010; Schlieder et al. 2012a, 2010, 2012b; Malo et al. 2013; Rodriguez et al. 2013; Liu et al. 2013b; Rice et al. 2010; Kraus et al. 2014b; Naud et al. 2014), en plus de 28 provenant d'articles présentés dans le cadre de cette thèse (Chapitres 2, 4 et 5). Nos observations ont donc plus que doublé le nombre de candidats membres d'AJs de types spectraux M5 ou plus tardifs précédemment identifiés.

Nous avons utilisé ce nouvel échantillon d'objets jeunes, complémenté de 41 objets jeunes connus dans la littérature, pour construire de nouvelles séquences dans 16 diagrammes de

type spectral–magnitude absolue et couleur–magnitude absolue. Nous avons ensuite comparé nos observations aux modèles théoriques d'évolution et d'atmosphère afin de mettre en lumière leurs limitations actuelles. En particulier, nous confirmons que les modèles d'atmosphère reproduisant le mieux les distributions d'énergie spectrale des naines brunes jeunes sont systématiquement plus froids que dans le cas des naines brunes vieilles, à un type spectral donné. Cet effet avait déjà été démontré dans le cas de la naine brune jeune HD 203030 B (Metchev & Hillenbrand 2006) et des exoplanètes géantes gazeuses TWA 27 b (Barman et al. 2011b) et HR 8799 b (Barman et al. 2011a).

Finalement, nous discutons du fait que nous avons identifié un nombre surprenant (12) de nouvelles candidates jeunes à l'association Tucana-Horologium situées à moins de 50 pc et dont la masse estimée se trouve dans l'intervalle 12.5–14 $M_{\rm Jup}$. Nous avons ainsi identifié $36.4^{+16.6}_{-12.5}$ fois plus d'objets dans cet intervalle de masses que les prédictions basées sur une FMI typique et sur la population d'étoiles massives dans Tucana-Horologium. Cette nouvelle population aux faibles masses correspond à une naine brune de 12.5–14 $M_{\rm Jup}$ pour chaque $17.5^{+6.6}_{-5.0}$ étoiles sur la séquence principale dans Tucana-Horologium. Il reste à déterminer si cette sur-population est limitée à cette association seulement, ou si elle trahit les premiers signes d'une remontée dans la FMI qui pourrait correspondre à une populations d'exoplanètes géantes éjectées de leur système en jeune âge (voir Sumi et al. 2011).

7.4 La connection entre les naines brunes et les exoplanètes géantes – Perspectives futures

Les travaux effectués au sein de cette thèse nous ont permis d'identifier un nombre significatif de nouvelles naines brunes jeunes. En connaissant l'âge de celles-ci via leur appartenance aux AJs, nous avons pu estimer leur masse et constater que certaines d'entre elles ont une masse inférieure à 13 $M_{\rm Jup}$. Leur masse et température étant similaires à celles des exoplanètes géantes gazeuses, elles seront utiles en tant que références pour comprendre les processus atmosphériques en jeu chez ces dernières. L'étude du système planétaire HR 8799 (Marois et al. 2008) a permis de montrer que les atmosphères d'exoplanètes géantes possèdent dans leur

haute atmosphère des nuages beaucoup plus épais que celles des naines brunes du champ de même température (Currie et al. 2011). Cette propriété est aussi partagée par les naines brunes jeunes, ce qui renforce l'interprétation selon laquelle les naines brunes jeunes sont similaires aux exoplanètes géantes.

Il sera donc intéressant d'étudier davantage la population des naines brunes jeunes pour mieux comprendre les exoplanètes géantes. Par exemple, les atmosphères d'exoplanètes géantes très froides ($T < 1500\,\mathrm{K}$) sont encore très mal connues (Naud et al. 2014). Une prolongation logique de cette thèse sera donc de rechercher les naines brunes de type spectral $>$ T0 membres d'AJs. Nous savons que les propriétés des naines brunes du champ changent de façon drastique à ces températures, étant donné que leurs nuages plongent sous la photosphère. Ce dégagement des nuages dans la photosphère est visible par les couleurs proche-infrarouges $J - K$ graduellement plus bleues aux basses températures (Figure 7.1).

Il est probable que le même phénomène se produise dans le cas des exoplanètes géantes très froides, cependant celles-ci sont très peu lumineuses en comparaison avec leur étoile-hôte très brillante et la technologie actuelle ne nous permet pas de les étudier à cause du grand contraste lumineux en jeu. Il serait cependant déjà possible d'effectuer une telle étude via les naines brunes jeunes, cependant nous ne connaissons encore que quelques naines brunes de type spectral T qui sont potentiellement jeunes (Delorme et al. 2012; Naud et al. 2014). Nous présentons à la Figure 7.1 un ensemble préliminaire de candidates membres d'AJs de type spectral $>$ T0 (cercles bleus), identifiées par une méthode semblable à celle employée au sein de ce projet (Section 3.3), mais en utilisant cette fois des contraintes de couleur et qualité photométrique moins strictes. Ces candidates ne sont pas encore confirmées spectroscopiquement, cependant nous pouvons déjà remarquer une possible transition aux couleurs $J - K$ plus bleues.

À la suite de cette thèse, nous entreprendrons ainsi un suivi des naines brunes jeunes très froides de type spectral T. Comme mentionné ci-haut, ceci nous permettra de mieux comprendre les atmosphères des exoplanètes géantes plus froides, mais les retombées scientifiques potentielles ne s'arrêtent pas là. La découverte de ces objets nous permettra de confirmer ou infirmer les résultats récents comme quoi la densité spatiale des naines brunes de masse

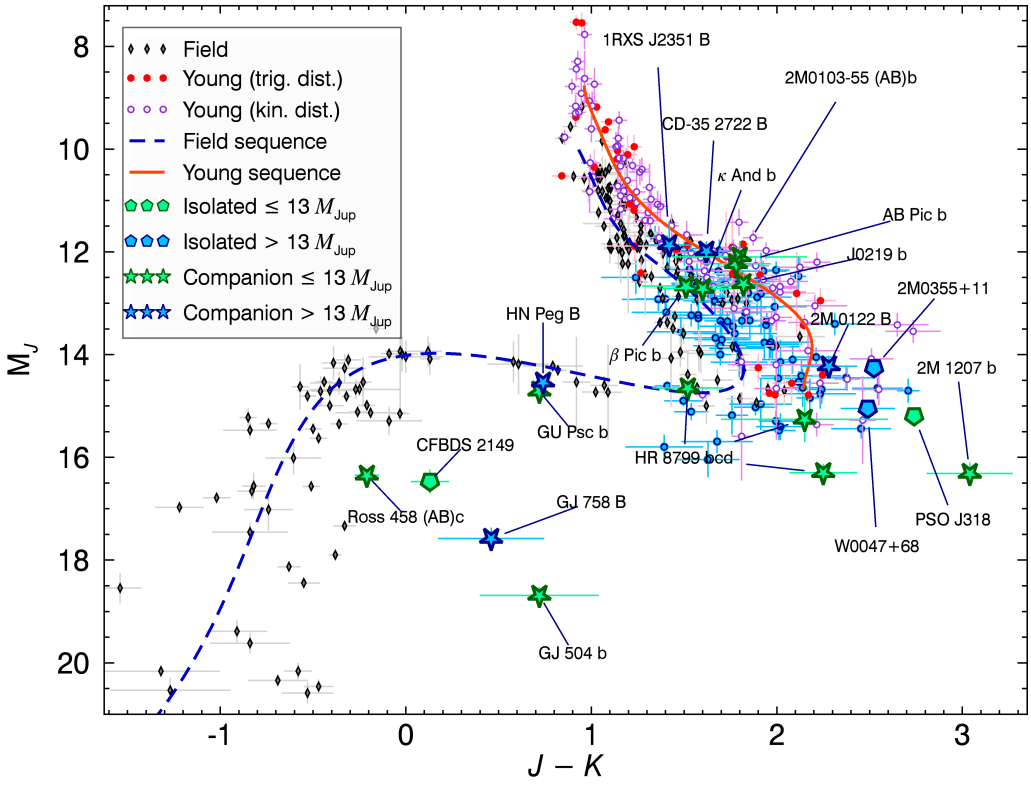

FIGURE 7.1 Séquence couleur–magnitude proche-infrarouge pour les étoiles de faible masse et naines brunes du champ (losanges noirs) et les naines brunes jeunes (points rouges et cercles mauves). Les étoiles bleues et vertes indiquent indiquent plusieurs compagnons connus de masses sub-stellaires ou planétaires, respectivement. Les pentagones bleus et verts indiquent plusieurs naines brunes et objets de masses planétaires isolés, respectivement. Cette figure suit le même format que la Figure 6.13, mais on y a ajouté plusieurs candidates de type spectral T identifiées pour la suite de ce projet (petits cercles bleus). On peut remarquer que ces candidates suivent la tendance attendue, correspondant à des couleurs graduellement plus bleues (vers la gauche) pour les objets les plus froids (et donc les moins brillants).

planétaire pourrait être significativement plus grande que prévu (Sumi et al. 2011). Plus généralement, nous pourrons potentiellement amener des éléments de réponse à une question fondamentale de l'astrophysique : les naines brunes isolées de masse planétaire se sont-elles toutes formées de la même façon que les naines brunes plus massives, ou certaines d'entre elles sont-elles en réalité des exoplanètes géantes errantes, éjectées de leur système stellaire peu après leur formation ?

Plusieurs projets futurs de l'astrophysique nous permettront de pousser encore plus loin les recherches présentées au sein de cette thèse. Parmi ceux-ci, la mission GAIA (Perryman et al. 2001) mesurera la parallaxe, le mouvement propre et la vitesse radiale d'un milliard d'étoiles. Le *Large Synoptic Survey Telescope* (LSST; Krabbendam et al. 2012) effectuera pour sa part un sondage de l'entièreté de l'hémisphère sud à chaque quelques jours. La quantité phénoménale de nouvelles données que GAIA et LSST nous apporteront nous permettra de révolutionner notre compréhension des associations cinématiques jeunes, notamment en les combinant avec l'efficacité de l'outil BANYAN.

L'instrument SPIRou (*Spectro-Polarimètre InfraRouge*; Delfosse et al. 2013), le *James Webb Space Telescope* (JWST; Gardner et al. 2006), le *Thirty Meter Telescope* (TMT; Nelson & Sanders 2008), le *European Extremely Large Telescope* (EELT; Gilmozzi & Spyromilio 2008) et le *Giant Magellan Telescope* (GMT; Johns et al. 2014) permettront une caractérisation sans précédent des naines brunes jeunes de masse planétaire découvertes au sein de cette thèse, notamment par leur sensitivité décuplée et leur large couverture spectrale. Les observations qui seront rendues possibles par ces nouvelles technologies avanceront significativement nos connaissances sur les propriétés et les procédés physiques en jeu dans l'atmosphère des exoplanètes géantes gazeuses. Ces observations permettront aussi de jeter plus de lumière sur les mécanismes de formation stellaire et planétaire.

Chapitre 8

Conclusion (*English*)

The work presented in this thesis focuses on identifying and characterizing the population of brown dwarfs and low-mass stars members of young moving groups (YMGs) in the solar neighborhood. The principal interest of this work is the identification of young brown dwarfs whose mass and physical properties are similar to those of the gaseous giant exoplanets detected with high contrast direct-imaging methods. It also aims at identifying the low-mass population of YMGs, which will allow for a detailed characterization of their initial mass function (IMF) in the substellar regime.

8.1 The BANYAN II tool

The first part of this thesis was dedicated to developing an algorithm that allows for the identification of very low-mass ($\lesssim 0.11\,M_{\odot}$ or $\lesssim 115\,M_{\rm Jup}$) candidate members of YMGs, corresponding to spectral types M5 or later. This algorithm, named BANYAN II, takes several observables as inputs, including celestial coordinates, proper motion and near-infrared magnitudes in the J, H, K_S, $W1$ and $W2$ bands. It then compares the $XYZUVW$ coordinates of an object with spatial and kinematic models of YMGs in the solar neighborhood and a field model of the Galaxy by assuming a series of distances and radial velocities. This comparison is performed using bayesian inference and results in a probability density distribution for every hypothesis as a function of distance and radial velocity. These two parameters, when unknown, are then marginalized by integrating the probability density distribution over the

full domain, thus yielding a membership probability for every YMG and the field.

This tool, inspired from BANYAN I (Malo et al. 2013, 2014a), includes several modifications and important improvements. In particular, two color–magnitude diagrams in near-infrared wavelengths are used to target young objects with unusually red colors, a consequence of the thicker dust clouds in their high atmospheres. In comparison, BANYAN I used one color–magnitude diagram in visible and near-infrared wavelengths, limiting its use to objects with spectral types earlier than M5. Furthermore, the spatial (XYZ) and kinematic (UVW) models describing YMGs were made more general by describing them with gaussian ellipsoids whose axes can freely rotate in space. Finally, the prior probabilities used in Bayes' theorem were made more realistic, and extensive false-positive and false-negative analyses were carried out with a Monte Carlo method. Before establishing the updated spatial and kinematic YMG models used in our analysis, we updated the compilation of bona fide members of YMGs in the solar neighborhood that was presented by Malo et al. (2013), by complementing it with 16 new members identified by Shkolnik et al. (2012) and Weinberger et al. (2013a).

We used BANYAN II to identify 25 new $\geq$M5 candidate members of YMGs in the solar neighborhood among a list of 158 known young low-mass stars and brown dwarfs from the literature. One of these membership predictions has already been confirmed by another team through the measurement of the candidate's radial velocity and trigonometric distance (Gizis et al. 2015). A similar follow-up is ongoing for several other candidates (J. K. Faherty et al., in preparation). We made the BANYAN II tool available to the community on a web page [1], which received more than 4 000 unique visits by users from 23 countries to this day.

8.2 The BASS survey

Equipped with the BANYAN II tool, we have then initiated the *BANYAN All-Sky Survey* (BASS), which allowed us to identify 228 new candidate members of YMGs in the solar neighborhood with spectral types in the M4–L6 range. In a first step, we have set up a list of 98 870 objects with spectral types potentially later than M4 in the solar neighborhood, and measured their proper motion from a cross-match of the 2MASS and WISE catalogs. We have

[1] http://www.astro.umontreal.ca/~gagne/banyanII.php

validated our method by cross-matching these 228 candidates with information available in the literature, which has allowed us to confirm or reject several candidates, as well as estimate a false-positive rate of 13%. This analysis has allowed us to identify the 2MASS J01033563–5515561 (AB)b system as a new bona fide member of the Tucana-Horologium association. This system includes a binary M5+M5 star and a 12–14 $M_{\rm Jup}$ companion at a projected orbital separation of $\sim$84 AU.

The BASS survey has allowed us to set up a list of 275 additional candidates whose near-infrared colors are only marginally redder than the field sequence (this constitutes the *Low-Priority BASS*, or LP-BASS, which is presented in detail in Annex 3.B). It is expected that this list includes several real members of YMGs, however its false-positive rate is estimated to be higher, at 26%.

We used this set of new YMG candidate members to identify the first signs of mass segregation (Section 1.1.4) in the AB Doradus, Tucana-Horologium and Columba associations. To achieve this, we have used the method of *Minimum Spanning Trees* (MSTs; Borůvka 1926; Barrow et al. 1985; Cartwright & Whitworth 2004; Allison et al. 2009b), which had already been successfully applied to measure mass segregation in several open clusters (e.g., Allison et al. 2009a; Hasan & Hasan 2011; Olczak et al. 2011; Pang et al. 2013), but was never before used on YMGs of the solar neighborhood.

The BASS survey also includes a list of 98 970 objects in the solar neighborhood with spectral types potentially later than M4, which served as our input sample. This list will be particularly useful for the search of exoplanets around late M dwarfs with high precision near-infrared radial velocity measurements and the method of transits, in particular with the *Transiting Exoplanet Survey Satellite* (TESS) mission that will survey more than 500 000 stars distributed on the whole Celestial sphere. Furthermore, this sample will be useful to search for new field brown dwarfs in the solar neighborhood.

8.3 The discovery and characterization of new young brown dwarfs

The third part of this thesis (Chapter 6) focused on a near-infrared spectroscopic follow-up of 240 candidate members of YMGs in the solar neighborhood that were identified as part of this thesis. These candidate members come both from the BASS and LP-BASS catalogs as well as from a preliminary version of the BASS catalog. This follow-up has allowed us to identify 110 new young low-mass stars and brown dwarfs with spectral types in the M5–L5 range, which are probable members of the YMGs under study. These new discoveries have allowed us to define for the first time spectroscopic templates for the L3 β, L4 β and L5 β spectral types, which are anchored on their optical classification while remaining consistent with the method of Allers & Liu (2013). These discoveries have allowed us to refine the estimated rate of false-positives in the BASS sample to 20%, which is slightly higher than the first estimation presented in Chapter 3 (13%), but that still represents a significant progress over previous methods. Before the publication of this paper, only 66 candidate members of YMGs with spectral types $\geq$ M5 were known (Song et al. 2003; Allers et al. 2009; Looper et al. 2007a; Riedel et al. 2014; Gizis 2002; Mamajek 2005; Looper et al. 2010a; Reiners & Basri 2009; Teixeira et al. 2009; Bowler et al. 2013; Shkolnik et al. 2012; Kirkpatrick et al. 2010; Schlieder et al. 2012a, 2010, 2012b; Malo et al. 2013; Rodriguez et al. 2013; Liu et al. 2013b; Rice et al. 2010; Kraus et al. 2014b; Naud et al. 2014), as well as 28 others that were reported in previous Chapters of this thesis (Chapters 2, 4 and 5). Our observations have thus boosted the number of known $\geq$ M5 candidate members of YMGs by a factor of more than two.

We used this new sample of young objects, complemented with 41 young dwarfs from the literature, to build new sequences in 16 spectral type–magnitude and color–magnitude diagrams. We have then compared our observations to theoretical evolutionary and atmospheric models to shed light on their present limitations. In particular, we confirmed that atmosphere models that best reproduce the spectral energy distribution of young brown dwarfs are systematically cooler than those that best fit old brown dwarfs of the same spectral type. This effect had already been demonstrated for the young brown dwarf HD 203030 B (Metchev &

Hillenbrand 2006) and for the giant gaseous exoplanets TWA 27 b (Barman et al. 2011b) and HR 8799 b (Barman et al. 2011a).

Finally, we discussed the fact that we have identified a surprising number (12) of new young brown dwarf candidate members of the Tucana-Horologium association within 50 pc and for which the estimated mass is located in the 12.5–14 $M_{\rm Jup}$ range. We have thus identified $36.4^{+16.6}_{-12.5}$ times too many objets in this mass range compared to what would have been expected from the predictions based on a typical IMF and the population of massive members of Tucana-Horologium. This new population corresponds to one young brown dwarf of 12.5–14 $M_{\rm Jup}$ for every $17.5^{+6.6}_{-5.0}$ main-sequence stars in this association. It remains to be determined whether this over-population is only observed in Tucana-Horologium or if it betrays the first signs of a turn-up in the IMF that could correspond to a population of giant, gaseous exoplanets that were ejected from their stellar system in their young age (e.g., see Sumi et al. 2011).

8.4 The connection between brown dwarfs and giant exoplanets – Future perspectives

The work presented in this thesis allowed us to identify a significant number of new young brown dwarfs. By knowing their age via membership to YMGs, we have been able to estimate their masses and noted that several of them have estimated masses below 13 $M_{\rm Jup}$. Their mass and temperature being similar to those of giant, gaseous exoplanets, they will be useful benchmark objects to understand the atmospheric processes that take place in these latter objects. Studies of the HR 8799 planetary system (Marois et al. 2008) have shown that the atmospheres of giant gaseous exoplanets host much thicker dust clouds in their high atmospheres compared to old brown dwarfs of similar temperatures (Currie et al. 2011). This property is also shared by young brown dwarfs, which reinforces the interpretation that they share similar properties with gaseous giant exoplanets.

It will thus be interesting to study the population of young brown dwarfs further to improve our understanding of giant exoplanets. For example, the atmospheres of very cool

($T < 1500\,\mathrm{K}$) giant exoplanets are still poorly known (e.g., Naud et al. 2014). A logical prolongation of this thesis will thus be to search for late-type $\geq$T0 brown dwarf members of YMGs. We know that the cloud properties of such cold objects change drastically in the case of old, field brown dwarfs, e.g. when their atmospheric clouds fall below their photosphere. This cloud clearing process causes cold brown dwarfs to have gradually bluer near-infrared colors (e.g., $J - K$) at lower temperatures (Figure 7.1).

It is probable that the same phenomenon happens to very cool giant exoplanets, yet these objects are so much fainter than their host stars that current technology does not allow us to study them because of this large contrast in brightness. It would nevertheless already be possible to perform a similar study on young, isolated brown dwarfs, but only a few such potentially young T-type brown dwarfs are currently known (e.g., Delorme et al. 2012; Naud et al. 2014). We present in Figure 7.1 a sample of preliminary candidate T-type YMG members (blue circles) that we identified with a method similar to that described in this thesis (Section 3.3), except that several color and quality filters were relaxed. These candidates are not yet confirmed spectroscopically, however we can already note a possible transition to bluer $J - K$ colors.

Following this thesis work, we will thus lead a survey for very cool young brown dwarfs of the T spectral class. As mentioned above, this will allow us to better understand the atmospheres of cooler giant exoplanets, however the potential scientific benefits of such a project do not stop there. The discovery of such very low-mass isolated objects will allow us to confirm or invalidate the recent results that the spatial density of planetary-mass brown dwarfs could be significantly larger than expected (Sumi et al. 2011). More generally, we will directly address the following fundamental question in astrophysics: do planetary-mass brown dwarfs all form in the same way than massive brown dwarfs, or are at least part of them really rogue giant exoplanets that were ejected from their host stellar system shortly after their formation ?

Several future projects in astrophysics will allow us to push the research presented in this thesis even further. Among those, the GAIA mission (Perryman et al. 2001) will measure the parallax, proper motion and radial velocity of a billion stars. The *Large Synoptic Survey Te-*

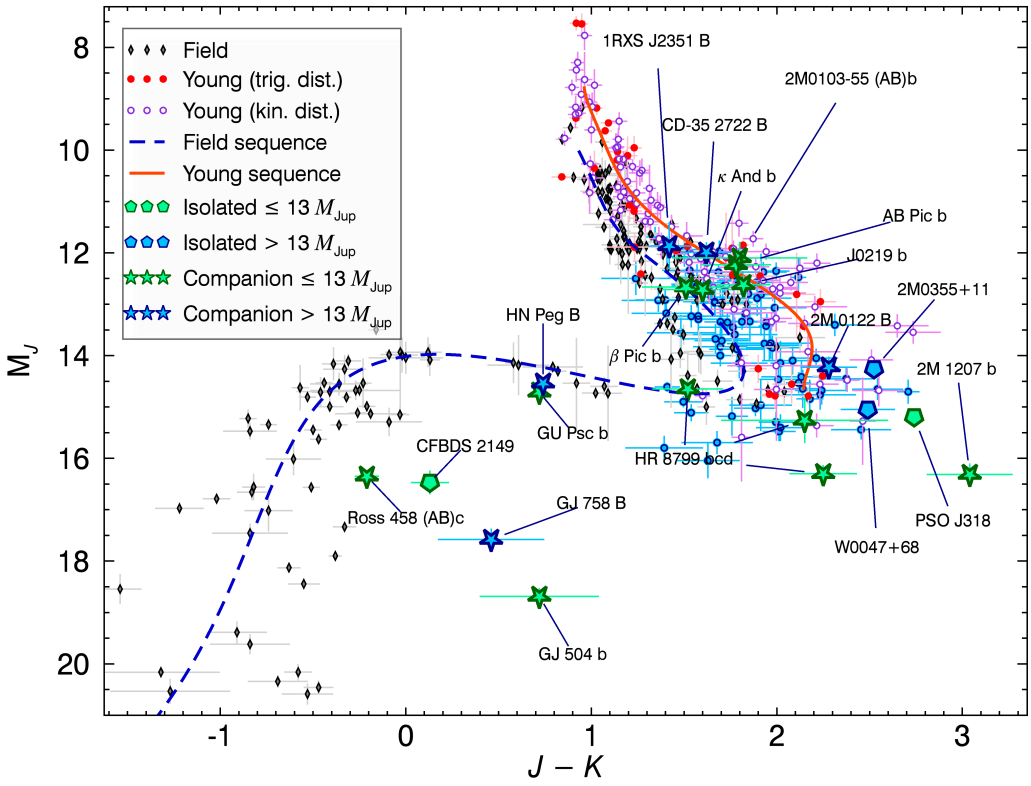

FIGURE 8.1 Near-infrared color–magnitude sequence for field low-mass stars and brown dwarfs (black diamonds) and young brown dwarfs (red dots and purple circles). The blue and green stars mark the position of known sub-stellar or planetary-mass companions, respectively. The blue and green pentagons indicate several isolated substellar and planetary-mass objects, respectively. This figure follows the same format as that of Figure 6.13, except that we have added several candidate young T dwarfs that were identified in the first version of a future survey for T dwarf members of YMGs (blue circles). We can see that these candidates display the expected behavior that corresponds to gradually bluer colors for colder (and thus fainter) objects.

lescope (LSST; Krabbendam et al. 2012) will obtain exposures of the whole southern Celestial sphere once every few days. The phenomenal quantity of data generated by GAIA and LSST will allow us to revolutionize our comprehension of YMGs, in particular by combining them with the efficiency of the BANYAN tool.

The SPIRou camera (*Spectro-Polarimètre InfraRouge*; Delfosse et al. 2013), the *James Webb Space Telescope* (JWST; Gardner et al. 2006), the *Thirty Meter Telescope* (TMT; Nelson & Sanders 2008), the *European Extremely Large Telescope* (EELT; Gilmozzi & Spyromilio 2008) and the *Giant Magellan Telescope* (GMT; Johns et al. 2014) will enable an unprecedented characterization of the young planetary-mass brown dwarfs discovered as part of this thesis, in particular because of their vastly augmented sensitivity and their large spectral coverage. The observations that will be made possible with these new technologies will significantly advance our knowledge of the physical properties and processes that take place in the atmospheres of giant gaseous exoplanets. These observations will also allow us to shed more light on the stellar and planetary formation mechanisms.

Appendice A

Spectroscopie optique d'étoiles de faible masse candidates membres d'associations jeunes

Nous avons effectué un suivi spectroscopique des candidates dont le type spectral est plus précoce que M8 dans les longueurs d'onde optiques, à l'aide des caméras GMOS-N et GMOS-S, respectivement situées aux télescopes Gemini-North et Gemini-South. Nous avons ainsi obtenu un spectre couvrant 600–1000 nm avec un pouvoir de résolution $R \sim 1000$ pour 156 étoiles de faible masse candidates membres d'associations jeunes entre 2012 et 2015. De celles-ci, 48 proviennent du catalogue BASS, 18 du catalogue LP-BASS et 90 du catalogue PRE-BASS (voir les Sections 3.4, 6.3 et l'Annexe 3.B pour une description de ces catalogues).

Ces données nous permettront d'effectuer la classification spectrale des objets en question et de mesurer leur activité magnétique à l'aide de la raie d'émission Hα à 656 nm. De plus, la mesure de la largeur équivalente de leurs raies d'absorption nous permettra d'évaluer leur gravité de surface et d'identifier les candidates dont l'âge consistant avec l'appartenance à une association jeune du voisinage solaire.

Nous présentons à la Figure A.1 les résultats d'une analyse préliminaire d'un sous-ensemble de notre échantillon composé de 31 étoiles de faible masse. On peut y voir que la largeur équivalente des raies d'absorption du Na I, K I et CrH en fonction du type spectral des étoiles

du champ forme une séquence (trait plein bleu foncé). La déviation standard des étoiles du champ autour de cette séquence est représentée par la région en rose délimitée par le trait pointillé bleu pâle.

Les triangles violets orientés à gauche correspondent à des étoiles géantes rouges en fin de vie (classes de luminosité I à III), dont la température et le type spectral sont similaires aux étoiles de faible masse du champ, mais dont le rayon est significativement plus grand. La gravité de surface des étoiles géantes est donc beaucoup plus faible et la largeur équivalente de leurs raies d'absorption forme ainsi une séquence distincte, située en-deçà de celle du champ. Les étoiles et naines brunes très jeunes membres de régions de formation d'étoiles (0–3 Man) sont représentées par les triangles verts pointant à droite. On peut voir que ces objets forment une séquence située légèrement au-dessus des géantes rouges. Nous nous attendons donc à ce que les membres d'associations jeunes (10–125 Man) forment une séquence intermédiaire entre ces derniers objets et les étoiles du champ ($\gtrsim$500 Man). Nous avons représenté les quelques cas confirmés avec les triangles oranges pointant vers le haut, ceux-ci semblant concorder avec cette attente. Les étoiles noires affichés à la Figure A.1 représentent les 31 candidates membres d'associations jeunes que nous avons déjà analysées.

Cette analyse préliminaire semblerait démontrer qu'il est possible d'identifier les membres d'associations jeunes dont le type spectral est plus tardif que M5, autrement la séquence jeune se trouve à l'intérieur de l'enveloppe définissant la séquence du champ. Ces résultats préliminaires ont été présentés dans l'affiche et le compte-rendu de conférence *Results from BASS, the BANYAN All-Sky Suvey*, présentés par J. Gagné *et al.* à la conférence *Cool Stars 18* en Juin 2014 à Flagstaff, Arizona. Les résultats complets seront présentés dans un article futur, dans lequel nous tenterons aussi d'identifier de nouvelles caractérstiques spectrales permettant de différencier les étoiles jeunes plus de types spectraux M0–M5 de la séquence du champ.

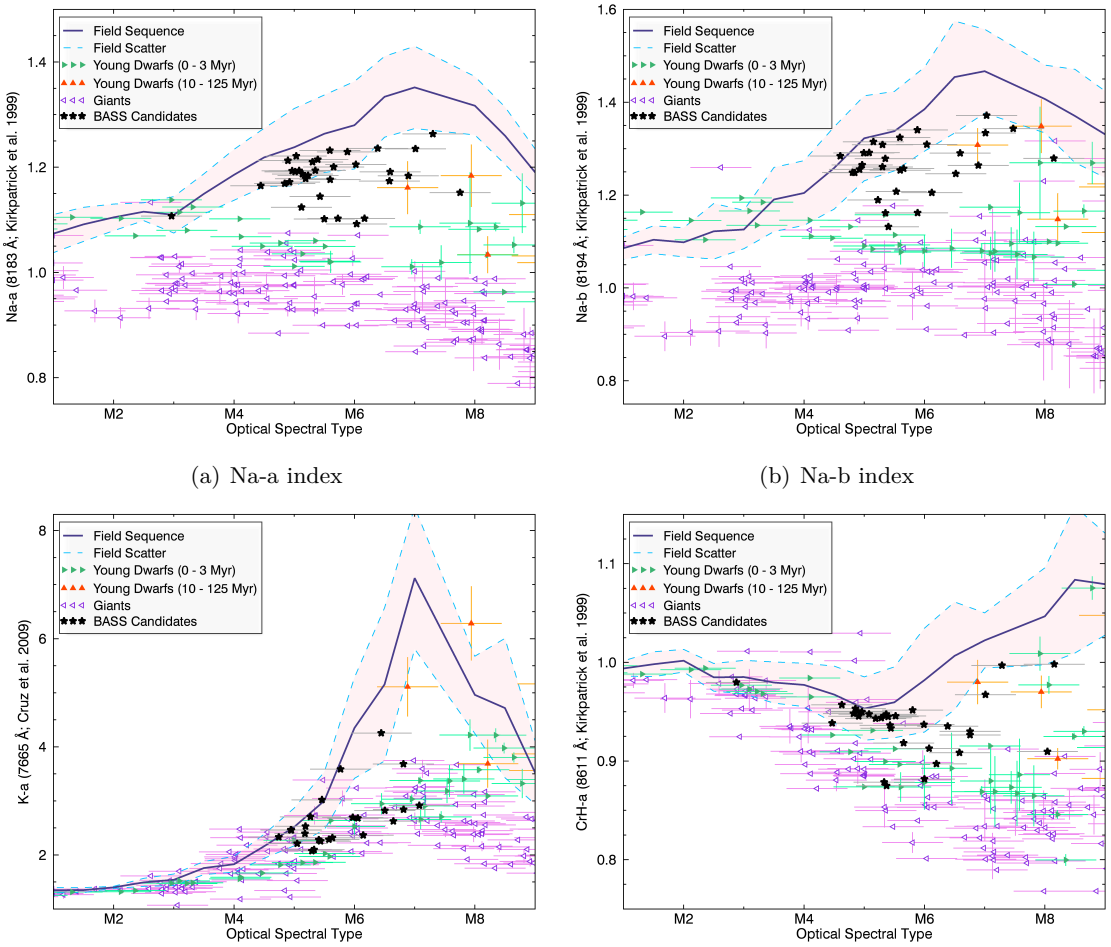

(a) Na-a index

(b) Na-b index

(c) K-a index

(d) CrH-a index

FIGURE A.1 Indices spectraux optiques sensibles à la gravité de surface pour des étoiles du champ ($\gtrsim$ 500 Man; trait bleu foncé et région rose délimitée par le trait bleu pâle pointillé), étoiles géantes rouges (triangles violets orientés à gauche), étoiles très jeunes (0–3 Man; triangles verts orientés à droite), étoiles jeunes (10–125 Man; triangles oranges orientés vers le haut) et candidates membres d'associations jeunes (10–125 Man) identifiés dans le cadre de ce projet (étoiles noires). On peut voir que ces indices spectraux sont de bons diagnostics d'âge pour les types spectraux > M5.

Appendice B

CFBDSIR2149–0403: A 4–7 JUPITER-MASS FREE-FLOATING PLANET IN THE YOUNG MOVING GROUP AB DORADUS ?

Philippe Delorme[1], Jonathan Gagné[2], Lison Malo[2], Céline Reylé[3], Étienne Artigau[2], Loïc Albert[2], Thierry Forveille[1], Xavier Delfosse[1], France Allard[4], Derek Homeier[4]

[1] *UJF-Grenoble 1/CNRS-INSU, Institut de Planétologie et d'Astrophysique de Grenoble (IPAG) UMR 5274, 38041 Grenoble, France*

[2] *Département de Physique and Observatoire du Mont-Mégantic, Université de Montréal, C.P. 6128 Succ. Centre-ville, Montréal, Qc H3C 3J7, Canada*

[3] *Université de Franche Comté, Institut UTINAM CNRS 6213, Observatoire des Sciences de l'Univers THETA de Franche-Comté, Observatoire de Besançon, BP 1615, 25010 Besançon Cedex, France*

[4] *CRAL, UMR 5574 CNRS, École Normale Supérieure, 69364 Lyon Cedex 07, France*

Received 2012 July 11; accepted 2012 September 25

Published in *Astronomy & Astrophysics*,

November 2012, *Vol.* 548, *page* 26

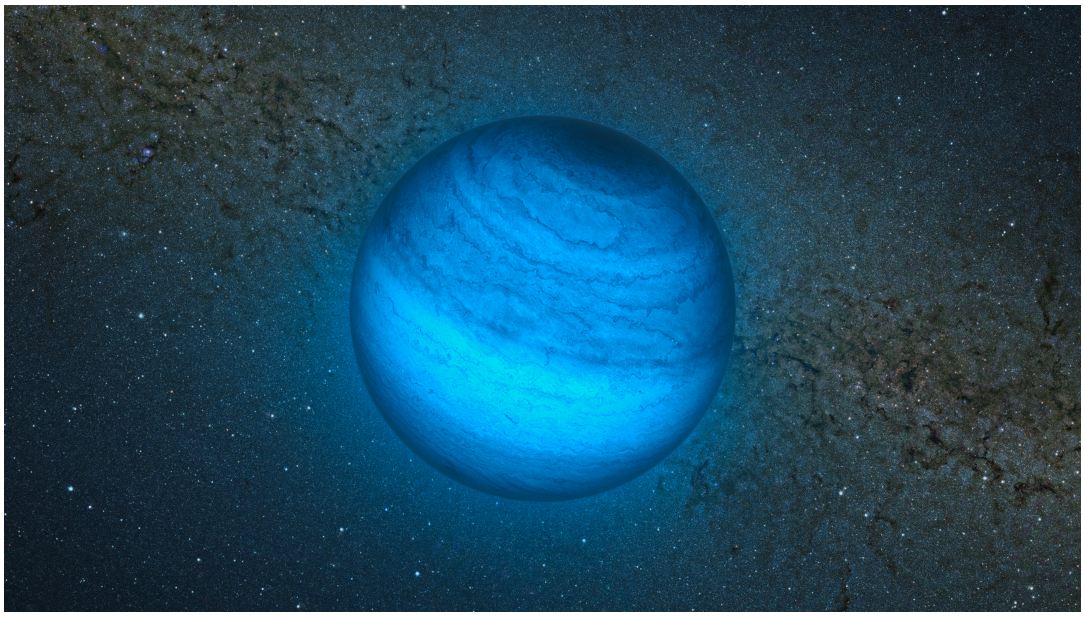

FIGURE B.1 Vue d'artiste de CFBDSIR J2149–0403 en lumière proche-infrarouge (crédit Nick Risinger).

Le sondage Canada-France Brown Dwarf Survey InfraRed (CFBDSIR; Delorme et al. 2010) a permis d'identifier plusieurs naines brunes très froides, dont CFBDSIR J214947.2–040308.9.

Nous présentons dans cet article une analyse cinématique faisant intervenir l'outil statistique BANYAN II, afin de démontrer que CFBDSIR J2149–0403 est une candidate membre de l'association cinématique jeune AB Doradus. À une température aussi faible, un objet de l'âge d'AB Doradus (110–130 Myr; Barenfeld et al. 2013) aurait une masse attendue de seulement 4 à 7 fois celle de Jupiter.

Nous y discutons la possibilité que CFBDSIR J2149–0403 soit une exoplanète éjectée, et effectuons une analyse spectroscopique démontrant que la température de CFBDSIR J2149–0403 se situe entre 650–750 K. De plus, nous identifions certaines propriétés spectroscopiques qui la différencient des naines brunes du champ et pouvant être attribuées à un plus jeune âge (voir Figure B.2).

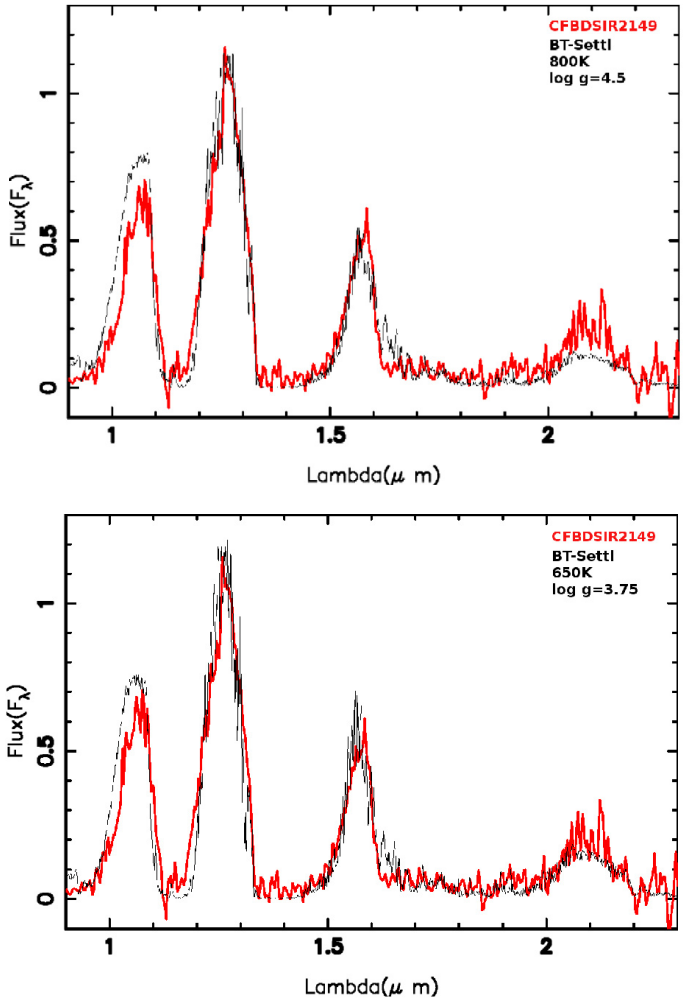

FIGURE B.2 Spectroscopie proche-infrarouge de la naine brune CFBDSIR J2149–0403 (trait rouge). Gauche : Comparaison avec le spectre d'un modèle atmosphérique correspondant à une naine brune du champ (trait noir). Droite : Comparaison avec le spectre d'un modèle atmosphérique correspondant à un objet jeune de masse planétaire (trait noir). Le flux élevé de CFBDSIR J2149–0403 entre 2.0 et 2.2 μm est une indication que celle-ci n'a pas terminé sa phase de contraction gravitationnelle et qu'elle a donc un jeune âge.

Appendice C

DIRECT-IMAGING DISCOVERY OF A 12–14 JUPITER-MASS OBJECT ORBITING A YOUNG BINARY SYSTEM OF VERY LOW-MASS STARS

Philippe Delorme[1], Jonathan Gagné[2], Julien H. Girard[3], Anne-Marie Lagrange[1], Gaël Chauvin[1], Marie-Eve Naud[2], David Lafrenière[2], René Doyon[2], Adric R. Riedel[4], Mickaël Bonnefoy[5], and Lison Malo[2]

[1] *UJF-Grenoble 1/CNRS-INSU, Institut de Planétologie et d'Astrophysique de Grenoble (IPAG) UMR 5274, 38041 Grenoble, France*

[2] *Département de Physique and Observatoire du Mont-Mégantic, Université de Montréal, C.P. 6128 Succ. Centre-ville, Montréal, Qc H3C 3J7, Canada*

[3] *European Southern Observatory, Alonso de Córdova 3107, Vitacura, Cassilla 19001, Santiago, Chile*

[4] *Department of Astrophysics, American Museum of Natural History, Central Park West at 79th Street, New York, NY 10034, USA*

[5] *Max Planck Institute for Astronomy, Königstuhl 17, 69117 Heidelberg, Germany*

Received 2013 January 25; accepted 2013 March 18

Published in *Astronomy & Astrophysics Letters*,

November 2013, *Vol.* 553, *page* L5

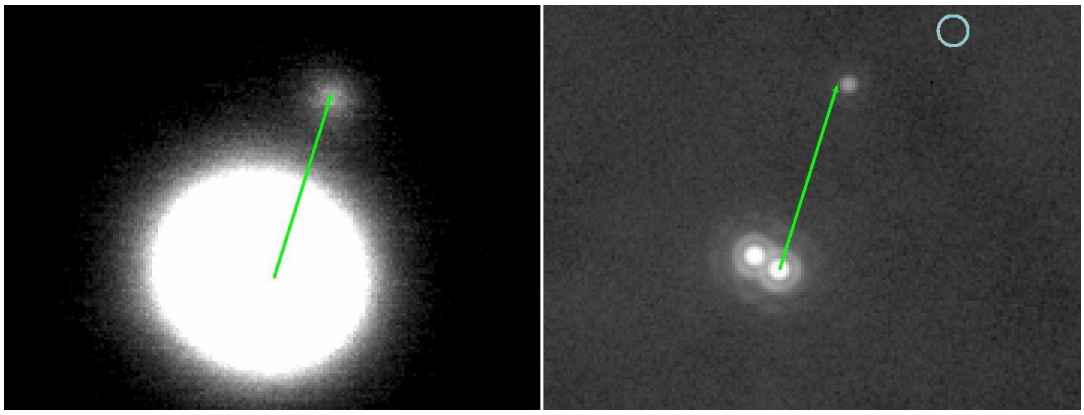

FIGURE C.1 Imagerie directe du compagnon planétaire 2MASS J0103–5515 (AB)b. Gauche : Observations NACO d'archive en Octobre 2002 en bande H. Droite : Nouvelles observations NACO obtenues en Novembre 2012, en bande L'. La flèche verte identifie la position relative du compagnon en 2002 et le cercle bleu identifie la position attendue en 2012 si le compagnon était plutôt une étoile d'arrière-plan.

Nous avons présenté dans cet article la découverte par imagerie directe d'un compagnon de masse planétaire (voir Figure C.1) orbitant 2MASS J01033563–5515561 AB, une étoile de faible masse binaire de type spectral M5.5. L'étoile-hôte en question a été identifiée comme une candidate membre de l'association Tucana-Horologium au cours du sondage BASS effectué dans le cadre de cette thèse (Gagné et al. 2015, voir Chapitre 3).

Le ratio de masse élevé entre la planète (12–14 $M_{\rm Jup}$) et l'étoile-hôte (masse systémique de $\sim 0.36\,M_{\odot}$) serait compatible avec un mécanisme de formation du compagnon semblable à celui des étoiles. Ainsi, ce système pourrait représenter un cas extrême d'étoile triple hiérarchique du point de vue de la formation. Ce système jeune aux propriétés extrême sera d'une grande utilité pour contraindre les simulations théoriques de formation planétaire.

Appendice D

BANYAN. VI. DISCOVERY OF A COMPANION AT THE BROWN DWARF/PLANET-MASS LIMIT TO A TUCANA-HOROLOGIUM M DWARF

Étienne Artigau[1], Jonathan Gagné[1], Jacqueline Faherty[2], Lison Malo[3], Marie-Eve Naud[1], René Doyon[1], David Lafrenière[1], Yuri Beletsky[4]

[1] *Institut de Recherche sur les Exoplanètes (iREx), Département de Physique, Université de Montréal, C.P. 6128, Succ. Centre-Ville, Montréal, QC, H3C 3J7, Canada*

[2] *Department of Terrestrial Magnetism, Carnegie Institution of Washington, Washington, DC 20015, USA*

[3] *Canada-France-Hawaii Telescope Corporation, 65-1238 Mamalahoa Highway, Kamuela, HI 96743, USA*

[4] *Las Campanas Observatory, Carnegie Institution of Washington, Colina el Pino, Casilla 601, La Serena, Chile*

Received 2015 January 13; accepted 2015 May 7

Accepted for publication in *The Astrophysical Journal*,

FIGURE D.1 Imagerie directe du compagnon planétaire J0219–3925 b en longueurs d'onde proche-infrarouge. On peut voir dans l'image à large champ (gauche) que l'étoile primaire est rouge en comparaison avec les autres étoiles du champ : Ceci est dû à sa faible température. On peut voir dans l'image recadrée (droite) que le compagnon J0219 b est encore plus rouge que son étoile-hôte, pour la même raison.

Nous avons identifié dans cet article 2MASS J02192210–3925225 b (J0219 b; voir Figure D.1), un compagnon de 12–15 $M_{\rm Jup}$ orbitant une étoile jeune de faible masse dans l'association Tucana-Horologium. L'étoile-hôte a été découverte et confirmée comme étant jeune dans le cadre du sondage *BASS*.

Le compagnon J0219 b se trouve sur une orbite relativement large : sa séparation physique est de 160 AU et la séparation angulaire projetée sur le ciel est de $4''$. Ceci nous a permis d'obtenir un spectre proche-infrarouge du compagnon à relativement haute résolution ($R \sim 5000$; voir Figure D.2). Nous avons ainsi pu identifier que le compagnon possède des propriétés physiques similaires à celles d'une naine brune et estimer sa température à ~ 1700 K.

Nous avons pu identifier plusieurs caractéristiques spectroscopiques trahissant le jeune âge du compagnon, tels qu'une pression atmosphérique plus basse et une couverture nuageuse plus épaisse. Ceci résulte entre autres en un continuum plus rouge et une forme plus triangulaire de la bande H (1.4–1.8 μm à la Figure D.2).

Cette nouvelle découverte pourra servir de référence pour mieux comprendre la connection

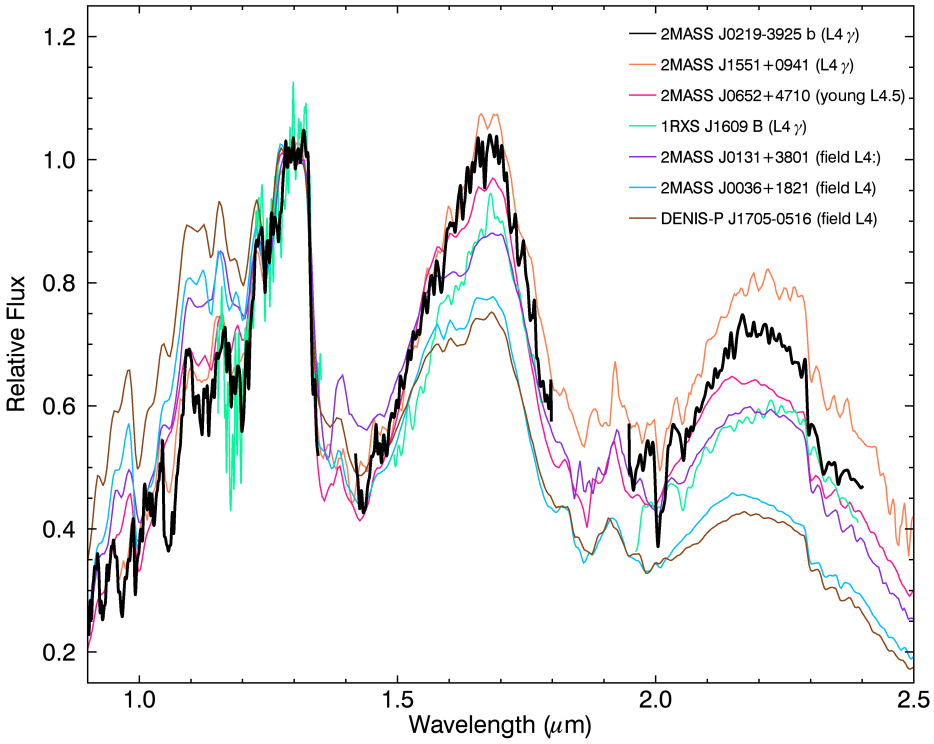

FIGURE D.2 Spectroscopie proche-infrarouge du compagnon J0219–3925 b (trait noir), en comparaison avec des naines brunes du champ (trais mauve, bleu et brun) ou membres d'associations jeunes (traits orange, magenta et vert) de types spectraux semblables.

entre les exoplanètes géantes gazeuses et les naines brunes, étant donné que J0219 b est un cas intermédiaire entre ces deux régimes dont l'âge est bien connu par son appartenance à l'association Tucana-Horologium (20–40 Myr). Il sera aussi possible de calibrer la métallicité du compagnon à l'aide de son étoile-hôte, ce qui n'est pas possible pour les objets similaires isolés dans l'espace.

Appendice E

Autres travaux

E.1 Articles à titre de premier auteur

E.1.1 SDSS J111010.01+011613.1: A mew planetary-mass T-type member of the AB Doradus moving group

Auteurs : Jonathan Gagné, Adam J. Burgasser, Jacqueline K. Faherty, David Lafrenière, René Doyon, Emily Bowsher, Christine Nicholls.

E.2 Articles à titre de co-auteur

E.2.1 Discovery of two L and T binaries with wide separations and peculiar photometric properties

Auteurs : Étienne Artigau, David Lafrenière, René Doyon, Michael C. Liu, Trent J. Dupuy, Loïc Albert, Jonathan Gagné, Lison Malo, Damien Gratadour.

Contribution : Analyse spectrale des deux composantes de la naine brune binaire à l'aide des diagnostics développés par Burgasser et al. (2010), afin de vérifier si l'une d'entre elles pourrait être une binaire non-résolue.

E.2.2 CFBDSIR2149-0403: A 4-7 Jupiter-mass free-floating planet in the young moving group AB Doradus ?

Auteurs : Philippe Delorme, Jonathan Gagné, Lison Malo, Céline Reylé, Étienne Artigau, Loïc Albert, Thierry Forveille, Xavier Delfosse, France Allard, Derek Homeier.

Contribution : Analyse de la cinématique de CFBDSIR 2149 à l'aide de l'algorithme BANYAN II. Plusieurs discussions avec l'auteur principal et commentaires généraux sur l'article. Écriture d'une partie du paragraphe 4.2 et création de la Figure 5.

E.2.3 Bayesian analysis to identify new star candidates in nearby young stellar kinematic groups

Auteurs : Lison Malo, René Doyon, David Lafrenière, Étienne Artigau, Jonathan Gagné, Frédérique Baron, Adric R. Riedel.

Contribution : Développement du schéma pour un traitement des incertitudes sur les observables mesurés dans l'algorithme Bayésien BANYAN et commentaires généraux sur l'article.

E.2.4 Direct-imaging discovery of a 12-14 Jupiter-mass object orbiting a young binary system of very low-mass stars

Auteurs : Philippe Delorme, Jonathan Gagné, Julien H. Girard, Anne-Marie Lagrange, Gaël Chauvin, Marie-Eve Naud, David Lafrenière, René Doyon, Adric R. Riedel, Mickaël Bonnefoy, Lison Malo.

Contribution : Communication privée d'une liste de candidates membres d'associations jeunes non publiées (inculant l'étoile-hôte J0103–5515 AB). Spectroscopie optique et proche-infrarouge de l'étoile primaire. Classification spectrale et caractérisation de l'émission Hα de l'étoile primaire et application de l'algorithme BANYAN II au système. Calcul du ratio de masse et commentaires généraux sur l'article. Recherche d'une contrepartie ROSAT de la primaire en rayons X et écriture du paragraphe 2.2.

E.2.5 Discovery of a wide planetary-mass companion to the young M3 star GU Psc

Auteurs : Marie-Eve Naud, Étienne Artigau, Lison Malo, Loïc Albert, René Doyon, David Lafrenière, Jonathan Gagné, Didier Saumon, Caroline Morley, France Allard, Derek Homeier, Anne Boucher.

Contribution : Observations et analyse spectroscopiques de la primaire GU Psc en longueurs d'onde proche-infrarouge. Calcul de la métallicité de GU Psc à l'aide des schémas développés par Mann et al. (2013a) et Newton et al. (2012). Application de l'algorithme BANYAN II au compagnon GU Psc b et commentaires généraux sur l'article.

E.2.6 BANYAN. III. Radial velocity, rotation and X-ray emission of low-mass star candidates in nearby young kinematic groups

Auteurs : Lison Malo, Étienne Artigau, René Doyon, David Lafrenière, Loïc Albert, Jonathan Gagné.

Contribution : Participation au développement de l'algorithme BANYAN et commentaires généraux sur l'article.

E.2.7 BANYAN. IV. Fundamental parameters of low-mass star candidates in nearby young stellar kinematic groups – Isochronal age determination using magnetic evolutionary models

Auteurs : Lison Malo, René Doyon, Gregory A. Feiden, Loïc Albert, David Lafrenière, Étienne Artigau, Jonathan Gagné, Adric R. Riedel.

Contribution : Participation au développement de l'algorithme BANYAN et commentaires généraux sur l'article.

E.2.8 Discovery and characterization of wide binary systems with a very low mass component

Auteurs : Frédérique Baron, David Lafrenière, Étienne Artigau, René Doyon, Jonathan Gagné, Cassy Davison, Lison Malo, Jasmin Robert, Daniel Nadeau, Céline Reylé.

Contribution : Construction du pipeline de réduction pour les données de la caméra GMOS en language IDL et commentaires généraux sur l'article.

E.2.9 Characterization of low-mass, wide-separation substellar companions to stars in Upper Scorpius: near-infrared photometry and spectroscopy

Auteurs : François-René Lachapelle, David Lafrenière, Jonathan Gagné, Ray Jayawardhana, Markus Janson, Christiane Helling, Soeren Witte.

Contribution : Révision sur les classifications spectrales et calculs des indices spectroscopiques des compagnons présentés dans l'article et commentaires généraux sur l'article.

Contribution : Identification de la candidate, analyse cinématique et écriture de l'article.

E.2.10 BANYAN. VI. Discovery of a companion at the brown dwarf/planetary-mass limit to a Tucana-Horologium M dwarf

Auteurs : Étienne Artigau, Jonathan Gagné, Jacqueline K. Faherty, Lison Malo, Marie-Eve Naud, René Doyon, David Lafrenière.

Contribution : Découverte de l'étoile primaire, analyse cinématique, réduction des spectres proche-infrarouge, classification spectrale et analyse de faible gravité.

E.2.11 The Brown Dwarf Kinematics Project (BDKP). IV. Radial velocities of 85 late-M and L dwarfs with MagE

Auteurs : Adam J. Burgasser, Sarah E. Logsdon, Jonathan Gagné, John J. Bochanski, Jacqueline K. Faherty, Andrew A. West, Eric E. Mamajek, Sarah J. Schmidt, Kelle L. Cruz.

Contribution : Analyse cinématique et écriture de la section sur l'appartenance aux associations cinématiques jeunes.

E.3 Compte-rendus de conférence

E.3.1 Preserving the photometric integrity of companions in high-contrast imaging observations using locally optimized combination of images

Auteurs : Jérôme Maire, Jonathan Gagné, David Lafrenière, René Doyon, James R. Graham, Jean-Pierre Véran, Lisa A. Poyneer.

Contribution : Participation au développement du pipeline pour l'application de l'algorithme LOCI-PSF.

E.3.2 Brown dwarfs of planets ? Some direct imaging detections that blur the border

Auteurs : Philippe Delorme, Jonathan Gagné, Justine Lannier, Anne-Marie Lagrange, Gaël Chauvin.

Contribution : Caractérisation cinématique de CFBDSIR 2149 avec l'algorithme BANYAN II.

E.3.3 Bayesian analysis to identify very low-mass members of nearby young stellar kinematic groups

Auteurs : Jonathan Gagné, David Lafrenière, René Doyon, Lison Malo, Jacqueline K. Faherty, Étienne Artigau.

E.3.4 A wide planetary-mass companion to a young M3 star of the AB Dor moving group

Auteurs : Marie-Eve Naud, Étienne Artigau, René Doyon, Lison Malo, Loïc Albert, David Lafrenière, Jonathan Gagné.

Contribution : Observations et analyse spectroscopiques de la primaire GU Psc en longueurs d'onde proche-infrarouge. Calcul de la métallicité de GU Psc à l'aide des schémas développés par Mann et al. (2013a) et Newton et al. (2012). Application de l'algorithme BANYAN II au compagnon GU Psc b et commentaires généraux sur l'article.

E.3.5 High-fidelity photometry and astrometry of high-contrast imaged companions using LOCI processing

Auteurs : Jérôme Maire, Jonathan Gagné, David Lafrenière, James R. Graham, René Doyon.

Contribution : Participation au développement du pipeline pour l'application de l'algorithme LOCI-PSF.

E.3.6 Prospects for the BANYAN search of low-mass moving group members with Gaia; and the importance of magnetic fields for isochronal age determination

Auteurs : Lison Malo, Jonathan Gagné, René Doyon, David Lafrenière, Étienne Artigau, Loïc Albert.

Contribution : Co-écriture de plusieurs sections et commentaires généraux sur le compte-rendu.

E.3.7 Results from BASS, the BANYAN All-Sky Survey

Auteurs : Jonathan Gagné, David Lafrenière, René Doyon, Jacqueline K. Faherty, Lison Malo, Étienne Artigau.

E.3.8 Demonstration of a near-IR laser comb for precision radial velocity measurements in astronomy

Auteurs : Xu Yi, Kerry Vahala, Scott A. Diddams, Gabriel G. Ycas, Peter Plavchan, Stéphanie Leifer, Jagmit Sandhu, Gautam Vasisht, Pin Chen, Peter Gao, Jonathan Gagné, Elise Furlan, Michael Botton, Eduardo Martin, Michael P. Fitzgerald, Gregory W. Doppmann, Charles A. Beichman.

Contribution : Création du pipeline de réduction de données pour la caméra CSHELL avec le peigne laser. Création de la figure 4.

E.3.9 The BANYAN all-sky survey for brown dwarf members of young moving groups

Auteurs : Jonathan Gagné, David Lafrenière, René Doyon, Jacqueline K. Faherty, Lison Malo, Kelle L. Cruz, Étienne Artigau, Adam J. Burgasser, Marie-Eve Naud, Sandie Bouchard, John E. Gizis, Loïc Albert.

Liste de Références

Aarnio, A. N., Weinberger, A. J., Stassun, K. G., Mamajek, E. E., & James, D. J. 2008, The Astronomical Journal, 136, 2483

Ackerman, A. S., & Marley, M. S. 2001, The Astrophysical Journal, 556, 872

Adams, F. C., & Fatuzzo, M. 1996, Astrophysical Journal v.464, 464, 256

Allard, F., Homeier, D., Freytag, B., Schaffenberger, & Rajpurohit, A. S. 2013, Mem. Soc. Astron. Ital., 24, 128

Allen, P. R., Cruz, K. K., Koerner, D. W., McElwain, M. W., & Reid, N. I. 2007, AJ, 133, 971

Allen, P. R., Koerner, D. W., Reid, I. N., & Trilling, D. E. 2005, The Astrophysical Journal, 625, 385

Allers, K. N., & Liu, M. C. 2013, The Astrophysical Journal, 772, 79

Allers, K. N., Liu, M. C., Dupuy, T. J., & Cushing, M. C. 2010, ApJ, 715, 561

Allers, K. N., Jaffe, D. T., Luhman, K. L., et al. 2007, The Astrophysical Journal, 657, 511

Allers, K. N., Liu, M. C., Shkolnik, E., et al. 2009, The Astrophysical Journal, 697, 824

Allison, R. J., Goodwin, S. P., Parker, R. J., et al. 2009a, The Astrophysical Journal Letters, 700, L99

—. 2009b, Monthly Notices of the Royal Astronomical Society, 395, 1449

Alves de Oliveira, C., Moraux, E., Bouvier, J., & Bouy, H. 2012, A&A, 539, 151

Andrei, A. H., Smart, R. L., Penna, J. L., et al. 2011, The Astronomical Journal, 141, 54

Artigau, É., Doyon, R., Lafrenière, D., et al. 2006, ApJ, 651, L57

Artigau, É., Doyon, R., Vallee, P., Riopel, M., & Nadeau, D. 2004, in Ground-based Instrumentation for Astronomy. Edited by Alan F. M. Moorwood and Iye Masanori. Proceedings of the SPIE, Université de Montreal, Canada, 1479–1486

Artigau, É., Gagné, J., Faherty, J., et al. 2015, The Astrophysical Journal, 806, 254

Artigau, É., Lafrenière, D., Doyon, R., et al. 2009, Cool Stars, 1094, 493

Artigau, É., Radigan, J., Folkes, S., et al. 2010, The Astrophysical Journal Letters, 718, L38

Artigau, É., Lafrenière, D., Doyon, R., et al. 2011, The Astrophysical Journal, 739, 48

Bakos, G. Á., Hartman, J., Torres, G., et al. 2011, The Astrophysical Journal, 742, 116

Bannister, N. P., & Jameson, R. F. 2007, Monthly Notices of the Royal Astronomical Society: Letters, 378, L24

Baraffe, I., & Chabrier, G. 2010, Astronomy & Astrophysics, 521, A44

Baraffe, I., Chabrier, G., Barman, T. S., Allard, F., & Hauschildt, P. H. 2003, Astronomy & Astrophysics, 402, 701

Bardalez Gagliuffi, D. C., Burgasser, A. J., Gelino, C. R., et al. 2014, The Astrophysical Journal, 794, 143

Barenfeld, S. A., Bubar, E. J., Mamajek, E. E., & Young, P. A. 2013, The Astrophysical Journal, 766, 6

Barman, T. S., Macintosh, B., Konopacky, Q. M., & Marois, C. 2011a, The Astrophysical Journal, 733, 65

—. 2011b, The Astrophysical Journal Letters, 735, L39

Barrado Y Navascués, D. 1998, Astronomy & Astrophysics, 339, 831

Barrado y Navascués, D., Stauffer, J. R., & Randich, S. 1998, The Astrophysical Journal, 506, 347

Barrow, J. D., Bhavsar, S. P., & Sonoda, D. H. 1985, Monthly Notices of the Royal Astronomical Society (ISSN 0035-8711), 216, 17

Basri, G. 1998, Brown dwarfs and extrasolar planets, 134, 394

—. 2000, Annual Review of Astronomy & Astrophysics, 38, 485

Basri, G., & Brown, M. E. 2006, Annual Review of Earth and Planetary Sciences, 34, 193

Bastian, N., Covey, K. R., & Meyer, M. R. 2010, Annual Review of Astronomy & Astrophysics, 48, 339

Bazell, D., & Aha, D. W. 2001, ApJ, 548, 219

Beamín, J. C., Ivanov, V. D., Bayo, A., et al. 2014, Astronomy & Astrophysics, 570, L8

Beichman, C., Gelino, C. R., Kirkpatrick, J. D., et al. 2014, The Astrophysical Journal, 783, 68

Béjar, V. J. S., Zapatero Osorio, M. R., & Rebolo, R. 1999, ApJ, 521, 671

Bernat, D., Bouchez, A. H., Ireland, M., et al. 2010, ApJ, 715, 724

Biller, B. A., Liu, M. C., Wahhaj, Z., et al. 2013, The Astrophysical Journal, 777, 160

Binks, A. S., & Jeffries, R. D. 2014, Monthly Notices of the Royal Astronomical Society: Letters, 438, L11

Blake, C. H., Charbonneau, D., & White, R. J. 2010, The Astrophysical Journal, 723, 684

Blecic, J., Harrington, J., Madhusudhan, N., et al. 2013, The Astrophysical Journal, 779, 5

Bochanski, J. J., Gizis, J. E., Hawley, S. L., et al. 2005, AJ, 130, 1871

Bochanski, J. J., Hennawi, J. F., Simcoe, R. A., et al. 2009, Publications of the Astronomical Society of the Pacific, 121, 1409

Bodenheimer, P. 1995, Annual Review of Astronomy & Astrophysics, 33, 199

Boeshaar, P. C. 1976, Ph.D. Thesis Ohio State Univ., 14

Bonnefoy, M., Chauvin, G., Lagrange, A.-M., et al. 2014a, Astronomy & Astrophysics, 562, A127

Bonnefoy, M., Chauvin, G., Dumas, C., et al. 2009, A&A, 506, 799

Bonnefoy, M., Boccaletti, A., Lagrange, A.-M., et al. 2013, Astronomy & Astrophysics, 555, A107

Bonnefoy, M., Marleau, G. D., Galicher, R., et al. 2014b, Astronomy & Astrophysics, 567, L9

Borůvka, O. 1926

Bouchy, F., Bonomo, A. S., Santerne, A., et al. 2011a, Astronomy & Astrophysics, 533, A83

Bouchy, F., Deleuil, M., Guillot, T., et al. 2011b, Astronomy & Astrophysics, 525, A68

Bouy, H., Brandner, W., Martín, E. L., et al. 2003, The Astronomical Journal, 126, 1526

Bouy, H., Duchêne, G., Köhler, R., et al. 2004, Astronomy & Astrophysics, 423, 341

Bouy, H., Martín, E. L., Brandner, W., et al. 2008, A&A, 481, 757

Bovy, J., & Tremaine, S. 2012, The Astrophysical Journal, 756, 89

Bowler, B. P., Liu, M. C., Kraus, A. L., & Mann, A. W. 2014, The Astrophysical Journal, 784, 65

Bowler, B. P., Liu, M. C., Shkolnik, E. L., & Dupuy, T. J. 2013, The Astrophysical Journal, 774, 55

Bowler, B. P., Liu, M. C., Shkolnik, E. L., et al. 2012a, The Astrophysical Journal, 753, 142

Bowler, B. P., Liu, M. C., Shkolnik, E. L., & Tamura, M. 2012b, ApJ, 756, 69

Boyer, M. L., Srinivasan, S., van Loon, J. T., et al. 2011, AJ, 142, 103

Briceño, C., Luhman, K. L., Hartmann, L., Stauffer, J. R., & Kirkpatrick, D. J. 2002, ApJ, 580, 317

Broos, P. S., Getman, K. V., Povich, M. S., et al. 2011, ApJS, 194, 4

Buchhave, L. A., Bakos, G. Á., Hartman, J. D., et al. 2010, The Astrophysical Journal, 720, 1118

Buchhave, L. A., Latham, D. W., Carter, J. A., et al. 2011, The Astrophysical Journal Supplement, 197, 3

Burgasser, A. J. 2007, The Astrophysical Journal, 659, 655

Burgasser, A. J., Cruz, K. K., McElwain, M. W., et al. 2004, AJ, 127, 2856

Burgasser, A. J., Cruz, K. L., Cushing, M., et al. 2010, The Astrophysical Journal, 710, 1142

Burgasser, A. J., Cruz, K. L., & Kirkpatrick, J. D. 2007, The Astrophysical Journal, 657, 494

Burgasser, A. J., Geballe, T. R., Leggett, S. K., Kirkpatrick, J. D., & Golimowski, D. A. 2006, The Astrophysical Journal, 637, 1067

Burgasser, A. J., Gelino, C. R., Cushing, M. C., & Kirkpatrick, D. J. 2012, ApJ, 745, 26

Burgasser, A. J., Gizis, J. E., & Bardalez-Gagliuffi, D. C. 2011, AJ, 141, 70

Burgasser, A. J., Liu, M. C., Ireland, M. J., Cruz, K. L., & Dupuy, T. J. 2008a, The Astrophysical Journal, 681, 579

Burgasser, A. J., Looper, D. L., Kirkpatrick, J. D., Cruz, K. L., & Swift, B. J. 2008b, The Astrophysical Journal, 674, 451

Burgasser, A. J., & McElwain, M. W. 2006, AJ, 131, 1007

Burgasser, A. J., Kirkpatrick, J. D., Brown, M. E., et al. 1999, The Astrophysical Journal, 522, L65

Burnett, B., & Binney, J. 2010, MNRAS, 407, 339

Burningham, B., Pinfield, D. J., Leggett, S. K., et al. 2008, Monthly Notices of the Royal Astronomical Society, 391, 320

Burningham, B., Pinfield, D. J., Lucas, P. W., et al. 2010, Monthly Notices of the Royal Astronomical Society, 406, 1885

Burningham, B., Cardoso, C. V., Smith, L., et al. 2013, Monthly Notices of the Royal Astronomical Society, 433, 457

Burrows, A., Hubbard, W. B., Lunine, J. I., & Liebert, J. 2001, Reviews of Modern Physics, 73, 719

Burrows, A., Marley, M., Hubbard, W. B., et al. 1997, The Astrophysical Journal, 491, 856

Caballero, J. A. 2007, The Astrophysical Journal, 667, 520

Canty, J. I., Lucas, P. W., Roche, P. F., & Pinfield, D. J. 2013, Monthly Notices of the Royal Astronomical Society, 435, 2650

Cappetta, M., Saglia, R. P., Birkby, J. L., et al. 2012, Monthly Notices of the Royal Astronomical Society, 427, 1877

Carson, J., Thalmann, C., Janson, M., et al. 2013, The Astrophysical Journal Letters, 763, L32

Cartwright, A., & Whitworth, A. P. 2004, Monthly Notices of the Royal Astronomical Society, 348, 589

Casewell, S. L., Jameson, R. F., & Burleigh, M. R. 2008, MNRAS, 390, 1517

Castro, P. J., Gizis, J. E., Harris, H. C., et al. 2013, The Astrophysical Journal, 776, 126

Chabrier, G. 2005, The Initial Mass Function 50 years later. Edited by E. Corbelli and F. Palle, 327, 41

Chabrier, G., Baraffe, I., Allard, F., & Hauschildt, P. 2000, The Astrophysical Journal, 542, 464

Chabrier, G., Baraffe, I., Leconte, J., Gallardo, J., & Barman, T. 2009, COOL STARS, 1094, 102

Chauvin, G., Lagrange, A.-M., Dumas, C., et al. 2004, Astronomy & Astrophysics, 425, L29

Chauvin, G., Lagrange, A.-M., Zuckerman, B., et al. 2005, Astronomy & Astrophysics, 438, L29

Chauvin, G., Lowrance, P., Faherty, J. K., et al. 2012, A&A, 548, 33

Chiu, K., Fan, X., Leggett, S. K., et al. 2006, The Astronomical Journal, 131, 2722

Costa, E., Méndez, R. A., Jao, W. C., et al. 2005, The Astronomical Journal, 130, 337

—. 2006, The Astronomical Journal, 132, 1234

Crifo, F., Phan Bao, N., Delfosse, X., et al. 2005, Astronomy & Astrophysics, 441, 653

Crossfield, I. J. M., Biller, B., Schlieder, J. E., et al. 2014, Nature, 505, 654

Cruz, K. K., & Reid, N. I. 2002, AJ, 123, 2828

Cruz, K. L., Kirkpatrick, J. D., & Burgasser, A. J. 2009, The Astronomical Journal, 137, 3345

Cruz, K. L., & Núñez, A. 2012, in 17th Cambridge Workshop on Cool Stars, Stellar Systems and the Sun, Barcelona, Spain, June 24-29, 2012.

Cruz, K. L., Reid, I. N., Liebert, J., Kirkpatrick, J. D., & Lowrance, P. J. 2003, The Astronomical Journal, 126, 2421

Cruz, K. L., Reid, I. N., Kirkpatrick, J. D., et al. 2007, The Astronomical Journal, 133, 439

Currie, T., Daemgen, S., Debes, J., et al. 2014, The Astrophysical Journal Letters, 780, L30

Currie, T., Burrows, A., Itoh, Y., et al. 2011, The Astrophysical Journal, 729, 128

Cushing, M. C., Rayner, J. T., & Vacca, W. D. 2005, ApJ, 623, 1115

Cushing, M. C., Vacca, W. D., & Rayner, J. T. 2004, The Publications of the Astronomical Society of the Pacific, 116, 362

Cushing, M. C., Marley, M. S., Saumon, D., et al. 2008, The Astrophysical Journal, 678, 1372

Cushing, M. C., Kirkpatrick, J. D., Gelino, C. R., et al. 2011, The Astrophysical Journal, 743, 50

Cutri, R. M., & al, e. 2012, VizieR On-line Data Catalog, 2311, 0

da Silva, L., Torres, C. A. O., de La Reza, R., et al. 2009, Astronomy & Astrophysics, 508, 833

Dahn, C. C., Harris, H. C., Vrba, F. J., et al. 2002, The Astronomical Journal, 124, 1170

Dawson, P., Scholz, A., & Ray, T. P. 2011, MNRAS, 418, 1231

de La Reza, R., Jilinski, E., & Ortega, V. G. 2006, The Astronomical Journal, 131, 2609

de la Reza, R., Torres, C. A. O., Quast, G., Castilho, B. V., & Vieira, G. L. 1989, Astrophysical Journal, 343, L61

De Marchi, G., Paresce, F., & Portegies Zwart, S. 2010, The Astrophysical Journal, 718, 105

de Zeeuw, P. T., Hoogerwerf, R., de Bruijne, J. H. J., Brown, A. G. A., & Blaauw, A. 1999, The Astronomical Journal, 117, 354

Deacon, N. R., & Hambly, N. C. 2007, A&A, 468, 163

Deacon, N. R., Hambly, N. C., King, R. R., & McCaughrean, M. J. 2009, MNRAS, 394, 857

Deacon, N. R., Liu, M. C., Magnier, E. A., et al. 2014, The Astrophysical Journal, 792, 119

Deleuil, M., Deeg, H. J., Alonso, R., et al. 2008, Astronomy & Astrophysics, 491, 889

Deleuil, M., Bonomo, A. S., Ferraz-Mello, S., et al. 2012, Astronomy & Astrophysics, 538, A145

Delfosse, X., Donati, J. F., Kouach, D., et al. 2013, in SF2A-2013: Proceedings of the Annual meeting of the French Society of Astronomy and Astrophysics. Eds.: L. Cambresy, 497–508

D'Elia, V., Perri, M., Puccetti, S., et al. 2013, A&A, 551, 142

Delorme, P., Delfosse, X., Albert, L., et al. 2008a, Astronomy & Astrophysics, 482, 961

Delorme, P., Willott, C. J., Forveille, T., et al. 2008b, Astronomy & Astrophysics, 484, 469

Delorme, P., Albert, L., Forveille, T., et al. 2010, Astronomy & Astrophysics, 518, A39

Delorme, P., Gagné, J., Malo, L., et al. 2012, Astronomy & Astrophysics, 548, A26

Delorme, P., Gagné, J., Girard, J. H., et al. 2013, Astronomy & Astrophysics, 553, L5

Deshpande, R., Martín, E. L., Montgomery, M. M., et al. 2012, The Astronomical Journal, 144, 99

Dhital, S., Burgasser, A. J., Looper, D. L., & Stassun, K. G. 2011, AJ, 141, 7

Díaz, R. F., Damiani, C., Deleuil, M., et al. 2013, Astronomy & Astrophysics, 551, L9

Díaz, R. F., Montagnier, G., Leconte, J., et al. 2014, Astronomy & Astrophysics, 572, A109

Dieterich, S. B., Henry, T. J., Jao, W.-C., et al. 2014, The Astronomical Journal, 147, 94

Dittmann, J. A., Irwin, J. M., Charbonneau, D., & Berta-Thompson, Z. K. 2014, The Astrophysical Journal, 784, 156

Ducourant, C., Teixeira, R., Chauvin, G., et al. 2008, A&A, 477, L1

Ducourant, C., Teixeira, R., Galli, P. A. B., et al. 2014, Astronomy & Astrophysics, 563, A121

Dupuy, T. J., & Liu, M. C. 2012, The Astrophysical Journal Supplement, 201, 19

Dupuy, T. J., Liu, M. C., & Bowler, B. P. 2009a, The Astrophysical Journal, 706, 328

Dupuy, T. J., Liu, M. C., Bowler, B. P., et al. 2010, The Astrophysical Journal, 721, 1725

Dupuy, T. J., Liu, M. C., & Ireland, M. J. 2009b, The Astrophysical Journal, 692, 729

—. 2009c, The Astrophysical Journal, 699, 168

—. 2014, The Astrophysical Journal, 790, 133

Dupuy, T. J., Liu, M. C., Leggett, S. K., et al. 2015, arXiv.org, 6212

Eggen, O. J. 1958, Monthly Notices of the Royal Astronomical Society, 118, 65

—. 1991, Astronomical Journal (ISSN 0004-6256), 102, 2028

Eikenberry, S. S., Elston, R., Raines, S. N., et al. 2004, in Ground-based Instrumentation for Astronomy. Edited by Alan F. M. Moorwood and Iye Masanori. Proceedings of the SPIE, ed. A. F. M. Moorwood & M. Iye, University of Florida, USA (SPIE), 1196–1207

Eisenbeiss, T., Ammler-von Eiff, M., Roell, T., et al. 2013, Astronomy & Astrophysics, 556, A53

Elias, J. H. 1978, Astrophysical Journal, 224, 857

Epchtein, N. 1998, New Horizons from Multi-Wavelength Sky Surveys, 179, 106

Faherty, J. K., Burgasser, A. J., Bochanski, J. J., et al. 2011, The Astronomical Journal, 141, 71

Faherty, J. K., Burgasser, A. J., Cruz, K. L., et al. 2009, The Astronomical Journal, 137, 1

Faherty, J. K., Cruz, K. K., Rice, E., & Riedel, A. R. 2013a, Protostars and Planets VI

Faherty, J. K., Rice, E. L., Cruz, K. L., Mamajek, E. E., & Núñez, A. 2013b, The Astronomical Journal, 145, 2

Faherty, J. K., Burgasser, A. J., Walter, F. M., et al. 2012, The Astrophysical Journal, 752, 56

Famaey, B., Jorissen, A., Luri, X., et al. 2005, Astronomy & Astrophysics, 430, 165

Famaey, B., Siebert, A., & Jorissen, A. 2008, Astronomy & Astrophysics, 483, 453

Fitzpatrick, E. L. 1999, The Publications of the Astronomical Society of the Pacific, 111, 63

Forveille, T., Beuzit, J.-L., Delorme, P., et al. 2005, A&A, 435, L5

Fuhrmann, K. 2004, Astronomische Nachrichten, 325, 3

Gagné, J., Faherty, J. K., Cruz, K. L., et al. 2014a, The Astrophysical Journal Letters, 785, L14

Gagné, J., Lafrenière, D., Doyon, R., et al. 2014b, The Astrophysical Journal Letters, 792, L17

Gagné, J., Lafrenière, D., Doyon, R., Malo, L., & Artigau, É. 2014c, The Astrophysical Journal, 783, 121

—. 2015, The Astrophysical Journal, 798, 73

Gagné, J., Lafrenière, D., Doyon, R., et al. 2013, Memorie della Societa Astronomica Italiana, 84, 916

Gaidos, E. J. 1998, The Publications of the Astronomical Society of the Pacific, 110, 1259

Gálvez-Ortiz, M. C., Clarke, J. R. A., Pinfield, D. J., et al. 2010, Monthly Notices of the Royal Astronomical Society, 409, 552

—. 2011, Research, 16, 03007

Gálvez-Ortiz, M. C., Kuznetsov, M., Clarke, J. R. A., et al. 2014, Monthly Notices of the Royal Astronomical Society, 439, 3890

Gardner, J. P., Mather, J. C., Clampin, M., et al. 2006, Space Science Reviews, 123, 485

Gatewood, G., & Coban, L. 2009, AJ, 137, 402

Gatley, I., Becklin, E. E., Mattews, K., et al. 1974, Astrophysical Journal, 191, L121

Geballe, T. R., Knapp, G. R., Leggett, S. K., et al. 2002, The Astrophysical Journal, 564, 466

Geißler, K., Metchev, S., Kirkpatrick, J. D., Berriman, G. B., & Looper, D. 2011, The Astrophysical Journal, 732, 56

Geissler, K., Metchev, S., Kirkpatrick, J. D., Berriman, G. B., & Looper, D. 2011, 448, 1351

Gilmozzi, R., & Spyromilio, J. 2008, Ground-based and Airborne Telescopes II. Edited by Stepp, 7012, 701219

Gizis, J. E. 2002, The Astrophysical Journal, 575, 484

Gizis, J. E., Allers, K. N., Liu, M. C., et al. 2015, The Astrophysical Journal, 799, 203

Gizis, J. E., Hawley, S. L., & Reid, N. I. 1997, Astronomical Journal v.113, 113, 1458

Gizis, J. E., Monet, D. G., Reid, I. N., et al. 2000, The Astronomical Journal, 120, 1085

Gizis, J. E., Reid, I. N., Knapp, G. R., et al. 2003, The Astronomical Journal, 125, 3302

Gizis, J. E., & Reid, N. I. 2005, PASP, 117, 676

Gizis, J. E., Faherty, J. K., Liu, M. C., et al. 2012, The Astronomical Journal, 144, 94

Glebocki, R., & Gnacinski, P. 2005, VizieR On-line Data Catalog, 3244, 0

Gliese, W., & Jahreiß, H. 1991, Preliminary Version of the Third Catalogue of Nearby Stars, Tech. rep.

Glover, S. C. O., & Mac Low, M.-M. 2007, The Astrophysical Journal, 659, 1317

Goldman, B., Marsat, S., Henning, T., Clemens, C., & Greiner, J. 2010, Monthly Notices of the Royal Astronomical Society, 405, 1140

Golimowski, D. A., Leggett, S. K., Marley, M. S., et al. 2004, The Astronomical Journal, 127, 3516

Gorlova, N. I., Meyer, M. R., Rieke, G. H., & Liebert, J. 2003, The Astrophysical Journal, 593, 1074

Goto, M., Kobayashi, N., Terada, H., et al. 2002, The Astrophysical Journal, 567, L59

Gould, A., & Chanamé, J. 2004, The Astrophysical Journal Supplement Series, 150, 455

Groom, S., Howell, J. H., & Teplitz, H. I. 2010, AAS, 215, 393

Guenther, E. W., & Wuchterl, G. 2003, A&A, 401, 677

Hambly, N. C., MacGillivray, H. T., Read, M. A., et al. 2001, MNRAS, 326, 1279

Hand, D. J., & Yu, K. 2001, Int Statistical Rev, 69, 385

Hasan, P., & Hasan, S. N. 2011, Monthly Notices of the Royal Astronomical Society, 413, 2345

Hawley, S. L., Covey, K. R., Knapp, G. R., et al. 2002, The Astronomical Journal, 123, 3409

Hearty, T., Magnani, L., Caillault, J. P., et al. 1999, A&A, 341, 163

Hébrard, G., Almenara, J. M., Santerne, A., et al. 2013, Astronomy & Astrophysics, 554, A114

Henry, T. J. 1991, Ph.D. Thesis Arizona Univ., 11

Henry, T. J., Jao, W.-C., Subasavage, J. P., et al. 2006, The Astronomical Journal, 132, 2360

Herter, T. L., Henderson, C. P., Wilson, J. C., et al. 2008, Ground-based and Airborne Instrumentation for Astronomy II. Edited by McLean, 7014, 70140X

Hinkley, S., Pueyo, L., Faherty, J. K., et al. 2013, The Astrophysical Journal, 779, 153

Høg, E., Fabricius, C., Makarov, V. V., et al. 2000, A&A, 355, L27

Horne, K. 1986, Astronomical Society of the Pacific, 98, 609

Huff, E. M., & Stahler, S. W. 2006, The Astrophysical Journal, 644, 355

Irwin, J. M., Quinn, S. N., Berta, Z. K., et al. 2011, The Astrophysical Journal, 742, 123

Jameson, R. F., Casewell, S. L., Bannister, N. P., et al. 2008, MNRAS, 384, 1399

Janson, M., Carson, J., Thalmann, C., et al. 2011, The Astrophysical Journal, 728, 85

Janson, M., Hormuth, F., Bergfors, C., et al. 2012, ApJ, 754, 44

Jao, W.-C., Henry, T. J., Subasavage, J. P., et al. 2003, AJ, 125, 332

Jappsen, A. K., Klessen, R. S., Larson, R. B., Li, Y., & Mac Low, M. M. 2005, Astronomy & Astrophysics, 435, 611

Jeffries, R. D. 2012, Low-Mass Stars and the Transition Stars/Brown Dwarfs - EES2011, 57, 45

Jeffries, R. D., Naylor, T., Mayne, N. J., Bell, C. P. M., & Littlefair, S. P. 2013, Monthly Notices of the Royal Astronomical Society, 434, 2438

Jenkins, J. S., Ramsey, L. W., Jones, H. R. A., et al. 2009, ApJ, 704, 975

Jilinski, E., Ortega, V. G., & de La Reza, R. 2005, The Astrophysical Journal, 619, 945

Jilinski, E., Ortega, V. G., de La Reza, R., Drake, N. A., & Bazzanella, B. 2009, The Astrophysical Journal, 691, 212

Johns, M., Hull, C., Muller, G., et al. 2014, in Proceedings of the SPIE, ed. L. M. Stepp, R. Gilmozzi, & H. J. Hall, The Giant Magellan Telescope Project Corp. (United States) (SPIE), 91451F

Johnson, D. R. H., & Soderblom, D. R. 1987, Astronomical Journal (ISSN 0004-6256), 93, 864

Johnson, H. L., & Knuckles, C. F. 1955, Astrophysical Journal, 122, 209

Joyce, R. R., Hinkle, K. H., Wallace, L., Dulick, M., & Lambert, D. L. 1998, The Astronomical Journal, 116, 2520

Kastner, J. H., Zuckerman, B., Weintraub, D. A., & Forveille, T. 1997, Science, 277, 67

Kendall, T. R., Delfosse, X., Martín, E. L., & Forveille, T. 2004, Astronomy & Astrophysics, 416, L17

Kendall, T. R., Jones, H. R. A., Pinfield, D. J., et al. 2007a, Monthly Notices of the Royal Astronomical Society, 374, 445

Kendall, T. R., Tamura, M., Tinney, C. G., et al. 2007b, Astronomy & Astrophysics, 466, 1059

Kharchenko, N. V., Scholz, R. D., Piskunov, A. E., Roeser, S., & Schilbach, E. 2007, VizieR On-line Data Catalog, 3254, 0

Khovritchev, M. Y., Izmailov, I. S., & Khrutskaya, E. V. 2013, MNRAS, 435, 1083

King, J. R., Villarreal, A. R., Soderblom, D. R., Gulliver, A. F., & Adelman, S. J. 2003, The Astronomical Journal, 125, 1980

Kirkpatrick, D. J., Cutri, R. M., Skrutskie, M. F., et al. 2003, VizieR On-line Data Catalog: II/246. Originally published in: University of Massachusetts and Infrared Processing and Analysis Center, 2246, 0

Kirkpatrick, J. D. 2005, Annual Review of Astronomy & Astrophysics, 43, 195

Kirkpatrick, J. D., Barman, T. S., Burgasser, A. J., et al. 2006, The Astrophysical Journal, 639, 1120

Kirkpatrick, J. D., Henry, T. J., & McCarthy, D. W. J. 1991, Astrophysical Journal Supplement Series (ISSN 0067-0049), 77, 417

Kirkpatrick, J. D., Reid, I. N., Liebert, J., et al. 1999, The Astrophysical Journal, 519, 802

—. 2000, The Astronomical Journal, 120, 447

Kirkpatrick, J. D., Cruz, K. L., Barman, T. S., et al. 2008, The Astrophysical Journal, 689, 1295

Kirkpatrick, J. D., Looper, D. L., Burgasser, A. J., et al. 2010, The Astrophysical Journal Supplement, 190, 100

Kirkpatrick, J. D., Cushing, M. C., Gelino, C. R., et al. 2011, The Astrophysical Journal Supplement, 197, 19

Kirkpatrick, J. D., Gelino, C. R., Cushing, M. C., et al. 2012, The Astrophysical Journal, 753, 156

Kirkpatrick, J. D., Schneider, A., Fajardo-Acosta, S., et al. 2014, The Astrophysical Journal, 783, 122

Kiss, L. L., Moór, A., Szalai, T., et al. 2011, Monthly Notices of the Royal Astronomical Society, 411, 117

Kleinmann, S. G., & Hall, D. N. B. 1986, Astrophysical Journal Supplement Series (ISSN 0067-0049), 62, 501

Klutsch, A., Freire Ferrero, R., Guillout, P., et al. 2014, Astronomy & Astrophysics, 567, A52

Knapp, G. R., Leggett, S. K., Fan, X., et al. 2004, The Astronomical Journal, 127, 3553

Konopacky, Q. M., Ghez, A. M., Barman, T. S., et al. 2010, The Astrophysical Journal, 711, 1087

Kordopatis, G., Gilmore, G., Steinmetz, M., et al. 2013, The Astronomical Journal, 146, 134

Krabbendam, V., Gressler, W., Andrew, J. R., et al. 2012, American Astronomical Society, 219

Kraus, A. L., Ireland, M. J., Cieza, L. A., et al. 2014a, The Astrophysical Journal, 781, 20

Kraus, A. L., Shkolnik, E. L., Allers, K. N., & Liu, M. C. 2014b, The Astronomical Journal, 147, 146

Kuzuhara, M., Tamura, M., Kudo, T., et al. 2013, The Astrophysical Journal, 774, 11

Lafrenière, D., Jayawardhana, R., & van Kerkwijk, M. H. 2008, The Astrophysical Journal, 689, L153

—. 2010, ApJ, 719, 497

Lagrange, A.-M., Gratadour, D., Chauvin, G., et al. 2009, A&A, 493, L21

Lagrange, A.-M., Bonnefoy, M., Chauvin, G., et al. 2010, Science, 329, 57

Lane, B. F., Zapatero Osorio, M. R., Britton, M. C., Martín, E. L., & Kulkarni, S. R. 2001, The Astrophysical Journal, 560, 390

Lane, R. R., Kiss, L. L., Lewis, G. F., et al. 2011, A&A, 530, 31

Larson, S., Brownlee, J., Hergenrother, C., & Spahr, T. 1998, AAS, 30, 1037

Lasker, B. M., Lattanzi, M. G., McLean, B. J., et al. 2008, AJ, 136, 735

Law, N. M., Hodgkin, S. T., & Mackay, C. D. 2008, MNRAS, 384, 150

Lawson, W. A., Crause, L. A., Mamajek, E. E., & Feigelson, E. D. 2001, Monthly Notices of the Royal Astronomical Society, 321, 57

Lee, K.-G., Berger, E., & Knapp, G. R. 2010, ApJ, 708, 1482

Leggett, S. K., Allard, F., Geballe, T. R., Hauschildt, P. H., & Schweitzer, A. 2001, The Astrophysical Journal, 548, 908

Leggett, S. K., Morley, C. V., Marley, M. S., & Saumon, D. 2015, The Astrophysical Journal, 799, 37

Leggett, S. K., Morley, C. V., Marley, M. S., et al. 2013, The Astrophysical Journal, 763, 130

Leggett, S. K., Saumon, D., Burningham, B., et al. 2010, The Astrophysical Journal, 720, 252

Leggett, S. K., Geballe, T. R., Fan, X., et al. 2000, The Astrophysical Journal, 536, L35

Leggett, S. K., Golimowski, D. A., Fan, X., et al. 2002, The Astrophysical Journal, 564, 452

Leggett, S. K., Currie, M. J., Varricatt, W. P., et al. 2006, Monthly Notices of the Royal Astronomical Society, 373, 781

Leggett, S. K., Cushing, M. C., Saumon, D., et al. 2009, The Astrophysical Journal, 695, 1517

Lépine, S. 2005, AJ, 130, 1680

Lépine, S., & Bongiorno, B. 2007, AJ, 133, 889

Lépine, S., & Simon, M. 2009, The Astronomical Journal, 137, 3632

Lépine, S., Thorstensen, J. R., Shara, M. M., & Rich, R. M. 2009, AJ, 137, 4109

Liebert, J., & Gizis, J. E. 2006, The Publications of the Astronomical Society of the Pacific, 118, 659

Littlefair, S. P., Casewell, S. L., Parsons, S. G., et al. 2014, Monthly Notices of the Royal Astronomical Society, 445, 2106

Liu, M. C., Dupuy, T. J., & Allers, K. N. 2013a, Astronomische Nachrichten, 334, 85

Liu, M. C., Dupuy, T. J., & Ireland, M. J. 2008, ApJ, 689, 436

Liu, M. C., Dupuy, T. J., & Leggett, S. K. 2010, ApJ, 722, 311

Liu, M. C., & Leggett, S. K. 2005, The Astrophysical Journal, 634, 616

Liu, M. C., Magnier, E. A., Deacon, N. R., et al. 2013b, The Astrophysical Journal Letters, 777, L20

Lodieu, N., Dobbie, P. D., & Hambly, N. C. 2011, A&A, 527, 24

Lodieu, N., Hambly, N. C., Jameson, R. F., & Hodgkin, S. T. 2008, Monthly Notices of the Royal Astronomical Society, 383, 1385

Lodieu, N., Scholz, R. D., McCaughrean, M. J., et al. 2005, Astronomy & Astrophysics, 440, 1061

Lodieu, N., Pinfield, D. J., Leggett, S. K., et al. 2007, Monthly Notices of the Royal Astronomical Society, 379, 1423

Looper, D. L., Bochanski, J. J., Burgasser, A. J., et al. 2010a, AJ, 140, 1486

Looper, D. L., Burgasser, A. J., Kirkpatrick, J. D., & Swift, B. J. 2007a, The Astrophysical Journal, 669, L97

Looper, D. L., Gelino, C. R., Burgasser, A. J., & Kirkpatrick, J. D. 2008a, The Astrophysical Journal, 685, 1183

Looper, D. L., Kirkpatrick, J. D., & Burgasser, A. J. 2007b, The Astronomical Journal, 134, 1162

Looper, D. L., Kirkpatrick, J. D., Cutri, R. M., et al. 2008b, The Astrophysical Journal, 686, 528

Looper, D. L., Mohanty, S., Bochanski, J. J., et al. 2010b, ApJ, 714, 45

López-Santiago, J., Montes, D., Crespo-Chacón, I., & Fernández-Figueroa, M. J. 2006, The Astrophysical Journal, 643, 1160

Low, C., & Lynden-Bell, D. 1976, Monthly Notices of the Royal Astronomical Society, 176, 367

Lucas, P. W., Roche, P. F., Allard, F., & Hauschildt, P. H. 2001, Monthly Notices of the Royal Astronomical Society, 326, 695

Lucas, P. W., Tinney, C. G., Burningham, B., et al. 2010, Monthly Notices of the Royal Astronomical Society: Letters, 408, L56

Luhman, K. L. 2004, ApJ, 617, 1216

—. 2007, The Astrophysical Journal Supplement Series, 173, 104

—. 2014, The Astrophysical Journal Letters, 786, L18

Luhman, K. L., Liebert, J., & Rieke, G. H. 1997, Astrophysical Journal Letters v.489, 489, L165

Luhman, K. L., Mamajek, E. E., Allen, P. R., & Cruz, K. L. 2009, The Astrophysical Journal, 703, 399

Luhman, K. L., Stauffer, J. R., & Mamajek, E. E. 2005, The Astrophysical Journal, 628, L69

Luhman, K. L., Patten, B. M., Marengo, M., et al. 2007, The Astrophysical Journal, 654, 570

Lutz, T. E., & Kelker, D. H. 1973, Publications of the Astronomical Society of the Pacific, 85, 573

Luyten, W. J. 1941, Annals of the New York Academy of Sciences, 42, 201

—. 1977, Proper motion survey with the 48-inch Schmidt telescope. LI. Hertzsprung diagrams for one hundred and fifteen thousand proper motion stars., 51, 1

Mace, G. N. 2014, ProQuest Dissertations And Theses; Thesis (Ph.D.)–University of California, 56

Mace, G. N., Kirkpatrick, J. D., Cushing, M. C., et al. 2013a, The Astrophysical Journal Supplement, 205, 6

—. 2013b, The Astrophysical Journal, 777, 36

Mahabal, A., Djorgovski, S. G., Turmon, M., et al. 2008, Astron. Nachr., 329, 288

Mainzer, A., Grav, T., Bauer, J., et al. 2011, The Astrophysical Journal, 743, 156

Makarov, V. V. 2007, ApJ, 658, 480

Makarov, V. V., & Urban, S. 2000, MNRAS, 317, 289

Makarov, V. V., Zacharias, N., Hennessy, G. S., Harris, H. C., & Monet, A. K. B. 2007, ApJ, 668, L155

Males, J. R., Close, L. M., Morzinski, K. M., et al. 2014, The Astrophysical Journal, 786, 32

Malmquist, K. G. 1936, Stockholms Observatoriums Annaler, 12, 7

Malo, L., Artigau, É., Doyon, R., et al. 2014a, The Astrophysical Journal, 788, 81

Malo, L., Doyon, R., Feiden, G. A., et al. 2014b, The Astrophysical Journal, 792, 37

Malo, L., Doyon, R., Lafrenière, D., et al. 2013, The Astrophysical Journal, 762, 88

Mamajek, E. E. 2005, The Astrophysical Journal, 634, 1385

—. 2006, The Astronomical Journal, 132, 2198

—. 2010, American Astronomical Society, 215, 473

—. 2012, ApJL, 754, L20

Mamajek, E. E., & Bell, C. P. M. 2014, Monthly Notices of the Royal Astronomical Society, 445, 2169

Mamajek, E. E., Bartlett, J. L., Seifahrt, A., et al. 2013, The Astronomical Journal, 146, 154

Manjavacas, E., Bonnefoy, M., Schlieder, J. E., et al. 2014, Astronomy & Astrophysics, 564, A55

Mann, A. W., Brewer, J. M., Gaidos, E., Lépine, S., & Hilton, E. J. 2013a, Astronomische Nachrichten, 334, 18

—. 2013b, AJ, 145, 52

Mann, A. W., Deacon, N. R., Gaidos, E., et al. 2014, AJ, 147, 160

Marleau, G. D., & Cumming, A. 2014, Monthly Notices of the Royal Astronomical Society, 437, 1378

Marley, M. S., Seager, S., Saumon, D., et al. 2002, The Astrophysical Journal, 568, 335

Marocco, F., Smart, R. L., Jones, H. R. A., et al. 2010, Astronomy & Astrophysics, 524, A38

Marocco, F., Andrei, A. H., Smart, R. L., et al. 2013, The Astronomical Journal, 146, 161

Marocco, F., Day-Jones, A. C., Lucas, P. W., et al. 2014, Monthly Notices of the Royal Astronomical Society, 439, 372

Marocco, F., Jones, H. R. A., Day-Jones, A. C., et al. 2015, Monthly Notices of the Royal Astronomical Society, 449, 3651

Marois, C., Macintosh, B., Barman, T., et al. 2008, Science, 322, 1348

Marsh, K. A., Wright, E. L., Kirkpatrick, J. D., et al. 2013, The Astrophysical Journal, 762, 119

Martin, D. C., Fanson, J., Schiminovich, D., et al. 2005, ApJ, 619, L1

Martín, E. L., Delfosse, X., Basri, G., et al. 1999, The Astronomical Journal, 118, 2466

Martín, E. L., Rebolo, R., & Zapatero Osorio, M. R. 1996, Astrophysical Journal v.469, 469, 706

Martín, E. L., Phan Bao, N., Bessell, M., et al. 2010, Astronomy & Astrophysics, 517, A53

Mason, B. D., Wycoff, G. L., Hartkopf, W. I., Douglass, G. G., & Worley, C. E. 2001, AJ, 122, 3466

McGovern, M. R., Kirkpatrick, D. J., McLean, I. S., et al. 2004, ApJ, 600, 1020

McLean, I. S., McGovern, M. R., Burgasser, A. J., et al. 2003, The Astrophysical Journal, 596, 561

McLean, M., Berger, E., & Reiners, A. 2012, The Astrophysical Journal, 746, 23

Messina, S., Desidera, S., Lanzafame, A. C., Turatto, M., & Guinan, E. F. 2011, Astronomy & Astrophysics, 532, A10

Metchev, S. A., & Hillenbrand, L. A. 2006, The Astrophysical Journal, 651, 1166

Metchev, S. A., Kirkpatrick, J. D., Berriman, G. B., & Looper, D. 2008, The Astrophysical Journal, 676, 1281

Miller, G. E., & Scalo, J. M. 1979, and J. M. Scalo. Astrophysical Journal Supplement Series, 41, 513

Monet, D. 1998, USNO-A2.0, by Monet, David.~ [Flagstaff, AZ] : U.S.~Naval Observatory, c1998.~.~United States Naval Observatory. (Flagstaff, AZ: USNO-A2.0)

Monet, D. G., Dahn, C. C., Vrba, F. J., et al. 1992, Astronomical Journal (ISSN 0004-6256), 103, 638

Monet, D. G., Levine, S. E., Canzian, B., et al. 2003, AJ, 125, 984

Monnier, J. D., Che, X., Zhao, M., et al. 2012, ApJL, 761, L3

Montes, D., López-Santiago, J., Gálvez, M. C., et al. 2001, Monthly Notices of the Royal Astronomical Society, 328, 45

Montet, B. T., Johnson, J. A., Muirhead, P. S., et al. 2014, arXiv.org, 4047

Moór, A., Szabó, G. M., Kiss, L. L., et al. 2013, Monthly Notices of the Royal Astronomical Society, 435, 1376

Moraux, E., Bouvier, J., Stauffer, J. R., & Cuillandre, J. C. 2003, Astronomy & Astrophysics, 400, 891

Morgan, W. W., Keenan, P. C., & Kellman, E. 1943, Chicago, -1

Morley, C. V., Fortney, J. J., Marley, M. S., et al. 2012, ApJ, 756, 172

Moutou, C., Bonomo, A. S., Bruno, G., et al. 2013, Astronomy & Astrophysics, 558, L6

Murphy, S. J., & Lawson, W. A. 2015, Monthly Notices of the Royal Astronomical Society, 447, 1267

Naud, M.-È., Artigau, É., Malo, L., et al. 2014, The Astrophysical Journal, 787, 5

Nelson, J., & Sanders, G. H. 2008, Ground-based and Airborne Telescopes II. Edited by Stepp, 7012, 70121A

Newton, E. R., Charbonneau, D., Irwin, J., et al. 2014, AJ, 147, 20

Newton, E. R., Irwin, J., Charbonneau, D., et al. 2012, American Astronomical Society, 219

Nidever, D. L., Marcy, G. W., Butler, R. P., Fischer, D. A., & Vogt, S. S. 2002, The Astrophysical Journal Supplement Series, 141, 503

Norlén, G. 1973, Physica Scripta, 8, 249

Norman, C., Ptak, A., Hornschemeier, A., et al. 2004, ApJ, 607, 721

Ochsenbein, F., Bauer, P., & Marcout, J. 2000, A&AS, 143, 23

Olczak, C., Spurzem, R., & Henning, T. 2011, Astronomy & Astrophysics, 532, A119

Opitz, D., & Gallardo, J. 2011, Boletín de la Asociación Argentina de Astronomía, 54, 93

Ortega, V. G., de La Reza, R., Jilinski, E., & Bazzanella, B. 2002, The Astrophysical Journal, 575, L75

Ortega, V. G., Jilinski, E., de La Reza, R., & Bazzanella, B. 2007, Monthly Notices of the Royal Astronomical Society, 377, 441

Pang, X., Grebel, E. K., Allison, R. J., et al. 2013, The Astrophysical Journal, 764, 73

Parviainen, H., Gandolfi, D., Deleuil, M., et al. 2014, Astronomy & Astrophysics, 562, A140

Pecaut, M. J., & Mamajek, E. E. 2013, The Astrophysical Journal Supplement, 208, 9

Pecaut, M. J., Mamajek, E. E., & Bubar, E. J. 2012, The Astrophysical Journal, 746, 154

Pérez-Garrido, A., Lodieu, N., Béjar, V. J. S., et al. 2014, Astronomy & Astrophysics, 567, A6

Perryman, M. A. C., Lindegren, L., Kovalevsky, J., et al. 1997, Astronomy and Astrophysics 323, 323, L49

Perryman, M. A. C., de Boer, K. S., Gilmore, G., et al. 2001, Astronomy & Astrophysics, 369, 339

Phan-Bao, N. 2011, Astron. Nachr., 332, 668

Phan-Bao, N., & Bessell, M. S. 2006, A&A, 446, 515

Phan-Bao, N., Guibert, J., Crifo, F., et al. 2001, A&A, 380, 590

Phan Bao, N., Bessell, M. S., Martín, E. L., et al. 2008, Monthly Notices of the Royal Astronomical Society, 383, 831

Picaud, S., Robin, A. C., & Bastian, U. 2005, in "Proceedings of the Gaia Symposium "The Three-Dimensional Universe with Gaia" (ESA SP-576). Held at the Observatoire de Paris-Meudon, 467

Pinfield, D. J., Burningham, B., Tamura, M., et al. 2008, Monthly Notices of the Royal Astronomical Society, 390, 304

Pinsonneault, M. H. 2010, Light Elements in the Universe, 268, 375

Ptak, A. 2007, Statistical Challenges in Modern Astronomy IV ASP Conference Series, 371, 429

Quinn, S. N., White, T. R., Latham, D. W., et al. 2014, arXiv.org, 4666

Rajpurohit, A. S., Reylé, C., Allard, F., et al. 2013, A&A, 556, 15

Rameau, J., Chauvin, G., Lagrange, A.-M., et al. 2013, The Astrophysical Journal Letters, 779, L26

Rayner, J. T., Toomey, D. W., Onaka, P. M., et al. 2003, PASP, 115, 362

Reid, I. N., Cruz, K. L., Kirkpatrick, J. D., et al. 2008a, The Astronomical Journal, 136, 1290

Reid, I. N., Lewitus, E., Allen, P. R., Cruz, K. L., & Burgasser, A. J. 2006, The Astronomical Journal, 132, 891

Reid, N. I., & Cruz, K. K. 2002, AJ, 123, 2806

Reid, N. I., Cruz, K. K., & Allen, P. R. 2007, AJ, 133, 2825

Reid, N. I., Cruz, K. K., Burgasser, A. J., & Liu, M. C. 2008b, AJ, 135, 580

Reid, N. I., Gizis, J. E., Kirkpatrick, D. J., & Koerner, D. W. 2001, AJ, 121, 489

Reid, N. I., Gizis, J. E., Kirkpatrick, D. J., et al. 2002, AJ, 124, 519

Reid, N. I., Kirkpatrick, D. J., Gizis, J. E., et al. 2000, AJ, 119, 369

Reid, N. I., Cruz, K. K., Lowrance, P., et al. 2003, AJ, 126, 3007

—. 2004, AJ, 128, 463

Reiners, A. 2009, ApJL, 702, L119

Reiners, A., & Basri, G. 2009, The Astrophysical Journal, 705, 1416

—. 2010, ApJ, 710, 924

Reiners, A., Seifahrt, A., & Dreizler, S. 2010, A&A, 513, L9

Reylé, C., Scholz, R. D., Schultheis, M., Robin, A. C., & Irwin, M. 2006, MNRAS, 373, 705

Reylé, C., Delorme, P., Willott, C. J., et al. 2010, Astronomy & Astrophysics, 522, A112

Riaz, B., Gizis, J. E., & Harvin, J. 2006, AJ, 132, 866

Ribas, I. 2003, Astronomy & Astrophysics, 400, 297

Rice, E. L., Faherty, J. K., & Cruz, K. L. 2010, The Astrophysical Journal Letters, 715, L165

Rice, E. L., Faherty, J. K., Cruz, K., et al. 2011, 16th Cambridge Workshop on Cool Stars, 448, 481

Riedel, A. R. 2012a, ProQuest Dissertations And Theses; Thesis (Ph.D.)–Georgia State University, 100

—. 2012b, Young Star convergence, doi:10.6084/m9.figshare.104613

Riedel, A. R., Murphy, S. J., Henry, T. J., et al. 2011, The Astronomical Journal, 142, 104

Riedel, A. R., Finch, C. T., Henry, T. J., et al. 2014, The Astronomical Journal, 147, 85

Robin, A. C., Marshall, D. J., Schultheis, M., & Reylé, C. 2012, A&A, 538, 106

Robin, A. C., Reylé, C., Fliri, J., et al. 2014, A&A, 569, 13

Rodriguez, D. R., Bessell, M. S., Zuckerman, B., & Kastner, J. H. 2011, The Astrophysical Journal, 727, 62

Rodriguez, D. R., Zuckerman, B., Kastner, J. H., et al. 2013, The Astrophysical Journal, 774, 101

Roeser, S., Demleitner, M., & Schilbach, E. 2010, AJ, 139, 2440

Rojas-Ayala, B., Covey, K. R., Muirhead, P. S., & Lloyd, J. P. 2012, The Astrophysical Journal, 748, 93

Russek, E., Kronmal, R. A., & Fisher, L. D. 1983, Computers and Biomedical Research, 16, 537

Sahu, K. C., Casertano, S., Bond, H. E., et al. 2006, Nature, 443, 534

Salpeter, E. E. 1955, Astrophysical Journal, 121, 161

Sandage, A. 1957, Astrophysical Journal, 125, 422

Sartori, M. J., Lépine, J. R. D., & Dias, W. S. 2003, Astronomy & Astrophysics, 404, 913

Saumon, D., & Marley, M. S. 2008, The Astrophysical Journal, 689, 1327

Schlafly, E. F., & Finkbeiner, D. P. 2011, ApJ, 737, 103

Schlafly, E. F., Green, G., Finkbeiner, D. P., et al. 2014, The Astrophysical Journal, 786, 29

Schlieder, J. E., Lépine, S., & Simon, M. 2010, The Astronomical Journal, 140, 119

—. 2012a, The Astronomical Journal, 143, 80

—. 2012b, The Astronomical Journal, 144, 109

Schmidt, M. 1959, Astrophysical Journal, 129, 243

Schmidt, S. J., Cruz, K. K., Bongiorno, B. J., Liebert, J., & Reid, N. I. 2007, AJ, 133, 2258

Schmidt, S. J., Hawley, S. L., West, A. A., et al. 2015, The Astronomical Journal, 149, 158

Schmidt, S. J., West, A. A., Hawley, S. L., & Pineda, J. S. 2010, The Astronomical Journal, 139, 1808

Schneider, A., Melis, C., & Song, I. 2012a, The Astrophysical Journal, 754, 39

Schneider, A., Song, I., Melis, C., Zuckerman, B., & Bessell, M. 2012b, The Astrophysical Journal, 757, 163

Schneider, A. C., Cushing, M. C., Kirkpatrick, J. D., et al. 2014, The Astronomical Journal, 147, 34

Scholz, R. D. 2014, Astronomy & Astrophysics, 561, A113

Scholz, R. D., McCaughrean, M. J., Zinnecker, H., & Lodieu, N. 2005, A&A, 430, L49

Seifahrt, A., Reiners, A., Almaghrbi, K. A. M., & Basri, G. 2010, A&A, 512, 37

Shkolnik, E. L., Anglada-Escudé, G., Liu, M. C., et al. 2012, The Astrophysical Journal, 758, 56

Shkolnik, E. L., Liu, M. C., Reid, I. N., Dupuy, T., & Weinberger, A. J. 2011, The Astrophysical Journal, 727, 6

Shkolnik, E. L., Liu, M. C., & Reid, N. I. 2009, ApJ, 699, 649

Shporer, A., O'Rourke, J. G., Knutson, H. A., et al. 2014, The Astrophysical Journal, 788, 92

Simcoe, R. A., Burgasser, A. J., Bernstein, R. A., et al. 2008, Ground-based and Airborne Instrumentation for Astronomy II. Edited by McLean, 7014, 70140U

Simcoe, R. A., Burgasser, A. J., Schechter, P. L., et al. 2013, Publications of the Astronomical Society of the Pacific, 125, 270

Simons, D. A., & Tokunaga, A. 2002, The Publications of the Astronomical Society of the Pacific, 114, 169

Siverd, R. J., Beatty, T. G., Pepper, J., et al. 2012, The Astrophysical Journal, 761, 123

Skemer, A. J., Hinz, P. M., Esposito, S., et al. 2012, The Astrophysical Journal, 753, 14

Skrutskie, M. F., Cutri, R. M., Stiening, R., et al. 2006, The Astronomical Journal, 131, 1163

Slesnick, C. L., Hillenbrand, L. A., & Carpenter, J. M. 2004, The Astrophysical Journal, 610, 1045

Soderblom, D. R. 2010, Annual Review of Astronomy & Astrophysics, 48, 581

Soderblom, D. R., Fedele, S. B., Jones, B. F., Stauffer, J. R., & Prosser, C. F. 1993a, Astronomical Journal (ISSN 0004-6256), 106, 1080

Soderblom, D. R., Jones, B. F., Balachandran, S., et al. 1993b, Astronomical Journal (ISSN 0004-6256), 106, 1059

Soderblom, D. R., Oey, M. S., Johnson, D. R. H., & Stone, R. P. S. 1990, Astronomical Journal (ISSN 0004-6256), 99, 595

Soderblom, D. R., Pilachowski, C. A., Fedele, S. B., & Jones, B. F. 1993c, Astronomical Journal (ISSN 0004-6256), 105, 2299

Song, I., Zuckerman, B., & Bessell, M. S. 2003, The Astrophysical Journal, 599, 342

Southworth, J. 2010, Monthly Notices of the Royal Astronomical Society, 408, 1689

Spite, F., & Spite, M. 1982, Astronomy & Astrophysics, 115, 357

Stassun, K. G., Kratter, K. M., Scholz, A., & Dupuy, T. J. 2012, The Astrophysical Journal, 756, 47

Stassun, K. G., Mathieu, R. D., & Valenti, J. A. 2006, Nature, 440, 311

Stauffer, J. R., Barrado y Navascués, D., Bouvier, J., Lodieu, N., & McCaughrean, M. 2003, Brown Dwarfs in the Alpha Persei Cluster, ed. E. Martín, Vol. 211 (Astronomical Society of the Pacific, 2003: Proceedings of IAU Symposium #211)

Stephens, D. C., & Leggett, S. K. 2004, The Publications of the Astronomical Society of the Pacific, 116, 9

Stephens, D. C., Leggett, S. K., Cushing, M. C., et al. 2009, The Astrophysical Journal, 702, 154

Strauss, M. A., Fan, X., Gunn, J. E., et al. 1999, The Astrophysical Journal, 522, L61

Subasavage, J. P., Henry, T. J., Hambly, N. C., Brown, M. A., & Jao, W.-C. 2005, AJ, 129, 413

Subasavage, J. P., Jao, W.-C., Henry, T. J., et al. 2009, AJ, 137, 4547

Sumi, T., Kamiya, K., Bennett, D. P., et al. 2011, Nature, 473, 349

Tanner, A. M., Law, N. M., & Gelino, C. R. 2010, PASP, 122, 1195

Teegarden, B. J., Pravdo, S. H., Hicks, M., et al. 2003, The Astrophysical Journal, 589, L51

Teixeira, R., Ducourant, C., Chauvin, G., et al. 2009, Astronomy & Astrophysics, 503, 281

—. 2008, A&A, 489, 825

Terrien, R. C., Mahadevan, S., Bender, C. F., et al. 2012, ApJL, 747, L38

Thackrah, A., Jones, H., & Hawkins, M. 1997, MNRAS, 284, 507

Thalmann, C., Carson, J., Janson, M., et al. 2009, The Astrophysical Journal Letters, 707, L123

Thé, P. S., & Staller, R. F. A. 1974, A&A, 36, 155

Thompson, M. A., Kirkpatrick, J. D., Mace, G. N., et al. 2013, Publications of the Astronomical Society of the Pacific, 125, 809

Tingley, B., Endl, M., Gazzano, J. C., et al. 2011, Astronomy & Astrophysics, 528, A97

Tinney, C. G. 1996, MNRAS, 281, 644

—. 1998, MNRAS, 296, L42

Tinney, C. G., Burgasser, A. J., & Kirkpatrick, J. D. 2003, The Astronomical Journal, 126, 975

Tinney, C. G., Faherty, J. K., Kirkpatrick, J. D., et al. 2014, The Astrophysical Journal, 796, 39

Torres, C. A. O., da Silva, L., Quast, G. R., de La Reza, R., & Jilinski, E. 2000, AJ, 120, 1410

Torres, C. A. O., Quast, G. R., da Silva, L., et al. 2006, A&A, 460, 695

Torres, C. A. O., Quast, G. R., de La Reza, R., et al. 2003a, in Open Issues in Local Star Formation. Proceedings of the Ouro Preto Colloquium, 83

Torres, C. A. O., Quast, G. R., Melo, C. H. F., et al. 2010, Star clusters: basic galactic building blocks throughout time and space, 266, 544

Torres, C. A. O., Quast, G. R., Melo, C. H. F., & Sterzik, M. F. 2008, Handbook of Star Forming Regions, I, 757

Torres, G., Guenther, E. W., Marschall, L. A., et al. 2003b, AJ, 125, 825

Torres, R. M., Loinard, L., Mioduszewski, A. J., & Rodríguez, L. F. 2007, The Astrophysical Journal, 671, 1813

Triaud, A. H. M. J., Hebb, L., Anderson, D. R., et al. 2013, Astronomy & Astrophysics, 549, A18

Vacca, W. D., Cushing, M. C., & Rayner, J. T. 2003, The Publications of the Astronomical Society of the Pacific, 115, 389

van Altena, W. F., Lee, J. T., & Hoffleit, E. D. 1995, New Haven

van Leeuwen, F. 2007a, in ASSL, ed. F. van Leeuwen, ASSL

van Leeuwen, F. 2007b, Astronomy & Astrophysics, 474, 653

—. 2009, Astronomy & Astrophysics, 497, 209

van Rhijn, P. J. 1936, Publications of the Kapteyn Astronomical Laboratory Groningen, 47, 1

Voges, W., Aschenbach, B., Boller, T., et al. 1999, Astronomy & Astrophysics, 349, 389

—. 2000, IAU Circ., 7432, 1

Vrba, F. J., Henden, A. A., Luginbuhl, C. B., et al. 2004, AJ, 127, 2948

Wahhaj, Z., Liu, M. C., Biller, B. A., et al. 2011, The Astrophysical Journal, 729, 139

Warren, S. J., Mortlock, D. J., Leggett, S. K., et al. 2007, Monthly Notices of the Royal Astronomical Society, 381, 1400

Webb, R. A., Zuckerman, B., Platais, I., et al. 1999, ApJ, 512, L63

Weinberger, A. J., Anglada-Escudé, G., & Boss, A. P. 2013a, The Astrophysical Journal, 762, 118

Weinberger, A. J., Becklin, E. E., Zuckerman, B., & Song, I. 2004, AJ, 127, 2246

Weinberger, A. J., Boss, A. P., & Anglada-Escud, G. 2013b, AAS, 221

West, A. A., Hawley, S. L., Bochanski, J. J., et al. 2008, The Astronomical Journal, 135, 785

Whitworth, A. P., & Stamatellos, D. 2006, Astronomy & Astrophysics, 458, 817

Wilson, J. C., Miller, N. A., Gizis, J. E., et al. 2003, Brown Dwarfs, 211, 197

Wilson, R. E. 1953, Washington, 0

Winn, J. N., Holman, M. J., Torres, G., et al. 2008, The Astrophysical Journal, 683, 1076

Witte, S., Helling, C., Barman, T., Heidrich, N., & Hauschildt, P. H. 2011, Astronomy & Astrophysics, 529, A44

Wolberg, J. 2006, Data Analysis Using the Method of Least Squares, Extracting the Most Information from Experiments (Springer Science & Business Media)

Wood, D. O. S., Myers, P. C., & Daugherty, D. A. 1994, Astrophysical Journal Supplement Series (ISSN 0067-0049), 95, 457

Wright, E. L., Eisenhardt, P. R. M., Mainzer, A. K., et al. 2010, The Astronomical Journal, 140, 1868

York, D. G., Adelman, J., Anderson, J. E. J., et al. 2000, The Astronomical Journal, 120, 1579

Zacharias, N., Finch, C. T., Girard, T. M., et al. 2012, VizieR On-line Data Catalog, 1322, 0

Zacharias, N., Finch, C., Girard, T., et al. 2009, VizieR On-line Data Catalog, 1315, 0

Zapatero Osorio, M. R., Béjar, V. J. S., Miles-Páez, P. A., et al. 2014, Astronomy & Astrophysics, 568, A6

Zapatero Osorio, M. R., Martín, E. L., Bouy, H., et al. 2006, The Astrophysical Journal, 647, 1405

Zhang, H. 2004, AA

Zuckerman, B. 2001, Young Stars Near Earth: Progress and Prospects, 244, 122

Zuckerman, B., Bessell, M. S., Song, I., & Kim, S. 2006, The Astrophysical Journal, 649, L115

Zuckerman, B., Rhee, J. H., Song, I., & Bessell, M. S. 2011, The Astrophysical Journal, 732, 61

Zuckerman, B., & Song, I. 2004, Annual Review of Astronomy &Astrophysics, 42, 685

Zuckerman, B., Song, I., & Bessell, M. S. 2004, ApJ, 613, L65

Zuckerman, B., Song, I., Bessell, M. S., & Webb, R. A. 2001a, The Astrophysical Journal, 562, L87

Zuckerman, B., Song, I., & Webb, R. A. 2001b, The Astrophysical Journal, 559, 388

Zuckerman, B., Vican, L., Song, I., & Schneider, A. 2013, The Astrophysical Journal, 778, 5

Zuckerman, B., & Webb, R. A. 2000, The Astrophysical Journal, 535, 959

Zwitter, T., Siebert, A., Munari, U., et al. 2008, AJ, 136, 421